IntechOpen

# Emerging Waveguide Technology

*Edited by Kok Yeow You*

# EMERGING WAVEGUIDE TECHNOLOGY

Edited by **Kok Yeow You**

**Emerging Waveguide Technology**
http://dx.doi.org/10.5772/intechopen.71142
Edited by Kok Yeow You

**Contributors**

Yanan Xu, Matthew Tanzy, Jun Ren, Nadege Courjal, Maria-Pilar Bernal, Alexis Caspar, Florent Bassignot, Ludovic Gautier-Manuel, Gwenn Ulliac, Miguel Suarez, Patrick Steglich, Prashant Patel, Satish Hamde, Afonso José Do Prado, Luis Henrique Jus, Melissa De Oliveira Santos, Elmer Mateus Gennaro, André Alves Ferreira, Thainá Guimarães Pereira, Aghatta Cioqueta Moreira, Juliana Semiramis Menzinger, Caio Vinícius Colozzo Grilo, Marinez Cargnin Stieler, José Pissolato Filho, Trung-Thanh Le, Duy-Tien Le, Zion Menachem, Dmitry Svistunov, Jian-Chiun Liou, Young Chul Lee, Isaac Medina, Primo Calva, Sergey Sharangovich, Artem Semkin, Xianglian Song, Yuanjiang Xiang, Xiaoyu Dai, Tomislav Rajić, Muhammad Rizwan Saleem, Yogesh Tyagi, Pratik Mevada, Dmitry Usanov, Alexander Skripal, Shankar Kumar Selvaraja, Purnima Sethi



**Notice**

Statements and opinions expressed in the chapters are these of the individual contributors and not necessarily those of the editors or publisher. No responsibility is accepted for the accuracy of information contained in the published chapters. The publisher assumes no responsibility for any damage or injury to persons or property arising out of the use of any materials, instructions, methods or ideas contained in the book.

First published in London, United Kingdom, 2018 by IntechOpen
eBook (PDF) Published by IntechOpen, 2019
IntechOpen is the global imprint of INTECHOPEN LIMITED, registered in England and Wales, registration number: 11086078, The Shard, 25th floor, 32 London Bridge Street
London, SE19SG – United Kingdom
Printed in Croatia

British Library Cataloguing-in-Publication Data
A catalogue record for this book is available from the British Library

Additional hard and PDF copies can be obtained from orders@intechopen.com

Emerging Waveguide Technology
Edited by Kok Yeow You

p. cm.

Print ISBN 978-1-78923-492-3

Online ISBN 978-1-78923-493-0

eBook (PDF) ISBN 978-1-83881-516-5

# Meet the editor

Dr. You obtained his BSc Physics (Honors) degree from the Universiti Kebangsaan Malaysia (UKM) in 2001. He pursued his MSc degree in Microwave from the Faculty of Science in 2003 and his PhD degree in Wave Propagation from the Institute for Mathematical Research, Universiti Putra Malaysia (UPM), Serdang, Selangor, Malaysia, in 2006. His main personal research interest is on the theory, simulation, and instrumentation of electromagnetic wave propagation at microwave frequencies focusing on the development of microwave passive devices and sensors for medical and agricultural applications. For the past 17 years, Dr. You has been developing numerous projects concerning the microwave waveguide measurement systems for agri-food, biomedical processing and microwave devices for biomedical treatments, as well as numerical electromagnetic modeling.

# Contents

# Preface

This book is a self-contained collection of scholarly papers targeting the audience of practicing researchers, academics, postgraduate students and other scientists whose work relates to waveguide researches and waveguide technologies. This book intends to provide the readers with a comprehensive overview of the current state of the art in waveguide technologies. It is divided into three sections with a total of 19 chapters. These chapters are written by several authors: researchers, scientists and experts in specific research fields related to radio-frequency (RF)/microwave, photonic and optical engineering. The editor would like to take this opportunity to thank all the authors for their valuable contributions. In fact, each chapter provides an introduction on the specific waveguide technologies as well as a detailed explanation of the methodology on how to solve the raised issues, which include both academic and industry aspects.

The first section contains five chapters related to RF and microwave waveguide technologies. The second section consists of ten chapters that focus on photonic and optical waveguide technologies. Recently, the rapid development of waveguides has had a significant impact on the current industrial, electrical/electronic, clinical, and communication fields. The products of waveguide contributions are high-speed circuits, real-time and wireless control systems, high-quality information and communication (IC) components, low-attenuation transmission lines, nanoantennas, micro/nanoelectronic devices, and so on. In addition, waveguides are also used as biological and chemical sensory devices.

The third section includes four chapters on waveguide analytical solutions. Analytical analysis has played a very important role in the academic microwave engineering and associated industries. Engineers in the microwave field will be able to understand the operating background of waveguide devices through analytical analysis because this is the fundamental knowledge of waveguide designs before entering into further applications. Based on the analytical models, the time spent on waveguide (antennas, communication components, sensors, etc.) design and measurement setup can be shortened.

**Kok Yeow You, Editor**
Communication Engineering Department
Faculty of Electrical Engineering
Universiti Teknologi Malaysia
Malaysia

Section 1

# RF and Microwave Waveguides

Chapter 1

# Broadband Slotted Waveguide Array Antenna

Yogesh Tyagi and Pratik Mevada

Additional information is available at the end of the chapter

http://dx.doi.org/10.5772/intechopen.78308

**Abstract**

This chapter describes the design and development of broadband slotted waveguide array (SWA) antenna. Conventional SWA antenna offers a few percentages of bandwidth, which can be enhanced using proposed novel differential feeding technique which electrically divides large resonating SWA into wideband subarrays by creating virtual shorts. This chapter discusses concepts to achieve broadband nature of SWA antennas, design, development, and characterization of edge fed slotted waveguide array antenna, coupling slot fed SWA antenna, and high efficiency broadband slotted waveguide array. The developed SWA antennas are characterized and their measured results are presented. The developed prototype of proposed SWA antenna demonstrates measured return loss better than −17 dB over 7.6% bandwidth and achieves 90.2% antenna efficiency. This chapter also briefs about planar broadband SWA antenna and its prototype development and characterization.

**Keywords:** slotted waveguide array, broadband antenna, array antenna, high efficiency antenna, virtual short, coupling slot

## 1. Introduction

Slotted waveguide array (SWA) antenna technology has been utilized by many spaceborne missions such as Radarsat-1, SIR-X, ERS-1/2, and Sentinel-1, because SWA technology has several advantages like high efficiency, good mechanical strength, high power handling capacity, and manufacturing ease. However, the main drawback of this technology is narrow impedance bandwidth, which limits its applications to support high resolution SAR systems for civil and military applications. Moreover, the traveling wave type SWA provides wide bandwidth, but its efficiency is very low.

Various bandwidth improvement techniques have been explored and reported in the literature, which includes reducing waveguide wall thickness, reducing waveguide cross section, widening slot width, and modifying slot shapes, e.g., dumbbell shape and elliptical shape [1–4]. When SWA is targeted for space applications, the reduction in wall thickness may not be suitable as it has to survive severe vibration and thermal loads. When SWA is targeted for high power and low attenuation systems, the reduction in waveguide cross section shows inferior performance. Moreover, slot widening and slot shaping affect the cross-polarization performance. SWA with modified slot shapes also needs high manufacturing accuracy. Although these techniques provide bandwidth improvement, other antenna parameters are compromised due to the constraints of respective techniques.

Sub-arraying technique is widely used and considered as most effective to broaden the bandwidth of conventional SWA. In this technique, SWA is divided into subarrays [3], so that better control over variation of normalize impedance ($z$) or admittance ($y$) with frequency is achieved. Generally, coupling slots are used to feed these subarrays. Being the resonating structure, coupling slot restricts the bandwidth performance. Therefore, a novel differential feedingave technique has been presented to remove the constraints introduced by coupling slots. WR-90 (22.86 mm × 10.16 mm in cross section) waveguide has been selected and the design of broadband SWA has been carried out at 9.65 GHz center frequency. Design and demonstration of SWA with conventional feeding techniques, i.e., edge feeding and coupling slot feeding have also been discussed and compared with proposed broadband SWA design.

In this chapter, Section 2 discusses the conventional bandwidth enhancement approach and various feeding mechanisms of subarrays are followed in Section 3. Mathematical proof of the presence of virtual short created due to the proposed differential feeding technique has been discussed in Section 4. Design and simulation of 10 elements linear SWAs is outlined in Section 5. Design of linear array is extended to planar array and it is presented in Section 6. The measured results of developed prototypes are provided in Section 7 with brief discussion.

## 2. Subarray: conventional technique for bandwidth enhancement

Many techniques have been discussed in the literature to enhance the bandwidth of traditional slotted waveguide array antenna. As it has been discussed in the previous section, the use of thin wall waveguides, reduced cross sectional waveguide, wide slots, and modified slot shapes are the reported techniques to improve the bandwidth. However, these techniques are capable to improve few percent of bandwidth. Hence, they are not suitable to achieve expected wideband performance.

Fundamentally, the bandwidth enhancement can be achieved by reducing the reactive effects of the input admittance over the frequency band of interest. By proper selection of number of slot elements in the edge fed linear SWA antenna for the required bandwidth, nearly zero reactive part of input admittance can be obtained for the desired frequency band, which subsequently results in wide bandwidth performance. **Figure 1(a)** shows the case study of variation of reactive part of input admittance with frequency for different number of slots in a single

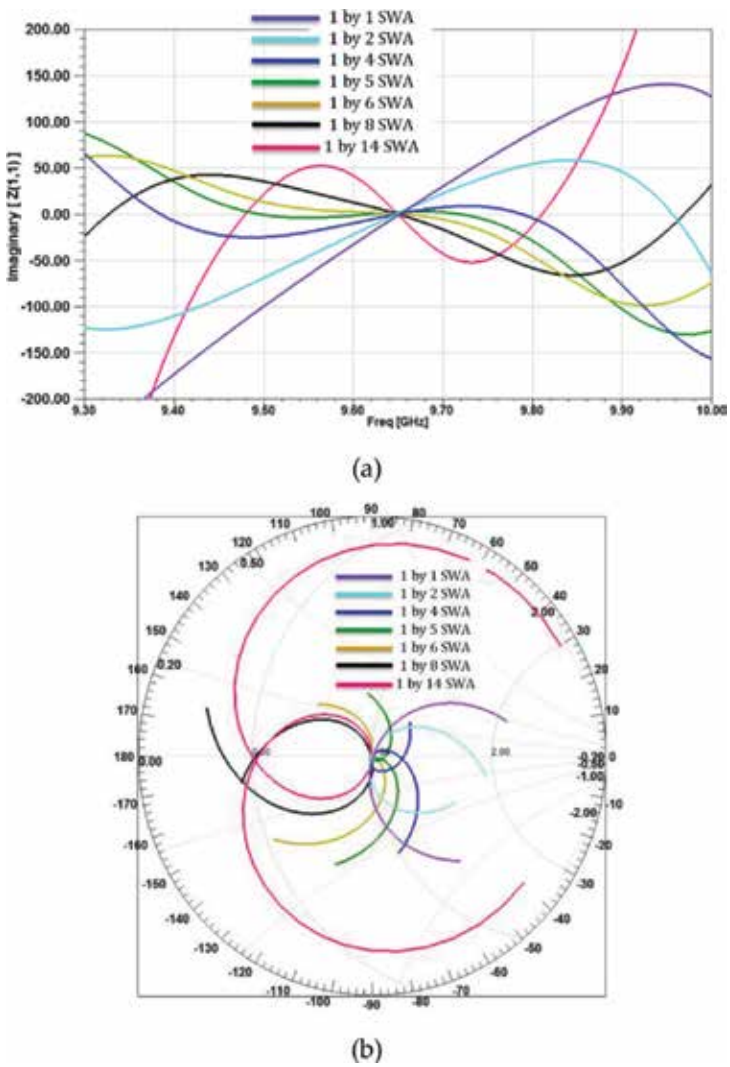


**Figure 1.** (a) Variation of reactive component of input admittance for different number of longitudinal slots and (b) variations of different number of longitudinal slots using smith chart.

branch of WR-90 waveguide. From **Figure 1(a)**, it can be observed that reactive part is very high and crosses zero at 9.65 GHz. The frequency at which zero crossing occurs is the resonance frequency of slot. When the number of slots reaches up to 6, the variation of reactive part of input admittance tends to zero over the frequency band of interest, which confirms the realizability of wideband SWA. When the number of slots is further increased, the reactive part of admittance starts to destabilize near zero and eventually provides strong resonant behavior. This phenomenon is also validated by plotting the impedance variation for different number of slots on smith chart, as shown in **Figure 1(b)**. It can be observed that varying the number of slots results in variation in impedance loop. By adjusting this impedance loop near normalized impedance of 1 by proper selection of number of slots, the antenna bandwidth can be improved.

The optimum number of radiating slots is selected by properly adjusting the size of impedance loop in smith chart. However, the bandwidth enhancement is not achieved by only size adjustment. Once the size of the impedance loop is adjusted which indicates the optimum number of radiating slots are selected, the impedance loop is moved to normalized impedance of 1 by using the impedance matching section. The impedance matching section maintains the variation of reflection coefficient below desired value, resulting in wide bandwidth performance. The discussed concept has been verified using circuit simulation in Advanced Design Studio (ADS). In this simulation, slotted waveguide array antenna having three longitudinal slots has been modeled using three parallel *RLC* network and inbuilt waveguide transmission line component. The circuit equivalent of three elements resonant SWAs is shown in **Figure 2(a)**. Here, slots are modeled as parallel *R*, *L* and *C* and they are connected by transmission line section having $Z_0$ and $\beta$ equivalent to WR-90 waveguide at 9.6 GHz. The values of *L* and *C* have been selected such that LC network resonates at center frequency of 9.6 GHz. The value of *R* has been selected to provide normalized admittance of 1 at the input of the array. The circuit schematic in ADS is shown in **Figure 2(c)**. Here, separate extra impedance matching section has been added to adjust the location of impedance loop in smith chart. The return loss plot and impedance on smith chart with/without impedance matching section are presented in **Figure 3**. It can be observed that, without matching section at the input, the circuit shows highly resonating behavior. After adding matching section, the impedance loop has been shifter around the normalized impedance of 1, which results in wider impedance bandwidth.

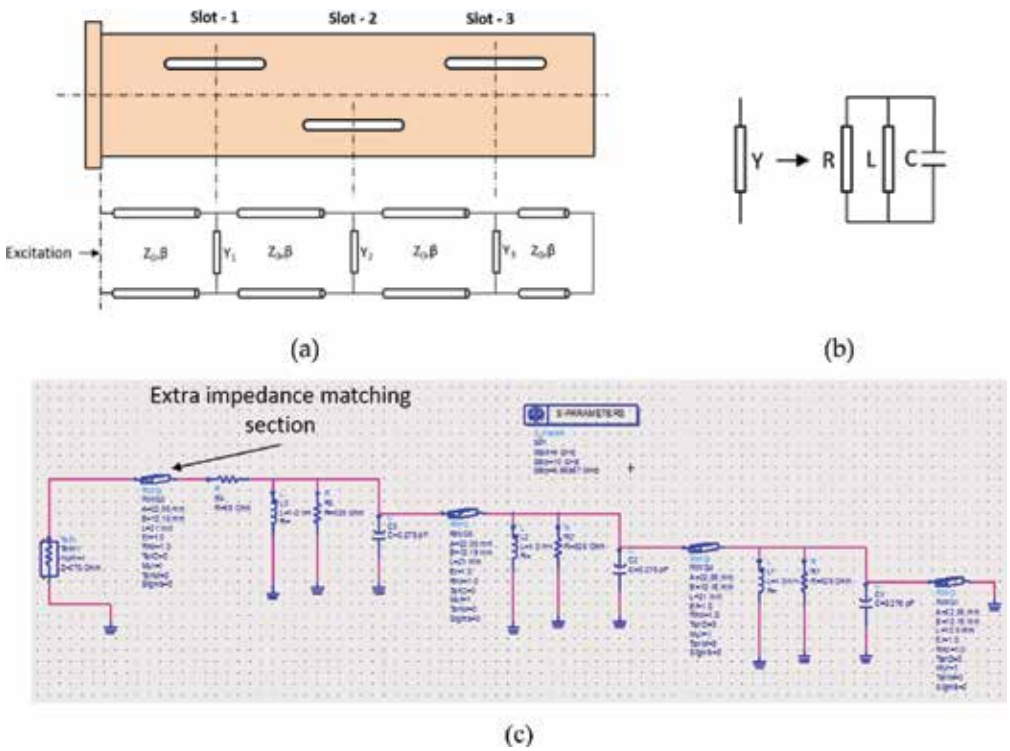


**Figure 2.** (a) Equivalent circuit representation of three elements resonant SWAs, (b) admittance modeling as parallel RLC, and (c) circuit layout of SWA in ADS.

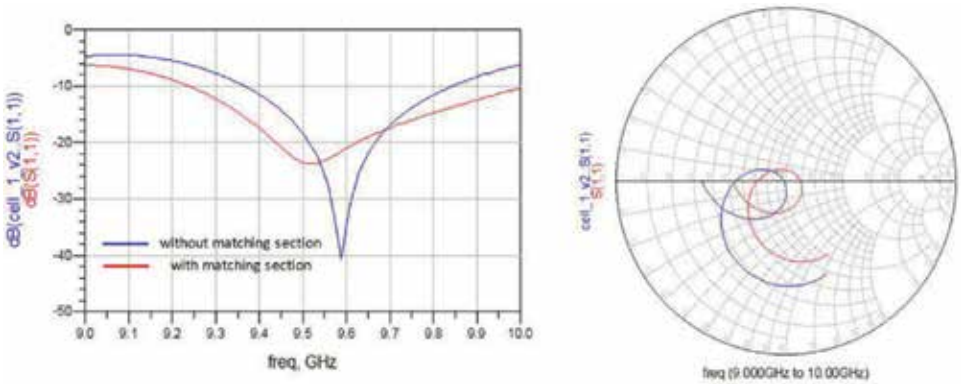


**Figure 3.** Simulation results of circuit layout.

In the case of slotted waveguide array antenna, the concept of impedance overloading of slots can be used as impedance matching technique to shift the impedance loop in smith chart, in place of adding extra impedance matching section. To validate the concept, five elements linear slotted waveguide array antenna has been designed as shown in **Figure 4(a)**. From **Figure 4(b)**, it can be observed that the selection of five radiating slots for the array provides optimum bandwidth.

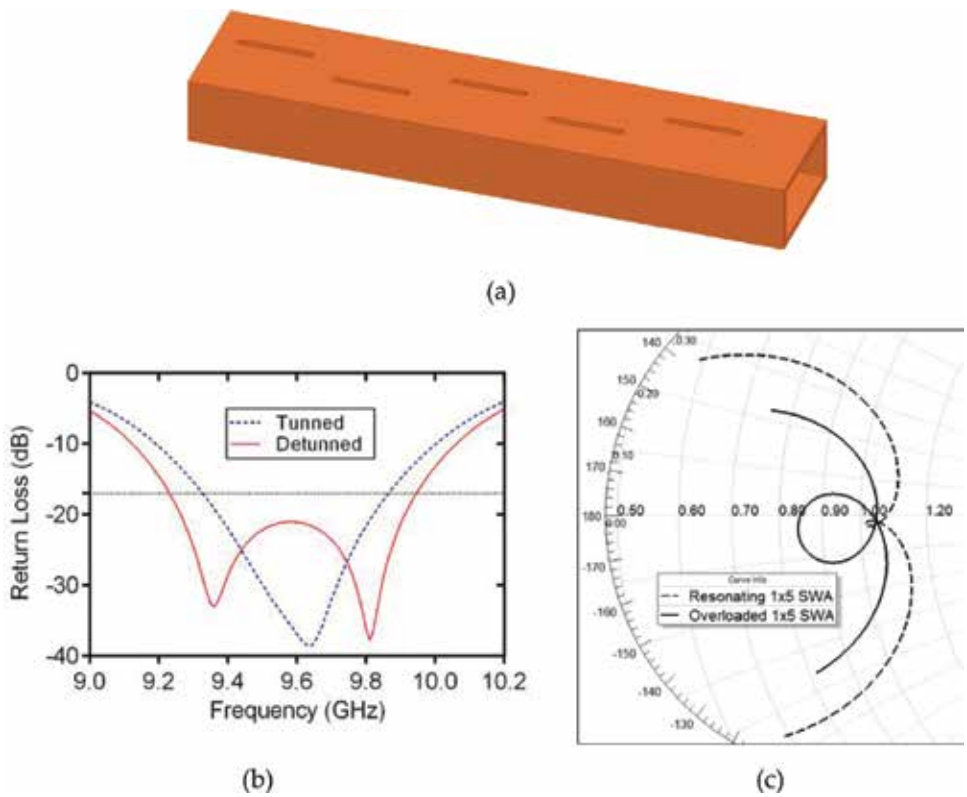


**Figure 4.** (a) Five elements linear slotted waveguide array antenna, (b) return loss performance, and (c) smith chart.

| | Without admittance overloading | With admittance overloading |
|---|---|---|
| Slot admittance | 0.1945 – j*0.016 | 0.2291 – j*0.016 |
| Slot length | 15.37 | 15.40 |
| Slot offset | 3.28 | 3.60 |

**Table 1.** Slot parameters.

Mutual coupling between the elements may be neglected due to considerably small array size. Therefore, Stevenson's formula can be used to compute slot lengths and offsets. Stevenson's formula provides the slot parameters for designed frequency only. Hence, the design of SWA with the computed slot parameters shows highly resonating nature, as shown in **Figure 4(b)**. It can be observed that the achieved return loss bandwidth is 2%. As it has been discussed earlier, the bandwidth of slotted waveguide array antenna can be improved using impedance overloading. To implement impedance over loading, slot length and offsets are tuned so that resultant admittance value slightly deviates from normalized value 1. For small SWA, this process can be carried out manually. **Table 1** lists slot admittance and their physical parameters for impedance overloading and non-overloading cases. **Figure 4(b)** shows the return loss performance of slotted waveguide array antenna incorporated with impedance overloading concept. It can be observed that the achieved return loss bandwidth is 15%, which is noteworthy improvement. Moreover, more detail about impedance overloading is explained in [4].

Furthermore, the linear array of five slots does not provide required gain, beamwidth, and desired gain ripples, if the pattern is shaped. Therefore, most effective approach to achieve overall performance of slotted waveguide array antenna is subarray approach. This technique exploits the advantages provided by dividing the large narrowband array into small wideband array ("Subarray"). The concept of subarray and its related theoretical studies have been published in the literature. But, the physical process of bandwidth broadening using subarray is not explained in detail.

## 3. Feeding mechanisms for subarray

The feeding mechanism of subarrays of the slotted waveguide array antenna plays a crucial role in limiting its bandwidth performance. Conventionally, the power to each subarray branch is delivered using feeding waveguide connected with subarrays by means of coupling slots. **Figure 5** shows the geometry of the 10-element slotted waveguide array antenna excited using coupling slots. Being the resonating element, coupling slots have their own resonant behavior and hence, the variation of reactive part of input admittance with frequency. Overall antenna resulting input admittance behavior is governed by the combined effect of radiating slots and coupling slots. Therefore, inherent wide bandwidth behavior of radiation slots, achieved using sub-array technique is degraded. Furthermore, coupling slots are used in feeding section of SWA which has to handle larger power than radiation branch of waveguide. Multipaction margin is also affected as narrow gap structures (i.e., coupling

slots) which are added in the path of high power signal. These factors are the major causes to limit the use of coupling slot feeding technique for large wideband SWAs. The design and simulation of 10 elements linear SWAs excited with coupling slot has been carried out and discussed in subsequent sections.

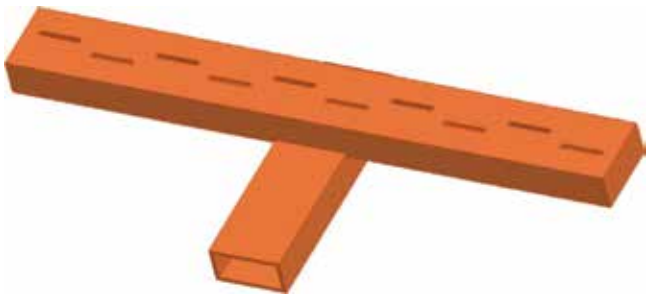

**Figure 5.** Geometry of 10 elements slotted waveguide array antenna fed coupling slots.

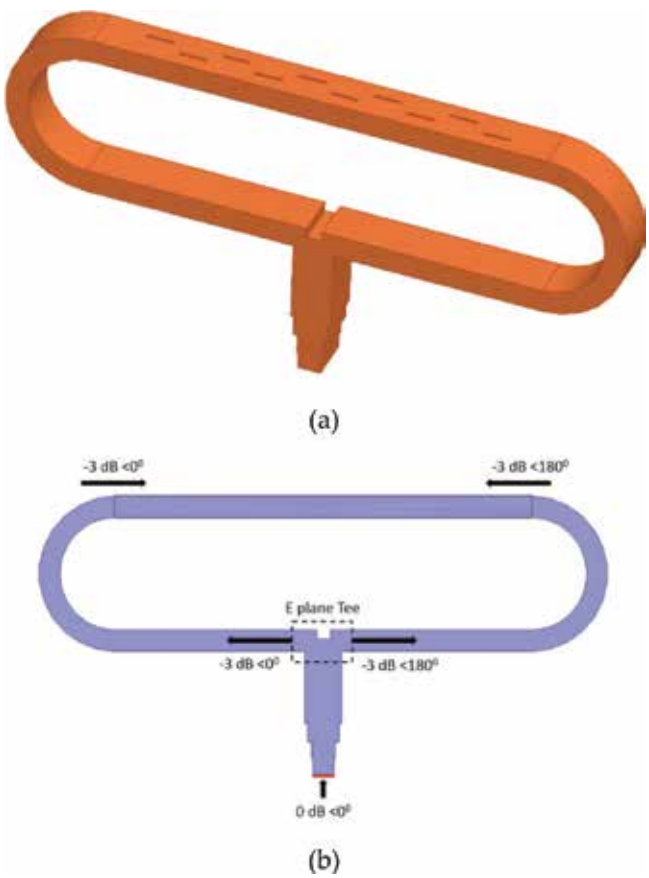


**Figure 6.** (a) Geometry of 10 elements slotted waveguide array antenna excited using differential feeding technique and (b) presence of virtual short.

Bandwidth and power handling performance of SWA can be preserved by eliminating resonating components from waveguide feed network design. This chapter describes the differential feeding technique which does not add any resonating structure in waveguide feeder network and maintains the effective bandwidth of subarray. **Figure 6(a)** shows the geometry of the proposed technique. Here, the edges of SWA are fed with 180° out of phase signal, which creates virtual short in the center of SWA. Presence of virtual short bifurcates the linear array and hence, effectively preserves the bandwidth achieved by subarraying. The presence of virtual short can be substantiated by observing current distribution on differentially excited waveguide, as shown in **Figure 6(b)**. The mathematical proof to validate the theory of virtual short is also detailed in Section 4. Moreover, two edges can be fed using E-plane T-junction which has inherent characteristics to provide 180° out of phase signals, irrespective of frequency of operation [5]. Therefore, the compensation of 180° phase over broadband of frequency can be achieved. Furthermore, the feeding network does not contain any resonating structures like coupling slots, to limit power handling capacity. The design and simulation results of 10 elements linear slotted waveguide array antenna incorporating the differential feeding technique is discussed in Section 5.

## 4. Theory of virtual short

Circuit theory has been applied to establish the virtual short theory in SWA. A branch in a circuit can be considered as short when the potential difference between two nodes of a branch is zero and the current flow is high in that branch. The presence of virtual short can be proved using similar concept in waveguide. In waveguide, *E*-field and *H*-field are used to derive the short circuit condition. The cross section of waveguide along length direction is shown in **Figure 7**. Here, operating frequency of 9.65 GHz has been selected. As WR-90 waveguide having cross sectional dimension of ($W_a$ = 22.86 mm) × ($W_b$ = 10.16 mm) is used, only $TE_{10}$ mode is supported at these frequency. As it can be seen in **Figure 7**, $Z = 0$ end is excited with 1 < 0° and $Z = Z_l$ is excited with 1 < 180°. Therefore, $E_y$ component of the signals is canceled and $H_x$ components of it are added at the center of waveguide, which satisfy the short circuit condition. Here, there is no conductor at the center of waveguide. However, the short circuit condition is fulfilled, which substantiate the presence of virtual short at the center of waveguide.

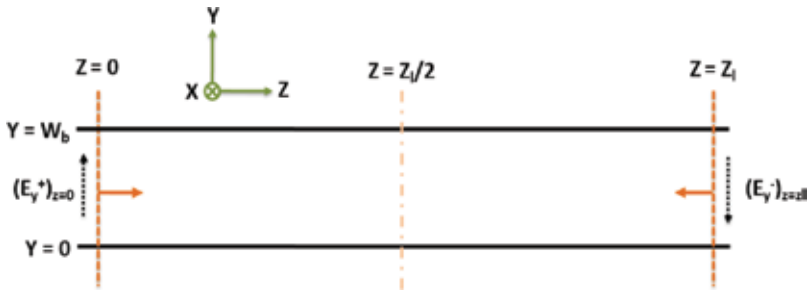


**Figure 7.** Cross section of WR-90 waveguide along length direction.

For $TE_{10}$ mode,

$$E_x^+ = 0$$

$$E_y^+ = -\frac{A_{10}}{\varepsilon}\frac{\pi}{a}\sin\left(\frac{\pi x}{a}\right)e^{-j\beta_z z}$$

$$E_z^+ = 0$$

$$H_x^+ = A_{10}\frac{\beta_z}{\omega\mu\varepsilon}\frac{\pi}{a}\sin\left(\frac{\pi x}{a}\right)e^{-j\beta_z z}$$

$$H_y^+ = 0$$

$$H_z^+ = -j\frac{A_{10}}{\omega\mu\varepsilon}\left(\frac{\pi}{a}\right)^2\cos\left(\frac{\pi x}{a}\right)e^{-j\beta_z z}$$

Here, excitation coefficient $A_{10}$ for both inputs are $(A_{10})_z = 0 = 1$ and $(A_{10})_z = z_l = -1$ (180° out of phase). For $E_y$ field component, at $z = 0$ (+ve $z$ directed wave)

$$\left(E_y^+\right)_{z=0} = -\frac{\pi}{\varepsilon a}\sin\left(\frac{\pi x}{a}\right)e^{-j\beta_z z}$$

at $z = z_l$ (−ve $z$ directed wave)

$$\left(E_y^+\right)_{z=z_l} = \frac{\pi}{\varepsilon a}\sin\left(\frac{\pi x}{a}\right)e^{-j\beta_z(z_l - z)}$$

Hence,

$$\left(E_{ytotal}\right)_{z=\frac{z_l}{2}} = \left(E_y^+\right)_{z=0} + \left(E_y^+\right)_{z=z_l}$$

$$\left(E_{ytotal}\right)_{z=\frac{z_l}{2}} = 0$$

Now, for $H_x$ field component,

$$\left(A_{10}\right)_z = 0 = \left(A_{10}\right)_z = z_l = 1$$

$$\left(H_x^+\right)_{z=0}, \left(H_x^+\right)_{z=z_l} = \frac{\beta_z \pi}{\omega\mu\varepsilon a}\sin\left(\frac{\pi x}{a}\right)e^{-j\beta_z\left(\frac{z_l}{2}\right)}$$

at $z = z_l/2$.

Hence,

$$\left(H_{xtotal}\right)_{z=\frac{z_l}{2}} = 2\left(H_x^+\right)_{z=0}$$

Now, for $H_z$ field component,

$$\left(A_{10}\right)_z = 0 = 1 \text{ and } \left(A_{10}\right)_z = z_l = -1$$

Hence,

$$\left(H_{ztotal}\right)_{z=\frac{z_l}{2}} = 0$$

Therefore,

$$\left(E_{ytotal}\right)_{z=\frac{z_l}{2}} = 0$$

$$\left(H_{xtotal}\right)_{z=\frac{z_l}{2}} = 2\left(H_x^+\right)_{z=0}$$

$$\left(H_{ztotal}\right)_{z=\frac{z_l}{2}} = 0$$

This fulfills the condition of short circuit node.

## 5. Design and simulation of linear slotted waveguide array antenna

Elliot's design technique has been applied to design SWA [6–8]. Elliot's design technique synthesizes slot lengths and offsets and incorporate mutual coupling between slots. This technique uses admittance variation of isolated shunt slot as a function of slot lengths and resonant length and the offset from center. Ansys HFSS 2014 has been used to compute the admittance variation and the real and imaginary part of admittance is plotted in **Figure 8(b)** and **(c)**. These plots are fed as input to Elliot's design technique and slot lengths and offsets are synthesized such that normalized input admittance (y) obtains value '1' at center frequency 9.65 GHz. Ten-element conventional edge fed SWA using synthesized slot lengths and offsets has been designed and shown in **Figure 9**.

3D simulation of conventional edge fed SWA has been carried out and the results are presented in Section 7. Simulation shows 2.8% 17-dB impedance bandwidth which does not cater to current need of bandwidth for communication and remote sensing applications. As it has been discussed in previous sections, 10 elements array can be split into two five element arrays, which will considerably increase the return loss bandwidth. Here, five element arrays

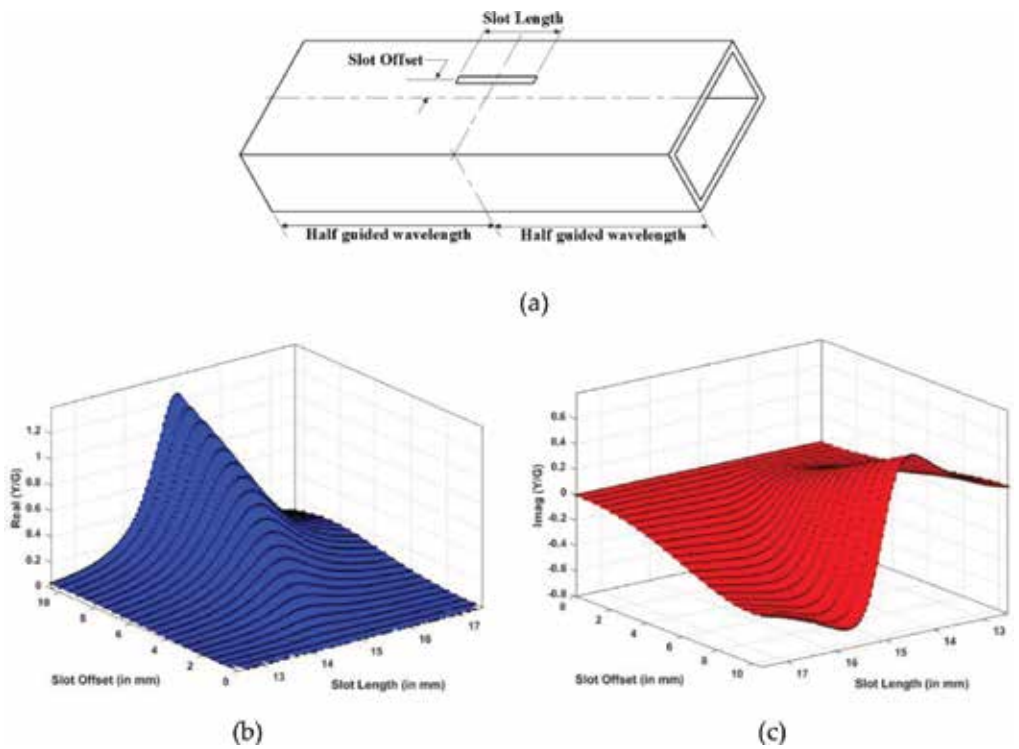


**Figure 8.** (a) Dimensional details of isolated shunt slot, variations of (b) real part of slot admittance, and (c) imaginary part of slot admittance functions of slot length and slot offset.

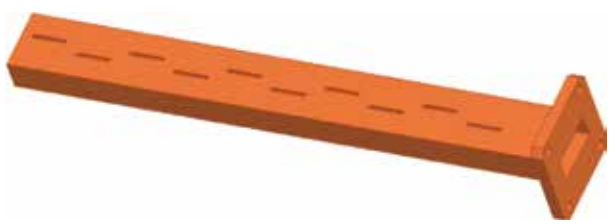

**Figure 9.** Geometry of conventional SWA with 15 mm slot length and 3.5 mm slot offset.

are combined in parallel. Therefore, slot lengths and offsets are to be adjusted so that normalized input impedance of each subarray becomes value '2'. Consequently, parallel combination of five element array results normalized admittance of 1 at input.

Subarrays can be excited by proper waveguide plumbing incorporated with coupling slots and waveguide tees. Such feeding network effectively governs the impedance bandwidth of SWA. In Section 3, the conventional coupling slot-based excitation technique and proposed differential feeding technique have been broadly detailed. To compare these techniques, 10-elements linear SWAs have been designed and optimized to achieve maximum bandwidth

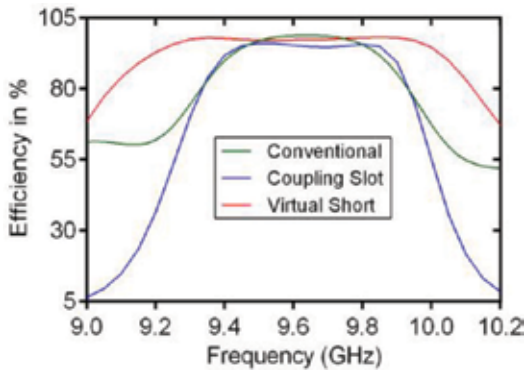


**Figure 10.** Comparison of total antenna efficiency between edge fed, coupling slot fed, and differential fed SWA.

for both type of feeding techniques. The simulated and their measured performances are compared and discussed in Section 7. When SWA is excited with coupling slots, 4.6% 17-dB RL bandwidth has been achieved, which is considerably less as compared to the expected bandwidth from subarray technique. The reduction in bandwidth can be ascribed to the addition of admittance variation of resonating coupling slots to the admittance variation of subarrays.

The chapter discusses the differential feeding technique which does not require resonating elements and hence, maintains the impedance bandwidth of subarray. After proper design and optimization of 10-elements linear SWAs with proposed feeding technique, 7.5% 17-dB RL bandwidth has been achieved, which is significantly large as compared to the RL bandwidth achieved when subarrays are fed using coupling slots. However, the achieved return loss bandwidth is not same as the RL bandwidth provided by a single subarray because of frequency sensitive nature of waveguide bends and E plane T junction.

Antenna efficiency is one of the important factors and it is the function of the reflection coefficient while considering other parameters constant. Therefore, if the variation of reflection coefficient with frequency is maintained below certain desired level (here, it is −17 dB), the antenna efficiency remains the same over the band of interest. Total antenna efficiency variation

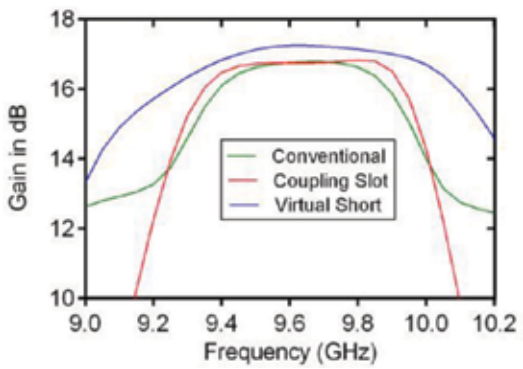


**Figure 11.** Comparison of realized antenna gain between edge fed, coupling slot fed, and differential fed SWA.

with frequency for various designed SWAs is shown in **Figure 10**. As it can be observed from **Figure 10**, ~90% efficiency is achieved over the band of interest for the proposed broadband SWA. Furthermore, SWA fed using coupling slots shows lowest efficiency, which can be attributed to high insertion loss added by coupling slots. **Figure 11** shows the plot of variation of realized gain with frequency for the presented SWAs. As it can be observed, the behaviors of realized gain and antenna efficiency with frequency are same. Moreover, gain flatness of proposer SWA has significant improvement as compared to conventional edge fed SWA and coupling slot fed SWA.

## 6. Design and simulation of planar slotted waveguide array antenna

In SWA, resonant slots are cut on the broadwall of the waveguide. Therefore, when any radiating structure working on the same band of interest is placed near these resonant slots, strong coupling between the resonant slots on waveguide and radiating structure occurs and reduces the impedance bandwidth of the SWA. This effect has been examined for the proposed broadband SWA by designing 2 × 10 planar broadband SWA using proposed differential feeding technique. **Figure 12** shows the design model of planar SWA. Here, two linear broadband SWAs are placed in proximity and combined using 1:2 waveguide feeder network employed with E- and H-plane tees. As it has been discussed, coupling between two linear SWAs should degrade the impedance bandwidth of planar SWA. However, proper optimization of feeder network can cancel the coupled energy, subsequently preserving the bandwidth of planar broadband SWA. About 7.8% 17-dB return loss bandwidth has been achieved in simulation. Section 7 shows the plots of simulated RL and far field patterns.

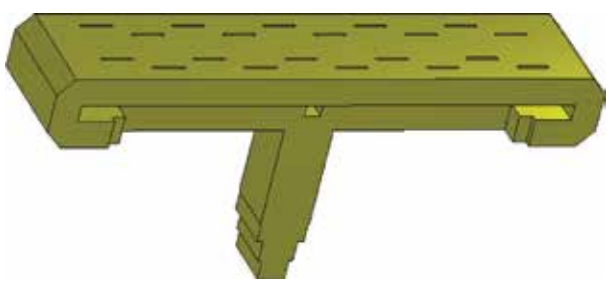

**Figure 12.** Geometry of 2 × 10 planar broadband SWA antenna with differential feeding mechanism.

## 7. Prototype fabrication and measurement

The presented antenna designs are fabricated and characterized for experimental validation of proposed technique. The realized prototypes of conventional SWA, SWA excited with coupling slots, and SWA with differential feeding technique are shown in **Figure 13**. Agilent E8363B microwave network analyzer with SOLT WR-09 calibration kit has been used to measure the return loss performance of these prototypes. **Figure 14** shows the comparison

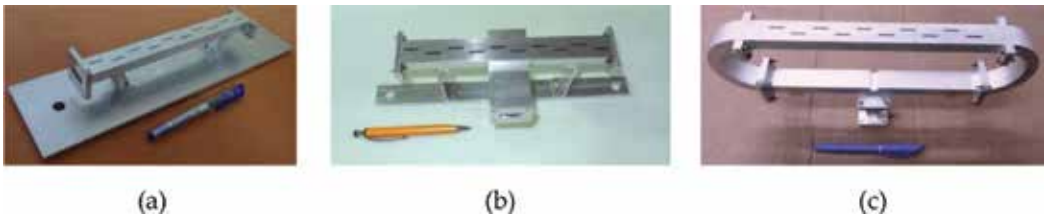


**Figure 13.** Fabricated structures (a) conventional slotted waveguide array, (b) slotted waveguide array antenna using coupling slots, and (c) SWA using differential feeding mechanism.

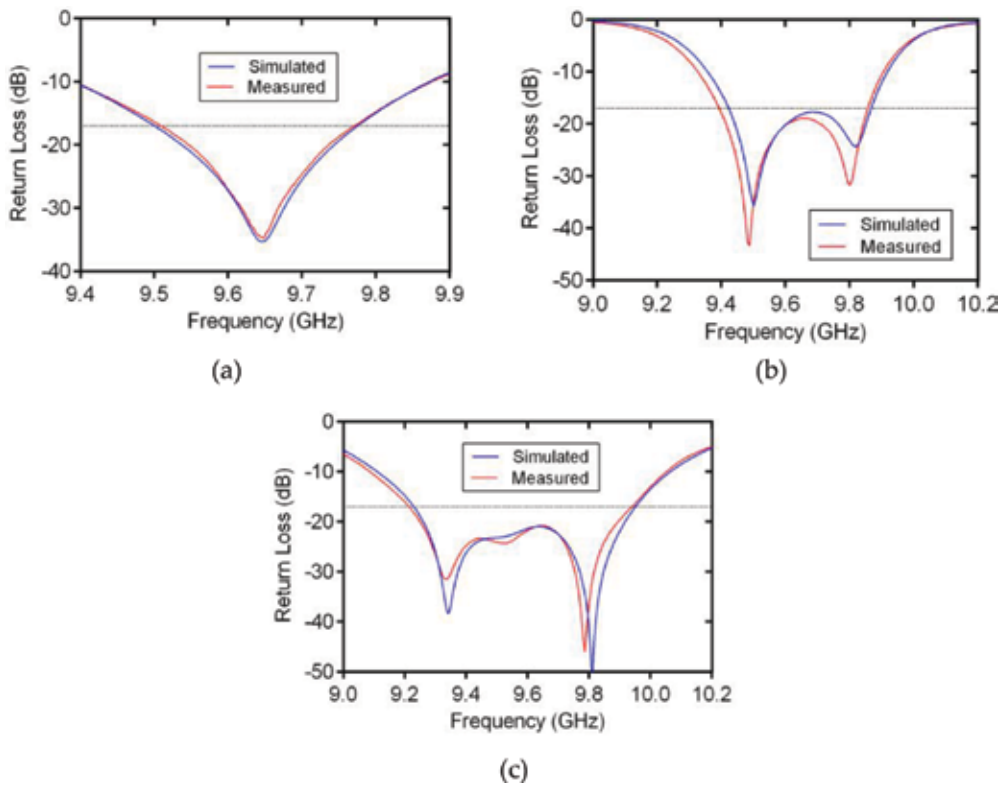


**Figure 14.** Simulated and measured return loss performance of (a) conventional slotted waveguide array, (b) slotted waveguide array antenna using coupling slots, and (c) SWA using differential feeding mechanism.

between measured and simulated return loss performance and **Table 3** lists the simulated and measured percentage bandwidth of each prototype. From **Figure 14**, it can be said that the simulated and measured results are in close agreement. Moreover, **Table 2** also compares the size of the fabricated SWA structure. The fabricated structures include the baseplates and interface plates which are not actual part of the antenna. They are connected with structure to perform S-parameter and far field characterization.

To validate the theory of virtual short in SWA, analysis has been carried out by placing physical short in the location of virtual short and its return loss performance is shown in **Figure 15**. No deviation from return loss performance of SWA with virtual short can be observed.

| | Length (mm) | Height (mm) | Width (mm) |
|---|---|---|---|
| Conventional slotted waveguide array | 36 | 14 | 50 |
| Slotted waveguide array antenna using coupling slots | 36 | 14 | 9.5 |
| SWA using differential feeding mechanism | 35 | 17 | 50 |

**Table 2.** Dimensions of fabricated SWA structures.

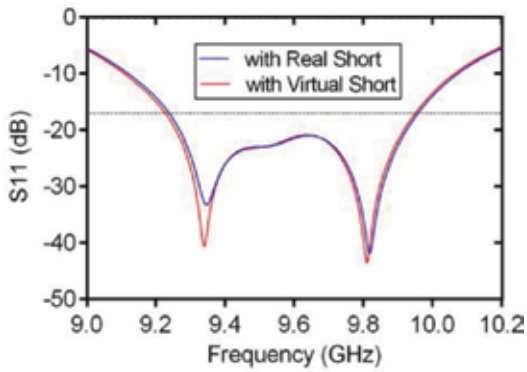


**Figure 15.** Simulated return loss performance of SWA with physical short and virtual short.

The radiation pattern and gain measurement of each fabricated prototype has also been carried out at in-house anechoic chamber. **Figure 16** shows proposed SWA antenna mounted on device under test (DUT) unit at anechoic chamber for far field measurement. Measured radiation patterns at 9.65 GHz for each prototype are shown in **Figure 17**. To obtain the gain of the array under test, the received power level difference between array under test and a standard gain horn has been measured and the results are presented in **Table 3** with their simulated performance. Good correlation between simulated and measurement of far-field parameters is obtained. Moreover, **Figure 18** shows the variation of measured gain with frequency of

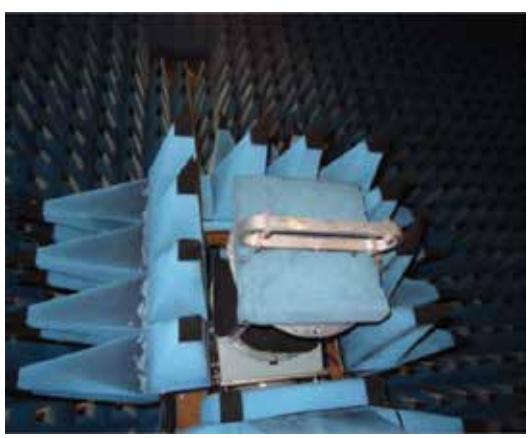

**Figure 16.** SWA using differential feeding mechanism mounted on DUT of anechoic chamber.

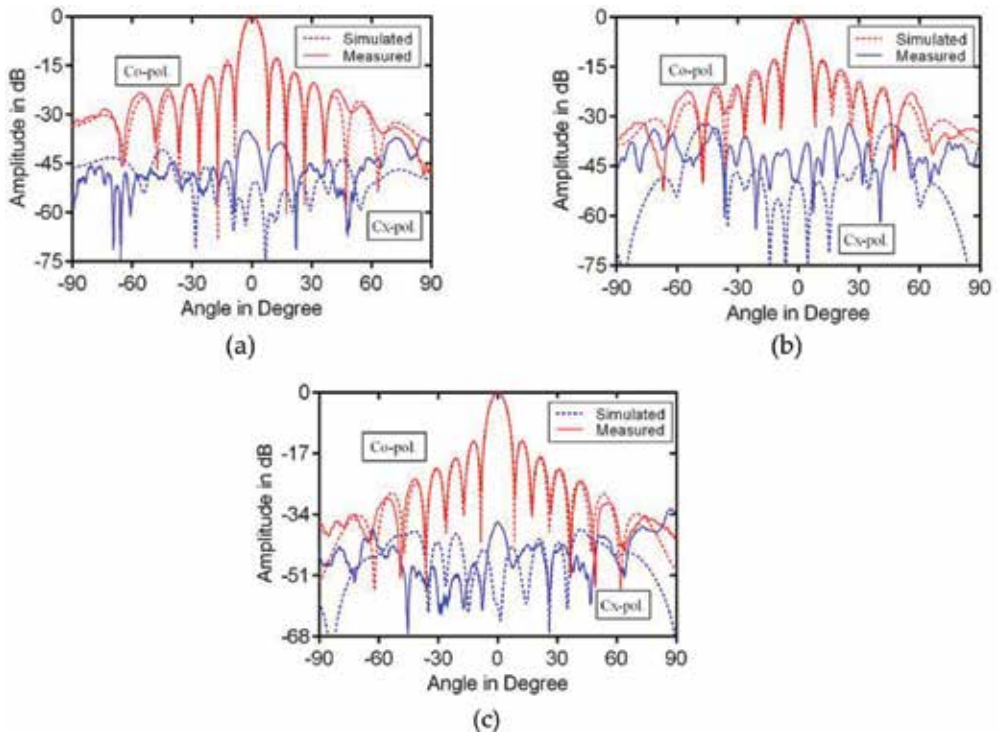


**Figure 17.** Simulated and measured radiation pattern of (a) conventional slotted waveguide array, (b) slotted waveguide array antenna using coupling slots, and (c) SWA using differential feeding mechanism.

| 9.65 GHz | Simulated BW (%) | Measured BW (%) | Simulated gain (dB) | Measured gain (dB) |
|---|---|---|---|---|
| Edge fed SWA | 2.8 | 2.7 | 16.60 | 16.35 |
| SWA fed by coupling slot | 4.6 | 4.8 | 16.61 | 16.21 |
| SWA fed by differential feeding mechanism | 7.5 | 7.6 | 16.62 | 16.32 |

**Table 3.** Measured bandwidth.

SWA with differential feeding mechanism. 0.88 dB gain variation over 800 MHz frequency range has been achieved.

Moreover, another most important mechanical aspects are antenna mass and its fabrication. Although the proposed SWA has high mass as compared to conventional SWAs, it can be reduced by the optimization of waveguide feeder network while incorporating mass as important factor in cost function and by using CFR- (Carbon Fiber Reinforced Plastic) based waveguides. In addition, the proposed SWA is complex to fabricate as compared to conventional SWAs. But, the recent evolution in mechanical fabrication processes has expanded the scope of fabricating complex waveguide structure within desired mass.

A prototype of 2 × 10 planar SWA antenna has also been realized and characterized to verify the simulation data. The developed prototype model is shown in **Figure 19** and its measured RL performance and far field pattern with their simulation data is plotted in **Figures 20** and **21**.

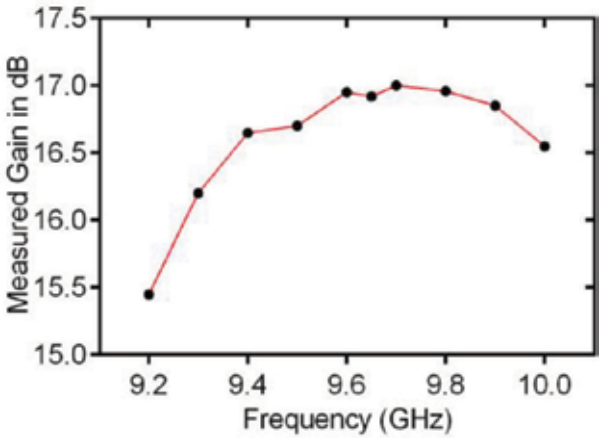


**Figure 18.** Variation of measured gain with frequency for SWA with differential feeding mechanism.

**Figure 19.** Fabricated structures of 2 × 10 planar SWA using differential feeding mechanism.

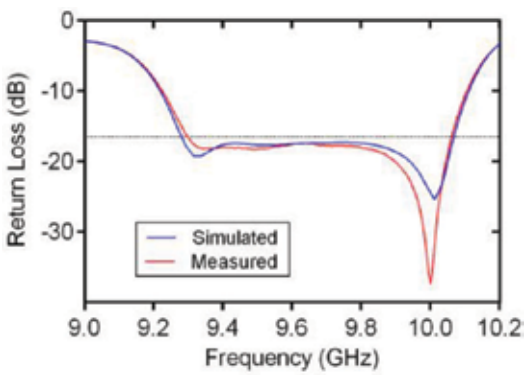


**Figure 20.** Simulated and measured return loss performance of 2 × 10 planar SWA using differential feeding mechanism.

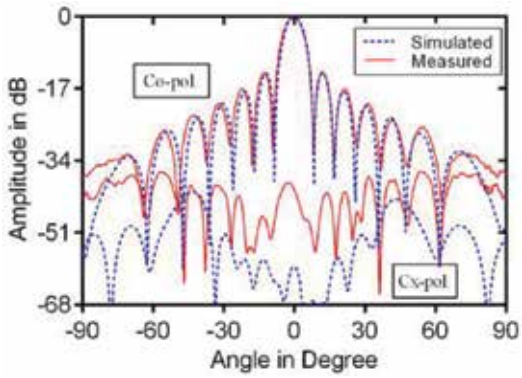


**Figure 21.** Simulated and measured radiation pattern of 2 × 10 planar SWA using differential feeding mechanism.

From **Figure 20**, it can be concluded that the planar array preserves the RL bandwidth of single linear array and the measured and simulated performances are in close match.

## 8. Conclusion

In this chapter, high efficiency broadband 10-element linear SWA integrated with differential feeding technique has been discussed in detail and also compared with conventional SWAs. The differential feeding technique has been proposed to eliminate the drawbacks of conventional SWAs excited with edge feeding and/or coupling slots. Mathematical justification of virtual short transpired due to differential feeding has also been presented and validated.

Ten-element linear SWAs employed with edge feeding, coupling slot feeding, and differential feeding have designed and simulated. The simulated results are also compared to validate the proposed advantages of differential feeding. About 7.5% return loss bandwidth has been achieved using differential feeding. Moreover, antenna efficiency and gain flatness performances are superior in the case of differential feeding. Presented designs of SWA are fabricated and characterized. In addition, 2 × 10 planar broadband SWA has also been designed, developed, and characterized. About 7.8% return loss bandwidth has been achieved in simulation. The measured performance of planar broadband SWA is also compared with simulated performance and good agreement has been achieved between them.

Furthermore, the proposed differential feeding techniques have shown many advantages like broad bandwidth, high power handling capacity, and the requirement of low fabrication tolerances. Therefore, this technique is the best suitable for SWA designs at millimeter wave and sub-millimeter wave.

## Acknowledgements

The authors thank and appreciate the support and encouragement provided by Shri Tapan Misra, Director, SAC during the course of this work. The authors also wish to thank all

engineers of Microwave Sensors Antenna Divison (MSAD) and Antenna Measurment Facility (AMF) for their help.

## Author details

Yogesh Tyagi and Pratik Mevada*

*Address all correspondence to: pratik@sac.isro.gov.in

Microwave Sensors Antenna Division (MSAD), Space Applications Centre (SAC), Indian Space Research Organization (ISRO), Ahmedabad, India

## References

[1] Wang W, Zhong S-S, Zhang Y-M, Liang X-L. A broadband slotted ridge waveguide antenna array. IEEE Transactions on Antennas and Propagation. August 2006;**54**(8). DOI: 10.1109/TAP.2006.879216

[2] Sekretarov SS, Vavriv DM. A wideband slotted waveguide antenna array for Sar systems. Progress In Electromagnetics Research M. 2010;**11**:165-176. DOI: 10.2528/PIERM10010606

[3] Zhao HC, Xu RR, Wu W. Broadband waveguide slot array for SAR. Electronics Letters. January 2011;**47**(2). DOI: 10.1049/el.2010.3009

[4] Silver S. Microwave Antenna Theory and Design. 1st ed. The United States of America: MacGraw-Hill Book Company, Inc.; 1949

[5] David M. Pozar, Microwave Engineering. 3rd ed. Singapore: John Wiley & Sons, Inc.; 2005

[6] Elliott RS, Kurtz LA. The Design of Small Slot Arrays. IEEE Transactions on Antennas and Propagation. March 1978;**AP-26**(2). DOI: 10.1109/TAP.1978.1141814

[7] Elliott RS. An improved design procedure for small arrays of shunt slots. IEEE Transactions on Antennas and Propagation. January 1983;**AP-31**(1). DOI: 10.1109/TAP.1983.1143002

[8] Kim DY, Elliott RS. A design procedure for slot arrays fed by single-ridge waveguide. IEEE Transactions on Antennas and Propagation. November 1988;**36**(11). DOI: 10.1109/8.9701

Chapter 2

# Photonic Crystal Waveguides

Dmitry Usanov and Alexander Skripal

Additional information is available at the end of the chapter

http://dx.doi.org/10.5772/intechopen.76797

**Abstract**

The original results of theoretical and experimental studies and the properties of microwave one-dimensional waveguide photonic crystals have been generalized. Methods for describing the electrodynamic characteristics of photonic crystals and their relationship with the parameters of periodic structures filling the waveguides have been presented. The results of an investigation on the characteristics of microwave waveguide photonic crystals made in the form of dielectric matrices with air inclusions have been presented. The model of effective dielectric permittivity has been proposed for describing the characteristics of the investigated photonic crystals containing layers with a large number of air inclusions. New types of microwave low-dimensional waveguide photonic crystals containing periodically alternating elements that are sources of higher type waves have been described. The possibility of effective control of the amplitude-frequency characteristics of microwave photonic crystals by means of electric and magnetic fields has been analyzed. Examples of new applications of waveguide photonic crystals in the microwave range have been given: the measuring parameters of the materials and semiconductor nanostructures that play the role of the microwave photonic crystals' periodicity defect; the resonators of near-field microwave microscopes; small-sized matched loads for centimeter and millimeter wavelength ranges on the basis of microwave photonic crystals.

**Keywords:** microwave photonic crystals, forbidden bands, defect mode, electrically controlled characteristics, measurement of micro- and nanostructures, microwave matched loads, low-dimensional photonic crystal

## 1. Introduction

The idea of the possibility of a continuous spectrum of electron energies decay into a set of alternating allowed and forbidden bands in the direction of electron motion and wave propagation in the presence of spatial periodicity of the deformation field was for the first

time proposed by Keldysh [1]. Periodic semiconductor structures with predetermined parameters of layers were called semiconductor superlattices. The wide interest to the problem of their creation appeared after the article was published in 1970 by Esaki and Tsu, who proposed to make such structures by changing the doping or composition of the layers [2]. The periods in such structures had values from 5 to 20 nm. The number of layers reached several hundred.

The author [3] gave the definition of photonic crystals as materials whose crystal lattice has a periodicity of the permittivity leading to the appearance of the "forbidden" frequencies range, called the photonic band gap. Yablonovich [4] and John [5] proposed to create structures with a photonic band gap, which can be considered as an optical analog of the band gap in semiconductors. In this case, the forbidden band is the frequency range in which the existence of light in the inner part of the crystal is forbidden. The type of defect or disturbance of periodicity in this instance can be different. Such structures have to be created artificially in contrast to natural crystals. In this case, the size of the basic unit element of a photonic crystal should be comparable with the light wavelength. The manufacturing of such structures involves the use of electron-beam and X-ray lithography [6].

As the advantage of such photonic crystals, the author [3] notes the possibility of an exact description of their properties that coincide with the experiment, in contrast to superlattices.

Structures with spatial periodicity of elements were also used in the microwave range to reduce the phase velocity of the wave in comparison with the speed of light in special waveguides, called delay-line structures [7]. The authors of [7] called them "a kind of artificial crystals, the cells of which have large sizes."

Delay-line structures are used in various types of vacuum microwave electronics devices. The specificity of the delay-line systems is the choice of their basic elements from metals and the need to take into account in the design the possibility of passing the electron beam interacting with the field. Examples of periodic structures used in delay-line systems are "meander," "counterpins," systems with alternating diaphragms, and so on.

In the microwave range, the photonic crystal can be realized both on waveguides with dielectric filling [8, 9] and on flat transmission lines with periodically changing stripe structure [10]. There are examples of the creation of photonic crystals in the optical, infrared, ultraviolet, microwave ranges. Creating a photonic crystal for the microwave range is the simplest. It should be noted that in the theoretical description of the properties of such structures, unlike, for example, from superlattices, it is not necessary to take into account the properties of transition layers, quantum size effects, the specificity of technological processes. This opens the possibility to more accurately examine the properties of photonic crystals associated with periodicity and, in particular, to use the results of a theoretical description to measure the parameters of their layers as a result of solving the corresponding inverse problem.

Materials with the properties of photonic crystals are also known in nature. They include, for example, noble opal [11], spicules of natural biomineral crystals, the basal spicules of glass sea sponges [12]. The time-varying forbidden band for the frequency region in the

vicinity of 6 GHz was observed in a solution with a chemical self-oscillating Briggs-Rauscher reaction characterized by the presence of periodically located regions with different permittivities [13].

## 2. One-dimensional microwave photonic crystals based on rectangular waveguides

### 2.1. Microwave photonic crystals: structures with forbidden bands

The results of theoretical analysis on the characteristics of one-dimensional microwave photonic crystals made on the basis of a rectangular waveguide and their experimental investigation are given, for example, in [14]. The one dimensionality of the crystal means that the dielectric structure that fills the waveguide has a periodicity of dielectric permittivity in one direction (along the wave propagation direction, along the Z axis). The authors of [14] studied structures in the form of alternating layers with high dielectric permittivity $h$ and low $l$ ($hl$-pairs) and layers of the $h_1lh_2$ type ($h_1$ and $h_2$ are dielectrics with different permittivities). In the theoretical description, the scattering matrix method was used. The arrangement of the dielectric layers in the waveguide can be characterized by the following relationships:

$$\varepsilon(x,y,z+d)=\varepsilon(x,y,z),\quad 0\le x\le a,\ \ 0\le y\le b, z<\infty, \tag{1}$$

$$\varepsilon(x,y,z+d)=\begin{cases}\varepsilon_1=\varepsilon_0\varepsilon_{r1}\ \ for\ \ -w\le z\le 0\\ \varepsilon_2=\varepsilon_0\varepsilon_{r2}\ \ for\ \ 0\le z\le v\end{cases}. \tag{2}$$

Here $\varepsilon_{r1}$ and $\varepsilon_{r2}$ are the relative permittivities of the two materials and $\varepsilon_0$ is the dielectric constant of the vacuum, $d=v+w$.

When continuity conditions are used on surfaces $z=0,\ \ z=v$ and $z=-w$ for tangential field components, the equation for finding the wave number $\gamma$ is obtained:

$$\gamma=\frac{1}{v+w}\arccos\left(L_{TE_{10}^z}\right), \tag{3}$$

where

$L_{TE_{10}^z}=\cos(\beta_1 w)\cos(\beta_2 v)-\frac{\beta_1^2+\beta_2^2}{2\beta_1\beta_2}\sin(\beta_1 w)\sin(\beta_2 v)$, $\beta_{1,2}^2=\omega^2\mu_0\varepsilon_{1,2}+k^2$, $k^2=(\pi/a)^2$.

The authors of [14] proposed to obtain reflection and transmission coefficients using the generalized scattering matrix, which is a result of the application of continuity conditions on media boundaries. The results of measurements and calculation of the transmission coefficient ($S_{21}$), characterized by the presence of a forbidden band for microwave photonic crystals consisting of 10 and 20 separate two-layer elements, are presented in [14]. The authors of [14] refer some of the differences between experiment and theory [14] to the imperfection of the waveguide walls.

To calculate the reflection $S_{11}$ and the transmission $S_{21}$, coefficients of the electromagnetic wave at its normal incidence on an $N$ layer structure, a matrix of wave transfer between regions with different values of wave propagation constants, can be used, similar to [15–17]:

$$\mathbf{T}(z_{j,j+1}) = \begin{pmatrix} \frac{\gamma_{j+1}+\gamma_j}{2\gamma_{j+1}} e^{(\gamma_{j+1}-\gamma_j)z_{j,j+1}} & \frac{\gamma_{j+1}-\gamma_j}{2\gamma_{j+1}} e^{(\gamma_{j+1}+\gamma_j)z_{j,j+1}} \\ \frac{\gamma_{j+1}-\gamma_j}{2\gamma_{j+1}} e^{-(\gamma_{j+1}+\gamma_j)z_{j,j+1}} & \frac{\gamma_{j+1}+\gamma_j}{2\gamma_{j+1}} e^{-(\gamma_{j+1}-\gamma_j)z_{j,j+1}} \end{pmatrix}, \tag{4}$$

which connects the coefficients $A_j$, $B_j$ and $A_{j+1}$, $B_{j+1}$, which determine the amplitudes of the incident and reflected waves on both sides of the boundary $z_{j,j+1}$, by the relation:

$$\begin{pmatrix} A_{j+1} \\ B_{j+1} \end{pmatrix} = \mathbf{T}(z_{j,j+1}) \cdot \begin{pmatrix} A_j \\ B_j \end{pmatrix}. \tag{5}$$

The coefficients $A_{N+1}$ and $B_0$, which determine the amplitudes of the wave transmitted through the multilayer structure (**Figure 1**) and the wave reflected from it, are connected to the coefficient $A_0$, determining the amplitude of the incident wave, by the following relation:

$$\begin{pmatrix} A_{N+1} \\ 0 \end{pmatrix} = \mathbf{T}_N \cdot \begin{pmatrix} A_0 \\ B_0 \end{pmatrix}, \tag{6}$$

where

$$\mathbf{T}_N = \begin{pmatrix} \mathbf{T}_N[1,1] & \mathbf{T}_N[1,2] \\ \mathbf{T}_N[2,1] & \mathbf{T}_N[2,2] \end{pmatrix} = \prod_{j=N}^{0} \mathbf{T}_{j,(j+1)} = \mathbf{T}(z_{N,N+1}) \cdot \mathbf{T}(z_{N-1,N})_{\ldots} \mathbf{T}(z_{1,2}) \cdot \mathbf{T}(z_{0,1}) \tag{7}$$

a transmission matrix of an $N$ layer structure.

The reflection $S_{11} = \frac{B_0}{A_0}$ and transmission $S_{21} = \frac{A_{N+1}}{A_0}$ coefficients of an electromagnetic wave interacting with a layered structure are determined by the following relationships:

$$S_{11} = -\frac{\mathbf{T}_N[2,1]}{\mathbf{T}_N[2,2]}, S_{21} = \frac{\mathbf{T}_N[1,1] \cdot \mathbf{T_N}[2,2] - \mathbf{T}_N[1,2] \cdot \mathbf{T}_N[2,1]}{\mathbf{T}_N[2,2]}. \tag{8}$$

When calculating $S_{11}$ and $S_{21}$, we used the matrixes of wave transfer between regions with different values of wave propagation constants $\gamma_j$ and $\gamma_{j+1}$.

The following expressions are used to calculate the reflection $|S_{11}|^2$ | and transmission $|S_{12}|^2$ coefficients of the electromagnetic wave expressed in terms of power (in dB unit):

$$|S_{11}|^2 = 10\log|S_{11}|^2, |S_{21}|^2 = 10\log|S_{21}|^2 \tag{9}$$

http://dx.doi.org/10.5772/intechopen.76797

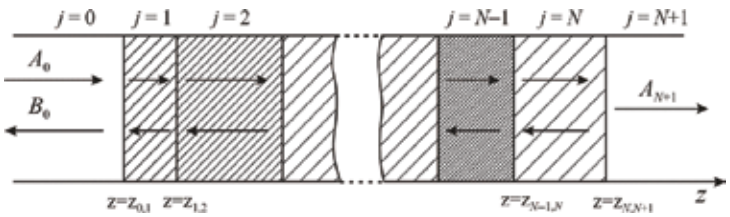


**Figure 1.** Structure consisting of $N$ layers.

The results of the theoretical and experimental investigation of the resonant features that appear in the allowed and forbidden bands of microwave photonic crystal in the case of creating periodicity disturbance are given in [18]. As a waveguide photonic crystal, a waveguide section with a structure that is periodically alternating layers of two types of dielectrics with different values of thickness and permittivity was used. The dimensions and materials of the layers were chosen in such a way that in the frequency range 8–12 GHz, two allowed and one forbidden band were observed for the propagation of electromagnetic waves. The parameters of the first and the last layers of the photonic crystal were the same. The results of calculating the power transmission coefficient $|S_{12}|^2$ of an electromagnetic wave using the abovementioned relationships for the 11-layer photonic crystal without disturbances in the case of $H_{10}$ wave propagation are shown in **Figure 2** (curve *1*).

From the results of the calculation presented in **Figure 3**, it follows that an increase of layers in number causes the decrease of the width of the first band gap completely located within the 3 cm wavelength range and the increase in the width of both the left and right allowed bands in this wavelength range. With a number of layers larger than 27, these changes are less than 10 MHz. This behavior of the characteristics of an electromagnetic propagation through a photonic crystal is due to the following circumstance. The allowed band has a "dissected" frequency response and consists of a set of resonances, the number of which is determined by the number of identical elements that form the photonic crystal. Therefore, the increase of the number of photon crystal layers causes the increase of the number of resonances determining the width of the allowed band and, consequently, its width increases. At the same time, the

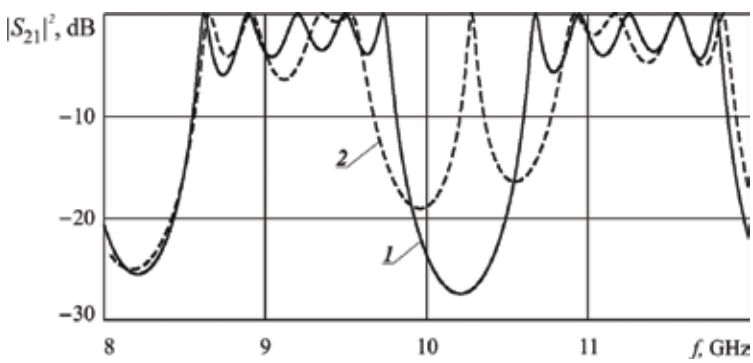


**Figure 2.** The results of calculating the square of the modulus of the transmission coefficient of an electromagnetic wave through the 11-layer structure without disturbance (curve *1*) and with the disturbed central layer (curve *2*).

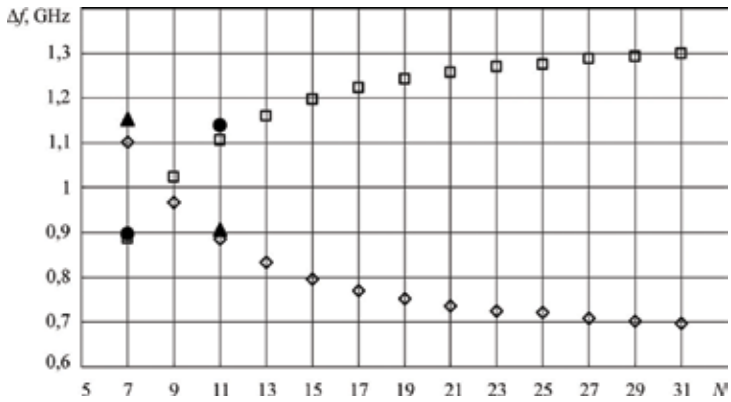


**Figure 3.** Dependences of the width of the forbidden and left allowed bands on the number of layers of a photonic crystal without disturbance: □, ●—theoretical and experimental values of the width of the left-allowed band, ◊, ▲—theoretical and experimental values of the band gap width.

width of the forbidden band decreases. The Q-value of the resonances that form the allowed band, the so-called "allowed levels," as follows from the results of calculations and experiments, is maximum near the lower and upper boundaries of the allowed band.

**Figure 2** (curve *2*) shows the calculations results of the frequency dependences of the square of the modulus of the electromagnetic wave transmission coefficient $S_{21}$ in the presence of a disturbance in the photonic crystal in the form of, for example, a central layer of smaller thickness $d_6$. In this case, a resonance feature with a transmission coefficient close to unit appears in the band gap. This feature is an impurity mode resonance whose location can be controlled by varying the dielectric layer thickness. The disturbance in a photonic crystal, as shown in [5], also leads to a change in the number of resonances formed in the allowed band and their positions on the frequency axis. When disturbance in the form of a central layer of a smaller thickness is created in a photonic crystal, the number of resonances in the allowed band decreases by one in comparison with the photonic crystal without disturbance, and the width of the forbidden band containing the impurity mode resonance increases substantially (**Figure 2**, curve *2*). This effect is especially evident for a small number of photonic crystal periods. It should be noted that the width of the forbidden band containing an impurity mode resonance with a number of layers tending to infinity turns out to be approximately equal to the width of the forbidden band of a photonic crystal without disturbances.

The one-dimensional waveguide photonic crystals consisting of 7 and 11 layers completely filling a cross-section of rectangular waveguide of a 3-cm wavelength were used in the experiments. The odd layers were made of $Al_2O_3$ ceramics ($\varepsilon_r = 9.6$), and the even ones were made of Teflon ($\varepsilon_r = 2.1$). The length of odd segments is 1 mm and the length of even segments is 44 mm. The disturbance was created by changing the length of the central layer, which led to the appearance of an impurity mode resonance in the forbidden band of a photonic crystal. The length of the central disturbed (Teflon) layer was chosen equal to 14 mm. The frequency dependences of the reflection and transmission coefficients of microwave radiation interacting with a photonic

crystal were measured with the Agilent PNA-L Network Analyzer N5230A. A comparison of the results of calculation and experiment shows their good quantitative coincidence.

In [19], the results of an investigation on the characteristics of a waveguide microwave photonic crystal made in the form of dielectric matrices with air inclusions are presented. Ceramics ($Al_2O_3$) with a large number of air inclusions and polystyrene were used as materials of dielectric layers. A waveguide photonic crystal consisting of 11 layers was studied in the frequency range 8–12 GHz (**Figure 4a**). Odd layers were made of $Al_2O_3$ ceramics ($\varepsilon_r = 9.6$), even layers were made of polystyrene ($\varepsilon_r = 1.05$). Thickness of odd lengths was $d_{Al_2O_3} = 1.0$mm, even $d_{foam} = 13.0$ mm. The layers completely filled the cross-section of the waveguide. In ceramic layers, a large number of air inclusions were created in the form of square-through holes, which form a periodic structure in the plane of the layer (**Figure 4b**).

On the basis of numerical modeling using the finite element method in the CAD ANSYS HFSS, the influence of the volume fraction of air inclusions on the amplitude-frequency characteristics of the transmission coefficient of a photonic crystal was studied. The volume fraction of air inclusions was controlled by changing the size of the holes $a_{hole}$ in the ceramics plates with a fixed amount of 36 in each of the plates. The simulation was carried out for three sizes of holes, equal to 0.75, 1.2 and 1.65 mm, which corresponds to a volume fraction of air inclusions equal to 8.5, 23 and 43%, respectively. The disturbance of the periodicity of the photonic structure was created by changing the thickness of the central (sixth) polystyrene layer. The thickness of the sixth modified (disturbed) polystyrene layer was 2.25, 2.75, 3.49 and 6.0 mm.

As follows from the results of numerical calculation of the amplitude-frequency characteristics of the transmission coefficient of a photonic crystal by the finite-element method in the absence of the periodicity disturbance in the photonic structure, the increase in the volume fraction of air inclusions in the ceramic layers leads to the shift of the forbidden band of the photonic crystal toward shorter wavelengths and to the decrease of its depth. The results of the calculation of the photonic crystal amplitude-frequency characteristics by the finite element method in the presence of the disturbance of the photonic structure periodicity in the form of a central polystyrene layer of different thickness are shown in **Figure 5** (solid curves).

The presence of the disturbance of the photonic structure periodicity in the form of the change of the thickness of the central (sixth) polystyrene layer led to the appearance of a transmission

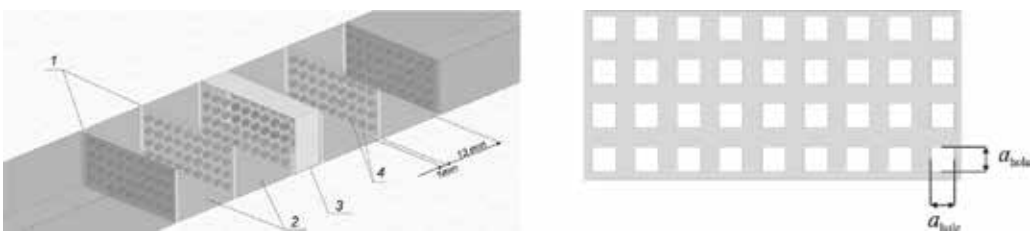


**Figure 4.** Model of the photonic crystal: 1—layers of ceramics with square through holes, 2—polystyrene layers, 3—disturbance in the form of a polystyrene layer with changed thickness (a). The ceramics layer with square through holes (b).

peak in the forbidden band of the photonic crystal, the position of which is determined by the size of this disturbance.

Measurement of the amplitude-frequency characteristic of the transmittance of the investigated photonic crystal in the 3 cm wavelength range was carried out using the Agilent PNA-L Network Analyzer N5230A. The results of experimental studies of the amplitude-frequency characteristics of the transmittance of a photonic crystal without disturbance and for different thicknesses of the disturbed polystyrene layer $d_{6\text{foam}}$ are shown in **Figure 5** (discrete curves). Comparison of the calculation and the experiment results indicates their good agreement.

The layers of investigated photonic crystals containing a large number of air inclusions can be considered as composite materials, which are dielectric matrices based on ceramics with fillers in the form of air inclusions. It is known that the dielectric properties of composite materials can be characterized by the value of the effective permittivity $\varepsilon_{\text{ef}}$ determined by the dielectric permittivities of the matrix $\varepsilon_1$ and filler $\varepsilon_2$ and their volume fractions. The results of the investigation on the possibility of describing the amplitude-frequency characteristics of the transmission coefficient of the investigated photonic crystal, using the model of the "effective" medium [20–22], are given in [19]. The photonic crystal consists of alternating homogeneous layers with effective dielectric permittivity and polystyrene. Its amplitude-frequency characteristic was calculated using a wave transfer matrix between regions with different values of the propagation constant of the electromagnetic wave, determined by the effective permittivity of the ceramic layers with air inclusions and the dielectric permittivity of the polystyrene.

To determine the effective permittivity $\varepsilon_{\text{ef}}$, it is necessary to solve the inverse problem [16]. According to the frequency dependences of the transmittance of a photonic crystal consisting of periodically alternating polystyrene and ceramic layers with air inclusions, the inverse problem was solved using the least squares method.

**Figure 6** shows the frequency dependences of the power transmission coefficient of the photonic crystal with a different fraction of air inclusion in ceramic layers with the disturbed sixth polystyrene layer of thickness $d_{6\text{foam}} = 6.0$ mm (circles) calculated using the finite element method in the CAD ANSYS HFSS and the frequency dependences of the transmission coefficients of a

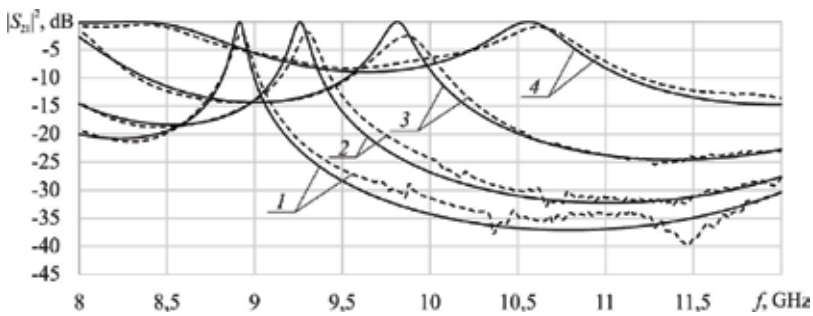


**Figure 5.** Calculated (continuous curves) and experimental (discrete curves) amplitude-frequency characteristics of the transmittance of a photonic crystal for various volume fractions of air inclusions with disturbed sixth polystyrene layer of 6.0 mm. The volume fraction of inclusions: 1–0, 2–8.5, 3–23.0 and 4–43.0%.

photonic crystal (curves) calculated at the values of the effective permittivity $\varepsilon_{ef}$ found from the inverse problem solution.

The dependence of the effective permittivity of the layers on the volume fraction of air inclusions, calculated from the solution of the inverse problem, coincides with the dependence described by Maxwell-Garnett ratio [20] with the error of 7.47%, the Bruggeman ratio [21] with the error of 4.50% and the Lichteneker ratio [22] with the error of 24.02%.

A distinctive feature of microwave photonic crystals is the ability to provide various functions necessary for the operation of microwave circuits [23–26] with a relatively small number of elements that make up a photonic crystal. A small number of elements forming microwave photonic crystals is associated with the need for compactness of the devices created on their basis. It is of scientific and practical interest to create multielement microwave photonic crystals characterized by small dimensions. To solve this kind of problem, it is possible to use as a photonic crystal the structure that excites higher type waves whose wavelengths are substantially shorter than the wavelength in the waveguide of the main type, as suggested by the authors in [27]. Therefore, the dimensions of devices at higher type waves become significantly smaller than similar devices on the main type of the wave. In this regard, they can be called low dimensional. The results of studies of waveguide photonic crystals in the form of alternating dielectric layers (even elements) of a photonic crystal and thin metal plates (odd elements) partially overlapping the waveguide cross-section are presented in [27]. Between the plates and the wide walls of the waveguide, there were gaps. Each of the plates created gap of the same width along the entire length of the plate. The gaps between the odd metal plates and the waveguide were created at one of the wide walls of the waveguide and the gaps between the even metal plates and the waveguide at the opposite wide wall of the waveguide. In this case, the gap is a source of higher type waves, forming in its vicinity the so-called near field. The structure of the investigated low-dimensional waveguide microwave photonic crystal is shown in **Figure 7**. The following materials were used as the dielectric material: polystyrene ($\varepsilon_r = 1.02$) and teflon ($\varepsilon_r = 2.1$). The dielectric layers completely filled the cross section ($23 \times 10$ mm) of the waveguide. The metal plates 50 μm thick were made of aluminum. The width of the gap $S$ did not exceed one-tenth of the size of the waveguide narrow wall.

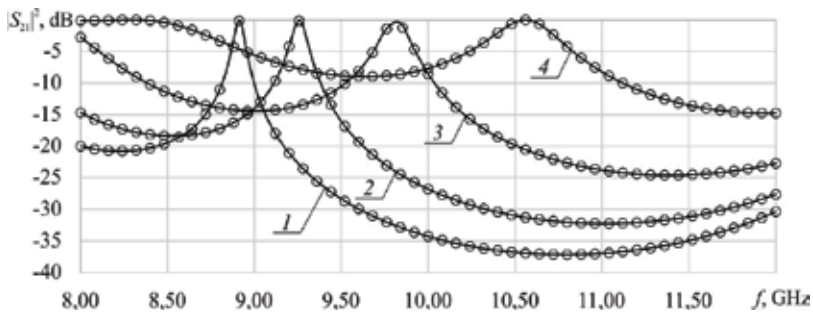


**Figure 6.** Amplitude-frequency characteristics of the transmission coefficients of a photonic crystal calculated using the values of the effective permittivity $\varepsilon_{ef}$, found from the inverse problem solution, of ceramics layers with different fraction of air inclusions with the disturbed sixth layer of 6.0 mm, $\varepsilon_{ef}$, rel. units: 1–9.6 ($x_1 = 0\%$), 2–8.44 ($x_1 = 8.5\%$), 3–6.78 ($x_1 = 23.0\%$), 4–4.82 ($x_1 = 43.0\%$).

Based on numerical simulation, using the finite element method in the CAD ANSYS HFSS, the influence of the thickness of dielectric layers, the gap width and the number of layers of the photonic crystal structure on the amplitude-frequency characteristics of the transmission and reflection coefficients of a photonic crystal was investigated.

The finite-element method was used to calculate the amplitude-frequency characteristic of the transmission $S_{12}$ and the reflection $S_{11}$ coefficients of a nine-layer photonic crystal consisting of five consistently alternating metal plates with gaps and four dielectric layers for different thicknesses of the dielectric layers $h$. It follows from the calculation results that the amplitude-frequency characteristic of the transmittance $S_{12}$ of the structure under study has a "band" character. The amplitude-frequency characteristic of such a photonic crystal consists of specific alternating "allowed" and "forbidden" bands. The frequency position of the resonance peaks of the coefficient $S_{11}$ corresponds to the position of the peaks of the coefficient $S_{12}$. The decrease in the thickness $h$ of the dielectric layers of the structure, as well as the increase in the width of the gap $S$, led to a shift in the amplitude-frequency characteristic of the photonic crystal toward shorter wavelengths and the increase in the width of the "allowed" band. At the same time, the width and depth of the "forbidden" band decreased. It was found that with the number of metal plates in the photonic crystal structure equal to $m$, the number of resonances on its amplitude-frequency characteristic is $m-1$.

Comparison of the results of calculations and experimental studies of a photonic crystal created in accordance with the model described above indicates their good qualitative agreement.

The use of metal plates with gaps in the structure of a photonic crystal has made it possible to substantially reduce its longitudinal dimension to 12.25 mm, which is approximately five times smaller than the longitudinal dimension of a photonic crystal created on elements made of alternating layers of dielectrics with different permittivity.

The disturbance of periodicity in a low-dimensional microwave photonic crystal, as well as in the ordinary one, should lead to the appearance of a defect (impurity) mode resonance. The theoretical definition of the conditions for its appearance and their experimental realization

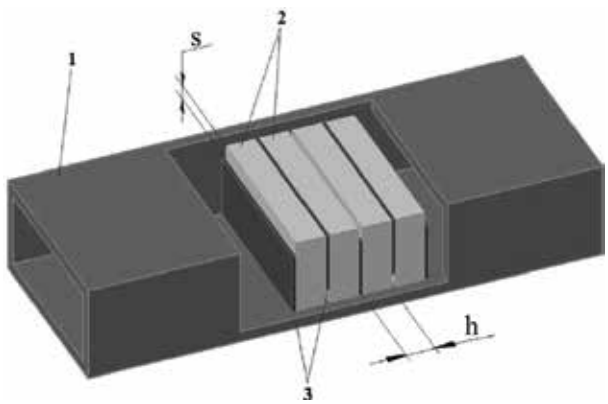


**Figure 7.** Model of a photonic crystal: *1*—rectangular waveguide segment, *2*—dielectric layers, *3*—thin metal plates, *S*—gap width, *h*—dielectric layer thickness.

was described in [28]. A violation of the periodicity of a photonic crystal can be a different size of the central dielectric layer or a modified size of the capacitive gap of the diaphragm adjacent to the disturbed layer. In [28], the results of studies of the low-dimensional photonic crystals described above (the inset to **Figure 8**) are presented. The diaphragms of 50 μm thick were made of aluminum. The thickness of each dielectric layer in the photonic crystal without "disturbances" was 3 mm. Thus, the total longitudinal dimension of the crystal without breaking the periodicity was ~15 mm. **Figure 8** shows the experimental and calculated using the ANSYS HFSS CAD the transmission coefficient $S_{21}$ of an eleven-layer photonic crystal without disturbance (curves *3*, *4*) and with disturbance (curves *1*, *2*) as a central dielectric (teflon, $\varepsilon_r = 2.1$) layer with thickness reduced to 1 mm, with a fixed value of the gap $S = 1$ mm.

The measurements were carried out using the Agilent PNA-L Network Analyzer N5230A. Comparison of the calculations and measurements results indicates their qualitative agreement. The existing difference may be due to ignoring the attenuation in the waveguide walls, which is essential for higher types of waves.

As follows from the results shown in **Figure 8**, the introduction of the disturbance in the form of a changed size of the central dielectric layer led to the appearance of a defect mode resonance and a significant change in the width and depth of the "forbidden" band. At the same time, the position of the defect mode on the frequency scale essentially depends not only on the thickness of the "disturbed" dielectric layer but also on the value of the capacitive gap of the diaphragms.

Periodic structures based on resonators as retarding systems for vacuum microwave devices and microwave filters have been described as early as in the 1960s [28, 29]. They were intended

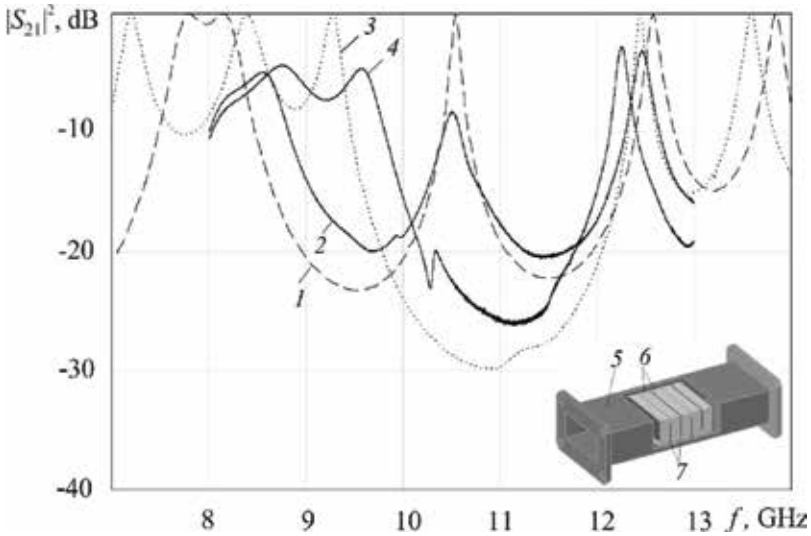


**Figure 8.** Calculated (dashed and doted curves) and experimental (solid curves) amplitude-frequency characteristics of transmittance $S_{12}$ of 11-layer low-dimensional photonic crystal: curves *1*, *2*—with "disturbed" sixth central teflon layer of 1 mm; curves *3* and *4*—without the periodicity disturbance. On the inset: a photonic crystal model: *5*—rectangular waveguide segment, *6*—dielectric layers, *7*—capacitive diaphragms.

to be used as delay-line structures in these devices, providing the optimal interaction of the electron beam with the electromagnetic wave. The investigated structure consists of periodically located metal resonant diaphragms at a distance $l$ from each other, deposited to a dielectric substrate (**Figure 9**) [30].

On the basis of numerical simulation using the finite element method in the CAD ANSYS HFSS, the influence of substrates with different dielectric permittivity on the microwave reflection and transmission coefficients of the structure was investigated. The amplitude-frequency characteristics of a photonic crystal made up of metal diaphragms deposited on a dielectric substrate with a through aperture for different widths of the aperture and the amplitude-frequency characteristics of a photonic crystal made up of diaphragms on dielectric substrates with apertures filled with a material with the permittivity $\varepsilon_2$ were analyzed. The increase in the width of the aperture, for a fixed permittivity of the substrate, causes the increase in the width and depth of the band gap. Moreover, the low-frequency edge of the band remains stationary around 9 GHz, and the extension occurs due to the shift from the high-frequency edge of the forbidden band to the high-frequency region. The same tendency is observed when the permittivity of insulator within the aperture increases.

The photonic crystal based on diaphragms without dielectric substrates consisted of 6 aluminum diaphragms of 10 μm fixed between two layers of 2 mm polystyrene placed in a rectangular waveguide. The width and height of the apertures of the diaphragms of the photonic crystal were chosen equal to 14 and 1 mm, respectively. This provided the appearance on the frequency dependences of the transmission and reflection coefficients (the dashed curves in **Figure 10a** and **b**, respectively) in the frequency range 8–12 GHz of one allowed and one forbidden bands. The same figures show the results of measurements of the amplitude-frequency characteristics of a photonic crystal with a disturbance of periodicity (solid curves) in the form of a modified distance $L$ between the central diaphragms.

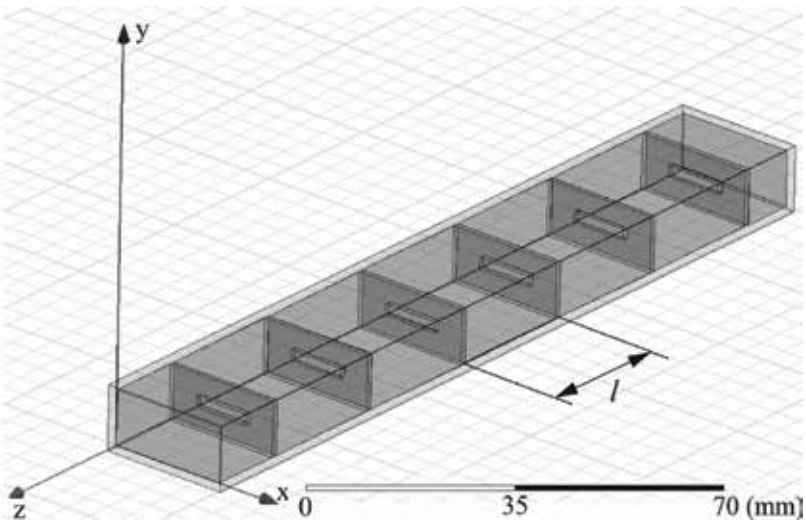


**Figure 9.** The scheme of the microwave photonic crystal, where $l$ is the distance between the diaphragms.

http://dx.doi.org/10.5772/intechopen.76797

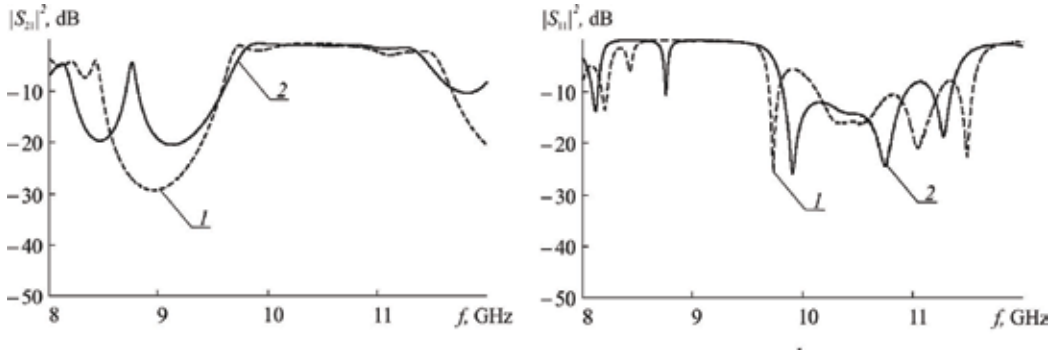


**Figure 10.** Experimental amplitude-frequency characteristics of the transmission coefficient (a) and reflection (b) of a photonic crystal based on diaphragms without dielectric substrates in the case of the disturbance absence (curve *1*) and the disturbance presence (curve 2). Distance between diaphragms $l = 27$ mm, length of slots $a_1 = 14$ mm, size of disturbance in the central layer $L = 20$ mm.

A comparison of the experimental dependences presented in **Figure 10** with the results of the calculation of the amplitude-frequency characteristics of the photonic crystal based on diaphragms without dielectric substrates in the case of the disturbance presence and the disturbance absence with parameters corresponding to the experimental sample described above indicates good qualitative and quantitative agreement.

### 2.2. Control of the characteristics of microwave photonic crystals

The ability to control the amplitude-frequency characteristics of microwave photonic crystals opens the prospect of expanding their field of application. This possibility was considered, in particular, in [31]. The authors of [31] took the design of the microwave photonic crystal used in [32] as a filter. Polystyrene, ceramics $Al_2O_3$ (thickness of 1 mm) and polycrystalline yttrium-iron garnet (YIG) (thickness of 1 mm) were used as the material forming the photonic crystal layer. The control of the amplitude-frequency characteristics of the investigated structures by magnetic field is provided by the increase in the real part of the ferrite magnetic susceptibility under increasing magnetic field. This leads to the increase in the microwave field concentration in the ferrite and to the increase in the phase shift of the wave as it passes through the ferrite plate and, as a consequence, to the shift of the amplitude-frequency characteristic.

In [33], the possibility of creating the waveguide photonic crystal with a tunable frequency position of a transparency window associated with the periodicity disturbance in the photonic crystal and with attenuation in this window controlled by *p-i-n* diodes was shown. The 11-layer microwave photonic crystal designed for operation in a 3-cm wavelength range was created, consisting of 11 alternating layers of ceramics $Al_2O_3$ ($\varepsilon_r = 9.6$, thickness of 1 mm) and polystyrene ($\varepsilon_r = 1.1$, thickness of 1 mm). The disturbance of periodicity was provided by using polystyrene plate as the sixth layer. To provide control of the transmittance in the transparency band the *p-i-n*-diode array was used, which was placed into the waveguide in conjunction with the photonic crystal (**Figure 11**).

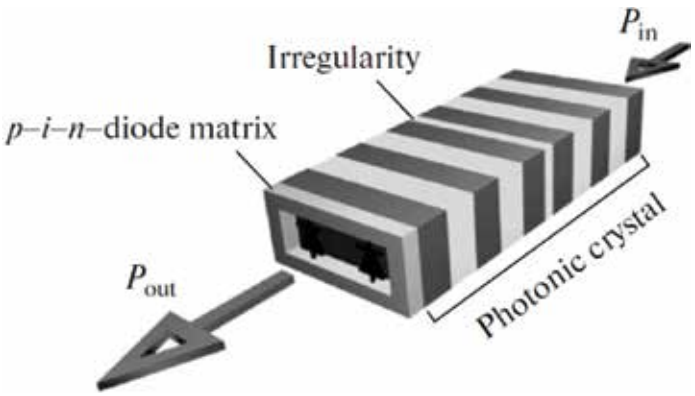


**Figure 11.** The arrangement of the photonic crystal and the *p-i-n*-diode array.

The control voltage regulated in the range 0–700 mV was applied to the *p-i-n*-diodes matrix. The matrix of *p-i-n*-diodes, in the absence of bias voltage, introduces a weak perturbation into the photonic crystal, and its characteristics remain practically unchanged. With increasing bias voltage, this perturbation increases due to the enrichment of the *i*-region by the charge carriers, and specificity for the photonic crystal resonant transmission decreases. The experimental frequency dependences $|S_{12}|^2$, $arg\ S_{12}$ and $|S_{11}|^2$, $arg\ S_{11}$ are shown in **Figure 12** for different bias voltage values on the *p-i-n*-diode with the thickness of the disturbed layer $d_6 = 5$ mm. As it follows from the results in this figure, the use of the microwave photonic crystal makes it possible to create the microwave switch with electrically adjustable characteristics from −1.5 to −25 dB when the bias voltage on *p-i-n* diodes varies from 0 to 700 mV.

It is known that the ring-type structures demonstrate properties of a photonic crystal, such as the presence of forbidden and allowed bands. The band nature of the spectrum in such structures is provided due to multiple reflections from the inhomogeneity in the structure. Such devices in microstrip design are given in [34, 35]. The characteristics of such structures in waveguide design are given in [36]. The element of the type "metal pin with a gap" is used in them as inhomogeneity. This inhomogeneity provides the appearance of a resonant feature in the forbidden band of the system under investigation, called the defect mode resonance or "transparency window." Accordingly, the blocking peak may appear in the allowed band (passband). **Figure 13** shows the design of a microwave element based on diaphragm, the system of coupled frame elements with "pin with a gap" type inhomogeneity located 20 mm to the right of the diaphragm and the semiconductor *n-i-p-i-n*-structure located in the gap between the pin and the frame element.

As it follows from the calculation results, the change in the conductivity of the control element from $10^{-3}$ to $10^5$ S/m leads to a change in the transmission coefficient at 9.44 GHz, corresponding to the blocking peak, in the range −36.79 to −1.01 dB. The system whose construction was described above was investigated experimentally. The bias voltage applied to the *n-i-p-i-n* structure in the 0–9 V range resulted in the change of the transmission coefficient from −25 to −1.5 dB at 9.644 GHz.

http://dx.doi.org/10.5772/intechopen.76797

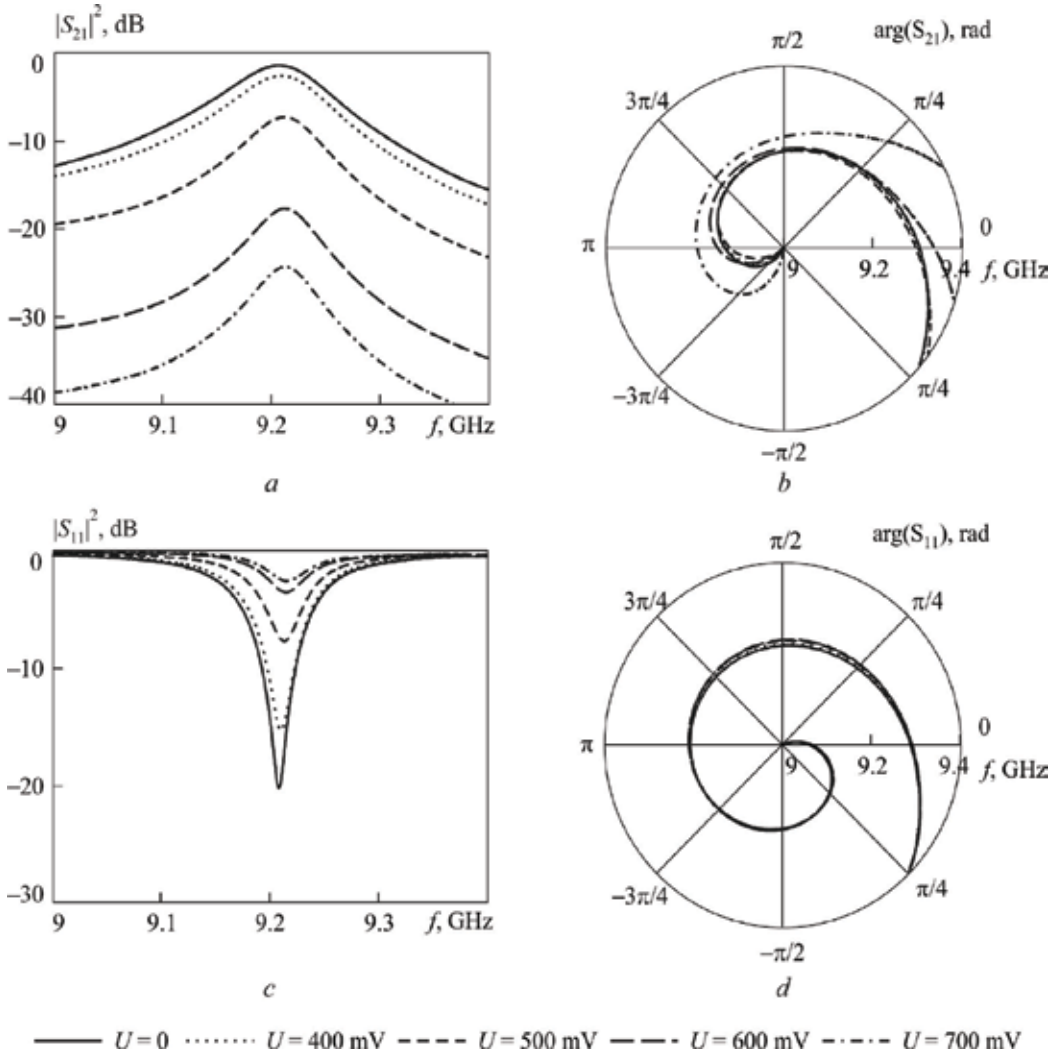


**Figure 12.** Experimental dependences of the square of the modulus (a, b) and phase (b, d) of the transmission (a, b) and the reflection (c, d) coefficients of electromagnetic radiation in the region of the transparency window of a photonic crystal for different values of the voltage on the *p*-*i*-*n*-diode, $d_6 = 5.5$ mm.

### 2.3. Application of microwave photonic crystals

Different directions of practical use of the unique characteristics of microwave photonic crystals were considered in [25]. One of the common names of microwave photonic crystals is structures with a forbidden band. At the same time, it is known that, in addition to the forbidden band (an analog of the band gap in semiconductors), microwave photonic crystals demonstrated the frequency band in which the wave propagates, practically without attenuation. The authors of [37] proposed to use this property to create waveguide broadband

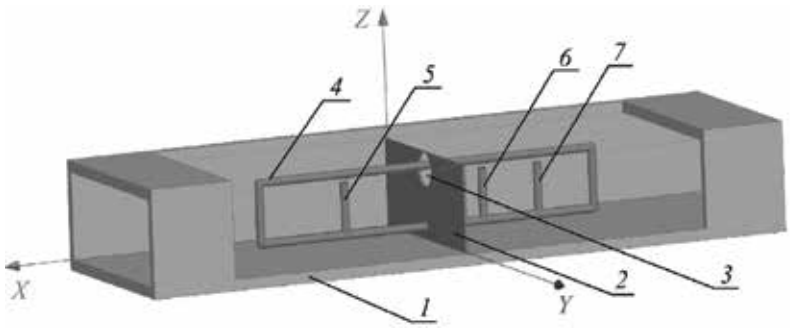


**Figure 13.** Model of the microwave element based on the diaphragm and the system of coupled frame elements containing inhomogeneity in the form of "pin with a gap" designs: 1—waveguide, 2—diaphragm, 3—aperture, 4—frame element, 5–7—inhomogeneities of "pin with a gap" type.

matched loads. The problem of constructing such loads remains one of the topical problems in microwave radioelectronics at the present time. Matched microwave loads are widely used both independently and as elements of complex functional devices: directional couplers, summators, power meters, measuring bridges, microwave filters, and so on [38, 39].

The results of studies of frequency dependences of the reflection coefficients of electromagnetic radiation from one-dimensional photonic crystals containing, along with periodically changing dielectric filling, nanometer metal layers are presented in [9, 10]. Computer simulations were carried to determine the possibility of using one-dimensional photonic crystals for creating matched loads. When calculating the reflection $S_{11}$ and the propagation $S_{21}$ coefficients of an electromagnetic wave, the matrix of wave transfer between regions with different values of the propagation constant of the electromagnetic wave was used, as was described in detail in [10, 16, 17]. During computer simulation in [2], the possibility of creating waveguide matched loads in an 8- and 3-cm wavelength bands was demonstrated.

The authors of [40] showed, as a result of solving the optimization problem, including the choice of the surface resistance of a nanometer metal film, that it was possible to create the matched load of the described above type with the voltage standing wave ratio (VSWR) not more than 1.1 in the frequency bands 8.15–12.05, 12.05–17.44 and 17.44–25.95 GHz. The longitudinal dimensions of the loads were less than 14.5, 10.0, 9.0 mm, respectively. For the frequency range 25.95–37.50 GHz (**Figure 14**), the VSWR of the created load was less than 1.15 with a longitudinal dimension of 6.5 mm.

It is known that reflection and transmission spectra of electromagnetic radiation can be used to measure the thickness and electrical conductivity of a semiconductor in metal-semiconductor structures [15–17]. The sensitivity of these methods depends significantly on how much these spectra are changed under changing the values of the semiconductor parameters. The determination of these parameters from the results of measurements of spectral dependences is called the solution of the inverse problem. The authors of [41] proposed to use for measurements of the parameters of nanometer metal layers on insulating substrates waveguide photonic structures in

http://dx.doi.org/10.5772/intechopen.76797

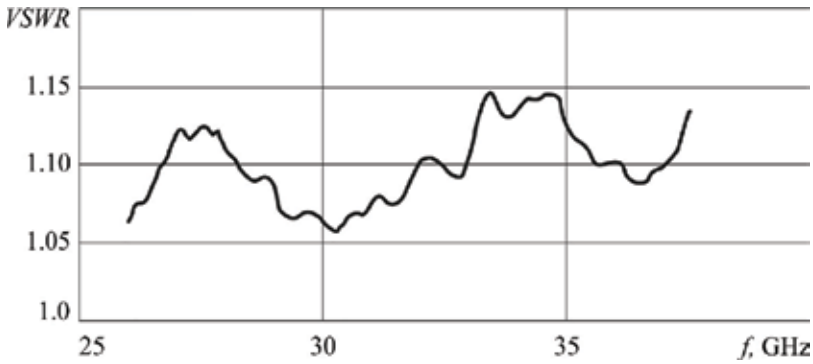


**Figure 14.** Experimental frequency dependence of VSWR in the range 25.95–37.50 GHz.

which the metal-dielectric structure was placed in a segment of a microwave photonic crystal that disturbed its periodicity. In the "forbidden" band of the photonic crystal, the transparency "window," that is sensitive to the sought parameters of the metal-dielectric structure, is seen.

One of the most successful and promising methods for diagnosing materials and structures that allow measurements with high spatial resolution is near-field microwave microscopy [42–44]. A key element of the near-field microwave microscope is a probe with an aperture size much smaller than the wavelength of the microwave radiation. In near-field microwave microscopes, the field of a non-propagating wave type is used as a probing source [16, 42, 43]. This field that is formed if the central conductor of the coaxial line goes beyond the outer conductor [15]. The authors [13] called the microwave resonator connected to the probe as the main element of the near-field microwave microscope, which provides to a greater extent its high sensitivity and resolution.

The increase in the sensitivity of the resonator to the perturbation introduced into it through the probe causes the increase in the sensitivity and resolution of the microwave microscope as a whole.

The design of the resonator in conjunction with the probe element for a near-field microwave microscope is described in [45]. In [46], the results of studying the possibility of using the one-dimensional photonic crystal in which a tunable resonator, serving as a load, allows to control the resonance features in the reflection spectrum of a near-field microwave microscope probe were presented. As such a load, the authors of [46] chose the cylindrical resonator with the coupling element extending beyond the cavity, the end of which is used as a probe of a near-field microscope to monitor the parameters of the dielectric plate with different values of the permittivity and the thickness of nanometer metal layers deposited on dielectric plates.

The general view of the probe of a near-field microwave microscope on the basis of a cylindrical microwave resonator with the coupling frame element and the one-dimensional photonic crystal is shown in **Figure 15**.

The probe based on the cylindrical resonator with a coupling frame element was connected to a segment of the waveguide photonic crystal 9 with the disturbance of the periodicity. The

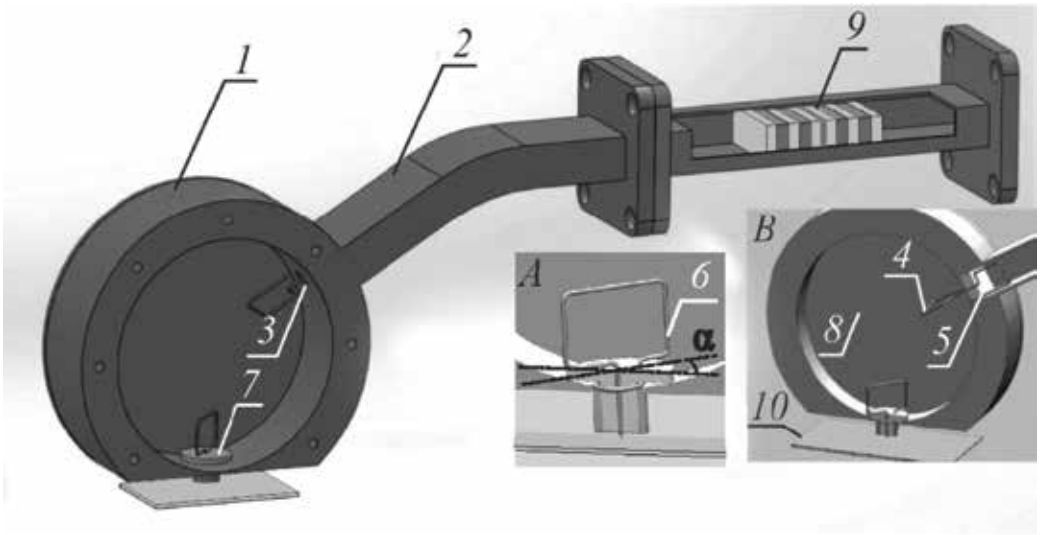


**Figure 15.** Probe of a near-field microwave microscope based on a cylindrical microwave cavity *1* with a communication coupler *6* and a one-dimensional photonic crystal *9*. Insert A is the frame coupling element. Insert B is the cylindrical microwave resonator with the coupling frame element and the measured sample *10*.

one-dimensional waveguide photonic crystal consisting of 11 layers was used in the frequency range 8–12 GHz. The odd layers were made of ceramics $Al_2O_3$ ($\varepsilon_r = 9.6$), even layers were made of teflon ($\varepsilon_r = 2.1$). The length of odd segments was 1 mm, of even segments varied in the range from 7 to 14 mm. The disturbance of periodicity was created by changing the length of the sixth central layer. The length of the disturbed sixth (teflon) layer varied in the range from 3 to 4 mm.

The tip of the probe approaching to the sample caused abrupt change in the input impedance of the probe and the reflection coefficient of the microwave wave from the probe. The magnitude of its change depends on the parameters of the test sample, such as electrical conductivity, permittivity, thickness.

**Figure 16** shows the results of measurements of the frequency dependence of the microwave reflection coefficient in the vicinity of the resonant frequency at a fixed gap (18 μm) between the probe and the samples under study with different dielectric permittivity. **Figure 16** shows the dependences of the microwave reflection coefficient measured at various fixed frequencies in the vicinity of the reflection coefficient minimum on the dielectric permittivity of the samples placed at a fixed distance near the tip of the probe.

The investigated resonance system can also be used to measure samples in the form of dielectric plates with nanometer metal layers of different thicknesses. **Figure 17** shows the results of measurements of the frequency dependences of the microwave reflection coefficient in the vicinity of the resonance frequency at a fixed gap (18 μm) between the probe and the samples under study with different thicknesses of the nanometer metal layer (Cr) in the metal-insulator structure. The thickness of the deposited nanometer metal layers was measured using the Agilent Technologies AFM5600 atomic force microscope.

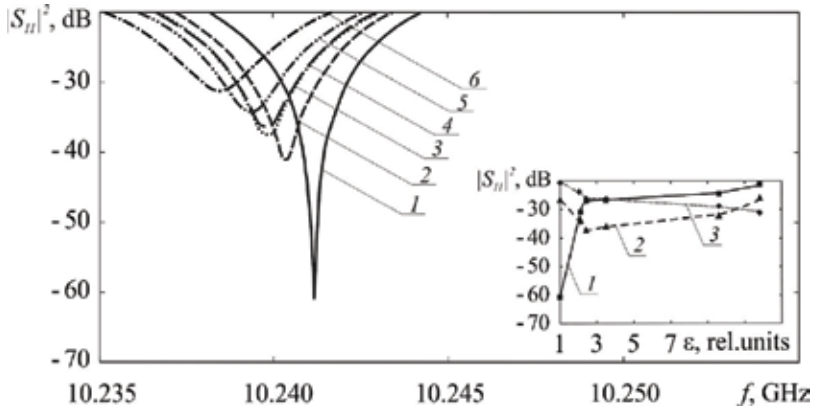


**Figure 16.** Frequency dependences of the microwave reflection coefficient in the vicinity of the resonance frequency at a fixed gap equal to 18 μm between the probe and samples with different dielectric permittivity. Curve 1 corresponds to the absence of the measured sample ($\varepsilon_r = 1$), 2—teflon ($\varepsilon_r = 2.0$), 3—paper-based laminate ($\varepsilon_r = 2.5$), 4—textolite; ($\varepsilon_r = 3.4$), 5—ceramics $Al_2O_3$ ($\varepsilon_r = 9.6$), 6—silicon ($\varepsilon_r = 11.7$).

The inset of **Figure 17** shows the dependences of the microwave reflection coefficient measured at various fixed frequencies (10.77908, 10.77895 and 10.77850 GHz) in the vicinity of the reflection coefficient minimum on the thickness of the nanometer metal layer on ceramics $Al_2O_3$ plates placed at a fixed distance near the tip of the probe.

In [47], it is proposed to implement a method for simultaneous measurement of the substrate thickness of a semiconductor structure, the thickness and conductivity of a heavily doped epitaxial layer, the mobility of free charge carriers in this layer using a one-dimensional microwave photonic crystal. The one-dimensional waveguide photonic crystal consisted of 11 layers, forming a structure of periodically alternating elements, each of which included two

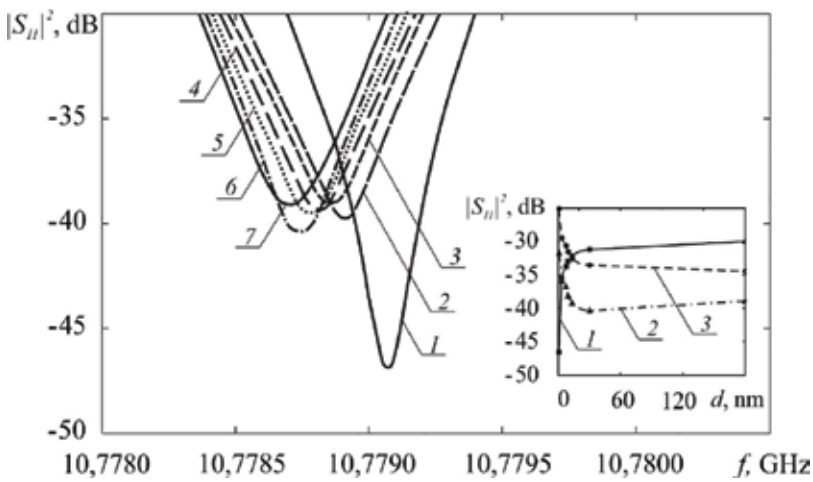


**Figure 17.** Frequency dependences of the microwave reflection coefficient in the vicinity of the resonance frequency at a fixed gap equal to 18 μm between the probe and the samples under study with different thicknesses of the nanometer metal layer Cr: (1) without metallization, (2) $d = 3$ nm, (3) $d = 7$ nm, (4) $d = 9$ nm, (5) $d = 13$ nm, (6) $d = 30$ nm, and (7) $d = 180$ nm.

layers, was considered. The measured structure, placed on the boundary of the disturbed central teflon layer and the next ceramics $Al_2O_3$ layer, was oriented in two ways relative to the direction of the electromagnetic wave propagation. The location of the sample inside the disturbed layer and its orientation relative to the disturbed layer in the photonic crystal are shown in **Figure 18** (configuration 1 and 2).

The investigated samples were epitaxial arsenide-gallium structures of thickness $t_s = t + t_{\text{sub}}$ consisting of an epitaxial layer with a thickness $t$ and electrical conductivity $\sigma$ and a semi-insulating substrate with thickness $t_{\text{sub}}$. The sought values of the investigated sample parameters are determined by the numerical method as a result of solving the system of equations:

$$\frac{\partial S(t_{\text{sub}}, t, \sigma)}{\partial t} = 0; \frac{\partial S(t_{\text{sub}}, t, \sigma)}{\partial t_{\text{sub}}} = 0; \frac{\partial S(t_{\text{sub}}, t, \sigma)}{\partial \sigma} = 0 \tag{10}$$

The residual function $S(t_{\text{sub}}, t, \sigma)$ defined by expression.

$$S(t_{\text{sub}}, t, \sigma) = \sum_{i=1}^{K} \left( \begin{array}{l} \left( |S_{211}(\omega_i,\ t_{\text{sub}}, t, \sigma)|^2 - \left|S_{21i1\ \text{exp}}\right|^2 \right)^2 + \left( |S_{111}(\omega_i,\ t_{\text{sub}}, t, \sigma)|^2 - \left|S_{11i1\ \text{exp}}\right|^2 \right)^2 + \\ + \left( |S_{212}(\omega_i,\ t_{\text{sub}}, t, \sigma)|^2 - \left|S_{21i2\ \text{exp}}\right|^2 \right)^2 + \left( |S_{112}(\omega_i, t_{\text{sub}},\ t, \sigma)|^2 - \left|S_{11i2\ \text{exp}}\right|^2 \right)^2 \end{array} \right), \tag{11}$$

for the case when the thickness of the heavily doped GaAs layer was 13.14 μm, its electrical conductivity $\sigma = 71.73$ Om$^{-1}$ m$^{-1}$, and the thickness of the substrate $t_{\text{sub}} = 480.3$ μm, has a

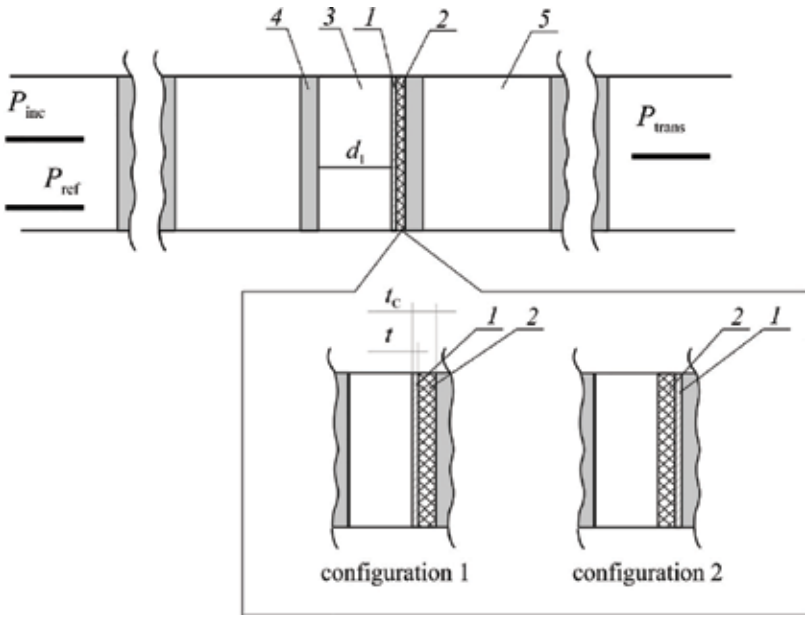


**Figure 18.** Arrangement of the semiconductor structure relative to the disturbed layer in the waveguide microwave 8 photonic crystal: (1) heavily doped semiconductor layer, (2) high-resistance substrate, (3) disturbed central layer, (4) and (5) periodically alternating layers with different values of permittivity.

http://dx.doi.org/10.5772/intechopen.76797

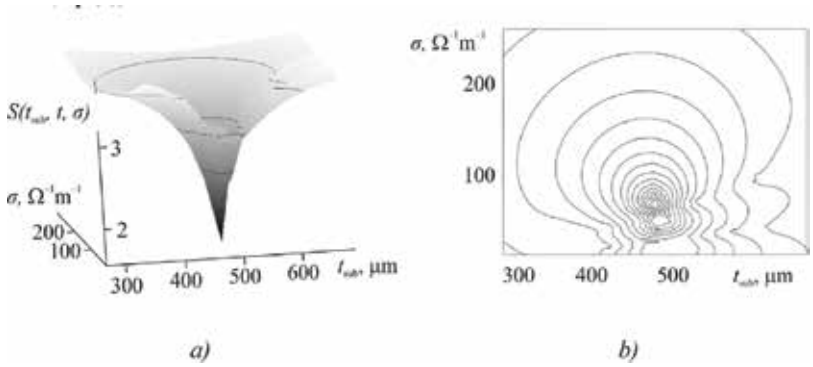


**Figure 19.** The form of the residual function in space and the contour maps in the planes of the sought parameters *a*), *b*) $-(t_{\text{sub}}, \sigma)$ for the gallium arsenide sample with an epitaxial layer of thickness $t = 13.14$ μm and electrical conductivity $\sigma = 71.73\ \text{Om}^{-1}\ \text{m}^{-1}$ grown on a high-resistivity substrate of thickness $t_{\text{sub}} = 480.3$ μm.

global minimum in the coordinate space $(t_{\text{sub}}, t, \sigma, S(t, \sigma))$, and the contour maps (**Figure 19**) are characterized by the presence of closed trajectories near the minimum. This fact determines possibility to obtain the thickness and electrical conductivity of the semiconductor layer from the solution of the system of equations (Eq. (9)).

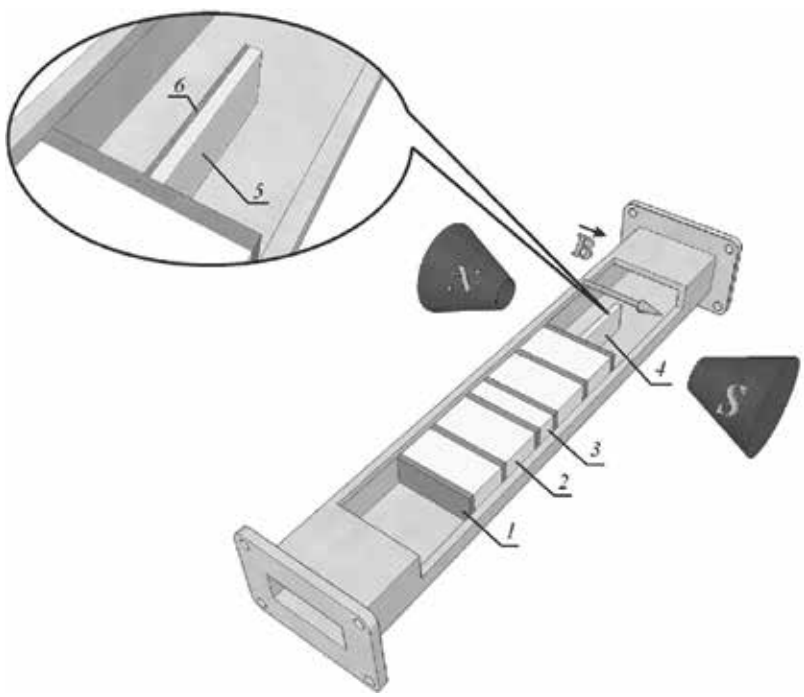


**Figure 20.** Arrangement of the photonic crystal and epitaxial semiconductor structure in the waveguide. 1—ceramics $Al_2O_3$ layer, 2—teflon layer, 3—disturbed teflon layer, 4—tested gallium arsenide structure, which includes: 5—high-resistance substrate, 6—heavily doped semiconductor layer. *N* and *S* are poles of the electromagnet.

To determine the mobility of free charge carriers of semiconductor heavily doped layers, the investigated epitaxial semiconductor structure was placed in the E plane at the center of the cross section of a rectangular waveguide after a waveguide photonic crystal. The magnetic induction vector of the magnetic field $\vec{B}$ was directed perpendicular to the narrow walls of the waveguide (**Figure 20**).

To find the mobility of free charge carriers by frequency dependences $S_{21}(\omega)$ and $S_{11}(\omega)$, the least squares method was used, in which the mobility value $\mu$ corresponding to the minimum value of the sum of the squares of the differences between the calculated $\left|S_{21}(\omega,\mu)\right|^2$ and $\left|S_{11}(\omega,\mu)\right|^2$ and the experimental $\left|S_{21_{\exp}}\right|^2$ and $\left|S_{11e_{xp}}\right|^2$ values of the squares of the modules of the transmission and reflection coefficients measured under the influence of the magnetic field and without it. The sought mobility values for two measured structures with thicknesses of heavily doped semiconductor layers of $t = 2.17$ and 13.14 μm were determined numerically and amounted to 0.591 $m^2$/(V*s) and 0.72 $m^2$/(V*s), respectively.

## 3. Conclusions

This chapter presents the results of theoretical and experimental studies of one-dimensional microwave photonic crystals based on rectangular waveguides characterized by the presence of forbidden and allowed bands for the propagation of electromagnetic waves. Methods for describing the electrodynamic characteristics of photonic crystals and their relationship with the parameters of periodic structures filling the waveguides have been presented. The change in the width of the allowed and forbidden bands of a photonic crystal has been described when a defect mode occurs because of the creation of the disturbance of the periodicity of the photonic crystal structure. The change in the amplitude-frequency characteristics of microwave photonic crystals has been considered. The types of disturbances and defect modes have been described. The results of the investigation on the characteristics of waveguide microwave photonic crystals created in the form of dielectric matrices with air inclusions have been presented. It has been shown that the layers of the investigated photonic crystals containing a large number of air inclusions can be considered as composite materials. New types of low-dimensional microwave waveguide photonic crystals containing periodically alternating elements that are the source of higher type waves have been described. The possibility of effective control of the amplitude-frequency characteristics of microwave photonic crystals by electric and magnetic fields has been analyzed. The examples of applications of waveguide microwave photonic crystals such as methods for measuring the parameters of materials and semiconductor nanostructures that play the role of periodicity disturbance of the microwave photonic crystals; resonators of near-field microwave microscopes; small-sized broadband matched loads of centimeter and millimeter wavelengths ranges based on microwave photonic crystals have been given.

## Acknowledgements

The research was carried out with the financial support of the Ministry of Education and Science of the Russian Federation (state task №8.7628.2017/BCH).

## Author details

Dmitry Usanov and Alexander Skripal *

*Address all correspondence to: skripala_v@info.sgu.ru

Saratov State University, Russia

## References

[1] Keldysh LV. The influence of ultrasound on the electronic spectrum of a crystal. Physics of the Solid State. 1962;**8**:2265-2267

[2] Esaki L, Tsu R. Superlattice and negative differential conductivity in semiconductors. IBM Journal of Research and Development. 1970;**14**:61-65. DOI: 10.1147/rd.141.0061

[3] Joannopulos J, Villeneuve PR, Fan S. Photonic crystals: Putting a new twist on light. Nature. 1997;**386**:143-146. DOI: 10.1038/386143a0

[4] Yablonovitch E. Inhibited spontaneous emission in solid-state physics and electronics. Physical Review Letters. 1987;**58**:2059-2063. DOI: 10.1103/PhysRevLett.58.2059

[5] John S. Strong localisation of fotons in certain disordered dielectric superlattices. Physical Review Letters. 1987;**58**:2486-2491. DOI: 10.1103/PhysRevLett.58.2486

[6] Zaitsev DF. Nanophotonics and Its Application. Moscow: Acteon; 2012. 445p

[7] Silin RA, Sazonov VP. Delay-Line Systems. Moscow: Soviet Radio; 1966. 628p

[8] Tae-Yeoul, Chang K. Uniplanar one-dimensional photonic-bandgap structures and resonators. IEEE Transactions on Microwave Theory and Techniques. 2001;**49**:549-553. DOI: 10.1109/22.910561

[9] Usanov D, Skripal Al, Abramov A, Bogolyubov A, Skvortsov V, Merdanov M. Measurement of the metal nanometer layer parameters on dielectric substrates using photonic crystals based on the waveguide structures with controlled irregularity in the microwave band. In: Proceedings of 37th European Microwave Conference; 8–12 October 2007; Munich, Germany. pp. 198-201. DOI: 10.1109/EUMC.2007.4405160

[10] Gulyaev YV, Nikitov SA. Photonic and magnetophotonic crystals—A new medium for information transfer. Radioengineering. 2003;**8**:26-30

[11] Samoilovich MI, Tsvetkov MY. Rare earth opal nanocomposites for nanophotonics. Nano- and Microsystem Technology. 2006;**10**:8-14

[12] Kul'chin YN, Bagaev SN, Bukin OA, Voznesenskiĭ SS, Drozdov AL, Zinin YA, Nagornyĭ IG, Pestryakov EV, Trunov VI. Photonic crystals based on natural oceanic biominerals. Technical Physics Letters. 2008;**8**:633-635. DOI: 10.1134/S1063785008080014

[13] Usanov DA, Rytik AP. Properties of a photonic crystal formed in a solution featuring the Briggs–Rauscher oscillating reaction. Technical Physics Letters. 2016;**42**:629-631. DOI: 10.1134/S1063785016060304

[14] Gomez A, Vegas A, Solano MA, Lakhtakia A. On one- and two-dimensional electromagnetic band gap structures in rectangular waveguides at microwave frequencies. Electromagnetics. 2005;**25**:437-460. DOI: 10.1080/02726340590957443

[15] Usanov DA, Skripa AV, Abramov AV, Bogolyubov AS. Determination of the metal nanometer layer thickness and semiconductor conductivity in metal-semiconductor structures from electromagnetic reflection and transmission spectra. Technical Physics. 2006;**5**:644-649. DOI: 10.1134/S1063784206050173

[16] Chaplygin YA, Usanov DA, Skripal AV, Abramov AV, Bogolyubov AS. The technique for measuring the electrical conductivity of nanometer metal films in layered structures from the reflection spectra of electromagnetic radiation. Electronics. 2006;**6**:27-35. In: Proceedings of the Universities

[17] Usanov DA, Skripal AV, Abramov AV, Bogolyubov AS, Kalinina NV. Measurements of thickness of metal films in sandwich structures by the microwave reflection spectrum. In: Proceedings of 36th European Microwave Conference; 10–15th September 2006; Manchester, UK; pp. 509-512. DOI: 10.1109/EUMC.2006.281071

[18] Usanov DA, Nikitov SA, Skripal' AV, Ponomarev DV. Resonance features of the allowed and forbidden bands of the microwave photonic crystal with periodicity defects. Journal of Communications Technology and Electronics. 2013;**58**:1035-1040. DOI: 10.1134/S1064226913110120

[19] Usanov DA, Skripal AV, Merdanov MK, Gorlitskii VO. Dielectric matrices with air cavities as a waveguide photonic crystal. Technical Physics. 2016;**61**:221-226. DOI: 10.1134/S1063784216020250

[20] Maxwell-Garnett JC. Colours in metal glasses and in metallic films. Philosophical Transactions of the Royal Society. 1904;**203**:385-420

[21] Bruggeman DAG. Dielectric constant and conductivity of mixtures of isotropic materials. Ann. Phys. 1935;**8**:636-679

[22] Lichtenecker K. Dielectric constant of natural and synthetic mixtures. Physikalische Zeitschrift. 1926;**4**:115-158

[23] Belyaev BA, Voloshin AS, Shabanov VF. Study of microstrip models of bandpass filters based on 1D photonic crystals. Doklady Physics. 2005;**50**:7-11. DOI: 10.1134/1.1862365

[24] Fernandes HCC, Medeiros JLG, Junior IMA, Brito DB. Photonic crystal at millimeter waves applications. PIERS Online. 2007;**3**:689-694. DOI: 10.2529/PIERS060901105337

[25] Ozbay E, Temelkuran B, Bayindir M. Microwave applications of photonic crystals. Progress In Electromagnetics Research. 2003;**41**:185-209. DOI: 10.1007/978-94-009-1665-4_19

[26] Saib A, Huynen I. Periodic metamaterials combining ferromagnetic nanowires and dielectric structures for planar circuits applications. Electromagnetics. 2006;**26**:261-277. DOI: 10.1080/02726340600570336

[27] Gulyaev YV, Nikitov SA, Usanov DA, Skripal AV, Posadskii VN, Tiazhlov VS, Baykin AV. Low-dimensional waveguide microwave photonic crystals. Doklady Physics. 2014;**59**:437-440. DOI: 10.1134/S1028335814100024

[28] Usanov DA, Skripal AV, Posadskii VN, Tiazhlov VS, Baykin AV. The defect mode in a low-dimensional waveguide microwave photonic crystal. Technical Physics Letters. 2016; **42**:550-552. DOI: 10.1134/S106378501605031X

[29] Cohn SB. Direct-coupled-resonator filters. Proceedings of the IRE. 1957;**45**:187-196

[30] Usanov DA, Skripal AV, Merdanov MK, Evteev SG. Waveguide photonic structures based on resonance diaphragms. Radioengineering. 2015;**10**:108-114

[31] Britun NV, Danilov VV. Photonic bandgap structures with electronically controlled characteristics. Technical Physics Letters. 2003;**29**:277-279. DOI: 10.1134/1.1573289

[32] Kuriazidou CA, Contopanagos HF, Alexopolos NG. Monolithic waveguide filters using printed photonic-bandgap materials. IEEE Transactions on Microwave Theory and Techniques. 2001;**2**:297-306. DOI: 10.1109/22.903089

[33] Usanov DA, Skripal AV, Abramov AV, Bogolyubov AS, Skvortsov VS, Merdanov MK. Waveguide photonic crystals with characteristics controlled by p-i-n-diodes. Electronics. 2010;**1**:24-29. In: Proceedings of the Universities

[34] Kim S-I, Jang M-Y, Kee C-S, Park I, Lim H. Characteristics of microwave filters based on microstrip photonic bandgap ring structures. Current Applied Physics. 2005;**5**:619-624. DOI: 10.1016/j.cap.2004.08.008

[35] Kee C-S, Jang M-Y, Kim S-I, Park I, Lim H. Tuning and widening of stop bands of microstrip photonic band gap ring structures. Applied Physics Letters. 2005;**86**:181109. DOI: 10.1063/1.1906315

[36] Usanov DA, Nikitov SA, Skripal' AV, Frolov AP, Orlov VE. Waveguides containing frame elements with electrically controlled characteristics of permitted and forbidden bands. Journal of Communications Technology and Electronics. 2014;**59**:1101-1106. DOI: 10.1134/S1064226914110230

[37] Usanov DA, Skripal AV, Abramov AV, Bogolyubov AS, Skvortsov VS, Merdanov MK. Broadband waveguide matched loads based on photonic crystals with nanometer metal layers. Radioelectronics. 2009;**1**:73-80. In: Proceedings of the Universities

[38] Helszajn J. Passive and Active Microwave Circuits. New York, Chichester, Brisbane, Toronto: John Wiley & Sons; 1978. 284p

[39] Lee KA, Guo Y, Stimson PA, Potter KA, Jung-Chih C, Rutledge DB. Thin-film power-density meter for millimeter wavelengths. IEEE Transactions on Antennas and Propagation. 1991;**39**:425-428. DOI: 10.1109/8.76347

[40] Usanov DA, Meshchanov VP, Skripal' AV, Popova NF, Ponomarev DV, Merdanov MK. Centimeter- and millimeter-wavelength matched loads based on microwave photonic crystals. Technical Physics. 2017;**62**:243-247. DOI: 10.1134/S106378421702027X

[41] Usanov DA, Skripal AV, Abramov AV, Bogolyubov AS, Skvortsov VS, Merdanov MK. Using waveguide photonic structures to measure the parameters of nanometer metal layers on insulating substrates. Electronics. 2007;**6**:25-32. In: Proceedings of the Universities

[42] Anlage SM, Steinhauer DE, Feenstra BJ, Vlahacos CP, Wellstood FC. Near-field microwave microscopy of materials properties. Microwave Superconductivity. 2001;**375**:239-269. DOI: 10.1007/978-94-010-0450-3_10

[43] Usanov DA. Nearfield Scanning Microwave Microscopy and Its Applications. Saratov: Saratov University Publishing House; 2010. 100p

[44] Usanov DA, Gorbatov SS. Near Field Effects in Electrodynamic Systems with Inhomogeneities and their Application in Microwave Technology. Saratov: Saratov University Publishing House; 2011. 392p

[45] Usanov DA, Skripal' AV, Frolov AP, Nikitov SA. Microwave near-field microscope based on a photonic crystal with a cavity and a controlled coupling element as a probe. Journal of Communications Technology and Electronics. 2013;**12**:1130-1136. DOI: 10.1134/S1064226913120176

[46] Usanov DA, Nikitov SA, Skripal AV, Orlov VE, Frolov AP. The patent of the Russian Federation for utility model 144 869 U1 IPC The device for measuring the permittivity of plates and thicknesses of nanometer conductive films. G01N 22/00 B82B 1/00 Application: 2013125178/07 dated 05/30/2013; Pub. 10/09/2014; Bul. 25

[47] Usanov DA, Nikitov SA, Skripal' AV, Ponomarev DV, Latysheva EV. Multiparametric measurements of epitaxial semiconductor structures with the use of one-dimensional microwave photonic crystals. Journal of Communications Technology and Electronics. 2016;**61**:42-49. DOI: 10.1134/S1064226916010125

Chapter 3

# High-Gain Amplifier Module Integrating a Waveguide into the Module Case for Millimeter Wave Applications

Young Chul Lee

Additional information is available at the end of the chapter

http://dx.doi.org/10.5772/intechopen.76622

**Abstract**

A high-gain amplifier module with integrated waveguide (WG) has been presented for millimeter wave applications. In order to improve the isolation between the amplification stages in the multi-stage amplifier module, an isolated WG is integrated into the module case. It is possible to effectively suppress the oscillation occurring in the high gain stage. Microstrip line (MSL)-to-WG transitions are designed and fabricated on a 5 mil thick RT5880 substrate for interconnection of the isolated WG, input/output WG and amplifier PCB in a cascaded two-stage high gain amplifier module. The transition loss of −0.44 dB is obtained at 40 GHz and return-loss ($S_{11}$) bandwidth below −10 dB is from 34.1 to 50 GHz. The fabricated high-gain amplifier module shows a high gain over 39.7 dB from 38 to 41 GHz. At 38.7 GHz, its maximum gain of 44.25 dB is achieved.

**Keywords:** waveguide, isolation, microstrip-to-waveguide transition, amplifier module

## 1. Introduction

Recently, millimeter-wave (mm-wave) frequency bands have attracted attention as various applications such as radar sensors [1–3] as well as wireless communication. In particular, due to very widely available bandwidth, frequency bands for a variety of wireless communication applications such as point-to-point wireless communications, radio-on-fiber (RoF) links [4], 5G cellular wireless networks [5], etc. are shifting to the mm-wave frequency band.

One of the key issues for the commercialization of mm-wave systems is reproducible and inexpensive packaging technology in addition to active integrated circuit (IC) technology.

Typically, active IC chips are assembled into metal or dielectric substrate carriers using wire-bonding or flip-chip [6] interconnect and eventually encapsulated in plastic packages or metal housings. Due to the integration of various materials and structures in a compact, limited packaging space, unwanted substrate modes [6], cavity resonance [7], feedback, or crosstalk [8, 9] occur within the packaging module. In the previous papers [6–9], this phenomenon was well analyzed and the causes were identified and design rules or various methods for suppressing them were presented. For example, the resistivity [6] of the flip chip carrier, the resonance condition of the cavity [7], the chip mounting design rule [8], and the resistance coating of the lid [10] were investigated. Several modules [1, 2, 6, 11] have been successfully developed to reflect these attempts. However, in the case of a high-gain amplification block requiring a gain of 30 dB or more, the stability problem is caused by the feedback effect [8, 9] of the reflected signal due to structural discontinuities in the packaging. That is, the radiated signals are reflected by the surrounding structures, enter the input stage of the amplification block, and are amplified, so that the entire module oscillates. Therefore, to eliminate the oscillation of the amplification block, small and medium gain amplifier modules [2, 12, 13] are connected in series using an external WG until the required gain is satisfied. An attenuator or filter is inserted between the amplifier modules to adjust the gain or remove unwanted waves [14]. However, these methods lead to bulky and expensive mm-wave radio system due to expensive additional components.

In this work, a 40 dB high-gain amplifier module integrating the isolation WG has been demonstrated for 40 GHz radio system applications. Because of the isolation WG as well as input and output WG into the metal case of the amplifier module, a low-loss and wideband MSL-to-WG transition is designed on the 5-mil thick RT5880 substrate to interconnect the amplifier IC mounted PCB with integrated WG. The simulated and tested results of the transition have been presented. The high-gain amplifier module was fabricated and its measured performance is analyzed.

## 2. Metal case integrating an isolation WG for high-gain amplifier module

In general, a proactive approach to suppressing this feedback effect is to effectively isolate the two adjacent amplification stages. **Figure 1** shows the metal case inserting a 15.7 mm long isolation WG between two cavities for high-gain amplifier module applications [15]. This method allows high-gain amplification without oscillation because of good isolation between two enclosed cavities in the metal case. In the each cavity, the PCB mounting an amplifier IC is assembled. Because signals radiated due to discontinuities in the metal case or PCB assembly are confined within each cavity, the amplifier IC assembled in another cavity is protected. In this work, the MSL-to-WG transition in the isolation WG as well as an input and output WG port should be designed. The WG is based on WR22 WG, whose size is $2.84 \times 5.68$ mm$^2$. Two commercial amplifier ICs [16] are used for high-gain amplification block with the gain of 40 dB. The signal line on the PCB is the 50 Ω microstrip line (MSL). Considering the inserted isolation WG and port WGs, four MSL-to-WG transitions are needed. The main key design issue is the low-loss and wide-band transition.

http://dx.doi.org/10.5772/intechopen.76622

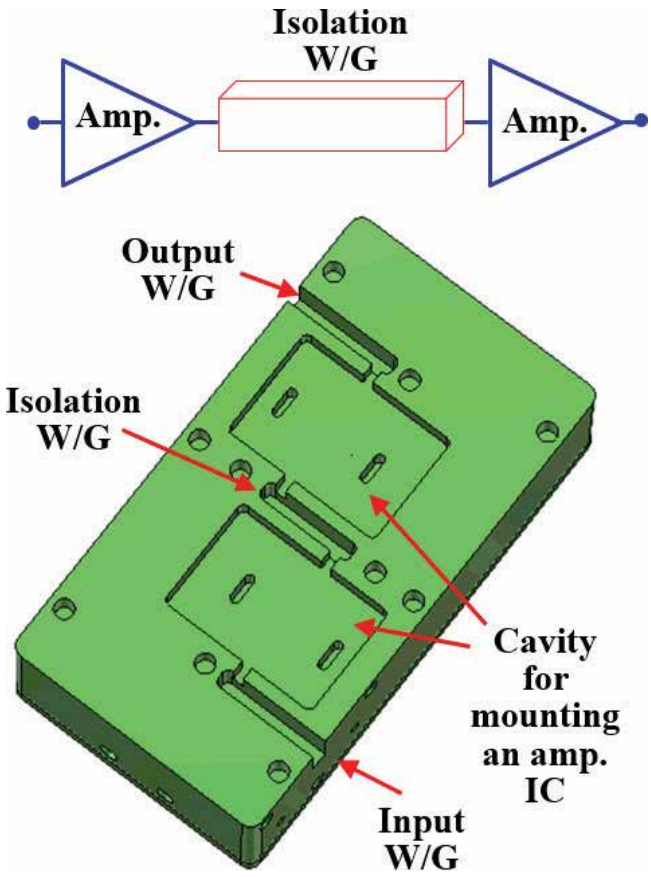


**Figure 1.** The metal case integrating an isolation WG for high-gain amplifier module applications.

## 3. Design and measurement of the low-loss and wideband MSL-to-WG transition

**Figure 2** presents a configuration of the MSL probe transition, transition module for measurement, and opening in the WG side to insert the transition. For this MSL-to-WG transition, a simple electric (E)-plane transition [17, 18] is used because of easy and simple design. In this transition, a TE10-mode energy in the WG couples to quasi-TEM-mode one in the MSL. The MSL transition consists of an E-plane probe, impedance transformer, and 50-Ω MSL. They are printed on a 5 mil thick substrate with a permittivity of 2.2 [19]. The size of the E-probe is 383 × 1465 μm$^2$. The simple high-impedance matching line with is designed for easy design and optimization. Its size is 295 μm × 1000 μm. The 363 μm wide MSL is designed for the 50-Ω impedance and its length between two transitions is 18.0 mm considering the cavity size in the metal case as shown in **Figure 2(b)**. A back-to-back structure is required for measurement of the fabricated MSL-to-WG transition. Two sets of the back-to-back structured transition are required to apply to the metal case as shown in **Figure 2(b)**. The E-probe of the transition is

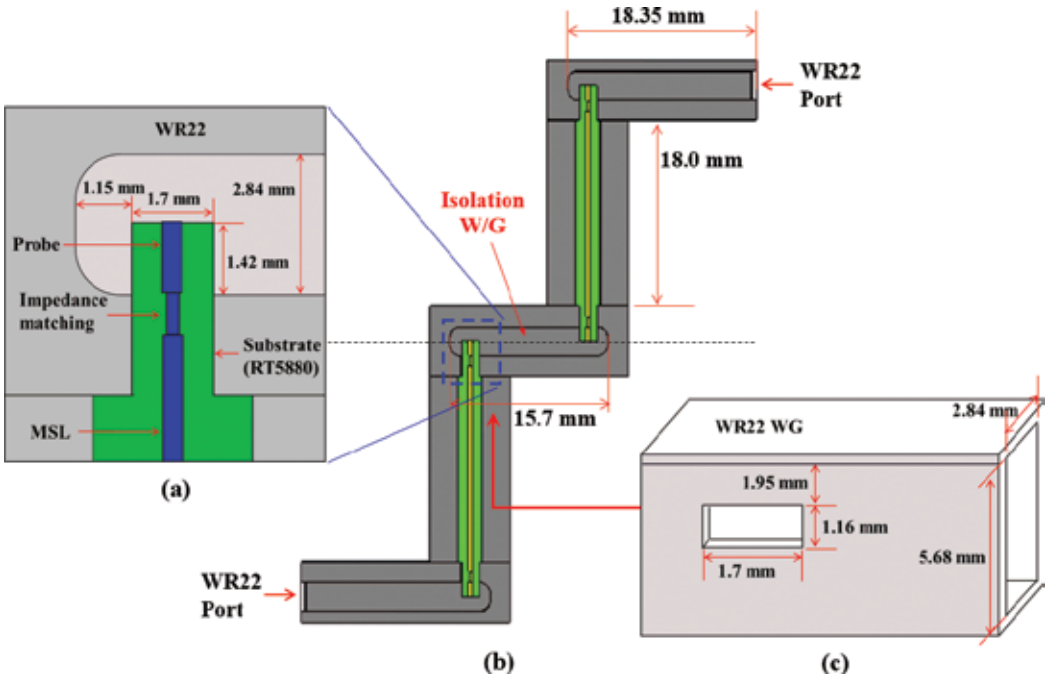


**Figure 2.** The configuration of the MSL probe transition (a), transition module consisting of four MSL-to-WG transitions (b), and opening in the WG side into which the transition is inserted.

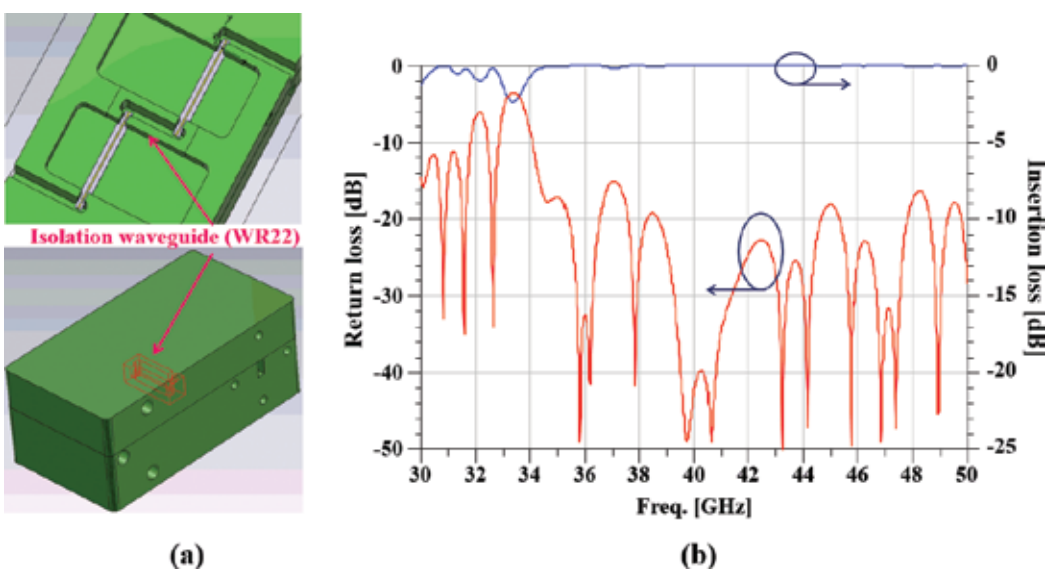


**Figure 3.** The metal case integrating transitions (a) and the designed results of the transition (b).

inserted into the side opening of the WG. Of course, its position and size should be optimized and the final dimensions are shown in **Figure 2(c)**.

Using electromagnetic (EM) analysis software [20], transitions were designed and analyzed. In **Figure 3**, the design model and results are presented. The transitions are designed to be assembled in the metal case. Since the WG must be integrated in the metal case, it is divided into two parts, the body and the lid. In **Figure 3(a)** and **(b)**, the metal case integrating transitions and the designed results are presented, respectively. In these designed results, an input

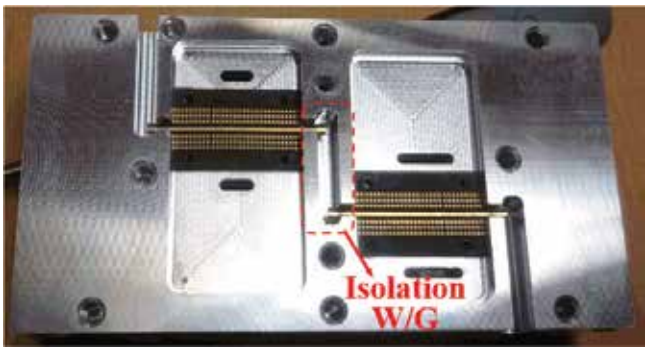


**Figure 4.** Fabricated transitions and assembled in the metal case.

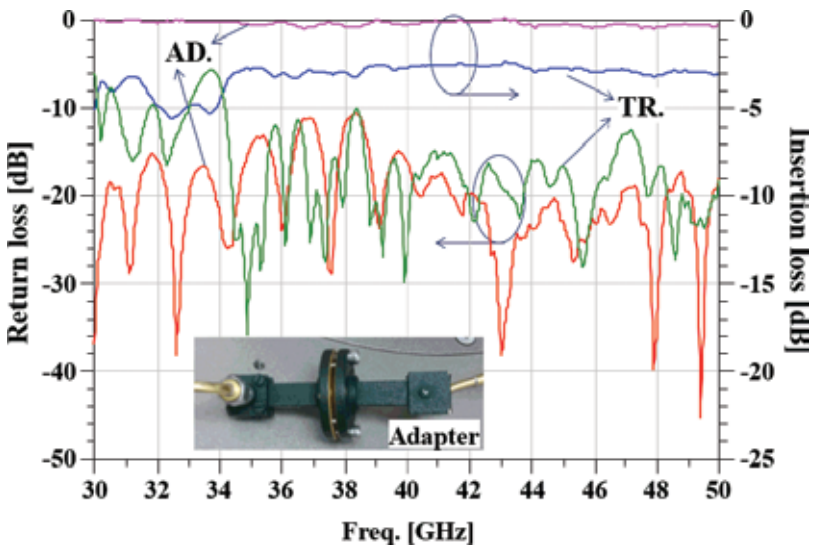


**Figure 5.** Measured results of the fabricated two-set transition (TR) in the back-to-back structure [an inset: an adapter connection, AD: adapters].

return loss (S11) less than −10 dB and insertion loss (S21) lower than −0.52 dB are obtained from 34.09 GHz up to 50 GHz.

The designed transitions were realized on the RT5880 substrate in commercial PCB foundry and two sets of the fabricated transitions were assembled on the metal case for the high-gain amplifier module as shown in **Figure 4**.

The measured loss characteristics of the adapters and fabricated transitions are presented as shown in **Figure 5**. Since the input and output port of the fabricated metal case is the WR22 WG, a 2.4 mm-male cable-to-WR22 WG adapters were used for connection with a vector network analyzer (VNA, Agilent N5250A) as shown in an inset of **Figure 5**. Losses of the adapters and the assembled two-set transitions were tested using the standard open-short-load (SOL) calibration from 30 to 50 GHz. The measured insertion and return loss of the adapters (AD) are from −0.26 to −0.33 dB and less than −10 dB, respectively, from 30 to 50 GHz. For the assembled two-set transitions (TR), the insertion losses of −2.9 and − 2.5 dB are observed at 38 and 41 GHz, respectively. This measured insertion loss of the transition includes several loss components came from the adapters, two 18 mm long MSLs with the loss of −0.0239 dB/mm, and the MSL-to-WG transitions. By considering these loss components, the loss per a single transition is −0.32 and −0.44 dB at 38 and 41 GHz, respectively. Its measured return loss of the transition is below −10 dB from 34.1 to 50 GHz. The operational bandwidth (BW) of the transition for a return loss of −10 dB is 15.9 GHz.

## 4. Fabrication and measurement of the high-gain amplifier module

The high-gain amplifier module was designed and fabricated for the purpose of demonstration of the isolation WG integrated in its metal case. **Figure 6** presents PCB layout to mount

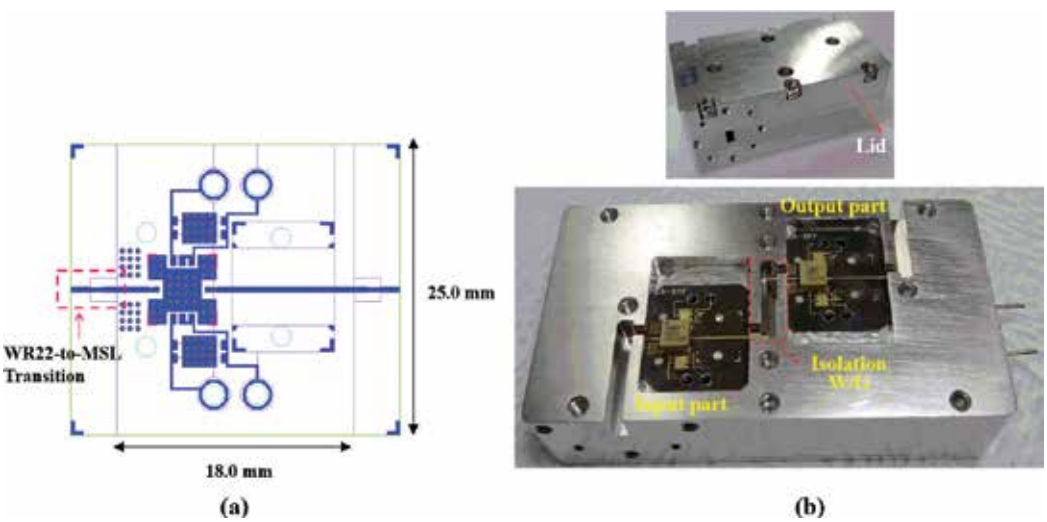


**Figure 6.** PCB layout to mount the amplifier IC (a) and the fabricated high-gain amplifier module (b).

the amplifier IC and the fabricated high-gain amplifier module. Landing patterns to mount a SMT-type amplifier IC [16] are designed on the RT5880 substrate by referring to application note [21] as shown in **Figure 6(a)**. In this substrate, MSL-to-WG transitions are also included to connect with WG. The designed PCB were fabricated and assembled with several components. Two PCBs were assembled in the metal case. The assembled high-gain amplifier module and the lid closed one are shown in **Figure 6(b)**. Its overall size is 79 × 42 × 32 $mm^3$.

The insertion and return losses of the fabricated high-gain amplifier module were measured at DC bias conditions (Vd = 5 V and Id = 1000 mA) and the measured results are presented in **Figure 7**. For comparison purposes, the characteristics plotted based on the data in a datasheet of the single amplifier IC [16] are also shown. For the high gain amplifier module, the gain more than 39.7 dB was measured at 38–41 GHz. At 38.7 GHz, the maximum gain of 44.25 dB is obtained [15].

Considering a single amplifier IC with the gain of 20 dB, a gain of 40 dB for the high-gain amplifier module connecting two amplifier ICs in series means that the transition loss is negligible. Therefore, these results demonstrate that the isolation WG provides good isolation between two amplifier ICs and suppress effectively feedback effects in the high-gain amplification block. Compared to the return losses (|S11| data and |S22| data) of the single amplifier IC, the return loss (|S22| meas) at output connection part of the high-gain amplifier module is

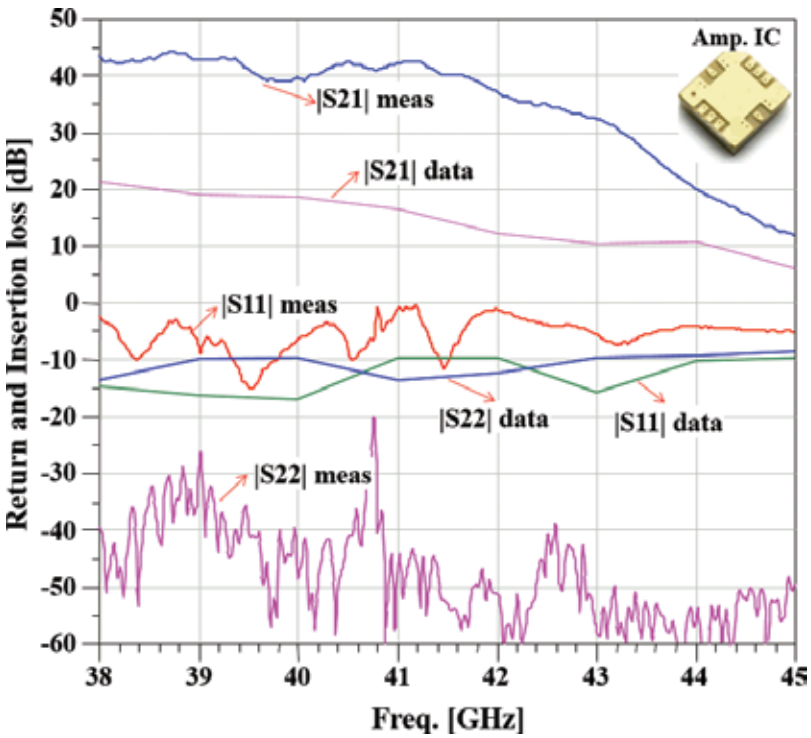


**Figure 7.** Measured results of the fabricated high-gain amplifier module, compared to amplifier IC (AMMP-6441) ones from its data sheet [M: measurement and amp. IC: data sheet of an amplifier IC].

noticeably improved, but the return loss (|S11| meas) at its input connection part is degraded. In general, the return loss of an assembled amplifier module follows the return loss characteristic of the transition. Therefore, the improvement of |S22| meas is due to the characteristics of the transition. However, the deterioration of |S11| meas at the input stage is caused by alignment and PCB fabrication process problems during assembly of the WG and PCB transitions.

## 5. Conclusion

The 40 dB high-gain amplifier module with the isolation waveguide (WG) has been presented for millimeter wave applications. For the purpose of suppressing the oscillation due to the feedback effect, the isolation WG was integrated into the metal case of the amplifier module. In addition to input/output WG of the amplifier module, additional MSL-to-WR22 WG transitions are required due to the isolation WG and low-loss and wide-band transition is designed and manufactured on the 5 mil thick RT5880 substrate. Its measured loss and operational bandwidth were less than −0.44 dB/a transition and 15.9 GHz, respectively at 40 GHz. The high-gain amplifier module was designed and fabricated for the purpose of demonstration of the isolation WG. The amplifier module operated stably without oscillation at high gain over 40 dB. The fabricated high-gain amplifier module showed a high gain over 39.7 dB from 38 to 41 GHz. Its maximum gain of 44.25 dB was obtained at 38.7 GHz.

## Author details

Young Chul Lee

Address all correspondence to: rfleeyc@gmail.com

Division of Marine Mechatronics, Mokpo National Maritime University, Republic of Korea

## References

[1] Tessmann A, Kudszus S, Feltgen T, Riessle M, Sklarczyk C, Haydl WH. A 94 GHz single-chip FMCW radar module for commercial sensor. In: IEEE MTT-S International Microwave Symposium. Vol. 3. 2002. pp. 1851-1854. DOI: 10.1109/MWSYM. 2002.1012223

[2] Tessmann A, Leuther A, Kuri M, Massler H, Riessle M, Essen H, Stanko H, Sommer R, Zink M, Stibal R, Reinert W, Schlechtweg M. 220 GHz low-noise amplifier modules for radiometric imaging applications. In: The 1st European Microwave Integrated Circuits Conference. 2006. pp. 137-140. DOI: 10.1109/EMICC.2006.282770

[3] Kim J-G, Kang D-W, Min B-W, Rebeiz GM. A single-chip 36-38 GHz 4-element transmit/receive phased-array with 5-bit amplitude and phase control. In: IEEE MTT-S International Microwave Symposium. 2009. pp. 561-564. DOI: 10.1109/MWSYM.2009.5165758

[4] Yaakob S, Samsuri NM, Mohamad R, Farid NE, Azmi IM, Hassan SMM, Khushairi N, Rahim SAEA, Rahim AIA, Rasmi A, Zamzuri AK, Idrus SM, Fan S. Live HD video transmission using 40GHz radio over fibre downlink system. In: IEEE 3rd International Conference on Photonics (ICP). 2012. pp. 246-249. DOI: 10.1109/ICP.2012.6379854

[5] Al-Falahy N, Omar YA. Technologies for 5G networks: Challenges and opportunities. IT Professional. 2017;**19**(1):12-20. DOI: 10.1109/MITP.2017.9

[6] Tessmann A, Riessle M, Kudszus S, Massler H. A flip-chip packaged coplanar 94 GHz amplifier module with efficient suppression of parasitic substrate effects. IEEE Microwave and Wireless Components Letters. 2004;**14**:145-147. DOI: 10.1109/LMWC.2004.827115

[7] Dhar J, Arora RK, Dasgupta A, Rana SS. Enclosure effect on microwave power amplifier. Progress in Electromagnetics Research C. 2011;**19**:163-177

[8] Krems T, Tessmann A, Haydl WH, Schmelz C, Heide P. Avoiding cross talk and feedback effects in packaging coplanar millimeter-wave circuits. In: IEEE MTT-S International Microwave Symposium. Vol. 2. 1998. pp. 1091-1094. DOI: 10.1109/MWSYM.1998.705183

[9] Beilenhoff K, Heinrich W. Excitation of the parasitic parallel-plate line mode at coplanar discontinuities. In: IEEE MTT-S International Microwave Symposium. Vol. 3. 1997. pp. 1789-1792. DOI: 10.1109/MWSYM.1997.596891

[10] Yook J-G, Katehi LPB, Simons RN, Shalkhauser KA. Experimental and theoretical study of parasitic leakage/resonance in a K/Ka-band MMIC package. IEEE Transactions on Microwave Theory and Techniques. 1996;**44**(2):403-410. DOI: 10.1109/22.554569

[11] Lee YC, Chang W-I, Park CS. Monolithic LTCC SiP transmitter for 60GHz wireless communication terminals. In: IEEE MTT-S International Microwave Symposium. 2005. pp. 1015-1018. DOI: 10.1109/MWSYM.2005.1516839

[12] Radisic V, Mei X, Sarkozy S, Yoshida W, Liu P-H, Uyeda J, Lai R, Deal WR. A 50 mW 220 GHz power amplifier module. In: IEEE MTT-S International Microwave Symposium. 2010. pp. 45-48. DOI: 10.1109/MWSYM.2010.5515248

[13] Tessmann A, Leuther A, Hurm V, Massler H, Zink M, Kuri M, Riessle M, Losch R, Schlechtweg M, Ambacher O. A 300 GHz mHEMT amplifier module. In: IEEE International Conference on Indium Phosphide & Related Materials. 2009. pp. 196-199. DOI: 10.1109/ICIPRM.2009.5012477

[14] Samoska L, Church S, Cleary K, Fung A, Gaier TC, Kangaslahti P, Voll P. Cryogenic MMIC low noise amplifiers for W-band and beyond. In: International Symposium on Space Terahertz Technology. 2011

[15] Lee YC. Waveguide integrated high-gain amplifier module for millimeter-wave applications. Progress in Electromagnetics Research Letters. 2015;**57**:125-130

[16] Avago Technologies. AMMP-6441 36-40 GHz, 0.4 W Power Amplifier in SMT Package [Internet]. Available from: http://www.datasheetlib.com/datasheet/168419/ammp-6441-tr2g_avago-technologies.html

[17] Leong Y-C, Weinreb S. Full band waveguide-to-microstrip probe transitions. In: IEEE MTT-S International Microwave Symposium; 1999. pp. 1435-1438. DOI: 10.1109/MWSYM.1999.780219

[18] Shireen R, Shi S, Prather DW. W-band microstrip-to-waveguide transition using via fences. Progress in Electromagnetics Research Letters. 2010;**16**:151-160

[19] Rogers Corporation. Available from: http://www.rogerscorp.com

[20] CST Microwave Studio. Available from: https://www.cst.com

[21] Avago Technologies. Application note 5520-AMxP-XXXX Production Assembly process (Land Pattern A) [Internet]. Available from: http://www.avagotech.com/docs/AV02-2954EN

Chapter 4

# Mathematical Analysis of Electrical Breakdown Effects in Waveguides

Isaac Medina and Primo-Alberto Calva

Additional information is available at the end of the chapter

http://dx.doi.org/10.5772/intechopen.76973

**Abstract**

The designers of microwave devices in the industry use the analytical solutions of the corona discharge equation to determine the minimum power breakdown threshold, in a particular device, such as waveguides and filters, and know whether it is in the established margins. There are two main ways to determine the breakdown threshold of a waveguide analytically; the most commonly used describes the plasma density generation completely as a function of the geometry by using the characteristic diffusion length, while the second is a more thorough method that involves the use of the effective diffusion length which considers collision frequency and electric field into the equations. Hence the aim of the designers is to obtain the closest results to experimental results, both methods must be considered in addition to the environmental changes so that they know the operational limits. This chapter describes the different methods to obtain analytical results for the breakdown threshold in any rectangular waveguide device, the influence of environmental conditions in the analysis and the inhomogeneous electric field effect inside the devices.

**Keywords:** electrical breakdown threshold, corona, characteristic diffusion length, waveguide filters, effective diffusion length

## 1. Introduction

Traffic capacity in a high-frequency scenario where waveguides are involved is generally limited by two main factors: bandwidth and input power [1]. In cases where the atmospheric pressure is a factor, such as satellite communications, the maximum input power of the signal is determined by several factors, among which are the geometry of the device, the collision

frequency of the molecules and free electrons and the intrinsic characteristics of the propagating medium itself, that is, air or nitrogen [2].

Waveguides are conductor hollow tubes, generally consisting of a circular, elliptical, or rectangular cross-section. The cross-section dimensions are chosen by designers in such a way that electromagnetic waves propagate inside the guide. A waveguide can have several shapes and sizes, and frequently its performance is a function of the radiofrequency (RF) routing signals; this means that the way the wave is propagating inside the guide. Rectangular waveguides are the most commonly used; this is because they are easily fabricated, they have a very broad bandwidth and they present low losses within their operating frequencies [3].

Rectangular waveguides operate only in certain frequency bands, depending on the cross-section dimensions. Waveguide geometry determines the highest operating wavelength, this means, higher waveguide sizes operate at lower frequencies.

Waveguide filters are responsible of eliminating unwanted radiations and interferences in a communication scheme. These devices are also hollow conductor tubes, made generally of aluminium, with the difference that inside them are distance variations or obstructions that generate the wanted filtering effect. **Figure 1** shows different types of waveguide filters.

The reason waveguide filters are analysed in terms of breakdown power is because this device is with the shortest cross-section of all the communications system, reaching even distances of 1 mm. In these sections, electric field density can be so high that it leads to electrical breakdown, rendering the components useless. **Figure 2** shows a low-pass corrugated filter after breakdown has occurred [4].

The continuous miniaturization tendency in electronic devices and the increasing demand of services lead to higher component integration. In a transponder system, passive components are allocated, such as filters and waveguides, where, due to the used power, high densities of electric field are reached, presenting mainly the corona and multipactor effects [5].

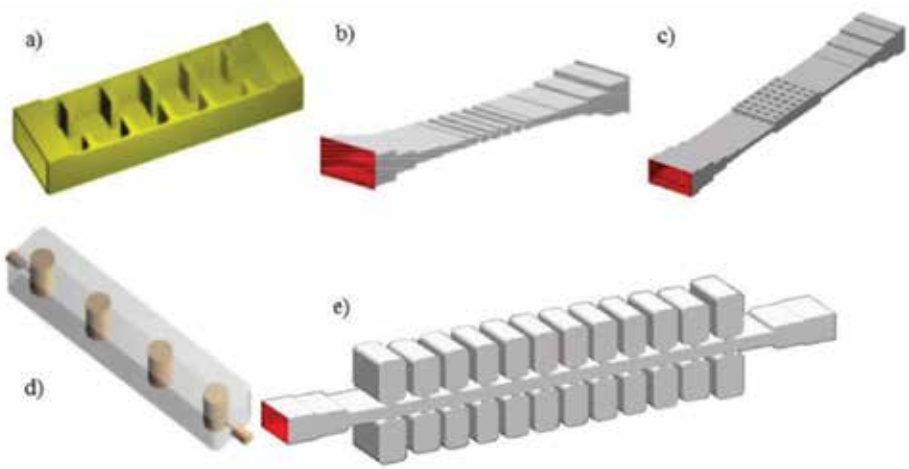


**Figure 1.** (a) Coupled iris filter, (b) corrugated waveguide filter, (c) waffle iron filter, (d) posts filter, and (e) guarded waveguide filter.

http://dx.doi.org/10.5772/intechopen.76973

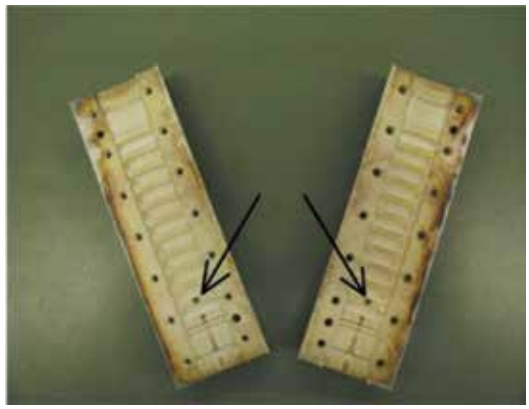

**Figure 2.** Low-pass corrugated filter after breakdown has occurred, as reported in [4].

High-performance RF filters are widely used in communications systems, where it is necessary to know its capabilities for input power handling. Since increasing the power levels is the simpler way to impulse the reach of the system and its capability for data transmission, the design for the high-power operation filters must consider the next effects: electrical breakdown by ionization (corona effect), multipactor effect and passive intermodulation interferences (PIM).

Multipactor is a breakdown mechanism in vacuum, in which a resonant increase of free-electron space charge develops between two surfaces. The applied field intensity is such that the electrons collide at ultra-high speeds against the walls of the device, causing the continuous release of secondary electrons in the medium and leading to a breakdown. However, this is not the critical stage for design implications.

Ionization breakdown is a phenomenon that occurs in gases where the normally low electron density increases in a way similar to an avalanche, turning the isolating gas into conducting plasma; this happens at higher pressures than multipactor. In satellite communications, breakdown analysis must be considered for the components located on Earth and for the ones destined for space operations, since the RF components that are designed to operate in space must be tested frequently on Earth at their highest power and are fully operational during the launching stage for telemetry purposes. This is the reason the analysis is made for low-pressure applications.

Waveguide breakdown analysis follows the next three stages: breakdown threshold determination, circuit and field analysis to determine the maximum voltage or field values and comparison of the experimental worst case with breakdown threshold.

Air ionization is caused because of the electrons' impact against air molecules. These electrons are accelerated by an RF field. If the energy level (provided by the RF field) is enough to cause ionization of neutral molecules, and the free electron total created by ionization exceeds the total losses of electrons due to attachment and recombination, the exponential growth of the electron density generates electron plasma and, eventually, leads to breakdown.

In low pressures, particles have a higher mean free path. Eventually, the mean free path increases until it reaches $d$ (gap distance), where the multipactor effect takes place. By reducing

the atmospheric pressure, there is a lower input power handling capacity until it reaches a minimum operation power; this is called critical pressure [4].

This chapter covers the ionization breakdown in atmospheric air analysis; the equations that describe this consider different processes, such as the ionization, attachment and collision frequencies. Also, the analysis considers as variables the atmospheric pressure and electric field intensity, considering contaminant-free dry air as the propagating medium. Nevertheless, due to the breakdown variability, the design of filters and waveguides is a controversial topic for designers, who consider a wide tolerance range from 0 dB to 3 dB according to minimum breakdown power [4, 5].

Corona breakdown is the process when electron plasma is created due to the ionization of the gas in areas where the electrical fields are high. Electrical fields in filters and waveguides can lead to corona effects at relatively low pressures (from 1 to 100 Torr), which, in atmospheric terms, are reached in the ionosphere (from 80 to 800 km). This phenomenon cannot occur in vacuum conditions, since it is necessary for the presence of a gas to ionize [4].

## 2. Breakdown power threshold

There are different processes that can generate ions; these are by electronic impact, field effect, photo-ionization and thermos-ionization. For the analysis of filters and waveguides, the most relevant is by electronic impact, being directly proportional to the collision frequency between electrons and molecules. The equation that describes the time evolution of free-electron generation is [4, 6–8]:

$$\frac{\partial n}{\partial t} = \nabla(D\nabla n) - \vec{v} \cdot \nabla n + (v_i - v_a)n - \beta n^2 + P \tag{1}$$

where $v_i$ and $v_a$ are the ionization and attachment frequencies, respectively, $D$ is the diffusion coefficient, $\beta$ is the recombination coefficient and $P$ is the electron production rate by external sources; $\nabla(D\nabla n)$ is the term that defines the diffusion of the electron cloud, from a high-density area to a lower-density area, and is entirely space dependent; and $\vec{v} \cdot \nabla n$ is the convective term that considers the possible movement of the gas.

For the corona effect analysis and from the pre-breakdown stage point of view, the recombination term is discarded, since it is only relevant once the electron density is high enough, which only occurs when the electrical discharge has already begun. Also, the convective term has to be discarded, since a stationary medium is assumed inside the waveguide devices, that is, there is no relevant movement of the gas molecules. Additionally, the diffusion coefficient is considered as space independent, since it is electric field independent [4]. The simplified equation is:

$$\frac{\partial n}{\partial t} = D\nabla^2 n + (v_i - v_a)n \tag{2}$$

Breakdown criteria are based on the fact that the electron density grows very fast once there are more freed electrons than captured. Considering a scenario where there is no diffusion, and

http://dx.doi.org/10.5772/intechopen.76973

a homogeneous field, due to the similar geometry among the parallel walls of the filter and waveguides. Then, Eq. (2) results in:

$$\frac{\partial n}{\partial t} = (v_i - v_a)n \tag{3}$$

and solving the derivative results in:

$$n(t) = n_0 e^{(v_i - v_a)t}. \tag{4}$$

When $v_i > v_{a,}$ there is an electron avalanche, and the breakdown condition for the continuous waves can be simplified as:

$$\frac{dn}{dt} = 0. \tag{5}$$

As a consequence, the general equation to solve the breakdown threshold stage is:

$$D\nabla^2 n + (v_i - v_a)n = 0. \tag{6}$$

Solving the Laplacian term from Eq. (6), and considering a Cartesian coordinate system, since the devices analysed are rectangular waveguides and filters, the equation leads to:

$$\frac{\partial^2 n}{\partial x^2} + \frac{\partial^2 n}{\partial y^2} + \frac{\partial^2 n}{\partial z^2} + \frac{\nu}{D}n = 0 \tag{7}$$

where $\nu = v_i - v_a$ is the effective ionization frequency. The rectangular waveguide device must be analysed from the cross-section, so the third term can be discarded, considering only the width and height of the guide.

$$\frac{\partial^2 n}{\partial x^2} + \frac{\partial^2 n}{\partial y^2} + \frac{\nu}{D}n = 0 \tag{8}$$

Establishing the solution as the product of two functions:

$$n(x, y) = X(x)Y(y) \tag{9}$$

Substituting (9) in (8), knowing that the equation components are independent between them, it results in:

$$Y\frac{d^2X}{dx^2} + X\frac{d^2Y}{dy^2} + \frac{\nu}{D}XY = 0 \tag{10}$$

and dividing by (9) we get:

$$\frac{1}{X}\frac{d^2X}{dx^2} + \frac{1}{Y}\frac{d^2Y}{dy^2} + \frac{\nu}{D} = 0. \tag{11}$$

This equation can be solved by proposing exponential solutions. Due to the independency among terms, the first term can be solved proposing a negative constant as a result:

$$\frac{1}{X}\frac{d^2X}{dx^2} = -\sigma$$

$$\frac{d^2X}{dx^2} + \sigma X = 0. \tag{12}$$

An exponential solution for (12) is proposed and derived twice:

$$X(x) = e^{\gamma x} \tag{13}$$

$$X''(x) = \gamma^2 e^{\gamma x}. \tag{14}$$

Substituting (13) and (14) in (12), we get:

$$\gamma^2 e^{\gamma x} + \sigma e^{\gamma x} = 0 \tag{15}$$

It can be determined that:

$$\begin{gathered} \gamma^2 + \sigma = 0 \\ \gamma = \pm\sqrt{-\sigma} \end{gathered} \tag{16}$$

So, the general equation for $X(x)$ is:

$$Ae^{i\sqrt{\sigma}x} + Be^{-i\sqrt{\sigma}x}. \tag{17}$$

By Euler, Eq. (17) can be rewritten as:

$$\begin{gathered} A[\cos\sqrt{\sigma}x + i\sin\sqrt{\sigma}x] + B[\cos\sqrt{\sigma}x - i\sin\sqrt{\sigma}x] \\ (A+B)\cos\sqrt{\sigma}x + (A-B)\sin\sqrt{\sigma}x \\ k_1\cos\sqrt{\sigma}x + k_2\sin\sqrt{\sigma}x. \end{gathered} \tag{18}$$

Considering the next border conditions, since there are no free electrons on the walls of the waveguide:

$$X(0) = 0, \qquad X(a) = 0 \tag{19}$$

where $a$ is the waveguide width distance. Then:

$$\begin{gathered} \mathrm{X}(0) = \mathrm{k}_1 = 0 \\ X(x) = k_2\sin\sqrt{\sigma}x \\ X(a) = k_2\sin\sqrt{\sigma}b = 0 \end{gathered} \tag{20}$$

The only possibility for a non-trivial solution is: $\sin\sqrt{\sigma}b = 0 \Rightarrow \sqrt{\sigma}b = m\pi$; resulting in $\sigma = \left(\frac{m\pi}{a}\right)^2$ where $m = 1, 2, 3, \ldots$. By the same method, the second component of Eq. (11) is: $\sigma_2 = \left(\frac{n\pi}{b}\right)^2$ where $n = 1, 2, 3, 4, \ldots$

This analysis considers the first harmonic. Then, Eq. (8) results in:

$$\left(\frac{\pi}{a}\right)^2 + \left(\frac{\pi}{b}\right)^2 = \frac{\nu}{D} \tag{21}$$

where $a$ and $b$ are the width and height of the rectangular waveguide. MacDonald defined the characteristic diffusion length as [8]:

$$\frac{\nu}{D} = \frac{1}{\Lambda^2} \tag{22}$$

This proves that diffusion processes are entirely dependent on the geometry. If one of the dimensions is much bigger than the other, as in a parallel plates experiment, the characteristic diffusion length is $\pi$ divided by the squared gap distance. This is valid for rectangular waveguides, due to the fact that they have a constant width and height. For the case of waveguide filters, the shortest height area must be considered for the analysis.

Nevertheless, a more realistic approach implies the presence of non-homogeneous fields, which renders the ionization frequency also non-homogeneous, and, consequently, the free electron density is also affected. To characterize diffusion losses in these situations, the concept of effective diffusion length is described by Ulf Jordan et al. [9].

## 3. Effective diffusion length

For homogeneous values of $D$, $v_i$ and $v_a$, the electron density increasing curve is constant, determined only by the border conditions of the analysed geometry. For non-homogeneous values in space, the free-electron density diffusion curve varies [9].

The inhomogeneity of these parameters occurs because of the inhomogeneity of the microwave electric field, which implies that $D$ and $v_a$ are approximately constant in space, the only inhomogeneous value being $v_i = v_i(x)$.

Ulf Jordan et al. [9] determined that the diffusion length in the presence of non-homogeneous fields also depends on the atmospheric pressure, as shown in Eq. (23). This equation was obtained using computational methods:

$$\frac{1}{\Lambda_{eff}^2} = a^{-2}\sqrt{\pi^4(1 + 0.3677\beta) + \frac{\pi^2\beta q}{2}} + \left(\frac{\pi}{b}\right)^2 \tag{23}$$

where

$$q = \left(\frac{a}{L_a}\right)^2 + \left(\frac{\pi a}{b}\right)^2$$

$a$ and $b$ are the width and height of the waveguide, respectively, $\beta$ is a parameter that depends on the used gas (for air $\beta = 5.33$) and the value of $L_a$ is:

$$L_a = \sqrt{\frac{D}{\nu_a}}$$

Consequently, as the pressure increases, the effective diffusion length decreases, and the calculated breakdown thresholds are the same as the ones obtained by using the characteristic diffusion length.

## 4. Ionization, attachment and diffusion in air

When a microwave field is applied, the energy transfer depends on the field's frequency and the environmental conditions (atmospheric pressure and humidity). An effective electric field is defined as [8]:

$$E_{eff} = \frac{E_{rms}}{\left(1 + \frac{\omega^2}{\nu_c^2}\right)^{\frac{1}{2}}} \tag{24}$$

where $E_{rms}$ is the root mean square electric field, $\omega$ is the angular frequency ($2\pi f$) and $\nu_c$ is the collision frequency between electrons and molecules. For air, the general equation for the collision frequency is [8]:

$$\nu_c = 5 \times 10^9 p \ \left[\mathrm{s}^{-1}\right] \tag{25}$$

$p$ is the atmospheric pressure in Torr. From Eq. (24) it can be deduced that in high-pressure cases, the effective field is equal to the RMS field, since the collision frequency increases along with the atmospheric pressure.

The diffusion coefficient in air is determined by [8]:

$$D = \frac{10^6}{p}\left[\mathrm{cm}^2\mathrm{s}^{-1}\right]. \tag{26}$$

The ionization frequency can be obtained by [6]:

$$\nu_i = 5.14 \times 10^{11} p \exp\left(-73\alpha^{-0.44}\right)\left[\mathrm{s}^{-1}\right] \tag{27}$$

with

$$\alpha = \frac{E_{rms}}{p\left(1 + \frac{\omega^2}{\nu_c^2}\right)^{\frac{1}{2}}} \equiv \frac{E_{eff}}{p} \tag{28}$$

$\alpha$ is known as the reduced electric field. Eq. (27) is valid in the range of $32 < \alpha < 100$ [4, 6]. The effective field term is very useful, since it relates the properties of the corona in direct current (DC) and alternating current (AC). The effective field produces the same energy transfer as in a DC field, so experimental data can be analysed in DC instead of AC [4, 10, 11]. The attachment frequency is two- and three-body phenomena.

$$\nu_a = \nu_{a2} + \nu_{a3} \tag{29}$$

$\nu_{a2}$ is only valid in the range $0 < \alpha < 60$ and is defined as [4, 6]:

$$\nu_{a2} \approx 7.6 \times 10^{-4} p\alpha^2(\alpha + 218)^2 \quad \left[\mathrm{s}^{-1}\right] \tag{30}$$

The three-body attachment is field independent and is obtained as follows [4]:

$$\nu_{a3} = 10^2 p^2 \left[\mathrm{s}^{-1}\right] \tag{31}$$

For electrostatic homogeneous fields:

$$E_b = \frac{V}{d} \tag{32}$$

where $d$ is the structure width and $V$ is the breakdown voltage. Finally, the breakdown power can be obtained by:

$$P = \frac{V^2}{Z} \tag{33}$$

$Z$ is the characteristic impedance of the device. For waveguides and filters, $Z$ is determined by:

$$Z \frac{\sqrt{\mu_0/\varepsilon_0}}{\sqrt{1 - \left(\frac{1}{2fa\sqrt{\mu_0\varepsilon_0}}\right)^2}} \tag{34}$$

$\mu_0$ and $\varepsilon_0$ are the magnetic permeability and the electrical permittivity on vacuum, respectively, and f is the operating frequency.

## 5. Analytical results' comparison

Commonly, the analytical results obtained by using the characteristic diffusion length are considerably lower than the experimental results at the critical pressure; this minimum power breakdown is known as Paschen minimum. **Figure 3** shows the experimental values obtained by Carlos et al. [4] compared to the analytical results using the characteristic diffusion length, for a low-pass Ku band filter at 12.5 GHz. The experimental and analytical results differ by 16%.

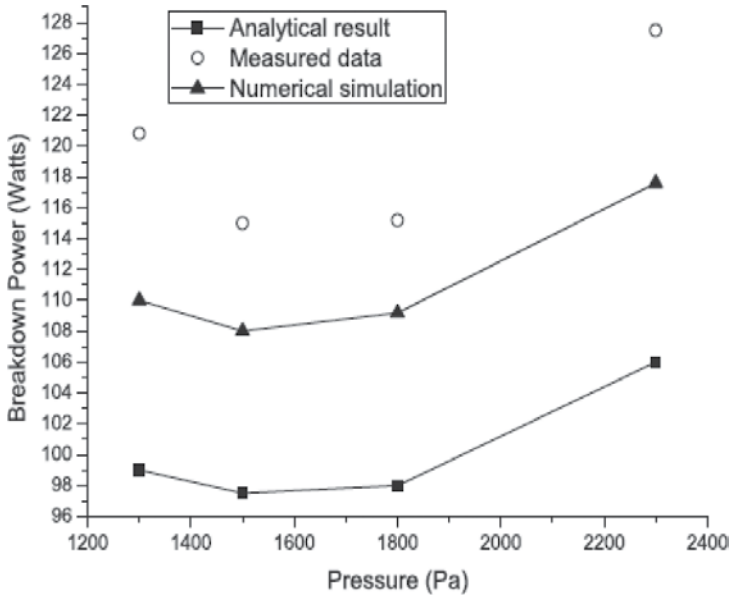


**Figure 3.** Low-pass Ku band filter operating at 12.5 GHz [4].

The results shown imply that it is necessary to consider the inhomogeneity of the electric fields, not due to geometry but due to the diffusion process that occurs at low pressures [12]. Then, instead of using the characteristic diffusion length, the effective diffusion length is used. **Figure 4** shows the experimental and analytical results using the characteristic diffusion length compared to the analytical results using the effective diffusion length for the same low-pass filter.

**Figure 5** shows another result comparison but for a corrugated waveguide filter operating at 12.2 GHz.

**Figures 4** and **5** show a slight increase in breakdown power, proving that the effective diffusion length from Eq. (23) is a more suitable equation for the cases of waveguide devices where the field inhomogeneity is greater.

These results can be explained because microwave breakdown in an RF device is manifested by an avalanche-like growth in time of the free-electron density in the gas filling the device. The difference between these power threshold results resides not only in their operating frequency but in their geometries and the number of irregularities the filter contains. A bigger amount of irregularities, or irises (steps that help in the filtering process), contributes to generating more inhomogeneity on the electric field.

**Figure 6** shows the transversal configuration and measures of each filter [4].

For the analysis of each filter, the minimum length located in the middle is considered.

The filter operating at 12.5 GHz is affected by the electric field inhomogeneity more than the other because of its high number of irises. Predicting mathematically the breakdown

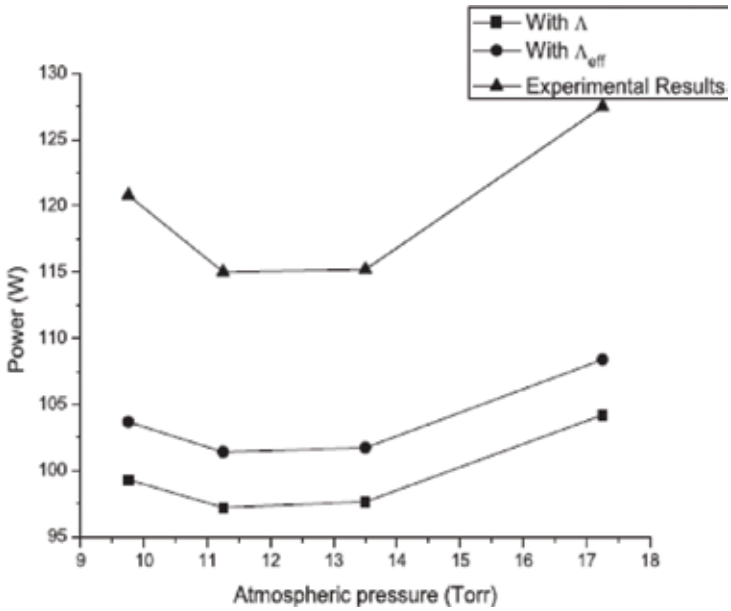


**Figure 4.** Experimental and analytical results using $\Lambda$ and $\Lambda_{eff}$ for a Ku band filter operating at 12.5 GHz.

threshold of a device with high amount of irregularities, such as **Figure 6** (b), requires modifications to the equations, more specifically, the use of an effective field-dependent collision frequency equation. The large number of irises generates a much higher space charge density than for a conventional obstruction-free waveguide. Further analysis of space charge density and the correct equations for these cases are considered in Section 6.

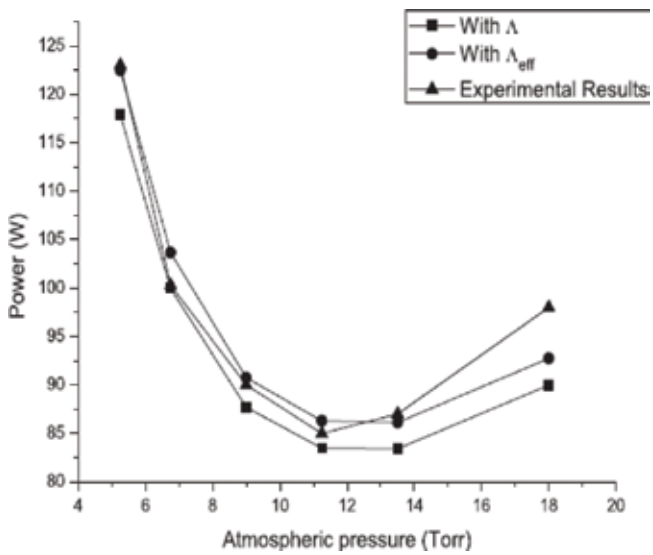


**Figure 5.** Experimental and analytical results using $\Lambda$ and $\Lambda_{eff}$ for a Ku band filter operating at 12.2 GHz.

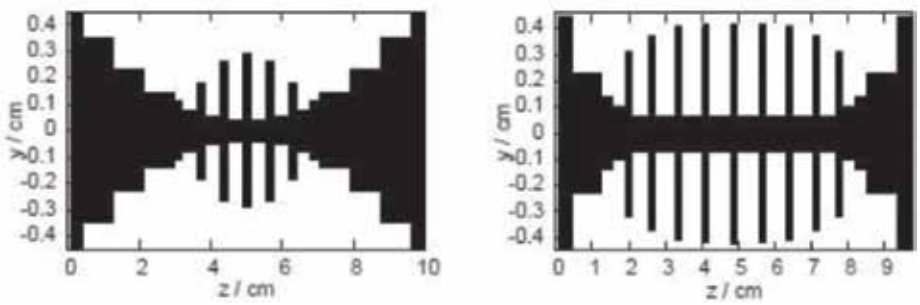


**Figure 6.** Transversal configuration of waveguide filters. (a) Operating at 12.2 GHz. (b) Operating at 12.5 GHz [4].

| Analysed filter | | Minimum breakdown power [W] | Data rate [Gb/s] |
|---|---|---|---|
| 12.2 GHz | $\Lambda$ | 83.5 | 4175 |
| | $\Lambda_{eff}$ | 86.1 | 4305 |
| 12.5 GHz | $\Lambda$ | 97.2 | 4860 |
| | $\Lambda_{eff}$ | 101.4 | 5070 |

**Table 1.** Calculated bit rate from power obtained by characteristic diffusion length and effective diffusion length for two different Ku band filters.

According to Witting [13], the transmission capacity of a communication network in terms of the number of users, power and data rate is:

$$\frac{R_B \cdot N}{P} \leq 20 \times 10^{18} \left[\mathrm{W}^{-1}\mathrm{s}^{-1}\right] \tag{35}$$

where $R_B$ is the data rate in bits/s, $N$ is the number of users and $P$ is the power in watts. **Table 1** shows the difference of bit rate obtained with the power from characteristic diffusion length calculation and the one from effective diffusion length calculation for the two different Ku band filters.

By using (35), the resulting increase on the bit rate of the filters, when using the effective diffusion length, is of 4.3% in the case of the 12.5 GHz low-pass filter and of 3.1% for the 12.2 GHz low-pass filter. Therefore, a small raise in the power, even of 3 or 4 W, is heavily reflected on the data rate and an increase of almost 200 Gbps is achieved.

## 6. Space charge density effects

The microwave devices' designers use the analytical solution of the corona discharge to determine if the operating power is within the established margins. As shown previously, the experimental results differ considerably from the analytical when the characteristic diffusion length is considered. It has been proved by some authors [2, 9, 12, 14] that the criteria used until now for the design of waveguide filters can be improved if the effective diffusion length is used instead of the characteristic diffusion length.

http://dx.doi.org/10.5772/intechopen.76973

The two main processes responsible for the electron losses during the breakdown stages are the diffusion from high-density regions towards lower-density regions and the attachment by neutral molecules, forming essentially negatively charged unmovable ions. For sufficiently enough electron density, at breakdown threshold, the region saturates and the electric field propagation is affected by its reflection or absorption in the device walls.

The most important negative ions present in air are $O_2^-$ and $O^-$ and the most important positive ions formed during electrical breakdowns at atmospheric pressure are $N_2^+$, $N_4^+$ and $O_2^+$. There have not been negative ions detected for nitrogen experimentally [15].

The avalanche evolution can be affected by any agent that alters the space charge electronic density. **Figure 7** shows the electric field $E_r$ around the avalanche and the resulting modification of the applied field $E_0$. The space charge at the head of the avalanche is assumed as concentrated within a spherical volume, with the negative charge ahead because of the higher electron mobility. The field is enhanced in front of the head of the avalanche with field lines from the

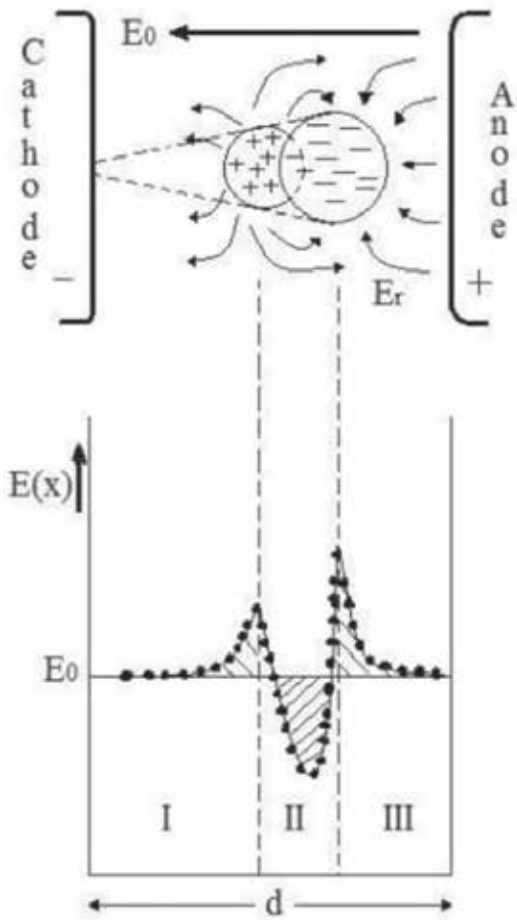


**Figure 7.** Schematic representation of electric field distortion in a gap caused by space charge of an electron avalanche [16].

anode terminating at the head, the region III. Further back in the avalanche, the field between the electrons and the ions left behind reduced the applied field ($E_0$), the region II. Still, further back, the field between the cathode and the positive ions is enhanced again, the region I [16].

The resultant field strength in front of the avalanche is thus ($E_0 + E_r$), whereas in the positive ion region just behind the head the field is reduced to a value ($E_0 - E_r$).

According to the results exhibited in **Figures 4** and **5**, where the analytical values of the breakdown power are lower than the experimental ones, this is an indication that the avalanche is mainly affected by the presence of positively charged ions instead of the negatively charged ions. The radial field produced by positive ions immediately behind the head of the avalanche can be calculated using the expression from [16]:

$$E_r = 5.3 \cdot 10^{-7} \frac{\alpha e^{\alpha_T x}}{\left(\frac{x}{p}\right)^{\frac{1}{2}}} \left[\frac{\text{Volts}}{\text{cm}}\right] \tag{36}$$

where $x$ is the distance in cm in which the avalanche has progressed, $p$ is the gas pressure in Torr and $\alpha$ is the Townsend first coefficient of ionization, denoted by:

$$\alpha_T x = 17.7 + \ln x \tag{37}$$

The Townsend first ionization coefficient indicates the number of ions generated by the electron collision by length unity. **Figure 8** shows the behaviour of $E_r$ and $E_0$ as a function of the pressure for different values of $x$, $x = a = 0.25$ cm, as this is the maximum height of the analysed Ku band filter.

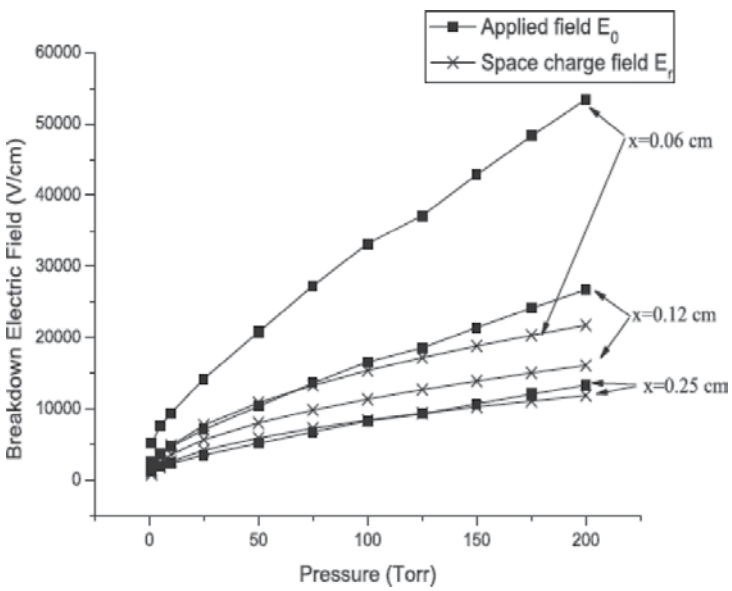


**Figure 8.** Applied electric breakdown $E_0$ versus space charge electric field $E_r$ for different values of $x$.

http://dx.doi.org/10.5772/intechopen.76973

It can be appreciated that the influence of the positive ionic space charge field is greater as a function of the development in the space of the avalanche.

For a more correct approach of the analytical results, Woo et al. [6] propose the collision frequency equation dependent on the reduced electric field as:

$$\nu_c = 5 \times 10^9 p \left[\frac{\alpha}{\alpha + 8}\right]^{1/2}. \tag{38}$$

**Figures 9** and **10** show the results of using this energy-dependent collision frequency equation and the effective diffusion length.

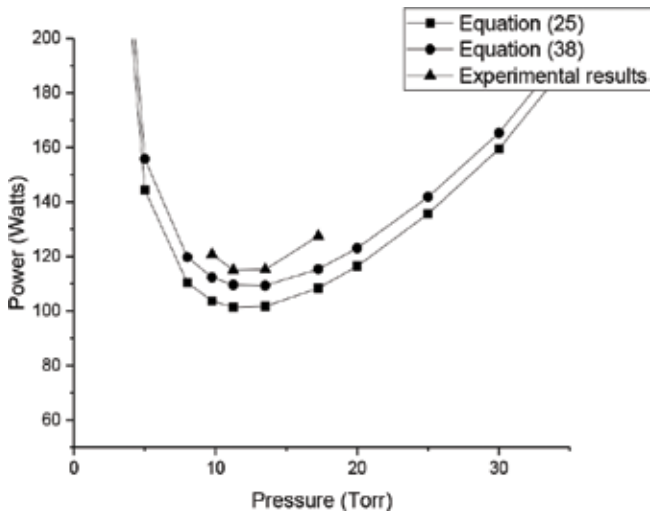


**Figure 9.** Breakdown power of a Ku band filter operating at 12.5 GHz using different collision frequency values.

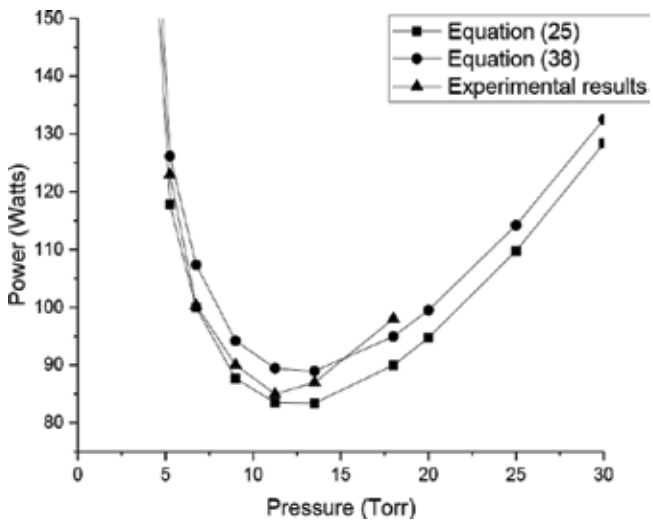


**Figure 10.** Breakdown power of a Ku band filter operating at 12.2 GHz using different collision frequency values.

It is shown that considering the diffusion length and the electric field-dependent collision frequency altogether, the results are far more similar to the experimental results, proving this to be an important approach towards the experimental results.

As minimal as these increases result, **Table 1** shows the importance of power, and the regulations for the design of these devices can be increased in terms of input power tolerance.

## 7. Plasmonic waveguide filters for increased data rate transmission

As the actual waveguide devices reach the technological limit, in terms of their data rate, it is necessary to develop new alternatives to overcome the continuously increasing demand of services [12]. By using encoding techniques, it is possible to send up to 16 bits of information per each Hertz sent [17]; the current Ku band analysed devices operate generally around 12.2 GHz, so the data rate is only of 195.2 Gbps. Much higher frequencies, such as those provided by optical communication, of about 350 THz, show a much promising environment, delivering up to 5600 Tbps.

Optical wireless communications demand different multiplexing and de-multiplexing techniques than traditional RF communication. For this, some proposals include a wavelength divisor multiplexer (WDM), this can be a polymer substrate mode for photonic interconnections and is used even for satellite communications [18]. This helps in a way that incoming signals are directly coupled with the system chip, leaving out any optical-electrical and electrical-optical conversions. This is a partial solution since the system needs power and wavelength management; for this, digital grating processors (DGPs) are implemented. There are many advantages that these photonic interconnections provide, among them are introducing a planar platform for space-saving purposes, efficiency against any external perturbation, low propagation losses, compatibility with other surface mount technologies and low cost. Nevertheless, DGPs are components that demand energy from the system to operate and generate interruptions in the transmission due to electronic processing. Other components can be responsible for the filtering of signals; as seen by Calva et al. [2], a plasmonic waveguide filter is a viable option.

Since the interconnection is very important, as the planar configuration of the devices, plasmonic waveguide filter proves a viable solution due to their capability of transfer information operating at different frequencies at the same time. Surface plasmons' inherent properties permit the signal to travel at the speed of light and also transport electrical and optical signals simultaneously [19]. The disadvantage of using these devices is that electrical breakdown due to ionization phenomena can occur.

These particular devices' operating principle is based on the light capability to penetrate some materials; for metals this can be up to 30 nm deep, helping in the generation of surface plasmons, which are oscillating free electrons in a coherent state that generate at the interface between any two materials. In some cases, incident light couples with the surface plasmon to generate self-sustaining propagating electromagnetic waves; these are known as surface plasmon polaritons (SPPs) [19]. A plasmonic waveguide filter example is shown in **Figure 11**; this is based on a metal–insulator–metal (MIM) structure [20].

http://dx.doi.org/10.5772/intechopen.76973

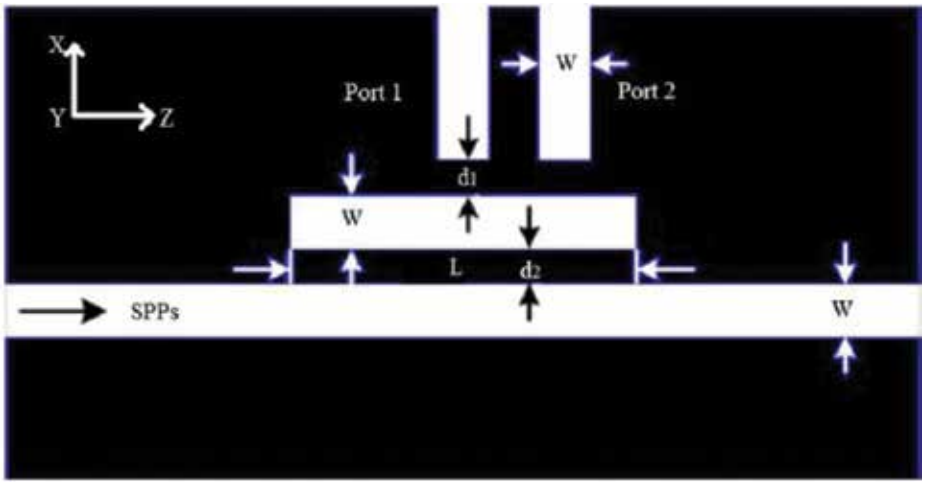


**Figure 11.** Two-channel plasmonic waveguide filter structure.

The configuration of these filters is formed by stacking nanometric waveguides of the same gap length. Multiple resonance modes are formed inside the devices; only the first and second mode can traverse through the next waveguides, the one in the middle of **Figure 11** and the port 1 and 2 vertical waveguides. The SPPs travel through the principal plasmonic waveguide; resonance happens if the SPPs are enclosed in the middle cavity. This mid-section is very important, since its size is responsible for the filtering effect; modifications of its length alter the delivered wavelength through ports 1 and 2. A wide range of wavelengths can be covered by using these filters, from 500 to 10,000 nm. However, some optimal configurations have been suggested; for distances of $L$=280, 320, 350, 360, and 390 nm, the transmitted resultant wavelengths are $\lambda$=575, 850, 1060, 1310, and 1550 nm, respectively [2]. As mentioned before, it is imperative to consider the field skin deep so that light can travel through the metal of these waveguide structures; $d_1$ and $d_2$ distances must be smaller than 30 nm in the case of silver [21]. The field skin deep distance describes the length of a given material, silver in this case, that an electromagnetic signal can penetrate, this distance depends on the signal frequency and the material properties. So, in this case, the distances are 10 and 15 nm, respectively, with a gap distance for all the waveguides of $W = 50$ nm. These filters have very good transmission spectra and can easily operate in wavelengths from 575 to 1500 nm, optimal for using them for an optical communication scheme.

The analysis of electromagnetic waves through a surface already excited contemplates that the electrons are in a non-equilibrium state and that they are generated because of light absorption, not only due to collisions. The absorption can be linear or multiple, resulting in many non-equilibrium electrons; then, considering the diffusion effect, electron–electron collisions occur and there is an energy exchange between the photon-excited electrons and the non-equilibrium electrons. The evolution in time of the free-electron density generated by excited photons and electron–electron collisions is [22]:

$$\frac{\partial n}{\partial t} = D\nabla^2 n + \frac{(1-R)\alpha_1 I}{\hbar\omega} + \frac{(1-R)^2\alpha_2 I^2}{2\hbar\omega} - \frac{n}{\langle\tau_{ee}\rangle} \tag{39}$$

where $D$ is the electronic diffusion coefficient, $\langle\tau_{ee}\rangle$ is the time between the electron–electron collisions, $I$ is the irradiance of light in watts per square meter, $R$ is the reflection coefficient, $\alpha_1$ is the linear photonic absorption coefficient and $\alpha_2$ is the two-photon absorption coefficient.

According to Bhushan et al. [23], there is no two-photon absorption for the cases where the plasmon has an angular momentum of $l > 1$ kgm$^2$/s. $l = 1$ corresponds to the bipolar resonance of the plasmon, which is the one that occurs in these types of filters [20]. Then, Eq. (39) is reduced to the following:

$$\frac{1}{\Lambda_{eff}} = \left(\frac{(1-R)\alpha_1 I}{\hbar\omega} - \frac{n}{\langle\tau_{ee}\rangle}\right)/nD \tag{40}$$

Substituting $\frac{1}{\langle\tau_{ee}\rangle} = \nu_c$:

$$\frac{1}{\Lambda_{eff}} = \frac{(1-R)\alpha_1 I}{\hbar\omega nD} - \frac{\nu_c}{D} \tag{41}$$

The lineal photonic absorption is obtained using the following [24]:

$$\alpha_1 = 4\pi\bar{k}/\lambda \ \left[\text{cm}^{-1}\right], \tag{42}$$

where $\bar{k}$ is the extinction coefficient. **Table 2** shows the experimentally obtained values in [24] for the extinction coefficients at a specific wavelength and the corresponding absorption coefficients.

The electron density in the electrical breakdown threshold is $n = 1.1 \times 10^{15}\text{cm}^{-3}$ [25]. The reflection coefficient of silver is $R = 0.95$. The $\hbar\omega$ term is the energy of a photon, where $\hbar$ is the Planck's constant divided by $2\pi$:

$$\hbar\omega = \frac{h2\pi f}{2\pi} = hf = 6.62 \times 10^{-34} f[\text{J}] \tag{43}$$

Using these equations and the effective diffusion length, as discussed before, in (39) the power breakdown threshold of a plasmonic waveguide filter can be obtained. **Figure 12** shows the power breakdown threshold of a plasmonic waveguide filter at different wavelengths.

| **Wavelength** [**nm**] | **Extinction coefficient** $\bar{k}$ | **Absorption coefficient** $\left[\text{cm}^{-1}\right]$ |
|---|---|---|
| 575 | 3.45 | 7.54E + 05 |
| 850 | 5.70 | 8.43E + 05 |
| 1060 | 7.33 | 8.69E + 05 |
| 1310 | 9.10 | 8.73E + 05 |
| 1550 | 10.60 | 8.59E + 05 |

**Table 2.** Experimental values for the extinction and linear photonic absorption coefficients.

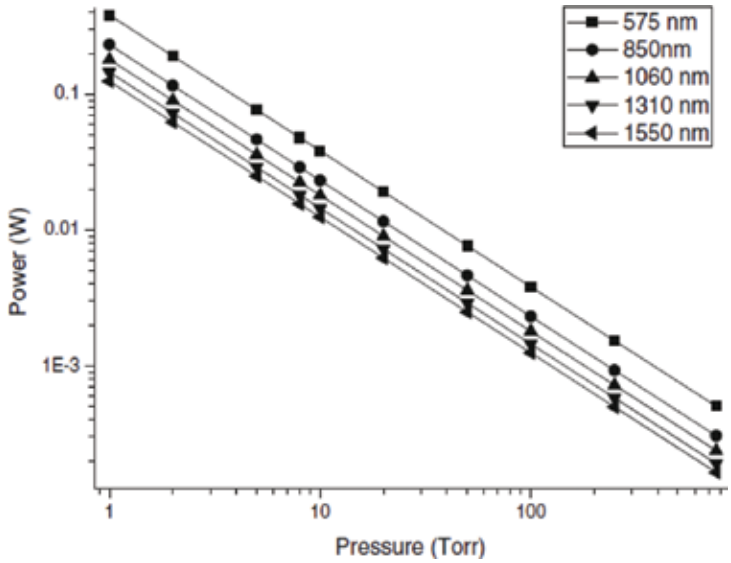


**Figure 12.** Power breakdown threshold of a two-channel plasmonic waveguide filter at different wavelengths.

These extremely low power values are not a problem in the data transmission, according to Radek Kvicala et al. [26]; the optical communication systems are capable of receiving very low optical powers of about $P = 4 \times 10^{-14}$ Watts.

## 8. Conclusions

The suggested modifications to the waveguide devices breakdown threshold analysis change the operating power in terms of the continuously increasing bandwidths and component integration. Increasing power handling in these devices by just a few watts have a considerable effect in the data rate, increasing its value, whereas avoiding the risk of breakdown to occur.

Waveguide designers use the free electrons in the time equation to obtain the lowest possible breakdown thresholds, which implies that homogeneous electric fields as a function of the geometry are considered. However, the presence of space charge inside the devices causes inhomogeneities in the electric field; therefore, it is important to determine the device structure for a correct analysis. When analysing a waveguide filter, the substructures inside it that generate the filtering effect, highly non-homogeneous areas are located. In these cases, the use of the effective diffusion length, along with the collision frequency equation that highly depends on the electric field, must be imperative for a correct approximation of the real values.

Plasmonic waveguide filters are a good proposal for the implementation of higher-frequency technologies. For wavelengths from 575 to 1500 nm, the power breakdown threshold is located between 0.1 and 0.4 Watts at 1 Torr atmospheric pressure. These power thresholds are

sufficient for the electronic processing required in an optical environment, since optical systems are capable of fully operating while receiving very low power, $P = 4 \times 10^{-14}\ W$.

## Author details

Isaac Medina[1,2]* and Primo-Alberto Calva[1,2]

*Address all correspondence to: ismesa@gmail.com

1 Centro de Desarrollo Aeroespacial del Instituto Politécnico Nacional, Delegación Cuauhtémoc, México, Ciudad de México

2 Instituto Politécnico Nacional, Colonia Barrio la Laguna Ticomán, Delegación Gustavo A. Madero, México, Ciudad de México

## References

[1] Elbert BR. Introduction to Satellite Communication. London: Artech House; 2008

[2] Calva PA, Medina I. Power Breakdown Threshold of a Plasmonic Waveguide Filter. Plasmonics, Springer US; January 2014

[3] Marcuvitz N. Waveguide Handbook. London, United Kingdom: Peter Peregrinus Ltd.; 1985

[4] Vicente Quiles CP. Passive intermodulation and corona discharge for microwave structures in communications satellites. Dissertation PhD Thesis, Germany: Technischen Universitat Darmstadt zur Erlangung der Wurde; 2005

[5] Ming Y. Power- handling capability for RF filters. IEEE Microwave Magazine. October 2007:88-97

[6] Woo W, DeGroot J. Microwave absorption and plasma heating due to microwave breakdown in the atmosphere. IEEE Physical Fluids. 1984;**27**(2):475-487

[7] MacDonald AD. Microwave Breakdown in Gases. New Jersey, United States: John Wiley & Sons; 1966

[8] MacDonald AD, Gaskell DU, Gitterman HN. Microwave breakdown in air, oxygen and nitrogen. Physical Review. June 1963;**130**:1841-1850

[9] Jordan U, Anderson D, et al. On the effective diffusion length for microwave breakdown. IEEE Transactions on Plasma Science. 2006;**34**(2):421-430

[10] Scharfman WE, Morita T. Voltage Breakdown of Antennas at High Altitude. Proceedings of the IRE, November 1960, pp. 1881-1887

[11] Ali AW. Intense and Short Pulse Electric Field (DC and Microwave) Air Breakdown Parameters. Washington, DC: Naval Research Laboratory; August 29, 1986. pp. 1-34

[12] Calva PA, Medina I. New solutions of the corona discharge equation for applications in waveguide filters in SAT-COM. IEEE Transactions on Plasma Science. April, 2013;**41**(4)

[13] Witting M. Satellite onboard processing for multimedia applications. IEEE Communications Magazine. June 2000;**38**(6):134-140

[14] Jordan U, Anderson D, Semenov V, Puech J. Discussion on the effective diffusion length for microwave breakdown. Institute of Applied Physics RAS. pp. 1-2

[15] Badaloni S, Gallimberti I. Basic data of air discharges: UPee - 72/05 Report, June 1972

[16] Kuffel E, Zaengl WS. High Voltage Engineering. London UK: Newnes; 2000

[17] International Telecommunications Union. Handbook on Satellite Communications. New York: Wiley; 2002

[18] Liu J, Gu L, Chen R, Craig D. WDM polymer substrate mode photonic interconnects for satellite communications. Photonics packaging and integration IV, Proceedings of SPIE, vol. 5358 (SPIE, Bellingham, WA); 2004

[19] Novotny L, Hecht B. Principles of Nano-Optics. Cambridge: Cambridge University Press; 2006

[20] Wen K, Yan L, Pan W, Luo B, Guo Z, Guo Y. Wavelength demultiplexing structure based on a plasmonic metal-insulator-metal waveguide. Journal of Optics, IOP Publishing. 2012; **14**(7):1-5

[21] Dionne JA, Sweatlock LA, Atwater HA. Plasmon slot waveguides: Towards chip-scale propagation with subwavelength-scale localization. Physical Review B. 2006;**73**(035407)

[22] Martsinovsky GA, et al. The role of plasmon-polaritons and waveguide modes in surface modification of semiconductors by ultrashort laser pulses, Fundamentals of laser assisted micro- and nanotechnologies. Proceedings of SPIE, Vol. 6985; 2008

[23] Bhushan B, Kundu T, Singh BP. Two photon absorption spectrum of silver nanoparticles. Optic Communication; **285**:5420-5424

[24] Palik ED. Handbook of Optical Constants of Solids. New York: Academic; 1991

[25] Unnikrishnan VK, Kamlesh A, et al. Measurements of plasma temperature and electron temperature in laser-induced copper plasma by time-resolved spectroscopy of neutral atom and ion emissions. Pramana-Journal of Physics. 2010;**74**

[26] Kvicala R, Hampl M, P Kucera. Satellite terrestrial (Earth) station optical communication. Northern Optics, Bergen, IEEE; 2006. pp. 83-85

Chapter 5

# Optical Waveguide for Measurement Application

Prashant Bansilal Patel and Satish T. Hamde

Additional information is available at the end of the chapter

http://dx.doi.org/10.5772/intechopen.76781

**Abstract**

The chapter provides the analysis of the behaviour of Mach Zehnder interferometer waveguide (MZIW) sensing structure and establishes the general design principles. Photonics interferometers have been widely used because of their highly sensitive detection technique. The present study is based on the MZIW structure for sensing application and deals with interferometer single-mode transmission. Theoretically, short wavelength and high difference in index ($\Delta\eta$) results in the low depth of the evanescence wave and increase in sensitivity. MZIW under consideration is very small in size hence it is very difficult to guide the light into waveguide. The output monitor detection sensitivity of the entire MZI structure depends on light-guiding efficiency. To maintain minimum losses at various micro-branches of the entire MZIW structure, effective light propagation is important and it is a critical parameter of the entire interferometer. Various tests have been carried out to study the effects of the $Y$ branch angle variation on light guiding into the MZIW structure especially in measurement application.

**Keywords:** interferometer, light propagation, waveguide

## 1. Introduction

Guided wave optics has revolutionized the photonic sensing technology. It covers both fibre and integrated optics technology. Photonics technology improves optical communication and minimizes the optical components used for communication as well as measurement applications [1]. Silicon nano-photonics waveguides strongly confine light in a submicron waveguide structure which has following advantages.

(i) allows sharp bends due to which compact and tiny components can be analysed and characterized;

(ii) gives tremendous reduction in footprints, which in turns open up new areas for the large-scale integration of photonics component circuits.

The fabrication of photonics circuits can be done on the similar line of complementary metal-oxide-semiconductor (CMOS) circuits [2]. Due to the similarity, CMOS compatibility opens up options for the interface of photonics functions with electronics functions. Photonics sensing technology has now gained a place in the vast portfolio of practical measurement technologies [3, 4].

However, current innovations in the photonics technique to manipulate the light are continue to provide both opportunity and challenge to the micro-optical components used in rapid measurement and sensing technologies. The development in the modern photonics sensors is due to the advances made in the LASER and optical fibre technology. The progress in the micro-electronics field accelerated the growth in silicon as well as polymer-based photonics devices.

Photonics technology also enhances precision as well as accuracy of the measurement. Photonics-based sensors reduce the measurement time which is not possible using conventional available techniques. The application of nanotechnology in the field of biology and biomedical field is known as bio-nano-technology or nano-bio-technology [5]. This technology gives rise to new devices and systems having improved sensitivity and accuracy for measurement application. Interferometer analysis using the *Y* branch is highlighted in this chapter for the MZIW structure and the general conclusions on optimization are drawn [6].

## 2. Interferometer technique

In interferometer phenomenon, two similar input waves are superimposed at an output waveguide to detect the phase difference between them. If the two waves are in phase, their electrical fields gets added (this is called as constructive interference). If they are out of phase (phase shift is 180° between them), the electric field received at the output waveguide gets cancelled (this is called as destructive interference).

Various interferometer configurations like Mach Zehnder interferometer, Fabry Perot interferometer and Michelson interferometer have been realized using optical methods. Out of all above techniques, the main consideration in this chapter is given to Mach Zehnder interferometer [7, 8].

## 3. Mach Zehnder interferometer waveguide (MZIW)

Interferometer is most suitable technique for analytical measurement with real-time interaction monitoring. Our main purpose is to provide the optimization and testing of MZIW. Interferometer based on MZIW consists of input waveguide structure (left *Y* branch) and output waveguide structure (right *Y* branch) [8]. In interferometer measurement, input light is equally guided into the two waveguides and light is recollected into the single

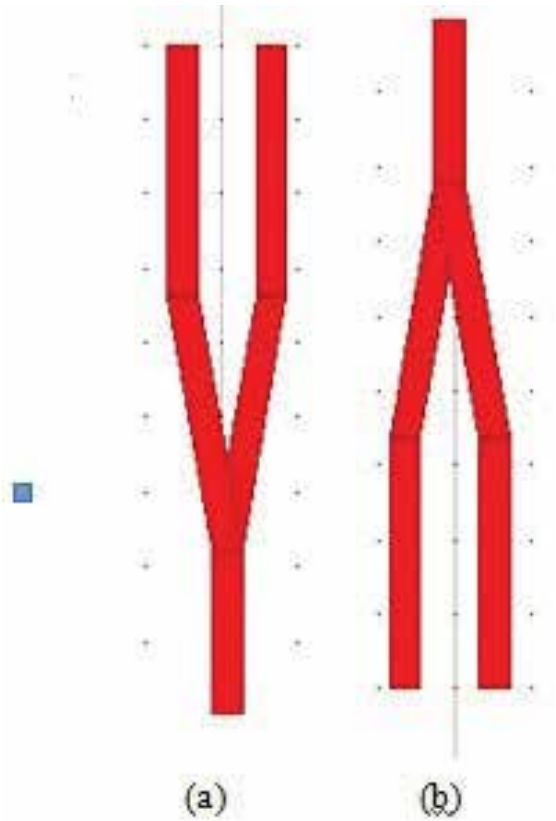


**Figure 1.** *Y* branches (a) Branch [1-2] (b) Branch [2-1].

waveguide as shown in **Figure 1**. One branch is 1-2 and other is the 2-1 branch. The sensing reaction changes the refractive index of sensing waveguide and it changes the speed (phase) of light [9]. The light intensity changes due to the optical interference at the output waveguide (2-1 branch) [10]. **Figure 1** demonstrates one-input and two-output (1-2 branches) and two-input one-output (2-1 branch)-type micro-*Y* branch for the MZIW structure. Many optical evanescent wave sensors in various forms have been used for highly sensitive sensing applications and MZIW is one class of such sensors. MZIW has been designed using one *Y* and one inverted *Y* branch to form an entire waveguide structure [11].

The simplest light waveguide component is the *Y* branch and is a three-port device that acts as a light divider, *Y* branch (1-2) and light collector and inverted *Y* branch (2-1) [12]. **Figure 1** shows a *Y* branch made by splitting a planer waveguide into two branches bifurcating at some angle. These components are very much similar to a fibre optic coupler which can also act as a power splitter except that it has only three ports. Conceptually it differs considerably from a fibre coupler since there is no coupling region in which modes of two different waveguides overlap. Function of the *Y* branch is very simple. With reference to **Figure 1**, in the branch region the waveguide is thicker and supports higher-order modes. However the geometrical symmetry forbids the excitation of asymmetric modes. If the thickness is changed gradually in an adiabatic manner, even higher-order symmetric modes are not excited, and power is

divided into two branches without much loss. In practice, a sudden opening of the gap violates the adiabatic condition, resulting in insertion losses associated with any *Y* branch. These losses depend on the branching angle θ and increases as angle $\theta$ increases.

In practice, what attracts our attention is the presence of a number of relatively primitive, that is, straight and curved waveguides. As it was mentioned earlier, the layout is very coarse and the light interactions actually occur just on a small fraction of the layout. For this reason waveguides are also called as micro-waveguides and the branches are also called as micro-branches. Various types of MZIW structures have been designed for sensing applications.

We have used beam propagation method (BPM) for the analysis of MZIW [13]. The physical propagation requires important information about the distribution of refractive index η(x, y, z) and input wave field, η(x, y, z = 0). From this we can detect the wave field throughout the rest of the domain u (x, y, z > 0).

In addition to above data, the BPM algorithm requires additional information in the form of numerical parameters like:

(i) finite computation domain $\{X \in (x_{min}, x_{max})\}$, $\{Y \in (y_{min}, y_{max})\}$, $\{Z \in (z_{min}, z_{max})\}$,

(ii) transverse grid size Δx and Δy,

(iii) longitudinal step size Δz.

Generally, smaller grid sizes give results with more accuracy. But due to a small grid size, simulation time increases [14]. It is very important and critical to perform a convergence study on the X and Y grid sizes to provide optimization and the tradeoff between speed and accuracy.

## 4. Waveguide configuration and analysis

**Figure 2** shows the MZIW structure in 3D (XYZ) format with reference to this proposed structure. We can join two *Y* branches (refer **Figure 1**) to form the entire MZIW structure (refer **Figure 2**) [15]. To perform this convergence study, we have used the scanning capabilities of beam propagation method, scanning and optimization tools. The MZI layout under the test is shown in **Figures 3** and **4**.

This scanning tool gives very good results. There are various configurations of photonic MZIW, which are used for sensing various physical parameters [16]. **Figure 3(a–d)** shows the experimental data for light output variation as a function of changes in the branch angle for *Y* branch (1-2).

We can use the proper numerical model for the design of the structure with appropriate characteristics.

**Figure 4(a–d)** shows experimental data for output variation as a function of changes in the branch angle for inverted *Y* branch (2-1) [17]. The performance of photonics interferometer depends upon various fibre geometry and fibre parameters.

For the successful design and working of sensor, the process of the parameter optimization is very critical and important.

http://dx.doi.org/10.5772/intechopen.76781

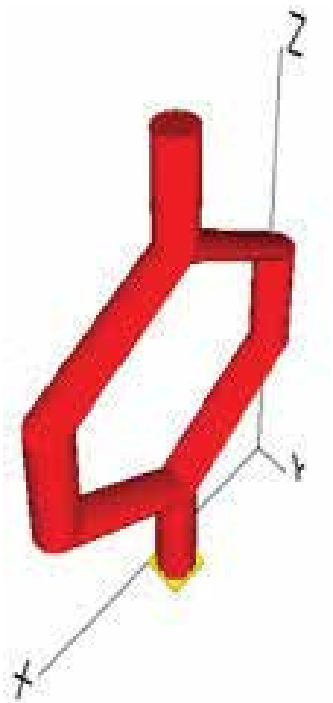


**Figure 2.** MZIW Structure in 3D format.

We have analysed monitor output behaviour with respect to variations in *Y* branch angle. **Figure 5(a–c)** shows the graph of *Y* branch angle variation versus output value.

From this, it is shown to split light and to combine light at *Y* branches already shown in **Figure 2**. The *Y* branch angle should be optimized. The angle should be less than 18°; above this, light propagation will not be appropriate through the MZIW structure. This reduces the output monitor value [18].

Also when light is guided through the bend structure, substantial radiation losses take place and significant distortion of the optical input launch field occurs when light proceeds through the MZIW structure [19]. As shown in **Figure 5(a)**, as we vary angle between 0° and 25°, monitor output value decreases, and as we increase angle variation beyond 25° that is up to 45°, monitor output value further decreases. This is represented in the graph shown in **Figure 5(b)**. In **Figure 5(c)** as we increase angle variation beyond 45° that is up to 75°, the monitor output value further goes on reducing.

The measuring sensitivity of the MZI structure is given by Eq. (1):

$$S = \frac{\Delta P}{\Delta n} \tag{1}$$

where $\Delta P$ is the monitor output power and $\Delta n$ is the refractive index change at measuring branch.

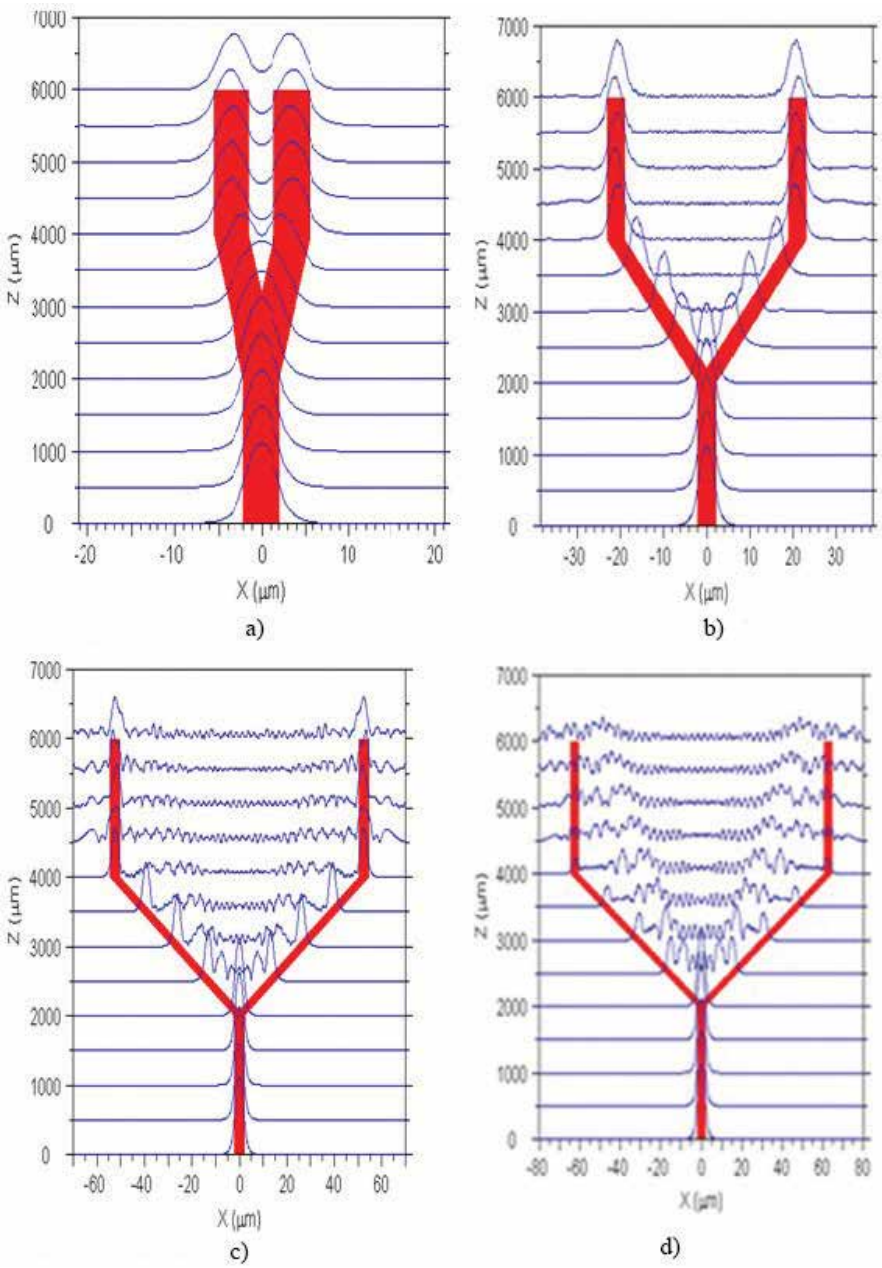


**Figure 3.** (a) Light guiding variation for *Y* branch at an angle of 18°; (b) light guiding variation for *Y* branch at an angle of 25°; (c) light guiding variation for *Y* branch at an angle of 45° and (c) light guiding variation for *Y* branch at an angle of more than 75°.

From **Figure 5(a–c)**, it is easily interpreted that beyond 18° it is difficult to guide light to the waveguide. These losses depend on the branching angle and increase as the angle increases.

**Figure 6(a** and **b)** shows the complete MZIW structure after optimum selection of *Y* branch angle (18°) for both the branches. This waveguide has a width of 3 μm and length of 40 μm. This structure is used for sensing applications like refractive index measurement of small

http://dx.doi.org/10.5772/intechopen.76781

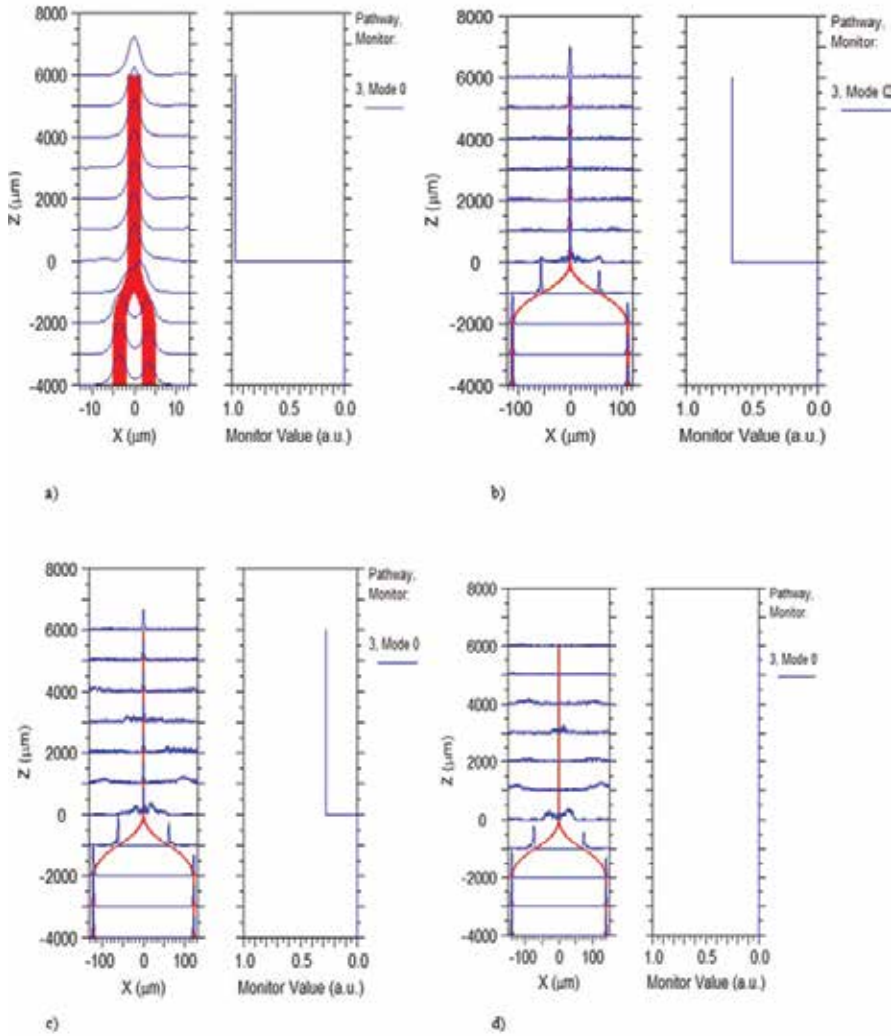


**Figure 4.** (a–d) Experimental data for output variation as a function of changes in branch angle for inverted *Y* branch (2-1). (a) Light guiding variation for *Y* branch at an angle of 18°; (b) light guiding variation for *Y* branch at an angle of 60°; (c) light guiding variation for *Y* branch at an angle of 75°; and (d) light guiding variation for *Y* branch at an angle more than 75°.

samples under measurement. The validation of the innovative approach is achieved by the characterization of the above MZIW structure. The sensitivity of the sensors is the most dominating and demanding parameter as it directly relates to how early the sensing parameters are detected [20].

According to the theory of interferometer, the intensity modulation scheme should be characterized by an output intensity of MZI behaving as a cosine function of the phase variation as shown in **Figure 5**. Indeed the detected light output power $I_{out}$ at the output of the *Y* branch (2-1) of the interferometer can be detected as given by Eq. (2).

$$I_{out} = I_r + I_{s+2\sqrt{}} I_s I_r \cos(\Delta\varphi) \tag{2}$$

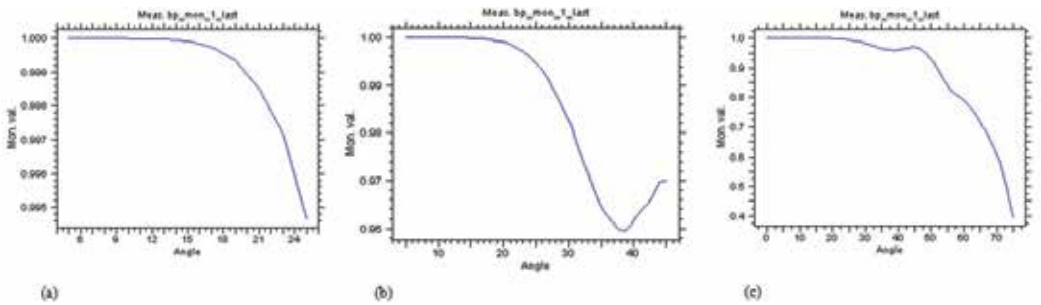


**Figure 5.** (a–c) Graph of angle variation between 0 and 75°. (a) Output value for angle variation between 0 and 25°; (b) output value for angle variation between 0 and 45°; (c) output value for angle variation between 0 and 75°.

where $I_r$ and $I_s$ are the optional powers of the reference and sensing waveguide observed in each arm of MZIW and $\Delta\phi$ is the phase difference between both waveguides.

The above result and study elucidates the influence of the *Y* branch angle on light guiding the MZIW structure and the MZIW variation in the angle changes light guiding efficiency, so the angle must be properly selected for sensing applications. From the above analysis and experimentation, it is observed that the optimum value for the angle is required to be below 18° (for 1-2 branch). In case of the MZIW interferometer, we know that one arm of the waveguide structure is acting as a reference arm and other arm is acting as a measurement arm. According to the graphs shown in **Figure 5(a–c)**, if light is not properly guided into the reference arm and other measurement arms of waveguides, it will produce considerable variations in the output monitor value. Due to these variations, the physical parameter that is to be

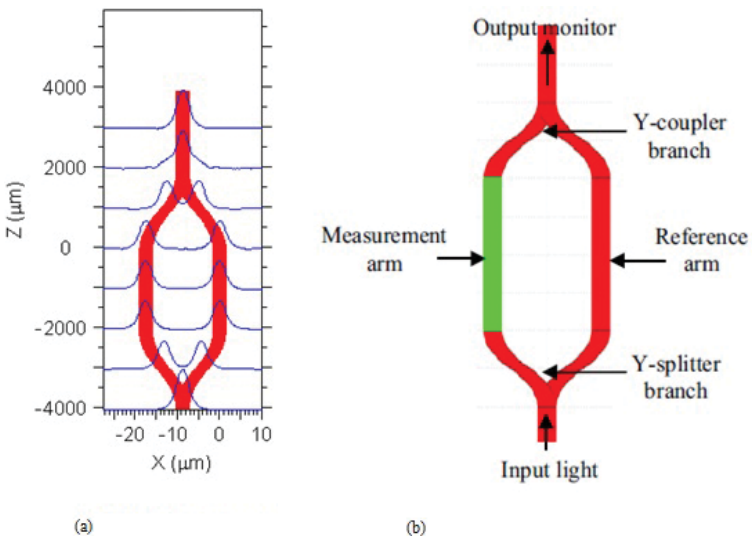


**Figure 6.** (a) MZIW structure using two *Y* branches and (b) complete MZIW structure used for sensing application.

http://dx.doi.org/10.5772/intechopen.76781

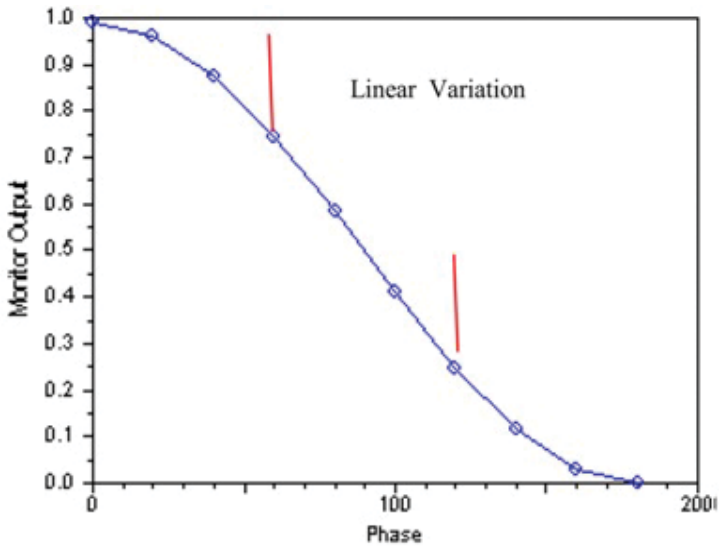


**Figure 7.** Graph of variation in phase shift and monitor output value for MZIW structure shown in **Figure 6**.

sensed using the interferometer will not be detected correctly. Output measurement becomes difficult. These types of waveguide structures are applicable to any measurement application that changes phase and amplitude of light passing through the waveguide. Generally branch angle should be maintained below 1 radian to reduce insertion losses below 1 dB and 18° for measurement applications.

Analysis and experimental characterization of MZIW is performed using a "beam propagation method" algorithm. Measurement is carried out by using an MZIW structure having branch angle as 18° (for the *Y* branch); however, the insertion loss of power divided also increases rapidly and often becomes intolerable after three or four bifurcation stages.

After the optimization of MZIW for the measurement application is completed, the next part is to analyse the structure for the refractive index (RI) measurement. **Figure 7** shows the phase shift variation due to refractive index variation and corresponding changes in the output monitor value. Due to proper light splitting and combining, changes in phase shift produced due to variations in the refractive index of the sample can be measured.

## 5. Conclusion

Measurements are carried out by using an MZI structure having branch angle of 18° (for the *Y* branch); however, the insertion loss of power divided also increases rapidly and often becomes intolerable after three or four bifurcation stages. The next step of this chapter consists of the characterization of rib waveguide-based MZI optical sensor.

## Acknowledgements

The authors would like to thank University of Pune and also appreciate the help extended by the University for providing funding under the Research and Development Program for this proposed research study work [Reference: BCUD/14, 2008–2010].

We also thank the Management of Dr. D.Y. Patil Institute of Technology, Pune, and S.G.G.S. Institute of Engineering and Technology, Nanded, for providing the necessary facilities for carrying out this work.

## Author details

Prashant Bansilal Patel[1]* and Satish T. Hamde[2]

*Address all correspondence to: prashantbgpatel@gmail.com

1 Dr. D.Y. Patil Institute of Technology (DIT), Pune, Maharashtra, India

2 S.G.G.S. Institute of Engineering and Technology (SGGSIET), Nanded, Maharashtra, India

## References

[1] Patel PB, Hamde ST. Analysis of the Mach-Zehnder interferometer waveguide structure for refractive index measurement. Journal of Optics. 2017;**46**(4):398-402

[2] Yuan D, Dong Y, Liuand Y, Li T. Mach-Zehnder interferometer biochemical sensor based on silicon-on-insulator rib waveguide with large cross section. Sensors. 2015;**15**: 21500-21517

[3] Weisser M, Tovar G, Mittler-Neher S, Knoll W, Brosinger F, Freimuth H, Lacher M, Ehrfeld W. Specific bio-recognition reactions observed with an integrated Mach-Zehnder interferometer. Biosensors and Bioelectronics. 1999;**14**:409-415

[4] Bosch ME, Sánchez AJR, Rojas FS, Ojeda CB. Recent development in optical fiber biosensors. Sensors. 2007;**7**:797-859

[5] Patel PB, Hamde ST. Characterization of the properties of optical wavefields—An investigations. Journal of Environmental Research and Development (JERAD). 2009;**4**(2):1-2

[6] Patel PB, Hamde ST. Miniaturized Fiber Optic Integrated Biosensor Platforms for Human Health Monitoring, International Conference on Emerging Technologies and Application in Engineering, Technology and Sciences (ICETAETS-08) at Saurashtra University; 13 and 14th January-2008; Rajkot, Gujrat

[7] Heideman RG, Kooyman RPH, Greve J. Performance of a highly sensitive optical waveguide Mach-Zehnder interferometer immunosensor. Sensors & Actuators B. 1993; **10**:209-217

[8] Hu MH, Huang JZ, Scarmozzino R, Levy M, Osgood RM. Tunable Mach-Zehnder polarization splitter using height-tapered Y-branches. IEEE Photonics Technology Letters. 2001;**6**:09

[9] Greivenkamp JE, editor. Handbook of Optics. Vol. 1. 2nd ed. University of Arizona, Tucson, Arizona: Interference, Optical Science Centre. Chapter 2

[10] Estevez MC, Alvarez M, Lechuga LM. Integrated optical devices for lab-on-a-chip biosensing applications. Laser & Photonics Reviews. 2012;**6**:463

[11] Sasaki H, Shiki E, Mikoshiba N. Propagation characteristic of optical guided waves in asymmetric branching waveguides. IEEE Journal of Quantum Electronics. 1981;**QE-17**(6): 1051-1057

[12] Thylen L. The beam propagation method: An analysis of it applicability. Optical and Quantum Electronics. 1983;**15**:433-439

[13] Neyer A, Mevenkamp W, Thylen L, Bo L. A beam propagation method analysis of active and Pasive waveguide crossing. IEEE Journal of Lightwave Technology. 1985;**LT-3**(3): 635-642

[14] Doerr CR. Beam propagation method tailored for step-index waveguides. IEEE Photonics Letters. 2001;**13**(2):2-3

[15] Patel PB, Hamde ST. Photonics sensing techniques based on various Mach Zehnder Interferometer Waveguide (MZIW) structures. In: International Conference on Biomedical Engineering; NIT Jalandhar; 17-19th Dec, 2010

[16] Qi Z-m, Matsuda N, Itoh K, Murabayashi M, Lavers CR. A design for improving the sensitivity of a Mach-Zehnder interferometer to chemical and biological measurements. Sensors and Actuators, B. 2002;**81**:254-258

[17] Sethi RS. Transducer aspects of biosensors. Biosensors & Bioelectronics. 1994;**9**:243-264

[18] Iqbal M, Gleeson MA, Spaugh B, Tybor F, Gunn WG, Hochberg M, Baehr-Jones T, Bailey RC, Gunn LC. Label-free biosensor arrays based on silicon ring resonators and high-speed optical scanning instrumentation. IEEE Journal of Selected Topics in Quantum Electronics. 2010;**16**:654-661

[19] Adams MJ. An Introduction to Optical Wave Guides. Chapter 7. New York: Wiley;

[20] Levy R, Peled A, Ruschin S. Waveguided SPR sensor using a Mach-Zehnder interferometer with variable power splitter ratio. Sensors and Actuators B. 2006;**119**:20-26

Section 2

# Photonic and Optical Waveguides

Chapter 6

# Review on Optical Waveguides

Shankar Kumar Selvaraja and Purnima Sethi

Additional information is available at the end of the chapter

http://dx.doi.org/10.5772/intechopen.77150

**Abstract**

Optical devices are necessary to meet the anticipated future requirements for ultrafast and ultrahigh bandwidth communication and computing. All optical information processing can overcome optoelectronic conversions that limit both the speed and bandwidth and are also power consuming. The building block of an optical device/circuit is the optical waveguide, which enables low-loss light propagation and is thereby used to connect components and devices. This chapter reviews optical waveguides and their classification on the basis of geometry (Non-Planar (Slab/Optical Fiber)/Planar (Buried Channel, Strip-Loaded, Wire, Rib, Diffused, Slot, etc.)), refractive index (Step/Gradient Index), mode propagation (Single/Multimode), and material platform (Glass/Polymer/Semiconductor, etc.). A comparative analysis of waveguides realized in different material platforms along with the propagation loss is also presented.

**Keywords:** optical waveguides, integrated optics, optical devices, optical materials, photonics integrated circuits

## 1. Introduction

Waveguides are indispensable for communication and computing applications as they are immune to electromagnetic interference and induced cross talk and also counter diffraction. Next-generation high-end information processing (bandwidths >1 Tb/s and speed >10 Gb/s) is immensely challenging using copper-based interconnects. Optical interconnects transmit data through an optical waveguide and offer a potential solution to improve the data transmission [1, 2]. There are predominantly two classes of optical waveguide: those in which "classical optical elements, placed periodically along the direction of propagation of the wave, serve to confine the wave by successive refocusing in the vicinity of the optical axis (laser resonators and multiple lens waveguides); and those in which the guiding mechanism is that of multiple

total internal reflection from interfaces parallel to the optical axis" (fiber optical waveguides, slab waveguides, and resonators) [3].

Historically, high-frequency microwave sources had created a furore on guided wave photonics pioneered by Rayleigh and Sommerfeld. The first theoretical description of mode propagation along a dielectric guide was done by Hondros and Debye in 1910 [3]. The first dielectric waveguide to be examined at optical frequencies was the glass fiber used primarily for fiber optics imaging applications [4].

A waveguide can be defined as any structure (usually cylindrical) used for guiding the flow of electromagnetic wave in a direction parallel to its axis, confining it to a region either within or adjacent to its surfaces. In order to understand the propagation of light in a waveguide, it is imperative to derive the wave equation. The electromagnetic wave equation can be derived from the Maxwell's equation, assuming that we are operating in a source free ($\rho = 0,\ J = 0$), linear ($\varepsilon$ and $\mu$ are independent of $E$ and $H$), and an isotropic medium. $E$ and $H$ are the electric and magnetic field amplitudes, respectively, $\varepsilon$ is the electric permittivity of the medium, and $\mu$ is the magnetic permeability of the medium. The equations are:

$$\nabla \times \overline{E} = -\frac{\partial \overline{B}}{\partial t} \tag{1}$$

$$\nabla \times \overline{H} = \frac{\partial \overline{D}}{\partial t} \tag{2}$$

$$\nabla . \overline{D} = 0 \tag{3}$$

$$\nabla . \overline{B} = 0 \tag{4}$$

Here, $B$ and $D$ are magnetic and electric fluxes, respectively. The wave equation derived from the above expressions is:

$$\nabla^2 \overline{E} - \mu\varepsilon \frac{\partial^2 \overline{E}}{\partial t^2} = -\nabla\left(\overline{E}.\frac{\nabla\varepsilon}{\varepsilon}\right) \tag{5}$$

The right-hand side of Eq. (5) is nonzero when there is a gradient in permittivity of the medium. Guided wave medium has a graded permittivity; however, in most structures, the term is negligible. Thus, the wave equation can be written as:

$$\nabla^2 \overline{E} - \mu\varepsilon \frac{\partial^2 \overline{E}}{\partial t^2} = 0,\ \nabla^2 \overline{H} - \mu\varepsilon \frac{\partial^2 \overline{H}}{\partial t^2} = 0 \tag{6}$$

for electric and magnetic field amplitudes, respectively.

## 2. Classification of waveguides

Optical waveguides can be classified according to their geometry, mode structure, refractive index (RI) distribution, and material. A dielectric optical waveguide comprises a longitudinally

extended high-index medium called the *Core*, which is transversely surrounded by a low-index medium, called the *Cladding*. A guided optical wave propagates in the waveguide along the longitudinal direction. The characteristics of a waveguide are determined by the transverse profile of its dielectric constant *(x, y),* which is independent of the *z* coordinate. For a waveguide made of optically isotropic media, the waveguide can be characterized merely with a single spatially dependent transverse profile of the index of refraction, n*(x, y)*. Broadly, the waveguides can be classified as [5]:

- Planar/2-D waveguides: Optical confinement is only in one transverse direction, the core is sandwiched between cladding layers in only one direction (**Figure 1(a)**). Optical confinement is only in the *x*-direction with index profile *n(x).* They are primarily used for high-power waveguide lasers and amplifiers.
- Non-planar/3-D/channel optical waveguide: Comprises of two-dimensional transverse optical confinement, the core is surrounded by cladding in all transverse directions, and $n(x, y)$ is a function of both $x$ and $y$ coordinates as shown in **Figure 1(b)**. A channel waveguide (with guidance in both directions) has a guiding structure in the form of a stripe with a finite width. Examples: channel waveguides (Section 2.3.II) and circular optical fibers [6].

A waveguide in which the index profile changes abruptly between the core and the cladding is called a step-index waveguide, while one in which the index profile varies gradually is called a graded-index waveguide as shown in **Figure 2**. Recently, hybrid index profile waveguide was shown combining both inverse-step index waveguide and graded index waveguides for high-power amplification of a Gaussian single-mode beam [7].

### 2.1. Waveguide mode

A waveguide mode is an electromagnetic wave that propagates along a waveguide with a distinct phase velocity, group velocity, cross-sectional intensity distribution, and polarization. Each component of its electric and magnetic field is of the form $f(x, y)e^{i\omega t - ihz}$, where $z$ is the axis of the waveguide. Modes are referred to as the "characteristic waves" of the structures because their field vector satisfies the homogenous wave equation in all the media that make up the

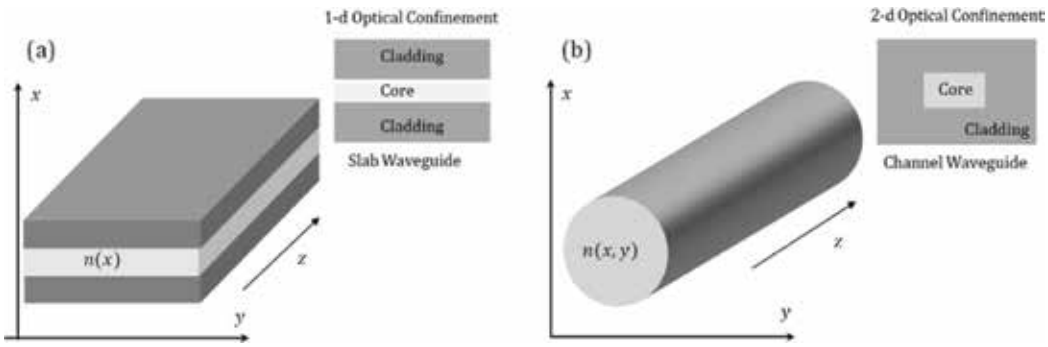


**Figure 1.** (a) Planar optical waveguide of 1-d transverse *(x)* optical confinement, (b) non-planar optical waveguide of 2-D transverse *(x, y)* optical confinement.

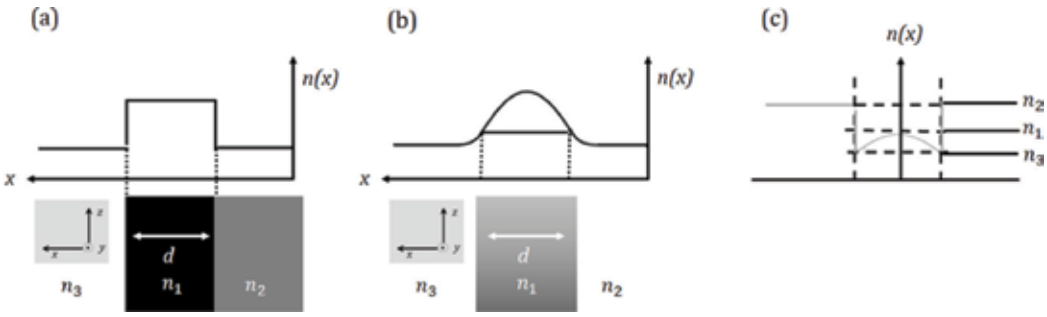


**Figure 2.** (a) Step-index type waveguide, (b) Graded-index waveguide, and (c) Hybrid waveguide.

guide, as well as the boundary conditions at the interfaces. The electric and magnetic fields of a mode can be written as $E_v(r,t) = E_v(x,y)\exp(i\beta_v z - i\omega t)$ and $H_v(r,t) = H_v(x,y)\exp(i\beta_v z - i\omega t)$, where ν is the mode index, $E_v(x,y)$ and $H_v(x,y)$ are the mode field profiles, and $\beta_v$ is the propagation constant of the mode.

A mode is characterized by an invariant transversal intensity profile and an effective index $(n_{eff})$. Each mode propagates through the waveguide with a phase velocity of $c/n_{eff}$, where $c$ denotes the speed of light in vacuum and $n_{eff}$ is the effective refractive index of that mode. It signifies how strongly the optical power is confined to the waveguide core. In order to understand modes intuitively, consider a simple step-index 2-D waveguide and an incident coherent light at an angle $\theta$ between the wave normal and the normal to the interface as shown in **Figure 3**. The critical angle at the upper interface is $\theta_c = \sin^{-1} n_c/n_f$ and lower interface $\theta_s = \sin^{-1} n_s/n_f$ and $n_s < n_c$ $(\theta_s < \theta_c)$.

Optical modes with an effective index higher than the largest cladding index are (1) **Guided modes** $(\theta_s < \theta < 90^\circ)$: As the wave is reflected back and forth between the two interfaces, it interferes with itself. A guided mode can exist only when a transverse resonance condition is satisfied so that the repeatedly reflected wave has constructive interference with itself. Modes with lower index are radiating and the optical power will leak to the cladding regions. They can be categorized as (2) **Substrate radiation modes** $(\theta_c < \theta < \theta_s)$: Total reflection occurs only at the upper interface resulting in refraction of the incident wave at the lower interface from either the core or the substrate, (3) **Substrate-cover radiation modes** $(\theta < \theta_c)$: No total reflection at either interface. Incident wave is refracted at both interfaces, and it can transversely extend to infinity on both sides of the waveguide, and (4) **Evanescent modes**: Their fields decay exponentially along the $z$ direction. For a lossless waveguide, the energy of an evanescent mode radiates away from the waveguide transversely.

The waveguide dimensions determine which modes can exist. Most waveguides support modes of two independent polarizations, with either the dominant magnetic (quasi-TM) or electric (quasi-TE) field component along the transverse (horizontal) direction. For most applications, it is preferable that the waveguides operate in a single-mode regime for each polarization. This single-mode regime is obtained by reducing the waveguide dimensions until all but

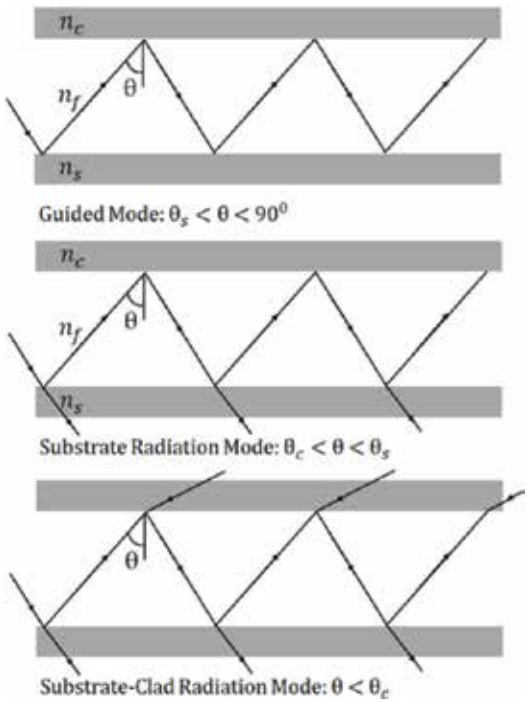


**Figure 3.** Ray-optical picture of modes propagating in an optical waveguide.

the fundamental waveguide modes become radiating. Fields in the waveguide can be classified based on the characteristics of the longitudinal field components, namely (1) **Transverse electric and magnetic mode** (TEM mode): $E_z = 0$, and $H_z = 0$. Dielectric waveguides do not support TEM modes, (2) **Transverse electric mode** (TE mode): $E_z = 0$ and $H_z \neq 0$, (3) **Transverse magnetic mode** (TM mode): $H_z = 0$ and $E_z \neq 0$, and (4) **Hybrid mode:** $E_z \neq 0$ and $H_z \neq 0$. Hybrid modes exist only in non-planar waveguide.

## 2.2. Planar waveguide

Homogeneous wave equations exist for planar slab waveguides of any index profile *n(x)*. For a planar waveguide, the modes are either TE or TM.

Infinite slab waveguide: The slab waveguide is a step-index waveguide, comprising a high-index dielectric layer surrounded on either side by lower-index material (**Figure 4**). The slab is infinite in

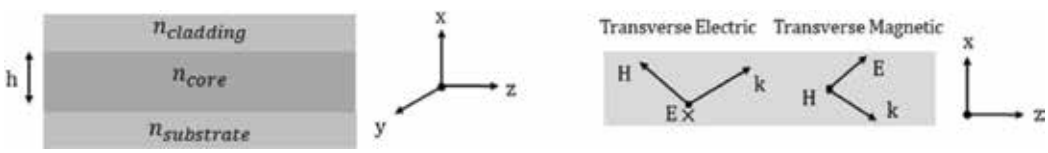


**Figure 4.** Planar slab waveguide and transverse electric (TE) and transverse magnetic configuration (TM).

the *y*-*z* plane and finite in *x* direction and the refractive index of $n_{core} > n_{cladding}, n_{substrate}$ to ensure total internal reflection at the interface. For case (1): $n_{cladding} = n_{substrate}$, the waveguide is denoted as **Symmetric** and for case (2): $n_{cladding} \neq n_{substrate}$, waveguide is **Asymmetric**.

For the electromagnetic analysis of the planar slab waveguide (infinite width), assuming $n_{core} > n_{substrate} > n_{cladding}$, we consider two possible electric field polarizations—TE or TM. The axis of waveguide is oriented in *z*-direction: *k* vector of the guided wave will propagate down the *z*-axis, striking the interfaces and angles greater than critical angle. The field could be TE which has no longitudinal component along *z*-axis (electric field is transverse to the plane of incidence established by the normal to the interface, and the *k* vector) or TM depending on the orientation of the electric field.

**I. For TE Asymmetric waveguide**: *E* field is polarized along the y-axis, and assuming that waveguide is excited by a source with frequency $\omega_o$ and a vacuum wave vector of magnitude $\frac{\omega_o}{c}$, the allowed modes can be evaluated by solving the wave equation in each dielectric region through boundary conditions. For a sinusoidal wave with angular frequency $\omega_o$, the wave equation for the electric field components in each region can be written as ($|k| = \omega\sqrt{\mu\varepsilon} = k$),

$$\nabla^2 E_y + {k_0}^2 {n_i}^2 E_y = 0 \tag{7}$$

here, $n_i$ can be the refractive index of either core, cladding, or the substrate. The solution to Equation (7) can be written as:

$$E_y(x, z) = E_y(x) e^{-j\beta z} \tag{8}$$

due to the translational invariance of the waveguide in z-direction. $\beta$ is the propagation constant along the *z*-direction (longitudinal). From Equation (8) and since $\frac{d^2 y}{dx^2} = 0$, we can write:

$$\frac{\partial^2 E_y}{\partial x^2} + \left({k_0}^2 {n_i}^2 - \beta^2\right) E_y = 0 \tag{9}$$

The solution to the wave equation can be deduced by considering Case (1) $\beta > k_0 n_i$ and $E_0$ is field amplitude at x = 0, solution is exponentially decaying and can be written as:

$$E_y(x) = E_0 e^{\pm\sqrt{\beta^2 - {k_0}^2 {n_i}^2}x} \tag{10}$$

The attenuation constant $\Upsilon = \sqrt{\beta^2 - {k_0}^2 {n_i}^2}$. Case (2) $\beta < k_0 n_i$, solution has an oscillatory nature and is given by:

$$E_y(x) = E_0 e^{\pm\sqrt{{k_0}^2 {n_i}^2 - \beta^2}x} \tag{11}$$

The transverse wave vector $\kappa = \sqrt{{k_0}^2 {n_i}^2 - \beta^2}$ and the relation between $\beta$, $\kappa$ and *k* are given by $k^2 = \beta^2 + \kappa^2$.

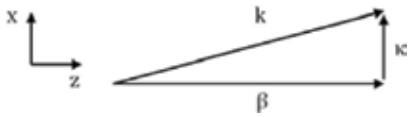


The longitudinal wave vector $\beta$ ($z$ component of $k$) must satisfy $k_0 n_{substrate} < \beta < k_0 n_{core}$ ($n_{cladding} \leq n_{core}$) in order to be guided inside the waveguide. Eigen values for the waveguide can be derived using transverse components of electric field amplitudes in three regions as $E_y(x) = Ae^{-\gamma_{cladding}x}$ for $0 < x; E_y(x) = Bcos(\kappa_{core}x) + Csin(\kappa_{core}x)$ for $-h < x < 0;$ $E_y(x) = De^{\gamma_{substrate}(x+h)}$ for $x < -h$, where $A$, $B$, $C$, and $D$ are amplitude coefficients to be derived using boundary conditions ($E_y, H_z, \frac{\partial E_y}{\partial x}$ $(at\ x = 0)$ are continuous). Solving the equation, we get $A = B, C = -\frac{A\Upsilon_{cladding}}{\kappa_{core}}$, $D = A[\cos(\kappa_{core}h) + \frac{\gamma_{cladding}}{k_{core}}\sin(k_{core}h]$, and thus:

$$\left.\frac{\partial E_y}{\partial x}\right|_{x=-h} = A\left[k_{core}\sin(k_{core}h) - \gamma_{cladding}\, cos\,(k_{core}h)\right](\text{Core})$$

$$= A\left[\, cos\,(k_{core}h) + \frac{\gamma_{cladding}}{k_{core}}\sin(k_{core}h)\right]\gamma_{substrate}(\text{Substrate}).$$

The Eigenvalue equation (**Figure 5(a)**) is given by:

$$\tan(hk_{core}) = \frac{\gamma_{cladding} + \gamma_{subtrate}}{k_{core}\left[1 - \frac{\gamma_{cladding}\gamma_{substrate}}{k_{core}^2}\right]} \tag{12}$$

**II**. **TM Asymmetric waveguide:** The field components of the waveguide can be written as:

$H_Y(x, y, t) = H_m(x)e^{-i\omega t}$, $E_x(x, z, t) = \frac{\beta}{\omega\varepsilon}H_m(x)e^{-i(\omega t - \beta z)}$, and $E_z(x, z, t) = \frac{-i}{\omega\varepsilon}$. The Eigen value for $\beta$ (**Figure 5(b)**) is given by:

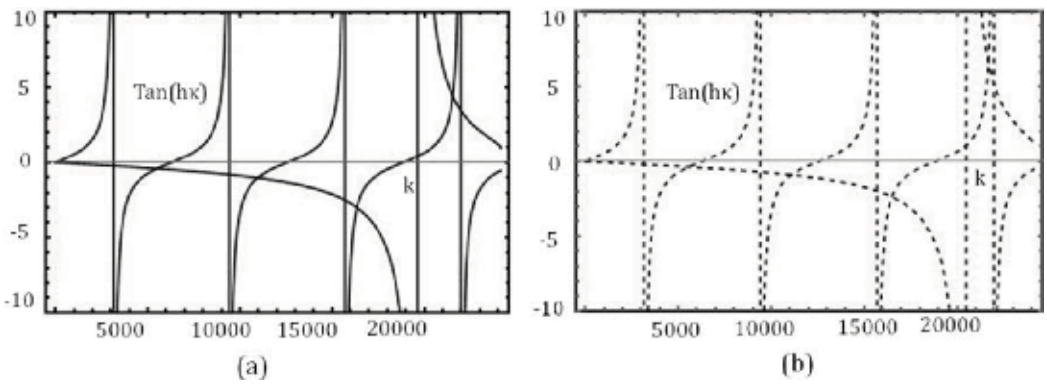


**Figure 5.** Plot for Eigen value equation for (a) Asymmetric TE mode slab waveguide, (b) Asymmetric TM mode slab Waveguide.

$$\tan(hk_{core}) = \frac{k_{core}\left[\frac{n_{core}^2}{n_{substrate}^2}\gamma_{substrate} + \frac{n_{core}^2}{n_{cladding}^2}\gamma_{cladding}\right]}{k_{core}^2 - \frac{n_{core}^4}{n_{cladding}^2 n_{substrate}^2}\gamma_{cladding}\gamma_{substrate}} \tag{13}$$

**III. TE Symmetric waveguide:** The field equation of a TE mode within the symmetric waveguide is given by:

$$\begin{aligned} E_y &= Ae^{-\gamma\left(x-h/2\right)} && \text{for } x \geq h/2 \\ E_y &= A\frac{\cos\kappa x}{\cos\kappa h/2} \text{ or } A\frac{\sin\kappa x}{\sin\kappa h/2} && \text{for } -h/2 \leq x \leq h/2 \\ E_y &= \pm Ae^{\gamma\left(x+h/2\right)} && \text{for } x \leq -h/2 \end{aligned} \tag{14}$$

The characteristic Eigen value equation for the TE modes in a symmetric waveguide is given by:

$$\begin{aligned} \tan\frac{\kappa h}{2} &= \gamma/k \text{ for even (cos) modes} \\ &= -k/y \text{ for odd (sin) modes} \end{aligned} \tag{15}$$

In order to plot the Eigen values of the TE modes of the symmetric waveguide, solutions of Eq. (15) are plotted for a wavelength of 1.55 μm and different "*h*" values (15 μm and 3 μm respectively) as shown in **Figure 6**.

The longitudinal wave vector β is quintessential to describe the field amplitudes in all regions of the waveguide. (i) Every Eigen value $\beta$ corresponds to a distinct confined mode of the system. The amplitude of the mode is established by the power carried in the mode; (ii) only a finite number of modes will be guided depending on the wavelength, index contrast, and

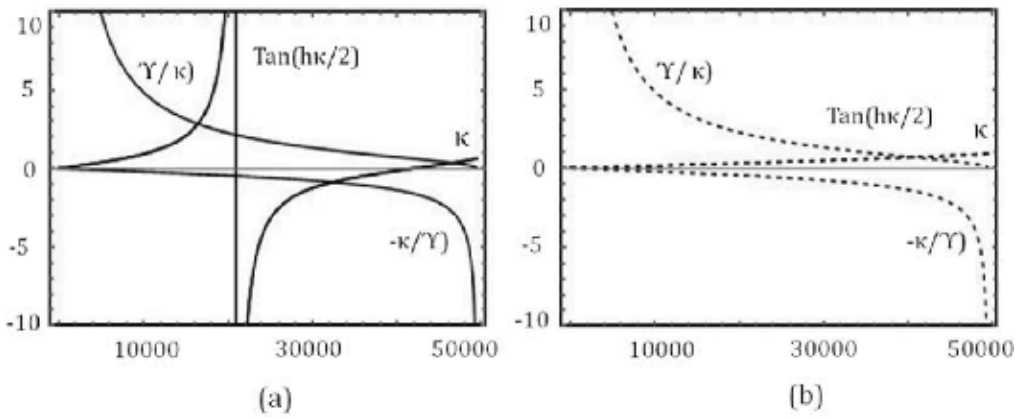


**Figure 6.** Plot for Eigen value equation for Symmetric TE mode slab waveguide at a wavelength of 1.55 μm for waveguide width of (a) 15 μm and (b) 3 μm. Thick waveguide supports multimode transmission.

waveguide dimensions; (iii) most modes will be unguided, and all modes are orthogonal to each other; (iv) some modes are degenerate. Degenerate modes will share the same value of $\beta$ but will have distinguishable electric field distributions. The **lower-order mode** is expressed by $\beta_{lowest\ order} \approx kn_{core}$ and **higher-order mode** by $\beta_{lowest\ order} \approx kn_{core}\cos\theta_{critical} \approx kn_{substrate}$. A waveguide is generally characterized by its normalized frequency, given by,

$$V = hk\left(n_{core}^2 - n_{subtrate}^2\right)^{1/2}.$$

The approximate number of modes ($m$) in the waveguide are given by $m \approx V/\pi$. Graphical solution to the waveguide can be evaluated by:

$$V = k_0 h\left(n_{core}^2 - n_{substrate}^2\right)^{1/2} \tag{16}$$

$$a = \left(n_{substrate}^2 - n_{cladding}^2\right) / \left(n_{core}^2 - n_{substrate}^2\right) \tag{17}$$

$$b = \left(n_{eff}^2 - n_{substrate}^2\right) / \left(n_{core}^2 - n_{substrate}^2\right) \tag{18}$$

where $a$ is asymmetry parameter (ranges from 0 (symmetric waveguide) to infinity), $b$ is normalized effective index (ranges from 0 (cutoff) to 1) and $n_{eff} = \beta/k_o$ is the effective index of the waveguide. The normalized dispersion relation is given by (**Figure 7**):

$$V\sqrt{1-b} = v\pi + \tan^{-1}\sqrt{b/(1-b)} + \tan^{-1}\sqrt{(b+a)/(1-b)} \tag{19}$$

where ν is an integer. The cut-off condition ($b = 0$) for modes in a step-index waveguide is given by $V = tan^{-1}\sqrt{a} + v\pi$. The numerical aperture is defined as the maximum angle that an

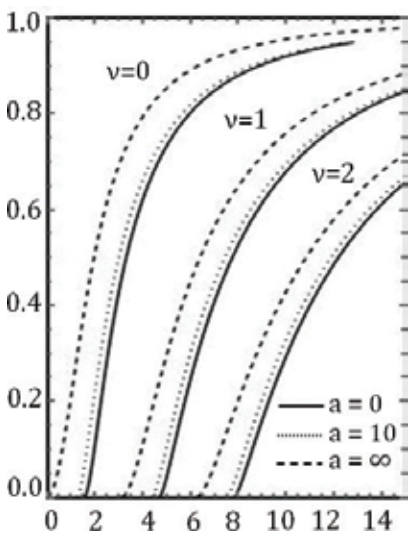


**Figure 7.** Normalized index $b$ versus normalized frequency $V$ for different values of asymmetry coefficient $a$ (a = 0, a = 10, a = ∞).

incident wave can have and still be guided within the waveguide. It is given by: $\mathrm{N}A = sin\,\theta_{max} = \sqrt{n_{core}^2 - n_{substrate/cladding}^2}$.

**IV. TM Symmetric waveguide:** The characteristic Eigen value equation for the TM modes in a symmetric waveguide is given by:

$$\begin{aligned}\tan\frac{\kappa h}{2} = &\quad (n_{core}/n_{substrate})^{2\gamma/\kappa} : \text{ even (cos) modes} \\ &= -(n_{core}/n_{substrate})^{2\kappa/\gamma} \text{ for odd (sin) modes}\end{aligned} \tag{20}$$

Graphical solution to the waveguide can be evaluated using:

$$V = k_0 h\left(n_{core}^2 - n_{substrate}^2\right)^{1/2} \tag{21}$$

$$a = \frac{n_{core}^2 n_{substrate}^2 - n_{cladding}^2}{n_{cladding}^2 n_{core}^2 - n_{substrate}^2} \tag{22}$$

$$b = \left(n_{eff}^2 - n_{substrate}^2\right) / \left(n_{core}^2 - n_{substrate}^2\right) \tag{23}$$

### 2.3. Non-planar waveguide

The following section describes step-index circular and channel waveguides.

**I. Step-index circular waveguide:** The wave equation for the step-index circular waveguides in cylindrical coordinates is given by:

$$E(r,\phi,z) = \hat{r}E_r(r,\phi,z) + \hat{\phi}E_\phi(r,\phi,z) + \hat{z}E_z(r,\phi,z) \tag{24}$$

At $z = 0$, field is purely radial (**Figure 8**).The $E_z$ component of the electric field couples only to itself and the scalar wave equation for $E_z$ is given by:

$$\frac{1}{r}\frac{\partial}{\partial r}\left(r\frac{\partial E_z}{\partial r}\right) + \frac{1}{r^2}\frac{\partial^2 E_z}{\partial \phi^2} + \frac{\partial^2 E_z}{\partial z^2} + k_0^2 n^2 E_z = 0 \tag{25}$$

One can write $E_z(r,\phi,z) = R(r)\phi(\varphi)Z(z)$, Eq. (24) can be written as:

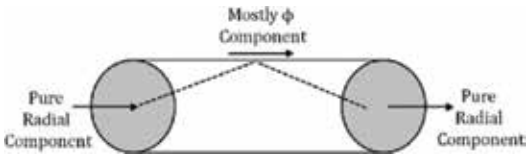


**Figure 8.** Schematic representation of step-index circular waveguide.

$$R''\Phi Z + \frac{1}{r}R'\Phi Z + \frac{1}{r^2}R\Phi'' Z + R\Phi Z'' + k_0^2 n^2 R\Phi Z = 0 \tag{26}$$

The solution to the wave equation is deduced from separation of variables, and we obtain:

$$r^2\frac{\partial^2 R}{\partial r^2} + r\frac{\partial R}{\partial r} + r^2\left(k_0^2 n^2 - \beta^2 - \frac{v^2}{r^2}\right)R = 0 \tag{27}$$

The solution is given by Bessel functions: (1),$J_\nu(\kappa r)$ when $k_0^2 n^2 - \beta^2 - \nu^2/r^2$ is positive ($\kappa^2 = k_0^2 n^2 - \beta^2$) and (2) $K_\nu(\Upsilon r)$ when $k_0^2 n^2 - \beta^2 - \nu^2/r^2$ is negative ($\gamma^2 = \beta^2 - k_0^2 n^2$). Bessel function (1) can be approximated by ($\kappa r$ is large) (**Figure 9**):

$$J_v(\kappa r) \approx \sqrt{\frac{2}{\pi\kappa r}}\cos\left(\kappa r - \frac{v}{\pi r} - \frac{\pi}{4}\right) \tag{28}$$

And solution to (2) is

$$K_v(\gamma r) \approx \frac{e^{-\gamma r}}{\sqrt{2\pi\gamma r}} \tag{29}$$

The equation for field distribution in the step-index fiber can be calculated through:

$E_r = \frac{-j\beta}{\kappa^2}\left[A\kappa J_v'(\kappa r) + \frac{j\omega\mu v}{\beta r}BJ_v(\kappa r)\right]e^{jv\phi}e^{-j\beta z}$, $E_\phi = \frac{-j\beta}{\kappa^2}\left[\frac{jv}{r}AJ_v(\kappa r) - \frac{\omega\mu}{\beta}B\kappa J_v'(\kappa r)\right]e^{jv\phi}e^{-j\beta z}$, $H_r = \frac{-j\beta}{\kappa^2}\left[B\kappa J_v'(\kappa r) - \frac{j\omega\epsilon_{core}v}{\beta r}AJ_v(\kappa r)\right]e^{jv\phi}e^{-j\beta z}$ and $H_\phi = \frac{-j\beta}{\kappa^2}\left[\frac{jv}{r}BJ_v(\kappa r) - \frac{\omega\epsilon_{core}}{\beta}A\kappa J_v'(\kappa r)\right]e^{jv\phi}e^{-j\beta z}$ for ($r<a$); $a$ is core's radius. In the cladding ($r>a$) $E_r = \frac{j\beta}{\gamma^2}\left[C\gamma K_v'(\gamma r) + \frac{j\omega\mu v}{\beta r}DK_v(\gamma r)\right]e^{jv\phi}e^{-j\beta z}$, $E_\phi = \frac{j\beta}{\gamma^2}\left[\frac{jv}{r}CK_v(\gamma r) - \frac{\omega\mu}{\beta}D\gamma K_v'(\gamma r)\right]e^{jv\phi}e^{-j\beta z}$ and $H_r = \frac{j\beta}{\gamma^2}\left[D\gamma K_v'(\gamma r) - \frac{j\omega\epsilon_{clad}v}{\beta r}CK_v(\gamma r)\right]e^{jv\phi}e^{-j\beta z}$.

The V-number or the normalized frequency is used to characterize the waveguide and is defined as:

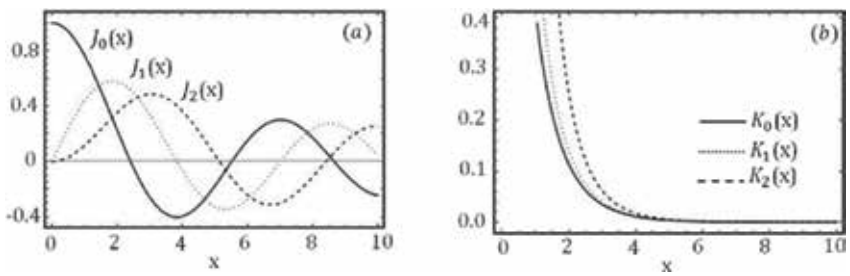


**Figure 9.** Bessel Function of the (a) first kind (behaves as a damped sine wave) and (b) second kind (monotonic decreasing function).

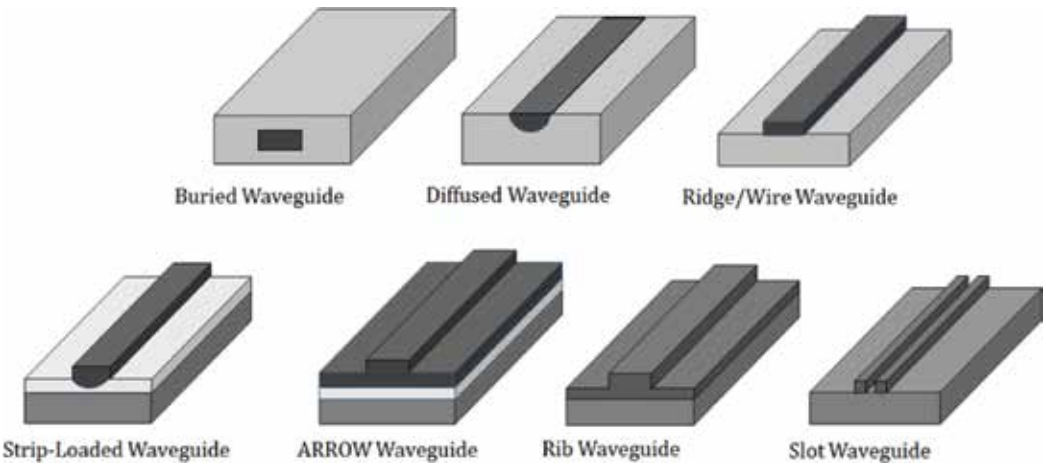


**Figure 10.** Schematic representation of various channel waveguides.

**II. Rectangular dielectric Waveguide:** Channel/rectangular waveguides are the most commonly used non-planar waveguides for device applications. Channel waveguides include buried waveguides, strip-loaded, ridge, rib, diffused, slot, ARROW, and so on. **Figure 10** shows the schematic of few of the channel waveguides. The wave equation analysis of a rectangular waveguide can be done by writing the scalar wave equation:

$$\frac{\delta^2 E}{\delta x^2} + \frac{\delta^2 E}{\delta y^2} + \left[k_0^2 n^2(x,y) - \beta^2\right] E = 0 \tag{30}$$

$$\text{V-number} = ak_0\sqrt{n_{core}^2 - n_{clad}^2} = \frac{2\pi a}{\lambda}\sqrt{n_{core}^2 - n_{clad}^2} \tag{31}$$

The general representation of the dielectric waveguide along with the electromagnetic field distribution in the regions is shown below:

| | | | | | |
|---|---|---|---|---|---|
| $\exp(-\gamma_3 x)$<br>$\exp(-\gamma_5 y)$ | | $Cos\,(\kappa_y y + \Phi_y)$<br>$\exp(-\gamma_3 x)$ | 3 | $\exp(-\gamma_3 x)$<br>$\exp(-\gamma_4 (y-b))$ | |
| $Cos\,(\kappa_x x + \Phi_x)$<br>$\exp(\gamma_5 x)$ | 5 | $Cos\,(\kappa_x x + \Phi_x)$<br>$Cos\,(\kappa_y y + \Phi_y)$ | 1 | $Cos\,(\kappa_x x + \Phi_x)$<br>$\exp(-\gamma_4 (y-b))$ | 4 |
| $\exp(-\gamma_2 (x-a))$<br>$\exp(\gamma_5 y)$ | | $Cos\,(\kappa_y y + \Phi_y)$<br>$\exp(-\gamma_2 (x-a))$ | 2 | $\exp(-\gamma_4 (y-b))$<br>$\exp(-\gamma_2 (x-a))$ | |

where $\phi_x$ and $\phi_y$ are phase constants. The characteristic equations are given by $tan\ \kappa_y b = \frac{\kappa_y(\gamma_4+\gamma_5)}{\kappa_y^2-\gamma_4\gamma_5}$ and $tan\ \kappa_x a = n_1^2 \frac{\kappa_x\left(n_2^2\gamma_3+n_3^2\gamma_2\right)}{n_2^2 n_3^2\kappa_x^2 - n_1^2\gamma_2\gamma_3}$ ($\gamma_i$) are exponential decay constants. The critical cut-off condition is given by:

$$V = k_0 \frac{a}{2} \sqrt{n_1^2 - n_2^2} \tag{32}$$

The following section describes various types of channel waveguides.

**1. Wire waveguide:** The schematic of silicon photonic wire waveguide is shown in **Figure 11(a)**. The waveguide consists of a silicon core and silica-based cladding. Since the single-mode condition is very important in constructing functional devices, the core dimension should be determined so that a single-mode condition is fulfilled. The primary requisite is single-mode guiding of the $TE_{00}$ and $TM_{00}$ mode. When the effective refractive index is larger than the cladding and smaller than the core, mode is guided in the waveguide, and guiding will be stronger for higher values of effective index $n_{eff}$. Thus, modes with effective indices above $n_{SiO_2}$ will not be radiated into the buffer layer and thus will be guided. **Figure 11(b)** depicts the quasi-TE mode of a 220-nm-high and 450-nm-wide silicon waveguide at wavelength of 1.55 μm [8].

Each mode propagates through the waveguide with a phase velocity of $c/n_{eff}$, where $c$ denotes the speed of light in vacuum and $n_{eff}$ is the effective refractive index felt by that mode. It signifies how strongly the optical power is confined to the waveguide core. Most waveguides support modes of two independent polarizations, with either the major magnetic (quasi-TM) or electric (quasi-TE) field component along the transverse (horizontal) direction.

**Figure 11(c)** shows $n_{eff}$ as a function of the width of the photonic wire. The $n_{eff}$ depends on the waveguide cross-section, waveguide materials, and the cladding material. Higher-order modes travel with a different propagation constant compared to the lowest-order mode and are less confined in the waveguides. As a consequence of the dissimilar propagation constants, there is modal dispersion which reduces the distance-bandwidth product of the waveguide. Due to the low confinement, first, a large field decay outside the waveguide reduces the maximum density of the devices and, second, in the waveguide bends the higher-order modes

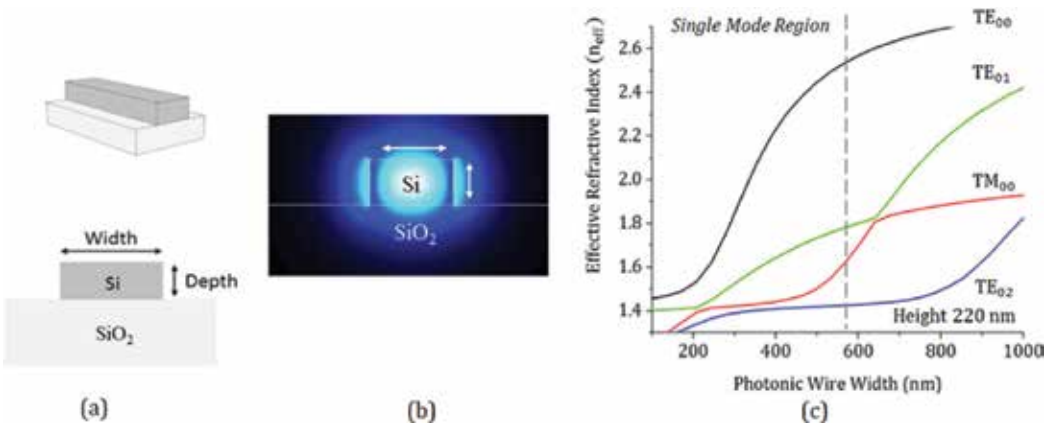


**Figure 11.** (a) Silicon-on-insulator wire waveguide, (b) quasi-TE mode of a 220-nm-high and 450-nm-wide silicon waveguide at wavelength of 1.55 μm, and (c) effective refractive index ($n_{eff}$) at 1550 nm for a 220-nm-high silicon photonic wire waveguide. The left of the hashed line is the single-mode region.

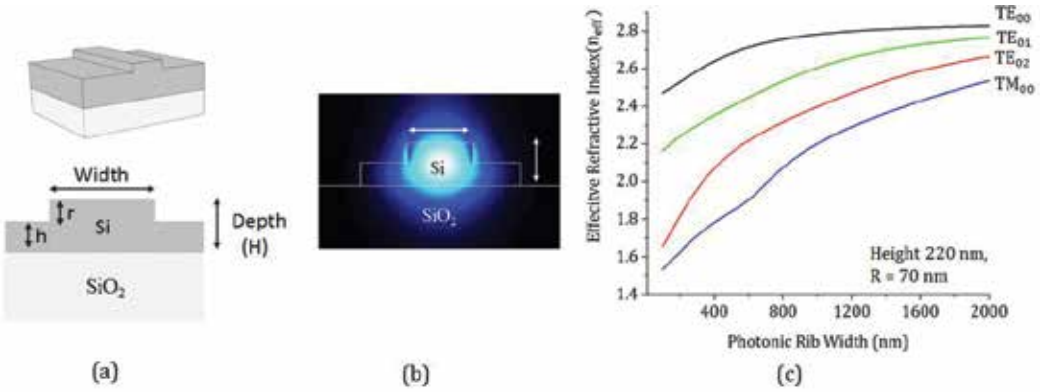


**Figure 12.** (a) Silicon-on-insulator rib waveguide, (b) quasi-TE mode of a 220-nm-high and 700-nm-wide silicon rib waveguide at wavelength of 1.55 μm, and (c) effective refractive index ($n_{eff}$) at 1550 nm for 220-nm-high silicon rib waveguide for ridge height ($r$) = 70 nm.

become leaky resulting in propagation losses. It is desirable that the difference between $n_{eff}$ of the fundamental quasi-TE and quasi-TM modes be large so that the coupling between the modes is limited due to difference in mode profiles and also the phase-mismatch. For widths below ~550 nm, silicon photonic wire will be single mode for each polarization.

**2. Rib waveguide: Figure 12(a)** and **(b)** shows the schematic and the fundamental quasi-TE mode of a silicon photonic rib waveguide ($H$ = 220 nm, $r$ = 70 nm). Although a rib waveguide can never truly be single mode, by optimizing the design, the power carried by the higher-order modes will eventually leak out of the waveguide over a very short distance, thus leaving only the fundamental mode. **Figure 12(c)** shows the dispersion $\left(n_{eff}\right)$ as a function of the width of the photonic rib waveguide. For widths below ~800 nm, silicon photonic rib waveguide will be single mode for each polarization.

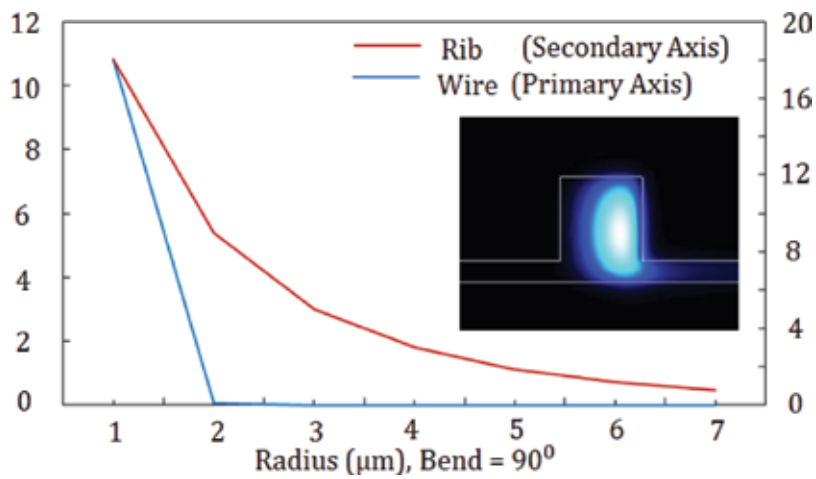


**Figure 13.** Mode loss for silicon wire (cross-section: 450 × 220 nm$^2$) and rib (cross-section: 600 × 220 nm$^2$) waveguides for a 90° bend with increasing bending radii.

Wire waveguides are advantageous as they provide a small bending radius and realization of ultra-dense photonic circuits. However, they have higher propagation losses. On the one hand, wire waveguide allows low-loss sharp bends in the order of a few micrometres, while, on the other hand, the device structures produced are susceptible to geometric fluctuations such as feature drift size (resulting in degradation of device performance) and waveguide sidewall roughness (resulting in propagation losses) [9, 10]. Rib waveguides typically require bend radii >50 μm in SOI to ensure low bend losses, which eventually result in a larger device/circuit footprint. **Figure 13** shows the TE mode loss in silicon wire and rib waveguide for a bend of 90°.

## 3. Slot waveguide

Slot waveguides are used to confine light in a low-index material between two high-index strip waveguides by varying the gap and dimensions (width and height) of the strip waveguides (**Figure 14(a)**). The normal component of the electric field (quasi TE) undergoes very high discontinuity at the boundary between a high- and a low-index material, which results into higher amplitude in the low-index slot region. The amplitude is proportional to the square of the ratio between the refractive indices of the high-index material (Si, Ge, $Si_3N_4$) and the low-index slot material (air). On the other hand, the effect of the presence of the slot is minimal on quasi-TM mode, which is continuous at the boundary. When the width of the slot waveguides is comparable to the decay length of the field, electric field remains across the slot and the section has high-field confinement [11–14], which results into propagation of light in the slot section; unlike in a conventional strip waveguide, where the propagating light is confined mainly in the high-index medium.

**Figure 14(c)** shows the variation in effective index with the waveguide width for different slot gaps. The advantage of a slot waveguide is the high-field confinement in the slot section, which normally cannot be achieved using a simple strip- or a ridge-based waveguide, making it a potential candidate for applications that require light-matter interaction such as sensing [12] and nonlinear photonics [13]. The launching of light into a slot waveguide is normally done by phase matching the propagation constant of the strip waveguide and the slot

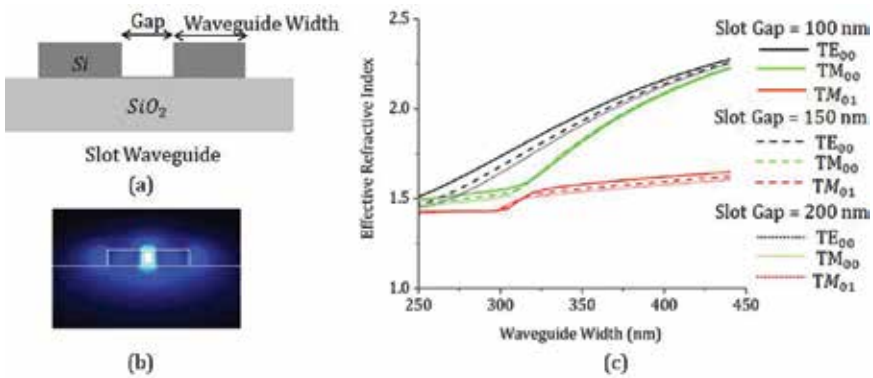


**Figure 14.** (a) Silicon-on-insulator slot waveguide, (b) Quasi-TE mode of a 220-nm-high (Gap = 100 nm) slot waveguide, (b) variation of effective refractive index with waveguide width for slot gap of 100, 150, and 200 nm, respectively, at a wavelength of 1.55 μm.

waveguide. However, efficient coupling still remains a challenge because of scattering loss and mode mismatch of the slot and strip waveguides, with a reported propagation loss between 2 and 10 dB/cm [14].

## 4. Strip-loaded waveguide

A strip-loaded waveguide is formed by loading a planar waveguide, which already provides optical confinement in the $x$ direction, with a dielectric strip of index $n_3 < n_1$ or a metal strip to facilitate optical confinement in the $y$ direction, as shown in **Figure 15(a)**. Strip-loaded waveguides do not require half-etching in waveguide fabrication and is therefore easier to fabricate. **Figure 15(a)** shows the schematic of a hydrogenated amorphous silicon strip-loaded waveguide where a thermal oxide is inserted between the layers for passivation [15]. **Figure 15(b)** shows the optical field for the waveguide for a 75-nm-thick and 800-nm-wide strip-loaded waveguide and **Figure 15(c)** depicts the variation in effective index with the strip waveguide width.

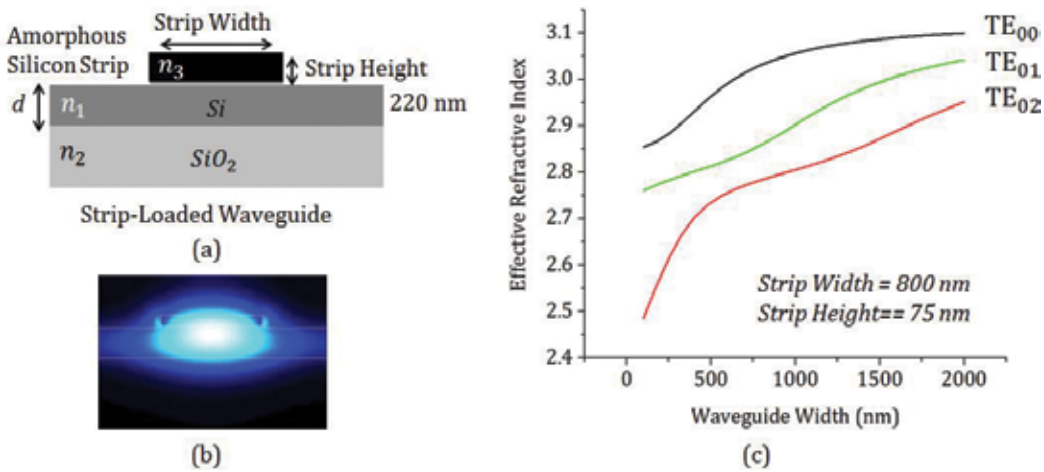


**Figure 15.** (a) Hydrogenated amorphous strip-loaded waveguide, (b) Quasi-TE mode of a 220-nm-high, 800-nm-wide, 75-nm-thick strip Waveguide, (c) Variation of effective refractive index with strip width at a wavelength of 1.55 μm.

## 5. Suspended waveguide

Suspended waveguides have enabled new types of integrated optical devices for applications in optomechanics, nonlinear optics, and electro-optics. Fabrication involves removing a sacrificial layer above or below a waveguide core layer to design these waveguides [16]. Increasing absorption loss of $SiO_2$ at longer wavelengths makes it challenging to utilize SOI for low-loss components in the mid-infrared (MIR) [17]. Removing the $SiO_2$ layer opens the possibility of extending the low-loss SOI wavelength range up to ~8 μm. For MEMS, it is imperative to have waveguides that can be mechanically actuated. This requires waveguides that are released

http://dx.doi.org/10.5772/intechopen.77150

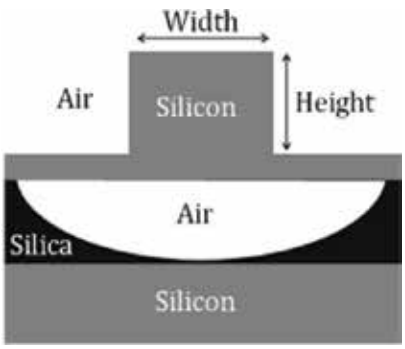


**Figure 16.** Schematic of a suspended waveguide.

from the substrate, for example, through surface micromachining [17]. **Figure 16** shows the schematic of a suspended waveguide [18].

## 6. Triplex$^{TM}$ technology

TriPleX waveguides are a family of waveguide geometries that is based on an alternating layer stack consisting of two materials: $Si_3N_4$ and $SiO_2$. The waveguide geometries are categorized as box shell, single stripe (propagation loss <0.03 dB/cm), symmetric double stripe (propagation loss <0.1 dB/cm), and asymmetric double stripe (propagation loss <0.1 dB/cm) as shown in **Figure 17(a)** [19]. Different confinement regimes can be optimized

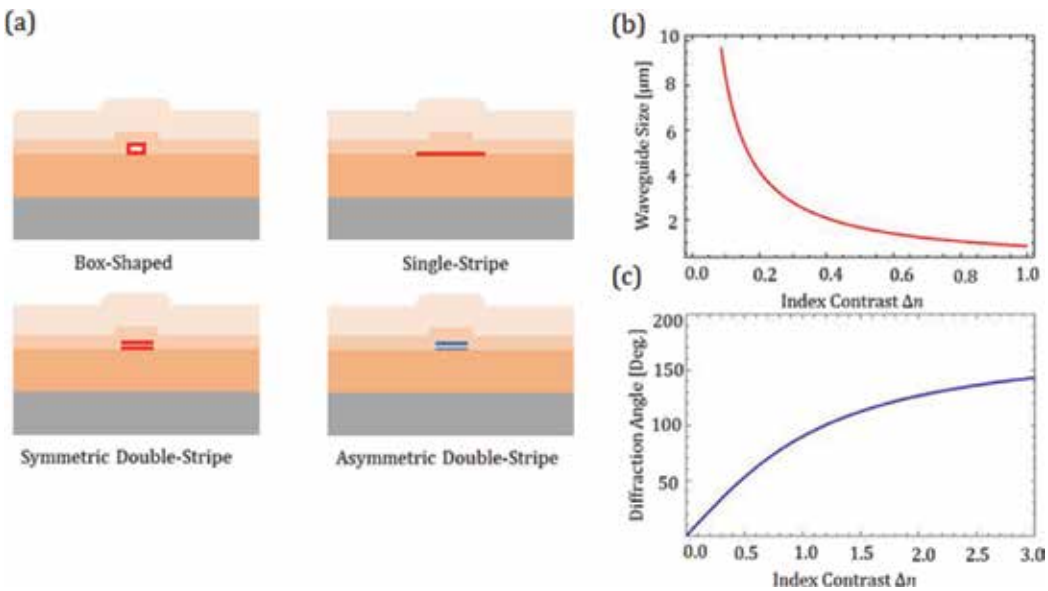


**Figure 17.** (a) Schematic of different type of TriPleX waveguides, (b) Variation in waveguide size of the box-shaped waveguide, and (c) its diffraction angle versus the index contrast.

for specific applications for these waveguides and tunable birefringence- and polarization dependent loss (PDL) can be achieved. Propagation losses (<0.1 dB/cm), very low PDL (< 0.1 dB/cm), and easy interconnection with optical fibers (<0.15 dB/facet) have been demonstrated in single-mode box-shaped waveguides [20]. Moreover, fabrication of the waveguide is a low-cost and simple process.

LioniX TriPleX technology is a versatile photonics platform suited for applications such as communications, biomedicine, sensing, and so on, over a broadband range of 0.4 to 2.35 μm [21]. **Figure 17(b)** and **(c)** depicts the variation in waveguide size and diffraction angle with index contrast of the box-shaped geometry for a wavelength of 1.55 μm.

## 7. Photonic crystal waveguide

Photonic crystal waveguides guiding mechanism is different from that of a traditional waveguide, which is based on internal reflection. A photonic crystal is a periodic dielectric structure with a photonic band gap, that is, a frequency range over which there is no propagation of light. The introduction of line defects into a photonic crystal structure creates an optical channel for propagation of light. If the line defect is properly designed, the resulting guiding mode falls within a photonic band gap, is highly confined, and can be used for guiding light. The guiding mode can also be designed to be broadband and thus gives rise to a compact, broadband photonic crystal waveguide [22]. Application of these waveguides includes nanofluidic tuning, RI measurements, optical characterization of molecule orientation, and biosensing.

## 8. Diffused waveguide

A diffused waveguide is formed by creating a high-index region in a substrate through diffusion of dopants, such as a $LiNbO_3$ waveguide with a core formed by Titanium (Ti) diffusion. Due to the diffusion process, the core boundaries in the substrate are not sharply defined. A diffused waveguide has a thickness defined by the diffusion depth of the dopant and a width defined by the distribution of the dopant. Alternatively, the material can be exchanged with the substrate. Ion-exchanged glass waveguide is fabricated by diffusing mobile ions originally in glass with other ions of different size and polarizability [23].The additional impurities cause a change in refractive index that is approximately proportional to their concentration. A material can also be implanted using an ion implanter within the waveguide. However, this process damages the lattice and is therefore followed by annealing.

## 9. ARROW waveguide

In anti-resonant reflecting optical (ARROW) waveguides, light confinement is realized by choosing the cladding layer thicknesses accordingly to create an anti-resonant Fabry-Perot reflector

for the transverse component of the wave vector at the desired wavelength. Even though the ARROW mode is leaky, low-loss propagation over large distances can be achieved. Yin *et al.* have designed an ARROW waveguide exhibiting single-mode confinement and low-loss light propagation in a hollow air core on a semiconductor chip [24]. ARROW waveguides with non-solid low-index cores have applications in gas and liquid sensing, quantum computing, quantum communications, and Raman scattering spectroscopy. Chalcogenide rib ARROW structures have also been shown with propagation loss ~6 dB/cm to design opto-chemical sensors in the near- and mid-IR region [25].

## 10. Augmented waveguide

Light confinement in a low-index media has been shown in ARROW, slot, and plasmonic waveguides. However, ARROW waveguide has low confinement and is thus leaky. Strong light confinement in the low-index medium can be achieved by using silicon slot and plasmonic waveguide. Fabrication of the slot waveguide is cumbersome and hybrid plasmonic waveguide suffers from additional propagation losses due to the presence of metal. Augmented waveguide confines light efficiently in the low-index region by reducing the reflection at the high index-low index interface in a high-index contrast waveguide, which results in enhancement of light confinement in the low-index region [26]. **Figure 18** shows the schematic of an augmented low-index waveguide.

Waveguides can be classified on the basis of different material platforms. Wavelength range, ease of fabrication, compactness, and CMOS compatibility are few of the determining factors when selecting a material for a specific application. **Table 1** compares various waveguide platforms along with their propagation losses [27]. **Figure 19** shows variation of index contrast with footprint for few material platforms.

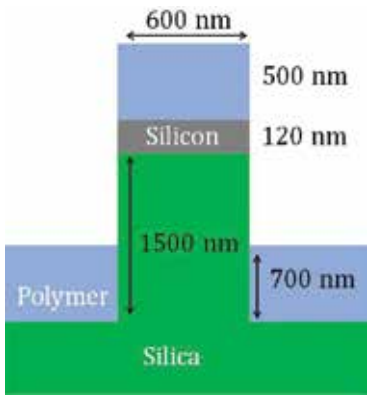


**Figure 18.** Schematic of an augmented waveguide.

| Material platforms | Waveguides | Range | Configuration | Propagation Loss |
|---|---|---|---|---|
| Semiconductor materials | Silicon | Mid-IR | Silicon nanophotonic waveguide | ∼4 dB/cm (2030 nm) ∼10 dB/cm (2500 nm) [28] |
| | | Mid/Near-IR | Suspended silicon-membrane ridge waveguide (TM mode) | $\sim 2.8 \pm 0.5$ dB/cm (3.39 μm) $\sim 5.6 \pm 0.3$ dB/cm (1.53 μm) [29] |
| | | Mid/Near-IR | Silicon on porous silicon (SiPSi) | $\sim 2.1 \pm 0.2$ dB/cm (1.55 μm) $\sim 3.9 \pm 0.2$ dB/cm (3.39 μm) [30] |
| | Germanium | Mid-IR | Germanium on silicon strip waveguide | $\sim 2.5 - 3$ dB dB/cm [31] (∼5.15-5.4 μm) |
| | | Far-IR | Germanium on silicon strip waveguide | ∼2.5 dB dB/cm [32] (∼5.8 μm) |
| | | Mid-IR | Germanium on silicon rib waveguide | $\sim 2.4 \pm 0.2$ dB/cm [33] (∼3.8 μm) |
| | | Mid-IR | Germanium-rich silicon germanium platform-based rib waveguide | $1.5 \pm 0.5$ dB/cm [34] (∼4.6 μm) |
| | | Mid IR/Far-IR | Silicon germanium/silicon-based graded index waveguides | ∼1 dB/cm (4.5 μm) ∼2 dB/cm (7.4 μm) [35] |
| | | Mid-IR | Germanium-on-silicon-on-insulator waveguides | 3.5 dB/cm (3.682 μm) [36] |
| | | Mid-IR | Silicon germanium ridge waveguide on a silicon substrate | 0.5 dB/cm (4.75 μm) [37] |
| | | Far-IR | Germanium on GaAs ridge waveguide | 4.2 dB/cm (10 μm) [38] |
| | Gallium arsenide (GaAS) | Near-IR | GaAS/$Al_{0.3}$ $Ga_{0.7}$As ridge waveguide for manipulation of single-photon and two-photon states | 1.6 dB/cm (1.55 μm) [39] |
| | | Near-IR | Suspended GaAs waveguide | 0.4 dB/mm (TE) (1.55 μm) and 6 dB/mm (TM) (1.03 μm) [40] |
| | | Near-IR | GaAs-based single-line defect photonic crystal slab waveguide | 0.76 dB/mm (1050–1580 nm) [41] |
| | Indium phosphide (InP) | Near-IR | InP waveguides based on localized Zn-diffusion process (MOVPE) to mitigate passive loss by p-dopants | 0.4 dB/cm (1.55 μm) [42] |
| | | Near-IR | Suspended InP dual-waveguide structures for MEMS-actuated optical buffering | 2.2 dB/cm (1.5–1.6 μm) [43] |
| | Gallium antimony | Mid-IR | GaSb waveguides based on quasi-phase matching (QPM) | ∼0.7/1.1 dB/cm [44] ∼(2/4 μm) |
| | Quantum dotes | Near-IR | Polymer waveguides containing infrared-emitting nanocrystal quantum dots (PbSe and InAs) | ∼5 dB/cm (inclusive of fiber coupling loss) [45] (∼1550 nm) |
| | Doped semiconductor | Vis/Near-IR | Rare-earth-doped GaN (gallium nitride) channel waveguide | ∼5.4/4.1 dB/cm [46] (∼633/1550 nm) |

| Material platforms | Waveguides | Range | Configuration | Propagation Loss |
|---|---|---|---|---|
| | | Near-IR | Erbium-Doped Phosphate Glass Strip-loaded Waveguide on Silicon | ∼4.1 dB/cm [47] (∼1535 nm) |
| | Semiconductor nanomaterials | Mid-IR | Silicon-on-Sapphire Suspended Nanowire | $\sim 1 \pm 0.3$ dB/cm [48] (∼4 μm) |
| | | Vis | Tin-oxide nanoribbons-based subwavelength waveguide | ∼10 dB/cm [49] (∼400-550 nm) |
| | | Near-IR | Amorphous silicon nanowire | ∼4.5 dB/cm [50] (∼1550 nm) |
| | | Near-IR | InP/benzocyclobutene optical nanowires on a GaAs substrate | ∼0.8 dB/mm [51] (∼1550 nm) |
| Silicon-on-insulator waveguides | Silicon-on-Silica | Near-IR | Silicon-on-silica strip waveguide | ∼0.6 dB/cm [52] (∼1550 and 2000 nm) |
| | | Near-IR | Silicon-on-silica rib (70-nm etch depth) waveguide | $\sim 0.1 - 0.2$ dB/cm [52] (∼1550 and 2000 nm) |
| | | Mid-IR | Silicon-on-silica rib (70-nm etch depth) waveguide | ∼1.5 dB/cm [53] (∼3800 nm) |
| | | Near-IR | Silicon-on-silica slot waveguide | $\sim 2.28 \pm 0.03$ dB/cm [54] (∼1064 nm) |
| | | Near-IR | Silicon-on-Silica slot waveguide | ∼3.7 dB/cm [55] (∼1550 nm) |
| | | Mid-IR | Suspended silicon waveguide | ∼3.1 dB/cm (7.67 μm) [56] |
| | | Near-IR | Silicon-on-silica strip waveguide coated with amorphous $(TiO_2)$ | $\sim 2 \pm 1$ dB/cm [57] (∼1550 nm) |
| | Silicon-on-Sapphire | Mid-IR | Silicon-on-sapphire ridge waveguide | $\sim 4.0 \pm 0.7$ dB/cm [58] (∼5.4-5.6 μm) |
| | | Mid-IR | Silicon-on-sapphire ridge waveguide | $\sim 4.3 \pm 0.6$ dB/cm [59] (∼4.5 μm) |
| | | Mid-IR | Silicon-on-sapphire slot waveguide | ∼11 dB/cm [60] (∼3.4 μm) |
| | | Near/Mid-IR | Silicon-on-sapphire nanowire waveguide | ∼0.8 dB/cm [61] (∼1550 nm). $\sim 1.1 - 1.4$ dB/cm [61] (∼2080 nm) ∼<2 dB/cm [61] (∼5.18 μm) |
| | Silicon-on-nitride | Mid-IR and Near-IR | Silicon-on-nitride ridge waveguide | $\sim 5.2 \pm 0.6$dB/cm [62] (∼3.39 μm) |
| | Thallium-doped SOI Rib/Indium-doped SOI Rib | Near-IR | Thallium-doped silicon waveguide | ∼3 dB/cm [63] (∼1.55 μm) |
| | | Near-IR | Indium-doped silicon waveguide, decrease in absorption coefficient ∼16 dB/cm [64] (wavelength ∼1.55 μm). | |
| Glass waveguides | Silica glass | Vis | Laser-written waveguide in fused silica for vertical polarization (VP)/ horizontal polarization (HP) beam | ∼0.06/0.1 dB/cm [65] (∼777 nm) |
| | | Mid-IR | 3D laser-written silica glass step-index high-contrast (HIC) waveguide | ∼1.3 dB/cm$^3$ [66] (∼3.39 μm) |

| Material platforms | Waveguides | Range | Configuration | Propagation Loss |
|---|---|---|---|---|
| | | Near-IR | Graded-index (GRIN) Cladding in HIC glass waveguides | ∼1.5 dB/cm [67] (∼1.55 μm) |
| | | Near-IR | High-index, doped silica glass material (Hydex) waveguides | ∼0.06 dB/cm [68] (∼1.55 μm) |
| | Silicon oxynitride (SiON) | Near-IR | SiON deposited by inductively coupled PECVD-based waveguides | $\sim 0.5 \pm 0.05$ dB/cm,$1.6 \pm 0.2$ dB/cm and $0.5 \pm 0.06$ dB/cm [69] (∼1330, 1550 and 1600 nm) |
| | Ion—exchanged glass | Vis | $Ti^{+}/Na^{+}$ ion-exchanged single-mode waveguides on silicate glass | $\sim 9 \pm 1$ dB/cm [70] (∼0.405 μm) |
| | | Near-IR | Alkaline aluminum phosphate glasses for thermal ion-exchanged waveguide | ∼0.53 dB/cm [71] (∼1.534 μm) |
| | Sol-gel glass | Near-IR | Hybrid organic-inorganic glass sol-gel ridge waveguides | ∼0.1 dB/cm [72] ∼(1.55 μm) |
| | | Vis | Sol-gel derived silicon titania slab waveguides films | ∼0.2 dB/cm [73] ( 677 nm) |
| | | Vis | Sol–gel-derived glass-ceramic photorefractive films-based waveguide | $\sim 0.5 \pm 0.2$ dB/cm [74] (∼635 nm) |
| | Tungsten tellurite glass | Near-IR | Optical planar channel waveguide-based on tungsten-tellurite glass fabricated by RF Sputtering | ∼0.44 dB/cm [75] (∼1.53 μm) |
| | Laser-written | Near-IR | Laser-written waveguide in planar light-wave circuit (PLC) glass doped with Boron and Phosphorous | ∼0.35 dB/cm [76] (∼1.55 μm) |
| | | Vis | Laser-written waveguide in fused silica for vertical polarization (VP)/ horizontal polarization (HP) beam | ∼0.06/0.1 dB/cm [65](∼777 nm) |
| | | Near-IR | Laser-written ferroelectric crystal in glass waveguide | ∼2.64 dB/cm [77] (∼1530 nm) |
| | | Vis | Femtosecond laser-written double-line waveguides in germanate and tellurite glasses | ∼2.0 dB/cm [78] (∼632 nm) |
| | | Near-IR | Ultrafast laser-written waveguides in flexible $As_2S_3$ chalcogenide glass tape | ⩽0.15 dB/cm [79] (∼1550 nm) |
| Electro-optic waveguides | Lithium niobate | Near-IR | Lithium niobate on insulator rib waveguide | ∼0.4 dB/cm [80] (∼1.55 μm) |
| | | Near-IR | Lithium niobate ridge waveguide | ∼0.3 dB/cm(TE) and 0.9 dB/cm (TM) [81] (∼1.55 μm) |
| | | Near-IR | Periodically poled lithium niobate waveguide | ∼<1 dB/cm [82] (∼1.55 μm) |
| | | Near-IR | Heterogeneous lithium niobate on silicon nitride waveguide | $\sim < 0.2 \pm 0.4$ dB/cm [83] (∼1.54 μm) |

| Material platforms | Waveguides | Range | Configuration | Propagation Loss |
|---|---|---|---|---|
| | | Near-IR | Lithium Niobate on Insulator Ridge Waveguide | ∼1 dB/cm [84] (∼1.55 μm) |
| | | Near-IR | Thin film strip-loaded (SiN) lithium niobate waveguide | ∼5.8 dB/cm (TE) 14dB/cm (TM) [85] (∼1.55 μm) |
| | | Near-IR | Thin film strip-loaded (a-Si) lithium niobate waveguide | ∼42 dB/cm (TE) 20dB/cm (TM) [86] (1.55 μm) |
| | | Near-IR | Thin film lithium niobate ridge waveguide | ∼0.268 dB/cm (TE) 1.3dB/cm (TM) [87] (∼1.55 μm) |
| | Lithium tantalate | Near-IR | $Ga^{3+}$-diffused lithium tantalate waveguide | ∼0.2 dB/cm (TE) 0.4 dB/cm (TM) [88] (∼1.55 μm) |
| | Barium titanate (BTO) | Vis | BTO thin films on MgO-based ridge waveguide | ∼2 dB/cm (TE) [89] (∼633 nm) |
| | | Mid-IR | BTO thin films on Lanthanum Aluminate (LAO) with a-Si ridge waveguide | ∼4.2 dB/cm [90] (∼3.0 μm) |
| | Electro-optic polymer | Near-IR | Hybrid Electro-Optic Polymer and $TiO_2$ Slot Waveguide | ∼5 dB/cm [91] (∼1550 nm) |
| | Liquid crystal | Near-IR | PDMS (poly (dimethyl siloxane))-liquid crystal-based optical waveguide | ∼8dB/cm [92] (∼1550 nm) |
| | | Vis | Liquid-crystal core channel waveguide encapsulated in semicircular grooves with glass substrate | ∼1.3 dB/cm [93] (∼632.8 nm) |
| | | Near-IR | Liquid crystal clad shallow-etched SOI waveguide | ∼4.5 dB/cm [94] (1570 nm) |
| Polymer-based | Conventional optical polymers | Vis | PMMA (poly(methyl methacrylate) )-based optical waveguide | ∼0.2 dB/cm [95] (∼850 nm) |
| | | Vis/Near-IR | Polyurethane (PU)-based optical waveguide | ∼0.8 dB/cm [95] (∼633 and 1064 nm) |
| | | Vis/Near-IR | Epoxy resin-based optical waveguide | ∼0.3/0.8 dB/cm [95] (∼633/1064 nm) |
| | | Vis | Polymer PMMA-based waveguide using femtosecond laser | ∼0.3 dB/cm [96] (∼638 and 850 mm) |
| | Novel optical polymers | Vis/Near-IR | Polymeric waveguides (WIR30 photopolymer) with embedded micro-mirror | ∼0.18 dB/cm [97] (∼850 nm ) |
| | | Vis/Near-IR | Acrylate-based waveguide pattern using photo exposure/laser ablation | ∼0.02/0.3 and 0.8 dB/cm [95] (∼840/1300 and 1550 nm) |
| | | Vis/Near-IR | Telephotonics-OASIC-based optical waveguide | ∼< 0.01, 0.03, 0.1 dB/cm [95] (∼840/1300/1550 nm) |
| | | Near-IR | Dow chemical perfluorocyclobutane(XU 35121)-based waveguide | ∼0.25 dB/cm [95] (∼1300/1550 nm) |

| Material platforms | Waveguides | Range | Configuration | Propagation Loss |
|---|---|---|---|---|
| | | Near-IR | Circular-core UV-curable epoxies-based optical waveguide | ∼0.79 dB/cm [98] (∼1550 nm) |
| | | Vis/Near-IR | Multi-mode Siloxane-based polymer waveguide, single-mode siloxane-based polymer waveguide | ∼0.05 dB/cm [99] (∼850 nm)/ ∼0.5/1 dB/cm [99] (∼1.31/ 1.55μm) |
| | Surface plasmon polariton waveguide | Near-IR | Polymer-Silicones-based long range surface plasmon polariton waveguide (LRSPPW) | $\sim 0.5 - 1$ dB/mm [100] (∼1.55 μm) |
| | | Near-IR | Exguide ZPU/LFR-based long range surface plasmon polariton waveguide (LRSPPW) | ∼1.72 dB/cm [101] (∼1.55 μm). |
| Hollow waveguides | Metal/ Dielectric Coated | THz | Gold-coated waveguide using liquid phase chemical deposition process | ∼1.98/1.89 dB/cm [102] (∼215/ 513 μm) |
| | | THz | Silver-coated waveguide using liquid phase chemical deposition Process | ∼1.77/1.62 dB/cm [102] (∼215/ 513 μm) |
| | | Mid-IR | Cadmium sulfide CdS) and PbS (Lead Sulfide) on Ag (Silver)-coated hollow glass waveguide | ∼0.037dB/cm [103] (∼2.94 μm) |
| | | THz | High-refractive index composite photonics band-gap Bragg fiber | ∼0.3 dB/cm [104] (∼300 μm) |
| | | THz | Silver/polystyrene-coated hollow glass waveguides | ∼1.9 dB/m [105] (∼300 μm) |
| | | Vis/Near-IR | Silver/cyclic olefin hollow glass waveguide | ∼0.549/0.095 and 0.298 dB/m [106] (∼808/1064 and 2940 nm) |
| | Hollow glass | Near-IR | Hollow-core optical waveguide (Si Substrate) | ∼1.7 dB/cm [107] (∼1.52-1.62 μm) |
| | | Far-IR | Tapered hollow-air core waveguide | ∼1.27 dB/cm [108] (∼6.2 μm) |
| | | Vis | Air-core anti-resonant reflecting Optical Waveguide (ARROW) | ∼4 dB/cm [109] (∼820-880 nm) |
| | Chalcogenide | Near-IR | Chalcogenide waveguides ($Ge_{23}Sb_7S_{70}$) fabricated through CMOS-compatible lift-off process: Strip/rib | 2-6 /<0.5 dB/cm [110] (∼1550 nm) |
| | | Mid-IR | Chalcogenide waveguides ($Ge_{11.5}As_{24}Se_{64.5}$) | <1 dB/cm (0.3dB at 2000 $cm^{-1}$ ) (1500-4000 $cm^{-1}$) [111] |
| | | Near-IR | Chalcogenide waveguides $Ge_{23}Sb_7S_{70}$ (chlorine-based plasma etching) | **<0.42 dB/$cm^{-1}$** (1550 nm) [112] |
| | Liquid core | Vis | Liquid core/(ethylene glycol) air-cladding waveguide | ∼0.14 dB/cm ( 464-596 nm) [113] |

| Material platforms | Waveguides | Range | Configuration | Propagation Loss |
|---|---|---|---|---|
| | | Vis | Nano porous solid liquid core Waveguide | ∼0.6 dB/cm ( 632.8 nm) [114] |
| Metamaterial optical waveguides | | Mid-IR | Suspended silicon waveguide with lateral cladding (subwavelength grating metamaterial) | ∼0.82 dB/cm (3.8μm) [115] |
| Titanium dioxide ($TiO_2$) | | Vis/Near-IR | Atomic layer deposition (ALD) $TiO_2$ slab waveguide | ∼2.0-3.5 dB/cm (633 nm) [116] <1 dB/cm (1530 nm) [65] |
| | | Near-IR | Amorphous $TiO_2$ strip waveguide | ∼2.4-0.2 dB/cm (1.55μm) [117] |
| Silicon carbide | | Near-IR | PECVD silicon-carbide-silicon oxide horizontal slot waveguide | $\sim 23.9 \pm 1.2$ dB/cm (1.3 μm)-TM mode [118] |
| Silicon nitride on silica[30] | | Vis | Silicon-nitride strip waveguide | ∼2.25 dB/cm. [119] (∼532 nm) |
| | | Vis | Silicon-nitride strip waveguide | ∼0.51 dB/cm. [120] (∼600 nm) |
| | | Vis | Silicon-nitride strip waveguide | ∼1.30 dB/cm. [119] (∼780 nm) |
| | | Near-IR | LPCVD Silicon-nitride strip waveguide | ∼0.04 dB/cm. [121] (∼1550 nm) |
| | | Near-IR | TripleX ™ LPCVD silicon-nitride planar waveguide | ∼0.02 dB/cm. [122] (∼1550 nm) |
| | | Near-IR | 900-nm-thick LPCVD Silicon-nitride strip waveguide | ∼0.37 dB/cm. [123] (∼1550 nm) |
| | | Mid—IR | LPVCD silicon-nitride strip waveguide | ∼0.60 dB/cm. [124] (∼2600 nm) |
| | | Mid-IR | Silicon-rich LPVCD silicon-nitride strip waveguide | ∼0.16 dB/cm. [125] (∼2650 nm)/ 2.10 dB/cm. [126] (∼3700 nm) |
| Tantalum pentoxide ($Ta_2O_5$)-core/silica-clad/ silicon substrate | | Near IR | Planar waveguide | ∼0.03 dB/cm. [127] (∼1550 nm) |
| Suspended silicon-on-insulator waveguide | | Mid-IR | Waveguide with Subwavelength grating | ∼3.4 dB/cm. [17] (∼3.8 μm). |
| Photonic crystal fibers based waveguides | | THz | Semiconductor silicon photonic crystal slab waveguides | ∼0.1/0.04 dB/cm. [128] (∼905.7/ 908 μm). |
| | | THz | 3-D printed THz waveguide based on Kagome photonic crystal structure | ∼0.1/0.04 dB/cm. [129] (∼905.7/ 908 μm). |
| | | THZ | Kagome-lattice hollow-core silicon photonic crystal slab-based waveguide | ∼0.875 dB/cm [129] (∼400 μm). |

**Table 1.** Material platforms.

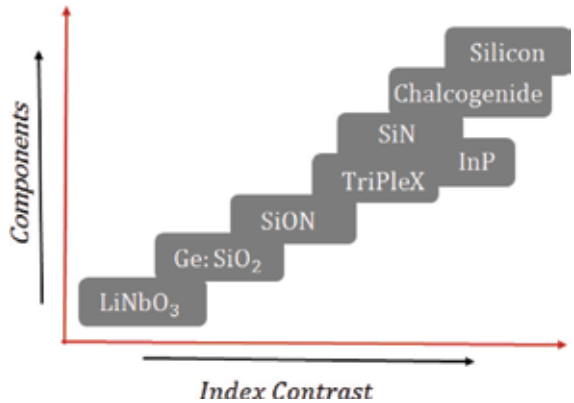


**Figure 19.** Comparison of different waveguide platforms as a function of index contrast and compactness.

## 11. Conclusion

Classification of waveguides on the basis of geometry (planar/non-planar), mode propagation (Single/Multi-Mode), refractive index distribution (Step/Gradient Index), and material platform is described briefly. An overview of different kinds of channel waveguides, namely wire, rib, slot, strip-loaded, diffused, TriPleX, suspended, photonic crystal, ARROW, and augmented waveguide is given. A comparative analysis of material platforms used along with their propagation losses and wavelength range is also shown.

## Author details

Shankar Kumar Selvaraja* and Purnima Sethi

*Address all correspondence to: shankarks@iisc.ac.in

Centre for Nano Science and Engineering, Indian Institute of Science, Bangalore

## References

[1] Hondros D, Debye P. Annals of Physics. 1910;**32**:465

[2] Kapany NS. Fiber Optics Principles and Applications. New York: Academic Press; 1967

[3] Kapany NS, Burke JJ. Optical Waveguides, Quantum Electronics Principles and Applications. New York: Academic Press; 1972

[4] Jia-Ming L. Photonic Devices: Cambridge university text; 2005

[5] Paschotta R. Field Guide to Lasers. Bellingham, WA: SPIE Press; 2008

[6] Pollock CR, Lipson M. Integrated photonics. 2003;**20**(25)

[7] Kim HS, Yoo S. Large mode area inverse index fiber with a graded index profile for high power single mode operation. Optics Express. 2017;**25**(18):21935-21946

[8] Shoji T, Tsuchizawa T, Watanabe T, Yamada K, Morita H. Low loss mode size converter from 0.3 μm square Si wire waveguides to singlemode fibres. Electronics Letters. 2002; **38**(25):1669-1670

[9] Inoue H, Hiruma K, Ishida K, Asai T, Matsumura H. Low loss GaAs optical waveguides. IEEE Transactions on Electron Devices. 1985;**32**(12):2662-2668

[10] Dai D, Tang Y, Bowers JE. Mode conversion in tapered submicron silicon ridge optical waveguides. Optics Express. 2012;**20**(12):13425-13439

[11] Xu Q et al. Experimental demonstration of guiding and confining light in nanometer-size low-refractive-index material. Optics Letters. 2004;**29**(14):1626-1628

[12] Passaro V, La Notte M. Optimizing SOI slot waveguide fabrication tolerances and strip-slot coupling for very efficient optical sensing. Sensors 12.3. 2012:2436-2455

[13] Wang Z, Zhu N, Tang Y, Wosinski L, Dai D, He S. Ultracompact low-loss coupler between strip and slot waveguides. Optics Letters. 2009;**34**(10):1498-1500

[14] Säynätjoki A et al. Low-loss silicon slot waveguides and couplers fabricated with optical lithography and atomic layer deposition. Optics Express. 2011;**19**(27):26275-26282

[15] Maegami Y, Cong G, Ohno M, Okano M, Yamada K. Strip-loaded waveguide-based optical phase shifter for high-efficiency silicon optical modulators. Photonics Research. 2016;**4**(6):222-226

[16] Stievater TH, Pruessner MW, Rabinovich WS, Park D, Mahon R, Kozak DA, Bradley Boos J, Holmstrom SA, Khurgin JB. Suspended photonic waveguide devices. Applied Optics. 2015;**54**(31):F164-F173

[17] Penadés JS, Alonso-Ramos C, Khokhar AZ, Nedeljkovic M, Boodhoo LA, Ortega-Moñux A, Molina-Fernández I, Cheben P, Mashanovich GZ. Suspended SOI waveguide with sub-wavelength grating cladding for mid-infrared. Optics Letters. 2014;**39**(19):5661-5664

[18] Li X, Zhou P, He S, Gao S. Dispersion engineering of suspended silicon photonic waveguides for broadband mid-infrared wavelength conversion. JOSA B. 2014;**31**(10):2295-2301

[19] Roeloffzen CGH, Hoekman M, Klein EJ, Wevers LS, Timens RB, Marchenko D, Geskus D, et al. Low-loss Si3N4 triPleX optical waveguides: Technology and applications overview. IEEE Journal of Selected Topics in Quantum Electronics. 2018;**24**(4):1-21

[20] Morichetti F, Melloni A, Martinelli M, Heideman RG, Leinse A, Geuzebroek DH, Borreman A. Box-shaped dielectric waveguides: A new concept in integrated optics? Journal of Lightwave Technology. 2007;**25**(9):2579-2589

[21] Melloni A, Costa R, Cusmai G, Morichetti F. The role of index contrast in dielectric optical waveguides. International Journal of Materials and Product Technology. 2009;**34**(4):421-437

[22] Lin S-Y, Chow E, Johnson SG, Joannopoulos JD. Demonstration of highly efficient waveguiding in a photonic crystal slab at the 1.5-μm wavelength. Optics Letters. 2000; **25**(17):1297-1299

[23] Tervonen A, Honkanen SK, West BR. Ion-exchanged glass waveguide technology: A review. Optical Engineering. 2011;**50**(7):071107

[24] Yin D, Schmidt H, Barber JP, Hawkins AR. Integrated ARROW waveguides with hollow cores. Optics Express. 2004;**12**(12):2710-2715

[25] Balan V, Vigreux C, Pradel A, Llobera A, Dominguez C, Alonso MI, Garriga M. Chalcogenide glass-based rib ARROW waveguide. Journal of Non-Crystalline Solids. 2003;**326**: 455-459

[26] Alam MZ, Sun X, Mo M, Stewart Aitchison J. Augmented low index waveguide for confining light in low index media. Laser & Photonics Reviews. 2017;**11**(3)

[27] Tong XC. Advanced Materials for Integrated Optical Waveguides: Springer; 2016.s

[28] Liu X, Jr RMO, Vlasov YA, Green WMJ. Mid-infrared optical parametric amplifier using silicon nanophotonic waveguides. Nature Photonics. 2010;**4**(8):557

[29] Chiles J, Khan S, Ma J, Fathpour S. High-contrast, all-silicon waveguiding platform for ultra-broadband mid-infrared photonics. Applied Physics Letters. 2013;**103**(15):151106

[30] Mashanovich GZ, Milošević MM, Nedeljkovic M, Owens N, Xiong B, Ee JT, Youfang H. Low loss silicon waveguides for the mid-infrared. Optics Express. 2011;**19**(8):7112-7119

[31] Malik A et al. Germanium-on-silicon mid-infrared arrayed waveguide grating multiplexers. IEEE Photonics Technology Letters. Sep. 2013;**25**(18):1805-1808

[32] Chang Y-C et al. Low-loss germanium strip waveguides on silicon forthe mid-infrared. Optical Letters. 2012;**37**:2883-2885

[33] Mashanovich GZ, Gardes FY, Thomson DJ, Hu Y, Li K, Nedeljkovic M, Penades JS, Khokhar AZ, Mitchell CJ, Stankovic S, Topley R. Silicon photonic waveguides and devices for near-and mid-IR applications. IEEE Journal of Selected Topics in Quantum Electronics. 2015;**21**(4):407-418

[34] Ramirez JM, Vakarin V, Gilles C, Frigerio J, Ballabio A, Chaisakul P, Le Roux X, et al. Low-loss Ge-rich Si 0.2 Ge 0.8 waveguides for mid-infrared photonics. Optics Letters. 2017;**42**(1):105-108

[35] Brun M, Labeye P, Grand G, Hartmann J-M, Boulila F, Carras M, Nicoletti S. Low loss SiGe graded index waveguides for mid-IR applications. Optics Express. 2014;**22**(1):508-518

[36] Younis U, Lim AE-J, Lo PG-Q, Bettiol AA, Ang K-W. Propagation loss improvement in Ge-on-SOI mid-infrared waveguides using rapid thermal annealing. IEEE Photonics Technology Letters. 2016;**28**(21):2447-2450

[37] Carletti L, Ma P, Yi Y, Luther-Davies B, Hudson D, Monat C, Orobtchouk R, et al. Nonlinear optical response of low loss silicon germanium waveguides in the mid-infrared. Optics Express. 2015;**23**(7):8261-8271

[38] Liao H-Y, Jung S, Chakravarty S, Chen RT, Belkin MA. Low-Loss Ge-on-GaAs platform for mid-infrared photonics. In: Lasers and Electro-Optics (CLEO), 2017 Conference on, pp. 1-2. IEEE. 2017

[39] Wang J, Santamato A, Jiang P, Bonneau D, Engin E, Silverstone JW, Lermer M, et al. Gallium arsenide (GaAs) quantum photonic waveguide circuits. Optics Communications. 2014;**327**:49-55

[40] Stievater TH, Mahon R, Park D, Rabinovich WS, Pruessner MW, Khurgin JB, Richardson CJK. Mid-infrared difference-frequency generation in suspended GaAs waveguides. Optics Letters. 2014;**39**(4):945-948

[41] Sugimoto Y, Tanaka Y, Ikeda N, Nakamura Y, Asakawa K, Inoue K. Low propagation loss of 0.76 dB/mm in GaAs-based single-line-defect two-dimensional photonic crystal slab waveguides up to 1 cm in length. Optics Express. 2004;**12**(6):1090-1096

[42] D'Agostino D, Carnicella G, Ciminelli C, Thijs P, Veldhoven PJ, Ambrosius H, Smit M. Low-loss passive waveguides in a generic InP foundry process via local diffusion of zinc. Optics Express. 2015;**23**(19):25143-25157

[43] Ng WH, Podoliak N, Horak P, Wu J, Liu H, Stewart WJ, Kenyon AJ. Design and fabrication of suspended indium phosphide waveguides for MEMS-actuated optical buffering. IEEE Journal of Selected Topics in Quantum Electronics. 2015;**21**(4):240-246

[44] Roux S, Cerutti L, Tournie E, Gérard B, Patriarche G, Grisard A, Lallier E. Low-loss orientation-patterned GaSb waveguides for mid-infrared parametric conversion. Optical Materials Express. 2017;**7**(8):3011-3016

[45] Olsson YK, Chen G, Rapaport R, Fuchs DT, Sundar VC, Steckel JS, Bawendi MG, Aharoni A, Banin U. Fabrication and optical properties of polymeric waveguides containing nanocrystalline quantum dots. Applied Physics Letters. 2004;**85**(19):4469-4471

[46] Steckl AJ, Heikenfeld JC, Lee D-S, Garter MJ, Baker CC, Wang Y, Jones R. Rare-earth-doped GaN: growth, properties, and fabrication of electroluminescent devices. IEEE Journal of Selected Topics in Quantum Electronics. 2002;**8**(4):749-766

[47] Yan YC, Faber AJD, De Waal H, Kik PG, Polman A. Erbium-doped phosphate glass waveguide on silicon with 4.1 dB/cm gain at 1.535 μm. Applied Physics Letters. 1997; **71**(20):2922-2924

[48] Singh N, Hudson DD, Yi Y, Grillet C, Jackson SD, Casas-Bedoya A, Read A, et al. Midinfrared supercontinuum generation from 2 to 6 μm in a silicon nanowire. Optica. 2015;**2**(9):797-802

[49] Sirbuly DJ, Law M, Yan H, Yang P. Semiconductor nanowires for subwavelength photonics integration. 2005:15190-15213

[50] Grillet C, Carletti L, Monat C, Grosse P, Ben Bakir B, Menezo S, Fedeli JM, Moss DJ. Amorphous silicon nanowires combining high nonlinearity, FOM and optical stability. Optics Express. 2012;**20**(20):22609-22615

[51] Carette M, Vilcot J-P, Bernard D, Decoster D. InP/benzocyclobutene optical nanowires. Electronics Letters. 2008;**44**(15):902-903

[52] Roelkens G. Photonic integration: Beyond telecom and datacom. European Conference Interventional Oncology. 2014. Roelkens, Günther

[53] Nedeljkovic M, Khokhar AZ, Hu Y, Chen X, Soler Penades J, Stankovic S, Chong HMH, et al. Silicon photonic devices and platforms for the mid-infrared. Optical Materials Express. 2013;**3**(9):1205-1214

[54] Li X et al. Experimental demonstration of silicon slot waveguide with low transmission loss at 1064 nm. Optical Communication. 2014;**329**:168-172

[55] Debnath K, Khokhar AZ, Boden SA, Arimoto H, Oo SZ, Chong HMH, Reed GT, Saito S. Low-loss slot waveguides with silicon (111) surfaces realized using anisotropic wet etching. Frontiers in Materials. 2016;**3**:51

[56] Penadés JS, Sanchez-Postigo A, Nedeljkovic M, Ortega-Moñux A, Wangüemert-Pérez JG, Xu Y, Halir R, et al. Suspended silicon waveguides for long-wave infrared wavelengths. Optics Letters. 2018;**43**(4):795-798

[57] Alasaarela T, Korn D, Alloatti L, Säynätjoki A, Tervonen A, Palmer R, Leuthold J, Freude W, Honkanen S. Reduced propagation loss in silicon strip and slot waveguides coated by atomic layer deposition. Optics Express. 2011;**19**(12):11529-11538

[58] Spott A, Yang L, Baehr-Jones T, Ilic R, Hochberg M. Silicon waveguides and ring resonators at 5.5 μ m. Applied Physics Letters. 2010;**97**(21):213501

[59] Baehr-Jones T, Spott A, Ilic R, Spott A, Penkov B, Asher W, Hochberg M. Silicon-on-sapphire integrated waveguides for the mid-infrared. Optics Express. 2010;**18**(12):12127-12135

[60] Zou Y et al. Grating-coupled silicon-on-sapphire integrated slot waveguides operating at mid-infrared wavelengths. Optics Letters. 2014;**39**:3070-3073

[61] Li F, Jackson SD, Grillet C, Magi E, Hudson D, Madden SJ, Moghe Y, et al. Low propagation loss silicon-on-sapphire waveguides for the mid-infrared. Optics Express. 2011; **19**(16):15212-15220

[62] Khan S, Chiles J, Ma J, Fathpour S. Silicon-on-nitride waveguides for mid-and near-infrared integrated photonics. Applied Physics Letters. 2013;**102**(12):121104

[63] Knights AP, Ackert JJ, Logan DF, Huante-Ceron E, Jessop PE. Deep-levels in silicon waveguides: A route to high yield fabrication. Optical and Quantum Electronics. 2012; **44**(12-13):575-580

[64] Logan DF, Velha P, Sorel M, De La Rue RM, Wojcik G, Goebel A, Jessop PE, Knights AP. Charge state switching of deep levels for low-power optical modulation in silicon waveguides. Optics Letters. 2011;**36**(19):3717-3719

[65] Guan J, Liu X, Salter PS, Booth MJ. Hybrid laser written waveguides in fused silica for low loss and polarization independence. Optics Express. 2017;**25**(5):4845-4859

[66] Martínez, Javier, Airán Ródenas, Toney Fernandez, Javier R. Vázquez de Aldana, Robert R. Thomson, Magdalena Aguiló, Ajoy K. Kar, Javier Solis, and Francesc Díaz. "3D laser-written silica glass step-index high-contrast waveguides for the 3.5 μm mid-infrared range." Optics Letters 40, no. 24 (2015): 5818-5821

[67] Hu J, Feng N-N, Carlie N, Petit L, Wang J, Agarwal A, Richardson K, Kimerling L. Low-loss high-index-contrast planar waveguides with graded-index cladding layers. Optics Express. 2007;**15**(22):14566-14572

[68] Duchesne D, Ferrera M, Razzari L, Morandotti R, Little BE, Chu ST, Moss DJ. Efficient self-phase modulation in low loss, high index doped silica glass integrated waveguides. Optics Express. 2009;**17**(3):1865-1870

[69] Rangarajan B, Kovalgin AY, Wörhoff K, Schmitz J. Low-temperature deposition of high-quality silicon oxynitride films for CMOS-integrated optics. Optics Letters. 2013;**38**(6):941-943

[70] Jordan E, Geoffray F, Bouchard A, Ghibaudo E, Broquin J-E. Development of Tl+/Na+ ion-exchanged single-mode waveguides on silicate glass for visible-blue wavelengths applications. Ceramics International. 2015;**41**(6):7996-8001

[71] Wang F, Chen B, Pun EYB, Lin H. Alkaline aluminum phosphate glasses for thermal ion-exchanged optical waveguide. Optical Materials. 2015;**42**:484-490

[72] Najafi SI, Ti T, Sara R, Andrews MP, Fardad MA. Sol-gel glass waveguide and grating on silicon. Journal of Lightwave Technology. 1998;**16**(9):1640

[73] Karasiński P, Tyszkiewicz C, Domanowska A, Michalewicz A, Mazur J. Low loss, long time stable sol–gel derived silica–titania waveguide films. Materials Letters. 2015;**143**:5-7

[74] Lukowiak A, Zur L, Tran TNL, Meneghetti M, Berneschi S, Conti GN, Pelli S, et al. Sol–gel-derived glass-ceramic photorefractive films for photonic structures. Crystals. 2017;**7**(2):61

[75] Gorshkov ON, Grishin IA, Kasatkin AP, Smetanin SV, Churbanov MF, Shushunov AN. Optical planar waveguides based on tungsten-tellurite glass fabricated by rf-sputtering. Journal of Non-Crystalline Solids. 2018;**480**:70-73

[76] Nasu Y, Kohtoku M, Hibino Y. Low-loss waveguides written with a femtosecond laser for flexible interconnection in a planar light-wave circuit. Optics Letters. 2005;**30**(7):723-725

[77] Stone A, Jain H, Dierolf V, Sakakura M, Shimotsuma Y, Miura K, Hirao K, Lapointe J, Kashyap R. Direct laser-writing of ferroelectric single-crystal waveguide architectures in glass for 3D integrated optics. Scientific Reports. 2015;**5**:10391

[78] da Silva, Diego S, Wetter NU, de Rossi W, Samad RE, Kassab LRP. Femtosecond laser-written double line waveguides in germanate and tellurite glasses. In: Laser Applications in Microelectronic and Optoelectronic Manufacturing (LAMOM) XXIII, vol. 10519, p. 105191B. International Society for Optics and Photonics. 2018

[79] Lapointe, Jerome, Yannick Ledemi, Sébastien Loranger, Victor Lambin Iezzi, Elton Soares de Lima Filho, Francois Parent, Steeve Morency, Younes Messaddeq, and Raman Kashyap. "Fabrication of ultrafast laser written low-loss waveguides in flexible As 2 S 3 chalcogenide glass tape Optics Letters 41, no. 2 (2016): 203-206

[80] Krasnokutska I, Tambasco J-LJ, Li X, Peruzzo A. Ultra-low loss photonic circuits in lithium niobate on insulator. Optics Express. 2018;**26**(2):897-904

[81] Hu H, Ricken R, Sohler W, Wehrspohn RB. Lithium niobate ridge waveguides fabricated by wet etching. IEEE Photonics Technology Letters. 2007;**19**(6):417-419

[82] Parameswaran KR, Route RK, Kurz JR, Roussev RV, Fejer MM, Fujimura M. Highly efficient second-harmonic generation in buried waveguides formed by annealed and reverse proton exchange in periodically poled lithium niobate. Optics Letters. 2002;**27**(3):179-181

[83] Chang L, Pfeiffer MHP, Volet N, Zervas M, Peters JD, Manganelli CL, Stanton EJ, Li Y, Kippenberg TJ, Bowers JE. Heterogeneous integration of lithium niobate and silicon nitride waveguides for wafer-scale photonic integrated circuits on silicon. Optics Letters. 2017;**42**(4):803-806

[84] Volk MF, Suntsov S, Rüter CE, Kip D. Low loss ridge waveguides in lithium niobate thin films by optical grade diamond blade dicing. Optics Express. 2016;**24**(2):1386-1391

[85] Li S, Cai L, Wang Y, Jiang Y, Hui H. Waveguides consisting of single-crystal lithium niobate thin film and oxidized titanium stripe. Optics Express. 2015;**23**(19):24212-24219

[86] Wang Y, Chen Z, Cai L, Jiang Y, Zhu H, Hui H. Amorphous silicon-lithium niobate thin film strip-loaded waveguides. Optical Materials Express. 2017;**7**(11):4018-4028

[87] Siew SY, Cheung EJH, Liang H, Bettiol A, Toyoda N, Alshehri B, Dogheche E, Danner AJ. Ultra-low loss ridge waveguides on lithium niobate via argon ion milling and gas clustered ion beam smoothening. Optics Express. 2018;**26**(4):4421-4430

[88] Ren S, Yang X-F, Zhang Z-B, Wong W-H, Yu D-Y, Pun EY-B, Zhang D-L. Crystalline phase, Ga3+ concentration profile, and optical properties of Ga3+-diffused lithium tantalate waveguide. Materials Letters. 2018;**213**:79-83

[89] Petraru A, Siegert M, Schmid M, Schubert J, Buchal C. Ferroelectic BaTiO 3 Thin Film Optical Waveguide Modulators. MRS Online Proceedings Library Archive. 2001;**688**

[90] Jin T, Li L, Zhang B, Lin H-YG, Wang H, Lin PT. Monolithic mid-infrared integrated photonics using silicon-on-epitaxial barium titanate thin films. ACS Applied Materials & Interfaces. 2017;**9**(26):21848-21855

[91] Qiu F, Spring AM, Maeda D, Ozawa M-a, Odoi K, Otomo A, Aoki I, Yokoyama S. A hybrid electro-optic polymer and $TiO_2$ double-slot waveguide modulator. Scientific Reports. 2015;**5**:8561

[92] d'Alessandro A, Martini L, Civita L, Beccherelli R, Asquini R. Liquid crystal waveguide technologies for a new generation of low-power photonic integrated circuits In: Emerging Liquid Crystal Technologies X, vol. 9384, p. 93840L. International Society for Optics and Photonics. 2015

[93] Wang T-J, Chaung C-K, Li W-J, Chen T-J, Chen B-Y. Electrically tunable liquid-crystal-core optical channel waveguide. Journal of Lightwave Technology. 2013;**31**(22):3570-3574

[94] Ako T, Hope A, Nguyen T, Mitchell A, Bogaerts W, Neyts K, Beeckman J. Electrically tuneable lateral leakage loss in liquid crystal clad shallow-etched silicon waveguides. Optics Express. 2015;**23**(3):2846-2856

[95] Ma H, Jen AK-Y, Dalton LR. Polymer-based optical waveguides: materials, processing, and devices. Advanced Materials. 2002;**14**(19):1339-1365

[96] Pätzold WM, Demircan A, Morgner U. Low-loss curved waveguides in polymers written with a femtosecond laser. Optics Express. 2017;**25**(1):263-270

[97] Dou X, Wang X, Huang H, Lin X, Ding D, Pan DZ, Chen RT. Polymeric waveguides with embedded micro-mirrors formed by metallic hard mold. Optics Express. 2010;**18**(1):378-385

[98] Xu X, Lin M, Jiang S, He Z. Circular-core single-mode polymer waveguide for high-density and high-speed optical interconnects application at 1550 nm. Optics Express. 2017;**25**(21):25689-25696

[99] Dangel R, Hofrichter J, Horst F, Jubin D, La Porta A, Meier N, Soganci IM, Weiss J, Offrein BJ. Polymer waveguides for electro-optical integration in data centers and high-performance computers. Optics Express. 2015;**23**(4):4736-4750

[100] Vernoux C, Chen Y, Markey L, Spârchez C, Arocas J, Felder T, Neitz M, et al. Flexible long-range surface plasmon polariton single-mode waveguide for optical interconnects. Optical Materials Express. 2018;**8**(2):469-484

[101] Kim JT, Park S, Jung Jin J, Park SK, Kim M-S, Lee M-H. Low-loss polymer-based long-range surface plasmon-polariton waveguide. IEEE Photonics Technology Letters. 2007; **19**(18):1374-1376

[102] Doradla P, Giles RH. Dual-frequency characterization of bending loss in hollow flexible terahertz waveguides In Terahertz, RF, Millimeter, and Submillimeter-Wave Technology and Applications VII, vol. 8985, p. 898518. International Society for Optics and Photonics. 2014

[103] Bledt CM, Melzer JE, Harrington JA. Theory and practical considerations of multilayer dielectric thin-film stacks in Ag-coated hollow waveguides. Applied Optics. 2014;**53**(4): A70-A82

[104] Ung B, Dupuis A, Stoeffler K, Dubois C, Skorobogatiy M. High-refractive-index composite materials for terahertz waveguides: trade-off between index contrast and absorption loss. JOSA B. 2011;**28**(4):917-921

[105] Bowden B, Harrington JA, Mitrofanov O. Silver/Polystyrene Coated Hollow Glass Waveguides for the Transmission of THz Radiation. In: Lasers and Electro-Optics, 2007. CLEO 2007. Conference on, pp. 1-2. IEEE. 2007

[106] Melzer JE, Harrington JA. Silver/cyclic olefin copolymer hollow glass waveguides for infrared laser delivery. Applied Optics. 2015;**54**(32):9548-9553

[107] Lo S-S, Wang M-S, Chen C-C. Semiconductor hollow optical waveguides formed by omni-directional reflectors. Optics Express. 2004;**12**(26):6589-6593

[108] Giglio M, Patimisco P, Sampaolo A, Kriesel JM, Tittel FK, Spagnolo V. Low-loss and single-mode tapered hollow-core waveguides optically coupled with interband and quantum cascade lasers. Optical Engineering. 2017;**57**(1). DOI: 011004

[109] Bappi G, Flannery J, Al Maruf R, Bajcsy M. Prospects and limitations of bottom-up fabricated hollow-core waveguides. Optical Materials Express. 2017;**7**(1):148-157

[110] Hu J, Tarasov V, Carlie N, Feng N-N, Petit L, Agarwal A, Richardson K, Kimerling L. Si-CMOS-compatible lift-off fabrication of low-loss planar chalcogenide waveguides. Optics Express. 2007;**15**(19):11798-11807

[111] Ma P, Choi D-Y, Yi Y, Gai X, Yang Z, Debbarma S, Madden S, Luther-Davies B. Low-loss chalcogenide waveguides for chemical sensing in the mid-infrared. Optics Express. 2013; **21**(24):29927-29937

[112] Chiles J, Malinowski M, Rao A, Novak S, Richardson K, Fathpour S. Low-loss, submicron chalcogenide integrated photonics with chlorine plasma etching. Applied Physics Letters. 2015;**106**(11):111110

[113] Lim J-M, Kim S-H, Choi J-H, Yang S-M. Fluorescent liquid-core/air-cladding waveguides towards integrated optofluidic light sources. Lab on a Chip. 2008;**8**(9):1580-1585

[114] Gopalakrishnan N, Sagar KS, Christiansen MB, Vigild ME, Ndoni S, Kristensen A. UV patterned nanoporous solid-liquid core waveguides. Optics Express. 2010;**18**(12):12903-12908

[115] Penadés JS, Ortega-Moñux A, Nedeljkovic M, Wangüemert-Pérez JG, Halir R, Khokhar AZ, Alonso-Ramos C, et al. Suspended silicon mid-infrared waveguide devices with subwavelength grating metamaterial cladding. Optics Express. 2016;**24**(20):22908-22916

[116] Alasaarela T, Saastamoinen T, Hiltunen J, Säynätjoki A, Tervonen A, Stenberg P, Kuittinen M, Honkanen S. Atomic layer deposited titanium dioxide and its application in resonant waveguide grating. Applied Optics. 2010;**49**:4321-4325

[117] Häyrinen M, Roussey M, Gandhi V, Stenberg P, Säynätjoki A, Karvonen L, Kuittinen M, Honkanen S. Low-loss titanium dioxide strip waveguides fabricated by atomic layer deposition. Journal of Lightwave Technology. 2014;**32**(2):208-212

[118] Pandraud G, Barbosa Neira A, Sarro PM, Margallo-Balbás E. PECVD SiC-SiO 2-SiC horizontal slot waveguides for sensing photonics devices. In: Sensors, 2010 IEEE, pp. 975-978. IEEE. 2010

[119] Subramanian AZ, Neutens P, Dhakal A, Jansen R, Claes T, Rottenberg X, Peyskens F, Selvaraja S, Helin P, Du Bois B, et al. Low-loss single mode PECVD silicon nitride photonic wire waveguides for 532–900 nm wavelength window fabricated within a CMOS pilot line. IEEE Photonics Journal. 2013;**5**:2202809-2202809. DOI: 10.1109/JPHOT.2013.2292698

[120] Romero-García S, Merget F, Zhong F, Finkelstein H, Witzens J. Silicon nitride CMOS-compatible platform for integrated photonics applications at visible wavelengths. Optics Express. 2013;**21**:14036-14046

[121] Luke K, Dutt A, Poitras CB, Lipson M. Overcoming Si3N4 film stress limitations for high quality factor ring resonators. Optics Express. 2013;**21**:22829-22833

[122] Bauters JF, Heck MJR, John D, Dai D, Tien M-C, Barton JS, Leinse A, Heideman RG, Blumenthal DJ, Bowers JE. Ultra-low-loss high-aspect-ratio Si 3 N 4 waveguides. Optics Express. 2011;**19**(4):3163-3174

[123] Epping JP, Hoekman M,Mateman R, Leinse A, Heideman RG, van Rees A, van der Slot PJM, Lee CJ, Boller KJ. High confinement, high yield Si3N4 waveguides for nonlinear optical applications. Optics Express. 2015;**23**:642-648

[124] Luke K, Okawachi Y, Lamont MRE, Gaeta AL, Lipson M. Broadband mid-infrared frequency comb generation in a Si3N4 microresonator. Optics Letters. 2015;**40**:4823-4826

[125] Lin PT, Singh V, Kimerling L, Agarwal AM. Planar silicon nitride mid-infrared devices. Applied Physics Letter. 2013;**102**. DOI: 10.1063/1.4812332

[126] Lin PT, Singh V, Lin HYG, Tiwald T, Kimerling LC, Agarwal AM. Low-stress silicon nitride platform for mid-infrared broadband and monolithically integrated microphotonics. Advanced Optical Materials. 2013;**1**:732-739

[127] Belt M, Davenport ML, Bowers JE, Blumenthal DJ. Ultra-low-loss $Ta_2O_5$-core/$SiO_2$-clad planar waveguides on Si substrates. Optica. 2017;**4**(5):532-536

[128] Tsuruda K, Fujita M, Nagatsuma T. Extremely low-loss terahertz waveguide based on silicon photonic-crystal slab. Optics Express. 2015;**23**(25):31977-31990

[129] Yang J, Zhao J, Cheng G, Tian H, Lu S, Chen P, Lin L, Liu W. 3D printed low-loss THz waveguide based on Kagome photonic crystal structure. Optics Express. 2016;**24**(20): 22454-22460

Chapter 7

# Graphene Based Waveguides

Xianglian Song, Xiaoyu Dai and Yuanjiang Xiang

Additional information is available at the end of the chapter

http://dx.doi.org/10.5772/intechopen.76796

**Abstract**

Graphene, which is well known as a one-atom thick carbon allotrope, has drawn lots of attention since its first announcement due to remarkable performance in mechanical, electrical, magnetic, thermal, and optical areas. In particular, unique properties of graphene such as low net absorption in broadband optical band, notably high nonlinear optical effects, and gate-variable optical conductivity make it an excellent candidate for high speed, high performance, and broadband electronic and photonics devices. Embedding graphene into optical devices longitudinally would enhance the light-graphene interaction, which shows great potential in photonic components. Since the carrier density of graphene could be tuned by external gate voltage, chemical doping, light excitation, graphene-based waveguide modulator could be designed to have high flexibility in controlling the absorption and modulation depth. Furthermore, graphene-based waveguides could take advantages in detection, sensing, polarizer, and so on.

**Keywords:** graphene, waveguide, photonics, tunable, optical

## 1. Introduction

With the increasing demand in data storage, high-performance computing, and broadband networks for communication, the requirement for high-performance optical devices with broadband working bandwidth could be imaged [1–3]. Among the whole process, integrating telecom network onto chips has irreplaceable importance [4]. Since waveguide is one of the most indispensable components in modern communication, its development surely means a lot, which would otherwise impede the whole progress of optical technology [5]. Silicon photonics could provide broad bandwidths, which have been applied to low-loss optical waveguides [6, 7]. Other photonic substrates such as germanium or compound semiconductors are required to achieve high performance at the same time [4, 8]. However, the common

use of such materials is restricted due to limited bandwidth, inevitable cross-talk, high-energy consumption, expensive cost, and so on [9, 10].

Two-dimensional (2D) materials, such as graphene, black phosphorus (BP), hexagonal boron nitride (hBN), and transition metal dichalcogenides ($MX_2$, such as $ReS_2$, $MoS_2$, $WS_2$, $WSe_2$), have been of tremendous interest for applications in electronics, optoelectronics, and integrated photonics due to their unique and distinctive properties from bulk ones [11, 12]. Among all these 2D materials, graphene plays a special role in leading the exploration of 2D materials, which was first isolated mechanically in 2004 [13, 14]. Graphene, which is well known for thinnest, strongest, and highest mobility, shows great potential in various applications. Besides, graphene absorbs only ~2.3% in normally incident waves in and optical range, as shown in **Figure 1**, and the interaction of graphene with electromagnetic wave covers a broadband from the visible to terahertz spectral range [16, 17]. Remarkably, the conduction and valence bands in a mono layer graphene meet at direct, leading to a gapless and semimetallic band structure, which could be adjusted by doping or some other external excitations [18–20].

The unique and extraordinary properties of graphene make it possible to be an ideal alternative in high-performance optoelectronic devices [21–25]. Hence, graphene, the unique 2D carbon atoms arranged in a honeycomb lattice, has been widely reported as an excellent plasmonic material for light-matter interactions from terahertz to the infrared (IR) region [18]. The gapless linear dispersion of Dirac fermions makes it possible for graphene integrated with other substrates to formulate modulators, polarizers, broadband waveguides, photodetectors, bio-sensors and so on [25–27]. Especially in the optical range, graphene-based waveguides play a critical role in photonic integrated circuits, optical fiber communication and sensing, as shown in **Figure 1**. It has been reported that coplanar integration which are planarized with

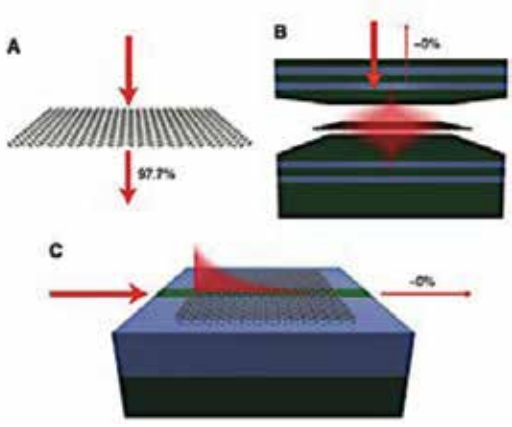


**Figure 1.** Different configurations for light-matter interaction in graphene. (A) For normal incident wave in optical range, graphene has the advantage of broadband absorption, the total absorption is quite small though. (B) When graphene is placed into an oical resonator, the absorption could be enhanced since the interaction between light and mater is enhanced. (C) When integrating graphene at the surface of photonics substrates, the interaction length would increase while the broadband optical bandwidth remains unchanged [15].

http://dx.doi.org/10.5772/intechopen.76796

cladding materials could be achieved by transferring and the lamination of graphene to the surface of silicon photonic substrates. Integrating graphene with photonic devices not only promotes the emergence of novel optoelectronic properties but also opens a new versatile platform to investigate more fundamental application of graphene.

Three independent research groups, Mueller's group [28] at Vienna University of Technology and Johannes Kepler University (Australia), Englund's group [29] at Columbia University, the Massachusetts Institute of Technology (MIT) and the IBM T.J. Watson Research Center (the USA), and Xu's group [30] at Chinese University of Hong Kong (China), reported almost at the same time, chip-integrated graphene photodetectors with high responsivities and speeds, for which the working wavelength is covered from 1.3 to 2.75 μm [31]. Graphene-based photodetectors have better performance than germanium-based devices, because germanium-based ones meet limitations to overcome the low efficiencies at wavelength above 1.5 μm. However, this problem does not exist in graphene due to the zero-bandgap intrinsic property. As a result, the optical absorption coefficient remains constant from visible to infrared range owing to the linear band structure. Thus, a nearly flat response covering almost the whole optical communication band would not be out of image.

Pospischil and Mueller et al. [24] achieved a new kind of graphene-band optical interconnect, which owned an ultra-wideband operation from the O to the U band, as shown in **Figure 2**. Besides, the operation speed of graphene-based transition has been proved to be really high, which could be a perfect candidate for high-speed data transmission. Moreover, this device could overcome the biggest obstacles in conventional ones; the energy consumption in a graphene-based modulator is quite low. Due to the strong optical interaction in graphene, small devices in single chips were possible. The mechanical flexibility of graphene plays a role in formulating active components in polymer-based optical circuits.

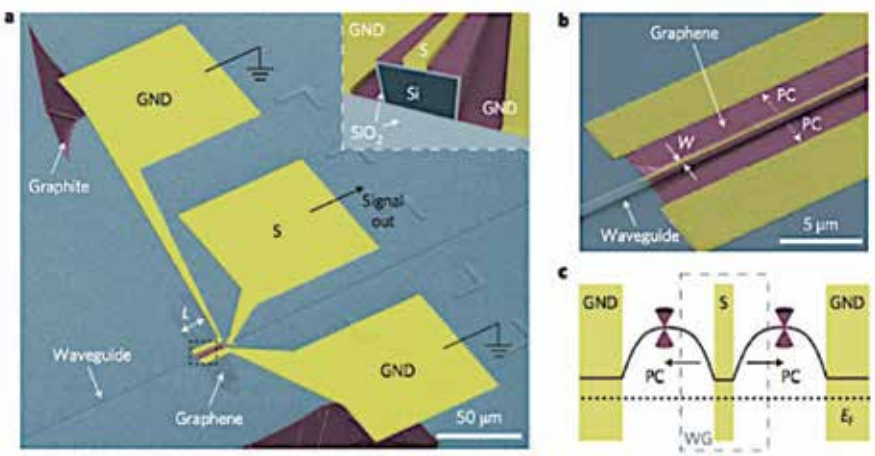


**Figure 2.** (a) Colored scanning electron micrograph of a waveguide-integrated graphene photodetector. The violet region represents graphene sheet. (b) enlarged view of the section highlighted by the black dashed rectangle in a. (c) Schematic illustration of the band diagram [24].

Gan et al. [29] achieved a photodetector which simultaneously exhibited high responsibility, high speed, and broadband spectral bandwidth by using a metal-doped graphene junction coupled evanescently with the waveguide, as shown in **Figure 3**. The absorption performance of

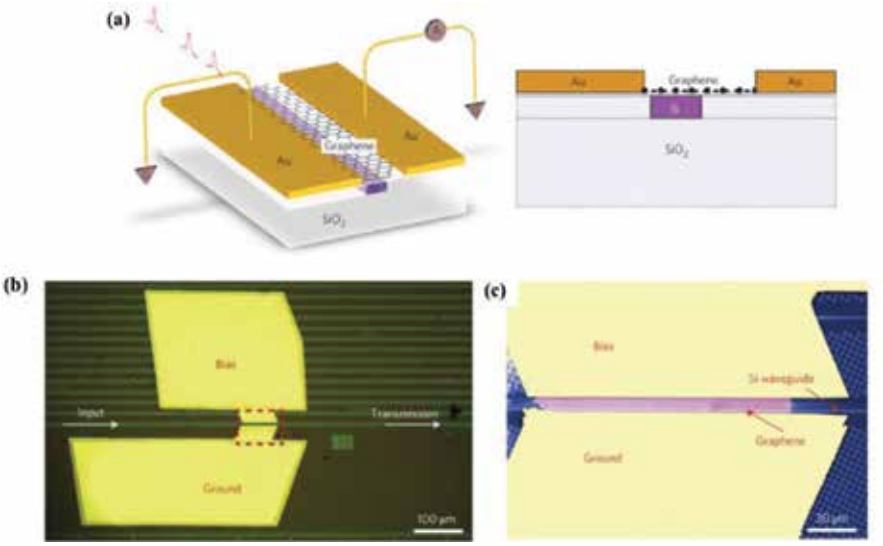


**Figure 3.** (a) Schematic of the waveguide-integrated graphene photodetector. (b) Optical microscopy top view of the device with a bilayer of graphene covering the waveguide. (c) SEM image showing the boxed region in (b) (false color), displaying the planarized waveguide (blue), graphene (purple) and metal electrodes (yellow) [29].

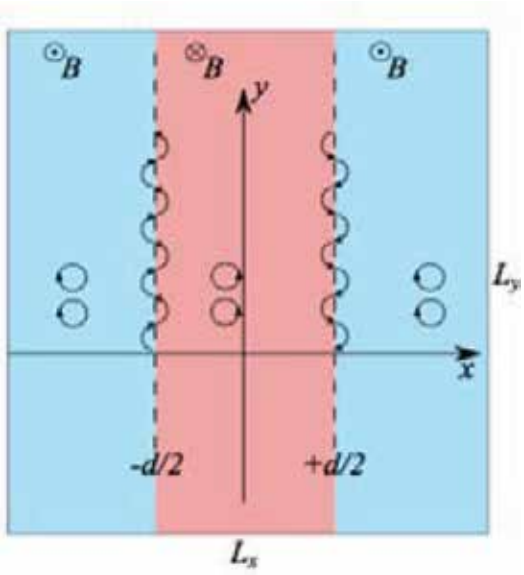


**Figure 4.** Schematic sketch of the MGW setup viewed from above. A magnetic field B is applied everywhere in the graphene plane except for the waveguide region $|x| < d/2$, where the field is reversed [32].

http://dx.doi.org/10.5772/intechopen.76796

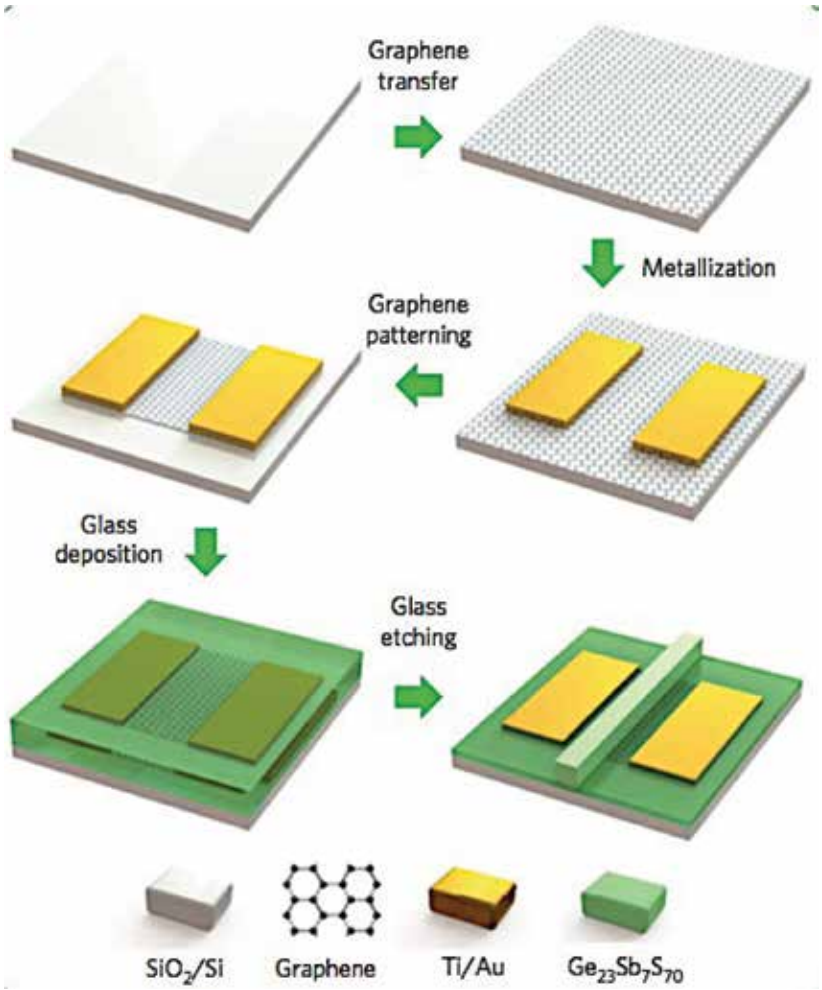


**Figure 5.** Schematic fabrication process flow to integrate chalcogenide glass photonic devices with graphene. Monolayer graphene had been grown on Cu foil by CVD method, which was then transferred onto the surface of target substrate by standard PMMA transformation process. Contract metals were then deposited and pattered on the surface of graphene. Subsequently, a standard electron-beam lithography process was adopted to patter graphene on the substrate. Then a glass film was deposited onto graphene surface by thermal evaporation, and the pattern of glass was defined by fluorine-based plasma etching [33].

graphene is improved by extending the length of graphene or by coupling graphene with a transverse-magnetic (TM) mode with a stronger evanescent field. Besides, the internal quantum efficiency of the photodetector can be improved by electrically grating the graphene layer to reshape the depth and location of the potential difference. In their research, they proved that graphene could be integrated with complementary-metal-oxide-silicon (CMOS), which made possible the realization of scalable ultra-high bandwidth graphene-based optical interconnectors.

The propagation of the electromagnetic field along the waveguide is summarized in two ways, which are known as transverse-electric (TE) and transverse-magnetic (TM) modes. Generally,

in the TE mode, the electric lines of flux are perpendicular to the axis of the waveguides. While in TM mode, the magnetic lines of flux are perpendicular to the axis of the waveguides. Normally, for waveguides using a single conductor, no transverse-electromagnetic (TEM) mode could be transmitted. Most research focus on the transmission of the TE mode, while Cohnitz et al. [32] investigated a magnetic graphene waveguide, in which a clean graphene is exposed to a static inhomogeneous magnetic field along one of the planar directions. As shown in **Figure 4**, when applying magnetic fields to a monolayer graphene, quantum modes exhibited like classical snake orbits near the field switch lines. While in the other regions far from these region, only Landau-quantized cyclotron orbits could be detected.

Usually, the integration of graphene with photonic devices relies on the transformation of exfoliated or delaminated or chemical vapor deposition (CVD)-fabricated 2D material onto pretreated devices, as shown in **Figure 5** [34]. However, the application of the transformation process is limited due to the shortcomings in uniformity and efficiency [35–37]. Most importantly, transferred 2D materials suffer from weak interaction with optical modes in pre-treated devices [37]. An atomic layer deposition (ALD) method has been adopted widely to obtain gate dielectric on graphene. Also, plasma-enhanced chemical vapor deposition (PECVD) could be another option for fabrication of silicon nitride on graphene. Last year, it was reported that the spin-coating process could be applied to directly fabricate the polymer waveguide modulator on graphene [38]. However, the fabrication technique of photonics devices integrating the graphene thin film needs to be improved for the difficulty of keeping the original properties of graphene after the following integrated progresses. Even though it's still a challenge to ensure the quality of integrated graphene up to date, the importance of optimized and the continuous study of graphene-based photonics devices, especially waveguides, are foreseen.

## 2. Electromagnetic properties of graphene-based waveguides

Most electromagnetic phenomena are governed by Maxwell equations, while the electromagnetic properties of materials are determined by two parameters, relative complex permittivity ($\varepsilon$) and relative complex magnetic permeability ($\mu$), which describe the coupling of a material with incident electromagnetic energy. Normally, in the optical range, refraction index ($n$) is used as well to describe the macroscopic effective parameters of the material, and the refraction has as a relationship with relative complex permittivity ($\varepsilon$) and relative complex permeability ($\mu$) the following:

$$n = \sqrt{\mu\varepsilon} \tag{1}$$

For most materials without magnetic properties, we treat $\mu = 1$ here. A conventional waveguide consists of a high-index core surrounded by a lower-index cladding.

### 2.1. Graphene's relative complex permittivity in vacuum

Graphene's optical properties can be determined by its relative complex permittivity. The equivalent in-plane component of graphene's relative permittivity is given by:

$$\varepsilon(\omega) = 1 + \frac{i\sigma(\omega)}{\omega\varepsilon_0 d} \tag{2}$$

where $d$ is the thickness of the graphene layer, $\varepsilon_0$ is relative complex permittivity in vacuum ($\varepsilon_0 = 8.854$ F/m), $\omega$ is the optical frequency, and $\sigma$ is graphene's optical conductivity. By using the Kubo method, we can calculate the optical conductivity ($\sigma$) which consists of intraband ($\sigma_{intra}$) and interband ($\sigma'_{inter} + i\sigma''_{inter}$) [39], as shown in **Figure 6**, thus:

$$\sigma_{total} = \sigma_{intra} + \sigma'_{inter} + \sigma''_{inter} \tag{3}$$

where

$$\sigma_{intra} = \sigma_0 \frac{4E_F}{\pi} \frac{1}{\hbar(\Gamma_1 - i\omega)} \tag{4}$$

$$\sigma'_{inter} = \sigma_0 \left[1 + \frac{1}{\pi}\tan^{-1}\left(\frac{\hbar\omega - 2E_F}{\hbar\Gamma_2}\right)\right] - \frac{1}{\pi}\tan^{-1}\left(\frac{\hbar\omega + 2E_F}{\hbar\Gamma_2}\right) \tag{5}$$

$$\sigma''_{inter} = -\sigma_0 \frac{1}{2\pi} In\left[\frac{(2E_F + \hbar\omega)^2 + (\hbar\Gamma_2)^2}{(2E_F - \hbar\omega)^2 + (\hbar\Gamma_2)^2}\right] \tag{6}$$

here, $\sigma_0 = e^2 4\hbar \cong 60.8$ μS is the universal optical conductance, $E_F$ is the Fermi level of graphene, $\hbar$ is Planck's constant, and $\Gamma_1 = 8.3 \times 10^{11}\text{s}^{-1}$ and $\Gamma_2 = 10^{13}\text{s}^{-1}$ are relaxation rates at room temperature associated with the interband and intraband transitions, respectively.

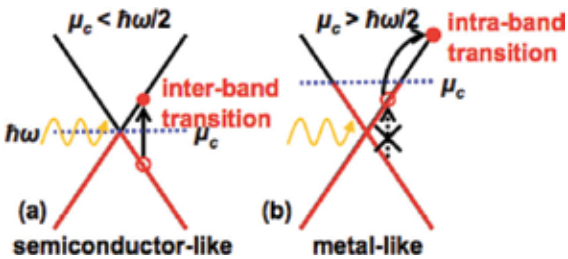


**Figure 6.** (a) Interband transition and (b) intraband transition in graphene [39].

Obviously, relative permittivity of this kind of waveguide is related to the conductivity of graphene, which would further influence the dispersion properties of the whole structure. When integrating graphene into the waveguide, the surface plasmon dispersion of graphene is strongly modified by the metal and other dielectric substrates; thus, the transmission of the incident electromagnetic wave in the waveguide is affected as well [40]. The characteristic plasmon dispersion relationship could be obtained by the following equation for the structure as described in **Figure 7(a)**:

$$\varepsilon_3 \frac{\varepsilon_4 + \varepsilon_3 \tanh qd_3}{\varepsilon_3 + \varepsilon_4 \tanh qd_3} + \varepsilon_2 \frac{\varepsilon_1 + \varepsilon_2 \tanh qd_2}{\varepsilon_2 + \varepsilon_1 \tanh qd_2} = -i\frac{q}{\omega}\sigma(q,\omega) \tag{7}$$

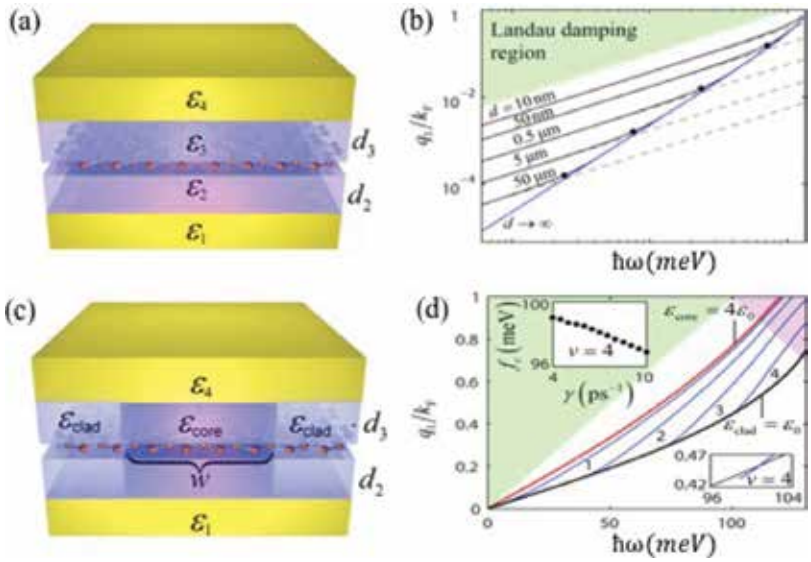


**Figure 7.** (a) Planar waveguide, and (c) non-planar rectangular waveguide. Dispersion characteristics of planar (b) and non-planar (d) waveguides [41].

for which the explanation of permittivity could be found in the **Figure 7(a)**. It should be noted here that the equation shows a good approximation when the thickness is much thicker than the skin depth [41]. As shown in **Figure 7(b)**, an enhanced confinement and an increased propagation distance can be obtained by adopting a metal slab within a certain spectral region. However, only the plasmonic field in the direction perpendicular to the surface could be confined to the model of **Figure 7(a)**. By adopting a non-planar structure as shown in **Figure 7 (c)**, 2D confinement could be obtained due to the dielectric boundaries in the other direction, of which the dispersion relationship could be obtained by an effective index method.

Graphene's relative permittivity can be easily tuned by electrostatic gating or chemical doping, which makes it easier to be applied for Talbot effect than metal-based devices [42]. Plasmonic Talbot carpets were experimentally obtained by using surface plasmon polariton (SPP) launching gratings, and a sub-wavelength focal spot can obtained.

### 2.2. The complex refraction index of graphene based waveguides

Borini's group estimated the optical index of graphene in visible range by dealing with universal optical conductivity and measured the optical spectrum within the framework of Fresnel's coefficient calculation [43]. Reflectometry is another method to acquire the reflection properties so as to obtain an average index over a broadband range by fitting the spectrum. Xu's group [44] calculated the complex refraction index of graphene at 1550 nm through reflectivity measurement on a $SiO_2$/Si substrate. And as reported by Wang [45], Notle's group applied picometrology to measure the refraction of graphene on thermal oxide on silicon at 488, 532, and 633 nm, respectively, in which the strong dispersion of the graphene index was observed in an optical range.

http://dx.doi.org/10.5772/intechopen.76796

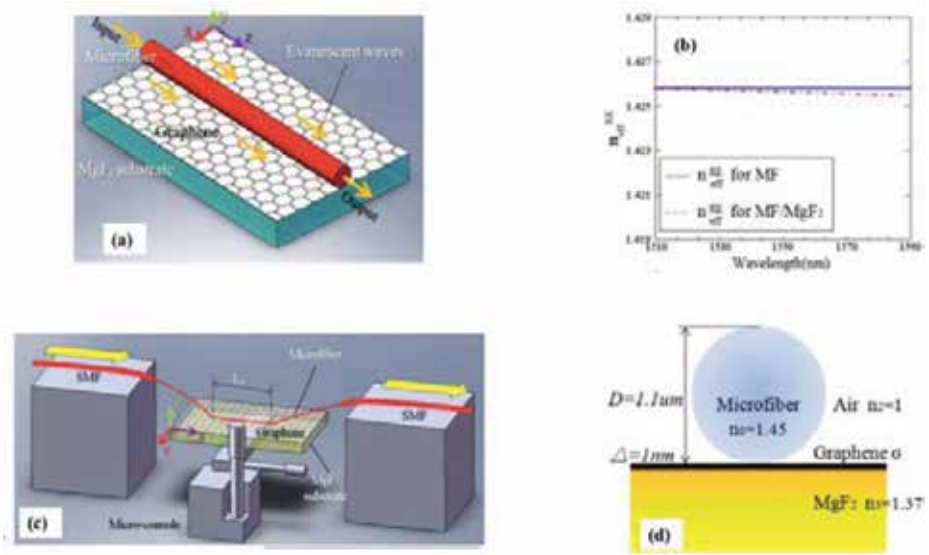


**Figure 8.** (a) Schematic diagram of the structure for the light propagating along the GMFW (red: Single mode fiber, white: Monolayer graphene, cyan: $MgF_2$ substrate). The orange arrows show the transmitting direction of the evanescent waves. (b) neffRE of the microfiber (blue solid) and the microfiber on $MgF_2$ (red dashed). (c) the experimental details of the GMHW. (d) Geometry of the cross-section of the GMHW [46].

However, in most conditions, graphene is regarded as a boundary condition when integrated into a waveguide due to the difficulty in a complex refraction index, while permittivity is regarded as a fundamental issue in graphene-based modern integrated photonics and devices. Yao's group [46] used a microfiber-based Mach-Zehnder interferometer to obtain the complex refraction index of the graphene waveguide from 1510 to 1590 nm, as shown in **Figure 8**. In this method, the microfiber acts as an effective mean to launch and collect the evanescent signal for the waveguide, for which, on the other hand, the contact length can adjusted if needed. As the results shown in **Figure 8(b)**, the complex refraction index of graphene-based waveguide varies from $2.91 - i3.92$ to $3.81 - i14.64$ in the experimental-range wavelength from 1510 to 1590 nm.

### 2.3. The tunability of graphene permittivity

When model graphene is infinitely thin, local two-sided surfaces with conductivity $\sigma$ could be obtained based on Kubo function as the following:

$$\sigma(\omega, \mu_c, \Gamma, T) = \frac{je^2(\omega - j2\Gamma)}{\pi\hbar^2} \times \left\{ \begin{array}{l} \dfrac{1}{(\omega - j2\Gamma)^2} \displaystyle\int_0^\infty \varepsilon \left[ \frac{\partial f_d(\varepsilon)}{\partial \varepsilon} - \frac{\partial f_d(-\varepsilon)}{\partial \varepsilon} \right] d\varepsilon \\ \\ - \displaystyle\int_0^\infty \left[ \frac{f_d(-\varepsilon) - f_d(\varepsilon)}{(\omega - j2\Gamma)^2 - 4(\varepsilon/\hbar)^2} \right] d\varepsilon \end{array} \right\} \tag{8}$$

where $\omega$ is radiated frequency, $\mu_c$ is chemical potential, $\Gamma$ refers to the phenomenological scattering rate that is assumed to be independent of energy, and T is temperature.

$$\mu_c = \hbar V_F \sqrt{\frac{\pi \varepsilon_{ox}}{e d_{ox}} (V - V_D)} \tag{9}$$

where $V_F$ stands for Fermi velocity, $\varepsilon_{ox}$, $d_{ox}$ corresponds to the permittivity and thickness of the dielectric, respectively, $V_D$ is the Dirac voltage, and $V$ is the externally applied voltage. Obviously, the chemical potential could be strongly tuned by the applied gate voltage, which, as a result, would impact the refraction index. Xu's group used the reflectivity measurement to obtain the complex refraction index of graphene on $SiO_2$/Si, which could be tuned by gate electric voltage, which agreed well with the Kubo function [44].

As shown in **Figure 9**, the real and imaginary part of the conductivity of graphene display a relationship with wavelength in the mid-infrared range [47]. Besides, the chemical potential which attributes the carrier density in graphene plays a critical role in controlling the conductivity. When $\hbar\omega > 2|\mu_c|$, the optical absorption of graphene is related to the real part of conductivity, which comes from the interband transition. Obviously, photocarriers are generated during the transition process, which could be used in applications such as photo-detection or modulators. While for $\hbar\omega < 2|\mu_c|$, the conductivity of graphene could be explained by Pauli's blocking theory. Thus, an electrostatic grating is always applied to adjust the chemical potential, and thus to tune the absorption of graphene, which lies as the principle to design optical modulators. Moreover, it's displayed in **Figure 9** that the imaginary part of intraband and interband conductivity has the opposite sign, which plays a critical role in determining whether the TE or TM mode could be propagated in graphene, which is always used in a polarizer.

### 2.4. Graphene integrated with nonlinear substrates

When integrating graphene with a nonlinear substrate, the relative complex permittivity of the substrate ($\varepsilon_{sub}$) could be explained by the following equation named Kerr-type medium [48]:

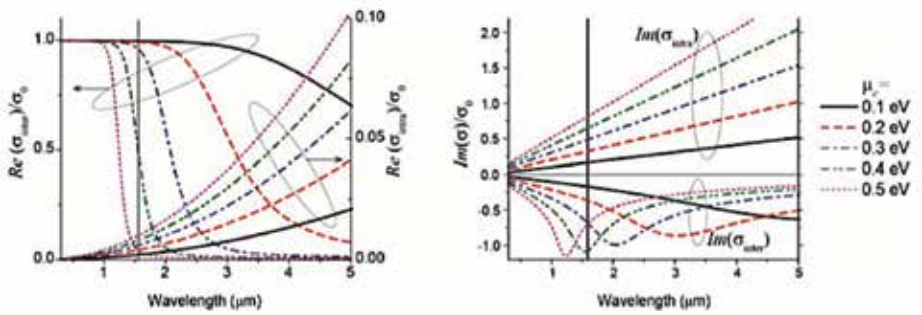


**Figure 9.** Interband (solid lines) and intraband (dashed lines) contribution to the dynamic conductivity in graphene. The vertical black line marks the telecommunication wavelength of $\lambda$ = 1.55 μm [47].

$$\varepsilon_{sub} = \varepsilon_L + \alpha E^2 \tag{10}$$

where $\varepsilon_L$ corresponds to the relative complex permittivity of substrate under linear incidence and $E$ corresponds to the external incident electric field. Besides, graphene with conductivity of $\sigma_g$ is treated as boundary here considering a one-atom scale thickness (**Figure 10**).

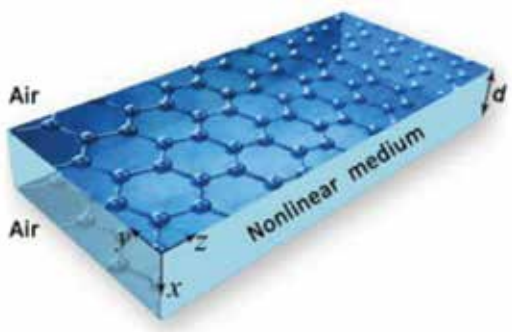


**Figure 10.** Schematic of waveguide constituted by graphene and nonlinear substrate [48].

For TM polarization with propagation constant β, three field components, *Ex*, *Ez*, and *Hy*, magnetic field $\boldsymbol{H}$ and electrical field $\boldsymbol{E}$ satisfy the following equations:

$$H = H_y y \tag{11}$$

$$E = E_x x + E_z z \tag{12}$$

$$\frac{dE_z}{d_x} = i\omega\mu_0 H_y + i\beta E_x \tag{13}$$

$$i\beta H_y = -i\omega\varepsilon_0\varepsilon E_x \tag{14}$$

$$\frac{dH_y}{dx} = i\omega\varepsilon_0\varepsilon E_z \tag{15}$$

where $\varepsilon_0$ and $\mu_0$ correspond to electric permittivity and magnetic permeability in the vacuum, exactly as $\varepsilon_0 = 8.854 \times 10^{-12}$F/m, $\mu_0 = 4\pi \times 10^{-7}$H/m. When integrating graphene at the top of the Kerr-type substrate, we get:

$$\varepsilon^2 E_x^2 = \frac{\beta^2}{\omega^2\varepsilon_0^2} H_y^2 \tag{16}$$

$$E_x^2 = \left(\varepsilon - \varepsilon_L - \alpha E_z^2\right)/\alpha \tag{17}$$

Thus, we further get:

$$\varepsilon^3 - \left(\varepsilon_L + \alpha E_z^2\right)\varepsilon^2 - \frac{\alpha\beta^2}{\omega^2\varepsilon_0^2}H_y^2 = 0 \tag{18}$$

By a mathematical transformation, we can finally get the discriminant of permittivity $\varepsilon$:

$$\Delta = -\left(\varepsilon_L + \alpha E_z^2\right)^3 \frac{\alpha\beta^2}{\omega^2\varepsilon_0^2}H_y^2 - 27\frac{\alpha^2\beta^4}{\omega^4\varepsilon_0^4}H_y^4 < 0 \tag{19}$$

if $\Delta < 0$, then there is only one solution for $\varepsilon$. The equation is useful when we numerically calculate permittivity in the relaxation method. We can get permittivity through its real root. In particular, the nonlinear conductivity of graphene cannot be ignored any more under this condition, which can be expressed as:

$$\sigma_g = \sigma_L + \sigma^{NL}|E_\tau|^2 \tag{20}$$

where $E_\tau$ is the tangential component of the electric field and $\sigma^{NL}$ contributes to nonlinear conductivity:

$$\sigma^{NL} = -i\frac{3}{8}\frac{e^2}{\pi\hbar^2}\left(\frac{eV_F}{\mu_c\omega}\right)^2\frac{\mu_c}{\omega} \tag{21}$$

in which $V_F$ stands for Fermi velocity. It should be noted here that the conductivity of graphene is regarded as Drude type only in THz and far IR range.

## 3. Applications

Graphene could be an ideal option to meet the increasing demand of high-performance optoelectronics or some other communication components when the incident wave is confined along the thin film surface [49]. The 2D structure of graphene and the planar configuration of silicon photonics are inherently compatible with each other [47]. Normally, the maximum absorption in the monolayer graphene integrating at the dielectric surface is about 10~20%, which would not make a big difference even applying highest practically achievable carrier concentrations [8]. This character could be enhanced when incorporating graphene on the surface of a passive silicon dielectric waveguide, and the modulation depth could be as high as 50% when applying voltage to the graphene sheet.

The application of graphene-based waveguides can be summarized to be modulators, detectors, sensors, polarizers and some other applications, as discussed in detail through the following.

### 3.1. Graphene-based waveguide integrated modulators

Thanks to the outstanding properties of graphene in conductivity, current density, and charge mobility, graphene-based waveguides are supposed to have promising potentials in applications

http://dx.doi.org/10.5772/intechopen.76796

such as unrivaled speed, low driving voltage, small physical footprints, and low power consumption [50], which can further be utilized in telecommunications and optoelectronics. While several graphene-based waveguides have been investigated, it still remains a challenge to combine graphene with plasmonic waveguides. How to control the intensity, phase, and polarization of the electromagnetic wave in an optical range through the waveguide attracts a lot of interest. When integrating graphene into a waveguide, the waveguide mode propagates along and is confined near a graphene sheet, which is regarded as the most promising for on-chip information processing. However, we have to admit here that even though the atomic thickness of graphene gives rise to lots of advantages, there are several challenges to deal with in such a device, such as unavoidable power consumption, slowdown response, and lower modulation depth.

Due to the tunable bandgap of graphene, waveguide modulators could be formed with broad flexibility [8, 50]. Besides, the carried density of graphene could be tuned manually through external gate voltage [51, 52], chemical doping [53, 54], and optical (laser) excitation [55]. As a result, the refraction index and the permittivity could be adjusted. It is worth mentioning here that the response of graphene in an optical range could be tuned by substrates as well [56], which may induce a bandgap opening in epitaxial graphene [57]. The transmission of 1.53 μm photons through the waveguide at a varied drive voltage is shown in **Figure 11**, which has been divided into three different regions from −6 to 6 V and the corresponding band structures are shown as insets. In the left region with drive voltage bellow −1 V, the Fermi level ($E_F$) was lower than half photonic energy ($\frac{1}{2}\hbar v$), and no electrons were available for further interband transition. In the middle region for drive voltage ranging from −1 to 3.8 V, the Fermi level was close to Dirac point; thus, it is possible for electrons in occupied regions transiting to unoccupied regions. In other words, graphene sheets showed potential in phonon absorbing, indicating its modulation ability. In the third region from 3.8 to 6 V, the transition was blocked again since all the electron states which were in resonance while the incident phonons were occupied.

Grigorenko's group reported a hybrid graphene-plasmon waveguide modulator for promising applications in telecom as shown in **Figure 12**, whose modulation depth was comparable with silicon-based waveguide modulators, showing a promising future for optical communication [50].

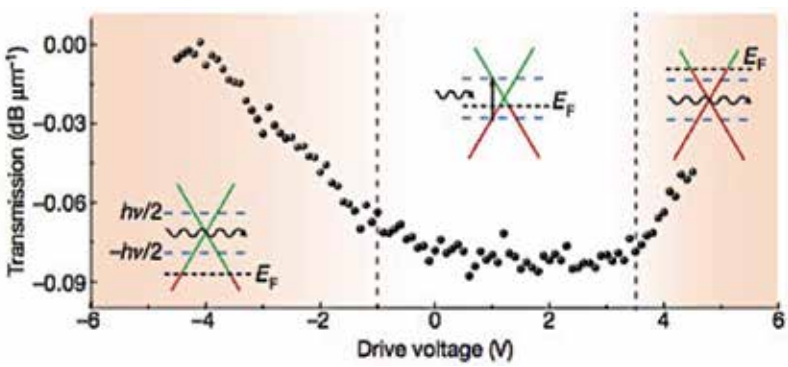


**Figure 11.** Displays the transmission of 1.53 μm photons through the waveguide at different drive voltages.

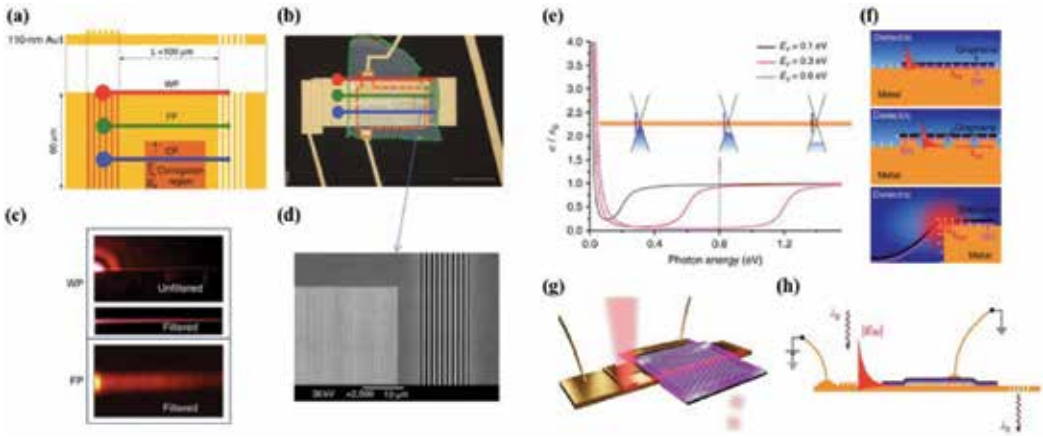


**Figure 12.** (a) The schematics of the hybrid graphene plasmonic waveguide modulators. (b) The optical micrograph of a typical hybrid graphene plasmonic modulator studied in this work. (c) Leakage radiation detection of wedge, upper panel, and flat, lower panel, plasmon-propagating modes. (d) A scanning electron micrograph of an area shown in b by the dotted box that shows corrugated waveguide and the semitransparent decoupling grating. (e) Optical Pauli blocking expressed in terms of graphene relative conductivity. (f) Sketches of three types of plasmonic modes under investigation —flat, corrugated and wedge plasmons. (g) 3D rendering of the experiment with the wedge plasmon mode. (h) The schematic of experiment where non-transparent grating couples light into plasmon modes [50].

The conductivity of graphene related to Fermi energy depends on the applied voltage between graphene layers and the thickness and permittivity of the dielectric layer located between two graphene layers. Asgari's group [58] applied bias voltage $V_b$ between two graphene layers which leads to an equal increase in electron density in the top layer and hole density in the bottom layer, as shown in **Figure 13**. Therefore, the absolute values of Fermi energies ($E_F$) in both graphene layers were identical but of opposite signs. Voltage application caused a potential difference between two graphene layers. Actually, when applying bias voltage between two graphene sheets, a capacitor effect could be observed. Besides, charge density in both sheets would increase with bias voltage, as well as Fermi energy. As a result, intraband conductivity would increase, while interband conductivity decreases.

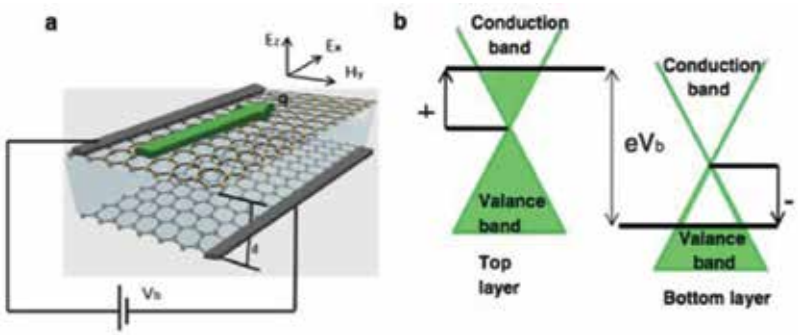


**Figure 13.** (a) Schematic illustration of the two-graphene layer structure and direction of electric and magnetic field components in TM mode. (b) The band scheme of the structure at bias voltage $V_b$ [58].

However, Murphy's group [8] designed a THz modulator formulated by setting large graphene sheets at the middle of two $SiO_2$ layers (300 nm) with Si wafers on both their sides based on ridge waveguides, as shown in the figure above. When applying voltage to graphene sheets, light-matter interaction could be modulated. As a result, the modulation depth could be achieved as high as 50%. Obviously, the carrier concentration in the graphene sheet would be modified by adjusting gate voltage. When voltage was guided through the graphene sheet in the waveguide, the electric field would penetrate into the graphene sheet and lead to absorption due to free carriers in the graphene sheet.

### 3.2. Graphene-based waveguide photodetectors

Conventionally, low band-gap semiconductors such as HgCdTe alloys or quantum-well and quantum-dot structures on III-V materials are adopted to formulate mid-infrared detectors [59]. With electrical tunability in light absorption and ultra-fast photo-response, graphene is regarded as a promising candidate for high-speed photo-detection applications [9]. It has been approved that graphene-based waveguide photodetectors could be applied from 300 nm to 6 μm or even longer [4]. It should be noted here that a dark current range may occur due to the gapless inherent properties of graphene, which should be avoided in practical application [60]. Thus, chemical potential must be tuned near the Dirac energy to ensure that incident field is illuminated to the graphene thin film.

Wang et al. [30] integrated monolayer graphene into a silicon optical waveguide on a silicon-on-insulator (SOI) from near-to-mid-infrared operational range, which indicated that the combination of the graphene silicon structure made it possible to overcome the shortcomings of the traditional junction-less photodetectors. As a result, a much higher sensitivity could be expected in graphene-based waveguides. The transverse electric mode light (~10 μm spot size) was coupled into the waveguide via a focusing sub-wavelength grating. Avouris' group [60] reported an efficient photodetection of the waveguide based on graphene, as shown in **Figure 14**, which shows gate-dependent response, and the response is nearly linear on the entire device of 10 mV. And the measurement from network analyzer showed the relative A.C photo-response, which could be further improved by applying a bias within the photocurrent generation path.

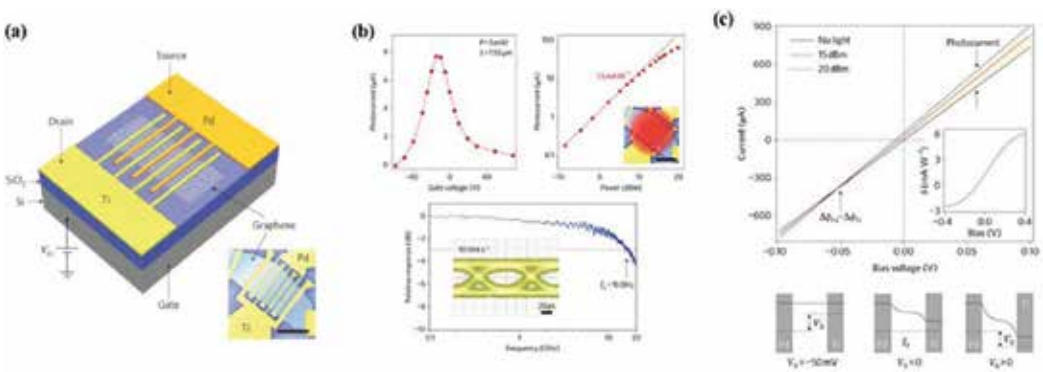


**Figure 14.** Photocurrent generation, high-frequency characterization of the MGM photodetector, and operation of the MGM photodetector at a data rate of 10 Gbit·s$^{-1}$ with 1.55 μm light excitation [60].

However, it's difficult to fabricate these materials which are challenging to operate at room temperature till now. Choi's group [61] integrated graphene with a $Bi_2Se_3$ heterostructure, in which graphene functioned as high mobility charge transport layers and $Bi_2Se_3$ functioned as a broadband IR absorber supplying holes in graphene. The graphene-$Bi_2Se_3$ structure showed broadband absorption and high-intensity response at room temperature.

### 3.3. Graphene-based waveguide sensors

Graphene is used in sensors, thanks to its unique electric properties, which show great potential in chemical or biology sensors. Among all varieties of chemical gas sensors, photonics gas sensors have advantages because of their high sensitivity and stability. Graphene plays a critical role in gas sensing due to the sensitivity of carried density to environment [62]. Graphene's conductivity can be changed drastically by adsorbed gas molecules which serve as charge carrier donors or acceptors to modulate the local carrier concentration of graphene. Cheng and Goda [63] conducted a graphene-based waveguide to measure $NO_2$ gas concentration based on germanium and silicon substrates, respectively, as shown in **Figure 15**, where sensitivity was about 20 times higher than that of the graphene-covered microfiber sensor. Li et al. [64] demonstrated a single graphene-based waveguide which simultaneously provides optical modulation and photodetection. For developing sensitive photonic gas sensors, it is important to consider the interaction of propagating light in the waveguide to the top graphene layer. Xiang's group [65, 66] conducted a series work on graphene waveguide bio-sensors, by coupling graphene surface plasmon polaritons (SPPs) and planar waveguides to realize the ultrasensitive response. The SPPs produced by graphene could be used for bio-sensors since the SPPs are extremely sensitive to changes in the dielectric constant; even small changes in molecular density could be detected [67]. Graphene-based waveguides could overcome the shortcomings in traditional bio-sensors such as low speed, more time, and insufficient sensitivity.

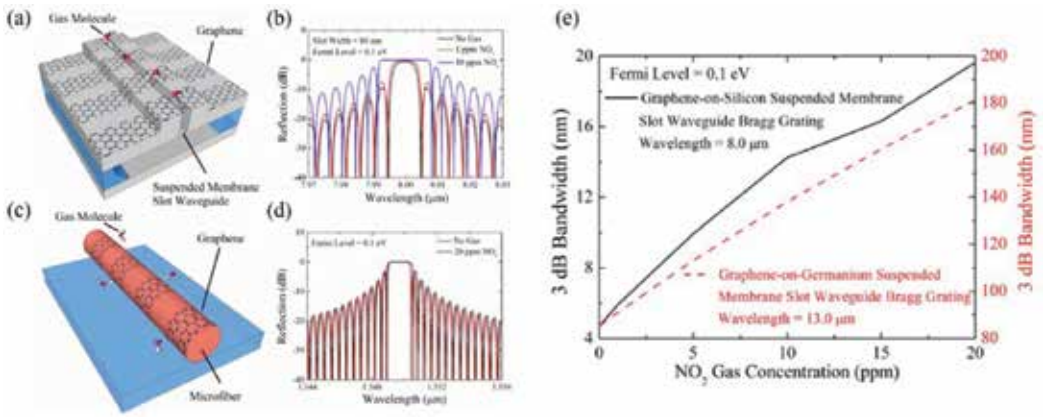


**Figure 15.** Design of graphene on silicon (GoG) and suspended membrane slot waveguide (SMSW) Bragg grating gas sensor in comparison with the graphene-covered microfiber Bragg grating gas sensor. The calculated 3 dB bandwidth of the proposed GoS-SMSW Bragg gratings as a function of the $NO_2$ gas concentration was shown [63].

### 3.4. Other waveguides

Usually, a fixed optical device works only on one particular polarization state, either the TE or the TM polarization state [68]. By coating silicon waveguides with graphene, a versatile polarizer works in two operation modes, which were based on the different effective mode index variations [69].

Waveguide integrated with graphene has nonlinear parameters which depend strongly on the Fermi level of graphene. It has been demonstrated that Integrating graphene with slot waveguide would benefit non-linear properties, owing to the interaction enhancement between graphene and incident electromagnetics [70].

When integrating graphene with nonlinear substrates on one or both sides, the surface plasmons' (SPs) localization length increased while their propagation length (PL) remained unchanged compared with the typical graphene waveguide [71, 72].

## 4. Conclusion

In conclusion, due to its unique electric and electromagnetic properties, graphene acts as a promising candidate for photonics and communication component of high performance. Especially, integrating graphene with waveguides makes it possible to overcome shortcomings such as limited bandwidth, inevitable cross-talk, high energy consumption, and expensive cost in conventional devices. Furthermore, the gapless linear dispersion of Dirac fermions makes it possible for graphene integrated with other substrates to formulate modulators, polarizers, broadband waveguides, photodetectors, bio-sensors, and so on. And the permittivity of graphene-based waveguides could be calculated based on Maxwell's function, even integrating with nonlinear substrates. The application of graphene waveguides expands the broadband range, from 300 nm to 6 μm or even longer. By tuning the carrier density of graphene through external gate voltage, chemical doping, or optical excitation, the relative complex permittivity of graphene is tuned. Thus, graphene waveguide modulators could be formed which adjusts absorption and modulation depth and so on. Besides, graphene waveguides show potential in fast and high-response detection and chemical sensing. The recent development in graphene synthesis and photonics components' fabrication technique ensures the compatibility in the integrated electronics platform, which shows a bright prospect in the near future.

## Author details

Xianglian Song, Xiaoyu Dai and Yuanjiang Xiang*

*Address all correspondence to: xiangyuanjiang@126.com

International Collaborative Laboratory of 2D Materials for Optoelectronic Science and Technology of Ministry of Education, College of Optoelectronic Engineering, Shenzhen University, China

## References

[1] Youngblood N, Chen C, Koester SJ, Li M. Waveguide-integrated black phosphorus photodetector with high responsivity and low dark current. Nature Photonics. 2015;**9**:247-252. DOI: 10.1038/nphoton.2015.23

[2] Ding Y, Guan X, Hu H. Efficient electro-optic modulation in low-loss graphene-plasmonic slot waveguides. Nanoscale. 2017;**9**:15576-15581. DOI: 10.1039/C7NR05994A

[3] Gao X, Cui TJ. Spoof surface plasmon polaritons supported by ultrathin corrugated metal strip and their applications. Nanotechnology Reviews. 2015;**4**:239-258. DOI: 10.515/ntrev-2014-0032

[4] Schuler S, Schall D, Neumaier D. Controlled generation of a p-n junction in a waveguide integrated graphene photodetector. Nano Letters. 2016;**16**:7107-7112. DOI: 10.1021/acs.nanolett.6b03374

[5] Chen M, Sheng P, Sun W. A symmetric terahertz graphene-based hybrid plasmonic waveguide. Optics Communications. 2016;**376**:41-46. DOI: 10.1016/j.optcom.2016.05.020

[6] Kovacevic G, Yamashita S. Waveguide design parameters impact on absorption in graphene coated silicon photonic integrated circuits. Optics Express. 2016;**24**:3584-3591. DOI: 10.1364/OE.24.003584

[7] Kou R, Tanabe S, Tsuchizawa T. Characterization of optical absorption and polarization dependence of single-layer graphene integrated on a silicon wire waveguide. Japanese Journal of Applied Physics. 2013;**52**:060203. DOI: 10.7567/JJAP.52.060203

[8] Mittendorff M, Li S, Murphy TE. Graphene-based waveguide-integrated terahertz modulator. ACS Photonics. 2017;**4**:316-321. DOI: 10.1021/acsphotonics.6b00751

[9] Shiue RJ, Gao Y, Wang Y. High-responsivity graphene-boron nitride photodetector and autocorrelator in a silicon photonic integrated circuit. Nano Letters. 2015;**15**:7288-7293. DOI: 10.1021/acs.nanolett.5b02368

[10] Ooi KJA, Leong PC, Ang LK. All-optical control on a graphene-on-silicon waveguide modulator. Scientific Reports. 2017;**7**:12748. DOI: 10.1038/s41598-017-13213-6

[11] Low T, Chaves A, Caldwell JD. Polaritons in layered two-dimensional materials. Nature Materials. 2016;**16**:182-194. DOI: 10.1038/nmat4792

[12] Nemilentsau A, Low T, Hanson G. Anisotropic 2D materials for tunable hyperbolic Plasmonics. Physical Review Letters. 2016;**116**:066804–5. DOI: 10.1103/PhysRevLett.116.066804

[13] Novoselov KS, Geim AK, Morozov AV. Electric field effect in atomically thin carbon films. Science. 2004;**306**:666-669. DOI: 10.1126/science.1102896

[14] Meyer JC, Geim AK, Mi K. The structure of suspended graphene sheets. Nature. 2007;**446**:60-63. DOI: 10.1038/nature05545

[15] Youngblood N, Li M. Integration of 2D materials on a silicon photonics platform for optoelectronics applications. Nano. 2017;**6**:1205-1218. DOI: 10.1515/nanoph-2016-0155

[16] Singh V, Joung D, Zhai L. Graphene based materials: Past, present and future. Progress in Materials Science. 2011;**56**:1178-1271. DOI: 10.1016/j.pmatsci.2011.03.003

[17] Hecht DS, Hu L, Irvin G. Emerging transparent electrodes based on thin films of carbon nanotubes, graphene, and metallic nanostructures. Advanced Materials. 2011;**23**:1482-1513. DOI: 10.1002/adma.201003188

[18] Nandamuri G, Roumimov S, Solanki R. Chemical vapor deposition of graphene films. Nanotechnology. 2010;**21**:145604. DOI: 10.1088/0957-4484/21/14/145604

[19] Edwards RS, Coleman KS. Graphene synthesis: Relationship to applications. Nanoscale. 2012;**5**:38-51. DOI: 10.1039/C2NR32629A

[20] Avouris P, Xia F. Graphene applications in electronics and photonics. MRS Bulletin. 2012; **37**:1225-1234. DOI: 10.1557/mrs.2012.206

[21] Sun Z, Martinez A, Wang F. Optical modulators with 2D layered materials. Nature Photonics. 2016;**10**:227-238. DOI: 10.1038/nphoton.2016.15

[22] Gan Q, Bartoli FJ, Kafafi ZH. Plasmonic-enhanced organic photovoltaics: Breaking the 10% efficiency barrier. Advanced Materials. 2013;**25**:2385-2396. DOI: 10.1002/adma.201203323

[23] Du W, Wang T, Chu HS. Highly efficient on-chip direct electronic–plasmonic transducers. Nature Photonics. 2017;**11**:623-627. DOI: 10.1038/s41566-017-0003-5

[24] Kim KS, Zhao Y, Jang H. Large-scale pattern growth of graphene films for stretchable transparent electrodes. Nature. 2009;**457**:706-710. DOI: 10.1038/nature07719

[25] De Arco LG, Zhang Y, Schienker CW. Continuous, highly flexible, and transparent graphene films by chemical vapor deposition for organic photovoltaics. ACS Nano. 2010; **4**:2865-2873. DOI: 10.1021/nn901587x

[26] Mikhailov SA. Electromagnetic response of electrons in graphene: Non-linear effects. Physica E: Low-dimensional Systems and Nanostructures. 2008;**40**:2626-2629. DOI: 10.1016/j.physe.2007.09.018

[27] Zhu H, Liu A, Shan F. One-step synthesis of graphene quantum dots from defective CVD graphene and their application in IGZO UV thin film phototransistor. Carbon. 2016;**100**: 201-207. DOI: 10.1016/j.carbon.2016.01.016

[28] Pospischil A, Humer M, Furchi MM. CMOS-compatible graphene photodetector covering all optical communication bands. Nature Photonics. 2013;**7**:892-896. DOI: 10.1038/nphoton.2013.240

[29] Gan X, Shiue RJ, Gao Y. Chip-integrated ultrafast graphene photodetector with high responsivity. Nature Photonics. 2013;**7**:883-887. DOI: 10.1038/nphoton.2013.253

[30] Wang X, Cheng Z, Xu K. High-responsivity graphene/silicon-heterostructure waveguide photodetectors. Nature Photonics. 2013;**7**:888-891. DOI: 10.1038/nphoton.2013.241

[31] Liu M, Zhang X. Silicon photonics: Graphene benefits. Nature Photonics. 2013;**7**:851-852. DOI: 10.1038/nphoton.2013.257

[32] Cohnitz L, Haeusler W, Zazunov A. Interaction-induced conductance from zero modes in a clean magnetic graphene waveguide. Physical Review B. 2015;**92**:085422. DOI: 10.1103/PhysRevB.92.085422

[33] Lin H, Song Y, Huang Y. Chalcogenide glass-on-graphene photonics. Nature Photonics. 2017;**11**:798-805. DOI: 10.1038/s41566-017-0033-z

[34] Liu LH, Zorn G, Castner DG. A simple and scalable route to wafer-size patterned graphene. Journal of Materials Chemistry. 2010;**20**:5041-5046. DOI: 10.1039/C0JM00509F

[35] Sun Z, James DK, Tour JM. Graphene chemistry: Synthesis and manipulation. Journal of Physical Chemistry Letters. 2011;**2**:2425-2432. DOI: 10.1021/jz201000a

[36] Tang Q, Zhou Z, Chen Z. Graphene-related nanomaterials: Tuning properties by functionalization. Nanoscale. 2013;**5**:4541-4583. DOI: 10.1039/C3NR33218G

[37] Yan Z, Peng Z, Sun Z. Growth of bilayer graphene on insulating substrates. ACS Nano. 2011;**5**:8187-8192. DOI: 10.1021/nn202829y

[38] Kleinert M, Herziger F, Reinke P. Graphene-based electro-absorption modulator integrated in a passive polymer waveguide platform. Optical Materials Express. 2016;**6**:1800-1807. DOI: 10.1364/OME.6.001800

[39] Kayoda T, Han JH, Takenaka M. Evaluation of chemical potential for graphene optical modulators based on the semiconductor-metal transition. In: IEEE 10th International Conference on Group IV Photonics, 2013. DOI: 10.1109/Group4.2013.6644446

[40] Kozina ON, Melnikov LA, Nefedov IS. Dispersion characteristics of hyperbolic graphene-semiconductors multilayered structure. In: Proceedings SPIE 9448, Saratov Fall Meeting 2014: Optical technologies in biophysics and medicine XVI; Laser physics and photonics XVI; and Computational biophysics. 2014. DOI: 10.117/12.2180053

[41] Lin I, Liu JM. Enhanced graphene plasmon waveguiding in a layered graphene-metal structure. Applied Physics Letters. 2014;**105**:011604. DOI: 10.1063/1.4889915

[42] Li K, Xia F, Wang M. Discrete Talbot effect in dielectric graphene plasmonic waveguide arrays. Carbon. 2017;**118**:192-199. DOI: 10.106/j.carbon.2017.03.047

[43] Bruna M, Borini S. Optical constants of graphene layers in the visible range. Applied Physics Letters. 2009;**94**:031901. DOI: 10.1063/1.3073717

[44] Xu F, Das S, Gong Y. Complex refractive index tunability of graphene at 1550 nm wavelength. Applied Physics Letters. 2015;**106**:031109. DOI: 10.1063/1.4906349

[45] Wang X, Chen Y, Nolte D. Strong anomalous optical dispersion of graphene: Complex refractive index measured by Picometrology. Optics Express. 2008;**16**:22105-22112. DOI: 10.1364/OE.16.022105

[46] Yao B, Wu Y, Wang Z. Demonstration of complex refractive index of graphene waveguide by microfiber-based Mach-Zehnder interferometer. Nature Photonics. 2013;**21**:29818-29826. DOI: 10.1364/OE.21.029818

[47] Koester S, Li M. Waveguide-coupled graphene optoelectronics. IEEE Journal of Selected Topics in Quantum Electronics. 2014;**20**:600021. DOI: 10.1109/JSTQE.2013.2272316

[48] Jiang X, Bao J, Zhang B. Dual nonlinearity controlling of mode and dispersion properties in graphene-dielectric plasmonic waveguide. Nanoscale Research Letters. 2017;**12**:395. DOI: 10.1186/s11671-017-2166-x

[49] Cheng B, Chen H, Jen Y. Tunable tapered waveguide for efficient compression of light to graphene surface plasmons. Scientific Reports. 2016;**6**:28799. DOI: 10.1038/srep28799

[50] Ansell D, Radko I, Han Z. Hybrid graphene plasmonic waveguide modulators. Nature Communications. 2015;**6**:8846. DOI: 10.1038/ncomms9846

[51] Vasko F, Zozoulenko I. Conductivity of a graphene strip: Width and gate-voltage dependencies. Applied Physics Letters. 2010;**97**:092115. DOI: 10.1063/1.3486178

[52] Hu H, Zhai F, Hu D. Broadly tunable graphene plasmons using an ion-gel top gate with low control voltage. Nanoscale. 2015;**7**:19493-19500. DOI: 10.1039/C5NR05175D

[53] Khan MF, Iqbal MZ, Iqbal MW. Improving the electrical properties of graphene layers by chemical doping. Science and Technology of Advanced Materials. 2014;**15**:055004. DOI: 10.1088/1468-6996/15/5055004

[54] Pi K, Han W, McCreary K. Manipulation of spin transport in graphene by surface chemical doping. Physical Review Letters. 2010;**104**:187201. DOI: 10.1103/PhysRevLett.104.187201

[55] Chen C, Park C, Boudouris B. Controlling inelastic light scattering quantum pathways in graphene. Nature. 2011;**471**:617-620. DOI: 10.1038/nature09866

[56] Jablan M, Buljan H, Soljačić M. Plasmonics in graphene at infrared frequencies. Physical review B. 2009;**80**:245435. DOI: 10.1103/PhysRevB.80.245435

[57] Zhou S, Gweon G, Fedorov A. Substrate-induced bandgap opening in epitaxial graphene. Nature Materials. 2007;**6**:770-775. DOI: 10.1038/nmat2003

[58] Doust S, Siahpoush V, Asgari A. The tunability of surface plasmon polaritons in graphene waveguide structures. Plasmonics. 2017;**12**:1633-1639. DOI: 10.1007/s11468-016-0428-6

[59] Zhang X, Yang S, Zhou H. Perovskite-erbium silicate nanosheet hybrid waveguide photodetectors at the near-infrared telecommunication band. Advanced Materials. 2017;**29**: 1604431. DOI: 10.1002/adma.201604431

[60] Mueller T, Xia F, Avouris P. Graphene photodetectors for high-speed optical communications. Nature Photonics. 2010;**4**:297-301. DOI: 10.1038/nphoton.2010.40

[61] Kim J, Park S, Jang H. Highly sensitive, gate-tunable, room temperature mid-infrared photodetection based on graphene-$Bi_2Se_3$ heterostructure. ACS Photonics. 2017;**4**:482-488. DOI: 10.1021/acsphotonics.6b00972

[62] Hwang T, Kim J, Kulkarni A. Graphene photo detector with integrated waveguide biochemical sensors. Sensors and Actuators B: Chemical. 2013;**187**:319-322. DOI: 10.1016/j.snb.2012.11.092

[63] Cheng Z, Goda K. Design of waveguide-integrated graphene devices for photonic gas sensing. Nanotechnology. 2016;**27**:505206. DOI: 10.1088/0957-4484/27/50/505206

[64] Youngblood N, Anugrah Y, Ma R. Multifunctional graphene optical modulator and photodetector integrated on silicon waveguides. Nano Letters. 2014;**14**:2741-2746. DOI: 10.1021/nl500712u

[65] Ruan B, Guo J, Wu L. Ultrasensitive terahertz biosensors based on Fano resonance of a graphene/waveguide hybrid structure. Sensors. 2017;**17**:1924. DOI: 10.3390/s17081924

[66] Wu L, Guo J, Xu H. Ultrasensitive biosensors based on long-range surface plasmon polariton and dielectric waveguide modes. Photonics Research. 2016;**4**:262-266. DOI: 10.1364/PRJ.4.000262

[67] Wijesinghe T, Premaratne M, Agrawal G. Low-loss dielectric-loaded graphene surface plasmon polariton waveguide based biochemical sensor. Journal of Applied Physics. 2015;**117**:213105. DOI: 10.1063/1.4922124

[68] Pei C, Yang L, Wang G. Broadband graphene/glass hybrid waveguide polarizer. IEEE Photonics Technology Letters. 2015;**27**:927-930. DOI: 10.1109/LPT.2015.2398352

[69] Hao R, Du W, Li E. Graphene assisted TE/TM-independent polarizer based on Mach-Zehnder interferometer. IEEE Photonics Technology Letters. 2015;**27**:1112-1115. DOI: 10.1109/LPT.2015.2408375

[70] Wang J, Cheng Z, Chen Z. High-responsivity graphene-on-silicon slot waveguide photodetectors. Nanoscale. 2016;**8**:13206-13211. DOI: 10.1039/C6NR03122F

[71] Hajian H, Soltani-Vala A, Kalafi M. Surface plasmons of a graphene parallel plate waveguide bounded by Kerr-type nonlinear media. Journal of Applied Physics. 2014;**115**:083104. DOI: 10.1063/1.4865435

[72] Yarmoghaddam E, Rakheja S. Dispersion characteristics of THz surface plasmons in nonlinear graphene-based parallel-plate waveguide with Kerr-type core dielectric. Journal of Applied Physics. 2017;**122**:083101. DOI: 10.1063/1.4991674

Chapter 8

# Lithium Niobate Optical Waveguides and Microwaveguides

Nadège Courjal, Maria-Pilar Bernal, Alexis Caspar,
Gwenn Ulliac, Florent Bassignot,
Ludovic Gauthier-Manuel and Miguel Suarez

Additional information is available at the end of the chapter

http://dx.doi.org/10.5772/intechopen.76798

**Abstract**

Lithium niobate has attracted much attention since the 1970s due to its capacity to modify the light by means of an electric control. In this chapter, we review the evolution of electro-optical (EO) lithium niobate waveguides throughout the years, from Ti-indiffused waveguides to photonic crystals. The race toward ever smaller EO components with ever-lower optical losses and power consumption has stimulated numerous studies, the challenge consisting of strongly confining the light while preserving low losses. We show how waveguides have evolved toward ridges or thin film-based microguides to increase the EO efficiency and reduce the driving voltage. In particular, a focus is made on an easy-to-implement technique using a circular precision saw to produce thin ridge waveguides or suspended membranes with low losses.

**Keywords:** integrated optics, $LiNbO_3$, electro-optics, optical grade dicing, photonics

## 1. Introduction

The electric control of light has fascinated people since the advent of electricity. The advent of cleanroom technologies in the early 1940s and the advances in fabrication technologies in the 1950s and 1960s have progressively opened up pathways toward integrated optics, offering the possibility of guiding light in small devices while controlling its flux. In this context, lithium niobate, also named $LiNbO_3$, has always played a prominent role. Indeed its refractive index—which governs the speed of light—is sensitive to electrical signals, thanks to its

electro-optical (EO) properties [1]. Hence, $LiNbO_3$ is often used when light modulation is required, as for example in fiber optic-based telecommunication systems.

As compared with semiconductors modulating electrically the absorption of light through the Franz-Keldysh effect, $LiNbO_3$-based modulators can change light intensity without any perturbation on the phase, that is, without chirp. Therefore, despite the great success of semiconductors for short-range telecommunication systems, the zero-chirp modulation provided by $LiNbO_3$-based components is still privileged when high-bit rate optical signals have to propagate through thousands of kilometers [2].

In comparison with polymers [3] or other ferroelectrics such as SBN [4], KTN [5], $BaTiO_3$ [6], which show even higher EO sensitivity than $LiNbO_3$, the material benefits from technological maturity based on Czochralski's process, so that numerous suppliers can be found around the world. Moreover, its physical properties are compatible with cleanroom fabrication processes. For example, its high Curie temperature (~ 1200°C) preserves the EO properties even during annealing steps, which is not the case for materials like SBN or KTN. Additionally, $LiNbO_3$ offers a wide transparency band [340–4.6 μm] which opens the range to applications from visible to mid-infrared. The low absorption losses (< 0.15%/cm at 1.06 μm) and its weak optical dispersion in the transparency band [7] also contribute to its success. As a result, lithium niobate has become indispensable for demanding applications such as broadband modulation for long-haul high-bit-rate optical telecommunication systems [2, 8], electromagnetic sensors [9], precision gyroscopes [10], and astronomy [11]. For each application, the challenge is to provide integrated configurations that are easy to implement, of low loss, low in energy consumption, and, if possible, compact. The basic element, namely the optical waveguide, is essential to meet these specifications.

First, we will provide some reminders about the classic electro-optical configurations. Then we will see the evolutions of $LiNbO_3$ optical waveguides from their first appearance in the 1970s to recent evolutions. Finally, we will show how nanoscale structuring can open up new perspectives for the material.

## 2. Electro-optical configurations in lithium niobate

The technological evolutions concerning electrooptical $LiNbO_3$ waveguides are oriented toward ever-lower propagation losses and lower coupling losses with fibers, while also seeking ever higher EO efficiency. The common specifications are summarized in Refs. [10, 12]. In what follows, we will take particular interest in optical losses and EO efficiency. Beforehand, we provide a quick reminder of the exploitation of the EO effect in lithium niobate.

$LiNbO_3$ EO modulators exploit the classic Pockels effect, which corresponds to a linear change of the refractive index as a function of the applied voltage. This index modification is due to the relative displacement of charges in the presence of an electric field $\vec{E}\ (E_1, E_2, E_3)$, which induces a macroscopic polarization inside the material. The modified index $n'_i$ can be deduced

from the intrinsic refractive index $n_i$ and the electrooptic tensor [$r$] by using Eq.(1) in the crystalline coordinate system:

$$\frac{1}{n_i'^2} = \frac{1}{n_i^2} + \sum_{j=1}^{3} r_{ij} E_j \tag{1}$$

The non-zero electrooptical coefficients $r_{13,}$ $r_{51}$, $r_{33}$, and $r_{22}$ of the [$r$] tensor are summarized in **Table 1** at 1550 nm wavelength for $LiNbO_3$ crystal substrates.

As $r_{33}$ is the highest electro-optic coefficient of the material, the most efficient EO configuration is achieved when both the electric field and the optical polarization are parallel with the third crystalline axis, that is, the Z-axis. This can be accomplished either by X-cut Y-propagating or by Z-cut waveguides. In what follows, we will mainly focus on X-cut waveguides (see **Figure 1**), which show better thermal stability than Z-cut ones.

In an X-cut Y-propagating waveguide, the crystalline X-axis is vertical, the Z-axis is in the plan of the wafer, and a waveguide is implemented along the Y-axis. Coplanar electrodes are placed on both sides of the waveguide (see **Figure 1**), and the gap $g$ between them is kept the same along the Y-axis. Therefore, a voltage applied on the electrodes generates an electric field over the optical guided mode, and this electric field is mainly horizontal and oriented along the Z-axis, as represented by the horizontal white arrows in **Figure 2(a)**.

| | | | | | |
|---|---|---|---|---|---|
| $r_{13}$ = 8.6 pm/V | $r_{51}$ = 28 pm/V | $r_{33}$ = 30.8 pm/V | $r_{22}$ = 3.4 pm/V | $n_o$ = 2.210 | $n_e$ = 2.138 |

$n_e$ and $n_o$ denote the extraordinary and ordinary index of the material.

**Table 1.** Electro-optical and optical properties of $LiNbO_3$ at 1550 nm wavelength [13].

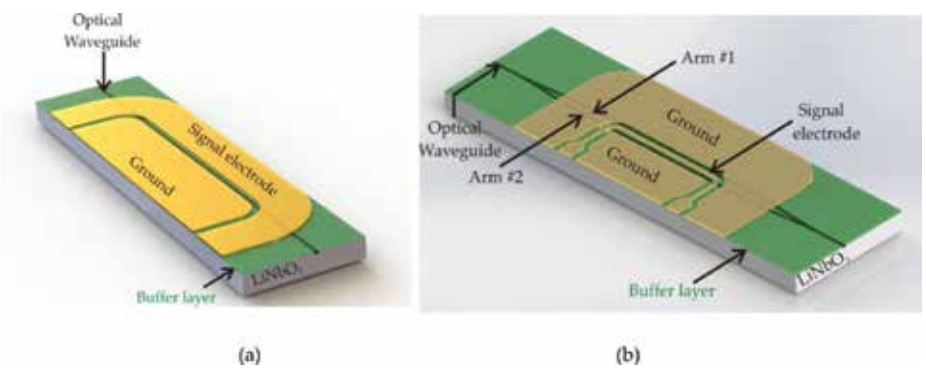


**Figure 1.** Standard configurations of integrated $LiNbO_3$ optical modulators in a X-cut substrate. (a) Phase modulator. (b) Mach-Zehnder modulator with push-pull electrodes: The signal electrode is placed between the two arms of the integrated interferometer. The buffer klayer helps preventing from optical leakage in the electrodes, and it also helps to achieve index matching between the electrical and optical propagating waves.

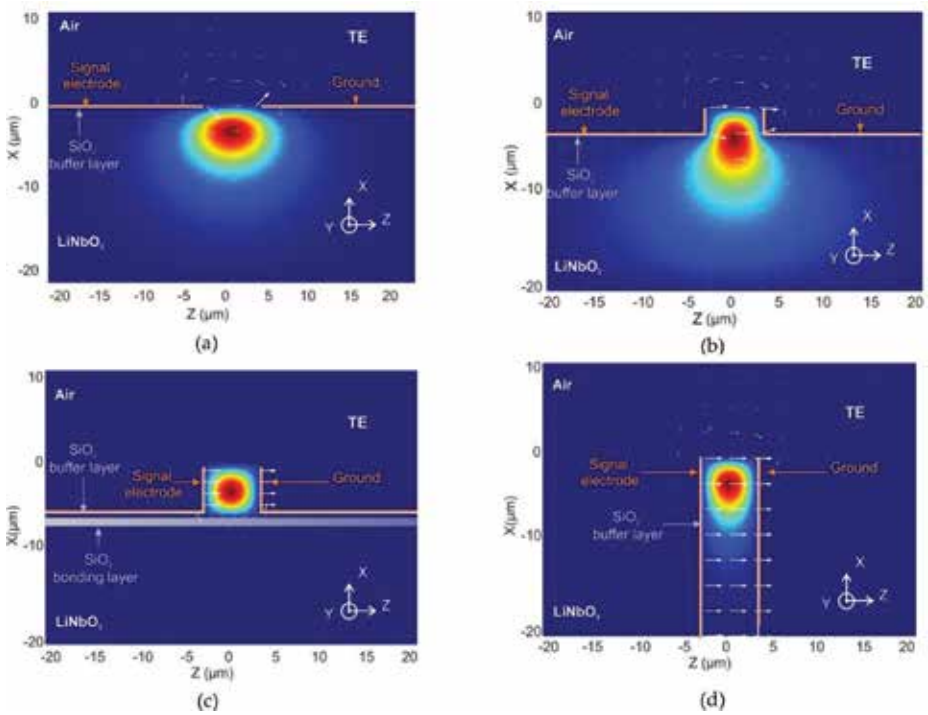


**Figure 2.** Cross-sections of optical waveguides. The electric optical guided mode and the applied electric field are calculated by F.E.M. (comsol® software) and represented with a color map and arrows respectively. (a) Standard Ti-indiffused waveguide with a gap $g$ = 6 μm between electrodes, a thickness buffer layer $t$ = 200 nm, and a $w$ = 6 μm wide titanium rib. (b) Same waveguide as in (a), but with a ridge height h = 3 μm. (c) Adhered ridge waveguide with a width of 6 μm, a ridge height of 6 μm, a $LiNbO_3$ layer thickness of 6 μm; and t = 200 nm. (d) High aspect ratio ridge waveguide done by Ti-indiffusion. The ridge height is 19 μm and the width is 6 μm; $t$ = 200 nm (a) Ti-indiffused waveguide, (b) standard ridge waveguide, (c) adhered ridge waveguide, (d) high-aspect ratio ridge waveguide.

In these conditions, the index modification induced by the voltage on the ordinary index and extraordinary index is evaluated through Eq. (2):

$$n_o' = n_o - \frac{n_o^3 \cdot r_{13} \cdot \Gamma \cdot V}{2 \cdot g} \text{ and } n_e' = n_e - \frac{n_e^3 \cdot r_{33} \cdot \Gamma \cdot V}{2 \cdot g} \tag{2}$$

where $\Gamma$ is the electro-optic overlap coefficient that takes into account the non-uniform behavior of the electric field over the optical mode cross-section:

$$\Gamma = \frac{\iint \varepsilon_Z^2 \cdot E_3 \cdot dS}{\iint \varepsilon_Z^2 \cdot dS} \cdot \frac{g}{V} \tag{3}$$

$\varepsilon_z$ denotes the third component of the electric optical field $\vec{\varepsilon}$ in the crystalline coordinate system, and $E_3$ is the electric field induced by the voltage $V$ applied on the electrodes. So in

| Configuration | Definition of the phase induced shift | Expression of $V_\pi$ |
|---|---|---|
| Phase modulation **Figure 1(a)** | $\varphi = \frac{\pi \cdot V}{\lambda \cdot g}\left(\Gamma \cdot n_e^3 \cdot r_{33}\right)L$ | $\frac{\lambda \cdot g}{\left(\Gamma \cdot n_e^3 \cdot r_{33}\right)L}$ |
| Intensity modulation **Figure 1(b)** | $\Delta\varphi = \frac{2\pi}{\lambda}\frac{n_e^3 \cdot r_{33} \cdot V}{2 \cdot g}(\Gamma_1 - \Gamma_2)L$ | $\frac{\lambda \cdot g}{n_e^3 \cdot r_{33} \cdot (\Gamma_1 - \Gamma_2)L}$ |

$\Gamma_1$ and $\Gamma_2$ denote the electro-optic overlap coefficients in arm #1 and arm#2 of the Mach-Zehnder device, respectively, when the polarization is parallel with (OZ). In a symmetric X-cut standard Mach-Zehnder configuration, $\Gamma_1 = -\Gamma_2$. Values of $\Gamma$ are strongly dependent on the electrode and buffer layer thickness.

**Table 2.** Evaluation of the electro-optic efficiency in classic configurations.

other words, $\Gamma$ is the average electric field seen by the optical electric field and normalized by $V$/g. Noteworthy, $\Gamma$ can be larger than 1 in specific cases.

Two basic configurations can be distinguished, the first one being the phase modulator for which only the phase of the optical signal is modified by the electric field (see **Figure 1(a)**) and the second one being the intensity modulator which exploits the interference between two signals having different paths in the material, such as the Mach-Zehnder illustrated schematically in **Figure 1(b)**. A precise evaluation of the electro-optic efficiency is given by the half-wave voltage, which is the voltage needed to obtain an induced phase shift of $\pi$. In the case of a phase modulator, the phase shift $\varphi$ denotes the phase accumulated through the electrode length $L$, and its expression is summarized in row #1 of **Table 2**. In a Mach-Zehnder intensity modulator, the phase shift $\Delta\varphi$ corresponds to the phase difference induced between the two arms at their output (see row #2 of **Table 2**).

From **Table 2** we can infer that the critical parameters for obtaining a low driving voltage $V_\pi$ and therefore low power consumption are the gap $g$, the active length $L$, and the electro-optic overlap coefficient $\Gamma$. In standard modulators, $g$ ranges from 6 to 30 μm, depending on the targeted performances in terms of impedance, bandwidth, and voltage, and $\Gamma$ is usually lower than 0.5, which is due to the weak overlap between the electrical field and optical guided mode. As an example, $\Gamma$ = 32% in the X-cut Ti-indiffused phase modulator with $g$ = 6 μm and with a $\delta$ = 0.2 μm silica buffer layer thickness calculated in **Figure 4(a)**. This means that an electrode longer than $L$ = 2 cm is needed to obtain a driving voltage lower than 5 V. So the achievement of compact modulators with low driving voltage requires an increase of $\Gamma$.

This latter is controlled by the fabrication technologies enabling more or less tight light confinement. In the following paragraphs we describe the evolutions from the first $LiNbO_3$ guides to the recent confined ones with increased $\Gamma$.

## 3. Standard waveguides

Titanium diffusion and proton exchange (PE) constitute the two main commercial techniques for the manufacture of $LiNbO_3$-based optical waveguides.

### 3.1. Titanium-indiffused waveguides

Since their discovery in 1974 by Schmidt et al. [14], Ti-indiffused optical waveguides have maintained continuous interest for commercial applications in high-bit-rate data-processing systems. More recently, they have attracted attention for mid-infrared applications dedicated to astrophysics [11, 15] or spectrometry [16].

Titanium-indiffused waveguides are fabricated through the diffusion of titanium ribs at a high temperature (~1000°C). The typical width of the Ti ribs is 6–7 μm and the thickness ranges from 80 to 100 nm for operations at 1550 nm wavelength. Extensive description of the process is given by Burns et al. [17]. Ti-indiffused waveguides have the advantages of low insertion losses (1 dB by Ramaswamy [18]). Their ability to guide two polarizations is also a specificity of interest, and they are good candidates over a very large spectral bandwidth from 1.0 to 4.7 μm.

The particularity of Ti-indiffused waveguides is their weak light confinement. Typically, the full width at half maximum (FWHM) of a standard X-cut Ti-indiffused waveguide working at 1550 nm is 7.5 μm in the horizontal direction and 4.8 μm in the vertical direction. This specificity allows a large $\eta$ overlap integral with single-mode fibers (SMF), expressed by Eq. (4):

$$\eta = \frac{\iint_S \varepsilon_{fiber}(x,z)\cdot\varepsilon^*_{guide}(x,z)\cdot dS}{\left(\iint_S \varepsilon_{fiber}(x,z)\cdot\varepsilon^*_{fiber}(x,z)\cdot dS\right)\left(\iint_S \varepsilon_{guide}(x,z)\cdot\varepsilon^*_{guide}(x,z)\cdot dS\right)} \tag{4}$$

where $E_{fiber}(x,z)$ denotes the spatial distribution of the optical guided electric field within the fiber, and $E_{guide}(x,z)$ is the spatial distribution of the optical guided electric field within the optical waveguide. $\eta$ can be larger than 85% in Ti-indiffused waveguides, which explains their low coupling losses with fibers and consequently their low insertion losses.

Although attractive for obtaining low losses, the weak light confinement is limiting for EO interaction, which is illustrated by a small $\Gamma$ of 32% in the example of **Figure 2(a)**. Therefore, Ti-indiffused waveguides are not the best candidates when compact and efficient EO modulators are required and alternative techniques have been considered.

### 3.2. Proton exchange-based waveguides

Proton exchange guides are well appreciated for non-linear periodically poled $LiNbO_3$ devices [19], due notably to a photorefractive threshold higher than Ti-indiffused waveguides [20]. The polarizing nature of PE waveguides also makes them prime waveguides for applications where polarization control is crucial. Fiber-optics gyroscopes [21] and polarizing phase modulators are particularly concerned [10].

Proton exchange [22] is a low-temperature process ($\sim$ 120–250°C) whereby Li ions from the $LiNbO_3$ wafer are exchanged with protons from an acid bath. Exchanged layers exhibit an increase in the extraordinary index and a slight decrease in the ordinary index, which is the origin of the polarizing nature of the PE-based waveguides. In the most general case, the

proton exchange zones may consist of several phase multilayers, which deteriorate their electro-optical performance. Several techniques have been successfully developed to design the index profile and to restitute the phase and optical properties. The mostly used techniques are:

- Annealed-PE [23], where annealing is performed subsequently to PE for obtaining mono-phase waveguides with restored EO properties;
- Soft-PE [24], where the proton exchange is done in soft conditions in buffered melts (i.e., lithium benzoate added to the benzoic acid) so that the optimal mono-phase waveguides are obtained in a one-step process;
- Reversed-PE, where the PE waveguides are immersed in a eutectic mixture of $LiNO_3$, $KNO_3$, and $NaNO_3$ to achieve buried waveguides with minimal loss connections with optical fibers.

Similar to Ti-indiffused waveguides, PE-based waveguides can yield very low insertion losses [25]. If light confinement is slightly tighter than their Ti-indiffused counterparts, PE-based waveguides are however not confined enough to reduce significantly the active length of EO modulators.

This observation led to strong efforts in the 1980s to obtain waveguides with both tight light confinement and low insertion losses. The first proposed solutions were based on ridge waveguides.

## 4. Ridge waveguides

As represented in **Figure 2(b)–(d)**, a ridge waveguide is an optical waveguide etched on both sides: the lateral confinement is ensured by a step index between $LiNbO_3$ and air. This configuration was firstly proposed by Kaminow et al. more than 40 years ago [26] to achieve a lateral confinement in planar Ti-outdiffused waveguides. Ridge waveguides are still a hot topic in research, with applications and manufacturing techniques evolving over the years.

### 4.1. Ridge made in standard waveguides by wet etching or plasma etching

The first generation of ridge waveguides was produced through Ti indiffusion or proton exchange techniques followed by dry or wet etching. The wafer thickness was about 500 μm and the ridge depth was typically lower than 10 μm. If their first apparition was in 1974, their attractiveness dates from the mid-1990s, when ridges were identified as the best solution to achieve both large bandwidth and impedance matching in EO Mach-Zehnder interferometers for long-haul high-bit-rate telecommunication systems [27]. Noteworthy, the moderate depth of the ridges was compatible with standard metal deposition techniques, which was convenient for the electrode deposition. Hence, ridge-based modulators with bandwidth as high as 100 GHz and driving voltage of 5.1 V were demonstrated [28] with 2-cm-long electrodes in

Mach-Zehnder modulators. The reported ridges were achieved through Ti indiffusion followed by selective dry etching with electron cyclotron resonance with argon and $C_2F_6$ gases.

More generally, most of the reported dry etching techniques use fluorine-based gases to exploit their chemical reactivity with $LiNbO_3$. Wet etching techniques associated with ion implantation, proton exchange, or domain inversion have also been widely studied [29, 30]. When followed by a subsequent step of annealing or Ti-in-diffusion at high temperature, the method is very efficient for the fabrication of ultra-smooth ridges with propagation losses as low as 0.05 dB/cm [31].

However, the etching step lasts for several hours to obtain depths of a few micrometers, and such small depths do not increase the EO efficiency significantly as compared with a standard waveguide. This is illustrated in **Figure 2(a)** and **(b)** where the increase of $\Gamma$ is only 18% in the 3-μm-deep ridge, as compared with the Ti-indiffused waveguide. According to finite element method (FEM) calculations, the ridge depth needs to be higher than 8 μm (see **Figure 2(d)**) or the substrate needs to be thinned down to a few micrometers (see **Figure 2(c)**) to achieve an increase larger than 60% in EO efficiency. Therefore, alternative techniques have been proposed, based on mechanical machining, to produce more efficient ridges.

### 4.2. Adhered ridge waveguides

Adhered ridge waveguides are made through mechanical processing. In a first step, the $LiNbO_3$ wafer is bonded to another one ($LiNbO_3$, $LaTiO_3$, Si…), and then the wafer is thinned down to a few micrometers by lapping polishing. Finally grooves are inscribed inside the thinned wafer by precise dicing [32] or by dry etching [33]. The adhered ridge waveguide is the remaining matter between two grooves. The first adhered ridge waveguide [32] aimed at replacing PE-based waveguides whose mobile protons induce long-term degradation of the optical response. The main application was nonlinear frequency conversion.

Since then, adhered ridge waveguides have been widely employed still for nonlinear (NL) applications [34, 35]. The typical thickness of the $LiNbO_3$ thinned layer ranges from 3 to 10 μm; the width of the ridge is typically 3–5 μm, and the depth is usually lower than the $LiNbO_3$ layer thickness (see **Figure 2(c)**). The pigtailing is performed by using lens coupling and laser welding [34]. Such pigtailed modules are now commercialized [36].

As attractive as they may be for NL applications, adhered ridge waveguides do not attract much attention for electro-optical modulation. One of the reasons is their multimode behavior which limits the modulation contrast. A step has been put forward with high-aspect ratio ridge waveguides having spot-size-converters, allowing for low insertion losses and for the filtering of optical modes.

### 4.3. High-aspect ratio ridge waveguides made by optical grade dicing

High-aspect ratio (HAR) ridge waveguides are ridges with depths larger than 10 μm (see **Figure 2(d)** and **3**). Such depths are achieved by optical grade dicing, meaning that the substrate is diced and polished at the same time [37]. In a first step, optical channels or planar

http://dx.doi.org/10.5772/intechopen.76798

waveguides are made simply through standard techniques (Ti indiffusion, proton exchange, ion implantation), and in a second step two grooves are diced along waveguide sides. If the machining parameters—such as translation and rotation speeds and nature and size of the blade—are properly chosen, the ridge patterns are diced and polished at the same time, which yield roughness lower than 20 nm and propagation losses lower than 0.1 dB/cm [37]. The resulting depths can be higher than 500 (see **Figure 3(a)**), but the preferred depth is between 10 and 50 μm [38] to obtain robust reproducible guided mode cross-sections that are independent on the ridge depth.

The uniform deposition of a buffer layer over the vertical edges of the ridge can be accomplished by atomic layer deposition (ALD), followed by a two-step side deposition of electrodes [39]. A schematic overview of the resulting EO ridge is seen in **Figure 4(a)**, while **Figure 4(b)** shows a standard electron microscope (SEM) image of the EO HAR ridge with ALD-deposited buffer layer.

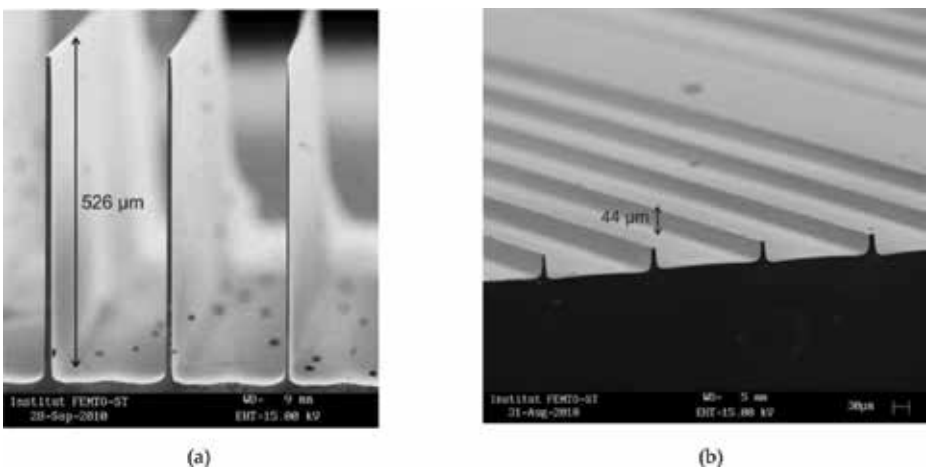


**Figure 3.** SEM images of high aspect ratio ridge waveguides. Record aspect ratio with a depth of 526 μm for a width of only 1 μm. (b) Optimal high aspect ratio waveguide, in term of robustness and losses [38].

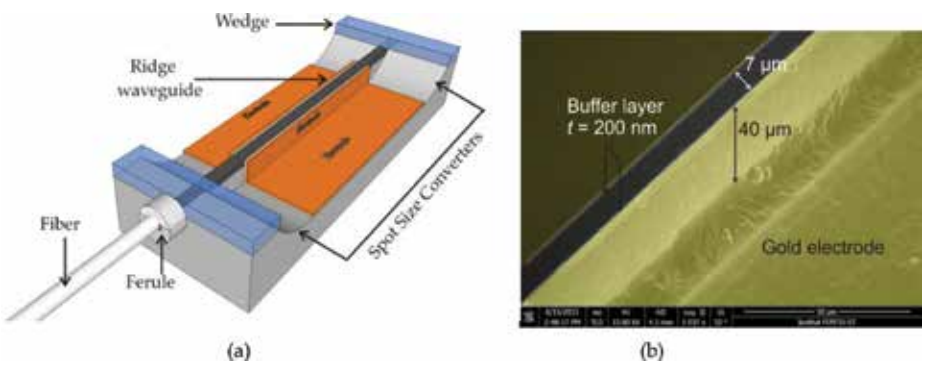


**Figure 4.** Ridge-based EO device. (a) Electro-optical ridge buffer layer with electrodes and spot-size-converters. (b) SEM image of an EO ridge with vertical buffer layer and electrodes.

Finite element method (FEM) simulations performed on HAR waveguides show that they are optimal in terms of EO efficiency, since the electric field is uniform over the optical waveguide. This is illustrated in **Figure 3(d)** with the white arrows representing the applied electric field. As a consequence, the electro-optical coefficient can be evaluated simply as a function of $g$:

$$\Gamma = \frac{g \cdot \varepsilon_{diel}}{2 \cdot \varepsilon_{LN} \cdot \delta + (g - 2 \cdot \delta) \cdot \varepsilon_{diel}} \tag{5}$$

where $\delta$ denotes the buffer layer thickness and $\varepsilon_{\mathrm{LN}}$ and $\varepsilon_{\mathrm{diel}}$ are the dielectric permittivities of $LiNbO_3$ and of the buffer layer, respectively. A quantitative comparison between a HAR ridge waveguide and a standard Ti-indiffused waveguide with the same gap and the same buffer layer shows that $\Gamma$ is increased twofold in favor of the HAR ridge waveguide. This was confirmed experimentally by Caspar et al. [39].

However, the counterpart of the strong lateral confinement is a weaker mode matching with SMFs: the $\eta$ coefficient is reduced down to 50%, meaning that 50% of the optical energy is lost per facet and consequently the insertion losses are ineluctably higher than 6 dB. This issue can be circumvented by using vertical spot-size converters such as the ones schematically depicted in **Figure 4(a)**. They are made simply by progressively decreasing the ridge depth, which can be done by lifting the blade before the end of the ridge. In this case, the total insertion losses are measured to be lower than 3 dB for a 2-cm-long ridge, and only the fundamental mode is allowed to propagate in the ridge [40].

If the high-aspect ratio ridge waveguide is the best configuration in terms of EO efficiency, there is however an interest in developing confined waveguides allowing more complex patterns than straight waveguides. This is the reason why thin films and membranes have also known to be a great success over the years.

## 5. Thin film-based and membrane-based waveguides

Thin film-based waveguides can be described as rib waveguides or gradient index-based waveguides integrated in $LiNbO_3$ thin films with a thickness lower than 5 mm. Ion slicing [41] is currently the prevailing manufacturing technique. These waveguides are also called microwaveguides.

### 5.1. Thin films fabricated by ion slicing

By combining wafer bonding and ion implantation, the ion slicing technique allows the wafer-scale production of thin layers of Z-cut and X-cut substrates with sub-micrometric thickness, and the roughness is lower than 0.5 nm [42]. More precisely, the fabrication process begins by $He^+$ ion implantation with a dose of about $4\times10^{16}$ ions/cm$^2$ to form an amorphous layer at a depth dependent on the implantation energy (typically a few hundreds of keV for submicronic $LiNbO_3$ layers). Then the implanted wafer is bonded to another one by using an intermediate layer with low refractive index, such as benzocyclobutene (BCB) or $SiO_2$ [42]. A thermal

treatment with temperature ramp is employed to split the samples along the implanted He layer. Hence, a thin $LiNbO_3$ layer bonded on another substrate remains. Afterward, annealing and chemical mechanical polishing are used to obtain a roughness of 0.5 nm. The technique is well mastered and thin-film $LiNbO_3$ layers are now commercialized [43, 44], which have boosted the development of compact $LiNbO_3$ components from low-loss ridge waveguides [45] to electro-optic microring resonators [46, 47], wire waveguide-based modulators [48], and nonlinear nanowires or ridges [49]. The lateral confinement can be ensured by proton exchange-based techniques or by direct etching of the thin layer. However, the insertion losses are often higher than 10 dB due to mode mismatch between the confined waveguides and the single mode fibers (SMFs) (see **Figure 5(b)**: the vertical confinement is significantly tighter than a standard SMF fiber, which leads to $\eta$ coefficient lower than 10%).

One approach to reduce the coupling losses is to guide the light in another material than $LiNbO_3$. As an example, as studied by Chen et al. [50], the light is guided in a silicon-on-insulator microring bonded to an ion-sliced $LiNbO_3$ film. The resulting low insertion losses (4.3 dB) are mitigated by a figure of merit of $V_\pi \cdot L$ = 9.1 V·cm, which is no better than what is reported in standard Ti-indiffused waveguides. The compacity is however made possible by using a microring resonator with small radius curvature and low radiation losses.

Another approach has been proposed recently, which relies on an easy-to-implement technique and allows low-loss free-suspended waveguides with calibrated thickness.

### 5.2. Suspended membranes fabricated by optical grade dicing

**Figure 6** shows how free-suspended waveguides can be made by optical grade dicing. A monomode optical waveguide is firstly fabricated through the diffusion of 6-μm-wide and 90 nm-thick Ti stripes at 1030°C for 10 h. Then, gold electrodes are sputtered over the substrate. Noteworthy, the electro-optical patterns are achieved by UV lithography, so that many other patterns can be envisioned with the same technology. Then, a curved slot is inscribed into

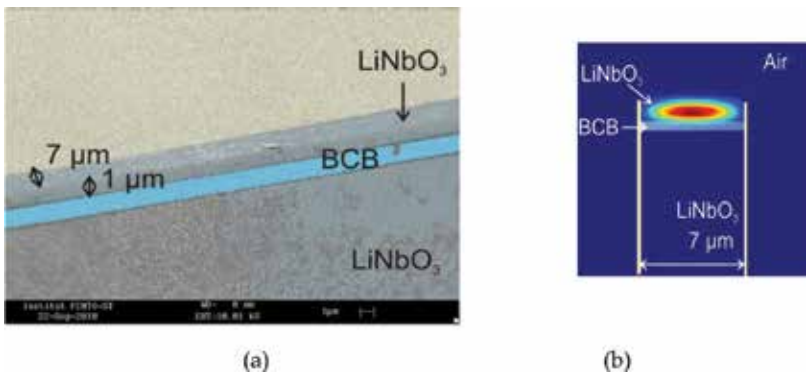


**Figure 5.** Thin film-based wire waveguides. (a) SEM image of a wire waveguide made by ion slicing. The dielectric bond layer is a BCB. (b) Amplitude of the electric field, TE optical mode calculated F.E.M. The overlap coefficient with a SMF mode is lower than – 10 dB.

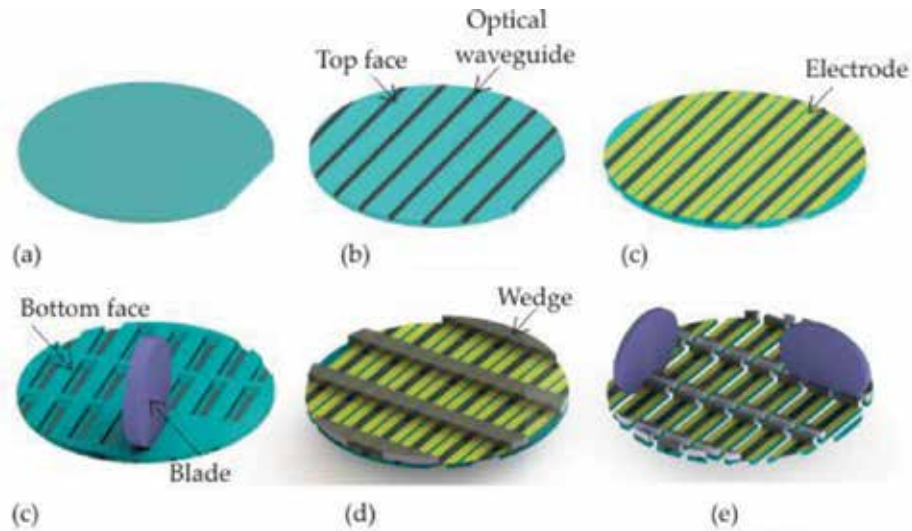


**Figure 6.** Process flow for the production of low-loss free-standing electro-photonic waveguides. The bottom face is the face of the wafer opposite to the waveguides.

the bottom face as schematically depicted in **Figure 6(c)** by optical grade dicing. The rotation speed and the moving speed of the 3350 DISCO DAD dicing saw are, respectively, 10,000 rpm and 0.2 mm/s. A resinoid blade progressively enters the wafers to a depth $\delta_b$ and inscribes a curved shape inside the bottom face of the sample. Then, the blade is translated along the waveguide and it is lifted before the end of the waveguide. The remaining matter is a membrane with a controlled thickness $t = e\text{-}\delta_b$ where $e$ is the wafer thickness. Thanks to this technique, vertical tapers are fabricated at the extremities of the membrane [51]. Indeed, they are created by the curved shape of the blade (see **Figure 6** and the tapers in **Figure 7**). Finally, wedges are bonded by UV adhesive on the top face of the wafer, and the chips are separated by optical grade dicing, enabling polished facets with an enlarged surface for pigtailing with fibers.

**Figure 7** shows a schematic diagram of a resulting membrane-based electro-optical waveguide. In the free-standing Section 1, the waveguide is thinned, and the thickness can take any value between 450 nm and 500 μm. This is achieved by a preliminar depth calibration in a dead zone of the wafer. The suspended waveguide is surrounded by electrodes allowing an electrical control of the effective refractive index. The cross-sections in **Figure 7** represent the optical guided mode along the suspended waveguide. In Section 1, the strongly confined mode allows an electro-optical coefficient twofold higher than in Section 3. On the other hand, the weakly confined mode in Section 3 allows mode matching and low coupling losses between the waveguide and the SMFs. Hence, the overlap coefficient $\eta$ can be as high as 85%. Additionally, to mode matching with fibers, the vertical tapers allow filtering in favor of the fundamental mode, which avoids parasitical beatings in the spectral transmission response [51].

The experimental measurements of losses are summarized in **Table 3** for both TE and TM polarizations and for different thicknesses. They are also reported by Courjal et al. [51]. They are compared with the average propagation losses of a non-thinned Ti-indiffused waveguide ($t$ = 500 μm) fabricated in the same conditions with the same total length. The measurements

http://dx.doi.org/10.5772/intechopen.76798

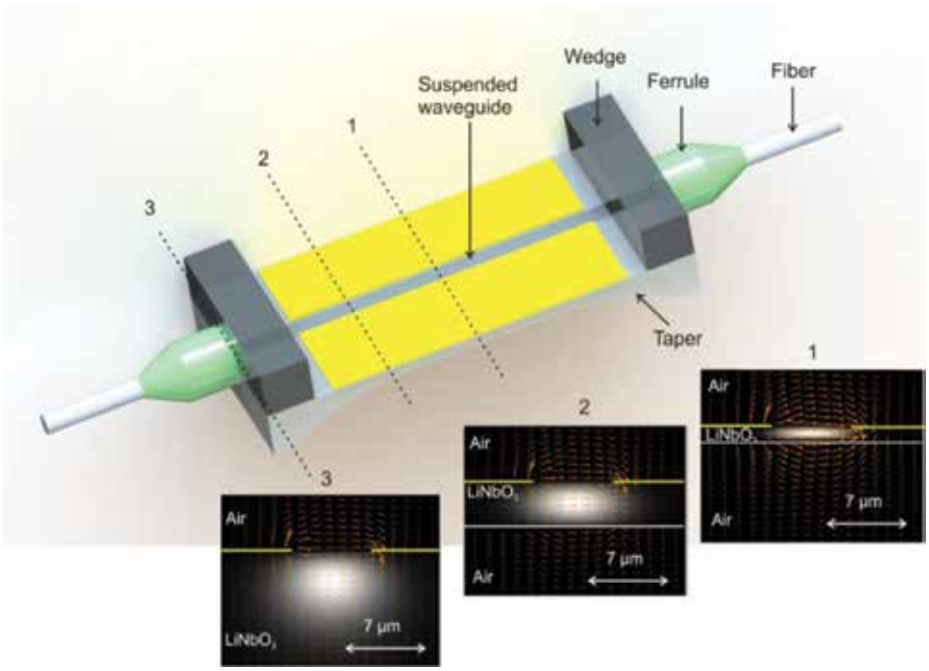


**Figure 7.** Schematic diagram of a free-suspended waveguide made by optical-grade-diving. The waveguide is thinned locally to get high EO efficiency. It is surrounded with tapers allowing mode matching. The inserts show the optical guided mode in different sections. Section#1: The layer thickness is 1 μm. Section#2: The layer thickness is 4 μm. Section#3: The layer thickness is 500 μm.

| $T$ (μm) | Pol. | $\alpha$ (dB/cm) | Total IL (dB) | ξ (dB) | $\Delta n_g/\Delta V$ (R.I.U./V) | $\Gamma$ (%) |
|---|---|---|---|---|---|---|
| 7500 | TE | 0.20 ± 0.06 | 2.8 ± 0.2 | 1.1 ± 0.3 | $7.8 \pm 1.0.10^{-6}$ | 34 |
| | TM | 0.22 ± 0.06 | 2.8 ± 0.2 | 1.1 ± 0.3 | $3.2 \pm 1.0{\cdot}10^{-6}$ | 35 |
| 4.50 | TE | 0.20 ± 0.06 | 2.8 ± 0.2 | 1.1 ± 0.3 | $13.4 \pm 1{\cdot}10^{-6}$ | 58 |
| | TM | 0.32 ± 0.06 | 2.9 ± 0.2 | 1.1 ± 0.3 | $15.8 \pm 1{\cdot}10^{-6}$ | 175 |
| 0.45 | TE | 3.20 ± 0.06 | 6.6 ± 0.5 | 1.1 ± 0.3 | — | — |
| | TM | 5.12 ± 0.06 | 8.1 ± 0.8 | 1.1 ± 0.3 | — | — |

$t$, $\alpha$, $IL$,$\xi$ are respectively the membrane thickness, the average propagation losses, the insertion losses, the reflection coefficient and the coupling losses per facet. $\Gamma$ is the overlap coefficient deduced from the measured $\Delta n_g/\Delta V$. The 450 nm-thick waveguides did not have electrodes so that the EO measurements could not be performed.

**Table 3.** Experimental assessment of losses for X-cut membrane-based waveguides with a total length of $L$ = 1.1 cm at 1550 nm wavelength.

were repeated five times for each waveguide and polarization. When the membrane has a thickness $t \geq 7$ μm, there is no difference observed between a membrane-based waveguide and non-thinned one. When the waveguide is thinned below 4.5 μm, the guided wave undergoes increased propagation losses, up to 5.1 dB/cm for the TM wave and 3.2 dB/cm for the TE wave when $t$ = 450 nm. Overall, the losses are lower for the TE waves than for TM waves, which is

due to an increased sensitivity of the TM waves to membrane roughness. It is noteworthy that the coupling losses remain the same regardless of the membrane thickness, which confirms the efficiency of the tapers to mode match with the fibers.

The EO overlap coefficient is deduced from the Fourier transform of the reflected spectral density (see **Figure 8**), which is also the autocorrelation of the impulse response. Due to the Fabry-Perot oscillations inside the cavity formed by the waveguide, a peak appears in the Fourier transform, which coincides with a round trip of the light between the two facets of the waveguide. From this peak, we can deduce the global effective group index: $n_{geff} = t_2 \cdot c_0/(2 \cdot L_{tot})$, $c_0$ being the speed of light and $L_{tot}$ denoting the waveguide length. The resulting effective group indexes are $n_{effTE} = 2.189 \pm 0.005$ and $n_{effTM} = 2.269 \pm 0.005$ for TE and TM polarizations, respectively, in an X-cut Y-propagating waveguide with a membrane thickness of 4.5 μm. The effective group index is measured voltage by voltage from **Figure 8**, for the assessment of the group index variation per voltage: $\Delta n_g/\Delta V$. The results are exposed in **Table 2**. $\Gamma$ is calculated from $\Delta n_g/\Delta V$ by using expressions (6) and (7) for the TE and TM waves, respectively:

$$\Gamma_{TE} = \frac{\Delta n_{eg}}{\Delta V} \cdot \frac{2 \cdot g}{n_e^3 \cdot r_{33}} \tag{6}$$

$$\Gamma_{TM} = \frac{\Delta n_{og}}{\Delta V} \cdot \frac{2 \cdot g}{n_o^3 \cdot r_{13}} \tag{7}$$

**Table 2** confirms the twofold enhancement of the EO interaction when the membrane is thinned down to 4.5 μm, and it shows that this enhancement is even higher for the TM-propagating wave, although this was not anticipated from the FEM calculations. This latter result can be of great interest to seek for isotropic EO behavior of the guided wave in the presence of an applied voltage.

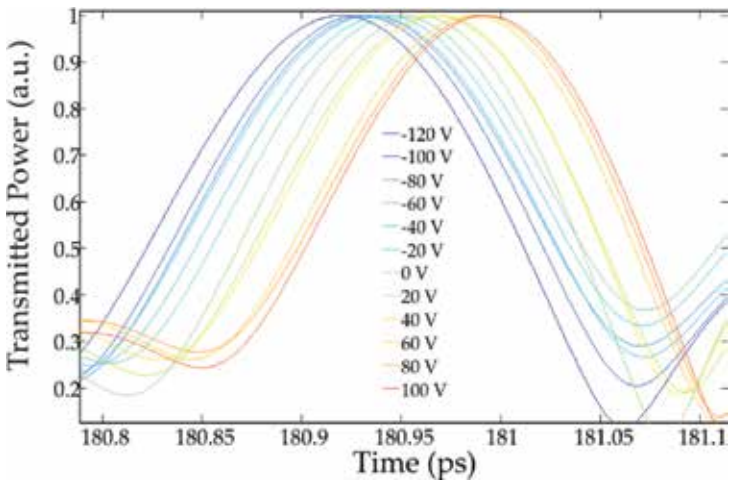


**Figure 8.** Zoom view of the Fourier transform of the reflected optical density spectrum. These measurements are achieved as a function of the applied voltage through a 12.0 mm long tapered-membrane-based waveguide with a width of 6 μm and a thickness of 4.5 μm. The total length was $L_{tot}$ = 1.2 mm.

http://dx.doi.org/10.5772/intechopen.76798

So membrane-based waveguides are good candidates to reduce the active length, without impacting the other parameters such as the losses. It is now tempting to go one step further toward compacity by inscribing nanostructures inside the membranes.

## 6. $LiNbO_3$ nanostructures and photonic crystals

It is well established that the machining of materials at the wavelength scale can yield a specific control of the light flux, which is of great interest to enhance significantly the electro-optical efficiency. In particular, photonic crystals (PhCs) are periodic structures that are designed to affect the motion of photons in a similar way that periodicity of a semiconductor crystal affects the behavior of electrons. The non-existence of propagating electromagnetic modes inside the structures at certain frequencies introduces unique optical phenomena such as tight light confinement. The part of the spectrum for which wave propagation is not possible is called the photonic bandgap (PBG).

The first reported PhC-based EO $LiNbO_3$ modulator [52] was configured to behave as an electro-absorbent modulator: it was designed to have a photonic bandgap, and the spectral edge was exploited for intensity modulation. Hence, an active length of 11 μm was sufficient to modulate the light with a driving voltage of 13 V [52]. A schematic diagram of such a device is seen in **Figure 9**. It consists of a square lattice PhC integrated on an annealed proton exchanged optical waveguide and surrounded by capacitive coplanar electrodes. The $LiNbO_3$ PhC was fabricated through focused ion beam (FIB) milling The refractive index was modified by the electric field *Ez* generated between the electrodes, which moved the spectral position of the PBG and consequently the transmitted intensity. The geometric properties of the PhC were chosen to benefit from slow light effects.

This compact modulator showed an EO interaction 312 times higher than the one predicted from Eq. (2): the extraordinary effect is shown in **Figure 10** where the PBG is spectrally shifted

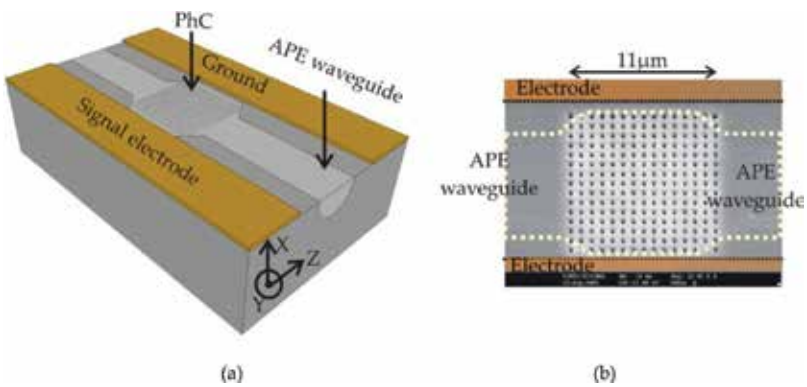


**Figure 9.** Image of the first reported PhC-based EO modulator [53]. (a) Schematic view of the ultra-compact modulator. (b) SEM image of the photonic crystal surrounded by electrodes.

by 100 nm when only 40 V is applied on the electrodes. This effect is attributed to an enhanced field factor *f* induced by slow light effect:

$$f = \sqrt{\frac{v_g^{BULK}}{v_g^{PC}}} \tag{8}$$

where $v_g^{BULK}$ is the group velocity in the bulk material and $v_g^{PC}$ is the group velocity in the photonic crystal. The EO enhancement is explained by Roussey et al. [53] by an effective EO coefficient being enhanced by the local field factor as follows:

$$r_{33}^{PC} = f^3 r_{33} \tag{9}$$

The local field factor was calculated by using the slope of the band dispersion diagram and was evaluated to be 6.8 which was in good agreement with the measurements. To our knowledge, this huge effect is still a record in terms of EO sensitivity. However, as performing and attractive as this configuration may appear, the transmission losses were of 10 dB (see **Figure 10(a)**), which is prohibitive for commercial applications. The small extinction ratio (12 dB) was also limiting for many demanding EO applications. These limitations are mainly due to the weak light confinement inside the APE waveguide, combined with the conical shape of photonic crystals that provoked deviation of light inside the substrate [54].

Since then, other approaches have been proposed, based on microring resonators or PhCs in thin films, enabling low propagation losses and high extinction ratio [42]. However, as mentioned in Section 5.1, these techniques are prohibitive in terms of fiber coupling, due to the mode mismatch between the fiber and the guided mode inside the thin film, which also induces insertion losses larger than 10 dB.

In this context, the suspended waveguides mentioned in Section 5.2 appear as good candidates for hosting photonic crystal and nanostructures. There are not many publications on the

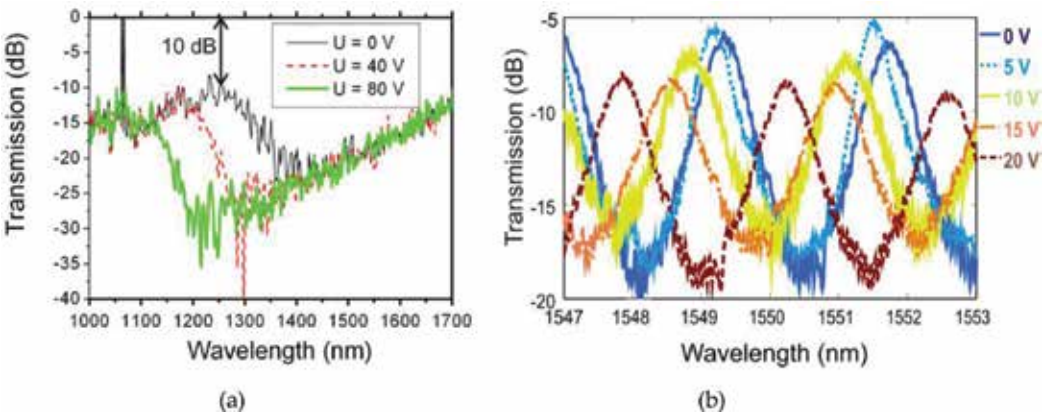


**Figure 10.** Spectral transmission responses through two PhC-based EO $LiNbO_3$ modulators, TE polarization. (a) Normalized transmission response through the modulator seen in **Figure 11**. (b) Normalized transmission response through a suspended Fabry-Perot [Caspar16]. The two measurements are done by direct butt-coupling with SMFs.

subject yet, but the inscription of a 1D-PhC cavity as reported by Courjal et al. [51] appears like a good start. The component is made of two 1D PhCs separated by 200 μm in a free-suspended membrane. The 1D PhCs are designed to be reflectors at 1550 nm wavelength and their pair constitutes a Fabry-Perot cavity. One of them can be visualized in **Figure 12(b)**. The free spectral range of 2.7 nm seen in **Figure 10(b)** is in good agreement with the theoretical prediction: $FSR=\lambda^2/(2\cdot\Delta\cdot n)$, where $\Delta$ is the distance between the two 1D PhCs. The quality factor is measured to be of 2580, revealing moderated reflectivity of the 1D PhC ($R \approx 50\%$). The spectral position of a resonance peak shown in **Figure 10(b)** is shifted by 40.0 pm/V, which is not as high as the shift reported in **Figure 10(a)**, but this is balanced with the transmission losses that are diminished by 5 dB.

The driving voltage is assessed by measuring the output optical power at 1550 nm. The measured electro-optical response reported in **Figure 11** shows a 9.6 V driving voltage for the TE-polarized wave and 25.2 V for the TM-polarized wave. So the figure of merit for each polarization is, respectively, 1.9 and 5 mV·m, for TE and TM waves, which is 40-fold higher than the ones classically measured in Mach-Zehnder intensity modulators. In the compact modulator of **Figure 9**, the EO interaction was enhanced by means of slow light effects. Here the remarkable EO sensitivity is rather attributed to a tip effect that enhances the electric field in the vicinity of the Bragg grating.

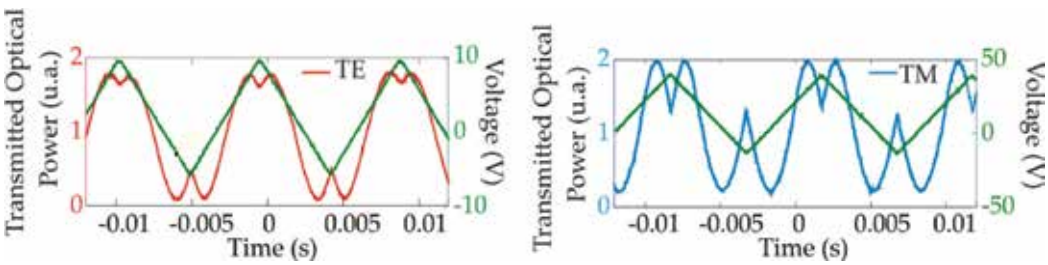


**Figure 11.** Experimental EO response of a TE wave (a) and TM wave (b) at the output of a 200 μm-long Fabry-Perot integrated in a 4.5 μm thick membrane.

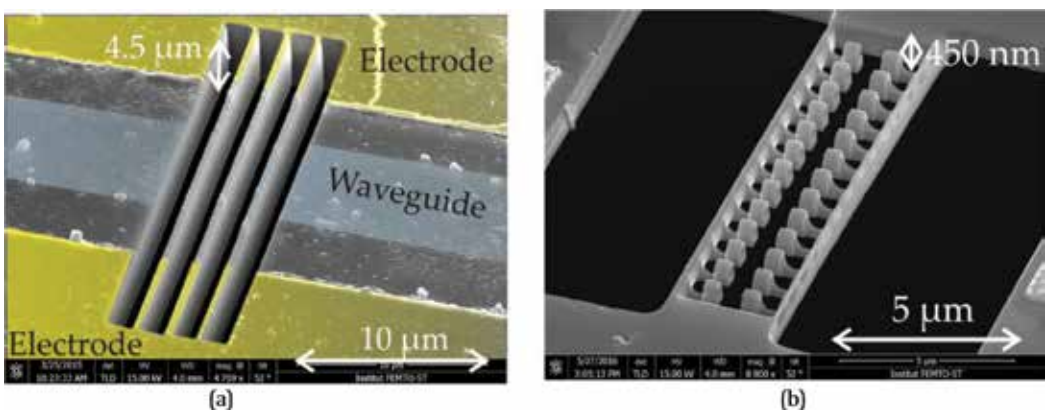


**Figure 12.** SEM views of $LiNbO_3$ free-suspended membranes done by optical-grade dicing. The patterns are inscribed by FIB milling. (a) 1D-PhC implemented in a 4.5 μm-thick waveguide. (b) Nanostructure in a 450 nm thick membrane. Such a thickness is a record for a free-suspended layer fabricated through mechanical approach.

So, PhC-based EO modulators are extremely promising for the achievement of low-power consuming and compact modulators either by exploiting slow light effects in the nanostructure or tip effects in structured electrodes. The recent developments reported on free-suspended membranes appear to be also very promising for preserving low losses. The achievement of commercial performances should be achieved by a better control in fabrication of the 1D PhCs.

Many other 2D suspended devices may be envisioned by using the same technique: as a perspective, **Figure 12** shows SEM images of diced membranes hosting micro- and nano-patterns that can be used as $LiNbO_3$ MEMs, opto-mechanical, or nonlinear wires.

## 7. Conclusion

In conclusion, lithium niobate is a material of current interest in both industry and research, thanks to its robust and reproducible properties and also thanks to the emergence of new technologies such as ion slicing or optical grade dicing. Hence, and even though the first modulators date from the 1970s, progress is still visible, to move toward ever more compactness with low energy consumption and low losses. In this chapter, we have taken particular interest in three important parameters: the $\Gamma$ electro-optical overlap coefficient that characterizes EO efficiency, the $\eta$ overlap integral with optical fibers, which quantifies coupling losses, and the propagation losses, the last two parameters being important contributors to overall insertion losses. We have shown how the use of confined guides (deep ridges or thin films) increases the EO efficiency by a factor of 2 and how tapers allow low integration losses. Finally, we have highlighted the spectacular effects of nanostructuring in confined guides to gain 1–2 orders of magnitude on the EO efficiency. These developments open the way toward compact and low-consuming photonic integrated circuit but also offer the promise of multi-control in optical circuits.

## Acknowledgements

This work was supported by the SATT Grand-Est under project μguide, partially by ANR under project ANR-16-CE24-0024-01, and by the Labex ACTION program (contract ANR-11-LABX-01-01). The work was partly supported by the French RENATECH network and its FEMTO-ST technological facility.

## Author details

Nadège Courjal[1]*, Maria-Pilar Bernal[1], Alexis Caspar[1], Gwenn Ulliac[1], Florent Bassignot[2], Ludovic Gauthier-Manuel[1] and Miguel Suarez[1]

*Address all correspondence to: nadege.courjal@femto-st.fr

1 FEMTO-ST Institute, Besançon, France

2 FEMTO-Engeeniring, Besançon, France

## References

[1] Turner EH. High frequency electro-optic coefficients of lithium niobate. Applied Physics Letters. 1966;**8**:303-306. DOI: 10.1063/1.1754449

[2] Wooten EL, Kissa KM, Yi-Yan A, Murphy EJ, Lafaw DA, Hallemeier PF, Maack D, Attanasio DV, Fritz DJ, McBrien GJ, Bossi DE. A review of lithium niobate modulators for fiber-optic communications systems. IEEE Journal on Selected Topics in Quatum Electronics. 2000;**6**:69-82. DOI: 10.1109/2944.826874

[3] DeRose CT, Enami Y, Loychik C, Norwood RA, Mathine D, Fallahi M, Peyghambarian N, Luo JD, Jen AK-Y, Katheperumal M, Yamamoto M. Pockel's coefficient enhancement of poled electro-optic polymers with a hybrid organic-inorganic sol-gel cladding layer. Applied Physics Letters. 2006;**89**:131102-131105. DOI: 10.1063/1.2357157

[4] Huang C, Bhalla AS, Guo R. Measurement of microwave electro-optic coefficient in $Sr_{0.61}Ba_{0.39}Nb_2O_6$ crystal fiber. Applied Physics Letters. 2005;**86**:211907-211910. DOI: 10.1063/1.1937997

[5] van Raalte JA. Linear electro-optic effect in ferroelectric KTN. Journal of the Optical Society of America. 1967;**57**:671-674. DOI: 10.1364/JOSA.57.000671

[6] Johnston AR, Weingart JM. Determination of the low-frequency linear electro-optic effect in tetragonal $BaTiO_3$. Journal of the Optical Society of America. 1965;**55**:828-834. DOI: 10.1364/JOSA.55.000828

[7] Gooch and Housego, lithium niobate optical crystal. [Internet]. 2017. Available from https://goochandhousego.com/wp-content/uploads/2013/12/LNmatProperties.pdf

[8] Eospace, electro-optic modulators [Internet]. 2017. Available from: http://www.eospace.com/

[9] Aydé R, Gaborit G, Dahdah J, Duvillaret L, Courjal N, Guyot C, Sablong R, Perrier AL, Beuf O. Unbiased electro-optic waveguide as a sensitive nuclear magnetic resonance sensor. IEEE Photonics Technology Letters. 2014;**26**:1266-1269. DOI: 10.1109/LPT.2014.2321099

[10] Photonics iXblue. Polarizing Y-Junction Phase Modulator for fiber optics gyros [Internet]. 2017. Available from: https://photonics.ixblue.com/files/files/pdf/Modulators/Y-JPX-LN_series.pdf

[11] Hsiao HK, Winick KA, Monnier JD, Berger JP. An infrared integrated optic astronomical beam combiner for stellar interferometry at 3-4 μm. Optics Express. 2009;**17**:18489-18500. DOI: 10.1364/OE.17.018489

[12] Newport, faq on electro-optic modulators [Internet]. 2017. Available from: https://www.newport.com/n/electro-optic-modulator-faqs

[13] Chen X, Zhang G, Zeng H, Guo Q, She W. Advances in Nonlinear Optics. Berlin, Boston: Walter de Gruyter GmbH & Co KG; 2015 978-3-11-030449-7

[14] Schmidt RV, Kaminow IP. Metal-diffused optical waveguides in $LiNbO_3$. Applied Physics Letters. 1974;**25**:458-461. DOI: 10.1063/1.1655547

[15] Heidmann S, Ulliac G, Courjal N, Martin G. Characterization and control of the electro-optic phase dispersion in lithium niobate modulators for wide spectral band interferometry applications in the mid-infrared. Applied Optics. 2017;**56**:4153-4157. DOI: 10.1364/AO.56.004153

[16] Thomas F, Heidmann S, de Mengin M, Courjal N, Ulliac G, Morand A, Benech P, Le Coarer E, Martin G. First results in near and mid IR lithium niobate-based integrated optics interferometer based on SWIFTS-Lippmann concept. Journal of Lightwave Technology. 2014;**32**:3736-3742

[17] Burns WK, Klein PH, West EJ. Ti diffusion in Ti:$LiNbO_3$ planar and channel optical waveguides. Journal of Applied Physics. 1979;**50**:6175-6179. DOI: 10.1063/1.325801

[18] Ramaswamy V, Alferness RC, Divino M. High efficiency single-mode fibre to Ti:$LiNbO_3$ waveguide coupling. Electronics Letters. 1982;**18**:30-31. DOI: 10.1049/el:19820022

[19] HC Photonics. (Reversed) Proton Exchange waveguides [Internet]. 2017. Available from: http://www.hcphotonics.com/products2.asp?area=1670&cat=1751&sn=939

[20] Glavas E, Cabrera JM, Townsend PD. A comparison of optical damage in different types of $LiNbO_3$ waveguides. Journal of Physics D: Applied Physics. 1989;**22**:611-616

[21] Suchoski Jr PG, Findakly TK, Ferrar CM, Leonberger FJ. Single-polarization, integrated optical components for optical gyroscopes. Patent US5223911 A; 1989

[22] Jackel JL, Rice CE, Veselka JJ. Proton exchange for high-index waveguides in $LiNbO_3$. Applied Physics Letters. 1982;**41**:607-608. DOI: 10.1063/1.93615

[23] Bortz ML, Fejer MM. Annealed proton-exchanged $LiNbO_3$ waveguides. Optics Letters. 1991;**16**:1844-1846. DOI: 10.1364/OL.16.001844

[24] Chanvillard L, Aschiéri P, Baldi P, Ostrowsky DB, de Micheli M, Huang L, Bamford DJ. Soft proton exchange on periodically poled $LiNbO_3$: A simple waveguide fabrication process for highly efficient nonlinear interactions. Applied Physics Letters. 2000;**76**:1089-1091. DOI: 10.1063/1.125948

[25] Suchoski PG, Findakly TK, Leonberger FJ. Stable low-loss proton-exchanged $LiNbO_3$ waveguide devices with no electro-optic degradation. Optics Letters. 1988;**13**:1050-1052. DOI: 10.1364/OL.13.001050

[26] Kaminow IP, Ramaswamy V, Schmidt RV, Turner EH. Lithium niobate ridge waveguide modulator. Applied Physics Letters. 1974;**24**:622-625. DOI: 10.1063/1.1655079

[27] Noguchi K, Mitomi O, Miyazawa H, Seki S. A broadband Ti:LiNbO3 optical modulator with a ridge structure. Journal of Lightwave Technology. 1995;**13**:1164-1168. DOI: 10.1109/50.390234

[28] Noguchi K, Mitomi O, Miyazawa H. Millimeter-wave Ti:$LiNbO_3$ optical modulators. Journal of Lightwave Technology. 1998;**16**:615-620. DOI: 10.1109/50.664072

[29] Laurell F, Webjorn J, Arvidsson G, Holmberg J. Wet etching of proton-exchanged lithium niobate—A novel processing technique. Journal of Lightwave Technology. 1992;**10**:1606-1609. DOI: 10.1109/50.184899

[30] Barry IE, Ross GW, Smith PGR, Eason RW. Ridge waveguides in lithium niobate fabricated by differential etching following spatially selective domain inversion. Applied Physics Letters. 1999;**74**:1487-1490. DOI: 10.1063/1.123589

[31] Hu H, Ricken R, Sohler W. Low-loss ridge waveguides on lithium niobate fabricated by local diffusion doping with titanium. Applied Physics B. 2010;**98**:677-679. DOI: 10.1007/s00340-010-3908-y

[32] Mizuuchi K, Sugita T, Yamamoto K, Kawaguchi T, Yoshino T, Imaeda M. Efficient 340-nm light generation by a ridge-type waveguide in a first-order periodically poled MgO: $LiNbO_3$. Optics Letters. 2003;**28**:1344-1346. DOI: 10.1364/OL.28.001344

[33] Kou R, Kurimura S, Kikuchi K, Terasaki A, Nakajima H, Kondou K, Ichikawa J. High-gain, wide-dynamic-range parametric interaction in Mg-doped $LiNbO_3$ quasi-phase-matched adhered ridge waveguide. Optics Express. 2011;**19**:11867-11872. DOI: 10.1364/OE.19.011867

[34] Umeki T, Tadanaga O, Asobe M. Highly efficient wavelength converter using direct-bonded PPZnLN ridge waveguide. IEEE Journal of Quantum Electronics. 2010;**46**:1206-1213. DOI: 10.1109/JQE.2010.2045475

[35] Chauvet M, Henrot F, Bassignot F, Devaux F, Gauthier-Manuel L, Pêcheur V, Maillotte H, Dahmani B. High efficiency frequency doubling in fully diced $LiNbO_3$ ridge waveguides on silicon. Journal of Optics. 2016;**18**:085503. DOI: 10.1088/2040-8978/18/8/085503/meta

[36] NTT. Wavelength Conversion Module for Visible, Near-IR, and Mid-IR Light Generation [Internet]. Available from https://www.ntt-electronics.com/en/products/photonics/conversion_module.html

[37] Courjal N, Guichardaz B, Ulliac G, Rauch J-Y, Sadani B, Lu H, Bernal M-P. High aspect ratio lithium niobate ridge waveguides fabricated by optical grade dicing. Journal of Physics D: Applied Physics. 2011;**44**:305101. DOI: 10.1088/0022-3727/44/30/305101

[38] Gerthoffer A, Guyot C, Qiu W, Ndao A, Bernal M-P, Courjal N. Strong reduction of propagation losses in $LiNbO_3$ ridge waveguides. Optical Materials. 2014;**38**:37-41. DOI: 10.1016/j.optmat.2014.09.027

[39] Caspar A, Ulliac G, Suarez M, Calero V, Bernal M-P, Courjal N, Roussey M, Häyrinen M, Laukkanen J, Honkanen S, Kuittinen M. High-aspect-ratio electro-optical ridge waveguide made by precise dicing and atomic layer deposition. 2017 Conference on Lasers and Electro-Optics Europe & European Quantum Electronics Conference (CLEO/Europe-EQEC); Munich. 2017. pp. 1–1. DOI: 10.1109/CLEOE-EQEC.2017.8086602

[40] Courjal N, Devaux F, Gerthoffer A, Guyot C, Henrot F, Ndao A, Bernal M-P. Low-loss $LiNbO_3$ tapered-ridge waveguides made by optical-grade dicing. Optics Express. 2015;**23**:13983-13990. DOI: 10.1364/OE.23.013983

[41] Levy M, Osgood RM Jr, Liu R, Cross LE, Cargill GS, Kumar A, Bakhru H. Fabrication of single-crystal lithium niobate films by crystal ion slicing. Applied Physics Letters. 1998;**73**: 2293-2296. DOI: 10.1063/1.121801

[42] Poberaj G, Hu H, Sohler W, Günter P. Lithium niobate on insulator (LNOI) for micro-photonic devices. Laser & Photonics Reviews. 2012;**6**:488-503. DOI: 10.1002/lpor.20110 0035

[43] NanoLN, LiNbO3 thin films [Internet]. 2017. Available from http://www.nanoln.com/en/pinfo.asp?ArticleID=13

[44] Partow Technologies LLC. Ino sliced thin films. [Internet]. 2017. Available from: http://www.partow-tech.com/thinfilms/

[45] Volk MF, Suntsov S, Rüter CE, Kip D. Low loss ridge waveguides in lithium niobate thin films by optical grade diamond blade dicing. Optics Express. 2016;**24**:1386. DOI: 10.1364/OE.24.001386

[46] Guarino A, Poberaj G, Rezzonico D, Degl'Innocenti R, Günter P. Electro-optically tunable microring resonators in lithium niobate. Nature Photonics. 2007;**1**:407-410. DOI: 10.1038/nphoton.2007.93

[47] Chen L, Chen J, Nagy J, Reano R. Highly linear ring modulator from hybrid silicon and lithium niobate. Optics Express. 2015;**23**:13255. DOI: 10.1364/OE.23.013255

[48] Lu H, Sadani B, Courjal N, Ulliac G, Smith N, Stenger V, Collet M, Baida FI, Bernal M-P. Enhanced electro-optical lithium niobate photonic crystal wire waveguide on a smart-cut thin film. Optics Express. 2012;**20**:2974-2981. DOI: 10.1364/OE.20.002974

[49] Geiss R, Saravi S, Sergeyev A, Diziain S, Setzpfandt F, Schrempel F, Grange R, Kley E, Tünnermann A, Pertsch T. Fabrication of nanoscale lithium niobate waveguides for second-harmonic generation. Optics Letters. 2015;**40**:2715-2718. DOI: 10.1364/OL.40.002715

[50] Chen L, Xu Q, Wood G, Reano RM. Hybrid silicon and lithium niobate electro-optical ring modulator. Optica. 2014;**1**:112-118. DOI: 10.1364/OPTICA.1.000112

[51] Courjal N, Caspar A, Calero V, Ulliac G, Suarez M, Guyot, Bernal MP. Simple production of membrane-based $LiNbO_3$ micro-modulators with integrated tapers. Optics Letters. 2016;**41**:5110-5113. DOI: 10.1364/OL.41.005110

[52] Roussey M, Bernal MP, Courjal N, Van Labeke D, Baida FI. Electro-optic effect exaltation on lithium niobate photonic crystals due to slow photons. Applied Physics Letters. 2006; **89**:241110-241113. DOI: 10.1063/1.2402946

[53] Roussey M, Baida FI, Bernal M-P. Experimental and theoretical observations of the slow-light effect on a tunable photonic crystal. JOSA B. 2007;**24**(6):1416-1422. DOI: 10.1364/JOSAB.24.001416

[54] Burr GW, Diziain S, Bernal M-P. The impact of finite-depth cylindrical and conical holes in lithium niobate photonic crystals. Optics Express. 2008;**16**:6302-6316. DOI: 10.1364/OE.16.00 6302

Chapter 9

# Raman Solitons in Nanoscale Optical Waveguides, with Metamaterials, Having Polynomial Law Nonlinearity Using Collective Variables

Yanan Xu, Jun Ren and Matthew C. Tanzy

Additional information is available at the end of the chapter

http://dx.doi.org/10.5772/intechopen.75121

**Abstract**

A mathematical analysis is conducted to illustrate the controllability of the Raman soliton self-frequency shift with polynomial nonlinearity in metamaterials by using collective variable method. The polynomial nonlinearity is due to the expanding nonlinear polarization $P^{NL}$ in a series over the field $E$ up to the seventh order. Gaussian assumption is selected to these pulses on a generalized mode. The numerical simulation of soliton parameter variation is given for the Gaussian pulse parameters.

**Keywords:** Raman solitons, polynomial nonlinearity, collective variables

## 1. Introduction

Much attention has been devoted to the understanding of metamaterials [1–4]. Through its engineered structures, researchers are able to control and manipulate the electromagnetic fields [5]. Using the freedom of design that metamaterials provide, electromagnetic fields can be redirected at will and propose a design strategy [6]. A general recipe for the design of media that create perfect invisibility within the accuracy of geometrical optics is developed. The imperfections of invisibility can be made arbitrarily small to hide objects that are much larger than the wavelength [7].

Especially, mathematical operations can be performed based on suitably designed metamaterials blocks, such as spatial differentiation, integration, or convolution [8]. Soliton pulse can evolve owning to delicate balance between dispersion and nonlinearity. However, it is

always a challenge to compensate for the loss when engineering these types of waveguide using metamaterials. The strong perturbation of a soliton envelope caused by the stimulated Raman scattering confines the energy scalability preventing the so-called dissipative soliton resonance [9]. It is important to know the limit we can reach expanding the nonlinear polarization $P^{NL}$ in a series over the field $E$ [10]. The fourth-order nonlinear susceptibility $\chi^{(4)}$, the fifth-order nonlinearity $\chi^{(5)}$, and the seventh-order nonlinearity $\chi^{(7)}$ have been measured [11, 12]. The polynomial mode nonlinearity is due to the nonlinear polarization of metamaterials in the power-series expansion form where terms are kept up to the seventh order in the field $E$ [10, 12–15]. This chapter conducts mathematical analysis to illustrate the controllability of the Raman soliton self-frequency shift with polynomial nonlinearity in metamaterials by using collective variable method.

## 2. Governing model

The dimensionless form nonlinear Schrödinger's equation (NLSE) that governs the propagation of Raman soliton through optical metamaterials, with polynomial law nonlinearity, is given by [16–24].

$$\begin{aligned} i\frac{\partial}{\partial t}\Phi(z,t) + a\frac{\partial^2}{\partial z^2}\Phi(z,t) + \left(c_1|\Phi(z,t)|^2 + c_2|\Phi(z,t)|^4 + c_3|\Phi(z,t)|^6\right)\Phi(z,t) \\ = i\alpha\frac{\partial}{\partial z}\Phi(z,t) + i\lambda\frac{\partial}{\partial z}\left(|\Phi(z,t)|^2\Phi(z,t)\right) + i\nu\frac{\partial}{\partial z}\left(|\Phi(z,t)|^2\right)\Phi(z,t). \end{aligned} \tag{1}$$

In this model, $\Phi(z,t)$ represents the complex valued wave function with the independent variables being $z$ and $t$ that represent spatial and temporal variables, respectively. The first term represents the temporal evolution of nonlinear wave, while the coefficient $a$ is the group velocity dispersion (GVD). The coefficients of $c_j$ for $j = 1,2,3$ correspond to the nonlinear terms. Together, they form polynomial mode nonlinearity. The polynomial mode nonlinearity is due to the nonlinear polarization of metamaterials in the power-series expansion form where terms are kept up to the seventh order in the field $E$ [10, 12–15]. It must be noted here that when $c_2 = c_3 = 0$ and $c_1 \neq 0$, the model Eq. (1) collapses to Kerr mode nonlinearity which is due to third-order polarization $P^{NL}$ [15]. However, if $c_3 = 0$ and $c_1 \neq 0$ and $c_2 \neq 0$, one arrives at parabolic mode nonlinearity, and it is from the fifth-order polarization $P^{NL}$ [15, 30]. Thus, polynomial mode stands as an extension version to Kerr and parabolic modes. Actually, the Raman effect is not influenced by the properties of the metamaterials; however, the Raman coefficient combines with the dispersive magnetic permeability of the metamaterials leading to additional higher-order nonlinear terms [10, 12, 14]. The group velocity and self-phase modulation term produce the delicate balance dispersion and nonlinearity that accounts for the formation of the stable soliton. On the right hand side, $\alpha$ describes intermodel dispersion, $\lambda$ represents the self-steepening term in order to avoid the formation of shocks, and $\nu$ is the complex higher-order nonlinear dispersion coefficient.

## 3. Mathematical formulation

The pulse may not only be able to translate as a whole entity, but it may also execute more or less complex internal vibrations depending on the type of the perturbations in the system. This particle-like behavior has led to the formulation of the collective variable $(CV)$ techniques [25]. The basic idea is that the soliton solution depends on a collective of variables, called CVs, symbolically $Z_j(j = 1, \ldots N)$, which represent pulse width, amplitude, chirp, frequency, and so on [25–28]. To this end, the original field is decomposed into two components, say $\Phi(z, t)$ at position $z$ in the metamaterials and at time t, in the following way:

$$\Phi(z, t) = f(Z_1, Z_2, \ldots, Z_N, t) + q(z, t), \tag{2}$$

where the first component $f$ constitutes soliton solution and the second one $q$ represents the residual radiation that is known as small amplitude dispersive waves. Introduction of these $N$ CVs increases the phase space of the dynamical system.

In order for the system to remain in the original phase space and best fit for the static solution, the CV method is obtained by configuring the function $f(Z_1, Z_2, \ldots, Z_N, t)$ and minimizes residual free energy (RFE) $E$, where

$$E = \int_{-\infty}^{\infty} |q|^2 dt = \int_{-\infty}^{\infty} |\Phi(z, t) - f(Z_1, Z_2, \ldots, Z_N, t)|^2 dt. \tag{3}$$

The approximation of neglecting the *residual field* is called "bare approximation" in condensed matter physics [27].

Let CVs evolve only in a particular direction to minimize the PFE in the dynamical system with the following simple way:

$$C_j = \frac{\partial E}{\partial Z_j} = \frac{\partial}{\partial Z_j}\left(\int_{-\infty}^{\infty} |q|^2 dt\right) = \int_{-\infty}^{\infty} \left(\frac{\partial q}{\partial Z_j} q^* + \frac{\partial q^*}{\partial Z_j} q\right) dt. \tag{4}$$

The rate of change of $C_j$ with respect to the normalized distance is defined as.

$$\dot{C}_j = \frac{dC_j}{dz} = 2\Re\left(\frac{d}{dz}\left(\int_{\infty}^{\infty} \frac{\partial q^*}{\partial Z_j} q dt\right)\right), \tag{5}$$

where $\Re$ stands for the real part. Here, the weak equality indicates that the constraints $C_j$ need not be exactly zero [28].

Then, we define a second set of constraints:

$$\frac{dC_j}{dz} \approx 0. \tag{6}$$

Through Eqs. (2)–(6), it leads to the equations of motion:

$$\dot{C}_j = -2\Re \sum_{k=1}^{N} \left( \int_{-\infty}^{\infty} \frac{\partial f^*}{\partial Z_j} \frac{\partial f}{\partial Z_k} dt - \int_{-\infty}^{\infty} \frac{\partial^2 f^*}{\partial Z_j \partial Z_k} q dt \right) \frac{dZ_k}{dt} + R_j, \tag{7}$$

where

$$R_j = 2\Re \int_{-\infty}^{\infty} \frac{\partial f^*}{\partial Z_j} \frac{d\Phi}{dz} dt, \tag{8}$$

for $1 \leq j \leq N$.

The set of Eqs. (5)–(8) is equivalent to the matrix equation:

$$\dot{C} = \frac{\partial C}{\partial z} \dot{z} + R, \tag{9}$$

where

$$z = \begin{pmatrix} Z_1 \\ Z_2 \\ \cdots \\ Z_N \end{pmatrix}, \tag{10}$$

$$R = \begin{pmatrix} R_1 \\ R_2 \\ \cdots \\ R_N \end{pmatrix}, \tag{11}$$

while the $N \times N$ Jacobian is given by

$$\frac{\partial C}{\partial z} = \frac{\partial (C_1, C_2, \ldots, C_N)}{\partial (Z_1, Z_2, \ldots, Z_N)} = \left( \frac{\partial C_j}{\partial Z_k} \right)_{N \times N}, \tag{12}$$

with

$$\frac{\partial C_j}{\partial Z_k} = -2\Re \left( \int_{-\infty}^{\infty} \frac{\partial f^*}{\partial Z_j} \frac{\partial f}{\partial Z_k} dt - \int_{-\infty}^{\infty} \frac{\partial^2 f^*}{\partial Z_j \partial Z_k} q dt \right), \tag{13}$$

for $1 \leq j, k \leq N$.

At this stage, through Eq. (6) we can solve Eq. (9) by the following CV equations of motion:

$$\dot{X} = \left( \frac{\partial C}{\partial z} \right)^{-1} R. \tag{14}$$

The set of Eqs. (4)–(14) represents the complete CV treatment for the generalized NLSE Eq. (1).

http://dx.doi.org/10.5772/intechopen.75121

## 4. Computational results

In this part the adiabatic parameter dynamics of solitons in optical metamaterials with polynomial nonlinearity will be obtained by CV method. A Gaussian is given by

$$f(Z_1, Z_2, Z_3, Z_4, Z_5, Z_6; t) = Z_1 \exp\left[-(t - Z_2)^{2m/X_3^2} + i\frac{Z_4}{2}(t - Z_2)^2 + iZ_5(t - Z_2) + iZ_6\right], \quad (15)$$

where $Z_1$ is the soliton amplitude, $Z_2$ is the center position of the soliton, $Z_3$ is the inverse width of the pulse, $Z_4$ is the soliton chirp, $Z_5$ is the soliton frequency, and $Z_6$ is the soliton phase. Also, $m$ is the Gaussian parameter, where $m > 0$.

In this case, with $N = 6$:

$$\frac{\partial C}{\partial z} = \begin{pmatrix} \frac{\partial C_1}{\partial Z_1} & \frac{\partial C_1}{\partial Z_2} & \frac{\partial C_1}{\partial Z_3} & \frac{\partial C_1}{\partial Z_5} & \frac{\partial C_1}{\partial Z_5} & \frac{\partial C_1}{\partial Z_6} \\ \frac{\partial C_2}{\partial Z_1} & \frac{\partial C_2}{\partial Z_2} & \frac{\partial C_2}{\partial Z_3} & \frac{\partial C_2}{\partial Z_5} & \frac{\partial C_2}{\partial Z_5} & \frac{\partial C_2}{\partial Z_6} \\ \frac{\partial C_3}{\partial Z_1} & \frac{\partial C_3}{\partial Z_2} & \frac{\partial C_3}{\partial Z_3} & \frac{\partial C_3}{\partial Z_5} & \frac{\partial C_3}{\partial Z_5} & \frac{\partial C_3}{\partial Z_6} \\ \frac{\partial C_4}{\partial Z_1} & \frac{\partial C_4}{\partial Z_2} & \frac{\partial C_4}{\partial Z_3} & \frac{\partial C_4}{\partial Z_5} & \frac{\partial C_4}{\partial Z_5} & \frac{\partial C_4}{\partial Z_6} \\ \frac{\partial C_5}{\partial Z_1} & \frac{\partial C_5}{\partial Z_2} & \frac{\partial C_5}{\partial Z_3} & \frac{\partial C_5}{\partial Z_5} & \frac{\partial C_5}{\partial Z_5} & \frac{\partial C_5}{\partial Z_6} \\ \frac{\partial C_6}{\partial Z_1} & \frac{\partial C_6}{\partial Z_2} & \frac{\partial C_6}{\partial Z_3} & \frac{\partial C_6}{\partial Z_5} & \frac{\partial C_6}{\partial Z_5} & \frac{\partial C_6}{\partial Z_6} \end{pmatrix}, \quad (16)$$

$$z = \begin{pmatrix} Z_1 \\ Z_2 \\ Z_3 \\ Z_4 \\ Z_5 \\ Z_6 \end{pmatrix}, \quad (17)$$

$$\mathcal{R} = \begin{pmatrix} R_1 \\ R_2 \\ R_3 \\ R_4 \\ R_5 \\ R_6 \end{pmatrix}, \quad (18)$$

where

$$\mathcal{R}_1 = -aZ_1(Z_4 + X_1Z_5)\frac{\Gamma\left(\frac{1}{2m}\right)}{m\left(\frac{2}{Z_3^2}\right)^{\frac{1}{2m}}} - \left(\frac{2aZ_1^2X_4}{m} + \frac{12\lambda Z_1^3}{Z_3^2}\right)\frac{\Gamma\left(\frac{1}{m}\right)}{\left(\frac{4}{Z_3^2}\right)^{\frac{1}{m}}} - 2\alpha Z_1 + 4Z_1^3\nu, \tag{19}$$

$$\mathcal{R}_2 = 2aZ_1^2((m-1)Z_4 + Z_1Z_5) + (1-2m)\left(\frac{aZ_1^2Z_5}{2m}\left(\frac{2}{Z_3^3}\right)^{\frac{1}{2m}} + \left(\frac{\alpha Z_1^2}{16} - \frac{\nu Z_1^5}{8m}\right)\left(\frac{4}{Z_3^2}\right)^{\frac{1}{2m}}\right)\Gamma\left(-\frac{1}{2m}\right)$$

$$= -\left(\frac{Z_1^2Z_4}{m}\left(c_1\left(\frac{Z_3^2}{4}\right)^{\frac{1}{m}} + c_2\left(\frac{Z_3^2}{6}\right)^{\frac{1}{m}} + C_3\left(\frac{Z_3^2}{8}\right)^{\frac{1}{m}}\right) - \frac{4\lambda Z_1^4Z_4Z_5}{\left(\frac{6}{Z_3^2}\right)^{\frac{1}{m}}}\right)\Gamma\left(\frac{1}{m}\right)$$

$$+\left(\frac{\alpha Z_1^2Z_5}{m\left(\frac{2}{Z_3^2}\right)^{\left(\frac{1}{2m}\right)}} - \frac{\lambda Z_1^4Z_5^2}{m\left(\frac{6}{Z_3^2}\right)^{\left(\frac{1}{2m}\right)}}\right)\Gamma\left(\frac{1}{2m}\right) + \frac{(m-1)\lambda Z_1^4Z_3^2}{3m}\left(\frac{6}{Z_3^2}\right)^{\left(\frac{1}{2m}\right)}\Gamma\left(-\frac{1}{m}\right), \tag{20}$$

$$\mathcal{R}_3 = \frac{\nu Z_1^5}{Z_3} - \frac{3aZ_1^3Z_3\left(\frac{2}{m}-1\right)}{m}Z_4\Gamma\left(\frac{1}{m}\right) - \frac{2\alpha Z_1^2}{X_3} - \frac{3\lambda Z_1^4}{2Z_3}$$

$$+\left(\frac{c_1Z_1^4}{2Z_3\left(\frac{4}{Z_3^2}\right)^{\left(\frac{1}{2m}\right)}} - \frac{aZ_1^2(Z_4 + Z_1Z_5)}{\left(\frac{2}{Z_3^2}\right)^{\left(\frac{1}{m}\right)}} + \frac{c_2Z_1^6}{3Z_3\left(\frac{6}{Z_3^2}\right)^{\left(\frac{1}{2m}\right)}} + \frac{c_3Z_1^8}{4Z_3\left(\frac{8}{Z_3^2}\right)^{\left(\frac{1}{2m}\right)}}\right)\frac{\Gamma\left(\frac{1}{2m}\right)}{2m^2}, \tag{21}$$

$$\mathcal{R}_4 = \left(\frac{aZ_1^2(1-2m)}{\left(\frac{2}{Z_3^2}\right)^{\left(\frac{1}{2m}\right)}}\right)\frac{\Gamma\left(\frac{1}{2m}\right)}{4m} - \left(\frac{aZ_1^3}{\left(\frac{2}{Z_3^2}\right)^{\left(\frac{1}{m}\right)}} - \frac{\lambda Z_1^4Z_5}{\left(\frac{4}{Z_3^2}\right)^{\left(\frac{1}{m}\right)}}\right)\frac{\Gamma\left(\frac{1}{m}\right)}{m} + \left(\frac{\alpha Z_1^2Z_4}{2\left(\frac{2}{Z_3^2}\right)^{\left(\frac{2}{m}\right)}} + \frac{2\lambda Z_1^5}{\left(\frac{4}{Z_3^2}\right)^{\left(\frac{2}{m}\right)}}\right)\frac{\Gamma\left(\frac{2}{m}\right)}{m}$$

$$-Z_1^2\left(\frac{c_1Z_1^2}{\left(\frac{4}{Z_3^2}\right)^{\left(\frac{3}{2m}\right)}} + \frac{c_2Z_1^4}{\left(\frac{6}{Z_3^2}\right)^{\left(\frac{3}{2m}\right)}} + \frac{c_3Z_1^6}{\left(\frac{8}{Z_3^2}\right)^{\left(\frac{3}{2m}\right)}} - \frac{\alpha Z_5}{\left(\frac{2}{Z_3^2}\right)^{\left(\frac{3}{2m}\right)}}\right)\frac{\Gamma\left(\frac{3}{2m}\right)}{m}, \tag{22}$$

$$\mathcal{R}_5 = 2a(1-2m)Z_1^2 - \left(\frac{aZ_1^3}{\left(\frac{2}{Z_3^2}\right)^{\left(\frac{1}{2m}\right)}}\right)\frac{\Gamma\left(\frac{1}{2m}\right)}{m} - 2\left(\frac{\alpha Z_1^2Z_4}{\left(\frac{2}{X_3^2}\right)^{\left(\frac{3}{2m}\right)}} - \frac{\lambda Z_1^4Z_4}{\left(\frac{4}{X_3^2}\right)^{\left(\frac{3}{2m}\right)}}\right)\frac{\Gamma\left(\frac{3}{2m}\right)}{m}$$

$$-2\left(\frac{\alpha Z_1^2X_5}{\left(\frac{2}{Z_3^2}\right)^{\left(\frac{1}{m}\right)}} - \frac{\lambda Z_1^4Z_5}{\left(\frac{4}{X_3^2}\right)^{\left(\frac{1}{m}\right)}}\right)\frac{\Gamma\left(\frac{1}{m}\right)}{m} - \frac{aZ_1^3\Gamma\left(\frac{1}{2m}\right)}{m\left(\frac{2}{Z_3^2}\right)^{\left(\frac{1}{2m}\right)}} + 2a(1-2m)aZ_1^2, \tag{23}$$

http://dx.doi.org/10.5772/intechopen.75121

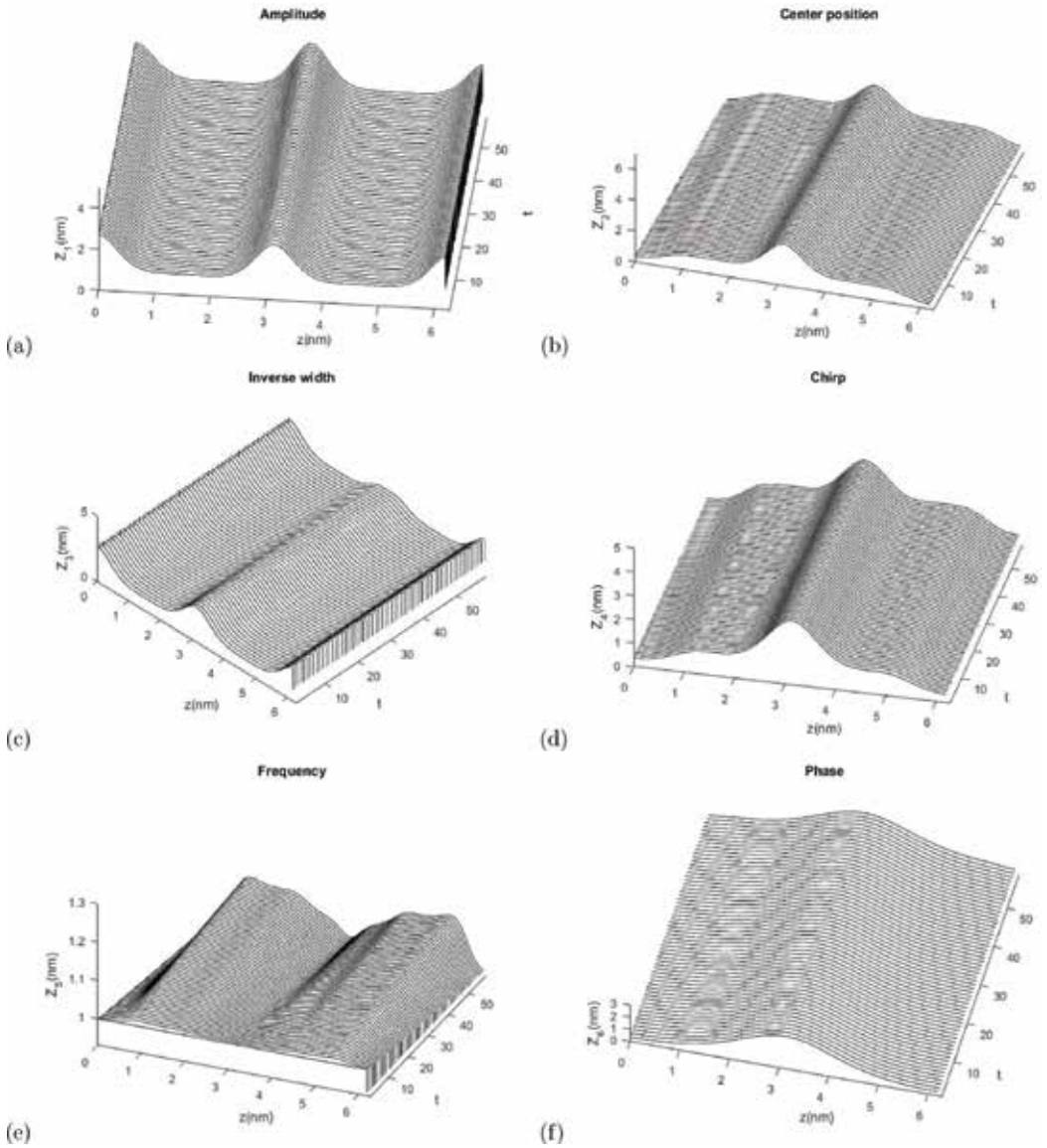


**Figure 1.** (a) Surface plot of soliton amplitude, (b) surface plot of soliton center position, (c) surface plot of soliton inverse width of the pulse, (d) surface plot of soliton chirp variation, (e) surface plot of soliton frequency, and (f) surface plot of soliton phase.

$$\mathcal{R}_6 = 2\left(\frac{\alpha Z_1 Z_4}{\left(\frac{2}{Z_3^2}\right)^{\left(\frac{1}{m}\right)}} + \frac{\lambda Z_1^4 Z_4}{\left(\frac{4}{Z_3^2}\right)^{\left(\frac{1}{m}\right)}}\right)\frac{\Gamma\left(\frac{1}{m}\right)}{m} + \left(\frac{\alpha Z_1 Z_5}{\left(\frac{2}{Z_3^2}\right)^{\left(\frac{1}{2m}\right)}} + \frac{\lambda Z_1^4 Z_5}{\left(\frac{4}{Z_3^2}\right)^{\left(\frac{1}{2m}\right)}}\right)\frac{\Gamma\left(\frac{1}{2m}\right)}{m} + \frac{aZ_1(2m-1)}{m}\left(\frac{Z_3^2}{2}\right)^{\left(\frac{1}{2m}\right)}\Gamma\left(-\frac{1}{2m}\right) - 2aZ_1^2. \tag{24}$$

## 5. Numerical simulation

The nonlinear dynamical system discussed in the previous section is plotted to illustrate the collective variables numerically; see **Figure 1**. The parameter values are as follows: $m = 1$, $a = 9.9 \times 10^{-2}$, $\lambda = 9.8 \times 10^{-2}$, $\alpha = 1 \times 10^{-1}$, $c_1 = 9.9 \times 10^{-1}$, $c_2 = -8 \times 10^{-2}$, $c_3 = -8 \times 10^{-3}$, and $v = 1.01 \times 10^{-1}$ [10, 12, 15, 30].

This continuous surface plot shows the dynamical relationship between the time and collective variables, in **Figure 1**. It shows soliton amplitude, center position, inverse width of the pulse, chirp, and phase keeping the original shape as time goes by. This is because group velocity and self-phase modulation term produce the delicate balance dispersion and nonlinearity that accounts for the formation of the stable soliton. It also describes Stokes Raman scattering that is due to transmitted wave at higher frequency and anti-Stokes Raman scattering where transmitted wave is at lower frequency by **Figure 1(e)** [29]. These results are consistent with Raman soliton scattering effect.

## 6. Conclusion

This chapter gives Raman soliton solutions in optical metamaterials that is studied with polynomial nonlinearity. The polynomial mode nonlinearity is due to expanding the nonlinear polarization $P^{NL}$ in a series over the field $E$ up to the seventh order [13–15]. The polynomial mode nonlinearity is an extension of the Kerr and parabolic mode nonlinearity, which are from third- and fifth-order polarization $P^{NL}$ [15, 30], respectively. The analytical results are supplemented with numerical simulation by collective variables. The continuous surface plot shows the dynamical relationship between the time and collective variables. It shows soliton amplitude, center position, inverse width of the pulse, chirp, and phase keeping the original shape as time goes by since group velocity and self-phase modulation term produce the delicate balance dispersion and nonlinearity. It also describes Stokes Raman scattering that is due to transmitted wave at higher frequency and anti-Stokes Raman scattering where transmitted wave is at lower frequency by **Figure 1(e)** [8, 29].

In the future, the set of plot with $m \neq 1$ will be plotted, and third-order dispersion (TOD) and fourth-order dispersion (FOD) will be included [15]. Nonlinear polarization of medium in the form of a power-series expansion, keeping the terms up to the ninth order, will be explored [10].

## Acknowledgements

This work was supported by NSF EAGER grants: 1649173.

## Author details

Yanan Xu[1]*, Jun Ren[2] and Matthew C. Tanzy[1]

*Address all correspondence to: yxu@desu.edu

1 Department of Mathematical Sciences, Delaware State University, Dover, DE, USA

2 Department of Physics and Engineering, Delaware State University, Dover, DE, USA

## References

[1] Liu Y, Zhang X. Recent advances in transformation optics. Nanoscale. 2012;**4**:5277-5292. DOI: 10.1039/C2NR31140B

[2] Schurig D, Mock JJ, Justice BJ, Cummer SA, Pendry JB, Starr AF, Smith DR. Metamaterials electromagnetic cloak at microwave frequencies. Science. 2006;**314**:977-979

[3] Pendry JB. Negative refraction makes a perfect lens. Physics Review Letter. 2000;**85**(18): 3966-3969

[4] Grzegorczyk TM, Kong JA. Review of left-handed metamaterials: Evolution from theoretical and numerical studies to potential applications. Journal of Electromagnetic Waves and Applications. 2006;**20**(14):2053-2064

[5] Li J. A literature survey of mathematical study of Metamaterials. International Journal of Numerical Analysis. 2016;**13**(2):230-243

[6] Pendry JB, Schurig D, Smith DR. Controlling electromagnetic fields. Science. 2006; **312**(5781):1780-1782

[7] Leonhardt U. Optical conformal mapping. Science. 2006;**312**(23):1777-1780

[8] Silva A, Monticone F, Castaldi G, Galdi V, Alu A, Engheta N. Performing mathematical operations with metamaterials. Science. 2012;**343**:160-163

[9] Kalashnikov VL, Sorokin E. Dissipative Raman solitons. Optics Express. 2014;**22**(24): 30118-30126

[10] Mitev VM, Pavlov LI, Stamenov KV. Seventh and ninth order nonlinear susceptibility measurement in alkali metal vapour. Optical and Quantum Electrics. 1979;**11**:229-236

[11] Ekvall K, Lundevall C, van der Meulen P. Studies of the fifth-order nonlinear susceptibility of ultraviolet-grade fused silica. Optics Letters. 2001;**26**(12):896-898

[12] Yang K, Kumar J. Susceptibilities of a poly(4BCMU) film through electroabsorption spectroscopy. Optics Letters. 2000;**25**(16):1186-1188

[13] Scalora M, Sychin MS, Akozbek N, Poliakov EY, D'Aguanno G, Mattiucci N, Bloemer MJ, Zheltikove AM. Generalized nonlinear Schrödinger equation for dispersive susceptibility and permeability: Application to negative index materials. Physical Review Letters. 2005; **95**:013902

[14] Powers PE. Fundamentals of Nonlinear Optics. 1st ed. Boca Raton, FL: CRC Press; 2011

[15] Syrchin MS, Zheltikov AM, Scalora M. Analytical treatment of self-phase-modulation beyond the slowly varying envelope approximation. Physical Review A. 2004;**69**:053803

[16] Biswas A, Khan KR, Mahmood MF, Belic M. Bright and dark solitons in optical metamaterials. Optik. 2014;**125**(13):3299-3302

[17] Biswas A, Mirzazadeh M, Savescu M, Milovic D, Khan KR, Mahmood MF, Belic M. Singular solitons in optical metamaterials by ansatz method and simplest equation approach. Journal of Modern Optics. 2014;**61**(19):1550-1555

[18] Ebadi G, Mohavir A, Guzman JV, Khan KR, Mahmood MF, Moraru L, Biswas A, Belic M. Solitons in optical metamaterials by F-expansion scheme. Optoelectronics and Advanced Materials: Rapid Communications. 2014;**8**(9–10):828-834

[19] Xiang Y, Dai X, Wen S, Guo J, Fan D. Controllable Raman soliton self-frequency shift in nonlinear metamaterials. Physical Review A. 2011;**84**:033815

[20] Krishnan EV, Al Gabshi M, Zhou Q, Khan KR, Mahmood MF, Xu Y, Biswas A, Belic M. Solitons in optical metamaterials by mapping method. Journal of Optoelectronics and Advanced Materials. 2015;**17**(3–4):511-516

[21] Biswas A, Mirzazadeh M, Eslami M, Milovic D, Belic M. Solitons in optical metamaterials by functional variable method and first integral approach. Frequenz. 2014;**68**(11–12):525-530

[22] Bhrawy AH, Alshaery AA, Hilal EM, Milovic D, Moraru L, Savescu M, Biswas A. Optical solitons with polynomial and triple power law nonlinearities and spatio-temporal dispersion. Proceedings of the Romanian Academy, Series A. 2014;**15**(3):235-240

[23] Biswas A, Milovic D. Traveling wave solutions of the nonlinear Schrodinger's equation in non-Kerr law media. Communications in Nonlinear Science and Numerical Simulation. 2009;**14**(5):1993-1998

[24] Xu Y, Savescu M, Khan KR, Mahmood MF, Biswas A, Belic M. Soliton propagation through nanoscale waveguides in optical metamaterials. Optics and Laser Technology. 2016;**7**:177-186

[25] Asseu O, Diby A, Yoboue P, Kamagete A. Spatio-temporal pulsating dissipative Solitons through collective variable methods. Journal of Applied Mathematics and Physics. 2016: 1032-1041

[26] Tchofo-Dinda P, Moubissi AB, Nakkeeran K. Collective variable theory for optical solitons in fibers. Physical Review E. 2011;**64**:016608(15)

[27] Boesch R, Stancioff P, Willis CR. Hamiltonian equations for multiple-collective-variable theories of nonlinear Klein-Gordon equations: A projection-operator approach. Physics Review B. 1988;**38**(10):6713-6735

[28] Tchofo Dinda P, Moubissi AB, Nakkeeran K. A collective variable approach for dispersion-managed solitons. Journal of Physics A: Mathematical and General. 2001;**34**: 103-110

[29] WIKIPEDIA. (2018, January 23). Retrieved from: https://en.wikipedia.org/w/index.php?title=Ramanscattering&action=history.

[30] Min X, Yang R, Tian J, Xue W, Christian JM. Exact dipole solitary wave solution in metamaterials with higher-order dispersion. Journal of Modern Optics. 2016;**63**(S3):S44-S50

Chapter 10

# Silicon-on-Insulator Slot Waveguides: Theory and Applications in Electro-Optics and Optical Sensing

Patrick Steglich

Additional information is available at the end of the chapter

http://dx.doi.org/10.5772/intechopen.75539

**Abstract**

This chapter deals with the basic concept of silicon-on-insulator (SOI) slot waveguides, including slot waveguide theory, fabrication steps, and applications. First, in the theory section, a modal field expression and the characteristic equation is derived, which is also valid for higher-order modes. SOI slot waveguide structures are simulated and characteristic values like the effective refractive indices and the field confinement factors are determined. The fabrication section describes typical SOI fabrication steps and the limits of current fabrication techniques. Additionally, developments regarding loss reduction in SOI slot waveguides are given from the fabrication point of view. This is followed by the theory and practice of slot waveguide based electro-optical modulators. Here, the SOI slot waveguide is embedded in an organic nonlinear optical material in order to achieve record-low voltage-length products. In the field of optical sensors, it is shown that slot waveguides enable remarkable waveguide sensitivity for both refractive index sensing and surface sensing.

**Keywords:** silicon-on-insulator (SOI), slot waveguide, polymer-based optical waveguides, silicon-organic hybrid waveguide, optical waveguides technology, electro-optic waveguides, waveguide sensing

## 1. Introduction

Recent developments in cloud computing, social media, and the Internet of things have heightened the need for integrated photonic communication systems. To compensate for the emerged data traffic, electro-optical (EO) modulators with large bandwidth and high-speed operation are necessary. This in turn needs novel material systems and waveguide structures since the established depletion-type modulators are speed limited due to carrier injection and

removal. In contrast, polymer-based EO modulators exhibit high-speed operation but suffer from process compatibility with the well-established silicon-on-insulator (SOI) technology, which makes high volume and cheap production challenging.

After the invention by Almeida et al. in 2004 [1], slot waveguides became one key element to combine the well-established SOI technology with nonlinear optical polymers [2]. In recent years, there has been an increasing interest in slot waveguide structures. An SOI slot waveguide consists of a small gap in between two silicon rails, where a nonlinear optical polymer can be deposited. This narrow gap has two effects. First, the guided light is partly confined inside the gap. Second, the gap leads to an extremely large electric field, while voltages as low as 1 V are applied. Consequently, a record-high operation speed and large bandwidth with low energy consumption has been demonstrated using the silicon-organic hybrid (SOH) photonics [3].

Researchers have also discovered the advantages of slot waveguides for optical sensing. In this case, the slot waveguide takes advantage from the fact that more than 70% of the guided light can be confined near the silicon rails. Therefore, the light has a stronger interaction with the analyte compared to common strip waveguides, where only a fraction, 20%, of the light can be interacting. This strong light-analyte interaction leads to a large waveguide sensitivity, which has pushed the development of recent integrated optical sensors.

This work examines the theory and applications of SOI slot waveguides for EO modulators and optical sensors. We provide a theoretical guideline for a deeper understanding of SOI slot waveguides. The present work is structured as follows. The following section focuses on a detailed theoretical description and analysis of slot waveguide structures. This is followed by a section on the fabrication scheme using standard SOI technology. Finally, application notes in electro-optics and optical sensing are given in Sections 4 and 5, respectively.

## 2. Silicon-on-insulator slot waveguide

This section deals with the basic concepts of SOI slot waveguides. For a deeper understanding of slot waveguide structure, the breakthrough paper of Almeida et al. [1] is recommended. However, the modal field expression given in [1] has some transcription errors and the given characteristic equation is not explicit for solving higher-order modes. Therefore, the correct modal field expression and the characteristic equation, which is also valid for higher-order modes is provided in this chapter, following the comprehensive work of Liu et al. [4].

### 2.1. Introduction to silicon-on-insulator waveguides

In general, silicon waveguides can be readily fabricated from SOI wafers using standard CMOS (complementary metal-oxide-semiconductor) processes. A typical SOI wafer consists of a buried oxide (BOX) layer between the silicon wafer and a thin silicon layer. Optical lithography and etching techniques are used to form the silicon waveguide. The most common silicon waveguide is the strip waveguide. This waveguide has a rectangular geometry as

http://dx.doi.org/10.5772/intechopen.75539

shown in **Figure 1**. During the last decade, a new waveguide approach based on vertical silicon slot waveguides has been proposed [1] and experimentally demonstrated to be suitable as an optical phase shifter [2]. An SOI slot waveguide consists typically of two silicon rails with a height of $h = 220$ nm. This thickness of 220 nm has become a standard used in particular by most multi-project wafer foundries [5]. As illustrated in **Figure 1**, both silicon rails are located on top of a buried oxide (BOX) substrate and are separated from each other by a slot width $s$. The width of the silicon rails is denoted as $wg$. Slot waveguides enable a high field confinement in a narrow low-index region. Infiltration of the interior of the slot waveguide with an EO polymer allows the use of the Pockels effect. Because of this effect, slot wave guides have high potential in the field of optical switching and high-speed modulation even at frequencies of 100 GHz [3]. As a consequence, various devices like Mach-Zehnder interferometers and ring resonators have been recently developed using slot waveguide phase shifters [6]. In fact, slot waveguides have become the key element in order to implement organic materials into silicon photonics. Beside the strip and slot waveguide, the strip-loaded slot waveguide is utilized in this work. The cross section of each waveguide type is shown in **Figure 1**.

The overwhelming advantage of SOI slot waveguides lies in its compatibility with CMOS fabrication processes. This compatibility ensures a cost efficient mass production environment for such integrated photonic devices. **Figure 2** shows, as an example, a scanning electron microscopy (SEM) picture of three slot waveguides with different slot widths from the top view and one slot waveguide in the cross-sectional view recorded with a focused ion beam (FIB). They were fabricated in an SiGe BiCMOS pilot line at the Institute of High-Performance Microelectronics (IHP) in Frankfurt (Oder) using 200 mm SOI wafers and 248 nm lithography.

### 2.2. Silicon-on-insulator slot waveguide theory

One major advantage of slot waveguides compared to strip waveguides is the fact that the guided light is partially confined in between two silicon rails. Consequently, the light is forced

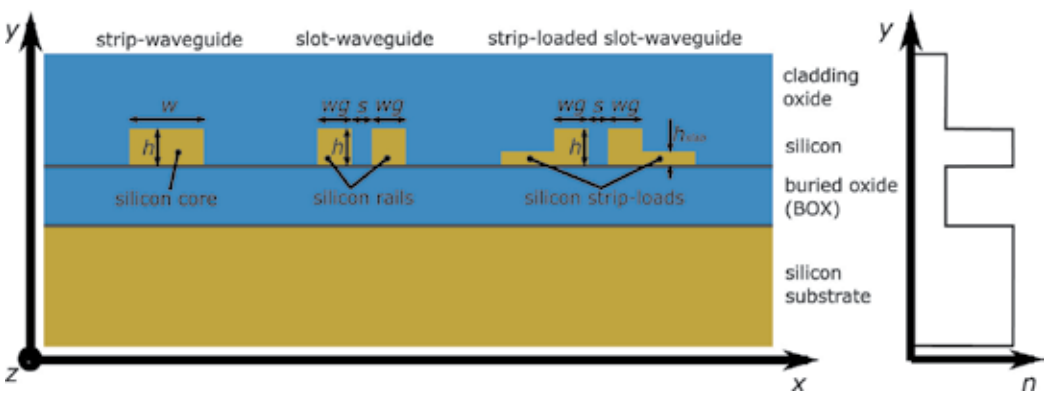


**Figure 1.** Typical silicon-on-insulator waveguide types. The most common waveguide type is the strip waveguide, where the light is highly confined inside the silicon core. In case of slot waveguides, the light is confined near two silicon rails. To apply a voltage to the silicon rails, strip-loads serve as electrical connections. The corresponding waveguide is called a strip-loaded slot waveguide.

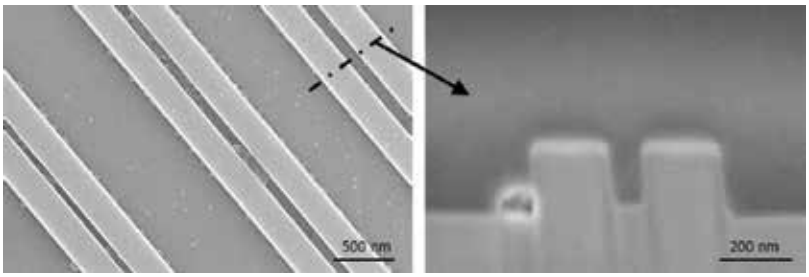


**Figure 2.** SEM image (left) of slot waveguides with different slot widths fabricated using 248 nm lithography. FIB image (right) of a slot waveguide cross section [13].

to interact directly with the cladding material. The reason for the high confinement is the large index contrast of the high-index silicon $n_{si}$ and the low-index cladding material $n_{clad}$. At the interface the normal electric field, which is according to **Figure 1**, the $E_x$ field component, undergoes a large discontinuity. This results in a field enhancement in the low-index region, which is proportional to the ratio of the refractive indices of the cladding material to that of silicon,

$$E_{x,slot} = \frac{n_{si}^2}{n_{clad}^2} E_{x,si} \tag{1}$$

Here, $E_{x,slot}$ and $E_{x,si}$ represent the electric field inside the slot and inside the silicon, respectively. From Eq. (1), it is apparent that the modal field distribution in the slot depends on the quotient of the refractive indices of silicon and the slot material. The larger the $n_{si}$ to $n_{clad}$ ratio, the stronger is the normal electric field component in the slot. Considering silicon with a refractive index of 3.48 and air as cladding material with a refractive index of 1.0, the resulting field amplitude is more than 12 times higher in the slot region according to Eq. (1). The high confinement inside the slot is of special benefit for EO and biosensing applications.

As shown in **Figure 2**, a conventional slot waveguide structure with finite height consists of two rectangle silicon rails. In the following, we will transform the three-dimensional (3D) rectangular silicon rails of the slot waveguide into a two-dimensional (2D) slab waveguide, where the height of the slot waveguide becomes infinite as illustrated in **Figure 3**. The coordinate system is set in the center of the slab-based slot waveguide. This slab waveguide approximation makes it easier to find an analytical solution and is simpler and more intuitive than numerical methods like the finite element method (FEM).

For the $E_x$ component of the fundamental TM (transverse magnetic) mode, the Helmholtz equation for each layer becomes

$$\frac{d^2E_x}{dx^2} + \left[k_0^2 n^2(x) - \beta^2\right] E_x = 0, \tag{2}$$

where

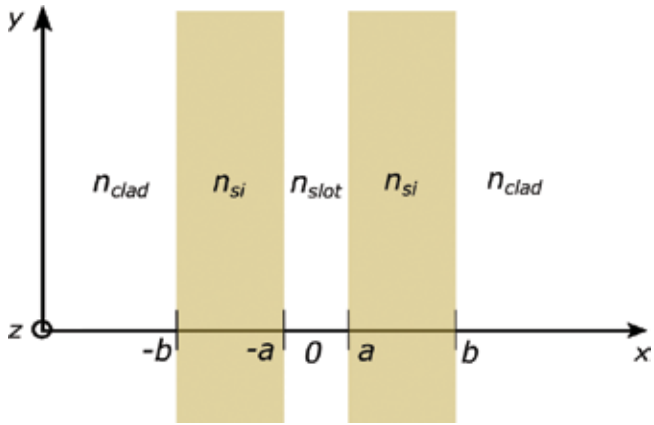


**Figure 3.** Schematic of the slot waveguide structure with infinite height (slab waveguide approximation). The refractive index of the slot is denoted as $n_{slot}$.

$$n(x) = f(x) = \begin{cases} n_{slot}, & if\ |x| < a \\ n_{si}, & if\ a < |x| < b \\ n_{clad}, & if\ |x| > b \end{cases} \tag{3}$$

and $\beta = k_0 n_{eff}$ denotes the mode propagation constant with the effective refractive index $n_{eff}$. Letting

$$\gamma_{slot}^2 = \beta^2 - k_0^2 n_{slot}^2 \tag{4}$$

$$\gamma_{si}^2 = k_0^2 n_{si}^2 - \beta^2 \tag{5}$$

$$\gamma_{clad}^2 = \beta^2 - k_0^2 n_{clad}^2 \tag{6}$$

the Helmholtz equation can be expressed as

$$\begin{cases} \dfrac{d^2 E_x}{dx^2} - \gamma_{slot}^2 E_x = 0, & if\ |x| < a \\ \dfrac{d^2 E_x}{dx^2} + \gamma_{si}^2 E_x = 0, & if\ a < |x| < b \\ \dfrac{d^2 E_x}{dx^2} - \gamma_{clad}^2 E_x = 0, & if\ |x| > b \end{cases} \tag{7}$$

The effective refractive index is obtained by solving the Eigen equation of the waveguide structure. In case of the TM fundamental mode, the following condition is assumed: $n_{si} > n_{clad} \geq n_{slot}$. The analysis of other cases like $n_{si} > n_{slot} > n_{clad}$ is out of the scope of this thesis. For a more detailed analysis the work of Liu et al. [4] is recommended. However, by choosing reasonable modal field functions in each layer of the slab-based slot waveguide and

employing the electromagnetic field boundary conditions, the modal field solution and the characteristic equation can be obtained. In consideration of the natural boundary condition and waveguide symmetry the general solution for the transverse E-field profile $E_x$ of the fundamental TM mode is

$$E_x(x) = \begin{cases} A_1 \cosh\left(\gamma_{slot} x\right), & if\ |x| < a \\ A_2 \cos\left(\gamma_{si}|x|\right) + B_2 \sin\left(\gamma_{si}|x|\right), & if\ a < |x| < b \\ A_3 e^{-\gamma_{clad}|x|}, & if\ |x| > b \end{cases} \tag{8}$$

Here, $A_1$, $A_2$, $A_3$ and $B_2$ are constants. Assuming that there is no free charge at the boundary, the boundary continuous conditions for the TM mode are the continuity of the normal component of the electric displacement field $\left(n_{clad}^2 E_{x,clad} = n_{si}^2 E_{x,si}\right)$ and $\left(n_{slot}^2 E_{x,slot} = n_{si}^2 E_{x,si}\right)$ and the continuity of $dE_x/dx$. At boundary surfaces $|x| = a$ and $|x| = b$, the boundary continuous conditions are used to derive the coefficients and the eigenvalue equation for $\beta$. The eigenvalue equation is a transcendental equation and is given by

$$\tan^{-1}\left(\frac{n_{si}^2}{n_{clad}^2}\frac{\gamma_{clad}}{\gamma_{si}}\right) + \tan^{-1}\left(\frac{n_{si}^2}{n_{slot}^2}\frac{\gamma_{slot}}{\gamma_{si}}\tanh\left(\gamma_{slot} a\right)\right) + m{\cdot}\pi = \gamma_{si}(b-a) \tag{9}$$

where $m$ is an integer. The analytical solution of the fundamental TM mode is obtained by substituting the coefficients into the general solution for $E_x$ (Eq. (8)), which leads to the modal field expression

$$E_x(x) = A\begin{cases} \dfrac{1}{n_{slot}^2}\cosh\left(\gamma_{slot} x\right), & if\ |x| < a \\ \dfrac{1}{n_{si}^2}\cosh\left(\gamma_{slot} a\right)\cos\left(\gamma_{si}(|x|-a)\right) \\ +\dfrac{1}{n_{slot}^2}\dfrac{\gamma_{slot}}{\gamma_{si}}\sinh\left(\gamma_{slot} a\right)\sin\left(\gamma_{si}(|x|-a)\right), & if\ a < |x| < b \\ \dfrac{1}{n_{clad}^2}\left(\cosh\left(\gamma_{slot} a\right)\cos\left(\gamma_{si}(b-a)\right)\right. \\ +\dfrac{n_{si}^2}{n_{slot}^2}\dfrac{\gamma_{slot}}{\gamma_{si}}\sinh\left(\gamma_{slot} a\right)\sin\left(\gamma_{si}(b-a)\right)\Big) e^{-\gamma_{clad}|x|}, & if\ |x| > b \end{cases} \tag{10}$$

where $A$ is an arbitrary constant. As an example, **Figure 4** shows the normalized $E_x$ field distribution of a typical silicon slot waveguide. This figure gives an evidence of the large discontinuity and the high E-field confinement inside the slot region.

### 2.3. Simulation of slot waveguides

In this section, a commercial full-vectorial finite element method (FEM) based mode solver from COMSOL Multiphysics is employed to simulate the slot waveguide structure with finite height.

http://dx.doi.org/10.5772/intechopen.75539

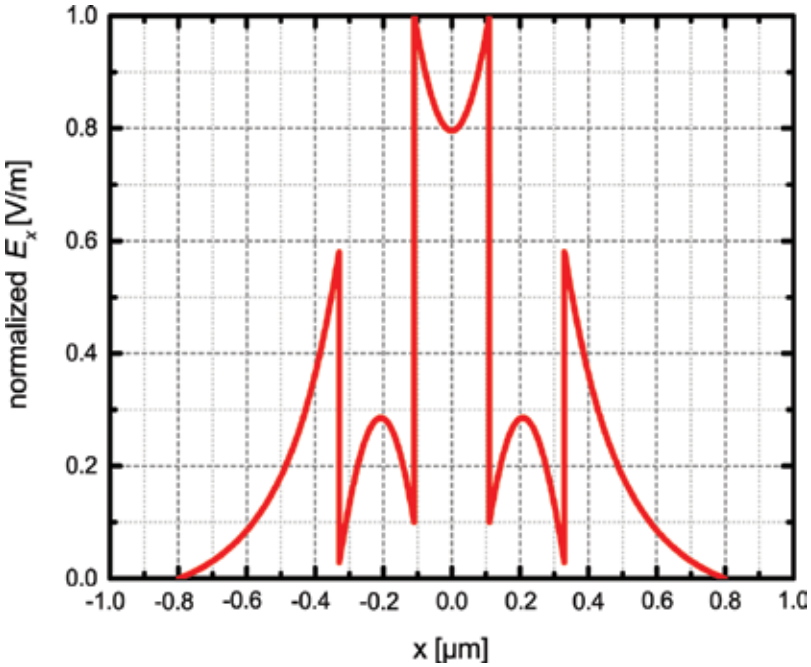


**Figure 4.** Calculated $E_x$ field (normalized) for a slot waveguide structure with infinite height. Parameters: $\lambda = 1550$ nm, $a = 110$ nm, $b = 220$ nm, $n_{slot} = n_{clad} = 1.44$, $n_{si} = 3.48$.

Here, the quasi-TE eigenmode presents the major E-field component along the x-direction [1]. Consequently, the quasi-TE eigenmode in the 3D slot waveguide structure is analogous to the TM eigenmode in the slab-based slot waveguide structure, which was studied in the previous section. In the following simulation study, the waveguide parameters, i.e., the silicon rail width *wg* and the slot width *s*, are variable whereas the height *h* is fixed to 220 nm (see **Figure 5**).

The wavelength is assumed to be $\lambda = 1550$ nm because it is a typical telecommunication wavelength in silicon photonics. Triangular vector elements with a maximum and minimum

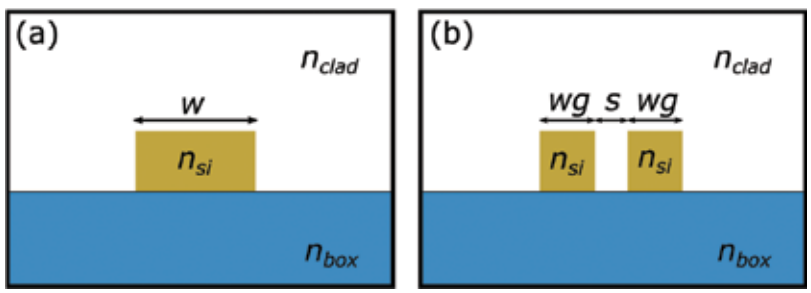


**Figure 5.** Cross-sectional view of an SOI strip waveguide (a) and an SOI slot waveguide (b). The cladding oxide is removed to hybridize the silicon waveguide with an EO polymer (EO modulator) or to bring the waveguide in contact with an analyte (biochemical sensor). The refractive indices are denoted as $n_{clad}$, $n_{si}$ and $n_{box}$ for the caldding material, silicon and buried oxide substrate, respectively.

element size of 6 and 2 nm, respectively have been adopted for meshing the profile with over $1.2 \times 10^4$ mesh elements. The overall simulation area was $3 \times 3\ \mu m$. In order to yield the mode field distribution and effective refractive index, the refractive index distribution $n(x, y)$ need to be declared to calculate eigenvalues and eigenfunctions of the wave equation. Finally, we get the E-field intensity distribution for the quasi-TE and quasi-TM mode as shown in **Figure 6**. In the following, we will neglect the quasi-TM mode because it is over two orders of magnitude smaller than the quasi-TE mode.

The material properties for our simulations were taken from a Sellmeier fit of the optical data from Malitson $(SiO_2)$ [16] and Salzberg and Villa $(Si)$ [17], which corresponds to having $n_{SiO_2} = n_{box} = 1.444$ and $n_{si} = 3.48$ at $\lambda = 1550$ nm. The refractive index of the surrounding material is in general variable because it can be gas, fluid or solid, depending on the application. For exemple, we chose $n_{clad} = 1.7$, which corresponds to a commercially available and reliable organic material named M3 (commercialized by GigOptix Inc.). M3 is successfully used for several slot waveguide based EO modulators like in [2, 18–20].

As result, the effective refractive index can be obtained from this simulation. **Figure 7** shows the calculated effective refractive indices $n_{eff}$ as a function of the slot width $s$ and the rail width $wg$. From this figure, it can be seen that the effective refractive index becomes higher by increasing the rail width $wg$ and by decreasing the slot width $s$. Therefore, such parameters have to be taken into account in order to design slot waveguide based mode coupler, ring resonators, or similar photonic components.

### 2.4. SOI slot waveguide optimization

In order to design and improve the waveguide geometry for applications in the field of EO modulators and optical sensors, it is necessary to calculate characteristic values, which describe the optical field confinement and therefore the interaction of light with the surrounding material.

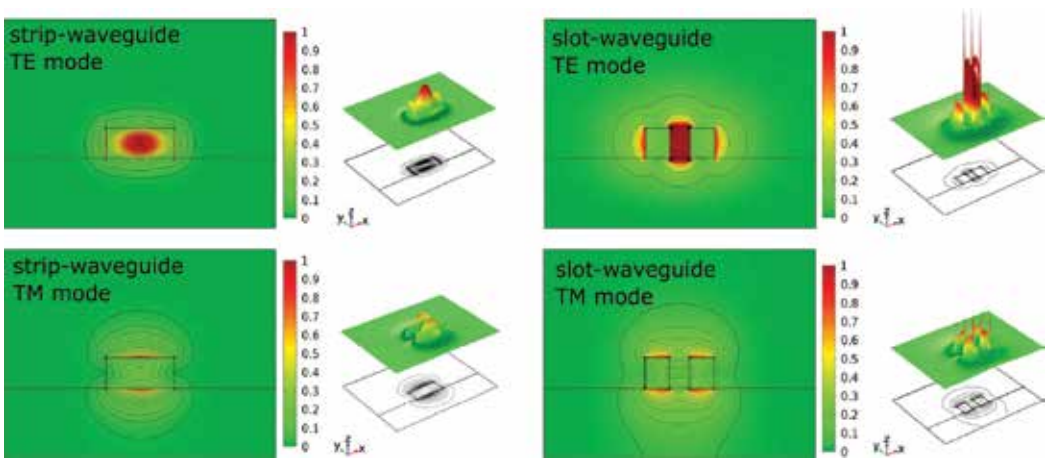


**Figure 6.** FEM simulation of the normalized E-field intensity $|E_x|^2 + |E_y|^2 + |E_z|^2$ for the first TE and first TM mode of SOI strip and slot waveguides. Parameters: $\lambda = 1550$ nm, $n_{box} = 1.444$, $n_{si} = 3.48$.

http://dx.doi.org/10.5772/intechopen.75539

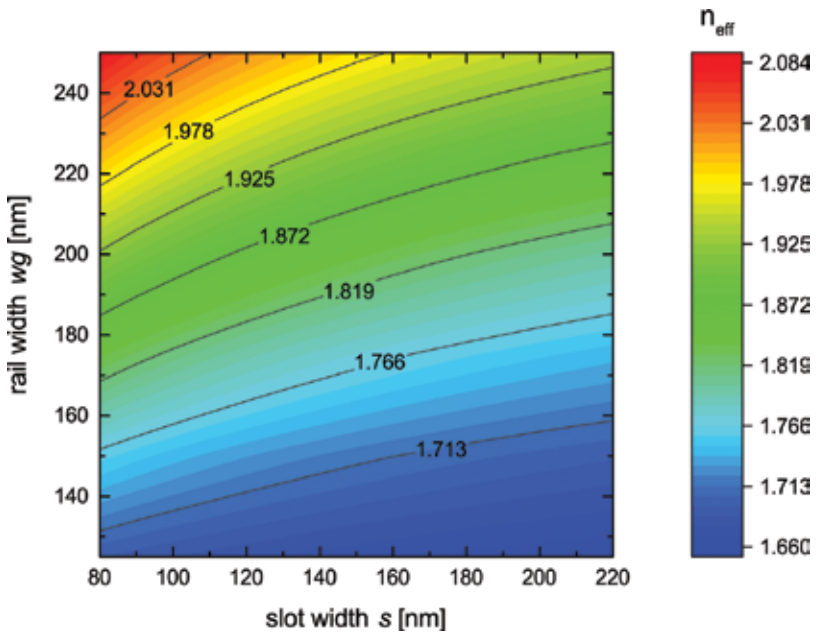


**Figure 7.** Calculated effective refractive indices $n_{eff}$ of SOI slot waveguides as a function of the slot width $s$ and the rail width $wg$.

One key figure of merit is the field confinement factor. In particular, it describes how well the guided modal field is confined in a certain region and is defined as the ratio of the time averaged energy flow through the domain of interest ($D_{int}$) to the time averaged energy flow through the total domain ($D_{tot}$)

$$\Gamma = \frac{\iint_{D_{int}} \mathrm{Re}\{E \times H^*\} e_z dxdy}{\iint_{D_{tot}} \mathrm{Re}\{E \times H^*\} e_z dxdy} \tag{11}$$

Here, $E$ and $H$ are the electric and magnetic field vectors, respectively, and $e_z$ is the unit vector in the $z$ direction. There are four different cases in order to choose the domain of interest, as illustrated in **Figure 8**. In case of common strip waveguides for electro-optics, the domain of interest is usually equal to the core region ($D_{int} = D_{core}$) because high confinement inside the core leads to lower optical losses. In contrast to that, for bio-sensing applications, the region of the cladding region is considered to be the domain of interest ($D_{int} = D_{clad}$), which is valid for strip and slot waveguides as well. The reason for this is that the main goal is to have a high light interaction with the surrounding material. Considering slot waveguides for electro-optics, the domain of interest is equal to the slot region ($D_{int} = D_{slot}$). There is also a change in refractive index outside the slot since the electric field is also located outside. This contribution is, however, very small compared to that one inside the slot if we assume the linear EO effect (Pockels effect). The Pockels effect requires indeed a non-centro-symmetrical orientation of the EO polymers or non-centro-symmetric organic crystals. Because of that, the main part of the electric field, which gives a contribution to the refractive index change, is the x-component.

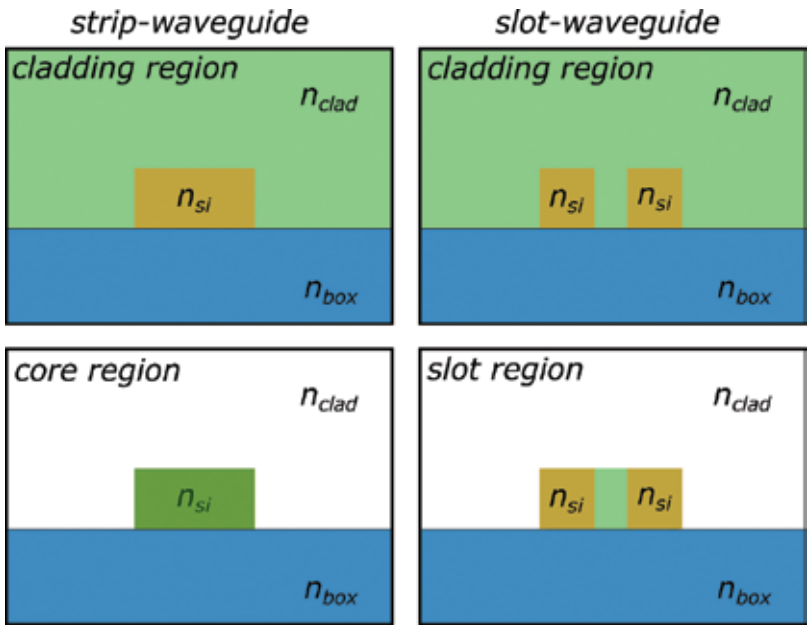


**Figure 8.** Domains of interest: core $D_{core}$, cladding $D_{clad}$ and slot $D_{slot}$ regions are highlighted in green. Please note that the substrate is not included in the cladding region because it does not contribute to the electro-optical or sensing effect. Only the amount of light, which is interacting with the cladding material, i.e. in the cladding or in the slot region, is of interest.

The x-component is homogeneous inside the slot. Outside there is just a little projection of the x-component which contributes as shown in **Figure 9**. This figure shows a simulation of the optical and electrical field in case of a strip-loaded slot waveguide. The strip-load serves as the electrical contact. In the following, however, the field confinement factor will be determined for slot waveguides without strip-load; the results are also valid for strip-loaded slot waveguides since the difference is negligible.

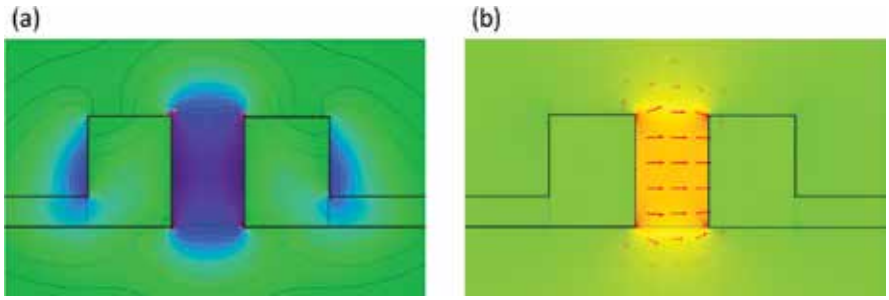


**Figure 9.** (a) The normalized optical field distribution for the quasi-TE eigenmode of a strip-loaded slot waveguide structure and (b) normalized x-component of the electric field ($E_x$). The largest overlap between optical and electrical field is achieved inside the slot. Because of that, Pockels effect outside the slot region is negligible and therefore, the field confinement factor in the slot region $\Gamma_{slot}$ should be taken into account in order to avoid an underestimation of the refractive index change $\Delta n$.

http://dx.doi.org/10.5772/intechopen.75539

To validate our simulation approach and compare it with literature data, the field confinement factors of standard SOI strip waveguides are investigated additionally and depicted in **Figure 10**. The domains of interest are the silicon core and the cladding in this case. Note that the substrate is not included in the calculated domains and, therefore, the sum of the core and cladding field confinement factor is not equal to unity. As can be seen from **Figure 10**, there is a large confinement of about 0.76 in the silicon core region of a strip waveguide with a typical waveguide width of $w = 500$ nm. These results are in good agreement with the literature [7].

However, to maximize the sensitivity of SOI slot waveguide based biochemical sensors, it is necessary to maximize the field confinement factor of the cladding (which will be referred to as $\Gamma_{clad}$) in order to increase the light-analyte interaction. From **Figure 11**, it can be seen that the confinement in the cladding region of a slot waveguide is increased by decreasing the rail width $wg$ and increasing the slot width $s$. We chose this parameter range to be compatible with typical semiconductor production platforms. For $wg = 180$ nm, the highest confinement in the cladding region is obtained in the parameter range of our simulation. For a slot waveguide with $wg = 180$ nm and $s = 180$ nm we obtain a field confinement factor of $\Gamma_{clad} = 0.69$. This is an enhancement of about five times compared to a conventional strip waveguide with a typical waveguide width of $w = 500$ nm. With that result, the high sensitivity of slot waveguide based label-free sensors as stated by Claes et al. can be explained [8]. However, due to the difficulty in functionalizing the interior of the slot, the sensitivity could be smaller than expected.

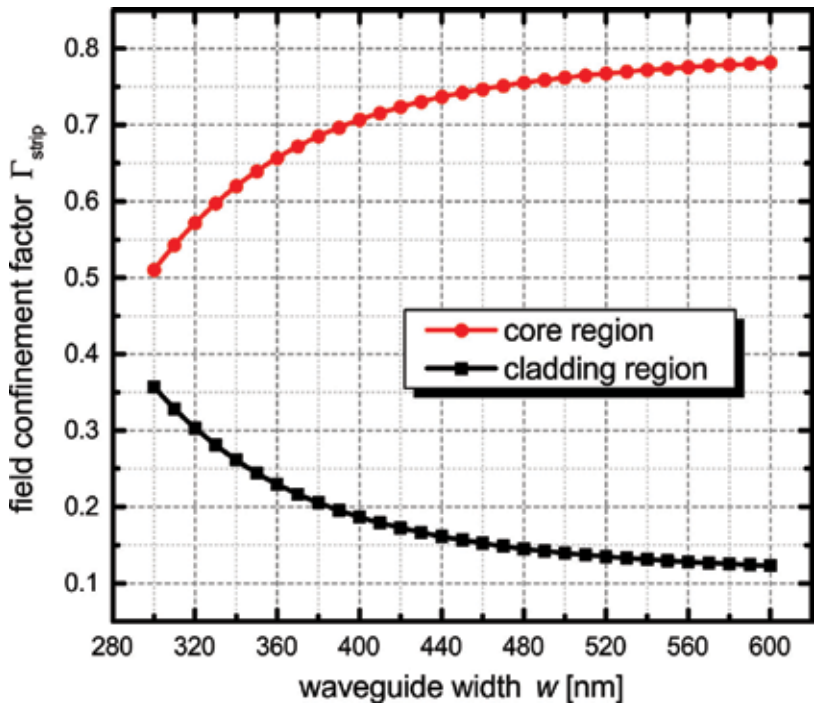


**Figure 10.** Calculated field confinement factor $\Gamma_{strip}$ of conventional SOI strip waveguides for the core and cladding region as a function of the waveguide width $wg$.

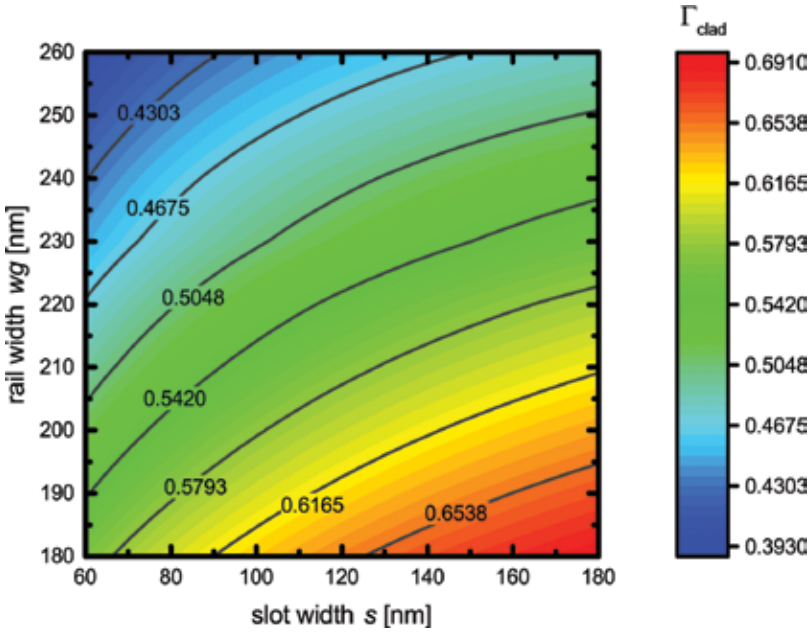


**Figure 11.** Calculated field confinement factor $\Gamma_{clad}$ of an SOI slot waveguide for the cladding region in dependence on the slot width $s$ and the rail width $wg$.

In order to improve SOI slot waveguides for EO applications, it is necessary to find the highest confinement in the slot region. **Figure 12** shows the calculated field confinement factors for the slot region $\Gamma_{slot}$ as a function of the slot width $s$ and the rail width $wg$ as parameter. As can be seen from this figure, there is one maximum of the highest field confinement of $\Gamma_{slot} = 0.216$ at a slot width of $s = 116$ nm and a rail width of $wg = 200$ nm. This is about three times smaller compared to an SOI strip waveguide (see **Figure 10**). However, in this case, it is more convenient to relate the field confinement factor $\Gamma_{slot}$ to the area where the light is confined as figure of merit, $\xi_{slot} = \Gamma_{slot}/A_{slot}$ and $\xi_{clad} = \Gamma_{clad}/A_{clad}$. In our case, $A_{slot}$ is equal to the slot domain of the slot waveguide and $A_{strip}$ is equal to the silicon core domain of the strip waveguide. For the optimized slot waveguide structure ($s = 116$ nm, $wg = 200$ nm), this figure of merit is about $\xi_{slot} = 7.83 \times 10^{12}\ \mathrm{m}^{-1}$ and for a typical strip waveguide ($w = 500$ nm), it is about $\xi_{slot} = 6.82 \times 10^{12}\ \mathrm{m}^{-1}$. Even $\xi_{slot}$ is 15% higher than $\xi_{strip}$; one should keep in mind that a modulator with extremely high field confinement usually suffers very high optical loss. This off-loss can make any modulator useless. With the calculated field confinement factor, an underestimation of the required interaction length for an EO phase modulator is ensured, but such estimation might lead to a field confinement factor that looks prohibitive for using such modulators. The key benefit of slot waveguides is nevertheless the use of organic materials with EO coefficients that are more than one order of magnitude higher compared to semiconductors like GaAs or strained silicon.

http://dx.doi.org/10.5772/intechopen.75539

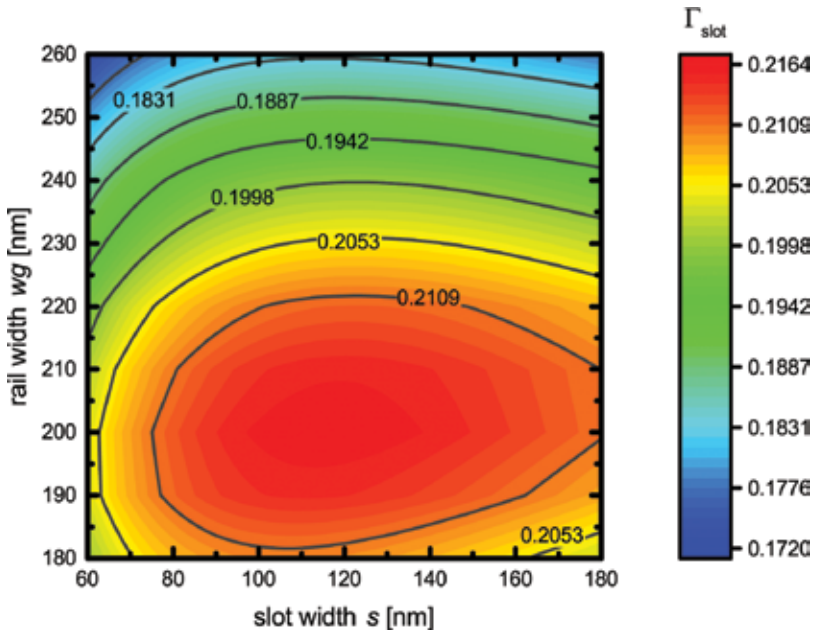


**Figure 12.** Calculated field confinement factor $\Gamma_{slot}$ of an SOI slot waveguide for the slot region as a function of the slot width $s$ and the rail width $wg$.

## 3. Fabrication of silicon-on-insulator slot waveguides

After the physical layout is developed and simulated, the optimized design need to be converted to a chip layout. Then the fabrication can be realized in an SOI pilot line. This section describes a typical process flow, which can be used with a 200 mm SOI wafer and 248 nm optical lithography or electron beam lithography. Commonly, SOI slot waveguides are fabricated by optical lithography, which enables slot width in the range of 120 nm to 200 nm. To reduce the slot width it is possible to use electron beam lithography.

The complete fabrication scheme is illustrated in **Figure 13**. The basis is an SOI wafer with a 220 nm silicon layer on top of a 2 $\mu m$ buried oxide layer. In fact, the silicon layer is the actual waveguide layer. It can be doped in a certain area (**Figure 13a–c**) with boron in order to reduce electric conductivity. In this case, the boron doping concentration is about $10^{17}$ $cm^{-3}$ and, hence, the resulting conductivity is about 11.3 $\Omega^{-1}cm^{-1}$. Then, the waveguide is reduced to create thin slabs, which will be used as the electric connection from the electrodes to the slot waveguide (**Figure 13d–e**). This is followed by etching the slot down until the substrate (**Figure 13f–h**). It is essential to etch it completely because a connection between both silicon rails would lead to a current flow, which in turn induces heat. To further reduce the electric conductivity, another doping step with higher boron doping concentration needs to be performed, as illustrated in **Figure 13i–k**. This higher doping area is placed a few hundreds

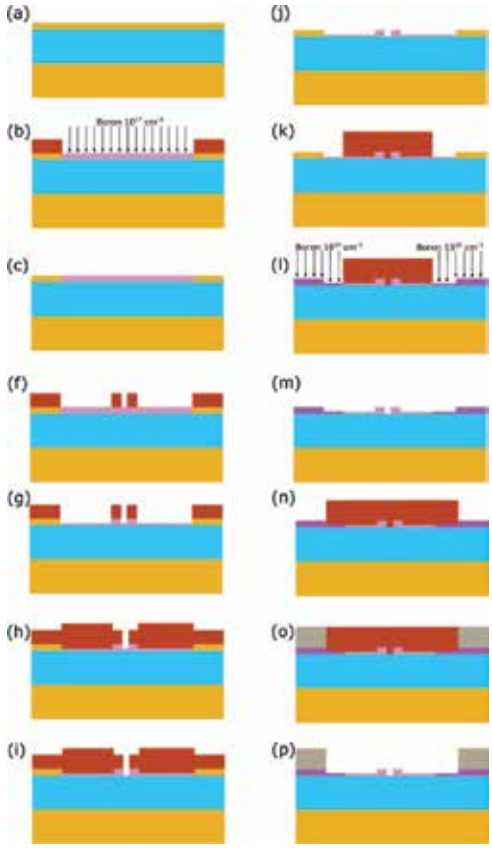


**Figure 13.** Schematic representation of the fabrication flow of a silicon-on-insulator slot waveguide.

of nanometers away from the slot waveguide (for example, 800 nm) to avoid optical losses due to two photon absorption and free carrier absorption. The boron doping concentration is $10^{20}$ $cm^{-3}$ and, hence, the resulting conductivity is about 1177.86 $\Omega^{-1}cm^{-1}$. Finally, the electric contacts are formed by depositing aluminum on the doped silicon (**Figure 13i–n**). A silicide intermediate layer can be used between the aluminum and doped silicon in order to reduce the resistivity.

However, only a few SOI slot waveguide-based ring resonators are published so far. The main reason for this fact is that slot-waveguide structures suffer from relatively high losses, mainly caused by sidewall roughness [24]. As a consequence, slot waveguide resonators like micro-ring resonators have typically small optical quality factors (Q-factors). One possible approach to tackle this problem is to reduce propagation losses in the slot waveguides by atomic layer deposition of thin dielectric films, for example, amorphous titanium dioxide ($TiO_2$) [25, 26]. This reduces, on the one hand, propagation losses but on the other hand, it is associated with additional and not economical production steps, which makes it rather unattractive from the commercial point of view. Another way to tackle this problem is to improve the coupling efficiency. For example, an improvement of 10 times mechanical, thermal the optical Q-factor was demonstrated recently [27].

http://dx.doi.org/10.5772/intechopen.75539

## 4. Electro-optic modulation in slot waveguides

Electro-optic modulators based on slot waveguides typically examine the linear EO effect, also known as Pockels effect, in organic materials such as organic crystals or polymers. In general, an EO polymer consists of a passive matrix of polymer chains that gives the material its mechanical, thermal, and chemical stability. This matrix is doped with active molecules that have a strong Pockels effect. Most EO devices based on organic EO materials use dipolar molecules embedded in or covalently attached to polymeric material lattices. A device-relevant EO activity requires a macroscopic non-centrosymmetric orientation, which is usually achieved by electric field poling of molecules endowed with their own lack of symmetry. This leads to a linear EO effect, which is appropriated for high-frequency applications.

The linear EO effect in terms of the refractive index change $\Delta n$ can be determined by

$$\Delta n = -\frac{1}{2} n_{eop}^3 r E = \frac{1}{n_{eop}} \chi^{(2)} E, \tag{12}$$

where $n_{eop}$ represents the refractive index of the EO polymer, $r$ is the linear EO coefficient, E is the electric field, and $\chi^{(2)}$ denotes the second-order susceptibility. In SOI slot waveguides, the electric field can be determined by $E = U/s$, where $U$ is the applied voltage. Comparing the coefficients in Eq. (12) gives the relation between linear EO coefficient and second-order susceptibility

$$r = -\frac{2\chi^{(2)}}{n_{eop}^4}. \tag{13}$$

The linear EO coefficient $r$ describes the EO activity of a centrosymmetric material and can be represented by [9].

$$r \propto N\beta \left\langle \cos^3\theta \right\rangle \tag{14}$$

Here, $N$ is the chromophore number density or the number of nonlinear molecules in the material contributing to the polarization, $\beta$ represents the molecular first hyperpolarizability, and $\left\langle \cos^3\theta \right\rangle$ denotes the average non-centrosymmetric order parameter.

$\theta$ denotes the angle between molecular dipole axis and the electric field vector. Eq. (14) suggests strategies to increase the linear EO effect:

1. Increasing the chromophore number density $N$.
2. Using chromophores with high first hyperpolarizability $\beta$.
3. Maximizing the average non-centrosymmetric order parameter $\left\langle \cos^3\theta \right\rangle$ by inducing a high molecular orientation.

Such requirements are best met by EO polymers which are dipolar and exhibit a highly polarizable donor-$\pi$-acceptor (D-$\pi$-A) system. This D-$\pi$-A system can support a charge transfer between electron donating and electron withdrawing groups [10]. For electron donating

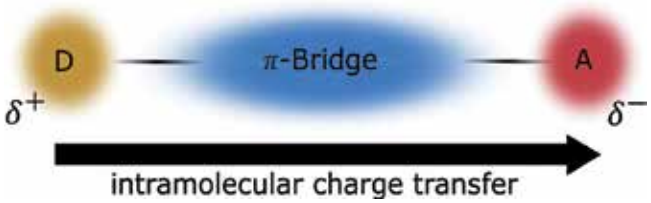


**Figure 14.** D-π-a system. EO polymers are typically composed of electron donating (D) and electron accepting (A) side groups.

usually the following side groups are used: $N(CH_3)_2$, $OCH_3$, OH, while for electron accepting groups the following ones: NO, $O_2N$, CHO, CN. The π-electron conjugated segment serves to transmit the charge, as illustrated in **Figure 14**.

In this work, we demonstrate EO modulation in an SOI slot waveguide using the azobenzene dye Disperse Red 1 doped in poly(methyl methacrylate). This guest-host polymer system is infiltrated into the slot waveguide by spin-coating. A ring resonator is employed to demonstrate intensity modulation. Here, the slot waveguide is partially introduced in the ring. The geometry values are the same as in our previous work in Ref. [11]. This ring resonator has been recently shown to operate efficiently as EO switch [12] and is fabricated in a SiGe BiCMOS pilot line on a 200 nm SOI wafer at the Institute of Innovative Microelectronics IHP in Frankfurt (Oder), Germany. This work, however, demonstrates intensity modulation by applying a function generator to the ground-signal-ground electrodes instead of a DC source. For this experiment, an external cavity laser operating the optical C-band is used as light source, which is polarized to obtain a quasi TE mode in the slot waveguide. A schematic of the complete experimental set-up is shown in **Figure 15**. For our demonstration, we applied a sine signal with a peak-to-peak voltage of 1 V at a frequency of 25 kHz. The oscilloscope traces in **Figure 16** show the applied electrical

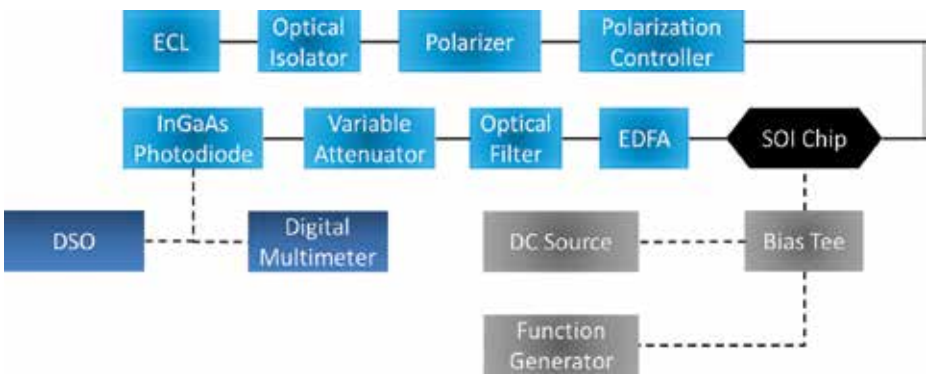


**Figure 15.** Schematic of the experimental set-up for EO modulation. An external cavity laser (ECL) is polarized and coupled to the SOI chip. An erbium doped fiber amplifier (EDFA) is used to amplify the outcoupled light. A 2 nm optical filter is applied to avoid signal noise from the EDFA and a variable attenuator is used to avoid damaging the InGaAs photodetector. Finally, the modulated signal is recorded with a digital sampling oscilloscope (DSO). The digital multimeter was used for wavelength adjustment.

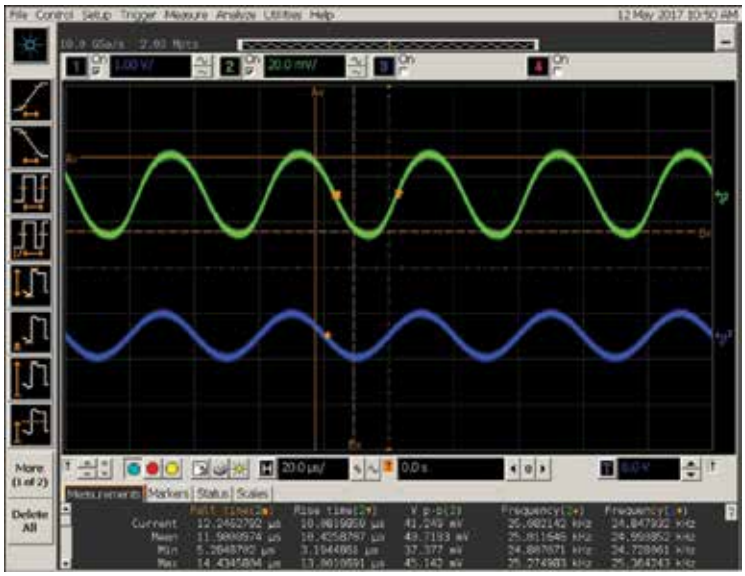

**Figure 16.** Oscilloscope traces of the electrical sine signal (blue) and the modulated optical signal (green). The peak-to-peak voltage of the electrical signal is 1 V and the modulation frequency is 25 kHz.

signal (blue) and the observed optical signal (green). The present experiment demonstrates the feasibility of a polymer filled SOI slot waveguide for EO modulation at low voltages. It is worthwhile to note that the applied voltage of 1 V is compatible with common CMOS-based drivers; making the present approach attractive from the commercial point of view.

## 5. Optical sensing in slot waveguides

The working principle of photonic ring resonators for biochemical sensing is based on refractive index sensing, i.e., the measurement of the resonance wavelength shift $\Delta\lambda$ due to a refractive index change $\Delta n_s$ of the solution containing the analyte in specific concentration. This refractive index change is typically subjected to a change in concentration. In order to measure the resonance wavelengths, the light of a tunable laser is in-coupled to the photonic chip out-coupled via an optical fiber, and detected by a photodiode. According to the resonance conditions, only selected wavelengths can propagate in the ring and distinct resonance peaks appear in the output spectrum.

In principle, the resonant wavelength $\lambda_{res}$ of the device depends on the effective refractive index $n_{eff}$ of the optical waveguide that, in turn, is determined by the refractive index of the analyte. Therefore, by detecting changes in the resonant wavelength $\Delta\lambda$ of the ring, small changes in refractive index $\Delta n_s$ of the solution can be determined. The wavelength shift can be calculated by [13].

$$\Delta\lambda = \frac{\lambda_{res}}{n_g}\Delta n_s \Gamma_{clad}, \tag{15}$$

where $\Gamma_{clad}$ is the field confinement factor in the cladding which has to satisfy the condition $\Delta n_{eff} = \Gamma_{clad} n_s$.

Generally, there are two types of sensing mechanisms, namely homogenous sensing and surface sensing, that a ring resonator can perform. The difference is the origin of sensing signal as shown in **Figure 17**. Homogeneous sensing signals results from the refractive index change induced by the presence of the analytes in the whole region of the evanescent field, which leads to a non-specific measurement. Detection of chemicals, for example, 2-propanol, sodium

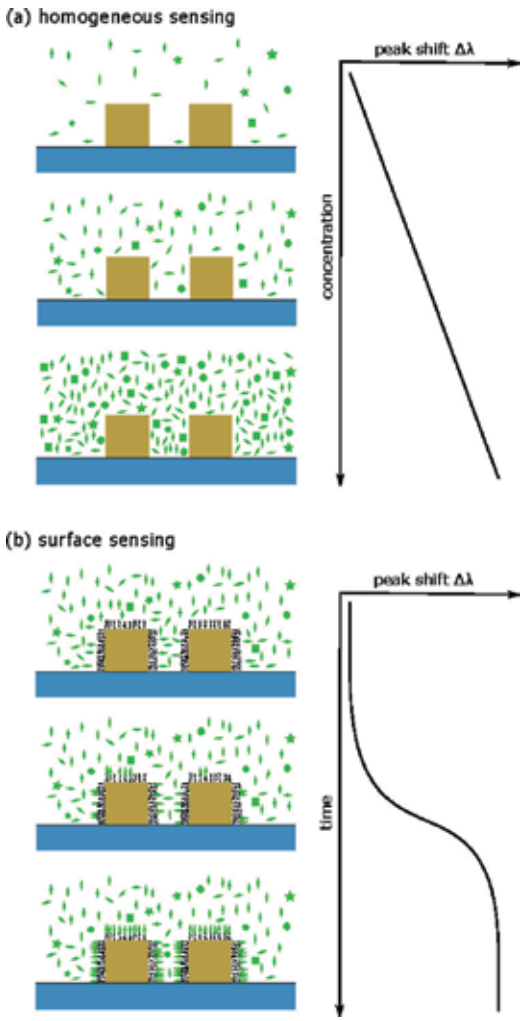


**Figure 17.** Schematic of the surface sensing principle. The cross section shows that the receptor molecules (antibody) are located on top of slot waveguide surface. The resonance peak is shifted due to a specific binding event. From this data the quantity of the adsorbed analyte is obtained.

chloride, and ethylene glycol, has been demonstrated using homogenous sensing [14]. However, homogeneous sensing usually lacks detection specificity.

In contrast, surface sensing signals originate from analytes in the close vicinity of the ring resonator surface [14]. In this case, the surface of the silicon waveguide is modified with an antibody. Only specific analytes can be attached to the antibody, i.e., this analyte-antibody binding leads to a specific measurement. Once the analyte-antibody binding takes place, the residuals can be removed by drying or flushing to enhance the specific measurement. When the antigen, for example, proteins or DNA, interacts with the antibody, the optical wave is influenced in its propagation, the resonance condition changes, and the resonance peak shifts by $\Delta\lambda$. The magnitude of the wavelength shift $\Delta\lambda$ provides information on the quantity of the adsorbed analyte, where the detection limit of the sensor is defined by the minimum resolvable wavelength shift. Moreover, by measuring the peak wavelength shift during the binding process, the binding kinetic can be observed.

However, the main advantage of SOI slot waveguides is the fact that more light can interact with the analyte. A possible explanation for this is the large field confinement factor in the cladding region [15]. This fact leads to an enhanced waveguide sensitivity defined as

$$S_{wg} = \frac{\delta n_g}{\delta n_s}. \tag{16}$$

The waveguide sensitivity, however, does not take into account the resonant structure of widely used ring resonators. Therefore, a second sensitivity is defined as the ring resonator sensitivity given by

$$S_{rr} = \frac{\delta \lambda_{res}}{\delta n_s}. \tag{17}$$

SOI slot waveguide based ring resonators have been demonstrated to achieve more than three times larger ring resonator sensitivities compared to conventional strip waveguide based ring resonators [8]. Notwithstanding this, slot waveguide based ring resonators have not been yet translated into a large overall sensitivity since the optical losses increase the detection limit described by the full width at half maximum (*FWHM*). At large *FWHM* the resonance peak shift may not be resolved. To take both into account (ring resonator sensitivity and the *FWHM*), we can define a figure of merit *FOM* given by

$$FOM = \frac{S_{rr}}{FWHM}. \tag{18}$$

However, the experimental demonstration of surface sensing is beyond the scope of this work, as it needs sophisticated surface modification techniques. Instead, this work focuses on homogenous sensing and demonstrates an exemplary detection of 2-propanol to prove the feasibility of the novel ring resonator concept. This demonstration has the aim of verifying that the concept has practical potential.

We will now turn to the experimental demonstration of homogeneous sensing. To validate our theoretical investigations we fabricated a hybrid-waveguide ring resonator with an SiGe

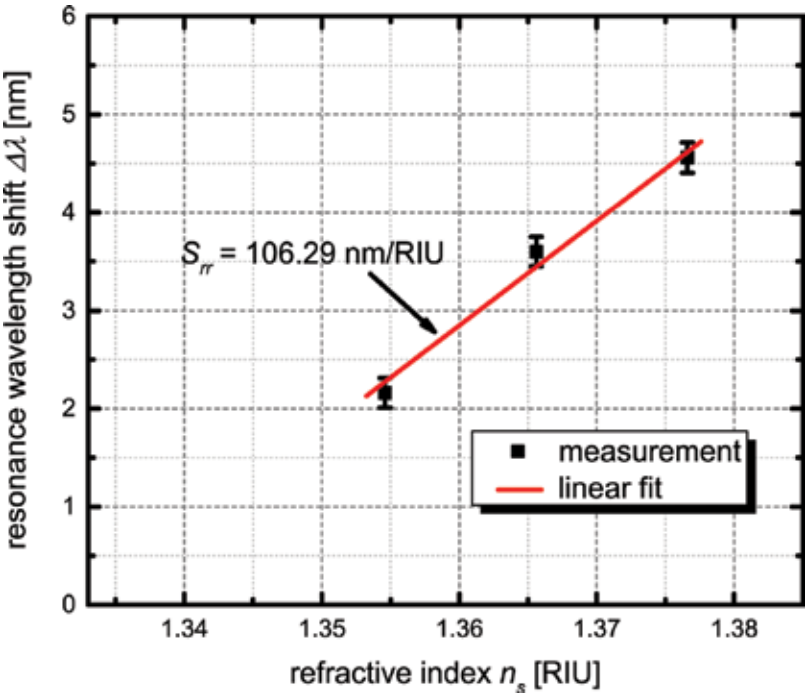


**Figure 18.** Measured resonance wavelength shift versus refractive index of the test liquid (100, 75, and 50% 2-propanol in deionized water). The slope of the linear fit gives the resonator sensitivity of $S_{rr} = 106.29$ nm/RIU [21].

BiCMOS pilot line. The slot width of the fabricated device is $s = 150$ nm and the rail width is $wg = 180$ nm. A comprehensive study and all geometric parameters of the hybrid-waveguide ring resonator can be found in Ref. [21].

As preliminary test, we measured 100, 75 and 50% concentrations of 2-propanol in de-ionized water. The test liquids are directly dropped onto the surface of the sensor. The refractive indices of the liquids were independently measured by means of a refractometer (Kern ORT 1RS) obtaining 1.3766, 1.3656, and 1.3546 for 100, 75, and 50%, respectively, in good agreement with literature values [22, 23]. **Figure 18** shows the resonance wavelength shift $\Delta\lambda$ versus refractive index $n_s$ of the liquid solutions [21]. Each measurement is carried out five times to prove reproducibility. Regression analysis was used to predict the ring resonator sensitivity. A ring resonator sensitivity of $S_{rr} = 106.29$ nm/RIU and a *FOM* of 1337 were observed. For comparison, a strip waveguide-based ring resonator has typically a ring resonator sensitivity of about 70 nm/RIU and a *FOM* of 903. This result demonstrates the feasibility of SOI slot waveguides for biochemical sensing and the advantage in terms of sensitivity with respect to SOI strip waveguides.

## 6. Summary

In conclusion, this work has theoretically and experimentally studied aspects of SOI slot waveguides. Simulation and analysis of SOI slot waveguides have been carried out using a

finite element method based mode solver. We have determined field confinement factors for the slot and cladding region for applications as EO modulator and optical sensor, respectively. According to the present simulation study, SOI slot waveguides provide about five times higher field confinement in the cladding region with respect to conventional SOI strip waveguides. These results can be used for design optimizations in order to achieve optimum SOI slot waveguide dimensions for sensing applications.

The present study was designed to determine the optical and electro-optical characteristics of SOI slot waveguide-based devices. The presented hybrid-waveguide ring resonator consisting of a slot waveguide implemented in a strip waveguide-based ring resonator has a set of characteristics, which makes it an excellent and unique candidate for low power switches and modulators in the field of optical communication systems. The device was fabricated using CMOS fabrication processes, which enables high integration density and scalable, large-volume manufacturing. One of the more significant findings to emerge from this study is the significantly improved EO response compared to common ring-based modulators making use of the plasma dispersion effect, giving rise to the perspective of sub-femtojoule EO switching. In addition, we have performed intensity modulation at 25 kHz. So far, these characteristics are not combined in any other ring resonator to our knowledge. Moreover, there is still significant room for enhancing the device performance in terms of EO response, for example, by taking advantage of the continuously improving EO polymers. Taken together, the presented results suggest that the slot waveguide-based ring resonators are promising candidates for future EO switches, modulators and tunable filters. Future work should investigate the poling procedure to achieve a larger linear EO effect and therefore, higher modulation frequencies using the same EO polymer. Another limitation is the utilized EO polymer. Using advanced EO polymers indicate that the current results could be further improved. Notwithstanding these limitations, the device performance observed in this study indicate the great promises of using EO polymers which are essential for various hybrid photonic devices particularly for low-power applications. The demonstrated ring resonator opens a new route toward promising applications in the realm of polymer-based non-linear photonics.

A further aspect investigated in this work was the use of SOI slot waveguides for optical sensing. As proof of principle, homogeneous sensing of different concentrations of 2-propanol in de-ionized water was performed. This study set out to determine the overall sensitivity, taking into account the optical losses and the ring resonator sensitivity. It turns out that the slot waveguide-based ring resonator has a higher overall sensitivity than most traditional ring resonator sensors based on strip waveguides. Thus, it appears to be promising for a wide range of sensing applications, including biochemical sensors.

## Author details

Patrick Steglich

Address all correspondence to: patrick.steglich@th-wildau.de

Technical University of Applied Sciences Wildau, Germany

## References

[1] Almeida VR, Xu Q, Barrios CA, Lipson M. Guiding and confining light in void nanostructure. Optics Letters. 2004;**29**(11):1209-1211. DOI: 10.1364/OL.29.001209

[2] Leuthold J, Koos C, Freude W, Alloatti L, Palmer R, Korn D, Pfeifle J, Lauermann M, Dinu R, Wehrli S, Jazbinsek M, Gunter P, Waldow M, Wahlbrink T, Bolten J, Kurz H, Fournier M, Fedeli J-M, Yu H, Bogaerts W. Silicon-organic hybrid electro-optical devices. Selected Topics in Quantum Electronics. 2013;**19**(6):114-126. DOI: 10.1109/JSTQE.2013.2271846

[3] Alloatti L, Palmer R, Diebold S, Pahl KP, Chen B, Dinu R, Fournier M, Fedeli J-M, Zwick T, Freude W, Koos C, Leuthold J. 100 GHz silicon-organic hybrid modulator. Light: Science and Applications. 2014;**3**(5):e173. DOI: 10.1038/lsa.2014.54

[4] Kong M, Jiang Y. Transverse magnetic modes in planar slot waveguides. Journal of the Optical Society of America B: Optical Physics. 2015;**32**(10):2052-2060. DOI: https://doi.org/10.1364/JOSAB.32.002052

[5] Chrostowski L, Hochberg M. Silicon Photonics Design: From Devices to Systems. 1st ed. Cambride: Cambridge University Press; 2015

[6] Baehr-Jones T, Hochberg M, Walker C, Scherer A. High-q optical resonators in silicon-on-insulator-based slot waveguides. Applied Physics Letters. 2005;**86**(8):081101. DOI: http://dx.doi.org/10.1063/1.1871360

[7] Vivien L, Pavesi L. Handbook of Silicon Photonics. 1st ed. Boca Raton: Taylor & Francis; 2013. 835 p

[8] Claes T, Molera JG, De Vos K, Schacht E, Baets R, Bienstman P. Label-free biosensing with a slot-waveguide-based ring resonator in silicon on insulator. IEEE Photonics Journal. 2009;**1**(3):197-204. DOI: 10.1109/JPHOT.2009.2031596

[9] Larry R. Dalton, Peter Günter, Mojca Jazbinsek, O-Pil Kwon, Philip A. Sullivan. Organic Electro-Optics and Photonics: Molecules, Polymers and Crystals. 1st ed. Cambridge University Press; 2015. 300 p

[10] Yesodha SK, Pillai CKS, Tsutsumi N. Stable polymeric materials for nonlinear optics: A review based on azobenzene systems. Progress in Polymer Science. 2004;**29**(1):45-74

[11] Steglich P, Mai C, Stolarek D, Lischke S, Kupijai S, Villringer C, Pulwer S, Heinrich F, Bauer J, Meister S, Knoll D, Casalboni M, Schrader S. Novel ring resonator combining strong field confinement with high optical quality factor. IEEE Photonics Technology Letters. 2015;**27**(20):2197-2200. DOI: 10.1109/LPT.2015.2456133

[12] Steglich P, Mai C, Stolarek D, Lischke S, Kupijai S, Villringer C, Pulwer S, Heinrich F, Bauer J, Meister S, Knoll D, Casalboni M, Schrader S. Partially slotted silicon ring resonator covered with electro-optical polymer. Proceedings of SPIE. 2016;**9891**(98910R):98910R-98910R-7. DOI: 10.1117/12.2217725

[13] Steglich P, Villringer C, Pulwer S, Casalboni M, Schrader S. Design optimization of silicon-on-insulator slot-waveguides for electro-optical modulators and biosensors. In: Ribeiro P, Raposo M, editors. Photoptics 2015. 1st ed. Cham: Springer International Publishing; 2016. pp. 173-187. DOI: 10.1007/978-3-319-30137-2_11

[14] Sun Y, Fan X. Optical ring resonators for biochemical and chemical sensing. Analytical and Bioanalytical Chemistry. 2011;**399**(1):205-211. DOI: 10.1007/s00216-010-4237-z

[15] Steglich P, Villringer C, Dümecke S, Michel YP, Casalboni M, Schrader S. Silicon-on-insulator slot-waveguide design trade-offs. In: Ribeiro P, Raposo M, editors. International Conference on Photonics, Optics and Laser Technology; Berlin. IEEE; 2015. pp. 47-52. DOI: http://ieeexplore.ieee.org/stamp/stamp.jsp?tp=&arnumber=7513125&isnumber=7513093

[16] Malitson IH. Interspecimen comparison of the refractive index of fused silica. Journal of the Optical Society of America. 1965;**55**:1205-1209. DOI: 10.1364/JOSA.55.001205

[17] Salzberg CD, Villa JJ. Infrared refractive indexes of silicon germanium and modified selenium glass. Journal of the Optical Society of America. 1957;**47**(3):244-246. DOI: 10.1364/JOSA.47.000244

[18] Korn D, Palmer R, Yu H, Schindler PC, Alloatti L, Baier M, Schmogrow R, Bogaerts W, Selvaraja SK, Lepage G, Pantouvaki M, Wouters JMD, Verheyen P, Van Campenhout J, Chen B, Baets R, Absil P, Dinu R, Koos C, Freude W, Leuthold J. Silicon-organic hybrid (SOH) IQ modulator using the linear electro-optic effect for transmitting 16QAM at 112 Gbit/s. Optics Express. 2013;**21**(11):13219-13227. DOI: 10.1364/OE.21.013219

[19] Palmer R, Alloatti L, Korn D, Schindler PC, Baier M, Bolten J, Wahlbrink T, Waldow M, Dinu R, Freude W, Koos C, Leuthold J. Low power Mach-Zehnder modulator in silicon-organic hybrid technology. IEEE Photonics Technology Letters. 2013;**25**(13):1226-1229. DOI: 10.1109/LPT.2013.2260858

[20] Palmer R, Alloatti L, Korn D, Schindler PC, Schmogrow R, Heni W, Koenig S, Bolten J, Wahlbrink T, Waldow M, Yu H, Bogaerts W, Verheyen P, Lepage G, Pantouvaki M, Van Campenhout J, Absil P, Dinu R, Freude W, Koos C, Leuthold J. Silicon-organic hybrid MZI modulator generating OOK, BPSK and 8-ASK signals for up to 84 Gbit/s. IEEE Photonics Journal. 2013;**5**(2):6600907-6600907. DOI: 10.1109/JPHOT.2013.2258142

[21] Steglich P, Villringer C, Pulwer S, Heinrich F, Bauer J, Dietzel B, Mai C, Mai A, Casalboni M, Schrader S. Hybrid-waveguide ring resonator for biochemical sensing. IEEE Sensors Journal. 2017;**17**(15):4781-4790. DOI: 10.1109/JSEN.2017.2710318

[22] Wei T, Han Y, Li Y, Tsai H-L, Xiao H. Temperature-insensitive miniaturized fiber inline Fabry-Perot interferometer for highly sensitive refractive index measurement. Optics Express. 2008;**16**(8):5764-5769. DOI: 10.1364/OE.16.005764

[23] Sun X, Dai D, Thylén L, Wosinski L. Double-slot hybrid Plasmonic ring resonator used for optical sensors and modulators. Photonics. 2015;**2**(4):1116. DOI: 10.3390/photonics2041116

[24] Ding R, Baehr-Jones T, Kim W-J, Xiong X, Bojko R, Fedeli J-M, Fournier M, Hochberg M. Low-loss strip-loaded slot waveguides in silicon-on-insulator. Optics Express. 2010;**18**(24): 25061-25067. DOI: 10.1364/OE.18.025061

[25] Alasaarela T, Korn D, Alloatti L, Saynatjoki A, Tervonen A, Palmer R, Leuthold J, Freude W, Honkanen S. Reduced propagation loss in silicon strip and slot waveguides coated by atomic layer deposition. Optics Express. 2011;**19**(12):11529-11538. DOI: 10.1364/OE.19.011529

[26] Saynatjoki A, Karvonen L, Alasaarela T, Tu X, Liow TY, Hiltunen M, Tervonen A, Lo GQ, Honkanen S. Low-loss silicon slot waveguides and couplers fabricated with optical lithography and atomic layer deposition. Optics Express. 2011;**19**(27):26275-26282. DOI: 10.1364/OE.19.026275

[27] Zhang W, Serna S, Roux XL, Alonso-Ramos C, Vivien L, Cassan E. Analysis of silicon-on-insulator slot waveguide ring resonators targeting high Q-factors. Optics Letters. 2015; **40**(23):5566-5569. DOI: https://doi.org/10.1364/OL.40.005566

Chapter 11

# Investigation of Ring Waveguide Add/Drop with Grating Couple

Jian-Chiun Liou

Additional information is available at the end of the chapter

http://dx.doi.org/10.5772/intechopen.76800

**Abstract**

The silicon photon technology platform is low transmission loss, small size, low cost of the process and easy integration with electronic components and other characteristics. It is designed to design high-density optical communication network system has a considerable advantage. Such as high-density wavelength division multiplexing (DWDM) system, that is through the different wavelengths of signal processing. So that it can be used for optical connection switches, routing and other applications. It composed of a DWDM system, through the Mach-Zehnder interferometer, ring resonator (Add/Drop), array waveguide grating (AWG) and grating coupler and other structural components. It is designed by components to filter, switch, adjust and detect functions. The characteristics of the ring resonator are for wavelength selection. It is suitable for the design of optical switches, signal switching and modulation applications. It is also the focus of this lab and this chapter to explore and study. The general edge coupling, between the optical fiber and the waveguide dimension is very different. As a result, larger insertion loss is caused. This study uses the vertical coupling method to investigate the characteristics of a ring resonator.

**Keywords:** ring waveguide, add/drop, grating couple

## 1. Introduction

Big data era is entering reality. However, due to the limitations of electronic physical characteristics, the traditional electrical interconnect [1–12] are increasingly faced with the challenge of rapidly expanding data transmission due to their technical development. In terms of bandwidth expansion, transmission delay, loss control, signal enhancement and other aspects of the urgent need for a fundamental breakthrough. This prompted researchers to start looking

for new solutions. Si-based photonic devices use optical transmission signals. Compared to electrons, photons travel much faster than the electron's velocity, and the mechanism by which light transmits signals is the wave impedance transformation, which consumes very little energy. The signal is not prone to distortion during transmission. In large bandwidth conditions can be greater transmission capacity. And silicon-based photonic devices also have complementary metal oxide semiconductor (CMOS) process compatible, small size, communication band transparent, anti-radiation and so on. It is precisely because of large bandwidth, low latency, low power consumption, low crosstalk and other advantages [13–21]. Emerging information technologies such as optical communications, optical interconnects and optical sensing based on the integration of silicon photonics demonstrate the development trend of building new information hardware. It is becoming an important foundation for a new generation of information systems and networks. A key issue that cannot be ignored for Si-based photonic integrated chips is the input and output of optical signals. In particular, silicon is an indirect bandgap material. Luminous efficiency has not yet reached the practical requirements. The prior art approach required the introduction of a separate light source from outside the photonic chip or the use of an on-chip hybrid integrated light gain material. Therefore, the photonic integrated chip needs among high efficiency, large bandwidth and easy integration of the optical coupling structure both in and out of the chip. Commonly used two kinds of coupling methods generally use the end level coupling structure or on-chip vertical coupling structure. It is compared to other various opto-couplers. The grating coupler uses the vertical diffractive optical field of the on-chip optical waveguide to realize the optical signal input or output of the wafer. It has the advantages of easy online on-chip testing, no wafer or wafer pretreatment, and no strict space limitations. Become a hot spot in the field of silicon-based photonics integration. With the gradual improvement of CMOS process accuracy. Silicon-based waveguides at or near the nanometer level are gradually getting out of the process limitations [22–36]. Raster coupler also gradually shows its unique technical advantages. This research mainly expounds the development status and future trend of grating coupler in recent years.

## 2. Grating coupler and characteristics

Silicon-based grating coupled devices can be divided into one-dimensional structure and two-dimensional structure. According to the grating cell cycle, duty cycle, etching depth, etching angle can be divided into uniform grating coupler, non-uniform grating coupler and blazed grating coupler. Gratings are coupling functional devices in silicon-based photonic integrated wafers. The main research contents of grating coupler include coupling efficiency, coupling angle, working wavelength bandwidth, polarization correlation and so on.

This uniform grating coupler refers to the unit period of each grating as shown in **Figure 1**, duty cycle, etching depth are constant. Its structure is that the slit is generally perpendicular to the interface. The diffraction mode field of a uniform periodic grating coupler decays exponentially. The mode field of single mode fiber is Gaussian distribution. The overlap between the two $\eta_3$ is limited. This is a classic model of a grating coupler. The coupling efficiency of the grating coupler is a coupling efficiency $\eta_3$ determined by the diffraction intensity, the

http://dx.doi.org/10.5772/intechopen.76800

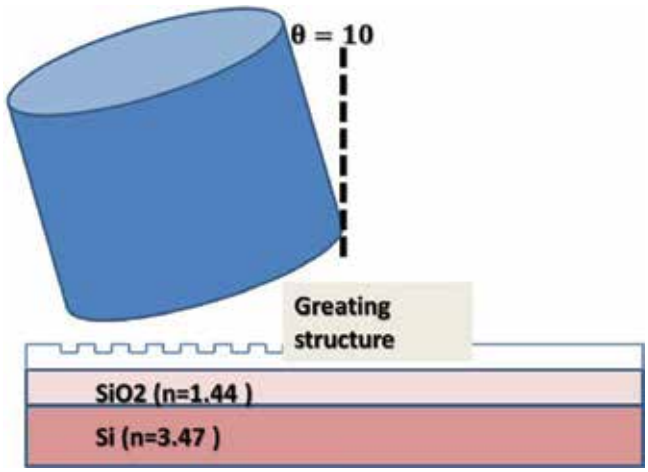


**Figure 1.** Silicon-based grating coupled.

directional efficiency and the overlapping integral of the coupling light field. Coupling efficiency is greatly affected. It is difficult to achieve efficient coupling. There are many ways to enhance the coupling efficiency. For example, an increase of multilayer dielectric mirrors, metal mirrors, overlays, and large duty cycle grating structures utilizing the slot effect. These methods either reduce reflection or enhance directivity, or reduce the reflection loss between the grating coupler and the optical fiber. This attenuated diffraction mode field and the optical mode field overlap integral is small. Coupling efficiency is greatly limited. The advantage of a uniform grating coupler is CMOS-compatible. The process is relatively simple. Moreover, the study of uniform structure is more comprehensive. Its processing method is more mature.

Non-uniform grating coupler effectively solves this mode field mismatch problem. The so-called non-uniform grating coupler, refers to the cycle and duty cycle or etching depth changes with the direction of light a quasi-periodic structure. Due to the fact that this structure no longer maintains a strict periodicity, the diffraction factor changes correspondingly as the grating cell structure changes. Therefore, the diffraction mode field no longer exhibits exponential decay. It is theoretically possible to achieve a Gaussian distribution of the diffracted light field. A non-uniform grating coupler structure exhibiting a Gaussian type in the diffraction mode field can be formed by a set of narrow-width-expanded slits. Etch depth from shallow to deep. This waveguide-to-grating reduction of the structure reduces the reflection loss, which is very helpful in improving the coupling efficiency due to the process challenges. This grating coupler structure developed slowly from the theory. One commonly used method of controlling the depth of etching is to take advantage of the load (hysteresis) effect of plasma etching. Optimize the correspondence between etching depth and slit width.

This is with the improvement of craftsmanship. Fine structures below 50 nm are also possible. The minimum width of the non-uniform grating coupler made by our research group is about 40 nm. The experimentally measured single-ended coupling loss is only 0.85 dB. Solve the problem of non-uniform periodic grating coupler on the fine processing requirements.

Researchers at OFC/NFOEC 2013 presented a method for double-depth etching, as shown in **Figure 3(a)** . This method uses several pairs of shallow etched raster to replace the front narrow groove grating pairs. This is due to the shallow depth of etching. It reaches the same coupling strength as the deep etched grating. It is necessary to increase the width of the groove. Reduce the technical difficulty. The minimum groove width in this article is 135 nm. The coupling loss is about 1.5 dB in the vertical coupling structure.

All along, to enhance the technology is to reduce the second-order reflections. It is improving the coupling efficiency. The grating coupler diffraction angle is about 10° angle. But this kind of declination not only has the limitation to the practical application. It caused packaging difficulties. Hinder the large-scale integration of the device. Vertical coupling becomes another problem to be solved that limits the practical application of the grating coupler after the coupling efficiency. For 0° declination, which is the need for vertical coupling is even more pressing. It is a uniform grating coupler or a non-uniform grating coupler. The problem of vertical coupling has not been well solved. There is second order reflection in resonance state. Second order reflection greatly reduces the coupling efficiency. In the detuning state, the second order reflections disappear. Coupling efficiency increases, but vertical coupling cannot be achieved. It can be seen from the Prague relations that it is to achieve vertical coupling. It must eliminate or reduce the second order reflections. Known methods have been the addition of distributed Bragg reflector (DBR) mirrors. The reflected light of the DBR mirror is canceled by the interference of the second order reflected light.

In this study, vertical coupling of 40% coupling efficiency was achieved by adding DBR mirrors. Its efficiency is close to the coupling efficiency (44%) without a DBR mirror. It is only weakening second-order reflections by process deviation. It cannot be completely eliminated. Coupling efficiency curve will fluctuate. And DBR reflector parameters of the process control are difficult. Changing the distance between the coupler and the mirror by 100 nm cancels out the interference and constructs the interference phase. The efficient is coupling into a great loss. Therefore, it is necessary to further study and improves the DBR mirror grating structure is the best way to eliminate second-order reflection is blazed grating. The slits of the blazed grating are not perpendicular to the wafer surface. Instead, there is a blaze angle in the normal direction of the raster plane. The diffraction mode field is the superposition of the total diffraction mode field. Blazed grating processing requirements is incompatible with CMOS process. For the process of the problem, the research proposed a gradual change of the gradient grating coupler. Use the multi-step structure instead of the inclined surface of the blazed grating. Asymmetric sub-grating structures proposed by researchers can theoretically be vertically coupled. At the same time coupling efficiency is not much loss.

## 3. Two-dimensional grating coupler

Two-dimensional grating coupler can be roughly divided into two kinds. One is a grating coupler similar to a photonic crystal structure. The other is the curved grating coupler. The two-dimensional photonic crystal grating coupler is proposed to solve the polarization problem in the grating waveguide as shown in **Figure 2**. The large difference is in the transmission

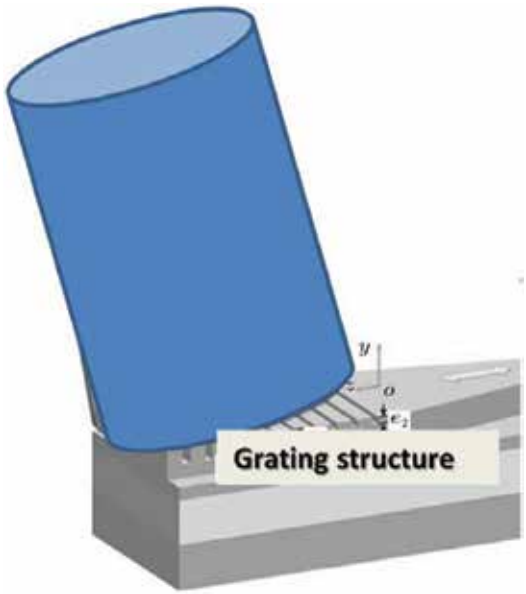


**Figure 2.** Two-dimensional grating coupler.

characteristics of the two transmission modes (TE, TM mode) in the grating coupler. A typical grating coupler can only transmit one mode. Transmission loss to another mode is relatively large. Waveguide birefringence is commonly used to describe polarization dependence. Defined as the difference between the effective refractive index or the group refractive index of the TE and TM modes, $\Delta n = nTE_{eff} - nTM_{eff}$. $TE_{eff}$ and $TM_{eff}$ are refractive index of the TE and TM modes. The ideal polarization correlation is zero. Zero birefringence is the inability to precisely control the waveguide size. Smaller size deviations result in changes in polarization dependence. In addition, the polarization dependence is also related to the heat outside the waveguide, pressure, etc., to achieve polarization insensitivity is very difficult.

A grating coupler for a two-dimensional photonic crystal is another solution. The light of different polarization state is separated in the grating coupler. In one path, the TM mode is changed into the TE mode, and the TE mode is transmitted in different waveguides. Finally, it received by another two-dimensional photonic crystal grating coupler. Compared with the former method, the process is relatively less difficult. This grating coupler requires exactly two waveguide devices. Otherwise there will be distortion in the synthesis. Arc grating coupler can effectively increase the degree of integration. Grating couplers and transmission waveguides typically have a pitch of more than 100 μm. An arcuate grating coupler takes advantage of the optical focusing characteristics of a circular or oval structure. All the arcs have a common focus. The waveguide is placed at this focus. This greatly reduces the spacing between the grating region and the waveguide. Arc grating coupler and waveguide spacing is generally 20 μm or less. Arc grating coupler increases the integration density at the same time. The additional loss between the waveguide and the waveguide is also reduced. The reported coupling efficiency of the curved grating coupler is 1.25 dB.

An infinitely long uniform grating with wavelength selectivity, in practical applications, the grating length is limited. This creates a spectral broadening. This broadening has a certain limit. Since the grating structure parameters of the non-uniform grating coupler are not fixed values. According to the Bragg formula, the diffracted waves no longer maintain a single wavelength. Chirp Structure in Non-uniform Grating Coupler. It is raised in order to improve the bandwidth. It compared to a uniform grating coupler. Chirped grating adds a concept of chirp. It is usually the grating cell cycle changes. The increase in bandwidth is mainly determined by the amount of chirp. The University of Hong Kong used a "fishbone" structure in the fabrication of sub-wavelength waveguide grating coupling devices. Compared to normal grating structures, this fishbone The 3 dB bandwidth of the structured grating coupler increases while reducing the back reflection, reaching 90 around 1530 nm, while the curved grating reduces the transmission loss with a theoretical result of 1.7 dB The grating coupling loss is 3.5 dB.

The chirped grating used in this study is a chirp structure with uniformly varying periods. The grating period changes linearly. Analogies show that the 3 dB bandwidth of a chirped grating increases to 140 nm at a grating average period of 700 nm, a chirp of 200 nm and a grating period of 20. The center wavelength is in the vicinity of 1550 nm. The experimentally measured 3 dB bandwidth is 120 nm, which is similar to the simulation results.

## 4. Ring waveguide add/drop

3D drawing of ring laterally coupled (left) and vertically coupled (right) to the straight waveguides.

The general application of this silicon-on-silicon micro-ring thermocouple switch is shown in **Figure 3**. The advantages of silicon nanocrystals are absorbing layers instead of polymer materials. It is compatible with standard micro-process technology. Silicone crystals have a wide absorption band which can extend close to the IR band. This system includes several features, the temperature dependence of refractive index. Silicon materials usually have higher refractive index temperature dependence than glass materials. Silicon temperature coefficient of about −0.075/°C grade. It is suitable for thermo-optic switch, silicon material refractive index temperature dependence. Other inorganic material temperature difference is relatively large and unstable. Silicon materials have low voltage, low current drive characteristics. It is switching time up to a few msec. It is suitable for wavelength tunable filter. It is heated silicon material refractive index increases. The wavelength of the optical filter will move towards long wavelengths. When the pulse wave is added, the rise time is about 25 msec and the fall time is about 30 msec. Waveform is high on (Pump on) 150 msec. The resulting power is 3.4 μW, low off (Pump off) 150 msec. It corresponds to the thermal optical switch displacement resonance wavelength of about 5 pm. Grating coupling effects via micro-cycle. This design structure is the most original resonant spectrum output to the optical detector. It observes resonance waves. It supplies a pulse of power to make the resonance wave read out by the optical detector displacement spectrum.

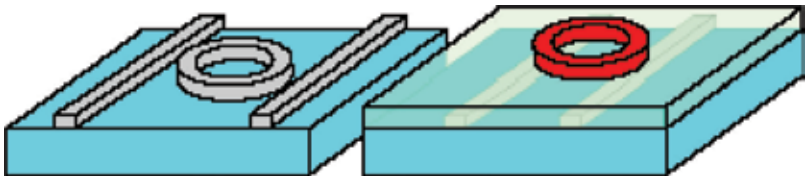

**Figure 3.** 3D drawing of ring laterally coupled (left) and vertically coupled (right) to the straight waveguides.

The thermo-optic switch calculates the switching energy, $H = hA\delta T$, where h is the total switching energy of the resonant center wavelength to be shifted, which is calculated by dividing the energy of the silicon (~ $10^{-5}$/° C). The material heat transfer coefficient in the air, A is the sphere size. This circle diameter is 150 μm, Q = 3 × $10^{-5}$ its resonance wavelength at 1450 nm, so the wavelength shift is ~ 4.8 pm. = 4.8/10 = 0.48° C, h = 81 W/m$^2$/° C for silicon rings. It calculate the required switching energy H = 2.9 μW.

The microsphere temperature reaches equilibrium after power is turned on and off. In other words, that in these microspheres must reach a certain temperature stable in the surrounding air. in order to make the desired resonant frequency shift very accurately fall in the desired band. The pulse signal has a very good control of the drive. This study based on micro-ring heat. The optical switch specially designs the precise power signal control circuit, which obtains better optical information processing efficiency for further breakthrough in the optical communication field.

## 5. Experiment and results

Edge coupler for wavelength selection platform is shown in **Figure 4**. The characteristics of a micro-switch ring wavelength selective switch are analyzed. The working states of the components and corresponding switching operations are analyzed. A new light intensity transfer function formula is used to numerically compare the spectral responses of different operating states and the switching responses of different switching operations. The results show that the device can realize the signal wavelength of four ways of simultaneous access of three channels, simultaneous access of two channels, single-channel access and no-channel access Selective access, multi-channel access to the open-circuit crosstalk performance deterioration, off-state crosstalk performance is not affected. The realization of the device access conversion between the switching operation can be divided into three categories. It switches operation to achieve the best off. The change of the index of refraction of small micro-rings during state crosstalk is about 6.0 × $10^{-3}$. The value of the change refraction index is in small micro-rings. It fully switched is less than 8.0 × $10^{-4}$. It indicates that it is easy to realize by thermo-optic effect Switching operation, and temperature control of the larger tolerance, the loss of the device switching characteristics of the results show that the loss can be based on the actual value. The refractive index of the micro-ring value of the passage is closed.

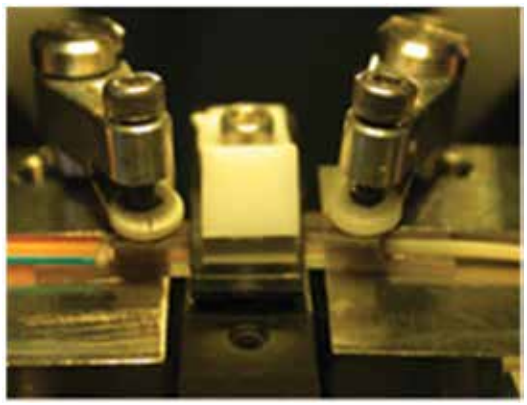

**Figure 4.** Edge coupler for wavelength selection platform.

In photonic multiplexing signal processing circuit, it can change the frequency and output amplitude of the size of the functional circuitry. Multiprocessing signal function lies in the large optical switch array selection (Addressing). It can quickly indicate which one of the optical switches is going to act as a thermo-optic effect as shown in **Figure 5**. It is fed into the desired temperature relative to the waveform and amplitude selected. It causes the temperature to be generated to correspond to this wavelength ($\lambda$). This so-called exchange of light signals is controlled by the thin film heating elements distributed in the polymer stack. The current through the heater cause the metal film heat as shown in **Figure 6**. It changes the distribution of heat within the branching area of the waveguide, causing the refractive index of the waveguide below it to change. It can guide the optical coupling from the main waveguide to the target branch waveguide, and realize the light switching action as shown in **Figure 7**.

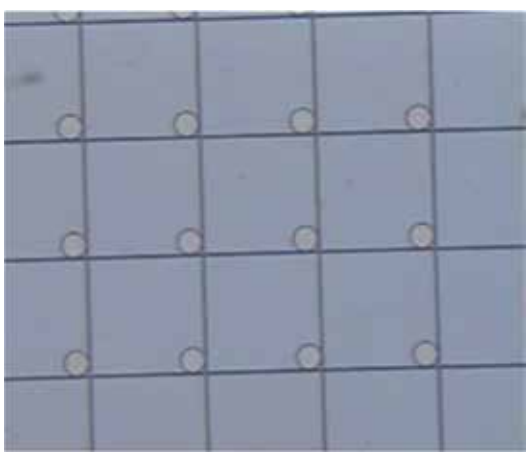

**Figure 5.** The optical micro-ring switches.

http://dx.doi.org/10.5772/intechopen.76800

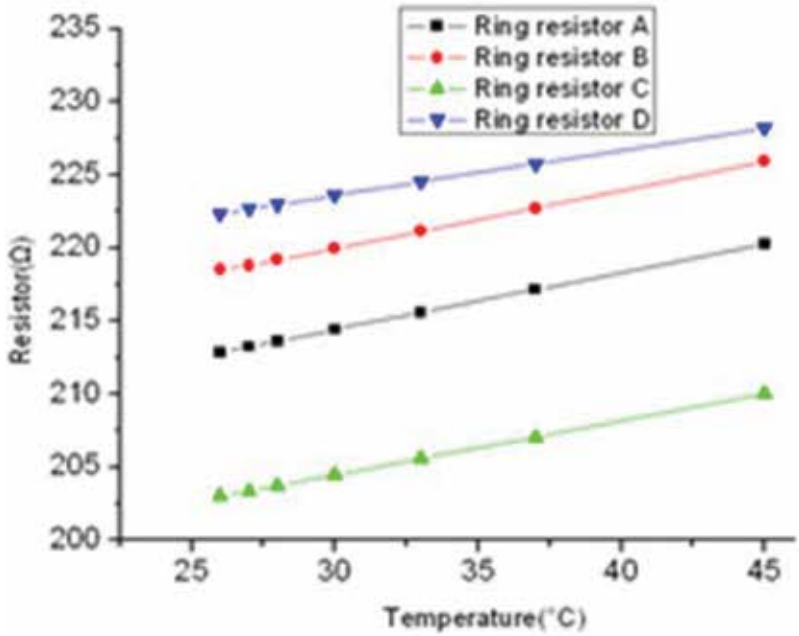


**Figure 6.** Different ring resister with difference value of temperature.

The system delivers laser light through a tunable laser (Yenista Tunicss-T100S) with a wavelength range of 1490 to 1640 nm and a resolution of 1 pico-meter. The laser light is transmitted through the fiber to a 2 × 2 splitter The splitter transmits the laser light to one end of the Gas cell and one end of the polarization controller respectively. Gas cell can generate absolute position at a specific wavelength. It is able to generate wavelength calibration position axis for the measurement of components. Through the polarization controller is the component side. It is through the polarization controller to control the maximum intensity of light detector straight. Laser light is TE polarized incident. It propagates through the fiber and is coupled through two grating couplers. At the same time through both ends of the InGaAs photodetector with amplification function to receive the last as shown in **Figure 8**. The system converts the measured optical signal into an electrical signal. It is through the BNC cable to send data to the computer.

In Add/drop condition is shown in **Figure 9**, an incident light enters from the input port of the optical waveguide. Part of the energy continues to propagate forward through the coupling region during transmission. A portion of the energy is coupled to the ring resonator. The energy coupled to the ring resonator is after a half-turn. A portion of the energy is coupled to the drop port. After the remaining energy is further circulated for half a turn, a part of the energy will be coupled back to the optical waveguide. The remaining energy will continue to maintain the above mechanism for dissemination. It is until the energy depleted so far. It is selectivity to wavelengths through the ring resonator. It can effectively filter or capture the wavelength of the action. It can achieve the effect of controlling the wavelength.

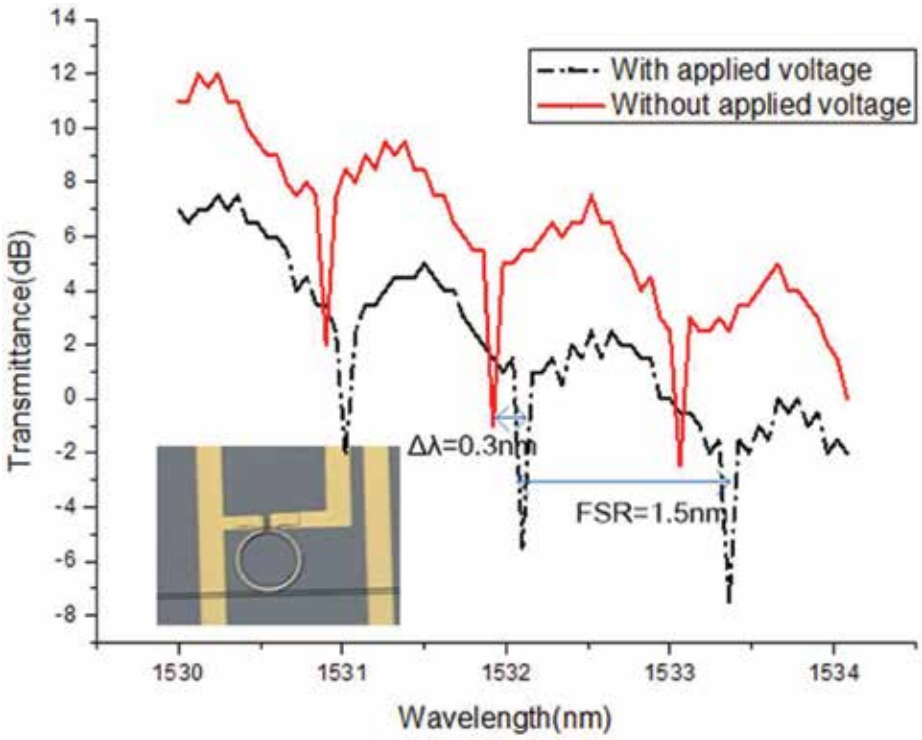


**Figure 7.** Wavelength shift of transmission spectrum in coupled-ring-resonator.

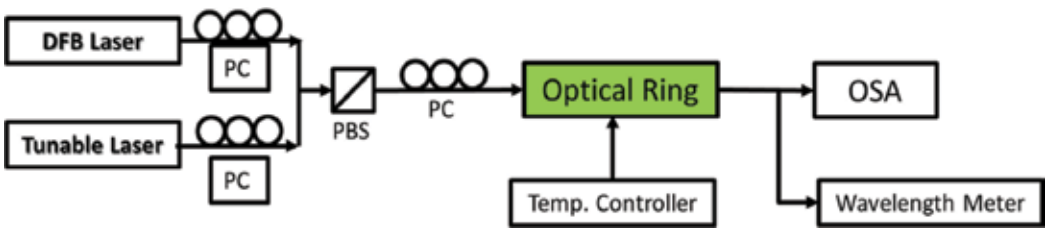


**Figure 8.** Optical micro-ring measurement platform.

With a linear raster coupler, the input light is coupled to this raster coupler for propagation, which is a linear raster structure limitation. Light requires longer focal length when traveling. If the focal length is not enough, easily lead to the scattering of light lead to energy loss. It causes the grating coupler coupling efficiency to drop.

In this study, the curvature-type grating structure is used for the measurement as shown in **Figure 10**. It can reduce the focusing length a lot. It is not loss of coupling efficiency.

Under the same coupling gap, the energy coupling coefficient and energy loss are relatively larger and larger in radius. The main reason is the large radius of the micro-ring coupling longer. Its energy coupling distance is longer. Therefore, a larger energy coupling coefficient

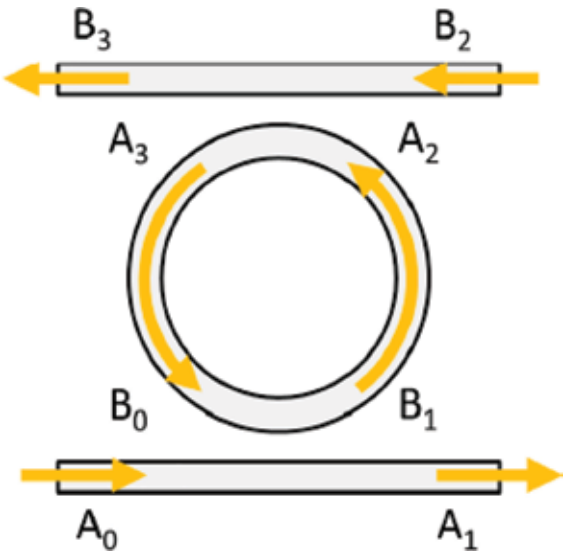


**Figure 9.** In add/drop condition.

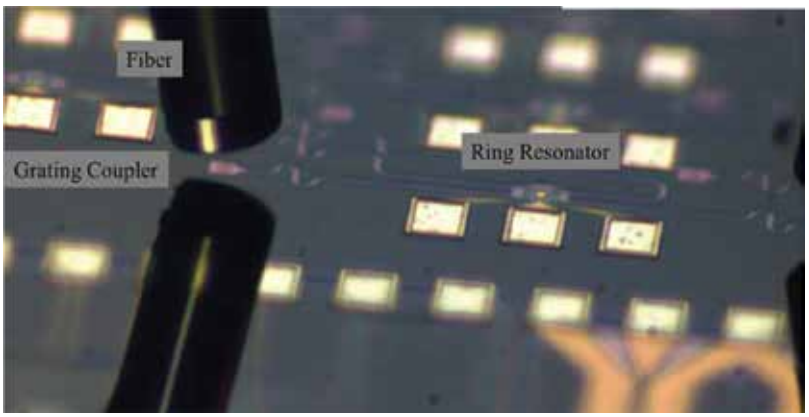


**Figure 10.** The vertical coupling system.

and coupling loss are generated. In addition, the total optical path of large radii in the ring resonator is larger than the small radius micro-rings. It produces extra spreading loss. Under the same coupling gap (200 μm) and radius 7.5 μm is shown in **Figure 11(a)**. Under the same coupling gap (200 μm) and radius 2.5 μm is shown in **Figure 11(b)**. Under the same coupling gap (200 μm) and radius 7.5 μm only drop is shown in **Figure 11(c)**.

It takes a drop of R2.5 Gap 200 at an approximate wavelength of 1546 nm. The dip curve with drop (with drop) and the dip curve with no drop (without drop) are shown in **Figure 12**.

It takes a drop of R7.5 Gap 200 at a wavelength of approximately 1555 nm. The dip curve with drop (with drop) and the dip curve with no drop (without drop) are shown in **Figure 13**. It is

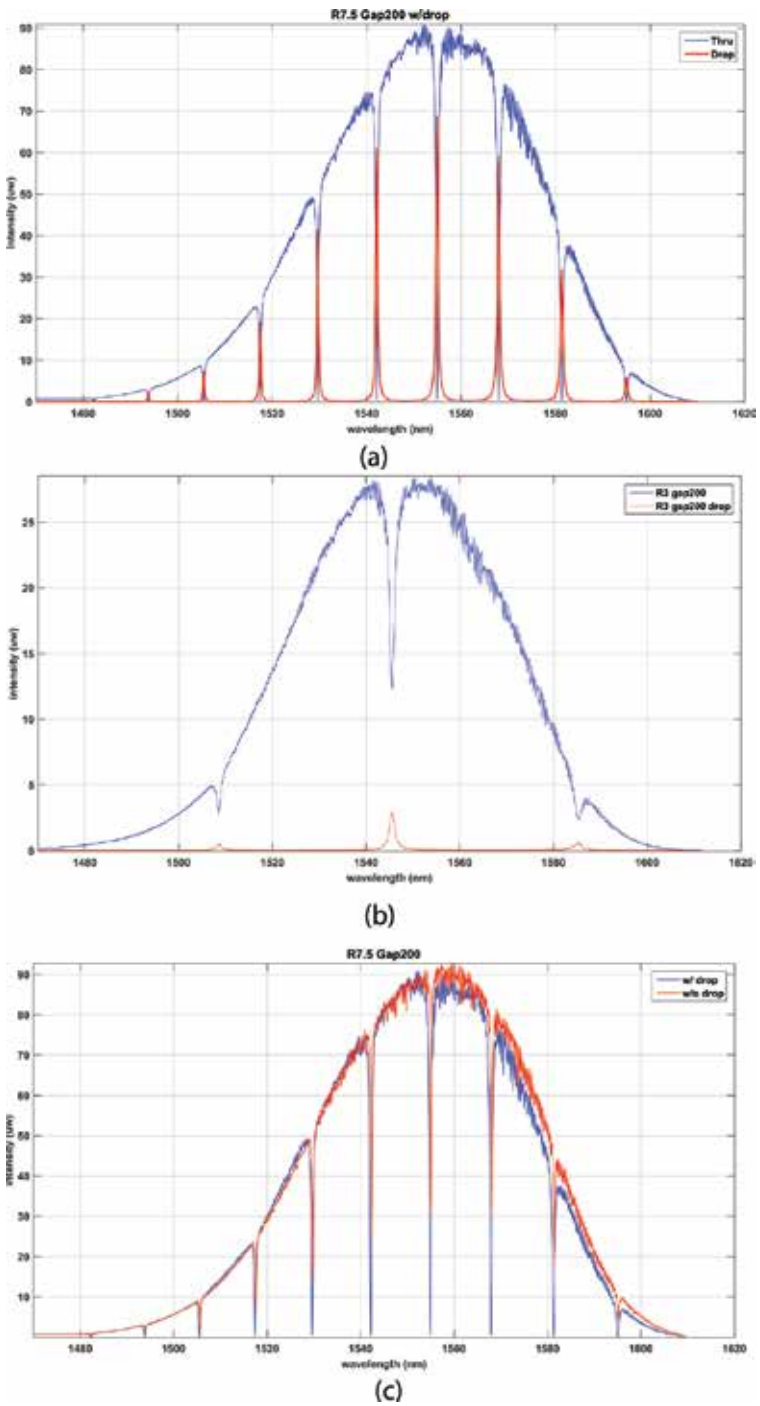


**Figure 11.** (a) Under the same coupling gap (200 μm) and radius 7.5 μm. (b). Under the same coupling gap (200 μm) and radius 2.5 μm. and (c). Under the same coupling gap (200 μm) and radius 7.5 μm only drop.

http://dx.doi.org/10.5772/intechopen.76800

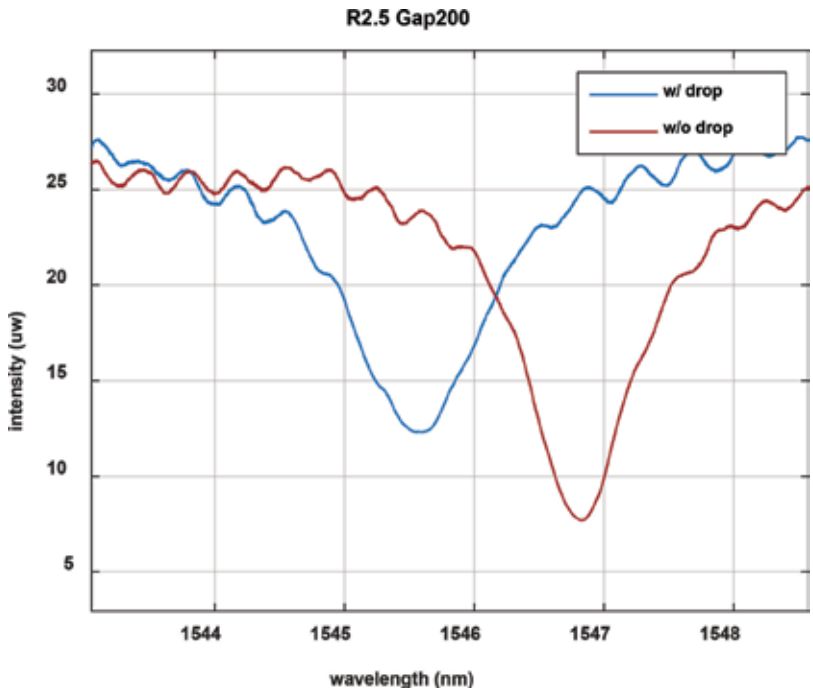


**Figure 12.** Take a drop of R2.5 gap 200 at an approximate wavelength of 1546 nm.

obviously very different. In the case of smaller micro-rings (R2.5 Gap 200), it presents a different drop wavelength. They differ by about 1 nm. In the case of large micro-rings (R7.5 Gap 200), it shows the same drop wavelength.

It adopts CMOS processing compatible processing methods. It has prepared a variety of types of grating coupler. Among them, it is in improving the coupling efficiency. It based on optimizing uniform grating structure parameters. It is reduce the reflection loss by covering the multilayer dielectric film. Use slot effect to increase the specific diffraction intensity. The non-uniform periodic structure is designed to realize the Gaussian field of diffraction field. Coupling efficiency continues to increase. It is 44% from conventional uniform grating couplers. It is 65% of the multilayer dielectric film grating structure. The coupling efficiency measurement of the non-uniform grating structure has reached 81.8%. In the vertical coupling by adding a DBR mirror. The second-order reflection at one end is canceled by the DBR reflected light interference. Vertical coupling was successfully achieved. In addition, the slope of the blazed grating is replaced by a step-change step structure. The analogy shows that the number of steps in a raster is 5. It could approximate the "shine" function.

The biggest advantage of a grating coupler lies in its testing and integration aspects. It compared to the face coupler. Grating couplers do not need to be polished. No strict space restrictions. Alignment tolerance, processing requirements are relatively simple. It greatly increased the flexibility of system design. It is more suitable for large-scale integration. It is in the

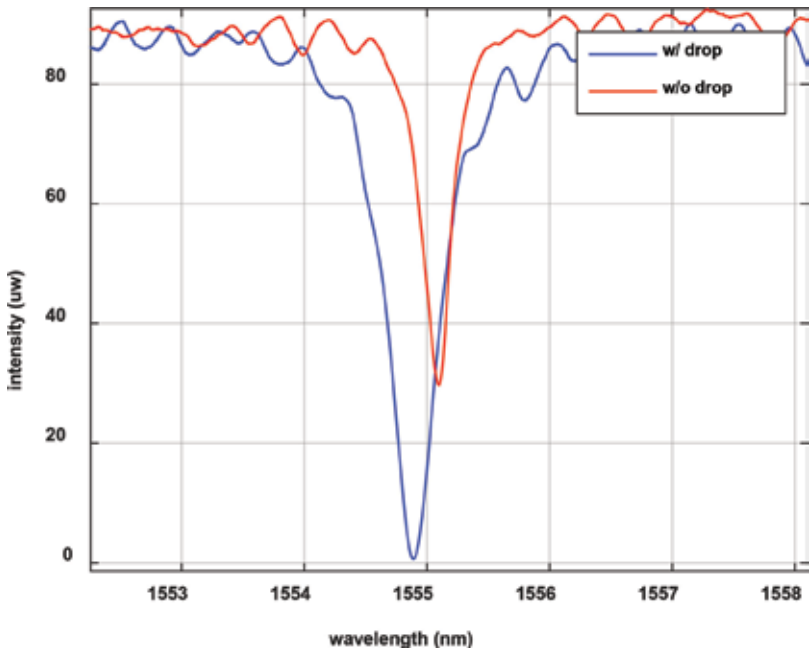


**Figure 13.** Take a drop of R7.5 gap 200 at a wavelength of approximately 1555 nm.

reported hybrid optoelectronic integration studies. Grating coupler compared with other coupling methods. Performance improvement is significant. The deepening of research work and the continuous development is preparation technology. The coupling efficiency of the grating coupler, working wavelength, polarization mode and other characteristics will continue to improve. It can be expected that grating couplers with high efficiency, large bandwidth and vertical coupling will rapidly develop and mature in the practical direction. A key element is in silicon-based photonics integration.

## 6. Author biography

Dr. Jian-Chiun Liou received a Ph.D. degree from the Institute of Nanoengineering and Microsystems, National Tsing Hua University, Hsinchu, Taiwan, in 2009. He joined the Printing Technology Development and Manufacturing Section of the Optoelectronics and Systems Laboratories at the Industrial Technology Research Institute (ITRI), Hsinchu, in 1999, where he focused on the ink-jet printing system. Since 2005, he has been a Project Leader working on a new MEMS architecture design and display application in the Electronics and Optoelectronics Research Laboratories, ITRI. In August 2014, he joined the faculty of the National Kaohsiung University of Applied Sciences (KUAS). In August 2017, he has joined the School of Biomedical Engineering, Taipei Medical University (TMU), Taipei 11,031, Taiwan. Currently, he is a Professor of School of Biomedical Engineering at the TMU. His research interests are in the fields of Optoelectronics, ASIC design, bio-chip technology, optical MEMS technology, integration of ink-jet printhead processes, and display technology. He is a holder of 71 patents on ink-jet printheads, MOEMS, MEMS, and has written more than 28 SCI Journal papers and

38 conference technical papers on MEMS, optical-N/MEMS, and display-related and micro−/nano-fluidics-related fields. He has also co-chaired many conference technical sessions and has been an invited speaker in many related events. In addition, he has performed the following tasks: Advance project leader (ITRI), SCI Journal paper reviewer (PIER, JEMWA, MEE), and Research fellow (NTHU). To add, Dr. Liou was the recipient of the following honors: ITRI/OES Research Achievement Award (2004), ITRI Research Paper Publication Award (2004), ITRI/EOL Research Achievement Award (Individual person Award, 2005), ITRI/EOL Outstanding Advanced Research Silver Award (2005), ITRI/EOL Research Achievement Award (2006), ITRI/EOL Patents Reviewer (2007), Outstanding Research Award (2007), ITRI/EOL Patents Reviewer(2008), Outstanding Research Award (2010), ITRI/EOL Patents Reviewer (2009), ITRI/EOL Outstanding Research Award (2010), International R&D 100 Awards (2010), 1st International Contest of Applications in Nano-Micro Technology Award (2010)—OPTO- MEMS Device Application, ITRI Paper Awards (2012), ITRI/EOL Outstanding Advanced Research Silver Award (2013), International Inventor Prize (2014), Nation Academic Award (2014). 2014 Invention Lifetime Achievement Award. 2015 "Design and fabrication of Monolithic CMOS/MEMS system with HV-ESD Clamp protected inkjet printhead." 2015 International Contest Application Contest in Nano-Micro Technology (Alaska, USA) "iCAN'15 7th Special Prize" 2015 International Contest of Application in Nano-Micro Technology (iCAN'15). Who's Who in the World® 2016 (33rd Edition). In 2016, "The 16th Wang Golden silicon semiconductor design and application contest winners": An ASIC designed to spray liquid medical wisdom DNA gene sequencing system. 2016 Third Prize Award and Best Supervisors: Jian-Chiun Liou, 2016 iCAN'16 France 2016 International Contest of Application in Nano-Micro Technology (iCAN'16 ESIEE Paris, July 7th, 2016): The Glove. 2017 "iCAN'17 Third Prize Award, and Education Star Award 2017 International Contest of Application in Nano-Micro Technology (iCAN'17 BEIJING): Cloud Health Care (CHC). 2017 Teaching Excellence Teacher Award. August 2017 Transferred to Taipei Medical University for medical electronics-related fields in-depth study. He is a member of the IEEE and a reviewer for more than 20 international journals including the Applied Physics Letters, JMEMS, Microfluidics and nano-fluidics, and micro-devices. He has also been a consultant to three Taiwanese companies.

## Author details

Jian-Chiun Liou

Address all correspondence to: jcliou@tmu.edu.tw

School of Biomedical Engineering, Taipei Medical University, Taipei, Taiwan

## References

[1] Kaalund CJ, Peng G. Pole-zero diagram approach to the design of ring resonator-based filters for photonic applications. Journal of Lightwave Technology. 2004;**22**(6):1548-1558

[2] Wang Z, ChenW, Chen YJ. Unit cell design of crossbar switch matrix using micro-ring resonators. ECOC 04, page we 3.7.2

[3] Chu ST, Little BE, Pan WG, Kaneko T, Kokubun Y. Cascaded microring resonators for crosstalk reduction and spectrum cleanup in adddrop filters. IEEE Photonics Technology Letters. 1999;**11**:1423-1425

[4] Chu ST, Little BE, Pan WG, Kaneko T, Sato S, Kokubun Y. An eight-channel add-drop filter using vertically coupled microring resonators over a cross grid. IEEE Photonics Technology Letters. 1999;**11**:691-693

[5] Ma X, Kuo GS. Optical switching technology comparison: Optical MEMS vs. other technologies. IEEE Communications Magazine. November, 2003;**41**(11):s16-s23

[6] Dey D. Towards an All-Optical WDM Slotted-Ring MAN with Support for Optical Multicasting. University of Twente. 19 Jun 2003. ISBNs:90-365-1930-6

[7] Smit MK, van Dam C. PHASAR-based WDM-devices: Principles, design and applications. IEEE Journal of Selected Topics in Quantum Electronics. 1996;**2**(2):236-250

[8] Smit MK. Arrayed Waveguide Devices: Where Do they Go from Here? Proc. Europ. Conf. Integrated Optics. France: Grenoble; 2005

[9] Fukazawa T, Ohno F, Baba T. Very compact arrayed-waveguide-grating demultiplexers using Si photonic wire waveguides. Japanese Journal of Applied Physics. 2004;**43**(5B):673-675

[10] Shibata T, Okuno M, Goh T, Watanabe T, Yasu M, Itoh M, Ishii M, Hibino Y, Sugita A, Himeno A. Silica-based waveguide-type 16 x 16 optical switch module incorporating driving circuits. IEEE Photonics Technology Letters. 2003;**15**(9):1300-1302

[11] Suzuki K, Mizuno T, Oguma M, Shibata T, Takahashi H, Hibino Y, Himeno A. Low loss fully reconfigurable wavelength-selective optical 1 x n switch based on transversal filter configuration using silica-based planar lightwave circuit. IEEE Photonics Technology Letters. 2004;**16**(6):1480-1482

[12] Kasahara R, Yanagisawa M, Goh T, Sugita A, Himeno A, Yasu M, Matsui S. New structure of silica based planar lightwave circuits for lowpower thermooptic switch and its application to 8 x 8 optical matrix switch. Journal of Lightwave Technology. 2002;**20**(6):993-1000

[13] Goh T, Yasu M, Hattori K, Himeno A, Okuno M, Ohmori Y. Low loss and high extinction ratio strictly nonblocking 16 x 16 thermooptic matrix switch on 6-in wafer using silica-based planar lightwave circuit technology. Journal of Lightwave Technology. 2001;**19**(3):371-379

[14] Mazumder MM, Hill SC, Chowdhury DQ, Chang RK. Dispersive optical bistability in a dielectric sphere. Journal of the Optical Society of America-B. 1995;**12**(2):297-310

[15] Haavisto J, Pajer GA. Resonance effects in low-loss ring waveguides. Optics Letters. 1980;**5**(12):510-512

[16] Weiershausen W, Zengerle R. Photonic highway switches based on ring resonators used as frequency-selective components. Applied Optics. 1996;**35**:5967-5978

[17] Little BE, Chu ST, Pan W, Kokubun Y. Microring resonator arrays for VLSI photonics. IEEE Photonics Technology Letters. 2000;**12**:323-325

[18] Suzuki S, Shuto K, Hibino Y. Integrated-optic ring resonators with two stacked layers of silica waveguide on Si. IEEE Xplore: IEEE Photonics Technology Letters. 1992;**4**(11): 1256-1258

[19] Madsen CK, Zhao JH. Optical Filter Design and Analysis. Wiley; 9 Oct 2001. (Print) ISBN: 9780471183730, (Online) ISBN: 9780471213758

[20] Driessen A, Geuzebroek DH, Hoekstra HJWM, Kelderman H, Klein EJ, Klunder DJW, Roeloffzen CGH, Tan FS, Krioukov E, Otto C, Gersen H, van Hulst NF, Kuipers L. Microresonators as building blocks for VLSI photonics. AIP Conference Proceedings. 2003;**709**:1-18

[21] Chao FL, Wang WS. Analysis of temperature profiles of thermo-optic waveguides. Fiber and Integrated Optics. 1994;**13**:397-406

[22] Wang WK, Lee HJ, Anthony PJ. Planar silica-glass optical waveguides with thermally induced lateral mode confinement. IEEE Journal of Lightwave Technology. 1996;**14**:429-436

[23] Hryniewicz JV. Higher order filter response in coupled microring resonators. IEEE Photonics Technology Letters. 2000;**12**:320-322

[24] Orta R, Savi P, Tascone R, Trinchero D. Synthesis of multiplering- resonator filters for optical systems. IEEE Photonics Technology Letters. 1995;**7**:1447-1449

[25] Rabus DG, Hamacher M, Heidrich H. Resonance frequency tuning of a double ring resonator in GaInAsP/InP: Experiment and simulation. Japanese Journal of Applied Physics. 2002;**41**(2B):1186-1189

[26] Madsen CK, Zhao JH. A general planar waveguide autoregressive optical filter. Journal of Lightwave Technology. 1996;**14**:437-447

[27] Little BE, Chu ST, Absil PP, Hryniewicz JV, Johnson FG, Seiferth F, Gill D, Van V, King O, Trakalo M. Very high-order microring resonator filters for WDM applications. IEEE Photonics Technology Letters. 2004;**16**(10):2263-2265

[28] Kim G-D, Lee S-S. Photonic microwave channel selective filter incorporating a thermooptic switch based on tunable ring resonators. IEEE Photonics Technology Letters. July1, 2007;**19**(13):1008-1010

[29] Tewary A, Digonnet MJF, Sung J-Y, Shin JH, Brongersma ML. Silicon-nanocrystal-coated silica microsphere thermooptical switch. IEEE Journal of Selected Topics in Quantum Electronics. November/December, 2006;**12**(6):1476-1479

[30] Tapalian HC, Laine J-P, Lane PA. Thermooptical switches using coated microsphere resonators. IEEE Photonics Technology Letters. August, 2002;**14**(8):1118-1120

[31] Il'chenko VS, Gorodetskii ML. Thermal nonlinear effects in optical whispering gallery microresonators. Laser Physics. 1992;**2**:1004-1009

[32] Davis MK, Digonnet MJF, Pantell RH. Thermal effects in doped fibers. Journal of Lightwave Technology. June, 1998;**16**(6):1013-1023

[33] Ng HY, Wang MR, Li D, Wang X, Martinez J, Panepucci RR, Pathak K. 1×4 wavelength reconfigurable photonic switch using thermally tuned microring resonators fabricated on silicon substrate. IEEE Photonics Technology Letters. May 1, 2007;**19**(9):704-706

[34] Lienhard JH IV, Lienhard JH V. A Heat Transfer Textbook. Cambridge Massachusetts: Phlogistron Press; 2003

[35] Ozisik MN. Boundary Value Problems of Heat Conduction. NewYork: Dover; 1989

[36] Worhoff K, Hilderink LTH, Driessen A, Lambeck PV. Silicon oxynitride—A versatile material for integrated optics applications. Journal of The Electrochemical Society. 2002;**149**(8):F85-F91

Chapter 12

# Multimode Waveguides on an SOI Platform for Arbitrary Power Splitting Ratio Couplers

Trung-Thanh Le and Duy-Tien Le

Additional information is available at the end of the chapter

http://dx.doi.org/10.5772/intechopen.76799

**Abstract**

Optical power couplers with arbitrary power splitting ratios are important components for many applications such as Mach-Zehnder interferometer-based structures, filters, switches, dispersion compensations, optical interconnects, and microring resonators. In this chapter, we present a new approach to achieve a very high compact coupler with arbitrary power splitting ratios on silicon on insulator (SOI) waveguides. The proposed device requires only one 4×4 multimode interference (MMI) coupler. We use a passive wide SOI waveguide to achieve the phase shifter. The footprint of the whole device is only about 6×150 μm$^2$. A large fabrication tolerance of ±50 nm can be achieved. The modified effective index method, beam propagation method, finite difference method, and finite difference-time difference method are used to optimally design the whole device.

**Keywords:** multimode interference, silicon on insulator, multimode waveguide, finite difference-time difference, finite difference method, modified effective index method

## 1. Introduction

Integrated optical couplers with arbitrary power coupling ratios are important components in optical communication applications. Such couplers can be used in Mach-Zehnder interferometer (MZI) structures, power taps, and microring resonators, and so on. In principle, any power coupling ratio can be achieved for standard 2×2 directional couplers [1]. The power coupling ratios can be controlled by adjusting the coupling length and/or the gap between the two waveguides of the directional coupler [2]. In practice, accurate fabrication of the gap requires

very tight control of the fabrication process. Moreover, additional loss due to mode conversion loss has been found to be a problem [3].

A multimode interference (MMI) power splitter plays an important role in the development of integrated photonics due to large fabrication tolerance, wide operation bandwidth, and compact size. Therefore, MMI couplers with unequal power splitting ratios have been found in many applications such as optical monitoring, optical microring resonators [4, 5], and optical reflectors [6]. In order to achieve a coupler with a variable power splitting ratios, a Mach-Zehnder interferometer (MZI) with a phase shifter at the arm can be used [7–11]. With a conventional MMI coupler with a rectangular shape, it has been shown that such device can only provide limited splitting ratios and therefore it has limited applications in all-optical signal processing and optical networks.

In the literature, there are some methods for obtaining variable power optical couplers based on MMI structures such as butterfly-like MMIs [12], exponential MMIs [13, 14], and angled MMIs [15, 16]. However, these methods require a very complicated fabrication processes, and they have a low fabrication tolerance. In addition, these methods are not suitable for silicon photonics because of high losses.

In recent years, we have presented some methods to overcome the limitations of the previous approaches such as by cascading three or four MMI couplers [17], using an MZI structure with a multimode waveguide [18], using slot waveguide [19]. Other approaches are to use MMI structure with QR code-like nanostructure [20, 21] or double MMI coupler [22]. However, such approaches still require a quite complex fabrication process and they have a large footprint.

In this chapter, we present a new approach to achieve a 2×2 coupler based on only one 4×4 MMI coupler with wide waveguide on silicon on insulator waveguides. Our new method has advantages of compact size, ease of fabrication with the current CMOS circuitry.

## 2. Theory of MMI matrix

Multimode interference coupler includes three regions: single mode input, output waveguides, and multimode waveguide connecting with two input and output regions. The multimode region has a large width to support some modes. The operation of the MMI coupler is based on Talbot effect [4, 23]. Based on locations of input field excitations, there are three main interference mechanisms: (1) general interference (GI) mechanism, which is independent of the modal excitation; (2) restricted interference (RI) mechanism, in which excitation inputs are placed at some special positions so that certain modes are not excited; (3) symmetric interference (SI) mechanism, in which the excitation input is located at the center of the multimode section.

An NxN GI-MMI coupler has length $L = L_{MMI} = \frac{p}{N} 3L_{\pi}$, where p is a positive integer such that p and N are without a common divisor. In practical designs, the shortest devices are obtained for p = 1. The resulting amplitudes from image input i (i = 1,…,N) to output j (j = 1,…,N) can be given in a compact form [23].

$$A_{ij} = A_{ji} = \sqrt{\frac{1}{N}} \tag{1}$$

where $|A_{ij}|^2$ is the normalized power of the output images. The phases $\phi_{ij}$ of the equal output signals at the output waveguides can be calculated by [23]: for i + j: even, $\phi_{ij} = \phi_0 + \pi + \frac{\pi}{16}(j-i)(8-j+i)$ and for i + j: odd, $\phi_{ij} = \phi_0 + \frac{\pi}{16}(i+j-1)(8-j-i+1)$; where the input ports i (i = 1, 2,…,N) are numbered from bottom to top and the output ports j (j = 1, 2,…, N) are numbered from top to bottom in the MMI coupler. $\phi_0 = -\beta_0 L_{MMI} - \frac{\pi}{2}$ is a constant phase that depends upon the MMI geometry and therefore can be implied in the following calculations.

In this chapter, the access waveguides are identical single mode waveguides with width $W_a$. The input and output waveguides are located at [24].

$$\mathrm{x} = \left(i + \frac{1}{2}\right)\frac{W_{MMI}}{N} \tag{2}$$

The electrical field inside the MMI coupler can be expressed by [25].

$$E(x,z) = \exp(-jkz)\sum_{m=1}^{M} E_m \exp\left(j\frac{m^2\pi}{4\Lambda}z\right)\sin\left(\frac{m\pi}{W_{MMI}}x\right) \tag{3}$$

We showed that the characteristics of an MMI device could be described by a transfer matrix [2]. This transfer matrix is a very useful tool for analyzing cascaded MMI structures. The phase $\phi_{ij}$ associated with imaging an input i to an output j in an MMI coupler. These phases $\phi_{ij}$ form a matrix $\mathbf{\Phi}$, with i representing the row number, and j representing the column number. Then the transfer matrix of the MMI coupler $\mathbf{M}$ is directly related to $\mathbf{\Phi}$, and the output field distribution emerging from the MMI coupler can be written as

$$\mathbf{b} = \mathbf{M}\mathbf{a} \tag{4}$$

where $\mathbf{a} = [a_1\ a_2 \ldots a_N]^T$, $\mathbf{b} = [b_1\ b_2 \ldots b_N]^T$ and $\mathbf{M} = \left[m_{ij}\right]_{NxN}$. The superscript T indicates the transpose of a matrix. $a_i$(i = 1,…,N) is the complex field amplitude at input waveguide i and $b_j$ (j = 1,…,N) is the complex field amplitude at output waveguide j. Elements of the transfer matrix $\mathbf{M}$ are $m_{ij} = m_{ji} = A_{ij}e^{j\phi_{ij}}$, where $A_{ij}$ is the field amplitude transfer coefficient and $\phi_{ij}$ is the phase shift when imaging from input i to output j.

Here, we propose a 4×4 MMI coupler with a width of $W_{MMI}$, length of $L_{MMI}$. A single 4×4 MMI coupler at a length of $L_1 = \frac{3L_\pi}{4}$ is described by the following transfer matrix [26–28].

$$\mathbf{M} = \frac{1}{2}\begin{bmatrix} -1 & -e^{j\frac{3\pi}{4}} & e^{j\frac{3\pi}{4}} & -1 \\ -e^{j\frac{3\pi}{4}} & -1 & -1 & e^{j\frac{3\pi}{4}} \\ e^{j\frac{3\pi}{4}} & -1 & -1 & -e^{j\frac{3\pi}{4}} \\ -1 & e^{j\frac{3\pi}{4}} & -e^{j\frac{3\pi}{4}} & -1 \end{bmatrix} \tag{5}$$

If the length is doubled to $L_{MMI} = 2L_1 = 3L_\pi/2$, a new 4×4 MMI coupler is formed and its transfer matrix is

$$\mathbf{S} = (\mathbf{M})^2 = \frac{1}{2}\begin{bmatrix} 1-j & 0 & 0 & 1+j \\ 0 & 1-j & 1+j & 0 \\ 0 & 1+j & 1-j & 0 \\ 1+j & 0 & 0 & 1-j \end{bmatrix} \tag{6}$$

## 3. Modified effective index and numerical methods

In this chapter, we use our proposed modified effective index method (MEIM) for designing MMI structures based on silicon waveguides as shown in [29]. The principle of this MEIM is to use the beat length $L_\pi$ of the MMI coupler as the invariant. Here, the beat length of an MMI structure can be defined as $L_\pi = \pi/(\beta_0 - \beta_1)$, where $\beta_0$ and $\beta_1$ are the propagation constants of the fundamental and first order modes, respectively. We shall find a matching value of the cladding index for the effective index method that forces the beat length $L_\pi$ in the equivalent 2D model to be equal to the beat length in an accurate 3D model. By this way, we find an optimal effective cladding index. For our silicon waveguide structure, in this chapter, we found that equivalent effective indices of the core waveguide and the cladding waveguide are to 2.82 and 2.19, respectively.

In order to optimally design the MMI coupler, we use the beam propagation method (BPM). We showed that the width of the MMI is optimized to be $W_{MMI}$ = 6 μm for compact and high performance device. **Figure 1** shows numerical simulations at optimal MMI length of $L_{MMI} = 141.7\ \mu m$ for signal at input port 1 and at input port 2. The simulations show that a very low insertion loss of 0.7 dB for both cases [2].

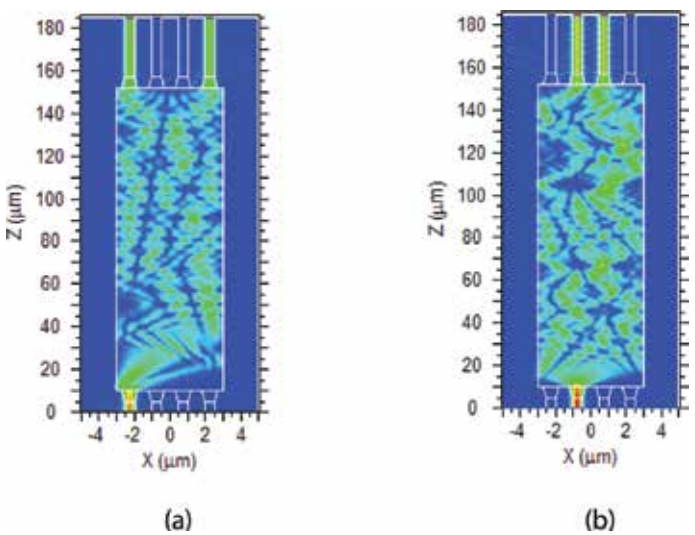


**Figure 1.** Power splitting ratio scheme based on 4×4 MMI coupler (a) Input 1 and (b) Input 2.

## 4. Arbitrary splitting ratio coupler based on a 4×4 MMI coupler

**Figure 2** shows the new scheme for achieving arbitrary coupling ratios in only one 4×4 MMI structure. We use two waveguides with different widths $W_{co1} = 300nm$ and $W_{co2} = 500nm$ at the two arms of the structure. The cross-sectional view of the SOI waveguide is shown in **Figure 3**. Here, the height of the SOI waveguide $h_{co} = 220nm$, the width of the SOI waveguide varies from 300 nm to 500 nm for single mode operation at wavelength of 1550 nm.

By using the FDM method, the effective refractive index of the SOI waveguide at different waveguide width of 300 nm to 500 nm can be calculated as shown in **Figure 4**. As an example, **Figure 5** shows the mode profile for the waveguide at the width of 300 nm and 500 nm, respectively.

A change in the effective index will induce the change in the phase shift. The phase difference between two waveguide then can be expressed by [30].

$$\Delta\varphi = \frac{2\pi}{\lambda}\Delta n_{eff} L_{arm} \tag{7}$$

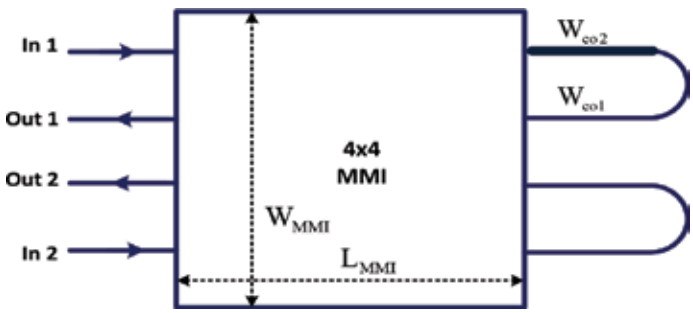


**Figure 2.** Power splitting ratio scheme based on 4×4 MMI coupler.

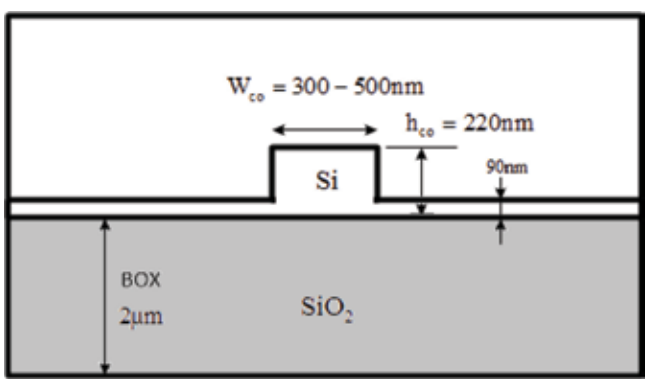


**Figure 3.** SOI waveguide structure.

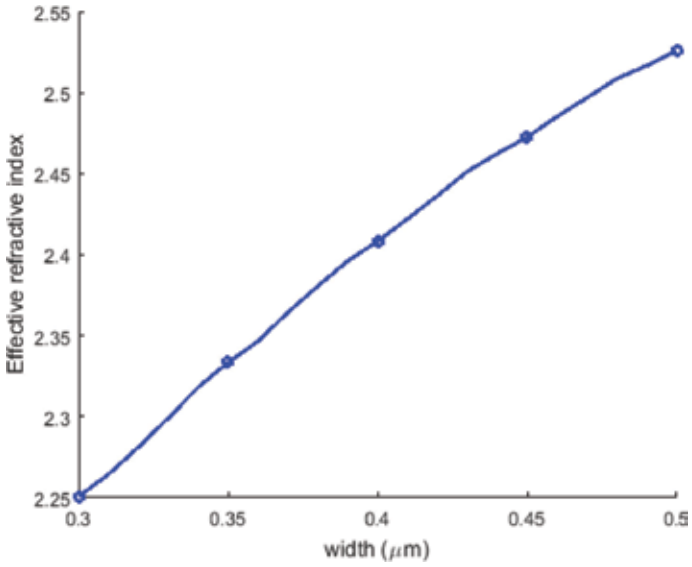


**Figure 4.** Effective refractive index of the SOI waveguide calculated by the FDM.

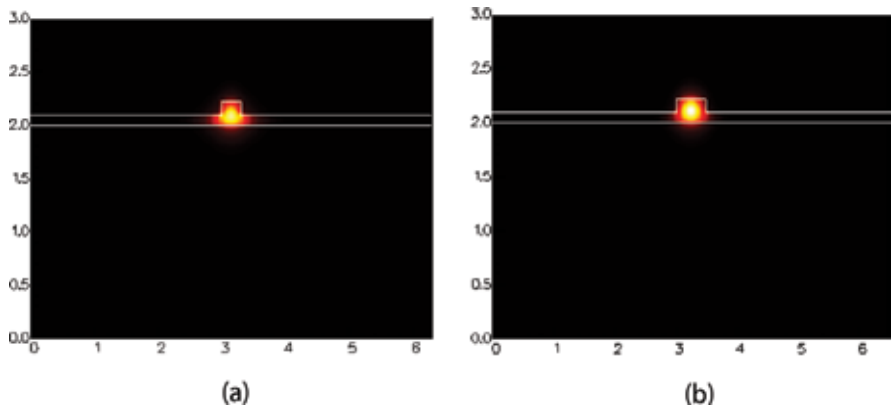


**Figure 5.** Field profile of the SOI waveguide (a) width of 300 nm and (b) width of 500 nm.

where $\Delta n_{eff}$ is the difference in the effective index, $L_{arm}$ is the length of the waveguide with the width of $W_{co2}$. As a result, the length of the waveguide $W_{co2}$ to achieve the phase shift from 0 to $\pi$ is presented in **Figure 6**. We see that the short length of 3.5035 μm is required to achieve a phase shift of $\pi$.

Due to the phase shift $\Delta\varphi$, the complex amplitudes at the input ports and output ports of the coupler of **Figure 2** can be described in terms of cascaded transfer matrices as

$$\mathbf{S} = \frac{1}{\sqrt{2}}\begin{bmatrix} 1 & j \\ j & 1 \end{bmatrix}\begin{bmatrix} e^{j\Delta\varphi} & 0 \\ 0 & 1 \end{bmatrix}\frac{1}{\sqrt{2}}\begin{bmatrix} 1 & j \\ j & 1 \end{bmatrix} = e^{j\frac{\Delta\varphi}{2}}\begin{bmatrix} \tau & \kappa \\ \kappa^* & -\tau^* \end{bmatrix} \tag{8}$$

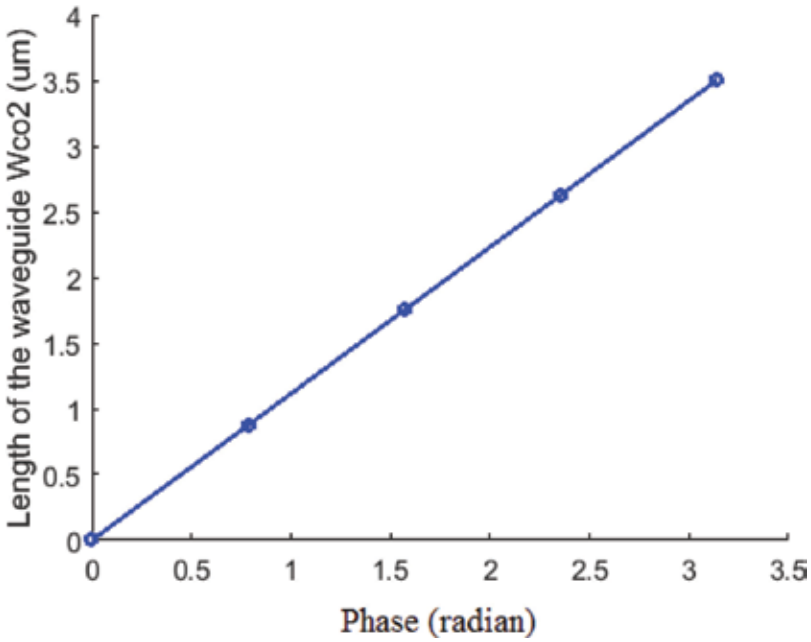


**Figure 6.** Length of the waveguide Wco2 required to achieve the phase shift from 0 to $\pi$.

where $\tau = \sin\left(\frac{\Delta\varphi}{2}\right)$, and $\kappa = \cos\left(\frac{\Delta\varphi}{2}\right)$. Therefore, if an input signal having power presented at input port 1 of the coupler in **Figure 2**, the normalized powers at output port 1 and output port 2 can be expressed by:

$$Out_1 = \sin^2\left(\frac{\Delta\varphi}{2}\right), \text{and } Out_2 = \cos^2\left(\frac{\Delta\varphi}{2}\right) \tag{9}$$

From Eqs. (7) and (9), the normalized output powers can be calculated and plotted in **Figures 7** and **8**. It is showed that any power splitting ratio can be achieved by changing the phase shift from 0 to $\pi$ or changing the length of the Wco2 waveguide from 0 to 3.51$\mu$m.

Consider the length of the Wco2 waveguide variation, the normalized output powers are shown in **Figure 9**. The simulation shows that the changes in normalized output powers are very small (nearly 0% in the range of −50 nm to +50 nm). It is feasible for the current CMOS circuitry [31].

Finally, we use FDTD method to simulate our proposed structure and then make a comparison with the analytical theory. In our FDTD simulations, we take into account the wavelength dispersion of the silicon waveguide. We employ the design of the MMI coupler presented in the previous section. A continuous light pulse of 15 fs pulse width is launched from the input to investigate the transmission characteristics of the device. The grid size $\Delta x = \Delta y = 20nm$ and $\Delta z = 20nm$ are chosen in our simulations. The FDTD simulations for the whole device are shown in **Figure 10**.

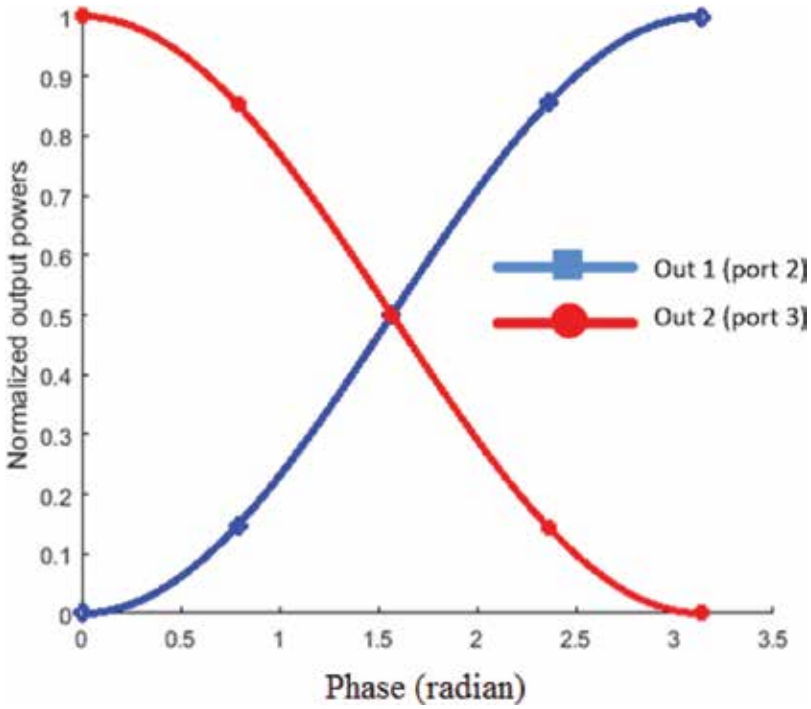


**Figure 7.** Normalized output powers at ports 2 (out1) and 3 (out2) for different phase shifts.

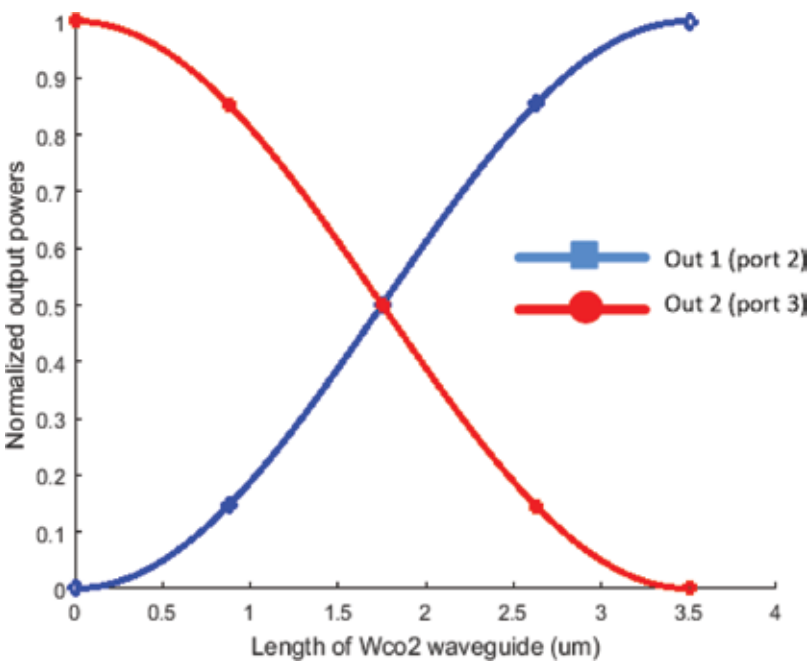


**Figure 8.** Normalized output powers at ports 2 and 3 for different Wco2 lengths.

http://dx.doi.org/10.5772/intechopen.76799

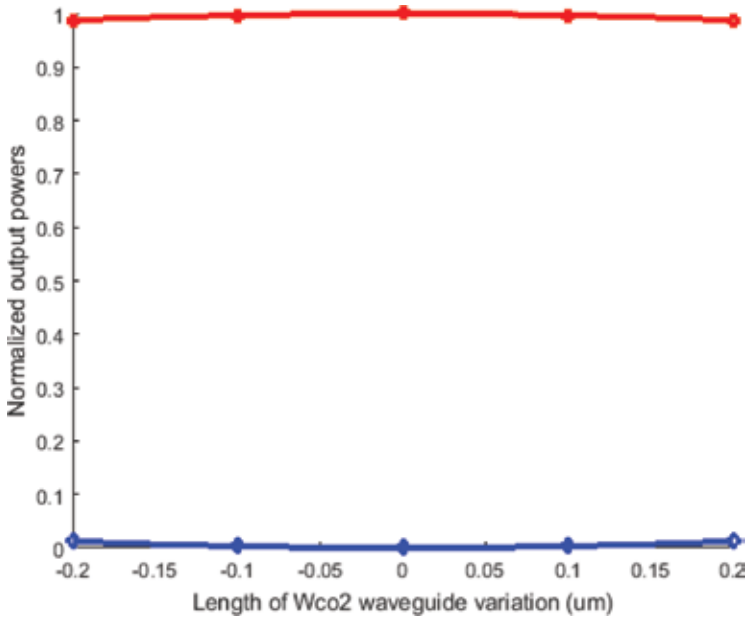


**Figure 9.** Normalized output powers at ports 2 and 3 for different Wco2 length variation.

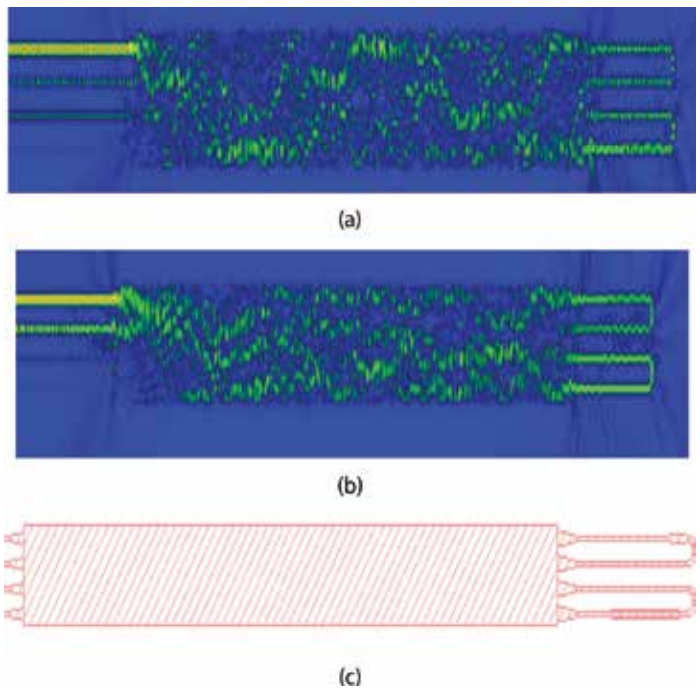


**Figure 10.** Optical field propagation through the coupler for input signal presented at port 1 and for length of the Wco2, (a) 1.75 μm and (b) 3.51 μm, and (c) mask design.

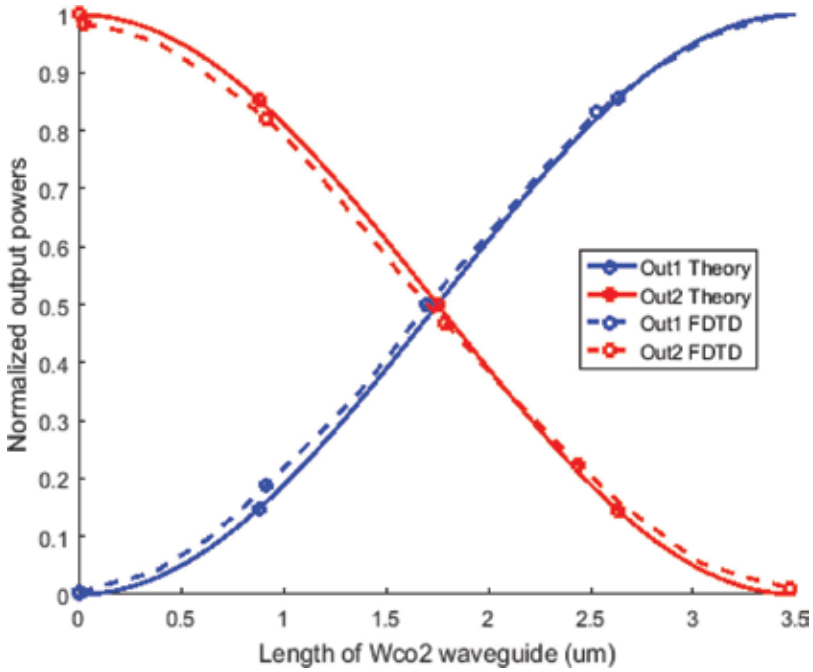


**Figure 11.** FDTD simulations compared with the theoretical analysis at different lengths of the Wco2 waveguide.

**Figure 11** shows the FDTD simulations compared with theoretical analysis. The simulations show that the device operation has a good agreement with our prediction by analytical theory.

## 5. Conclusions

We presented a compact structure with a footprint of $6\times150$ μm$^2$ based on silicon on insulator waveguides for 2×2 couplers with free of choice power splitting ratios. The new structure requires only one 4×4 multimode interference coupler. The wide SOI waveguide is used to achieve the phase shift. By changing the length of the wide waveguide from 0 to 3.51 μm, any power splitting ratios can be achieved. The device operation has been verified by using the FDTD. This coupler can be useful for optical interconnects, microring resonator applications.

## Author details

Trung-Thanh Le* and Duy-Tien Le

*Address all correspondence to: thanh.le@vnu.edu.vn

Vietnam National University (VNU), International School (VNU-IS), Hanoi, Vietnam

## References

[1] Payne F. Design principles of ring resonator waveguide devices. Private Communication. 2007

[2] Le T-T. Multimode Interference Structures for Photonic Signal Processing. Germany: LAP Lambert Academic Publishing; 2010

[3] Xia F, Sekaric L, Vlasov YA. Mode conversion losses in silicon-on-insulator photonic wire based racetrack resonators. Optics Express. 2006;**14**:3872-3886

[4] Soldano LB, Pennings ECM. Optical multi-mode interference devices based on self-imaging: Principles and applications. IEEE Journal of Lightwave Technology. 1995;**13**: 615-627

[5] Suzuki S, Kazuhiro O, Yoshinori H. Integrated-optic double-ring resonators with a wide free spectral range of 100 GHz. Journal of Lightwave Technology. 1995;**13**:1766-1771

[6] Jeong S, Matsuo S, Yoshikuni Y, et al. Flat-topped spectral response in a ladder-type interferometric filter. IEICE Transactions on Electronics. 2005;**E88-C**:1747-1754

[7] Oguma M, Jinguji K, Kitoh T, et al. Flat-passband interleave filter with 200 GHz channel spacing based on planar lightwave circuit-type lattice structure. Electronics Letters. 2000; **36**:1299-1300

[8] Takiguchi K, Jinguji K, Okamoto K, et al. Variable group-delay dispersion equalizer using lattice-form programmable optical filter on planar. IEEE Journal of Selected Topics in Quantum Electronics. 1996;**2**:270-276

[9] Yariv A. Critical coupling and its control in optical waveguide-ring resonator systems. IEEE Photonics Technology Letters. 2002;**14**:483-485

[10] Choi JM, Lee RK, Yariv A. Control of critical coupling in a ring resonator–fiber configuration: Application to wavelength-selective switching, modulation, amplification, and oscillation. Optics Letters. 2001;**26**:1236-1238

[11] Takiguchi K, Jinguji K, Ohmori Y. Variable group-delay dispersion equaliser based on a lattice-formprogrammable optical filter. Electronics Letters. 1995;**31**:1240-1241

[12] Besse PA, Gini E, Bachmann M, et al. New 2×2 and 1×3 multimode interference couplers with free selection of power splitting ratios. IEEE Journal of Lightwave Technology. 1996; **14**:2286-2293

[13] Dai D, He S. Proposal for diminishment of the polarization-dependency in a Si-nanowire multimode interference (MMI) coupler by tapering the MMI section. IEEE Photonics Technology Letters. 2008;**20**:599-601

[14] Dai D, He S. Design of an ultrashort Si-nanowaveguide-based multimode interference coupler of arbitrary shape. Applied Optics. 2008;**47**:38-44

[15] Levy DS, Li YM, Scarmozzino R, et al. A multimode interference-based variable power splitter in GaAs-AlGaAs. IEEE Photonics Technology Letters. 1997;**9**:1373-1375

[16] Lai Q, Bachmann M, Hunziker W, et al. Arbitrary ratio power splitters using angled silica on siliconmultimode interference couplers. Electronics Letters. 1996;**32**:1576-1577

[17] Truong C-D, Le T-T. Power splitting ratio couplers based on MMI structures with high bandwidth and large tolerance using silicon waveguides. Photonics and Nanostructures - Fundamentals and Applications. 2013;**11**:217-225

[18] Le TT, Cahill LW, Elton D. The design of 2×2 SOI MMI couplers with arbitrary power coupling ratios. Electronics Letters. 2009;**45**:1118-1119

[19] Le TT and Cahill LW. The design of multimode interference couplers with arbitrary power splitting ratios on an SOI platform. In LEOS 2008, Newport Beach, California, USA, 9-14 Nov 2008

[20] Ke X, Liu L, Wen X, et al. Integrated photonic power divider with arbitrary power ratios. Optics Letters. 2017;**42**:855-858

[21] Piggott AY, Petykiewicz J, Su L, et al. Fabrication-constrained nanophotonic inverse design. Scientific Reports. 2017;**7**:1786

[22] Cherchi M, Ylinen S, Harjanne M, et al. Unconstrained splitting ratios in compact double-MMI couplers. Optics Express. 2014;**22**:9245-9253

[23] Bachmann M, Besse PA, Melchior H. General self-imaging properties in N × N multimode interference couplers including phase relations. Applied Optics. 1994;**33**:3905-3911

[24] Le D-T, Le T-T. Coupled resonator induced transparency (CRIT) based on interference effect in 4×4 MMI coupler. International Journal of Computer Systems. 2017;**4**:95-98

[25] Heaton JM, Jenkins RM. General matrix theory of self-imaging in multimode interference (MMI) couplers. IEEE Photonics Technology Letters. 1999;**11**:212-214

[26] Le T-T. Two-channel highly sensitive sensors based on 4 × 4 multimode interference couplers. Photonic Sensors. 2017;**7**:357-364

[27] Le T-T, Cahill L. The design of 4×4 multimode interference coupler based microring resonators on an SOI platform. Journal of Telecommunications and Information Technology. 2009:98-102

[28] Le DT, Do DT, Nguyen VK, et al. Sharp asymmetric resonance based on 4×4 multimode interference coupler. International Journal of Applied Engineering Research. 2017;**12**: 2239-2242

[29] Le T-T. An improved effective index method for planar multimode waveguide design on an silicon-on-insulator (SOI) platform. Optica Applicata. 2013;**43**:271-277

[30] Petrone G, Cammarata G. Modelling and Simulation. Rijeka: InTech Publisher; 2008

[31] Dan-Xia X, Schmid JH, Reed GT, et al. Silicon photonic integration platform—Have we found the sweet spot? IEEE Journal of Selected Topics in Quantum Electronics. 2014;**20**: 8100217

Chapter 13

# Longitudinal Differential Protection of Power Systems Transmission Lines Using Optical Waveguide

Tomislav Rajić

Additional information is available at the end of the chapter

http://dx.doi.org/10.5772/intechopen.76621

**Abstract**

This chapter describes using optical waveguide for communication between two relays on the opposite ends of the power systems transmission line (or transmission line). Transmission lines are a very important part of the power system. Because of that, relay protection must be fast and safe. Longitudinal differential protection satisfies these requirements. Pilot wire differential relays are commonly used for the protection of short lines. The existence of the pilot wires is a disadvantage. This protection is limited to lines of a few tens of kilometers. However, if optical protection ground wires (OPGWs) are used, instead of pilot wires, the length of the line ceases to be a limiting factor. The following sections tell more about constructions, assembly and utilization of the optical waveguides in differential protection. Also, the newest algorithms of this protection are listed.

**Keywords:** differential protection, relay, communication, optical protection ground wires, transmission line

## 1. Introduction

Due to the transient stability of the power system, faults on the lines near the power plant or large substations must be switched off quickly. Longitudinal differential protection can be applied for fast and selective protection of lines.

The longitudinal differential protection principle is based on the comparison of the currents located at the beginning and at the end of the line, resulting in a quick, sensitive and simple protection concept that ensures that the faulted line is disconnected from the network. The protected zone is defined by the position of the current transformers from which signals are brought into the differential relay.

Analogue longitudinal differential protection is used for shorter, single-circuit transmission lines in double-fed networks. Pilot cable line connects secondary current transformers on the opposite sides of the protected line. A great disadvantage is the existence of pilot wire, and such protection is limited to short lines. If optical protection ground wires (OPGWs) are used, the length of the line ceases to be a limiting factor [1–3].

OPGW is a dual functioning cable performing the duties of a ground wire and also providing a patch for the transmission of voice, video or data signals. It is located at the top of the power line tower.

The second section presents a classic approach of longitudinal differential protection of transmission lines. The operating principle is explained [1–3].

The third section talks more about OPGW. It describes two different constructions of the OPGW. The same characteristics of them are mentioned and showed. The elements for connecting OPGW with the tower are enumerated and shown [4–8].

The next section describes relay protection realized with pilot wires [9–11].

The fifth section discusses the use of digital protection. The algorithms mentioned in recent works are listed. A short recapitulation is performed. Of course, all solutions or algorithms are difficult to be implemented without using OPGW [12–23].

## 2. Longitudinal differential protection: a classic approach

**Figure 1** shows the longitudinal differential protection operating principle. If the fault occurs outside the protected zone, the left- and right-end currents have the same direction and approximate intensities, that is, their difference is negligible and the protection does not trip. Should the fault occur within the protected zone, the right-end's current changes its direction, establishing a significant current through the differential relay M, causing its tripping. Differential current is the current difference that tends to initiate operation and stabilization current is the current proportional to thought current that tends to inhibit operation.

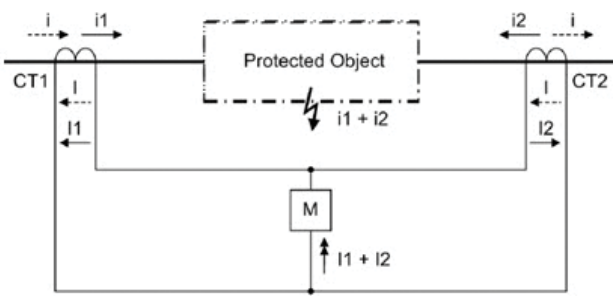


**Figure 1.** Longitudinal differential protection of transmission lines—Protection operating principle.

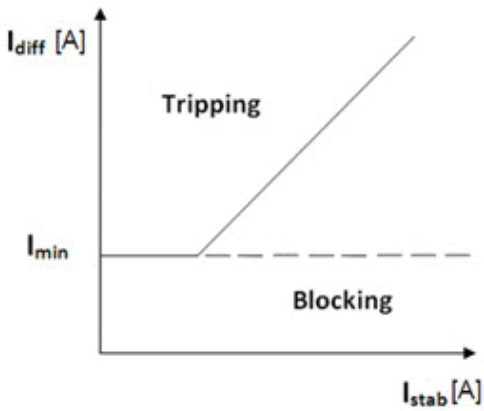


**Figure 2.** Differential relay tripping characteristic.

Equations (1) and (2) are used for calculating the stabilization and differential currents individually for each phase [1–3]:

$$I_{stab} = \left|\underline{I_L}\right| + \left|\underline{I_R}\right| \tag{1}$$

$$I_{diff} = \left|\underline{I_L} - \underline{I_R}\right| \tag{2}$$

with the following explanation:

*IL*—basic harmonic phasor of the left-end phase current.

*IR*—basic harmonic phasor of the right-end phase current.

**Figure 2** shows the tripping characteristic of the differential relay. The minimum tripping current ($I_{min}$) defines the minimum relay tripping threshold and is set to 20–50% of the rated transformer current. This quantity is defined since in an actual system, in a non-fault condition, there is always a difference between the currents measured on the opposite line ends due to the current transformers' imperfection and the charging current.

The relay trips if the operating point, defined by the differential and stabilization currents' RMS values, is located within the relay tripping area (**Figure 2**) [1–3].

## 3. Optical protection ground wires (OPGW)

OPGW is the high-technology equipment for sending/receiving different kinds of data through electrical transmission lines.

The transmission lines are perhaps the most important part of the power system. It connects other power system elements such as power plants and substations. Electrical energy finds

the way from plants to consumption, thanks to these lines. Electrical engineers found out a very easy way for data transmission using OPGW and mentioned lines.

Transmission lines have at least three phase conductors. These conductors transmit electrical power. For rated voltage above 110 kV, line towers have one or more earth wires on their top. It could be a metal wire with protective function. This earth wire conducts one part of the fault current and protects people around the tower from dangerous voltage. It serves as a lightning protection also because it is on the highest point of the tower.

OPGW could be used as the earth wire. It has the same protection functions like a metal earth wire (lightning and high over-voltages) but also includes communication that is especially important for relay protection. This fiber optic communication provides reliability in the power system protection and data transmission. OPGW construction and number of layers depend on the requirements (both mechanical and electrical). Originally, fiber is placed in the tube. Several metallic strands are located around the tube.

Nowadays, OPGW finds its place in electrical engineering. Displacing the metal earth wires by the OPGW is quite well represented. Dual function of these wires has been won.

**Figure 3** shows the position of the OPGW on the top of the tower [4–8].

However, OPGW could be used for fast-data signal transmission. These signals could be protection signals, operation system data, signals for line testing and monitoring signals. Instead of this, video material or voice could be also carried out from one end of the line to another. OPGW is a multi-function conductor. The most important thing is the absence of additional investments for the trace. Transmission lines have already existed, so the only investment is in replacing the old wire with the new one.

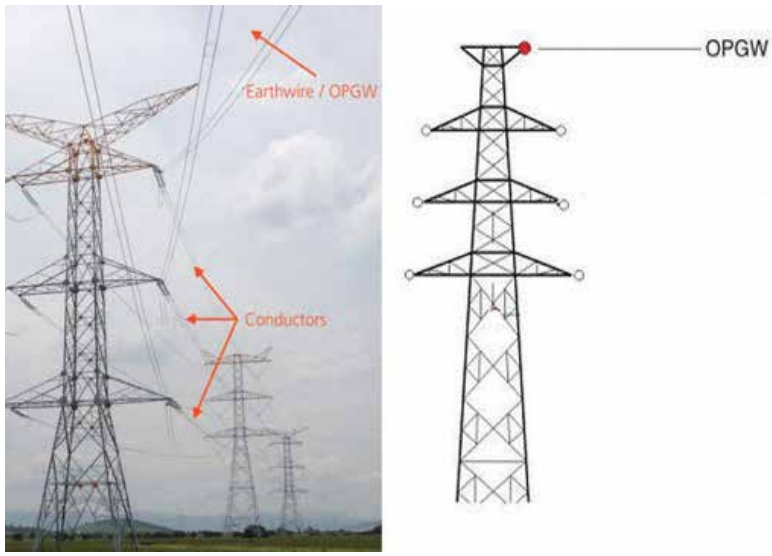


**Figure 3.** Position of OPGW.

### 3.1. OPGW cable constructions

Two types of the OPGWs are discussed. One is the central loose tube type and the other one is multi-loose tube type.

#### *3.1.1. Central loose tube type*

The steel tube is sealed and water resistant. The fibers are positioned in the center of the tube and are surrounded with water blocking gel. The stainless steel tube protects optical fibers from possible damages under abnormal operation conditions or during installation. The aluminum layer could be placed around this tube. Aluminum-clad steel wires create the external protection. This protection involves single or multiple layers of these wires. These aluminum wires provide compact construction. It has a dual function. One provides mechanical protection for sever conditions and the other one controls temperature rise during short-circuit conditions. **Figure 4** shows the cross-section of the central loose tube type.

It could be up to 48 fibers placed inside of the stainless steel tube. For easy identification, these optical wires are colored and are in different shapes. Wires are organized in many layers also. This organization provides high mechanical strength and good sag tension performance.

The core is much smaller. It is about 9 microns. This type of cable is suitable for greater distance than multimode cable. Only one light wave can travel through the fiber. This is the reason for distortion absence. The attenuation parameter for the single-mode fiber is typically 0.35 dB/km at 1310 nm and 0.23 dB/km at 1550 nm. This fiber is optimized for use in the 1300 nm & 1550 nm band [4].

#### *3.1.2. Multi-loose tube type*

The elements included in construction are almost the same. Optical fibers surrounded with water blocking gel are placed inside the stainless steel tube. This type has more than one tube. The tubes are helically positioned around the center of the cable. This is why it is called multi-loose tube type. The aluminum alloy is positioned in the external layer to give greater strength and resistance to corrosion.

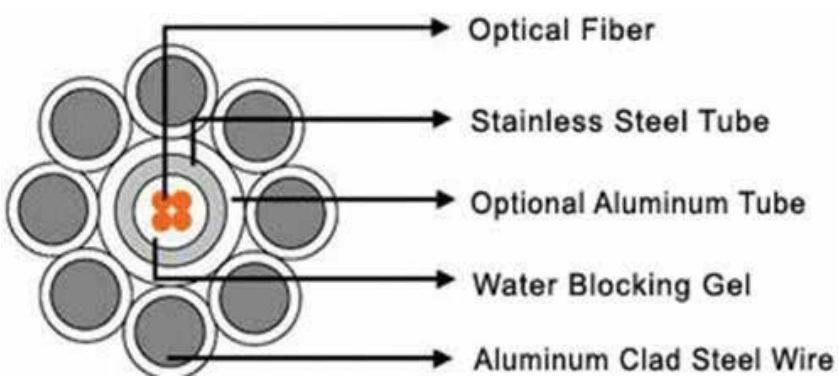


**Figure 4.** Central loose tube type.

The number of fibers is up to 144. The multi-loose tube type can meet the requirement of huge cross and large-current capacity.

This fiber has light traveling in the core in many rays called modes. It is made of glass fibers. The main application for multimode fibers is for short-reach optical transmission systems such as local area network (LAN) application. The attenuation parameter for multimode fiber is typically 0.8 dB/km at 1310 nm [4].

Telecom companies prefer this type of OPGW. Multi-loose tube type is good for video material transmission, internet connection and data for the SCADA system which is most important for electrical engineering. It is secure from accidental cutting due to construction work [4–8].

**Figure 5** shows cross-section of the multi-loose tube type.

**Tables 1–3** give some information on cable characteristics [7, 8].

### 3.2. OPGW cables' hardware

OPGW cables are connected with the tower and there are many elements which are used for that such as tension assembly, suspension assembly and attaching clamps and vibration dampers. These elements provide mechanical strength of OPGW and reduce oscillations. **Figures 6–9** show mentioned elements.

Sometimes, the distance between two nearest towers are longer then the length of OPGW. In that case, tension assembly has to be used. Connection with the tower is provided with tower clamps also [6].

An assembly with reinforced suspension clamp and neoprene inner covering, especially designed for OPGW cables, is shown in **Figure 8**.

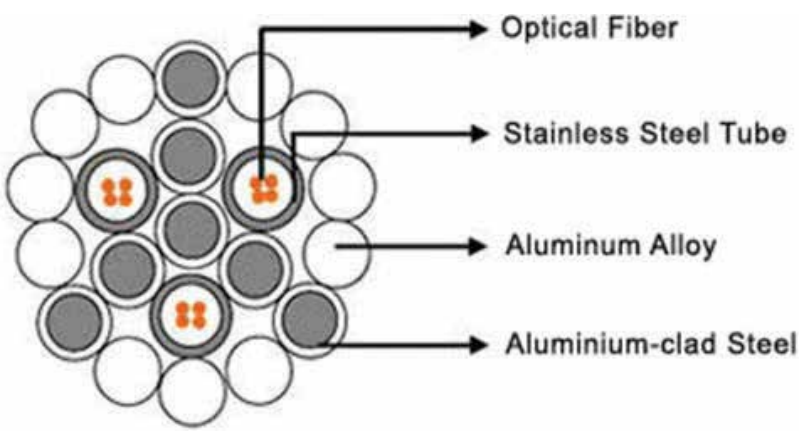


**Figure 5.** Multi-loose tube type.

| Fiber count | Diameter (mm) | Weight (kg/km) | Short circuit capacity ($KA^2s$) |
|---|---|---|---|
| 12 | 7.8 | 243 | 4.7 |
| 24 | 9 | 313 | 8.4 |
| 36 | 10.2 | 394 | 13.9 |
| 48 | 10.8 | 438 | 17.5 |

**Table 1.** Some characteristics of the single-layer central tube OPGW cable.

| Fiber count | Diameter (mm) | Weight (kg/km) | Short circuit capacity ($KA^2s$) |
|---|---|---|---|
| 12 | 13 | 671 | 42.2 |
| 24 | 15 | 825 | 87.9 |
| 28 | 16 | 857 | 132.2 |
| 36 | 17 | 910 | 186.3 |

**Table 2.** Some characteristics of the double-layer central tube OPGW cable.

| Fiber count | Diameter (mm) | Weight (kg/km) | Short circuit capacity ($KA^2s$) |
|---|---|---|---|
| 12 | 13.4 | 543,2 | 74.8 |
| 24 | 13.4 | 587,8 | 68.9 |
| 36 | 16.4 | 675,6 | 190.1 |
| 72 | 19.9 | 750 | 426.6 |
| 144 | 21.2 | 891,4 | 498.6 |

**Table 3.** Some characteristics of the multi-loose tube OPGW cable.

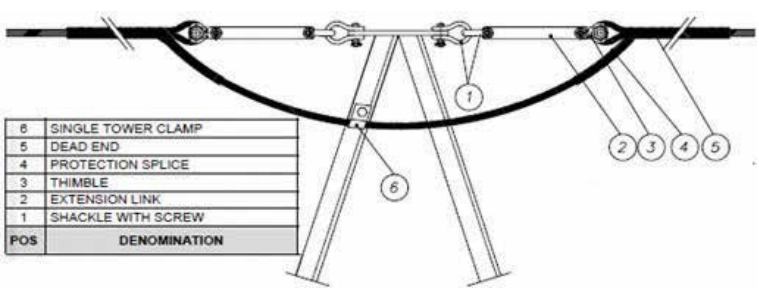


**Figure 6.** Double dead-end set passing for OPGW cable.

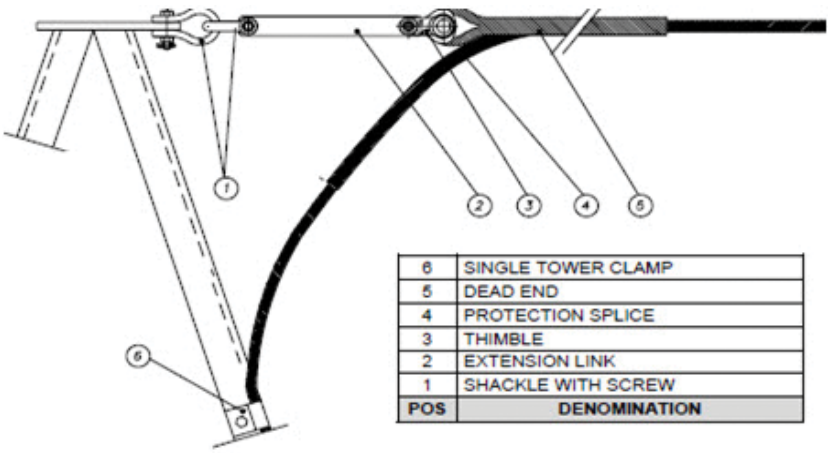


| POS | DENOMINATION |
|---|---|
| 6 | SINGLE TOWER CLAMP |
| 5 | DEAD END |
| 4 | PROTECTION SPLICE |
| 3 | THIMBLE |
| 2 | EXTENSION LINK |
| 1 | SHACKLE WITH SCREW |

**Figure 7.** Single dead-end set for OPGW cable.

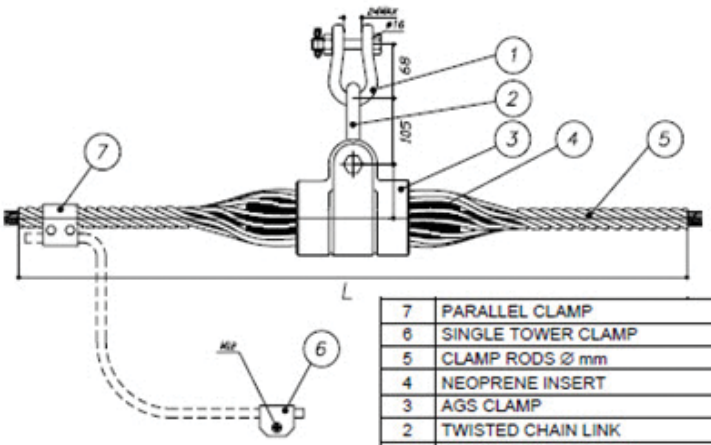


| POS | DENOMINATION |
|---|---|
| 7 | PARALLEL CLAMP |
| 6 | SINGLE TOWER CLAMP |
| 5 | CLAMP RODS Ø mm |
| 4 | NEOPRENE INSERT |
| 3 | AGS CLAMP |
| 2 | TWISTED CHAIN LINK |
| 1 | SHACKLE WITH SCREW |

**Figure 8.** Suspension assembly with twisted chain link for OPGW cable.

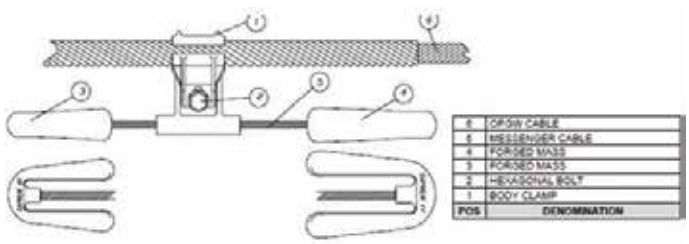

| POS | DENOMINATION |
|---|---|
| 6 | OPGW CABLE |
| 5 | MESSENGER CABLE |
| 4 | FORGED MASS |
| 3 | FORGED MASS |
| 2 | HEXAGONAL BOLT |
| 1 | BODY CLAMP |

**Figure 9.** Damper AMG—Four resonances asymmetric Stockbridge.

The dampers are used to absorb the cable vibrations as shown in **Figure 9**. The number of dampers is determined by the environmental conditions, the distance between towers, the type of OPGW cable and the installation parameters.

## 4. Differential transmission line protection with pilot relays

Pilot relays involve pilot wires. That is the main characteristic. It means that there is an interconnecting channel between two differential relays positioned at the opposite ends of the transmission line. Different types are used in practice. The distance between relays is the limiting factor. "Wire pilot", "Carrier-current pilot" and "Microwave pilot" are three different types of pilot conductors.

A wire pilot consists of a two-wire circuit of the telephone-line type. This is the easy solution because these circuits already exist as a part of the local telephone company system. Solution with a wire pilot is economical for distances up to 5–10 miles.

Beyond 10 miles of distances, a carrier-current pilot usually becomes more economical. The circuit consists of a power line as a conductor for low-voltage, high-frequency currents and the ground wire as the return conductor.

When the number of requiring pilot channels becomes larger than economic capabilities, microwave pilots are used. These are radio systems with ultra-high frequency.

**Figure 10** shows the schematic illustration of the a-c wire-pilot relaying principle.

It could be a d-c connection also but more elements have to be used. **Figure 11** illustrates pilot wire d-c connection to current transformers. This connection is provided via phase sequence networks and saturating transformers. Phase sequence networks are directly connected to current transformers. Three phase currents flow in and a single-phase voltage flows out of the network [9–11].

Impedances of relay circuits are not the same rate as the pilot wire impedance. Insulating transformers match these impedances.

Pilot wire has some requirements and limitations of equipment such as the insulation capability. High voltages may occur. Insulation capability depends on the highest values that could

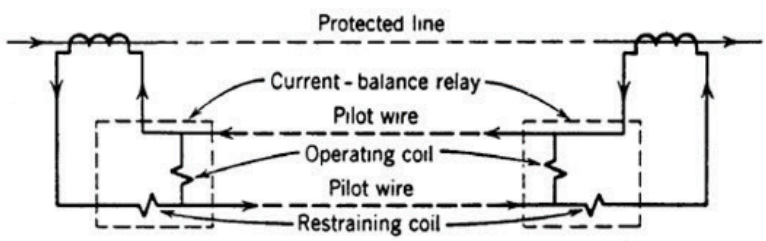


**Figure 10.** Schematic illustration of the opposed-voltage principle of the a-c wire-pilot relaying.

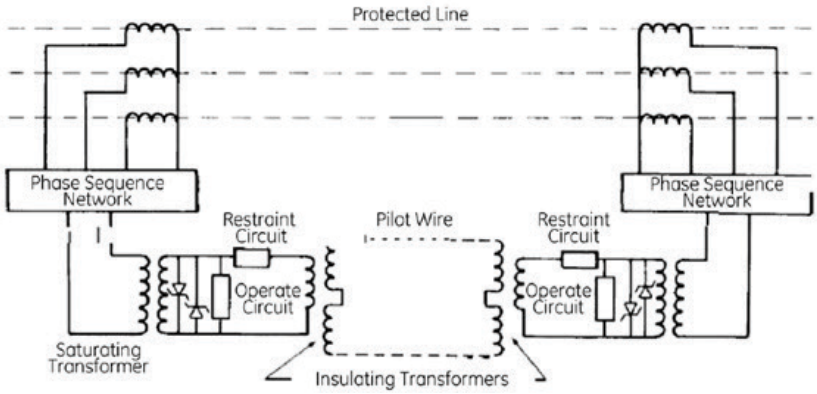


**Figure 11.** Pilot wire simplified arrangement.

occur. The main problem of the pilot wires is its length. It depends on loop resistance. There is a maximum value required. It is 2000 Ω. Shunt capacitance also has a limiting value. It is recommended that this capacitance be less than 1.5 microfarads.

Connection with the d-c wire pilot means that a lot of elements have to be used. This is one of the disadvantages. An a-c connection does not have these problems. Besides that, a-c connection also is immune to power swings. The good thing about d-c connection is the existence of these wires because of the telephone companies [10, 11].

## 5. Digital transmission line differential relays using digital communication

Natural disasters may be of significant impact on overhead transmission lines and cause communication outage related to pilot protection.

A dedicated fiber connection relies solely on optics residing within the relays to send IEEE C37.94 signaling bi-directionally, usually on a pair of single-mode strands of fiber from one relay to another. Potential sources of trouble for direct-connected current differential relay schemes normally can be traced to one of the following:

Most line-current differential relays use a 64 kbps communication interface even though designs with higher bandwidths (n × 64 kbps) are more common. The data frame length depends on the different relay designs. It varies between 15 bits and 200 or 400 bits. Sometimes it could be out of these bounds. The current data transmission has a large range also—from one to four per cycle, sometimes even more. There are some line current differential relays generally used for distribution line protection that uses slower-speed asynchronous serial communications. Presently, the use of Ethernet communications has not been widely implemented for line current differential relaying but is expected in future designs.

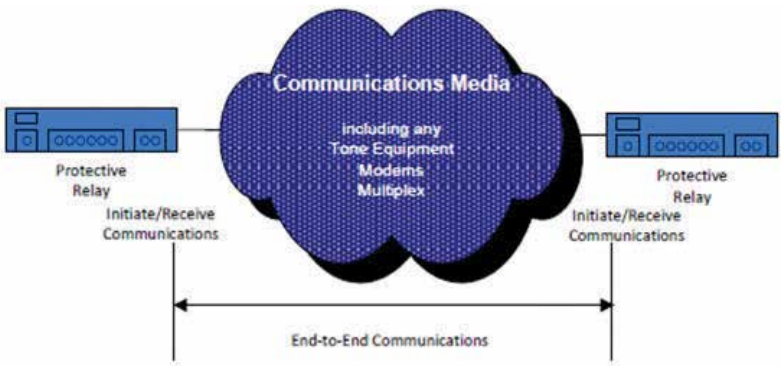


**Figure 12.** Protective relaying communications.

The communication channel can be over a dedicated fiber or over a multiplexed network, as shown in **Figure 12**. The dedicated fiber connection typically deploys LED or laser depending on the fiber's distance. The laser option can typically be applied for up to 100 km. The longer fiber lengths may need repeaters [12].

In order to guarantee the safe and stable operation of high-voltage transmission lines, differential protection is adopted as the main protection for the benefits of its phase-selection function and immunity to power swings and operation modes.

Many various principles for realization of the differential protection have been published in the recent literatures. The fast communication between relays installed at the opposite ends of the line is necessary [12].

There are a number of different relay measuring principles used by current differential relays:

- Percentage differential relays
- Charge comparison relays
- Power differential relays
- Alpha plane relay

These principles are briefly described in the following subsections.

### 5.1. Percentage differential relays

This is most like a classic approach. **Figures 1** and **2** show a basic arrangement. At each terminal, an evaluation of the sum of the local and remote current values is made in order to calculate a differential current. Under normal operating conditions or external faults, the current entering at one end of the protected circuit is practically the same as that leaving at the other end. Hence, the differential current value is practically zero and operation of the protection will not occur. For a fault on the protected power line, the differential current value

will exceed the operation threshold value and the protection will operate to clear the fault. There are so many modifications of the classic approach. Some of them use negative or zero-sequence current components.

There are two types of algorithms for differential protection: those that use phasors [13–16] and those that use instantaneous values of electrical quantities [17, 18].

### 5.2. Charge comparison operating principle

Charging current is a capacitive leakage current on the transmission line. The operating principles of charge comparison are similar to those of the more common percentage restraint current differential type of protective relay. Current differential relays compare the total currents entering and leaving the primary protection zone. They will trip if the difference between these currents exceeds some pre-defined restraint limit. For this comparison to be made, the current differential relay at the local station has to know the identical phase current recorded at the remote station(s) for the same interval being considered at the local station. This requires precise communications delay measurement and compensation. With current differential relays that compare instantaneous values, any error in compensation causes an error in the comparison and results in a variation of the pickup point. In addition, many samples per cycle are sent to the remote station, placing a burden on the communications channel [12].

The simple system shown in **Figure 13** is assumed.

Charging current compensation is a solution which removes charging current from the measured current and hence excludes the charging current from the differential current calculation. The charging current ($I_c$) can be estimated on the basis of operational capacitance:

$$I_C = \frac{2 \times \pi}{\sqrt{3}} \times U_n \times f_n \times c_d \times L \times 10^{-6} \tag{3}$$

where:

$I_c$—charging current (A),

$U_n$—rated network voltage (kV),

$f_n$—rated frequency (Hz),

$c_d$—longitudinal operational capacitance (nF/km),

$L$—line length (km).

Then the compensated current can be calculated as follows:

$$I_x = I_x' - I_C \tag{4}$$

where:

$I_x$—is compensated current at terminal x,

$I_x'$—is measured current at terminal x.

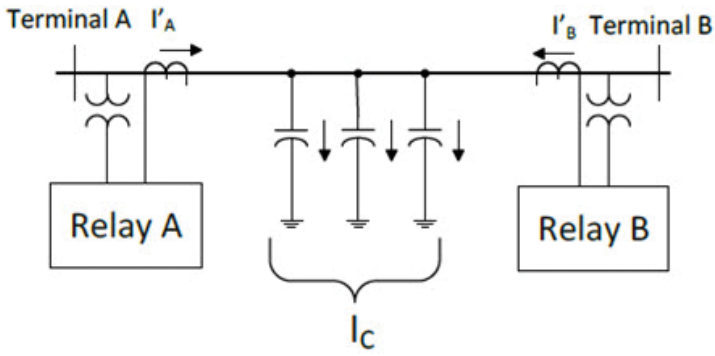


**Figure 13.** Charging current compensation.

Current that has a higher value should be compensated. It depends on the load flow direction. The higher value has current measured in the terminal where energy flows in.

Assuming a perfect alignment between local and remote currents, there is ±4 ms of error tolerance in the compensation. Given that line capacitance will cause a slight misalignment of the currents and that any compensation is going to have some resolution, it is practical to use ±3 ms as a limit for how much the communication channel delay can vary during normal operation without affecting the relaying. This is well within the normal operational limits of most communication channels in a dedicated fiber environment, even under adverse conditions.

### 5.3. Power differential relays

In addition to the classic approach, which uses current signals exclusively, there are solutions which require voltage inputs too [19–21].

Charging current is treated as the main cause of differential relay wrong operation in many papers. This current could be compensated with the power differential principle. This method proposes measuring currents and voltages at both ends of the transmission line. The original differential principle is saved. Operate and restrain values are compared but instead of currents, active powers at both ends are considered.

In this case, calculation time is reduced and length of line is not a limiting factor. These are the great advantages. Wrong operation during fault with low resistance and no faulted phase selection are the disadvantages of the mentioned technique.

There is a different method for realization of this protection based on power losses determination. It requires measuring currents and voltages at each end of the line too. Fault location could be determined in an easy way. This method compares difference in the real power at each end of the transmission line with the maximum power losses in the protected element. Every fault could be detected and the protection is secure and dependable. Fast communication between relays is very important [19–21].

### 5.4. Alpha plane relays

The alpha plane current differential protection principle compares individual magnitudes and angles of the currents. Magnitude and phase angle of each current at the opposite line ends are measured. According to these values, vector *r* is determined (its magnitude and angle). The alpha plane depicts the complex ratio of *IR*/*IL*, and it is shown in **Figure 14**.

Operating and restraining regions are presented in **Figure 15**. Comparison of the amplitudes and the angles lead to one of these decisions.

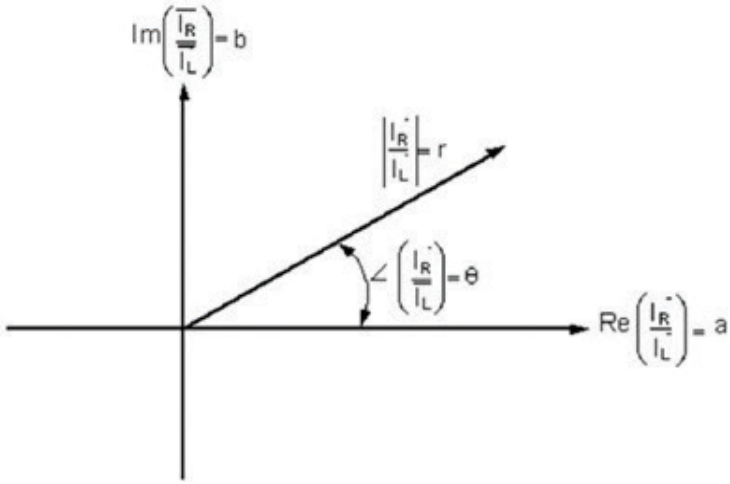


**Figure 14.** Complex current ratio plane (*α*-plane).

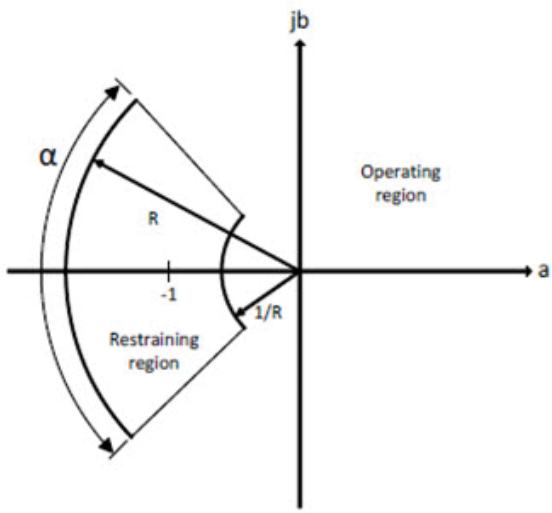


**Figure 15.** Current ratio plane.

The horizontal axis variable $a$ is the real part of the complex ratio of $IR/IL$, and the vertical axis variable $b$ is the imaginary part of the complex ratio of $IR/IL$. In the alpha plane element, the angular setting $\alpha$ [°] and the radius setting $R$ define restraining region. The first one allows the accommodation of current transformer and current alignment errors and the second one modifies sensitivity.

Data transmission delay has to be compensated. Current measuring and comparison depend on the communication channel. There are delays in two directions—transmit and receive. These delays sometimes are different. SONET/SDH systems could be the reason for this asymmetry. One technique for overcoming this problem, so-called ping-pong, involves measuring the round-trip channel delay. The communications path-delay differences are typically less than 2 ms. Delays of 3–5 ms are rare [12].

The papers that emphasize this method are authored by Almedia and Silva [22, 23].

## 6. Conclusion

This chapter describes using optical waveguide for communication between two differential relays on the opposite ends of the power systems' transmission line. Using the pilot wires limits utilizing this protection only for short lines. If optical protection ground wires are used, instead of pilot wires, the length of the line ceases to be a limiting factor. This chapter tells us more about constructions, assembly and utilization of the optical waveguides in differential protection. Also the newest algorithms of this protection are mentioned.

The sections present a classic approach of longitudinal differential protection of transmission lines, talk more about construction and installation of the OPGW cables and discuss digital protection algorithms. All the algorithms are difficult to be implemented without using OPGW.

## Author details

Tomislav Rajić

Address all correspondence to: rajic@etf.rs

University of Belgrade-School of Electrical Engineering, Belgrade, Serbia

## References

[1] Đurić M, Stojanović Z. Relay Protection. Belgrade: KIZ 'CENTER'; 2014

[2] Đurić M, Terzija V, Radojević Z, et al. Algorithms for Digital Relaying. Belgrade: ETA; 2012

[3] Ziegler G. Numerical Differential Protection: Principles and Applications. 2nd ed. Erlangen: Publicis Publishing; 2012. pp. 66-69 and 202-233

[4] Caledonian. Outdoor Fiber Cable [Internet]. Available from: http://www.caledonian-cables.com/Fiber%20Cable/New%20Fiber%20Cables/OPGW.html [Accessed: December 01, 2017]

[5] Elsewedy Electric. Fiber Optic Cables [Internet]. Available from: http://www.elsewedy-electric.com/fe/Common/ProductDivisions.aspx [Accessed: December 11, 2017]

[6] PRYSMIAN. Cables and Systems [Internet]. Available from: http://mcwadeproductions.co.za/wp-content/uploads/2015/08/Prysmian-Catalogue-Aug-2015.pdf [Accessed: December 05, 2017]

[7] W. T. Connect the World. Communication Cables [Internet]. Available from: https://www.alibaba.com/product-detail/Double-Layer-Stranded-Optical-Ground-Wire_60677017577.html [Accessed: December 11, 2017]

[8] American Wire Group. OPGW Optical Ground Wire—Multi Stainless Steel Tube [Internet]. Available from: http://wire.buyawg.com/viewitems/opgw-optical-ground-wire-2/opgw-optical-ground-wire? [Accessed: December 12, 2017]

[9] GE Grid Solutions. 5wire-Pilot Relays [Internet]. Available from: http://www.gegridsolutions.com/multilin/notes/artsci/art05.pdf [Accessed: December 02, 2017]

[10] GE Grid Solutions. 15line Protection with Pilot Relays [Internet]. Available from: http://www.gegridsolutions.com/multilin/notes/artsci/art15.pdf [Accessed: December 02, 2017]

[11] Voloh I, Johnson R. Applying digital line current differential relays over pilot wires. In: 2005 58th Annual Conference for Protective Relay Engineers; 5-7 April 2005; College Station, TX, USA. USA: IEEE; 2005

[12] C37.243-2015—IEEE Guide for Application of Digital Line Current Differential Relays Using Digital Communication. Date of Publication: 7 Aug. 2015. DOI: 10.1109/IEEESTD.2015.7181615

[13] Krishnanand K, Dash P, Naeem M. Detection, classification, and location of faults in power transmission lines. International Journal of Electrical Power & Energy Systems. 2015;**67**:76-86

[14] Hosny A, Sood VK. Transformer differential protection with phase angle difference based inrush restraint. Electric Power Systems Research. 2014;**115**:57-64

[15] Dambhare S, Soman SA, Chandorkar MC. Adaptive current differential protection schemes for transmission-line protection. IEEE Transactions on Power Delivery. 2009;**24**:1756-1762

[16] Adly A, El Sehiemy R, Abdelaziz A. A directional protection scheme during single pole tripping. Electric Power Systems Research. 2017;**144**:197-207

[17] Deng X, Yuan R, Li T, et al. Digital differential protection technique of transmission line using instantaneous active current: Theory, simulation and experiment. IET Generation Transmission and Distribution. 2015;**9**:996-1005

[18] Rajić T, Stojanović Z. An algorithm for longitudinal differential protection of transmission lines. International Journal of Electrical Power & Energy Systems. 2018;**94**:276-286

[19] Wen M, Chen D, Yin X. An energy differential relay for long transmission lines. International Journal of Electrical Power & Energy Systems. 2014;**55**:497-502

[20] Kawady T, Talaab A, Ahmed E. Dynamic performance of the power differential relay for transmission line protection. International Journal of Electrical Power & Energy Systems. 2010;**32**:390-397

[21] Aziz MMA, Zobaa AF, Ibrahim DK, et al. Transmission lines differential protection based on the energy conservation law. Electric Power Systems Research. 2008;**78**:1865-1872

[22] Almeida M, Silva K. Transmision lines differential protection based on an alternative incremental complex power alpha plane. IET Generation Transmission and Distribution. 2017;**11**:10-17

[23] Silva K, Bainy R. Generalized alpha plane for numerical differential protection applications. IEEE Transactions on Power Delivery. 2016;**31**:2565-2566

Chapter 14

# End-Fire Mode Spectroscopy: A Measuring Technique for Optical Waveguides

Dmitry V. Svistunov

Additional information is available at the end of the chapter

http://dx.doi.org/10.5772/intechopen.75558

**Abstract**

End-fire mode spectroscopy technique provides reliable measurement of the whole mode spectrum of optical waveguides having arbitrary cross refractive index profile. The method is based on registration of light beams radiated from the abrupt output edge of the waveguide, with each beam corresponding to the individual waveguide mode. Due to different values of mode propagation constants, modes of different orders demonstrate different refraction angles at the output waveguide face when modes reach that face under the same nonzero inclination angle. Just this feature is used in the technique. Mode excitation is performed directly through the input waveguide face, and therefore the technique can be applied to analyze mode spectrum of arbitrary waveguides, including the ones with non-monotonic index profiles (particularly, symmetric step-index profiles or buried graded-index waveguides with any burying depths).

**Keywords:** waveguides, integrated optics, mode index, refractive index, optical measurements

## 1. Introduction

Optical waveguides are the basic elements of any photonic device, and their parameters define the operating performances of the whole photonic unit. Optimization of those parameters requires performing the choice of appropriate technology conditions. Development of fabrication technology and further designing the waveguide elements having pre-defined properties need performing a control of the characteristics of trial waveguide samples. Furthermore, planar optical waveguides are used intensively in determination of the basic properties of optical materials. And the problem of reliable determination of the main waveguide performances is still actual.

Important part of examination of planar optical waveguides is measurement of the waveguide mode spectrum. Usually this procedure is performed by a well-known m-line spectroscopy technique (e.g., see [1–5]). The measured set of mode indices can be considered as initial data as for preliminary determination of the device operating performances as for reconstruction of cross refractive index profile in the formed trial sample. Traditional computing techniques allowing reconstruction of that profile are described in Refs. [6, 7]. However, in cases of planar waveguide structures with thick cover layers or so-called buried graded-index waveguides m-line spectroscopy does not provide reliable measurements. Thick cover layers or large burying depths do not allow tunneling the modes to the external prism and forming the corresponding spatial m-lines. In these cases, some modes (first of all, the lower-order modes) may be simply missed in examinations by m-line spectroscopy [8, 9]. The greater the burying depth the fewer number of modes can be measured by this method. To avoid missing the modes, a layer-by-layer etching of the sample surface could be applied [10, 11]. However, that procedure has many chances to cut a part of the refractive index profile occupied by the mode fields, and that should lead to distortion of the original waveguide mode spectrum. The use of nonlinear optical effects like second harmonic generation [9] can be successful only for limited number of optical materials demonstrating high values of the corresponding coefficients.

Here we describe a measuring technique named the end-fire mode spectroscopy which is suitable for examination of planar waveguides having arbitrary refractive index profiles including the case of buried waveguide structures with any burying depths, and the presented results of examination of buried waveguides prove this advantage of the technique. Furthermore, here we show that this technique allows also conducting direct measurements of another important characteristic – the maximal refractive index in graded-index waveguides, unlike conventional techniques that involve the set of measured mode indices and employ computing of the maximal value in the refractive index profile using different approximations.

## 2. Method content

### 2.1. Mode spectrum measuring

Usually waveguide mode spectrum is presented with a kit of mode indices $N_m$ (the value obtained from the mode propagation constant $\beta_m$ as $N_m = \beta_m / k$, where $k = \omega / c = 2\pi / \lambda$; $\omega$, c and $\lambda$ – the light frequency, velocity and wavelength in vacuum correspondingly, m – the mode number). These values relate to the mode phase velocity, and they are involved into expressions describing the mode fields which are derived as solutions of wave equations. We can write a well-known general form of such expression for mode electric field vector (magnetic component of light wave is of the same view): $\mathbf{E_m}(x,y,z,t) = \mathbf{E_0}(x,y) \times \exp[i(\omega t - \beta_m z)]$. That representation is applied for all kinds of waveguides: planar and 3D (including stripe and channel waveguides, fibers, etc.) having as different step-like cross index distributions as graded-index ones. The expression written in cylindrical coordinates has a similar view (that approach is more convenient for optical fibers). Depending on the mode type, corresponding nonzero field projections are considered. Evidently, that expression describes unidirectional

http://dx.doi.org/10.5772/intechopen.75558

propagation of light wave having some cross field distribution. That description means that the waveguide mode is represented by the equivalent model of plane wave propagating in homogeneous uniform medium with the same light phase velocity as the original waveguide mode. So, we can consider a waveguide transmitting several modes as an imaginary set of superimposed layers with uniform refractive indices $N_m$, each denoting the certain waveguide mode and transmitting the plane wave having corresponding cross field distribution as it is shown in **Figure 1**. Then our aim (to measure the mode spectrum) can be associated with the task of measuring the indices of different uniform media illuminated with plane light waves. That task can be performed by the technique like one of the usual methods of traditional bulk refractometry, for example by the goniometric technique that bases on the Snell's law and employs registration of the beam declination angle when the prism of tested optical material is illuminated with the collimated incident light. Thus we could try to provide similar experimental conditions in order to examine the waveguide samples.

The content of the end-fire mode spectroscopy is registration of light beams radiated from the abrupt output edge of a planar waveguide, with each beam corresponding to the individual waveguide mode. Due to different values of mode propagation constants, modes of different orders demonstrate different refraction angles at the output sample face if they are directed to that face under nonzero incidence angle into the waveguide. Just this feature is exploited by the technique in procedures of mode spectrum measurements. Both excitation and output of waveguide modes are performed at the sample faces by the end-fire coupling method which allows reliable launching and output of the whole mode spectrum in any planar waveguide. Therefore, the end-fire mode spectroscopy technique can be applied to examination of planar waveguides having arbitrary cross refractive index profiles including symmetric step-index ones and deep-buried graded-index waveguides.

The measuring block-scheme is shown in **Figure 2**. Collimated light beam is focused on the input waveguide face by the cylindrical lens. The whole mode spectrum can be launched in this manner in few-mode waveguides. Application of the input cylindrical lens provides obtaining collimated (in the sample planform) mode beams propagating into the examined waveguide. In the case of a thick multimode waveguide, a group of modes is excited simultaneously and can be registered. Further scanning the input sample face along the Y axis allows launching and registration of other mode groups until the whole waveguide mode spectrum is measured.

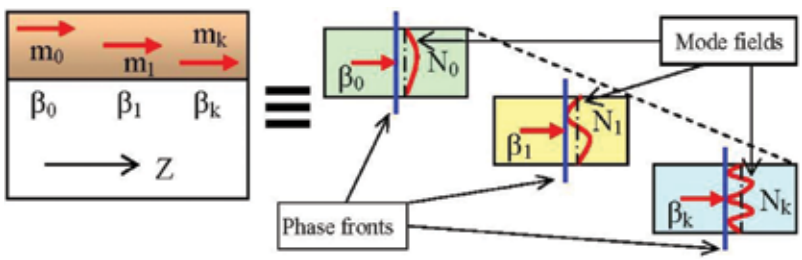


**Figure 1.** Equivalent representation of graded-index planar waveguide as a set of superimposed layers having uniform refractive indices.

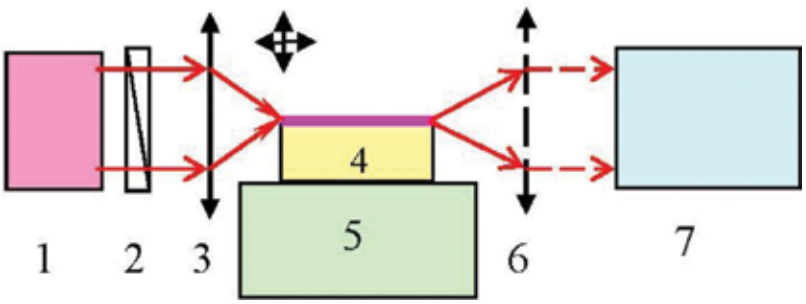


**Figure 2.** Measuring block-scheme. 1 – Laser with collimator, 2 – Polarizer, 3 and 6 – Cylindrical lenses, 4 – Examined waveguide sample, 5 – Goniometer sample mount, 7 – Goniometer telescope.

Cylindrical lens in the recording block is not necessary for measuring the mode spectrum. That lens should be installed in procedures of complex measuring as described below.

Two scheme variants providing skew incidence of waveguide beams to the sample output face have been proposed [12]. The former one uses the trapezoidal (in planform section) samples having non-parallel opposite (input and output) waveguide faces as it is shown in **Figure 3**. The latter one allows testing the samples having usual rectangular form with mode launching performed under special procedure by focusing the probe beam on the polished side face of the examined waveguide. Application of a cylindrical lens for mode excitation enables obtaining collimated (in planform XZ section) waveguide beams in both scheme variants. The latter variant is very attractive because of its non-destructive character, but the alternative former scheme is more convenient for conducting measurements.

The optical scheme has been built according to the former measuring variant in our experiments, and **Figure 3** demonstrates light ray paths in planform XZ section of the sample. Whereas the directions of simultaneously excited modes slightly differ due to different refraction at the input sample face, the rays of only one mode beam are shown into the waveguide in order to simplify the drawing. Each output light beam is associated with the individual waveguide mode, and the mode orders of the corresponding modes are identified by the

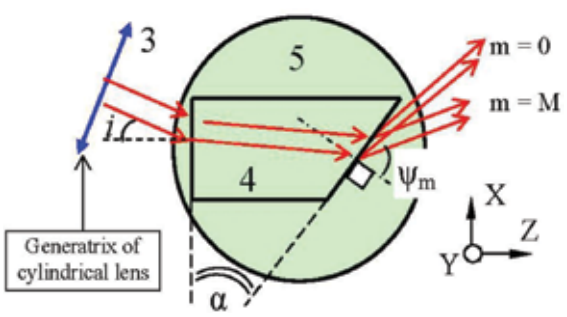


**Figure 3.** Planform of the sample on the goniometer mount. Two-sided arrow denotes here the cylindrical lens generatrix; other designations are the same as in **Figure 2**.

http://dx.doi.org/10.5772/intechopen.75558

inclination of a certain output beam to the output waveguide face: the lower the mode order, the bigger the output angle. The fundamental mode forms the light beam having maximal value of the output angle $\psi_{max}$. In the upright YZ projection, the output beams have large divergence (see **Figure 2**). Therefore, these beams appear on the cross screen apart of the sample as separate light strips.

Application of the Snell's law both to input and output sample faces leads to following expression for calculating the mode indices $N_m$:

$$N_m = \sqrt{(\sin \psi_m / \sin \alpha + \sin i / \tan \alpha)^2 + (\sin i)^2} \quad (1)$$

where $m$ is the mode order, $i$ and $\psi_m$ are the incident and output angles of the spatial light beams measured in the XZ plane, and $\alpha$ is the angle between the input and output waveguide faces.

Evidently, normal incidence of the probe beam to the input waveguide face (i.e., the condition $i = 0$) is the simplest scheme variant that is most suitable for measuring. For such scheme, Eq. (1) transforms to.

$$N_m = \sin \psi_m / \sin \alpha \quad (2)$$

When graded-index waveguides are examined, the pattern of output beams has a specific view as a set of slightly curved light strips on the cross screen. The simplest way to explain that pattern is application of the known ray approximation of waveguide light propagation. Following to that approach, **Figure 4** demonstrates the rays into shallow graded-index planar waveguide. All drawn rays represent the same waveguide mode.

One can see that the ray 3 is radiated being parallel to the sample surface from the output face point with the depth of so-called turning point which corresponds to the depth in the refractive index cross distribution where the mode index is equal to the refractive index value. So, just the direction of that ray in the planform XZ plane should be registered in measuring the waveguide mode spectrum. The ray scheme demonstrates also the rays 2 and 4 radiated from arbitrary point of the output face under equal opposite tilts. The presence of those rays means

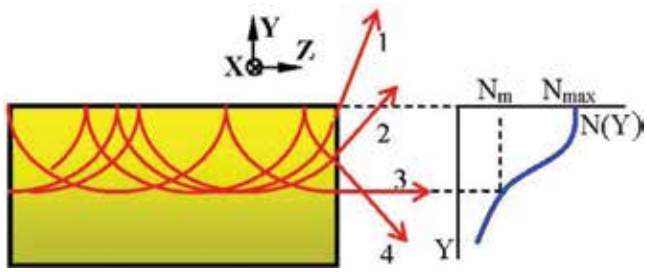


**Figure 4.** Ray approximation of mode propagation into graded-index planar waveguide. All plotted rays represent the same mode.

that the output light beam is symmetric relatively to the ray 3. Furthermore, the rays 1–3 are radiated from the sample points at different depths where the refractive index has different values. Therefore, the projections of those output rays to the planform XZ should have different directions in that plane. Thus the pattern of the output light beam (corresponding to the certain waveguide mode) on the cross screen apart the sample looks like a curved light strip which is symmetric relatively to the waveguide surface as it is shown in **Figure 5**. As we must register the rays that are analogous to the ray 3, we find those rays at the top of parabolic-like light strip.

Reliability of the results of mode spectrum measuring by the end-fire mode spectroscopy was proved in comparative examinations of graded-index planar waveguides fabricated in optical glasses. The mode spectrum of the same waveguides had been measured independently with the described technique and also by the traditional m-line spectroscopy method. Whereas the main advantage of the end-fire spectroscopy is its capability to analyze buried waveguides, several shallow graded-index samples had been chosen for comparative measuring because the traditional technique provides reliable results only for that type of waveguides.

**Figure 6** presents the photo of the typical pattern formed by output light beams on the cross screen apart from the sample in examinations by the end-fire mode spectroscopy.

The whole spectrum of TE modes was launched simultaneously in this experiment, and the light strips really demonstrate some curvature due to the cross graded-index profile in the examined waveguide layer (see **Figure 6a**). The centers of the parabolic-like light curves were used for measuring the output angles $\psi_m$. The enlarged view of those central parts of the light strips (**Figure 6b**) demonstrates good separation of the strips. So, they can be easily registered in measuring.

As an example, **Table 1** presents the results of comparative examinations of the planar waveguide fabricated on the substrate of commercial sodium-containing glass K8 by ion exchange in a potassium nitrate melt at 400°C. The probe light of 633 nm wavelength was used, and the bevel angle between the opposite sample faces was measured with the goniometer by the autocollimation method as $\alpha = 38^0\ 57'\ 08'' \pm 5''$.

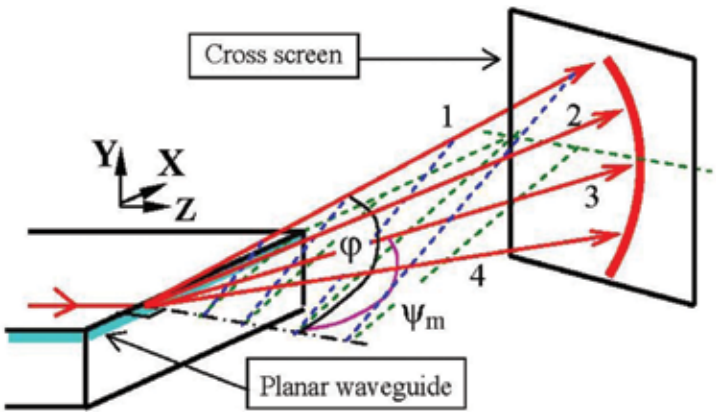


**Figure 5.** Spatial light beam radiated from the output waveguide face.

http://dx.doi.org/10.5772/intechopen.75558

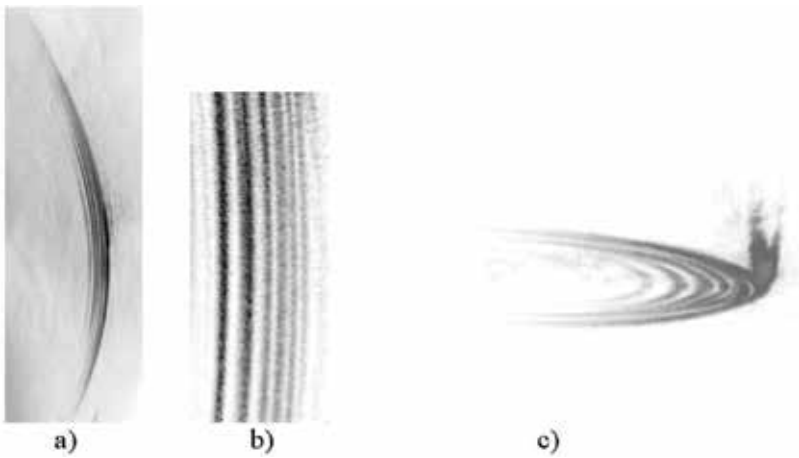


**Figure 6.** Photos of the patterns on the cross screen in procedures of mode spectrum measuring (a, b) and in complex measuring (c). $\lambda$ = 633 nm, planar K8:$K^+$ waveguide. (Here all photos – Negatives, colored positives – In online version).

| Mode order | 0 | 1 | 2 | 3 | 4 | 5 | 6 |
|---|---|---|---|---|---|---|---|
| m-line spectro-scopy | 1.51980 | 1.51822 | 1,51701 | 1.51611 | 1.51544 | 1.51493 | 1.51452 |
| End-fire mode spectro-scopy | 1.51985 | 1.51824 | 1.51711 | 1.51619 | 1.51549 | 1.51494 | 1.51456 |

**Table 1.** Comparative examination of planar K8: $K^+$ waveguide, TE modes, $\lambda$ = 633 nm.

A good agreement between the mode index values measured by both techniques is evident. The difference between the results obtained by those methods does not exceed $10^{-4}$, which is similar to the errors considered quite acceptable in traditional mode index measurements.

Furthermore, the samples of buried waveguide structures have been tested by the end-fire spectroscopy technique. Planar buried waveguides have been formed in optical glasses by two-staged ion exchange. First, the shallow planar waveguides having the maximal refractive index at the sample surface were fabricated. Then the samples were treated into another melt providing appearance of reverse direction of diffusion process into the sample. That procedure led to decreasing the surface refractive index while the maximum of the cross index distribution was shifted deeper to the sample depth. Performed choice of the stage's durations resulted in fabrication of buried waveguide structures.

Mode excitation was performed in examinations by focusing the light beam to the input sample face. However, no waveguide modes have been registered in examinations of those structures by traditional m-line spectroscopy while both direct watching and application of $40^x$

and 90$^x$ objectives proved the presence of the mode light spots at the output sample face. That means that the obtained burying depths were sufficient for the case when the "tails" of mode field distribution were so weak near the sample surface that their tunneling to the prism did not resulted in appearance of the output light beams which could be registered. Application of the end-fire mode spectroscopy technique allowed analyzing the waveguide structures that supported propagation of single TE mode. The results of performed examinations by the described technique are presented in **Table 2**.

Thus, the end-fire mode spectroscopy technique has demonstrated successfully its advantageous feature that is capability of examination of planar structures of any type.

### 2.2. Evaluation of maximal refractive index

Besides mode spectrum measuring, the technique enables evaluating the maximal refractive index in graded-index waveguides. A principle of that procedure can also be explained involving ray approximation of mode propagation. One can conclude from **Figure 4** that we should register the ray 1 radiated from the waveguide at the sample point having maximal refractive index in the graded-index layer. Determination of that index is performed using the output angle $\varphi$ of that boundary ray of the emitted light beam. That angle is marked in **Figure 5**, and we see that it must be measured in the plane formed by both the considered ray and the normal to the output sample face, and that plane is tilted to the planform XZ plane. Ray tracing performed for that boundary ray shows that the maximal refractive index $N_{max}$ can be determined by solving Eq. [13].

$$N_{max} \cdot \cos\left\{\arcsin\left[\left(N_m/N_{max}\right)\cos\,\alpha\right]\right\} = \sin\,\varphi \tag{3}$$

However, in our optical scheme the goniometer measures the angles lying in the XZ plane. So, we obtain in our measuring the values of the angle $\varphi_{xz}$ which is the projection of the angle $\varphi$ to the XZ plane, and the relation between those angles should be used in calculations. Another circumstance to be considered is following: both angular and linear apertures of the goniometer telescope are limited, but the registered beam is high-divergent in the upright projection YZ. Therefore, we should apply the cylindrical lens (drawn by dash line in **Figure 2**)

| Sample | K8 : $K^+$ : $Na^+$ | K8 : $K^+$ : $Na^+$ | K8 : $Ag^+$ : $Na^+$ |
|---|---|---|---|
| Stage 1 of treatment | Melt: $KNO_3$ 400 °C ; 24 hrs | Melt: $KNO_3$ 400 °C ; 24 hrs | Melt: 0.5% mol. $KNO_3$ + 99.5% mol. eut. (K – Na)$NO_3$ 348 °C ; 24 hrs |
| Stage 2 of treatment | Melt: $NaNO_3$ 400 °C ; 19.5 hrs | Melt: $NaNO_3$ 400 °C ; 15 hrs | Melt: $NaNO_3$ 348 °C ; 15 hrs |
| Mode index | 1.5156 | 1.5159 | 1.5162 |

**Table 2.** Examination of buried waveguides by end-fire mode spectroscopy, $TE_0$, $\lambda$ = 633 nm.

in the recording scheme block in order to collimate the measured light beam. Considering the parameters of the lens, relation between the mentioned angles can be deduced as.

$$\tan\varphi = \tan\varphi_{XZ}\sqrt{\left[1+(d/2f)^2\right]\left[(N_{\max}/N_m)^2-(\cos\alpha)^2\right]}/\sin\alpha \quad (4)$$

where $f$ is the focus length of the cylindrical lens, and $d$ is the size of the output curved light strip measured along the Y axis behind that lens. Considering (4) and also a known relation $\sec^2\varphi = 1 + \tan^2\varphi$, one can deduce from (3) the final equation containing the only unknown $N_{\max}$. Numerical solution of the obtained equation gives the desired value of the maximal refractive index in the graded-index waveguide.

It should be noted that mentioned collimation of the output beam is needed only in measurements of the maximal refractive index when one must register high-divergent boundary rays. Measurement of the mode spectrum is performed by registering the central parts of the output light beams, and it does not matter is the output cylindrical lens applied or not in that case.

As an example, let us consider the results of evaluation of the maximal refractive index in the K8: $K^+$ waveguide whose mode spectrum is presented above. The photo of the pattern of output light beam obtained in measuring by the described technique is shown in **Figure 6c**. For comparison, the maximal refractive index had been measured directly by the end-fire mode spectroscopy and also computed according to conventional methods using the measured mode spectrum. The White-Heidrich method [6] gives the result as $N_{\max,WH} = 1.52204$, and the Chiang method [7] is resulted in $N_{\max,Ch} = 1.52138$. So, these widespread computing techniques give different results for the same waveguide. Basing on the results obtained for waveguides of that type (see, for example, Ref. [14]), and also taking into account our previous experience we can guess that application of the White-Heidrich technique is more appropriate for reconstruction of refractive index profile in the examined sample because the used fabrication technology results in graded-index layers demonstrating cross refractive index distributions which are well described with the *erfc* function. Direct measuring conducted by the end-fire mode spectroscopy resulted in the value $N_{\max} = 1.5223$ when the highest-order mode was registered. This value is evidently closer to the result of the White-Heidrich method than the solution of the Chiang method. It means that the described technique provides direct measuring of the maximal refractive index in graded-index waveguides with rather good accuracy. We must note that some imprecision occurs in measuring caused by diffractive character of real output light beams that defines smudgy ends of registered light strips and therefore impedes obtaining a high accuracy. However, the deviation of the measured result from the actual one is less than the difference (and, consequently, uncertainty) between the results computed according to traditional techniques. In any way, the obtained value is to be considered as the result of maximal index estimation and can be used as itself for further estimations of treatment conditions or waveguide unit performances, as for choosing between the noted traditional computing techniques of index profile reconstruction.

The pattern shown in **Figure 6c** demonstrates that application of the cylindrical leans in the scheme recording block really does not affect the central parts of light strips and allows

conducting measurements of the mode spectrum also in that variant of optical scheme. So, the end-fire mode spectroscopy technique allows performing reliable direct complex measurements of the set of important optical characteristics of arbitrary planar waveguides (the mode spectrum and the maximal refractive index) in a single procedure.

## 3. Measuring conditions

### 3.1. Choice of the sample form

For enhancing the technique sensitivity and accuracy, we must consider the conditions providing maximal variation $\delta\psi_m$ of the light beam emission line related to mode index variation $\delta N_m$. Referring to Eq. (2), one can see that the value of the term $\partial\psi_m/\partial N_m = \sin\alpha/(1 - N^2_m \sin^2\alpha)^{1/2}$ increases with a rise in the bevel angle $\alpha$ between the opposite waveguide faces. So, in order to provide high method sensitivity we must maximize that angle. The same can be concluded from the dependence $\psi_m(\alpha)$ that is plotted in **Figure 7**.

However, when $\alpha$ approaches the value $\alpha_{lim} = \arcsin(1/N_m)$, total inner reflection appears at the output waveguide face, and the mode is reflected back to the waveguide (to the side sample face) instead of being emitted out through the output sample face. That limit value is marked in the graph with the dash line. Proper choice of the angle $\alpha$ should be performed considering the maximal refractive index value, which is expected to be obtained into the sample by the applied method of waveguide fabrication. Slightly overestimated value of that refractive index is substituted for $N_m$ to the expression for $\alpha_{lim}$. Being calculated in such a manner, angle limit represents the optimal value of the angle $\alpha$. Indeed, as the mode indices are always less than the maximal refractive index in a waveguide, described manner of the bevel angle choice prevents the occurrence of total inner reflection at the output sample face for all modes of the examined waveguide.

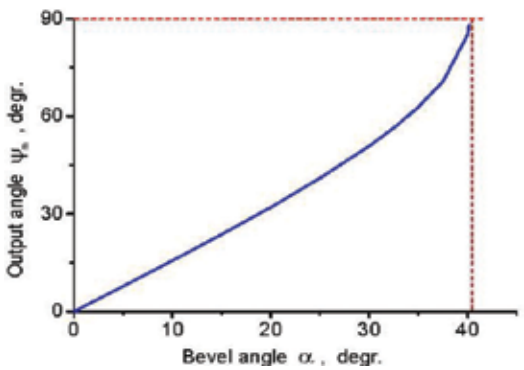


**Figure 7.** Influence of the sample bevel angle on the sensitivity of measuring. $N_m = 1.55$.

http://dx.doi.org/10.5772/intechopen.75558

### 3.2. Requirements to the collimator

Adjustment of the collimator must provide acceptable divergence of the collimated light beam. Let us first consider the axial section of that beam by the plane normal to the waveguide surface (the upright plane YZ in **Figure 2**). One can conclude from the drawn ray scheme that divergent (in that upright projection) beam causes a mismatch between apertures of waveguide mode and exciting focused spatial light beam. That mismatch results in decreasing the excitation efficiency. However, it does not influence on the registered angular values (they are measured into another planform projection XZ). Now let us consider the affect of beam divergence into that plane XZ (that coincides with the sample surface) on the results of angular measurements. One can conclude from **Figure 3** that if a divergence of the incident light beam is small, each output beam acquires a slight angular broadening, but it remains approximately axisymmetric relatively to the direction $\psi_m$. Therefore, registration of the central direction of each weakly divergent output light beam eliminates the affect of possible small maladjustment of the collimator.

Another requirement concerns performances of examined waveguides: the divergence of each output beam must be less than the angles between the output beams corresponding to waveguide modes of adjacent orders. Otherwise, overlapped different beams could not be distinguished and measured. Let us evaluate these angles basing on performances of graded-index waveguides which mostly demonstrate the closer mode indices (and, hence, would form the least beam spatial separation in the considered scheme) for higher-order modes. Considering the presented condition for the bevel angle $\alpha$, we can deduce following expression from Eq.(1) for adjacent higher-order modes: $N_m - N_{m+1} \approx N_{max} \times (\psi_m - \psi_{m+1}) \cos \psi_{av}$, where $\psi_{av} = (\psi_m + \psi_{m+1})/2$. On the other hand, we obtain from Eq. (1) that $\cos \psi_m = [1 - (N_{av}/N_{max})^2]^{1/2}$ where $N_{av}$ – the value corresponding to the mean direction between considered output beams, and $N_{av} \approx (N_m + N_{m+1})/2$. Hence the angle between those light beams $\delta\psi = \psi_m - \psi_{m+1} \approx (N_m - N_{m+1})/(N^2_{max} - N^2_{av})^{1/2}$. As an example, let us evaluate $\delta\psi$ for some planar graded-index waveguide fabricated by ion-exchanged diffusion in commercial glass. Defining the model values as $N_{max} = 1.53$, $N_{av} = 1.51$ and also $(N_m - N_{m+1}) = 10^{-4}$ for higher-order modes, we obtain $\delta\psi \approx 4 \times 10^{-4}$ radian ≈ 1.4 arcmin. So, the divergence of the collimated light beam must not exceed that limit. That condition can be easily met in adjusting the optical scheme.

Thus we can expect that the source of the main affect on the results could be deviations from the conditions of mode excitation occurring in the launching scheme unit.

### 3.3. Tolerance of incident beam direction

As Eq. (1) involves the angle of incidence *i*, that angle can be considered as a factor capable of affecting the reliability of the results of mode index measurements. Being considered together, Eqs. (1) and (2) allow evaluating the occurred errors caused by deviation of the incident beam from the condition of normal incidence to the input waveguide face. Indeed, in the basic measuring regime calculations of mode indices are executed according to Eq. (2). However, if the mode launching unit is adjusted inaccurately (i.e. when $i \neq 0$), substitution of

measured values $\psi_m$ to Eq. (2) leads to appearance of errors because the right way is application of Eq. (1) in this case.

Let us evaluate those errors. We can deduce from Eq. (2) that $\partial N_m/\partial\psi_m = (\cos\psi_m/\sin\alpha)$. Ray tracing that was performed for the scheme shown in **Figure 3** resulted in following $\psi_m(i)$ dependence: $\psi_m = \arcsin\{N_m \sin[\alpha - \arcsin(\sin i/N_m)]\}$. We could note that the operating variant of the measuring technique is the case $i \approx 0$. Then, considering negligibility of the angle $i$, the term $\partial\psi_m/\partial i$ can be written as $\partial\psi_m/\partial i \approx -\cos\alpha/\cos\psi_m$. Substituting that term into the expression for $\partial N_m/\partial\psi_m$ and defining $\Delta N_m = |\partial N_m|$, we can evaluate the mode index error as $\Delta N_m = \Delta i/\tan\alpha$. Here $\Delta i$ denotes the increment of angle $i$ from some value. Since we are considering the deviation from the condition of normal incidence of the input beam (i.e., from zero angle of incidence), just the small angle $i$ plays itself the role of the increment $\Delta i$ here. Then, replacing the values in the derived expression, we obtain the desired dependence of the mode index error on the angle of incidence:

$$\Delta N_m(i) = i/\tan\alpha \tag{5}$$

where $i$ is a small angle in radian measure. This expression indicates that the mentioned mode index errors caused by wrong application of Eq. (2) in the case of deviation from the condition of normal incidence of the input light beam will be identical for all modes in the examined waveguide.

To confirm that unobvious conclusion, we can consider the described sample of K8: $K^+$ waveguide and evaluate numerically the mentioned errors by another manner. In this case we assume that considered mode index error can be defined as $\Delta N_m(i) = N_m - N'_m$, where $N'_m$ is the incorrect value calculating according to Eq.(2) without involving the angle of incidence, and $N_m$ is the actual mode index value. The mode indices measured by the traditional m-line spectroscopy technique (see **Table 1**) are substituted for those actual values. Defining the angle of incidence $i$ as a variable and using the actual mode index values, we calculated from Eq. (1) the values of the output angle $\psi'_m$ that would be obtained in measurements for the given angles $i$. Then we substitute those angles $\psi'_m$ into Eq. (2) and find the corresponding $N'_m$ values. The errors of mode index determination are obtained by comparing the actual mode indices with those calculated $N'_m$ values. The results of determination of $\Delta N_m(i)$ values by that manner are shown in **Figure 8**.

It can be noted that the errors calculated for the modes of different orders are really identical in the most practical cases of small angles of incidence. The $\Delta N_m(i)$ dependence obtained for that waveguide sample by calculation according to Eq. (5) coincides completely with the one shown in this figure. So, the obtained results confirm a validity of the derived Eq. (5), and it can be applied for evaluation of mode index errors. We can note here that precise adjustment of the used GS-5 goniometer sample mount in our experiments allowed limiting the values of the angle of incidence within the range of 5 arcsec. Therefore the mentioned errors do not exceed $3 \times 10^{-5}$, and that is quite acceptable value corresponding to the usual level of errors occurred in measuring by the traditional m-line spectroscopy technique.

One can also see from Eq. (5) that the choice of the bevel angle $\alpha$ closer to the upper limit value makes it possible not only to increase the sensitivity of the end-fire mode spectroscopy

http://dx.doi.org/10.5772/intechopen.75558

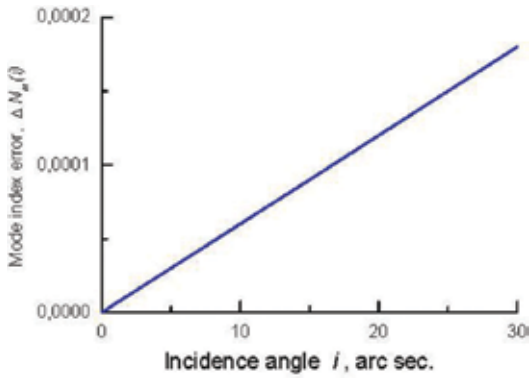


**Figure 8.** Errors caused by deviation from the condition of normal incidence of exciting beam.

technique but also to reduce the influence of deviation from the condition of normal beam incidence to the input waveguide face.

### 3.4. Adjustment of input cylindrical lens

Besides the inclination of the incident beam in the XZ plane, occurrence of some turn of the cylindrical lens generatrix relatively to the waveguide plane in the launching scheme block is possible in measuring. Let us consider that case of the lens rotated around its optical axis assuming that the lens axis is directed along the normal to the input sample face. The ray paths in waveguide mode excitation procedure are shown in **Figure 9**.

Let the lens generatrix be tilted toward the surface of the sample by angle γ. Then the plane of incidence of the focused light beam (that involves the two-sided arrow denoting the lens in the scheme) is turned to the vertical Y axis by the same angle as it is shown in **Figure 9**. Considering reversible character of light paths in optical systems containing the passive

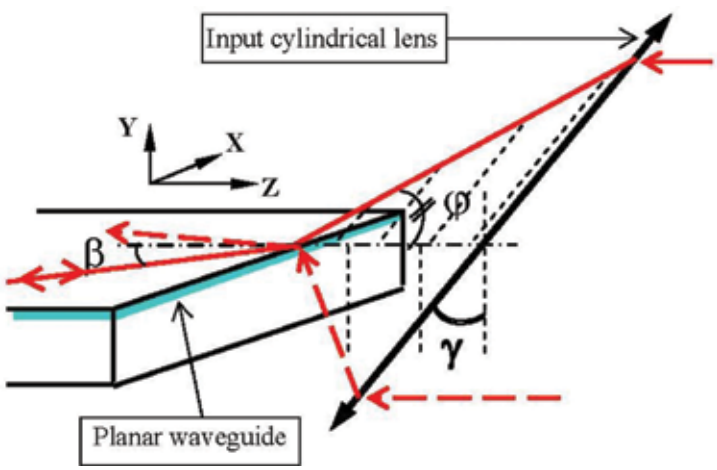


**Figure 9.** Waveguide mode excitation under the turn of input cylindrical lens.

elements only, we can consider our case in the reverse direction as an emission of the waveguide mode from the output waveguide face. That approach allows using the reasons and the results described above.

It is shown that the output mode beam looks like a curved light strip on the cross screen when a skew incidence of collimated beam to the output face is performed into the waveguide, and the strip edges demonstrate maximal inclinations from the longitudinal upright section. Then our studied case can be considered as reversible one – the tilted boundary rays of the incident light beam formed with the turned cylindrical lens excite the mode which is directed at some angle to the normal to the input sample face (see **Figure 9**) while the paraxial rays of the incident beam still meet the condition of normal incidence. That means excitation of divergent (in the planform XZ plane) waveguide mode beam, and consequently the spatial light beam which is radiated from the opposite output sample face should demonstrate angular broadening into that XZ projection.

If the numerical aperture of the exciting lens, as well as the size and position of the light spot at the input sample face are matched with the corresponding parameters of the excited mode, the output light beam is approximately axisymmetric relatively to the direction of unperturbed output beam, and that produces no additional errors neither in measuring the output beam direction nor in further calculation of the mode index. However, a set of waveguide modes is excited usually with the end-fire technique, and there is a natural wish to use this circumstance by measuring the characteristics of several modes under the single adjustment procedure. For this purpose, one scans the input end with the focused input beam and chooses a beam position that leads to optimizing the visibility of the mode's set. Then only the part of the shifted incident beam actually excites some individual mode. As the exciting lens is turned in the considered manner, the output light beam is broadened asymmetrically (relatively to the output mode direction that could be in the case of zero lens turn) as can be seen in **Figure 9**. Just that reason leads to additional errors in measuring. The detailed procedure of determination of dependence $\Delta N_m(\gamma)$ is presented in Ref. [15]. Here we show in **Figure 10** the example of that dependence calculated for the waveguide K8: $K^+$ considered above. Unlike the error type described in the preceding paragraph, one can see that the errors caused by lens turning differ one from another for modes of different orders, and the lowest-order mode indicate the minimum error. The noted difference between the errors decreases as the mode order increases, and for the two highest modes the mentioned errors almost coincide.

Whereas the considered error $\Delta N_m(\gamma)$ is substantially less than the error $\Delta N_m(i)$ for identical values of the angles $i$ and $\gamma$, the former error caused by the lens turning dominates in practice because the used standard equipment provides precise control of normal light incidence to the sample face, but does not enable accurate orienting the lens generatrix relatively to the sample surface. In those cases the expected errors of the lens orientation could be up to the order of arc minutes, and therefore just that range of angle $\gamma$ variations is used in the graph shown in **Figure 10**. It is seen that mode index errors are rather significant for those angles $\gamma$, and, in order to keep the errors within acceptable limits (no greater than $10^{-4}$), one should try to control the orientation of the cylindrical lens with accuracy of about 2–3 arcmin.

http://dx.doi.org/10.5772/intechopen.75558

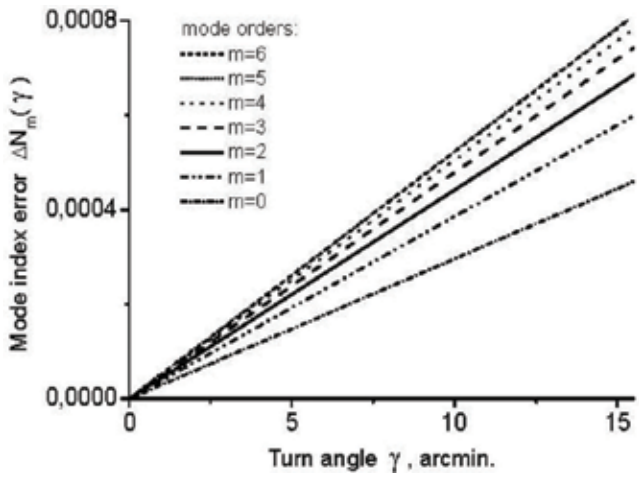


**Figure 10.** Errors caused by the turn of input cylindrical lens.

For tuning the lens turn, a rather simple technique associated with a variant of autocollimation method could be suggested. The performed procedures are illustrated by **Figures 11** and **12**.

First the tilt of the incident light beam should be registered by watching through the goniometer telescope or with the photoreceiver matrix. Then the reference glass cube (given in the goniometer tool kit) is installed on the goniometer sample mount, and the reflected light beam is registered near the opposite direction according to the scheme in **Figure 11**. Registered light strip patterns are shown in **Figure 12**.

If the measuring system is misadjusted in parameter $\gamma$, the strips representing direct and reflected beams demonstrate opposite inclinations at the angle of $2\gamma$ to each other. Turning

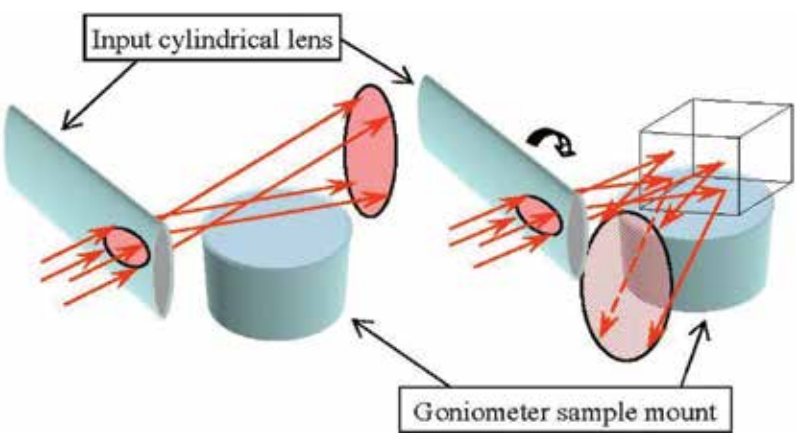


**Figure 11.** Adjusting the orientation of input cylindrical lens under consecutive registration of direct and reflected light beams.

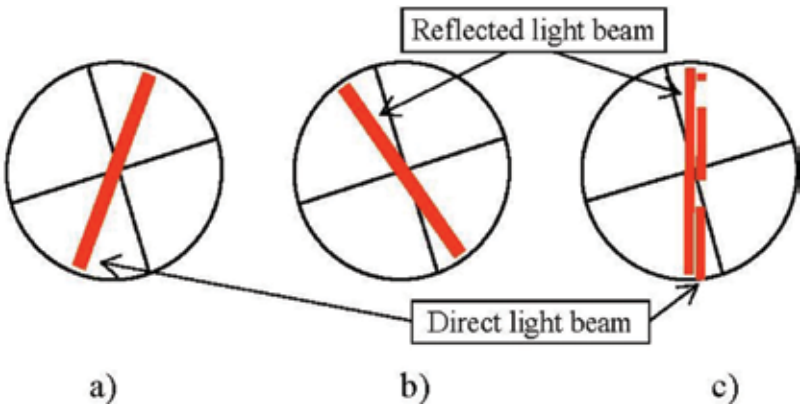


**Figure 12.** Patterns from the goniometer telescope in adjusting procedure: Direct (a) and reflected (b) light beams before, and also after (c) the procedure.

the lens around its ax and repeating the procedures one can obtain coincidence of orientations of those light strips. This will be the criterion for correct orientation of the cylindrical lens – the lens generatrix gets right orientation parallel to the sample mount surface. For example: using the micrometer ocular of the goniometer tool kit we were able to adjust the lens orientation with the accuracy of 2 arcmin. It can be concluded from the dependences shown in **Figure 10** that the corresponding mode index errors are reduced to an acceptable level. We can also note that our evaluation results in the maximum level of the measurement errors when the cylindrical lens is rotated around the axis, accompanied by the displacement of the input beam as it scans over the end of the waveguide. The mode index errors decrease as the incident beam is shifted toward the position that matches the region of localization of the measured mode, and the range of allowable lens tilts is broadened.

## 4. Conclusion

The presented materials prove applicability of the end-fire mode spectroscopy technique to analysis of planar optical waveguides with arbitrary cross refractive index profiles, and performed measurements of the characteristics of buried waveguides highlight this advantage of the technique. Furthermore, the technique allows conducting reliable direct complex measurements of the set of important optical characteristics of arbitrary planar waveguides (the mode spectrum and the maximal refractive index) in a single procedure. End-fire mode spectroscopy has a good potential for wide practical application in examinations of planar structures. Further developments should be aimed at modifying the measuring scheme in order to be able to analyze 3D optical guides. That could allow extending the area of technique applications by involving additional large group of waveguides including optical fibers.

## Author details

Dmitry V. Svistunov

Address all correspondence to: svistunov@mail.ru

Peter-the-Great St.-Petersburg Polytechnic University, St.-Petersburg, Russia

## References

[1] Tien PK, Ulrich R. Theory of prism-film coupler and thin-film light guides. Journal of the Optical Society of America. 1970;**60**(10):1325-1337. DOI: 10.1364/JOSA.60.001325

[2] Barnosky MK. Introduction to Integrated Optics. NY, London: Plenum Press; 1974. 515 p. DOI: 10.1007/978-1-4684-2082-1

[3] Wang X, Yin C, Cao Z. Progress in Planar Optical Waveguides. Berlin-Heidelberg: Springer-Verlag; 2016. XI,241 p. DOI: 10.1007/978-3-662-48984-0

[4] Lavchiev VM, Jakoby B, Hedenig U, Grille T, Kirkbride JMR, Ritchie GAD. M-line spectroscopy on mid-infrared Si photonic crystals for fluid sensing and chemical imaging. Optics Express. 2016;**24**(1):262-271. DOI: 10.1364/OE.24.000262

[5] Yulianto M, Marzuki A, Suryanti V. Diffusion processes for planar waveguides fabrication in soda-lime glasses. Journal of Physics: Conference Series. 2017;**909**(1):012022 (5 pp). DOI: 10.1088/1742-6596/909/1/012022

[6] White JM, Heidrich PF. Optical waveguide refractive index profiles determined from measurement of mode indices: A simple analysis. Applied Optics. 1976;**15**(1):151-155. DOI: 10.1364/AO.15.000151

[7] Chiang KS. Construction of refractive-index profiles of planar dielectric waveguides from the distribution of effective indexes. Journal of Lightwave Technology. 1985;**LT-3**(2):385-391. DOI: 10.1109/JLT.1985.1074194

[8] Rogozinski R. Determination of refractive index profiles of planar buried waveguides on the basis of a set of modal propagation constants. Optics Communication. 2003; **219**(1):199-214. DOI: 10.1016/S0030-4018(03)01286-0

[9] Marangoni M, Osellame R, Ramponi R, Giorgetti E. Second harmonic generation from radiation to guided modes for the characterization of reverse-proton-exchanged waveguides. Opitcs Express. 2004;**12**(2):294-298. DOI: 10.1364/OPEX.12.000294

[10] Glebov LB, Dokuchaev VG, Morozova IS. Simple method for reconstruction of refractive-index profile for planar wave-guides. Optics and Spectroscopy. 1989;**66**(5):1110-1114. WOS: A1989AC80700031

[11] Monir M, El-Refaei H, Khalil D. Single-mode refractive index reconstruction using an nm-line technique. Fiber and Integrated Optics. 2006;**25**(2):69-74. DOI: 10.1080/01468030500466230

[12] Svistunov DV. End-fire mode spectroscopy technique of examination of planar waveguides. Journal of Optics A: Pure and Applied Optics. 2008;**10**(8):085301(4 pp). DOI: 10.1088/1464-4258/10/8/085301

[13] Svistunov DV. New measuring method of examination of planar optical waveguides. In: Proceedings of Progress in Electromagnetics Research Symposium (PIERS 2009 in Beijing); 23-27 March 2009; Beijing. 2009. pp. 1689-1693. DOI: 10.2529/PIERS080904135015

[14] Zolotov EM, Kiselyov VA, Pelekhaty VM. Determination of characteristics of optical diffuse waveguides. Soviet J Quant. Electr. 1978;**8**(11):2386-2382. DOI: 10.1070/QE1978v008n11ABEH011261

[15] Svistunov DV. Optimizing the mode-excitation conditions when a planar waveguide is being investigated by means of end-fire mode spectroscopy. Journal of Optical Technology. 2014;**81**(1):1-5. DOI: 10.1364/JOT.81.000001

Chapter 15

# Polymer Resonant Waveguide Gratings

Muhammad Rizwan Saleem and Rizwan Ali

Additional information is available at the end of the chapter

http://dx.doi.org/10.5772/intechopen.76917

**Abstract**

This chapter deals with the advances in polymeric waveguide gratings for filtering and integrated optics applications. Optical polymer materials are widely used for planar and corrugated micro-optical waveguide grating structures ranging from down a micrometer to several hundred micrometers. Light in a polymeric waveguide is transmitted in discrete modes whose propagation orders depend on incident wavelength, waveguide dimensional parameters, and material properties. Diffracted optical structures are permittivity-modulated microstructures whose micro-relief surface profiles exhibit global/local periodicity. The resonant nature and location of such globally periodic structures (diffraction gratings) excite leaky waveguide modes which couple incident light into reflected/transmitted plane wave diffraction orders. It describes design & analysis, fabrication, and characterization of sub-wavelength polymer grating structures replicated in different polymeric materials (polycarbonate, cyclic olefin copolymer, Ormocomp) by a simple, cost-effective, accurate, and large scale production method. The master stamp (mold) for polymer replication is fabricated with an etchless process with smooth surface profile.

**Keywords:** resonant waveguide gratings, polymeric materials, nanoimprint lithography

## 1. Introduction

Conventional optical waveguides work on the principle to guide waves in a material surrounded by other material media, the refractive index of the material should be slightly higher than that of surrounded media such that light can bounce along the waveguide by means of total internal reflections at the boundaries between different media. The indefinite guiding progress the waves from successive boundaries which must interfere constructively to generate a continuous and stable interference pattern along the waveguide. If the interference pattern in not fully constructive, the waves cancel, owing to the self-destruction. The conventional

optical waveguides are primarily the most common type of thin film optical filters used widely as narrowband filters in laser cavities, optical telecommunications, and light modulators [1]. However, the realization of sub-nanometer narrowband filters with thin film technique require hundreds of optical thin-films stack with stringent tolerances over thicknesses and refractive index variations [2]. Resonant Waveguide Gratings (RWGs) are a new class of narrowband filters and are widely used in applications such as polarizers [3], laser cavity reflectors [3, 4], light modulators [5], biosensors [6], and wavelength division multiplexing [7]. Such narrowband reflectance/transmittance spectral characteristics can be observed by sub-wavelength grating structures in terms of resonance anomalies [8, 9] with numerous potential applications. RWG operates with resonance effects with relatively simpler structure of few layers. Owing to the resonant nature of the sub-wavelength grating, the leaky modes are supported by the structure (waveguide layer and a grating layer) [10]. In the absence of the grating layer, waveguide layer supports a true bound mode. This bound mode becomes leaky when a grating layer is added with the waveguide layer. Eventually, optical energy is coupled out of the waveguide into radiation modes. On the other hand, the incident plane wave energy is coupled to the waveguide. The incident plane wave energy is coupled into leaky modes and then back to one or more radiation modes. This coupling mostly depends on the wavelength, angle of incidence and other structural parameters of the grating layer. At resonance a sharp peak in reflected/transmitted light might be observed at a specific combination of these parameters.

Large scale demands for cost-effective yet reliable and efficient photonic components have led many researchers to consider polymer materials. Polymeric materials become widely useful and increasingly attractive in the fabrication of various micro and nanostructures with the potential replacement of conventional inorganic materials such as $SiO_2$ and $LiNbO_3$ or semiconductors. Novel polymers have been introduced for replication of nanostructure RWG through inexpensive and mass-production process [11]. The polymeric materials offer high thermal expansion coefficient (almost an order of magnitude) in comparison to traditional inorganic materials as well as thermo-optic coefficient which enable them to use as fast rate switches. Investigations to fabricate RWG in polymeric materials have been actively pursued throughout over the past two decades [12, 13].

The capability to fabricate precise novel structures at micro to nanoscale with a wide variety of materials imposes great challenges to the advancement of nanotechnology and the nanosciences. The semiconductor industry continues pushing to lower structural size and to manufacture smaller transistors and high density integrated circuits. The demanding industrial processes through newly developed lithographic methodologies need to address some critical issues such as speed, reliability, overlay accuracy, etc. Many alternative approaches have been used to manufacture nanostructures in past two decades, despite of using expensive tools such as deep-UV projection lithography and electron beam lithography techniques. These techniques include micro-contact printing, scanning probe based techniques, dip-pen lithography, and Nanoimprint Lithography (NIL) [14]. NIL can not only fabricate nanostructures in resists but can also imprint functional devices in many polymers through ease and cost-effective processes in a number of applications such as photonics, data storage, biotechnology, and electronics [15].

In this chapter we present details of design, fabrication, and characterization of polymeric RWG employing affordable techniques and mass production processes. The fabrication of master

stamp by electron beam lithography and subsequent replication in polymer materials by NIL is presented to target a number of applications in thermoplastics and UV curable polymers.

## 2. Theory of resonant waveguide gratings

The grating structure to enhance the resonance anomalies of a periodic profile (periodic modulation of refractive index) by coupling illuminating plane wave to the leaky modes of the waveguide of the grating is known as resonant waveguide gratings. Diffraction grating splits incident plane wave to propagate in different directions so-called diffraction orders. The periodic structure undergo complete interference and resonates with no transmission at a particular wavelength and incident angle [16]. As a result, light couples out of the waveguide, propagates up to smaller distances, and appears in the form of narrower reflectance peaks whose power varies from 0 to 100% over a range of structural parameters [10, 16, 17].

The propagation constant of a leaky mode is complex quantity and expressed as,

$$\beta = \beta_0 + i\gamma, \tag{1}$$

where $\beta_0$ and $\gamma$ are pure real numbers while the imaginary part ($\gamma$) of the propagation constant represents the propagation loss of the leaky modes [18]. Generally, the spectral width of a resonance curve is proportional to this propagation loss and the full width at half maximum is approximated by.

$$\Delta\lambda_{\mathrm{FWHM}} = \lambda_0 \frac{d\gamma}{\pi}, \tag{2}$$

where $\lambda_0$ is the resonant wavelength, $d$ is the periodicity.

In 1994, researchers used Effective Medium Theory (EMT) to model stratified media as a thin-film stack possessing some effective index. The attempts were made to achieve symmetric spectral response with low sidebands by varying thicknesses of thin-film stacks. This approach results in to design an effective thin-film layer to be antireflective at resonant wavelength [19, 20]. Several researchers considered thin-film model for the design of symmetric filters and suggested numerical solutions based on rigorous modeling methods [21]. To design grating layer, the effective index model was suggested for thin-film method [19]. In 1956, Rytov developed a transcendental equation based on EMT to correlate effective refractive index of a stratified medium to physical parameters and wavelength of light [22]. This equation can be applied to grating problems and written as for a TE-polarized light:

$$\left(n_{\mathrm{H}}^2 - n_{\mathrm{eff}}^2\right)^{1/2} \tan\left[\pi \left(n_{\mathrm{H}}^2 - n_{\mathrm{eff}}^2\right)^{\frac{1}{2}} \times \frac{fd}{\lambda}\right] = -\left(n_{\mathrm{L}}^2 - n_{\mathrm{eff}}^2\right)^{1/2} \tan\left[\pi\left(n_{\mathrm{L}}^2 - n_{\mathrm{eff}}^2\right)^{\frac{1}{2}} \times \frac{(1-f)d}{\lambda}\right], \tag{3}$$

where $n_{\mathrm{H}}$, $n_{\mathrm{L}}$, $n_{\mathrm{eff}}$ are the high, low, and effective indices of the grating, respectively, $f$ is the fill factor, $d$ is the grating periodicity, and $\lambda$ is the wavelength of the light. In the long wavelength limit $\left(\frac{d}{\lambda} \to 0\right)$, (Eq. (3)) can be solved in terms of an analytic relation:

$$n_{\text{eff}} = \left[f n_{\text{H}}^2 + (1-f) n_{\text{L}}^2\right]^{1/2}. \tag{4}$$

Eq. (3) is referred as the exact effective index model whereas (Eq. (4)) as zeroth order effective index model.

The fundamental structure of a RWG is shown in **Figure 1**. The waveguide grating consist of a substrate material with refractive index $n_t$, a coupled grating layer with refractive index distribution $n_2(x)$ along $x$-direction and a superstrate layer (generally air) with refractive index $n_i$. When light of wavelength $\lambda$ illuminates the grating at an incident angle $\theta_i$, it results in generation of various propagated diffraction orders through one-dimensional grating which can be calculated by fundamental grating equation, given as:

$$n_2 \sin\theta_m = n_i \sin\theta_{in} + m\frac{\lambda}{d}, \tag{5}$$

where $\lambda$ is the wavelength, $\theta_{in}$ is the incident angle of light, $d$ is the periodicity of the grating structure, $\theta_m$ is the diffraction order, $m$ = 0, ±1, ±2, ±3,… is the index of diffraction order, $n_i$, and $n_2$ are the indices before and after the interface. For reflection gratings $n_2$ is replaced by $n_i$ and for transmission gratings by $n_t$.

Narrow reflection or transmission peaks can be achieved by understanding the physics of the structure which depends on the excitation of leaky waveguide modes. Consider a reflection grating with periodicity smaller than the wavelength of light used to allow only zeroth-order diffraction under plane wave illumination as shown in **Figure 2**. The resulted reflecting fields from the gratings may be assumed to produce from two contributions, namely: a direct reflection and a scattered field reflection [22]. The inherent direct reflection from upper interface is primary reflection so-called *Fresnel reflection* whereas the secondary reflection from the grating structure is due to excitation and rescattering of leaky waveguide modes whose phase vary continuously to fulfill the coupling relation given below:

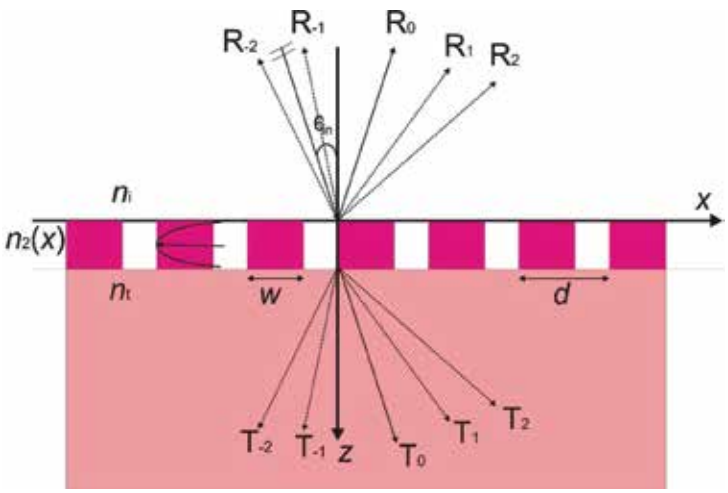


**Figure 1.** Schematic representation of resonant waveguide Grating's structure with forward and backward propagated diffraction orders.

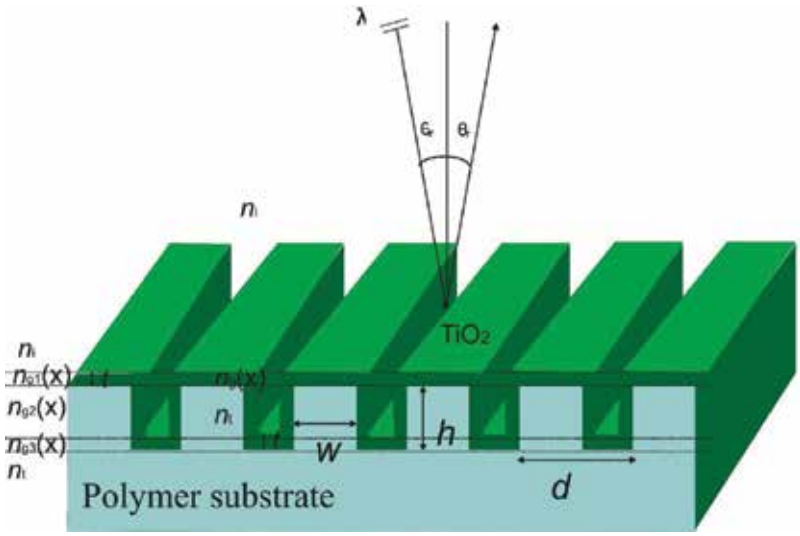


**Figure 2.** Schematic view of RWG with refractive index distributions and coated high index cover layer.

$$\gamma_0 = k_x + n\frac{2\pi}{d}, \tag{6}$$

where $d$ is periodicity of the grating, $\gamma_0$ is propagation constant of fundamental mode and $k_x$ is wave vector associated with the illuminating plane wave. At the resonance regime the rapidly varying phase of the secondary field with respect to the incident field (wave number) becomes similar in phase which gives rise resonance in the form of narrow reflected peak with wavelength or angle of incidence [23]. In **Figure 1**, the leaky waveguide modes in lateral direction are represented by propagation constant $\gamma$. Due to the leaky nature of propagated modes, they are shown to possess both real and imaginary parts and form a plane, so-called *complex $\gamma$-plane*. A leaky mode is described by a pole on this complex $\gamma$-plane. A planar waveguide supports at least one mode, the pole of which is represented by the real value on this $\gamma$-plane. Owing to the introduction of periodicity in the planar structure, such single mode splits into an infinite number of spatially diffracted orders whose poles are represented by complex values on this complex $\gamma$-plane with a separation of $\frac{2\pi}{d}$. Thus, the leaky waveguide modes are primarily associated with the periodicity of grating structure and much more closely spaced poles can be observed for sufficiently small periodic structure compared to incident wavelength. The magnitudes of real and imaginary parts of such complex poles show the extent of leaky modes excited by the input plane wave i.e., the coupling of the real part of modes (poles) with input filed and the associated coupling loss, respectively [24].

## 3. Selection of polymer materials for optical waveguide

Polymeric materials have become potential candidate with versatility optical device performance and functionality. In comparison to inorganic materials, polymeric materials possess many attributable characteristics. The properties of polymer materials can be changed

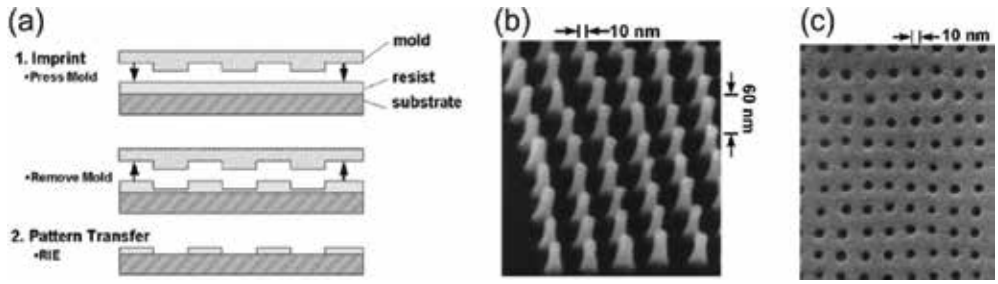


**Figure 3.** (a) Schematic representation of originally proposed NIL process by Chou. (b) Scanning Electron Microscopy (SEM) image of a mold possessing pillar array diameter of 10 nm. (c) Replicated structure of mold in PMMA polymer material with hole array of size 10 nm. Reproduced with permission from [27]. Copyright 1997, American Institute of Physics.

chemically after modifying the chemical structure of the monomers, polymer backbones, addition of functional groups or chromophores. Polymer materials can be made to manipulate easily by many conventional or unconventional fabrication methods such as reactive ion etching (dry etching), wet etching, soft lithography etc. [25]. Polymer materials offer a simple, low-cost, and reliable fabrication process irrespective to fragile silica or expensive semiconductor materials. Functional polymeric materials provide interesting properties for integrating several diversified materials with different functionalities.

Optical waveguide structures can be fabricated directly by electron beam lithography which is the most effective method to fabricate micro- and nanostructures [25]. Alternatively, soft lithography technique has been extensively developed during past 20 years and improving optical waveguide manufacturing by the use of a master stamp to generate several soft molds to reproduce its replicas [25, 26]. **Figure 3** shows schematic of the originally NIL process proposed by Chao almost two decades before [27, 28]. The master stamp or mold containing nanoscale surface relief features is pressed against a polymeric material on a substrate with tightly controlled temperature and pressure to create a thickness contrast in polymer material. Furthermore, a thin residual layer is made beneath the stamp protrusions as a cushioning layer to protect nanoscale structure on mold surface from a direct impact of mold on the substrate. However, this residual layer can be removed at the end of the process by an anisotropic $O_2$ plasma etching. **Figure 3b** and **c** shows Scanning Electron Microscopy (SEM) images of a mold with pillar array of diameter 10 nm and replicated hole array in poly (methyl methacrylate) (PMMA) [28].

## 4. RWG modeling tool

In this chapter the RWG structures are designed and modeled using most efficient method which is based on the Fourier expansion, commonly known as Fourier Modal Method (FMM) or the coupled wave method (CWM) [29]. FMM determines eigen-solution values of Maxwell's equations in a periodic or piecewise continuous medium by expanding the electromagnetic fields and permittivity functions to Fourier series and applying the boundary conditions to show fields inside the grating by an algebraic eigenvalue problem [30]. Employing FMM to periodic-modulated region, the modulated region sections in slabs

http://dx.doi.org/10.5772/intechopen.76917

where solution of Maxwell's equations is determined at each slab. Such solutions appear in the form of forward and backward propagated fields consisting of modal fields. These fields are pseudoperiodic in nature and expressed in the $e^{\pm i\beta z}$, where $\beta$ is the eigenvalue of a mode. The eigenvalue problem is shown in matrix form which expresses a set of allowed $\beta$ values and transverse field distributions for each polarization of light. The emerging fields from each slab are combined at each interface by applying boundary values. This computation shows an overall field inside the modulated region which is then matched with the fields in homogeneous regions surrounding the modulated region. At the end the problem is expressed in a matrix form to calculate complex transmission and reflection field amplitudes [31].

## 5. Cost-effective master stamp fabrication process by electron beam lithography (EBL) and hydrogen silsesquioxane (HSQ) resist

The properties of stamping material play a significant role in replication process to achieve a well-defined replicated features. In this section, patterns are defined on a resist material

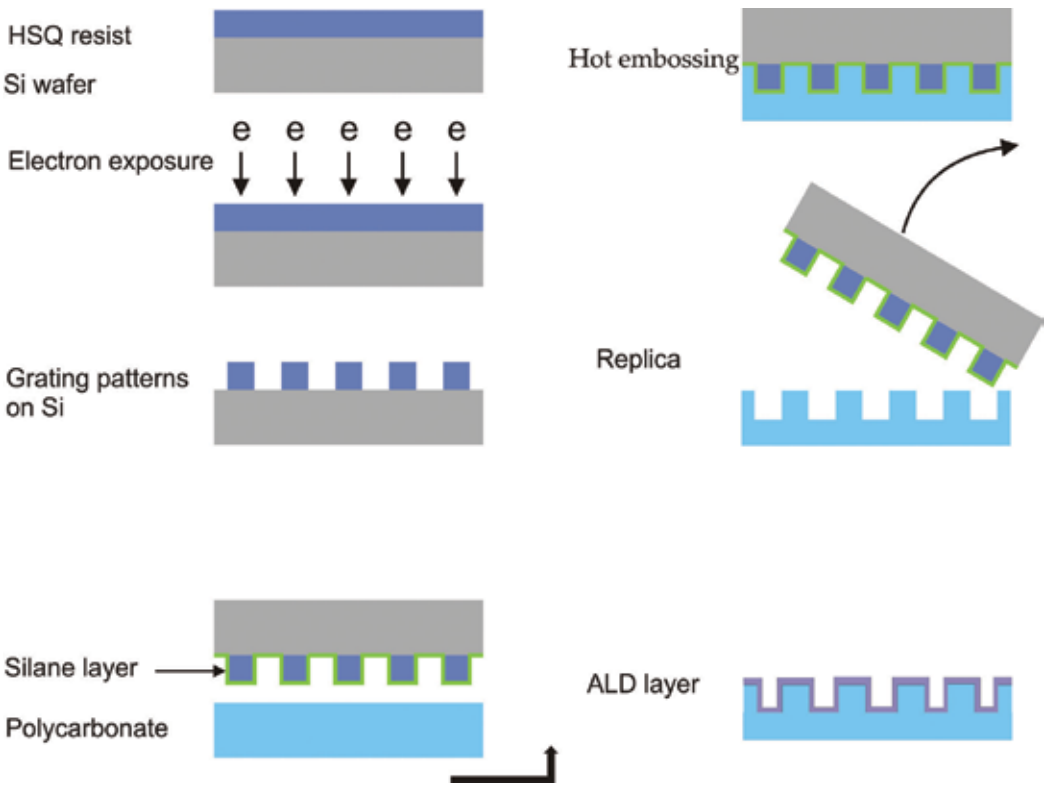


**Figure 4.** Schematic representation of fabrication and replication process of HSQ mold and polymeric binary grating structures with nanoscale surface-relief features. Reproduced with permission from [11]. Copyright 2012, SPIE.

which is coated on a silicon substrate and written by electron beam lithography (EBL) without reactive ion etching (RIE) of silicon. Moreover, accurate control to pattern depth is challenging and inaccuracies in depth profiles are inherent with different width structures. Furthermore, the associated EBL proximity effect increases with the pattern depths and become more pronounced when beam size becomes comparable to the pattern size. The line edge variations occurred due to incomplete suppression of resist after development process resulted in polymer molecule agglomerate formation at pattern line edges [20]. Hydrogen silsesquioxane (HSQ) is a high resolution, inorganic, negative tone EB resist material with small linewidth variations in comparison to positive EB resists such as PMMA and ZEP. To fabricate structures with high resolutions, the molecular size of resist material need to be smaller than the nanoscale features to be replicated for which HSQ resist possesses dominating properties with slight line roughness and high etch resistance in addition [32].

In this Chapter we show replication of nanoscale structures in thermoplastic thin films and UV curable polymers by using an HSQ mold. The mold is fabricated by spin coating HSQ resist layer on silicon substrate, direct e-beam writing followed by development process without reactive ion etching. The HSQ resist thickness is adjusted to obtain structure design height $h$. Additionally,

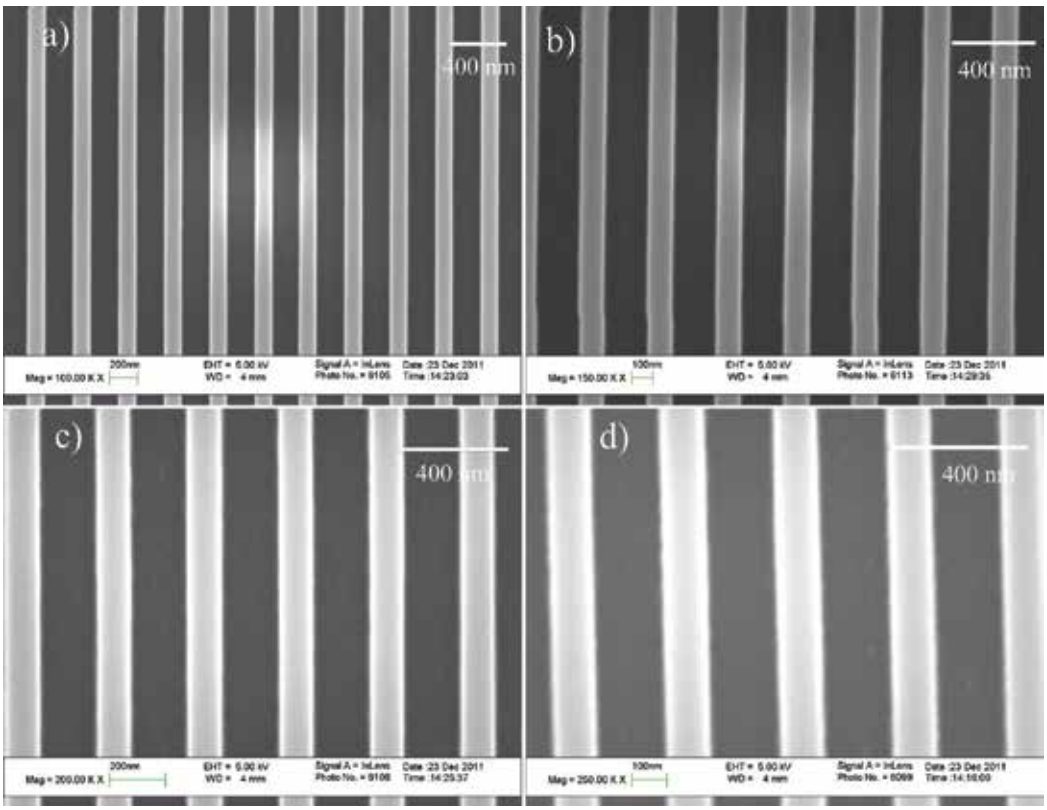


**Figure 5.** SEM images of top view of HSQ resist master stamp on silicon substrate with periodicity ($d$ = 325 nm) at different magnifications: (a) 100.00 KX, (b) 150.00 KX, (c) 200.00 KX, and (d) 250.00 KX.

the formed structure is heat treated to improve mechanical properties of the resist for 180 min at 300°C temperature. Such thermal treatment improves density and hardness of HSQ resist to enable it for the use of hard stamp with high imprint pattern fidelity. The heat treated mold(s) are surface treated in nitrogen environment to deposit a silane layer to act as an antiadhesive layer for imprinting. Finally, the imprinted polymeric gratings with several periodicities are coated with high index amorphous $TiO_2$ thin films by atomic layer deposition. Spectral characteristics of the replicated structures are investigated by a variable angle spectroscopic ellipsometer. **Figure 4** depicts schematic representation of complete process flow of HSQ mold fabrication and imprinting into polymeric materials (thermoplastics and UV curable) with high index $TiO_2$ thin layer.

**Figure 5** shows SEM images of top view of HSQ resist molds (grating structures) at different magnifications on silicon substrate with period *d* of 325 nm. **Figure 6a** and **b** shows cross-sectional view of SEM images of HSQ binary molds with period 425 nm and **Figure 6c** and **d** with period 325 nm [33].

**Figure 7** shows imprinted sub-wavelength grating structures in thermoplastic and UV curable plastic materials by NIL tool. **Figure 8** shows various thin films of amorphous $TiO_2$ coated on polycarbonate, cyclic olefin copolymer and UV curable Ormocomp by atomic layer deposition

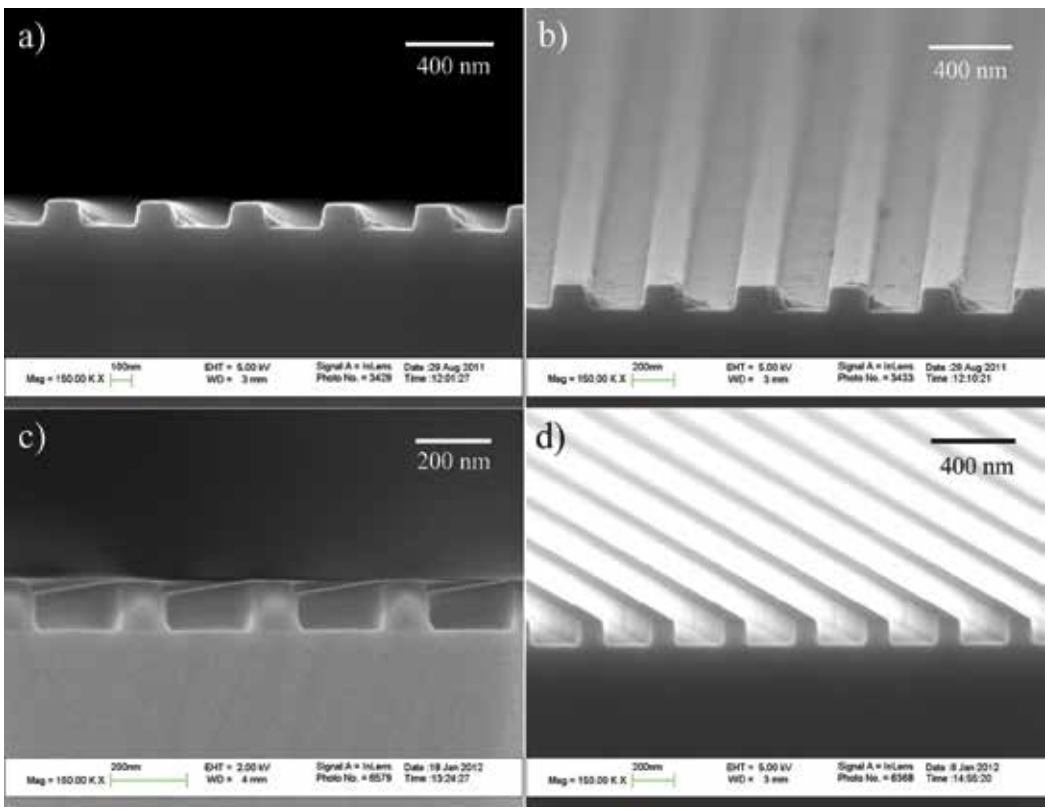


**Figure 6.** SEM images of cross-sectional view of HSQ resist master stamp on silicon with periodicities: (a and b) *d* = 425 nm and (c and d) *d* = 325 nm. Reproduced with permission from [33]. Copyright 2013, NUST.

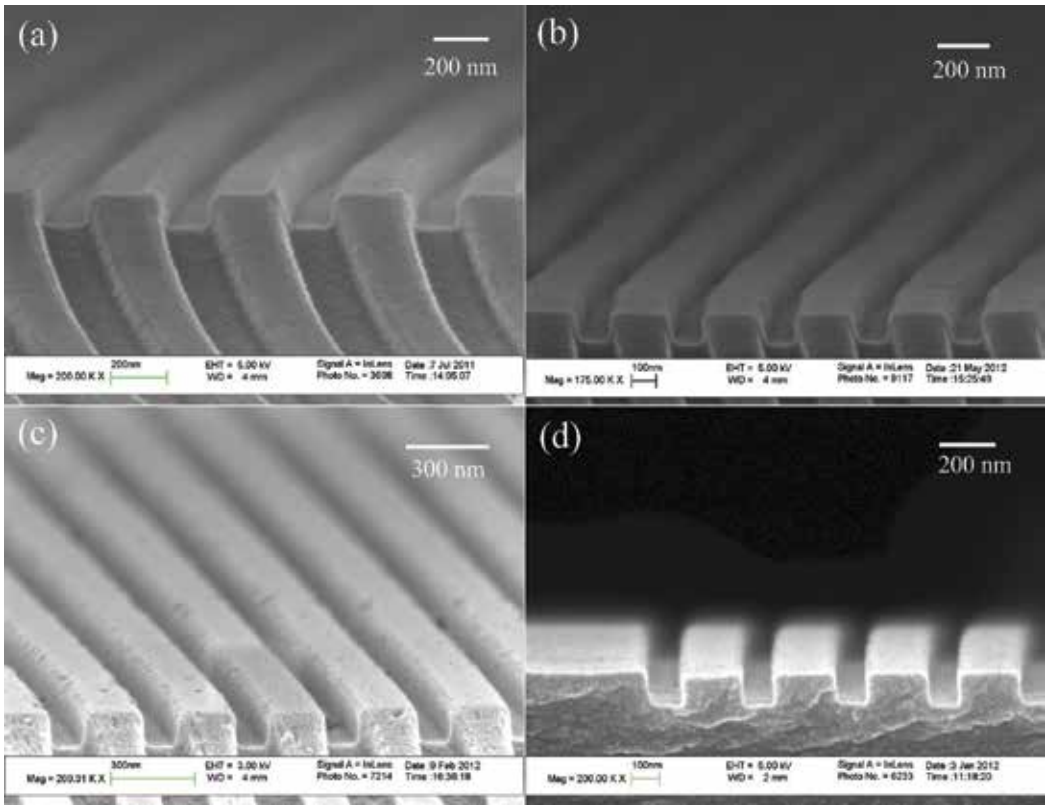


**Figure 7.** SEM images of cross-sectional view of imprinted structures in: (a and b) polycarbonate with period $d$ = 368 nm, (c) cyclic olefin copolymer with period $d$ = 325 nm and (d) UV curable material Ormocomp with period $d$ = 325 nm. Reproduced with permission from [33]. Copyright 2013, NUST.

as a waveguide layer [30]. The details of conformal growth of amorphous $TiO_2$ thin films by atomic layer deposition is described in Refs. [34, 35].

**Figure 9** shows the ellipsometric measurement setup when a linearly polarized plane wave (electric field vector is parallel called TE or perpendicular called TM to the grating lines) incident on the sample at an incident angle Φ with respect to normal of the RWG sample. The light-matter interaction results in specular reflectance/transmittance of the resonant gratings. The polarization state (TE or TM) of the illuminated light is selected by a polarizer stage which transforms the unpolarized light beam into a linearly polarized light beam. The polarization stage composed of a polarizer mounted on a continuously rotated stepper motor with high accuracy. The rotating polarizer changes the intensity of the light. The phase and amplitude of the modulated light represents the polarization state of the beam entering the analyzer/detector. In general, ellipsometer predicts the ellipticity of the polarization state of the light, optical constants ($n$ and $k$) of optical materials, and the thickness of the thin film. The ellipsometric measurement uses two parameters which are connected by Eq. (7) [36].

http://dx.doi.org/10.5772/intechopen.76917

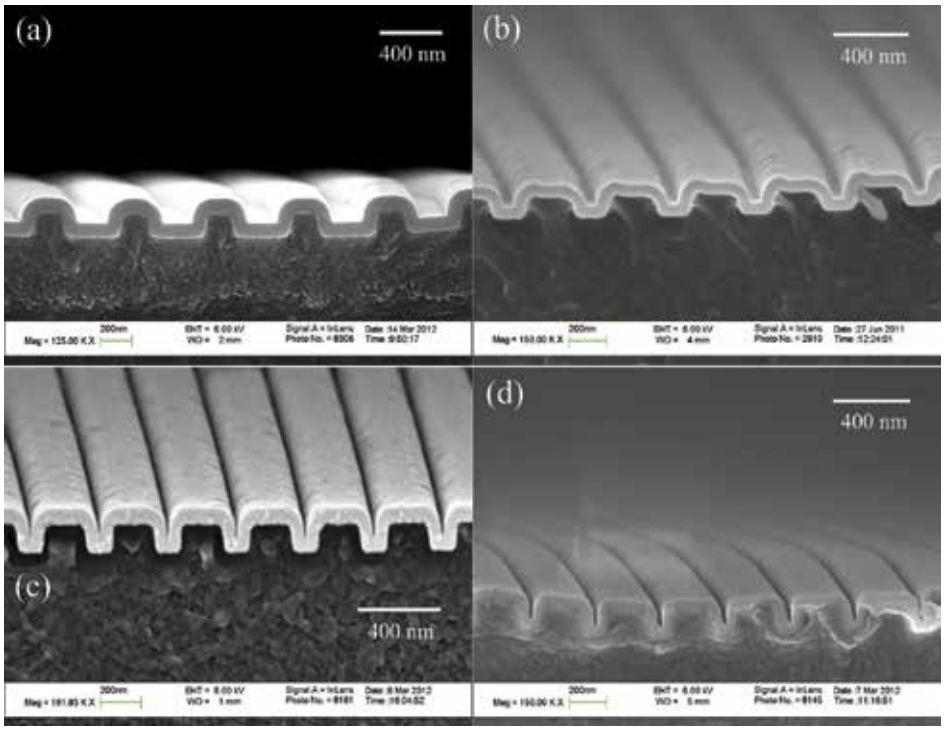


**Figure 8.** SEM images of amorphous $TiO_2$ coated replicated gratings: (a) polycarbonate with period $d$ = 368 nm and $TiO_2$ thickness $t$ = 80 nm, (b) polycarbonate with period $d$ = 368 nm and $TiO_2$ thickness $t$ = 60 nm, (c) cyclic olefin copolymer with period $d$ = 325 nm and $TiO_2$ thickness $t$ = 50 nm, and (d) UV curable material Ormocomp with period $d$ = 325 nm and $TiO_2$ thickness $t$ = 50 nm. Reproduced with permission from [33]. Copyright 2013, NUST.

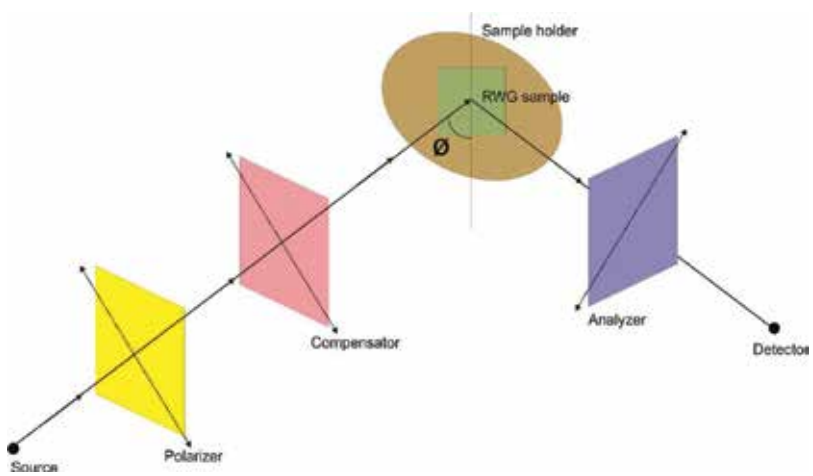


**Figure 9.** Experimental setup of an ellipsometer to measure specular reflectance or transmittance.

$$\tan\psi\, e^{i\Delta} = \frac{R_p}{R_s}, \tag{7}$$

Where $R_p$ and $R_s$ are the complex-amplitude reflectance coefficients for p- and s-polarization state of light, $\Psi$ represents elliptical state of polarization and $\Delta$ is the relative phase of the vibrations along $x$- and $y$-directions which can vary from zero to $2\pi$.

## 6. Results and discussion

**Figure 10** shows designed and experimentally predicted spectral response (specular reflectance) of replicated grating structures in polycarbonate (PC), cyclic olefin copolymer (COC), and UV curable polymer Ormocomp [33]. The measured specular reflectance of PC, COC, and Ormocomp show reflectance peaks at 698.6 nm, 631.4 nm, and 630.4 nm with peak reflectance efficiencies 0.71, 0.94, and 0.65, respectively as shown in **Figure 10d–f**. The resonance peaks occur at different spectral positions with lower diffraction efficiencies than those calculated theoretically as shown in **Figure 10a–c**. The spectral shifts might occur due to inaccuracies in the dimensional profile of the replicated structures including rounding of grating edges rather completely rectangular as shown in ideal profile of **Figures 1** and **2**. The reduction of measured peak efficiencies are most likely caused by scattering of light from surface roughness, slight irregularities in the straightness of the grating lines, porosity and volume variations in polymers that cause refractive index changes in microscopic scale.

The observed variations may also be explained by molecular orientations of the polymer chains. The stress induction during mold filling may result in a partial orientation and configuration of polymeric chain along principal stress directions. Such molecular orientations may relax in thermal environment over a certain length of time. If however, temperature environment is kept constant, for example, for a UV curable material, the molecular orientations can be frozen up in the glassy state of the polymers. Such frozen-in-stresses in the newly molecular chain orientations may lead to generate an anisotropic behavior in the refractive index and cause peak shift.

**Figure 11a** and **b** shows specular reflectance of two designed replicated gratings in polycarbonate (with periodicities $d$ = 425 nm and $d$ = 368 nm), illuminated with TE-polarized light (electric field is parallel to grating lines) at three different angles of incidence (18°, 19°, and 20°) with Full Width Half Maximum (FWHM) of about 11 nm. **Figure 11c** and **d** shows measured spectral reflectance of designed gratings (with periodicities $d$ = 425 nm and $d$ = 368 nm) with FWHM of 13.5 nm and 11 nm, respectively. The experimentally predicted spectra is in close agreement to that of calculated, however, the wavelength shifts may be attributed due to slight variations of refractive indices of materials interacted with light. **Figure 11e** shows the simulated reflectance efficiency variations of two gratings with $TiO_2$ thicknesses of 60 nm and 75 nm. **Figure 10f** shows experimentally measured spectral efficiencies verses calculated

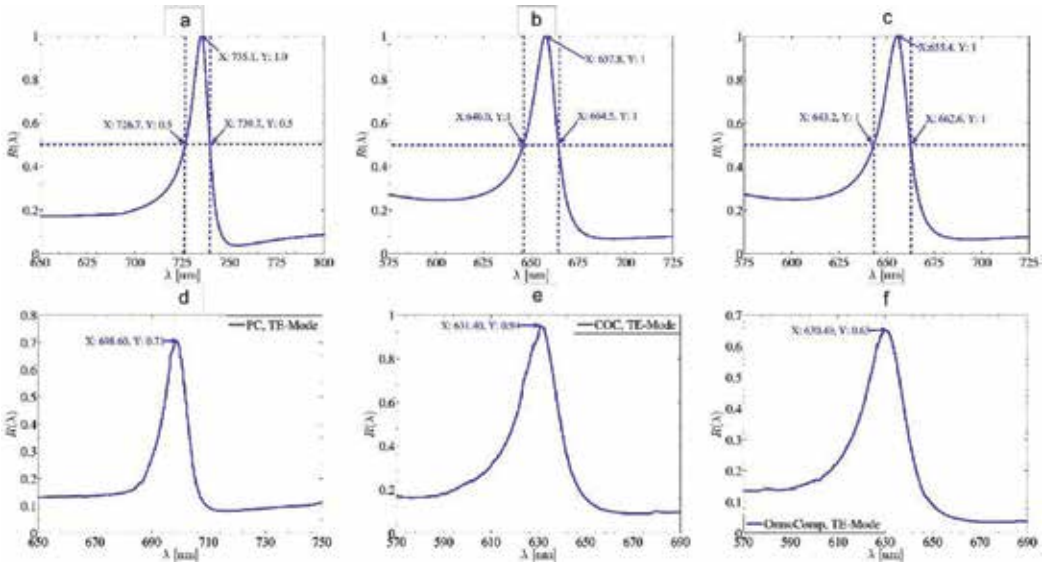


**Figure 10.** Theoretically calculated and experimentally measured specular reflectance of replicated gratings with grating height $h$ = 120 nm and $TiO_2$ thickness t = 50 nm: a) polycarbonate with periodicity ($d$ = 368 nm), b) cyclic olefin copolymer with periodicity ($d$ = 325 nm), c) Ormocomp with periodicity ($d$ = 325 nm); measured reflectance spectra of all three designed gratings: d) polycarbonate, e) cyclic olefin copolymer, and f) ormocomp. Reproduced with permission from [37]. Copyright 2013, Elsevier.

ones with two $TiO_2$ thicknesses. Both experimentally measured and calculated spectra are in agreement, provided few spectral shifts occur due to reasons described above.

For replication by thermal NIL, the temperature of the polymer materials are raised above glass transition temperature ($T_g$) of polymers. At such a condition ($T > T_g$), both Young's modulus and viscosity of polymers reduce by several orders of magnitude in comparison to their values at room temperatures. Moreover, below $T_g$ the value of Young's modulus of glassy polymers remains constant for many polymers, approximately $3 \times 10^9$ Pa in comparison to their respective values at room temperature. In general practice, the temperature rise for thermal NIL is 60–90°C above $T_g$ so that polymer transform into a viscous flow to fill micro and nanocavities, however, after imprinting process polymer is cooled down below $T_g$ to preserve imprinted pattern. In fact, $T_g$ is onset temperature for molecular motion in polymers. There are many factors which increase energy for molecular motion, such as, intermolecular forces, interchain steric hindrance (branching or cross-linking, bulky and stiff side groups). In some processes, it is desirable to use lower temperature values, which is then compensated by corresponding increase in the process pressure and time to obtain perfect imprinting. The requirement of high temperature and pressure for NIL process may restrict the production of NIL technology. Furthermore, the mismatch of thermal expansion coefficient between the mold material and substrate may impose limitations for pattern overlay for large substrates. Alternatively, liquid precursors having low Young's modulus and viscosity can be cured by UV light at ambient temperatures. Due to low viscosity of the fluid the imprinting process is facilitated and minimize pattern density effects.

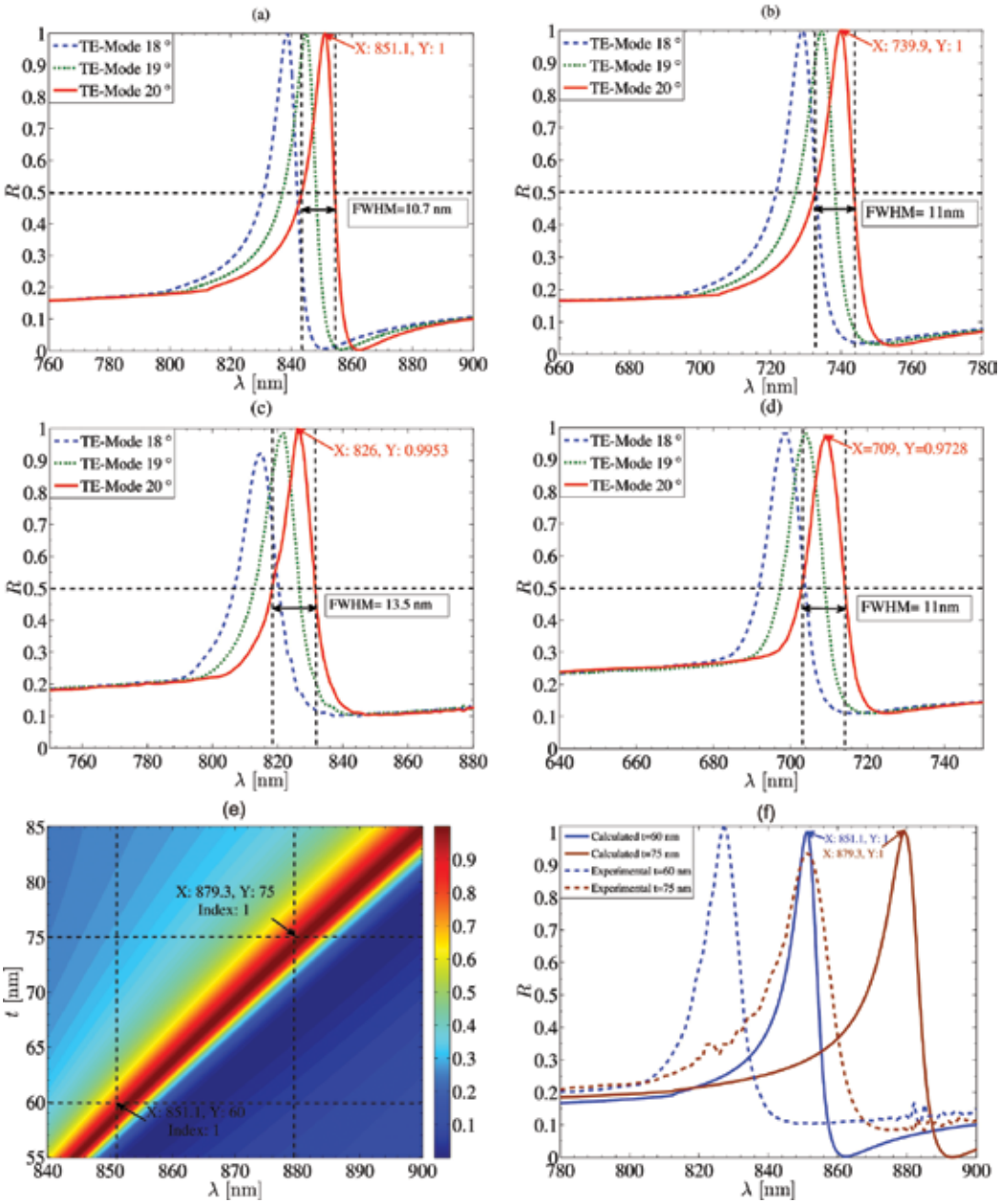


**Figure 11.** Theoretically calculated specular reflectance at three illuminating angles of replicated gratings: (a) with $d = 425$ nm, (b) with $d = 368$ nm. Experimentally calculated specular reflectance at three illuminating angles of replicated gratings: (c) with $d = 425$ nm, (d) with $d = 368$ nm, (e) variation in simulated spectral reflectance as a function of $TiO_2$ thickness $t$ and wavelength of illuminating TE light, and (f) theoretically calculated and experimentally predicted specular reflectance as a function of wavelength. Blue curves show layer thickness $t = 60$ nm and brown curves $t = 75$ nm. Reproduced with permission from [11]. Copyright 2012, American Optical Society.

## 7. Conclusions

The replication of nanophotonic components with sub-wavelength features in polymeric materials is demonstrated and described as the most promising technology to produce narrow band-pass filters which are efficient, reliable, cost-effective, environmentally stable and effective at bulk scale production. Nanoimprint lithography is an economic process which initially requires the manufacturing of a master stamp (mold) which is fabricated commonly by EBL and reactive ion etching (RIE) processes. These processes enhance cost, inaccuracies and a reduction in efficiency and device performance. This work presented the manufacturing of master stamp by EBL using a negative tone binary electron beam resist HSQ without RIE process. The sub-wavelength replicated structures' profile height was adjusted by the thickness of resist layer on silicon substrate by spin coating process. A direct pattern writing on HSQ resist was performed by EBL followed by development for sufficient time. The RIE process step was replaced by HSQ pattern resist heat treatment to improve the mechanical and physical properties such as hardness and density of HSQ resist, respectively. The simple etchless process of mold formation brings fast prototyping of nano-optical devices with rapid processing time and high pattern fidelity, superior optical performance and wide applicability to mass production.

In NIL two important steps performed are mold release and pattern transfer. The imprinting process lead strong adhesive forces between the mold and the resist at large contact area. A perfect mold release keeps both resist shape integrity and a complete mold-resist separation as well as suitable plasma-etching resistance for pattern transfer into substrate. This means, nanoimprint resists which give rise both mold-release, etch-resist properties and allow fast and precise nanoimprinting are highly desirable.

The replicated grating structures in polymer materials further coat by thin dielectric films of $TiO_2$ as waveguide layer to support optical modes. Theoretically simulated results agree with the experimentally measured for the RWG in a number of polymers such as polycarbonate, cyclic olefin copolymer and Ormocomp.

## Acknowledgements

The author is thankful to all professors, researchers, engineers, technicians, and students who contributed to the continuous development of various different processes of the nanofabrication at the Department of Physics and Mathematics, University of Eastern Finland, Joensuu, Finland. We are greatly thankful to HoD Prof. Dr. Seppo Honkanen for providing the financial fundings to publish this Chapter from Department of Physics and Mathematics, University of Eastern Finland under Project code 931351, which is highly appreciated. We greatly appreciate the editorial support from InTech in preparing this chapter. The chapter is dedicated to my Father-in Law Mr. Ehsan Elahi (late).

## Author details

Muhammad Rizwan Saleem[1,2]* and Rizwan Ali[1]

*Address all correspondence to: rizwan@casen.nust.edu.pk

1 Institute of Photonics, University of Eastern Finland, Joensuu, Finland

2 US-Pakistan Center for Advance Studies in Energy (USPCAS-E), National University of Sciences and Technology (NUST), Islamabad, Pakistan

## References

[1] Macleod HA, editor. Thin-Film Optical Filters. New York: American Elsevier; 1969

[2] Macleod HA. Challenges in the design and production of narrow-band filters for optical fiber communications. In: Fulton ML, editor. Optical and Infrared Thin Films, Proc. SPIE 4094. SPIE; 2000. pp. 46-57

[3] Magnusson R, Wang SS. New principle for optical filters. Applied Physics Letters. 1992;**61**:1022-1024

[4] Cox JA, Morgan RA, Wilke R, Ford CM. Guided-mode grating resonant filters for VCSEL applications. In: Cindrich I, Lee SH, editors. Diffractive and Holographic Device Technologies and Applications V, Proc. SPIE 3291. SPIE; 1998. pp. 70-76

[5] Sharon A, Rosenblatt D, Friesem AA, Weber HG, Engel H, Steingrueber R. Light modulation with resonant grating-waveguide structures. Optics Letters. 1996;**21**:1564-1566

[6] Norton SM. resonant grating structures: Theory, design, and applications [dissertation]. New York: University of Rochester, Rochester; 1997

[7] Golubenko GA, Sychugov VA, Tishchenko AV. The phenomenon of full 'external' reflection of light from the surface of a corrugated dielectric waveguide and its use in narrow-band filters. Soviet Physics/Lebedev Institute Reports. 1985;**1**(11):36-40

[8] Wang SS, Magnusson R. Design of waveguide-grating filters with symmetrical line shapes and low sidebands. Optics Letters. 1994;**19**:919-921

[9] Tibuleac S, Magnusson R. Reflection and transmission of guided-mode resonance filters. Journal of the Optical Society of America. 1997;**14**:1617-1626

[10] Muhammad Rizwan Saleem. Resonant waveguide gratings by replication and atomic layer deposition [dissertation]. University of Eastern Finland, Joensuu, Finland: Publication of the University of Eastern Finland; 2012

[11] Saleem MR, Stenberg PA, Khan MB, Khan ZM, Honkanen S, Turunen J. Hydrogen silsesquioxane resist stamp for replication of nanophotonic components in polymers. Journal of Micro/Nanolithography, MEMS, and MOEMS. 2012;**11**(1):013007

[12] Mai X, Moshrefzadeh R, Gibstingson UJ, Stegeman GI, Seaton CT. Simple versatile method for fabricating guided-wave gratings. Applied Optics. 1985;**24**:3155-3156

[13] Rochon P, Natansohmer A, Callender CL, Robitaille L. Guided mode resonance filters using polymer films. Applied Physics Letters. 1997;**71**:1008-1010

[14] Byron D, Gates QX, Stewart M, Ryan D, Grant Willson C, Whitesides GM. New approaches to nanofabrication: Molding, printing, and other techniques. Chemical Reviews. 2005;**105**(4):1171-1196. DOI: 10.1021/cr030076o

[15] Jay Guo L. Recent progress in nanoimprint technology and its application. Journal of Physics D. 2004;**37**(11):R123

[16] Golubenko GA, Svakhin AS, Sychugov AV, Tishchenko AV. Total reflection of light from a corrugated surface of a dielectric waveguide. Soviet Journal of Quantum Electronics. 1985;**15**:886-887

[17] Popov E, Mashev L, Maystre D. Theoretical study of the anomalies of coated dielectric gratings. Optica Acta. 1986;**33**:607-619

[18] Thurman ST, Michael Morris G. Controlling the spectral response in guided-mode resonance filter design. Applied Optics. 2003;**42**(16):3225-3233

[19] S.T. Thurman and G.M. Morris. Resonant-grating filter design: The appropriate effective-index model. In: Presented at the OSA Annual Meeting, Providence, R.I; 22-26 Oct; OSA; 2000

[20] Hessel A, Oliner AA. A new theory of Wood's anomalies on optical gratings. Applied Optics. 1965;**4**:1275-1297

[21] Hegedus Z, Netterfield R. Low sideband guided-mode resonant filters. Applied Optics. 2000;**39**:1469-1473

[22] Rytov SM. Electromagnetic properties of a finally stratified medium. Soviet Physics, JETP. 1956;**2**:466-475

[23] Rosenblatt D, Sharon A, Friesem AA. Resonant grating waveguide structures. Journal of Quantum Electronics. 1997;**33**:2038-2059

[24] Norton SM, Erdogan T, Morris GM. Coupled-mode theory of resonant-grating filters. Journal of the Optical Society of America. A. 1997;**14**:629-639

[25] Huang Y, Paloczi GT, Yariv A, Cheng Z, Dalton LR. Fabrication and replication of polymer integrated optical devices using electron-beam lithography and soft lithography. The Journal of Physical Chemistry. B. 2004;**108**:8606-8613

[26] Eldada L, Shacklette LW. Advances in polymer integrated optics. IEEE Journal of Quantum Electronics. 2000;**6**(1):54-68

[27] Chou SY, Krauss PR, Zhang W, Guo L, Zhuang L. Sub-10 nm imprinted lithography and applications. Journal of Vacuum Science and Technology B. 1997;**15**:2897. DOI: 10.1116/1.589752

[28] Jay Guo L. Nanoimprint lithography: Methods and material requirements. Advanced Materials. 2007;**19**:495-513. DOI: 10.1002/adma.200600882

[29] Moharam MG, Pommet DA, Gran EB. Stable implementation of the rigorous coupled-wave analysis for surface-relief gratings: Enhanced transmittance matrix approach. Journal of the Optical Society of America. A. 1995;**12**:1077-1086

[30] Li L. Use of Fourier series in the analysis of discontinuous periodic structures. Journal of the Optical Society of America. A. 1996;**13**:1870-1876

[31] Kim H, Park J, Lee B. Fourier Modal Method and its Applications in Computational Nanophotonics. Boca Raton: CRC Press; 2012

[32] Namatsu H et al. Three dimensional siloxane resist for the formation of nanopatterns with minimum linewidth fluctuations. Journal of Vacuum Science and Technology B. 1998;**16**(1):69

[33] Saleem MR. Design, fabrication and analysis of photonic device nanostructures [dissertation]. Islamabad, Pakistan: National University of Sciences and Technology (NUST); 2013

[34] Saleem MR, Silfsten P, Honkanen S, Turunen J. Thermal properties of $TiO_2$ films grown by atomic layer deposition. Thin Solid Films. 2012;**520**:5442-5446

[35] Saleem MR, Ali R, Honkanen S, Turunen J. Thermal properties of thin $Al_2O_3$ films and their barrier layer effect on thermo-optic properties of $TiO_2$ films grown by atomic layer deposition. Thin Solid Films. 2013;**542**:257-262

[36] Azzam RMA, Bashara NM. Ellipsometry and Polarized Light. Amsterdam: North Holland publishing Company; 1977

[37] Saleem MR, Honkanen S, Turunen J. Thermo-optic coefficient of Ormocomp and comparison of polymer materials in athermal replicated subwavelength resonant waveguide gratings. Optics Communications. 2013;**288**:56-65

Section 3

# Waveguide Analytical Solutions

Chapter 16

# Applications and Solving Techniques of Propagated Wave in Waveguides Filled with Inhomogeneous Dielectric Materials

Zion Menachem

Additional information is available at the end of the chapter

http://dx.doi.org/10.5772/intechopen.76793

**Abstract**

This chapter presents techniques to solve problems of propagation along the straight rectangular and circular waveguides with inhomogeneous dielectric materials in the cross section. These techniques are very important to improve the methods that are based on Laplace and Fourier transforms and their inverse transforms also for the discontinuous rectangular and circular profiles in the cross section (and not only for the continuous profiles). The main objective of this chapter is to develop the techniques that enable us to solve problems with inhomogeneous dielectric materials in the cross section of the straight rectangular and circular waveguides. The second objective is to understand the influence of the inhomogeneous dielectric materials on the output fields. The method in this chapter is based on the Laplace and Fourier transforms and their inverse transforms. The proposed techniques together with the methods that are based on Laplace and Fourier transforms and their inverse transforms are important to improve the methods also for the discontinuous rectangular and circular profiles in the cross section. The applications are useful for straight waveguides in the microwave and the millimeter-wave regimes, for the straight hollow waveguide and for infrared field, also in the cases of inhomogeneous dielectric materials in the cross section.

**Keywords:** wave propagation, inhomogeneous dielectric materials, rectangular and circular waveguides, dielectric profiles

## 1. Introduction

The methods of straight waveguides have been proposed in the literature. Review of numerical and approximate methods for the modal analysis of general optical dielectric waveguides with

emphasis on recent developments has been published [1]. Examples of important methods have been proposed such as finite-difference method, the integral-equation method, and methods based on series expansion. Full-vectorial matched interface and boundary method for modal analysis of dielectric waveguides has been proposed [2]. The method distinguishes itself with other existing interface methods by avoiding the use of the Taylor series expansion and by introducing the concept of the iterative use of low-order jump conditions.

A review of the hollow waveguide and the applications has been presented [3, 4]. A review of hollow waveguides, infrared transmitting, and fibers has been presented [5]. Hollow waveguides with metallic and dielectric layers have been proposed to reduce the transmission losses. A hollow waveguide can be made from any flexible or rigid tube, such as glass, plastic or glass, and the inner hollow surface is covered by a metallic layer and a dielectric overlayer. The structure of the layer enables to transmit both the TE and TM polarization with low attenuation [6, 7].

Selective suppression of electromagnetic modes in rectangular waveguides has been presented [8] by using distributed wall losses. Analytical model for the corrugated rectangular waveguide has been extended to compute the dispersion and interaction impedance [9].

A Fourier operator method has been used to derive for the first time an exact closed-form eigenvalue equation for the scalar mode propagation constants of a buried rectangular dielectric waveguide [10]. Wave propagation in an inhomogeneous transversely magnetized rectangular waveguide has been studied with the aid of a modified Sturm-Liouville differential equation [11]. A fundamental and accurate technique to compute the propagation constant of waves in a lossy rectangular waveguide has been proposed [12]. This method is based on matching the electric and magnetic fields at the boundary and allowing the wavenumbers to take complex values.

A method that relates to the propagation constant for the bound modes in the dielectric rectangular waveguides has been proposed [13]. An analysis of rectangular folded-waveguide slow-wave structure has been developed using conformal mapping by using Schwarz Christoffel transformation [14]. A simple closed form expression to compute the time-domain reflection coefficient for a transient $TE_{10}$ mode wave incident on a dielectric step discontinuity in a rectangular waveguide has been presented [15]. In this paper, an exponential series approximation was provided for efficient computation of the reflected and transmitted field waveforms.

The electromagnetic fields in rectangular conducting waveguides filled with uniaxial anisotropic media have been characterized [16]. In this paper, the electric type dyadic Green's function due to an electric source was derived by using eigenfunctions expansion and the Ohm-Rayleigh method. An improved generalized admittance matrix technique based on mode matching method has been proposed [17]. The generalized scattering matrix of waveguide structure and its discontinuity problems is obtained with relationship equations and reflection coefficients.

A full-vectorial boundary integral equation method for computing guided modes of optical waveguides has been proposed [18]. Method for the propagation constants of fiber waveguides

http://dx.doi.org/10.5772/intechopen.76793

of arbitrary cross section shape has been proposed [19]. In this paper, the proposed techniques used to solve problems of scattering by irregularly shaped dielectric bodies, and in the static limit, for solving the problem of an irregular dielectric or permeable body in an external field.

The rectangular dielectric waveguide technique for the determination of complex permittivity of a wide class of dielectric materials of various thicknesses and cross sections has been described [20]. In this paper, the technique has been presented to determine the dielectric constant of materials. The fields and propagation constants of dielectric waveguides have been determined within the scalar regime [21] by using two-dimensional Fourier series expansions. Propagation of modes in some rectangular waveguides using the finite-difference time-domain method has been proposed [22]. Analysis of rectangular waveguide using finite element method has been proposed [23].

Wave propagation and dielectric permittivity reconstruction in the case of a rectangular waveguide have been studied [24]. According to this paper, we study the electromagnetic wave propagation in a rectangular waveguide filled with an inhomogeneous dielectric material in the longitudinal direction. Light propagation in a cylindrical waveguide with a complex, metallic and dielectric function has been proposed [25]. Advancement of algebraic function approximation in eigenvalue problems of lossless metallic waveguides to infinite dimensions has been investigated [26]. The method of algebraic function approximation in eigenvalue problems of lossless metallic waveguides such as a closed uniform cylindrical waveguides has been proposed [27]. Analysis of longitudinally inhomogeneous waveguides using Taylor's series expansion has been proposed [28]. Analysis of longitudinally inhomogeneous waveguides using the Fourier series expansion has been proposed [29]. The method of external excitation for analysis of arbitrarily-shaped hollow conducting waveguides has been proposed [30].

A circular metallic hollow waveguide with inner dielectric multilayers has been designed by Miyagi and Kawakami [31] with the emphasis on low-loss transmission of the $HE_{11}$ mode for the infrared. According to this paper, the transmission losses of the dielectric-coated metal waveguides are drastically reduced when a multiple dielectric layer is formed instead of a single dielectric layer. The simplest and most efficient multilayer structure is a three-dielectric-layer stack deposited on a metal layer.

A transfer matrix function for the analysis of electromagnetic wave propagation along the straight dielectric waveguide with arbitrary profiles has been proposed [32]. According to this paper, the method is based on the Laplace and Fourier transforms, and the inverse Laplace and Fourier transforms. A rigorous approach for the propagation of electromagnetic fields along a straight hollow waveguide with a circular cross section has been proposed [33]. The cross section is made of a metallic layer, and only one dielectric layer upon it. The separation of variables is obtained by using the orthogonal-relations. The longitudinal components of the fields are developed into the Fourier-Bessel series. The transverse components of the fields are expressed as functions of the longitudinal components in the Laplace plane and are obtained by using the inverse Laplace transform by the residue method.

In order to solve more complex problems of coatings in the cross section of the dielectric waveguides, such as rectangular and circular profiles, then it is important to develop in each

modal an improved technique to calculate the dielectric profile, the elements of the matrix and its derivatives of the dielectric profile.

The main objective of this chapter is to develop the techniques that enable us to solve problems with inhomogeneous dielectric materials in the cross section of the straight rectangular and circular waveguides. The second objective is to understand the influence of the inhomogeneous dielectric materials on the output fields. Thus, we need to develop the technique and a particular application to calculate the profiles in the cross section. Namely, we need to calculate the dielectric profile, the elements of the matrix and its derivatives of the dielectric profile in the cases of the straight rectangular and circular waveguides. The proposed techniques are important to improve the methods that are based on Laplace and Fourier transforms and their inverse Laplace and Fourier transforms also for the discontinuous rectangular and circular profiles in the cross section (and not only for the continuous profiles).

## 2. Formulation of the problem

In this chapter, we present techniques for solving discontinuous problems of dielectric materials in the cross section of the straight waveguide for applications in the microwave and millimeter-wave regimes and in the cases of infrared regime. The proposed techniques are very effective in relation to the conventional methods because they allow the development of expressions in the cross section only according to the specific discontinuous problem. In this way, the mode model method becomes an improved method to solve discontinuous problems in the cross section.

Three examples of inhomogeneous dielectric materials in the cross section of the straight waveguides are shown in **Figure 1(a)–(c)**. **Figure 1(a)** shows an example of rectangular profile in the cross section of the straight rectangular waveguide. **Figure 1(b)** shows an example of

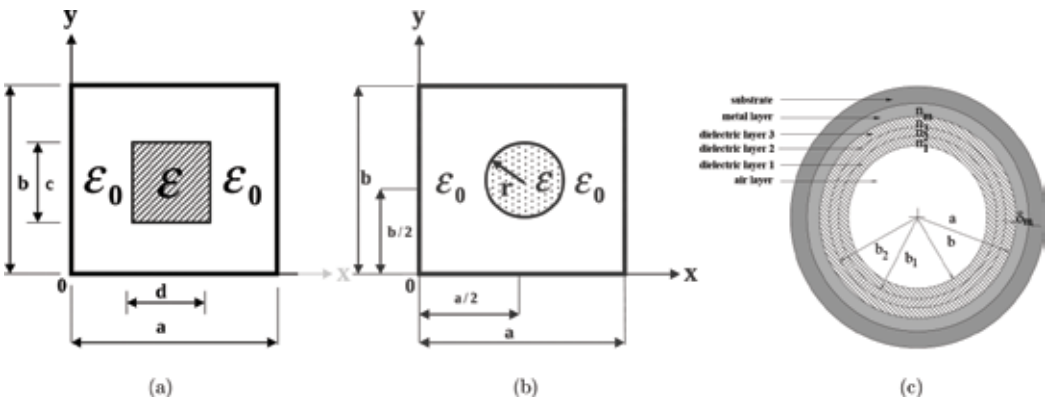


**Figure 1.** Three examples of inhomogeneous dielectric materials in the cross section of the straight waveguides. (a) Rectangular profile in the cross section of the straight rectangular waveguide; (b) Circular profile in the cross section of the straight rectangular waveguide; (c) Three dielectric layers and a metallic layer in the cross section of the hollow waveguide.

http://dx.doi.org/10.5772/intechopen.76793

circular profile in the cross section of the straight rectangular waveguide. **Figure 1(c)** shows an example for three dielectric layers and a metallic layer in the cross section of the straight hollow waveguide.

In order to solve these inhomogeneous dielectric materials, we need to calculate the dielectric profile, the elements of the matrix and its derivatives of the dielectric profile. In the next section, we explain the techniques to solve problems with inhomogeneous dielectric materials in the cross section of the straight rectangular waveguide (**Figure 1(a)** and **1(b)**) and also in the cross section of the straight circular waveguide (**Figure 1(c)**).

## 3. The technique to solve inhomogeneous dielectric profiles

The particular application is based on the $\omega_\varepsilon$ function [34]. The $\omega_\varepsilon$ function is used in order to solve discontinuous problems of the rectangular profile, and circular profile in the cross section of the straight waveguide. The $\omega_\varepsilon$ function is defined as $\omega_\varepsilon(r) = C_\varepsilon \exp\left[-\varepsilon^2/\left(\varepsilon^2 - |r|^2\right)\right]$ for $|r| > \varepsilon$, where $C_\varepsilon$ is a constant, and $\int \omega_\varepsilon(r)dr = 1$. In the limit $\varepsilon \to 0$, the $\omega_\varepsilon$ function is shown in **Figure 2**.

The technique that based on $\omega_\varepsilon$ function is very effective to solve complex problems, in relation to the conventional methods, especially when we have a large numbers of dielectric layers and a metal layer, as shown in **Figure 1(c)**. We will demonstrate how to use with the proposed technique for all the cases that are shown in the examples in **Figure 1(a)–(c)**.

### 3.1. The technique based on $\omega_\varepsilon$ function for the rectangular profile in the cross section of the straight rectangular waveguide

The elements of the matrix g(n, m) are calculated for an arbitrary profile in the cross section of the straight waveguide according to **Figure 3(a)** and **3(b)**. **Figure 3(a)** shows the arbitrary profile in the cross section of the straight waveguide. **Figure 3(b)** shows the rectangular profile in the cross section of the straight waveguide, according to **Figure 1(a)**.

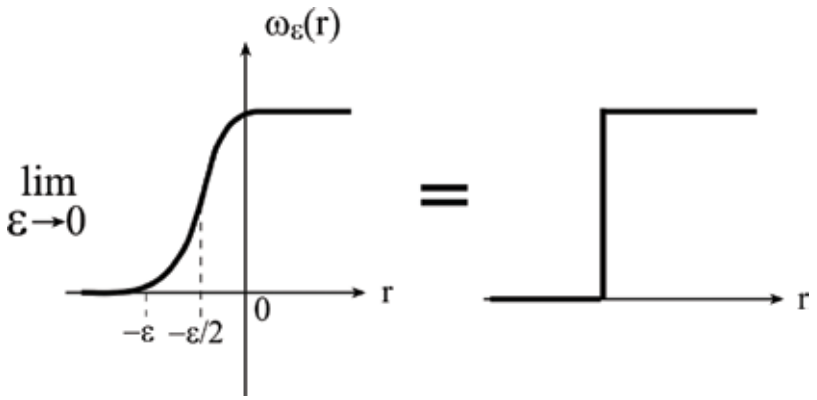


**Figure 2.** The technique based on $\omega_\varepsilon$ function in the limit $\varepsilon \to 0$ to solve discontinuous problems.

The dielectric profile $g(x,y)$ is given according to $\varepsilon(x,y) = \varepsilon_0(1+g(x,y))$. According to **Figure 3(a)** and **3(b)** and for $g(x,y) = g_0$, we obtain

$$g(n,m) = \frac{g_0}{4ab}\int_{-a}^{a} dx \int_{-b}^{b} \exp\left(-j\left(k_x x + k_y y\right)\right) dy$$

$$= \frac{g_0}{4ab}\left\{\int_{x_{11}}^{x_{12}} dx \int_{y_{11}}^{y_{12}} \exp\left(-j\left(k_x x + k_y y\right)\right) dy + \int_{-x_{12}}^{-x_{11}} dx \int_{y_{11}}^{y_{12}} \exp\left(-j\left(k_x x + k_y y\right)\right) dy \right. \quad (1)$$

$$\left. + \int_{-x_{12}}^{-x_{11}} dx \int_{-y_{12}}^{-y_{11}} \exp\left(-j\left(k_x x + k_y y\right)\right) dy + \int_{x_{11}}^{x_{12}} dx \int_{-y_{12}}^{-y_{11}} \exp\left(-j\left(k_x x + k_y y\right)\right) dy \right\}.$$

If $y_{11}$ and $y_{12}$ are not functions of x, then the dielectric profile is given by

$$g(n,m) = \frac{g_0}{ab}\int_{x_{11}}^{x_{12}} \cos\left(k_x x\right) dx \int_{y_{11}}^{y_{12}} \cos\left(k_y y\right) dy. \quad (2)$$

The derivative of the dielectric profile in the case of $y_{11}$ and $y_{12}$ are functions of x, is given by

$$g_x(n,m) = \frac{2}{am\pi}\int_{x_{11}}^{x_{12}} g_x(x,y) \sin\left[\frac{k_y}{2}\left(y_{12} - y_{11}\right)\right] \cos\left[\frac{k_y}{2}\left(y_{12} + y_{11}\right)\right] \cos\left(k_x x\right) dx, \quad (3)$$

where $g_x(x,y) = (1/\epsilon(x,y))(d\epsilon(x,y)/dx)$, $\epsilon(x,y) = \epsilon_0(1+g(x,y))$, $k_x = (n\pi x)/a$, and $k_y = (m\pi y)/b$. Similarly, we can calculate the value of $g_y(n,m)$, where $g_y(x,y) = (1/\epsilon(x,y))(d\epsilon(x,y)/dy)$.

For the cross section as shown in **Figures 1(a)** and **3(b)**, the center of the rectangle is located at (0.5 a, 0.5 b), $y_{12}$ = b/2 + c/2 and $y_{11}$ = b/2−c/2. Thus, for this case, $y_{12} - y_{11}$ = c and $y_{12} + y_{11}$ = b.

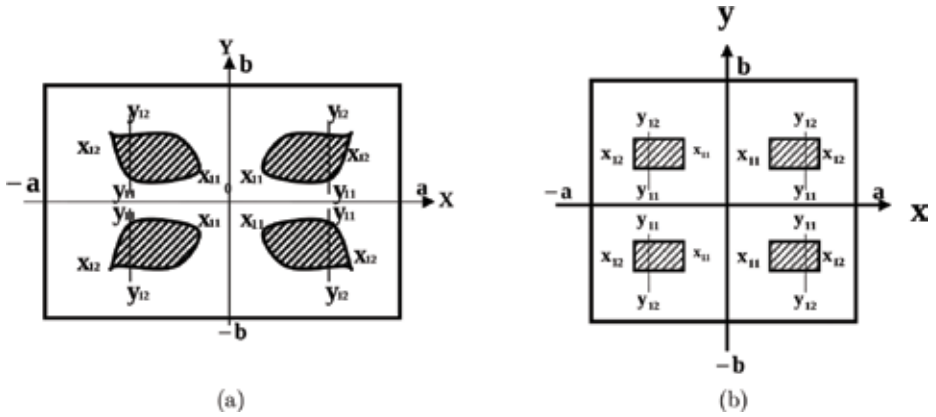


**Figure 3.** (a). The arbitrary profile in the cross section of the straight waveguide. (b). The rectangular profile in the cross section of the straight waveguide, according to **Figure 1(a)**.

### 3.2. The technique based on $\omega_\varepsilon$ function for the circular profile in the cross section of the straight rectangular waveguide

The equation of the circle is given by $(x-a/2)^2+(y-b/2)^2=r^2$. The center of the circle is located at (0.5 a, 0.5 b), as shown in **Figure 1(b)**. We obtain two possibilities without this $y_{11}(x)=b/2-\sqrt{r^2-(x-a/2)^2}$ and $y_{12}(x)=b/2+\sqrt{r^2-(x-a/2)^2}$, where $y_{12}-y_{11}=2\sqrt{r^2-(x-a/2)^2}$ and $y_{12}+y_{11}=b$.

The dielectric profile for the circle is given where the center is located at (0.5 a, 0.5 b) (**Figure 1(b)**) by

$$g(x,y)=\begin{cases} g_0 & 0\le r<r_1-\varepsilon_1/2 \\ g_0\exp\left[1-q_\varepsilon(r)\right] & r_1-\varepsilon_1/2\le r<r_1+\varepsilon_1/2 \end{cases}, \tag{4}$$

where

$$q_\varepsilon(r)=\frac{{\varepsilon_1}^2}{{\varepsilon_1}^2-\left[r-(r_1-\varepsilon_1/2)\right]^2}, \tag{5}$$

else $g(x,y)=0$. The radius of the circle is given by $r=\sqrt{(x-a/2)^2+(y-b/2)^2}$.

The derivatives of the dielectric profile for the circle are given where the center is located at (0.5 a, 0.5 b), as shown in **Figure 1(b)**, where $r_1-\varepsilon_1/2\le r<r_1+\varepsilon_1/2$ by

$$g_x=\frac{-2\ g_0\ \cos\theta exp\left[1-q_\varepsilon(r)\right]\left[r-(r_1-\varepsilon_1/2)\right]{\varepsilon_1}^2}{\left\{1+g_0\exp\left[1-q_\varepsilon(r)\right]\right\}\left[{\varepsilon_1}^2-\left[r-(r_1-\varepsilon_1/2)\right]^2\right]^2}, \tag{6}$$

$$g_y=\frac{-2\ g_0\ \sin\theta exp\left[1-q_\varepsilon(r)\right]\left[r-(r_1-\varepsilon_1/2)\right]{\varepsilon_1}^2}{\left\{1+g_0\exp\left[1-q_\varepsilon(r)\right]\right\}\left[{\varepsilon_1}^2-\left[r-(r_1-\varepsilon_1/2)\right]^2\right]^2}, \tag{7}$$

else $g_x=0$, and $g_y=0$.

The elements of the matrices for the circular profile are given where the center is located at (0.5 a, 0.5 b) (**Figure 1(b)**) by

$$g(n,m)=\frac{g_0}{ab}\left\{\int_0^{2\pi}\int_0^{r_1-\varepsilon_1/2}\cos\left[\frac{n\pi}{a}\left(r\cos\theta+\frac{a}{2}\right)\right]\cos\left[\frac{m\pi}{b}\left(r\sin\theta+\frac{b}{2}\right)\right]\right.$$
$$\left.+\int_0^{2\pi}\int_{r_1-\varepsilon_1/2}^{r_1+\varepsilon_1/2}\cos\left[\frac{n\pi}{a}\left(r\cos\theta+\frac{a}{2}\right)\right]\cos\left[\frac{m\pi}{b}\left(r\sin\theta+\frac{b}{2}\right)\right]\exp\left[1-q_\varepsilon(r)\right]\right\}rdrd\theta, \tag{8}$$

$$g_x(n,m)=-\frac{2g_0}{ab}\left\{\int_0^{2\pi}\int_{r_1-\varepsilon_1/2}^{r_1+\varepsilon_1/2}\frac{{\varepsilon_1}^2\left[r-(r_1-\varepsilon_1/2)\right]\exp\left[1-q_\varepsilon(r)\right]\cos\theta}{\left[{\varepsilon_1}^2-\left[r-(r_1-\varepsilon_1/2)\right]^2\right]^2\left[1+g_0\exp\left[1-q_\varepsilon(r)\right]\right]}\right.$$
$$\left.\cos\left[\frac{n\pi}{a}\left(r\cos\theta+\frac{a}{2}\right)\right]\cos\left[\frac{m\pi}{b}\left(r\sin\theta+\frac{b}{2}\right)\right]\right\}rdrd\theta, \tag{9}$$

$$g_y(n,m) = -\frac{2g_0}{ab}\left\{\int_0^{2\pi}\int_{r_1-\varepsilon_1/2}^{r_1+\varepsilon_1/2} \frac{{\varepsilon_1}^2[r-(r_1-\varepsilon_1/2)]\exp\left[1-q_\varepsilon(r)\right]\sin\theta}{\left[{\varepsilon_1}^2-[r-(r_1-\varepsilon_1/2)]^2\right]^2\left[1+g_0\exp\left[1-q_\varepsilon(r)\right]\right]} \right.$$
$$\left. \cos\left[\frac{n\pi}{a}\left(r\cos\theta+\frac{a}{2}\right)\right]\cos\left[\frac{m\pi}{b}\left(r\sin\theta+\frac{b}{2}\right)\right]\right\} r dr d\theta, \tag{10}$$

where $r = \sqrt{(x-a/2)^2+(y-b/2)^2}$.

The proposed techniques in this subsection and the subsection 3.1 relate to the method for the propagation along the straight rectangular metallic waveguide [32]. The techniques and the particular applications to solve the rectangular and circular profiles in the cross section of the straight rectangular waveguide are important in order to improve the mode model [32]. The method is based on the Laplace and Fourier transform and their inverse transforms. Laplace transform is necessary to obtain the comfortable and simple input-output connections of the fields. The output transverse field profiles are computed by the inverse Laplace and Fourier transforms.

The matrix **G** is given by the form.

$$\mathbf{G} = \begin{bmatrix} g_{00} & g_{-10} & g_{-20} & \cdots & g_{-nm} & \cdots & g_{-NM} \\ g_{10} & g_{00} & g_{-10} & \cdots & g_{-(n-1)m} & \cdots & g_{-(N-1)M} \\ g_{20} & g_{10} & \ddots & \ddots & \ddots & & \\ \vdots & g_{20} & \ddots & \ddots & \ddots & & \\ g_{nm} & \ddots & \ddots & \ddots & g_{00} & \vdots & \\ \vdots & & & & & & \\ g_{NM} & \cdots & \cdots & \cdots & \cdots & \cdots & g_{00} \end{bmatrix}. \tag{11}$$

Similarly, the $\mathbf{G}_x$ and $\mathbf{G}_y$ matrices are obtained by the derivatives of the dielectric profile. These matrices relate to the method that is based on the Laplace and Fourier transforms and their inverse [32].

Several examples will demonstrate in the next section in order to explore the effects of the rectangular and circular materials in the cross section (**Figure 1(a)** and **1(b)**) along the straight waveguide on the output field. All the graphical results will be demonstrated as a response to a half-sine ($TE_{10}$) input-wave profile and the rectangular and circular materials in the cross section of the straight rectangular waveguide.

### 3.3. The technique based on $\omega_\varepsilon$ function for the circular profile in the cross section of the straight circular waveguide

The cross section of hollow waveguide (**Figure 1(c)**) is made of a tube of various types of three dielectric layers and a metallic layer. The internal and external diameters are denoted as 2b,

$2b_1$, $2b_2$, 2a, and 2(a+$\delta_m$), respectively, where $\delta_m$ is the thickness of the metallic layer. In addition, we denote the thickness of the dielectric layers as $d_1$, $d_2$, and $d_3$, respectively, where $d_1 = b_1 - b$, $d_2 = b_2 - b_1$, and $d_3 = a - b_2$. The refractive index in the particular case with the three dielectric layers and the metallic layer in the cross section of the straight hollow waveguide (**Figure 1(c)**) is calculated as follows:

$$n(r) = \begin{cases} n_0 & 0 \le r < b - \varepsilon_1/2 \\ n_0 + (n_1 - n_0)\exp\left[1 - \dfrac{{\varepsilon_1}^2}{{\varepsilon_1}^2 - [r - (b + \varepsilon_1/2)]^2}\right] & b - \varepsilon_1/2 \le r < b + \varepsilon_1/2 \\ n_1 & b + \varepsilon_1/2 \le r < b_1 - \varepsilon_2/2 \\ n_1 + (n_2 - n_1)\exp\left[1 - \dfrac{{\varepsilon_2}^2}{{\varepsilon_2}^2 - [r - (b_1 + \varepsilon_2/2)]^2}\right] & b_1 - \varepsilon_2/2 \le r < b_1 + \varepsilon_2/2 \\ n_2 & b_1 + \varepsilon_2/2 \le r < b_2 - \varepsilon_2/2, \\ n_2 + (n_3 - n_2)\exp\left[1 - \dfrac{{\varepsilon_3}^2}{{\varepsilon_3}^2 - [r - (b_2 + \varepsilon_3/2)]^2}\right] & b_2 - \varepsilon_2/2 \le r < b_2 + \varepsilon_3/2 \\ n_3 & b_2 + \varepsilon_3/2 \le r < a - \varepsilon_3/2 \\ n_3 + (n_m - n_3)\exp\left[1 - \dfrac{{\varepsilon_4}^2}{{\varepsilon_4}^2 - [r - (a + \varepsilon_4/2)]^2}\right] & a - \varepsilon_3/2 \le r < a + \varepsilon_4/2 \\ n_m & else \end{cases} \tag{12}$$

where the parameters $\varepsilon_1$, $\varepsilon_2$, $\varepsilon_3$, and $\varepsilon_4$ are very small [e.g., $\varepsilon_1 = \varepsilon_2 = \varepsilon_3 = [a - b]/50$, $\varepsilon_4 = \delta_m/50$]. The refractive indices of the air, dielectric and metallic layers are denoted as $n_0$, $n_1$, $n_2$, $n_3$, and $n_m$, respectively. In this study, we suppose that $n_3 > n_2 > n_1$.

The transverse derivative of the dielectric profile is calculated as follows:

$$g_r(r) = \begin{cases} 0 & 0 \le r < b - \varepsilon_1/2 \\ \dfrac{-4(n_1 - n_0)\exp\left[1 - \dfrac{{\varepsilon_1}^2}{{\varepsilon_1}^2 - [r - (b + \varepsilon_1/2)]^2}\right][r - (b + \varepsilon_1/2)]{\varepsilon_1}^2}{n_0 + (n_1 - n_0)\exp\left[1 - \dfrac{{\varepsilon_1}^2}{{\varepsilon_1}^2 - [r - (b + \varepsilon_1/2)]^2}\right]\left[{\varepsilon_1}^2 - [r - (b + \varepsilon_1/2)]^2\right]^2} & b - \varepsilon_1/2 \le r < b + \varepsilon_1/2 \\ 0 & b + \varepsilon_1/2 \le r < b_1 - \varepsilon_2/2 \\ \dfrac{-4(n_2 - n_1)\exp\left[1 - \dfrac{{\varepsilon_2}^2}{{\varepsilon_2}^2 - [r - (b_1 + \varepsilon_2/2)]^2}\right][r - (b_1 + \varepsilon_2/2)]{\varepsilon_2}^2}{n_2 + (n_3 - n_2)\exp\left[1 - \dfrac{{\varepsilon_2}^2}{{\varepsilon_2}^2 - [r - (b_1 + \varepsilon_2/2)]^2}\right]\left[{\varepsilon_1}^2 - [r - (b_1 + \varepsilon_2/2)]^2\right]^2} & b_1 - \varepsilon_2/2 \le r < b_1 + \varepsilon_2/2 \\ 0 & b_1 + \varepsilon_2/2 \le r < b_2 - \varepsilon_3/2, \\ \dfrac{-4(n_3 - n_2)\exp\left[1 - \dfrac{{\varepsilon_3}^2}{{\varepsilon_3}^2 - [r - (b_2 + \varepsilon_3/2)]^2}\right][r - (b_2 + \varepsilon_3/2)]{\varepsilon_3}^2}{n_3 + (n_m - n_3)\exp\left[1 - \dfrac{{\varepsilon_3}^2}{{\varepsilon_3}^2 - [r - (b_2 + \varepsilon_3/2)]^2}\right]\left[{\varepsilon_1}^2 - [r - (b_1 + \varepsilon_2/2)]^2\right]^2} & b_2 - \varepsilon_3/2 \le r < b_2 + \varepsilon_3/2 \\ 0 & b_2 + \varepsilon_3/2 \le r < a - \varepsilon_4/2 \\ \dfrac{-4(n_m - n_3)\exp\left[1 - \dfrac{{\varepsilon_4}^2}{{\varepsilon_4}^2 - [r - (a + \varepsilon_4/2)]^2}\right][r - (a + \varepsilon_4/2)]{\varepsilon_4}^2}{n_3 + (n_m - n_3)\exp\left[1 - \dfrac{{\varepsilon_4}^2}{{\varepsilon_4}^2 - [r - (a + \varepsilon_4/2)]^2}\right]\left[{\varepsilon_4}^2 - [r - (a + \varepsilon_4/2)]^2\right]^2} & a - \varepsilon_4/2 \le r < a + \varepsilon_4/2 \\ 0 & else \end{cases} \tag{13}$$

The proposed technique in this subsection relates to the theoretical model that based on Maxwell's equations, Fourier-Bessel series, Laplace transform, and the inverse Laplace transform [33]. In this theoretical model, the longitudinal components of the fields are developed into the Fourier-Bessel series. The transverse components of the fields are expressed as functions of the longitudinal components in the Laplace plane and are obtained by using the inverse Laplace transform by the residue method. The separation of the variables is obtained by using the orthogonal relations.

The output transverse components of the fields of the straight hollow waveguide are finally expressed in a form of transfer matrix function, and the derivation has been already explained in detail in Ref. [33]. The contribution of the proposed technique to calculate the refractive indices ($n(r)$) and the transverse derivative of the dielectric profile ($g_r$) for three dielectric layers is important to improve the method that is based on the mode model [33]. This improved method is important to reduce the transmission losses of the dielectric coated metal waveguides.

## 4. Numerical results

Several examples for all geometry of the rectangular and circular waveguides and the dielectric profile are demonstrated in this section for three cases, as shown in **Figure 1(a)–(c)**.

### 4.1. Numerical results for the rectangular dielectric material in the cross section of the straight rectangular waveguide

The analytical method for the dielectric slab [35] is shown in **Figure 4(a)**. The slab profile in the cross section is based on transcendental equation, as follows:

$$E_{y1} = j\frac{k_z}{\varepsilon_0}\sin(\nu x) \qquad 0 < x < t \tag{14}$$

$$E_{y2} = j\frac{k_z}{\varepsilon_0}\frac{\sin(\nu t)}{\cos\left(\mu(t-a/2)\right)}\cos\left[\mu(x-a/2)\right] \qquad t < x < t+d \tag{15}$$

$$E_{y3} = j\frac{k_z}{\varepsilon_0}\sin\left[\nu(a-x)\right] \qquad t+d < x < a, \tag{16}$$

where $\nu \equiv \sqrt{k_o^2 - k_z^2}$ and $\mu \equiv \sqrt{\varepsilon_r k_o^2 - k_z^2}$ result from the transcendental equation.

$$\left(\frac{a-d}{d}\right)\frac{d\mu}{2}\tan\left(\frac{d\mu}{2}\right) - (t\nu)\cot(t\nu) = 0. \tag{17}$$

The criterion for the convergence of the solution is given by

http://dx.doi.org/10.5772/intechopen.76793

$$C(N) \equiv \log\left\{\frac{\max\left(|E_y^{N+2} - E_y^N|\right)}{|\max\left(E_y^{N+2}\right) - \min\left(E_y^N\right)|}\right\}, \tag{18}$$

for $N \geq 1$, where $(2N+1)^2$ is the number of the modes. By increasing the order $N$, then $E_y(N)$ approaches $E_y$.

**Figure 4(a)** shows the geometry of the slab profile for practical case of the slab dielectric material, where a = 20 mm, b = 10 mm, d = 3.3 mm, t = 8.35 mm, $\lambda = 6.9$ cm, and $\epsilon_r = 9$.

**Figure 4(b)** demonstrates the output result of the comparison between the theoretical model with the analytical solution [35].

**Figure 4(c)** shows the criterion of the convergence in Eq. (18). Between N = 7 and N = 9 the value of the criterion is equal to $-2$. According to **Figure 4(b)** and **4(c)**, the comparison has shown good agreement.

All the next graphical results are demonstrated as a response to a half-sine ($TE_{10}$) input-wave profile.

**Figure 5(a)–(f)** relates to discontinuous problem according to **Figure 1(a)**. **Figure 5(a)–(d)** shows the results of the output field as a response to a half-sine ($TE_{10}$) input-wave profile. In this case, c = d = 3.3 *mm* and the center of the rectangle is located at the point (0.5 a, 0.5 b), as shown in **Figure 1 (a)** for $\epsilon_r = 3, 5, 7$, and 10, respectively. The other parameters are a = b = 2 *cm* , z = 15 *cm*, $k_0 = 167\ 1/m$, $\lambda = 3.75$ *cm*, and $\beta = 58\ 1/m$. The output fields are strongly affected by the input wave profile ($TE_{10}$ mode), the rectangular profile, and the location of the center of the rectangle (0.5 a, 0.5 b).

**Figure 5(e)** shows the output amplitude and the Gaussian shape of the central peak in the same cross section of **Figure 5(a)–(d)**, where a = 2 cm, b = 2 cm, y = b/2 = 10 mm, c = 3.3 *mm*, d = 3.3 *mm*, z = 15 *cm*, $k_0 = 167\ 1/m$, and for $\epsilon_r$ =3, 5, 7, and 10, respectively.

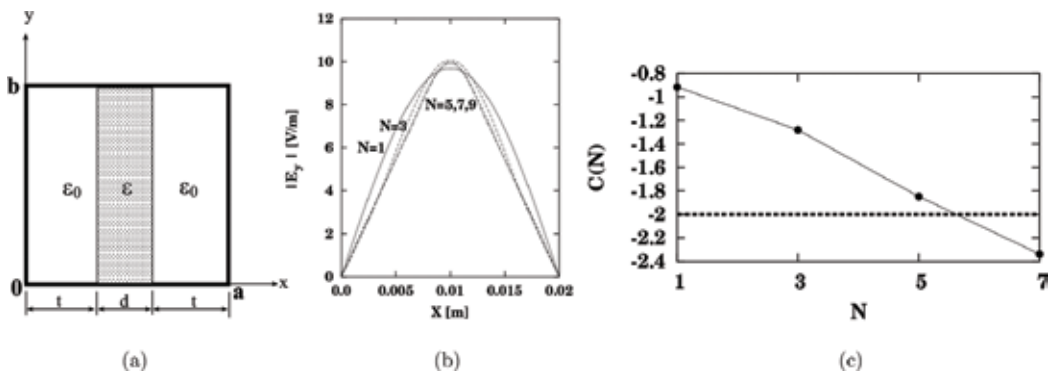


**Figure 4.** (a). The cross section of the straight rectangular waveguide. (b). The results between our model and the analytical method. (c). The criterion of the convergence according to Eq. (18).

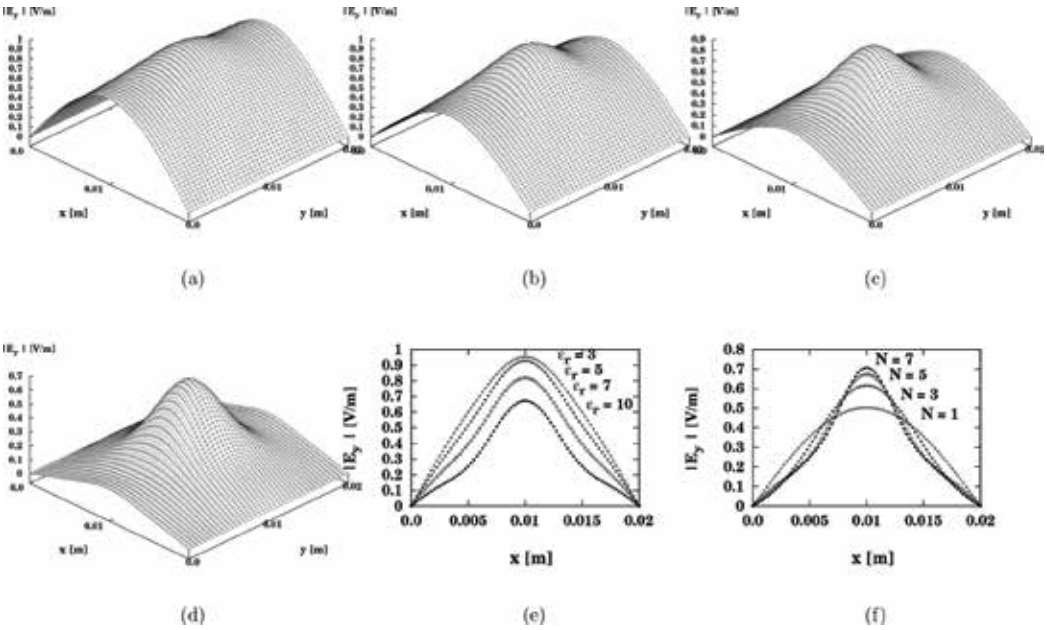


**Figure 5.** The output field as a response to a half-sine ($TE_{10}$) input-wave profile where c = d = 3.3 *mm* and the center of the rectangle is located at the point (0.5 a, 0.5 b) according to **Figure 1(a)**, where: (a). $\epsilon_r$ = 3; (b). $\epsilon_r$ = 5; (c). $\epsilon_r$ = 7; (d). $\epsilon_r$ = 10. The other parameters are a = b = 2 *cm*, z = 15 *cm*, $k_0$ = 167 $1/m$, $\lambda$ = 3.75 *cm*, and $\beta$ = 58 $1/m$ . (e). The output field for $\epsilon_r$ =3, 5, 7, and 10, respectively, where a = b = 2 cm, y = b/2 = 10 mm. (f). The output profiles for N = 1, 3, 5, and 7, where $\epsilon_r$ = 10.

By increasing only the value of $\epsilon_r$ of the rectangular dielectric profile, the $TE_{10}$ wave profile decreased, the Gaussian shape of the output field increased, and the relative amplitude decreased. In addition, by increasing only the value of $\epsilon_r$, the width of the Gaussian shape decreased.

The output profiles and the amplitudes for N = 1, 3, 5, and 7 are shown in **Figure 5(f)**, for $\epsilon_r$ = 10. By increasing only the parameter of the order N, the output field approaches to the final output field.

According to the results, we see that the output fields are strongly affected by the input wave profile ($TE_{10}$ mode), the rectangular profile, and the location of the center of the rectangle (0.5 a, 0.5 b).

### 4.2. Numerical results for the circular dielectric material in the cross section of the straight rectangular waveguide

**Figure 6(a)–(f)** relates to discontinuous problem according to **Figure 1(b)**. **Figure 6(a)–(d)** demonstrates the results of the output field as a response to $TE_{10}$ input-wave profile, for $\epsilon_r$ = 3, 5, 7, and 10, respectively. The radius of the circle in this case is equal to 2.5 *mm* and the center of the circle is located at the point (0.5 a, 0.5 b), as shown in **Figure 1(b)**.

The other parameters are a = b = 2 *cm* , z = 15 *cm*, $k_0$ = 167 $1/m$, $\lambda$ = 3.75 *cm*, and $\beta$ = 58 $1/m$.

**Figure 6(e)** shows the output amplitude and the Gaussian shape of the central peak in the same cross section of **Figure 6(a)–(d)**, where $\epsilon_r$ =3, 5, 7, and 10, respectively.

http://dx.doi.org/10.5772/intechopen.76793

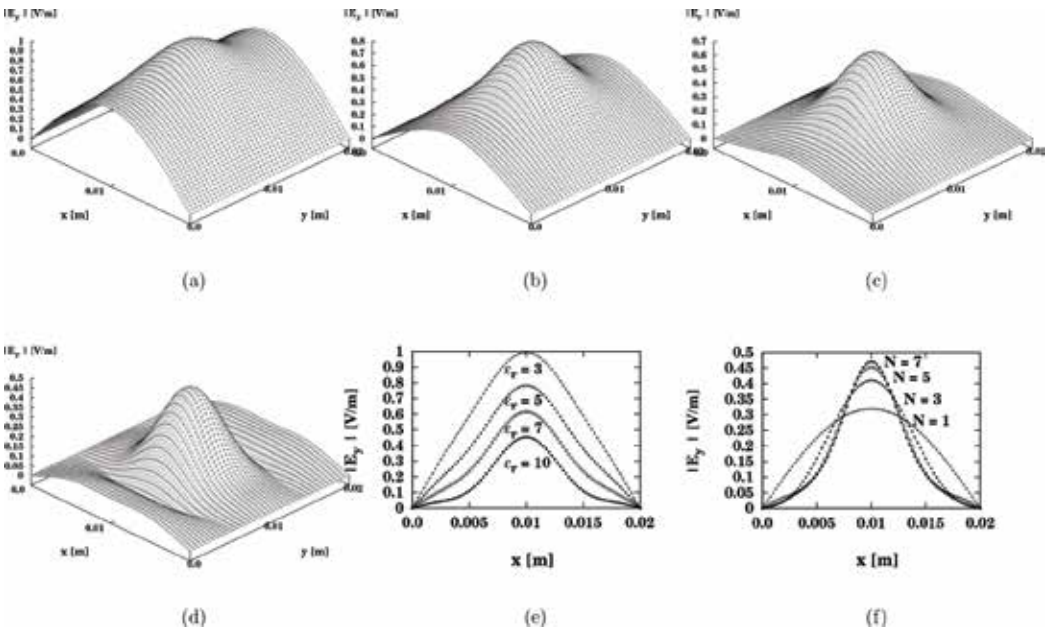


**Figure 6.** The output field as a response to a half-sine ($TE_{10}$) input-wave profile where the radius of all circle is equal to 2.5 *mm* and the center of the circle is located at the point (0.5 a, 0.5 b) according to **Figure 1(b)**, where: (a). $\epsilon_r = 3$; (b). $\epsilon_r = 5$; (c). $\epsilon_r = 7$; (d). $\epsilon_r = 10$. The other parameters are a = b = 2 *cm*, z = 15 *cm*, $k_0 = 167\ 1/m$, $\lambda = 3.75$ *cm*, and $\beta = 58\ 1/m$ . (e). The output field for $\epsilon_r$ =3, 5, 7, and 10, respectively, where a = b = 20 mm, y = b/2 = 10 mm. The radius of all circles is equal to 2.5 *mm*. (f). The output profiles for N = 1, 3, 5, and 7, where $\epsilon_r = 10$.

The output profiles are shown in **Figure 6(f)** for N = 1, 3, 5, and 7, where $\epsilon_r = 10$. The other parameters are a = b = 2 *cm*, z = 15 *cm*, $k_0 = 167\ 1/m$, $\lambda = 3.75$ *cm*, and $\beta = 58\ 1/m$.

By increasing only the parameter $\epsilon_r$ of the circular dielectric profile from 3 to 10, the Gaussian shape of the output transverse profile of the field increased, the $TE_{10}$ wave profile decreased, and the relative amplitude of the output field decreased.

The output fields of **Figure 6(a)–(f)** are strongly affected by the input wave profile ($TE_{10}$ mode), the circular profile, and the location of the center of the circle (0.5 a, 0.5 b).

It is interesting to see a similar behavior of the output results in the cases of rectangular profiles (**Figure 5(a)–(f)**) that relate to **Figure 1(a)** and in the cases of circular profiles (**Figure 6(a)–(f)**) that relate to **Figure 1(b)**, for every value of $\epsilon_r$, respectively. According to these output results, we see the similar behavior for every value of $\epsilon_r$, but the amplitudes of the output fields are different.

### 4.3. Numerical results for the three dielectric layers and a metallic layer in the cross section of the straight hollow waveguide

The comparison between our theoretical result of the output power density with the laboratory result in the case of the straight hollow waveguide with one dielectric layer and a metallic layer

is demonstrated in **Figure 7(a)** and **7(b)**. In this example, the diameter (2a) of the waveguide is 2 mm, the thickness of the dielectric layer [$d_{(AgI)}$] is 0.75 $\mu m$, and the minimum spot-size ($w_0$) is 0.3 mm. The length of the straight waveguide is 1 m. The refractive indices of the air, the dielectric layer (AgI) and the metallic layer (Ag) are $n_{(0)} = 1$, $n_{(AgI)} = 2.2$, and $n_{(Ag)} = 13.5 - j75.3$, respectively. The value of the refractive index of the material at a wavelength of $\lambda$=10.6 $\mu$m is taken from the table compiled by Miyagi et al. [36].

The results of the output power density ($|S_{av}|$) (e.g., **Figure 7(a)**) show the behavior of the solutions for the $TEM_{00}$ mode in excitation. The comparison between our theoretical result (**Figure 7(a)**) and the published experimental data [37], as shown also in **Figure 7(b)** shows good agreement of a Gaussian shape as expected, except for the secondary small propagation mode. The experimental result is taken into account the roughness of the internal wall of the waveguide, but our theoretical model is not taken the roughness.

Miyagi and Kawakami showed that transmission losses of the dielectric-coated metal waveguides are drastically reduced when a multiple dielectric layer is formed instead of a single dielectric layer [31]. The simplest and most efficient multilayer structure is three dielectric layers that deposited on a metal layer.

Thus, in this subsection, we present the output results that relate to the proposed technique and the particular application for the cross section of the straight hollow waveguide with three dielectric layers (and not only with one dielectric layer) and a metallic layer. In this case, we can improve the method [33], in the case of the three dielectric layers and a metallic layer in the cross section of the straight hollow waveguide.

**Figure 8(a)–(c)** relates to discontinuous problem according to **Figure 1(c)**. The output power density for the straight hollow waveguide with three dielectric layers is shown in **Figure 8(a)–(c)**. **Figure 8(a)** is shown for a = 0.8 mm and $w_0$ = 0.1 mm. **Figure 8(b)** is shown for a = 0.8 mm and $w_0$ = 0.3 mm. **Figure 8(c)** is shown for a = 0.6 mm and $w_0$ = 0.3 mm. The other parameters are b = 0.5 mm, $\lambda = 10.6\ \mu m$ , $n_{(0)}$ = 1, $n_1$ = 2.22−j $10^{-6}$, $n_2$ = 4−j $10^{-6}$, $n_3$ = 6−j $10^{-6}$, $n_m = n_{(Ag)}$ = 13.5−j 75.3, and the length of the straight waveguide is 1 m.

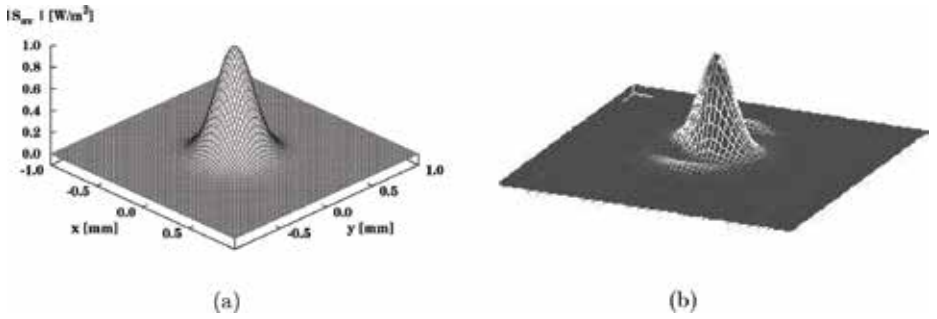


**Figure 7.** The comparison between our theoretical results of the output power density with the laboratory results in the case of the straight hollow waveguide with one dielectric layer. The parameters are a = 1 mm, $w_0$ = 0.3 mm, $d_{(AgI)}$= 0.75 $\mu m$, $\lambda$ = 10.6 $\mu m$, $n_{(0)}$ = 1, $n_{(AgI)}$ = 2.2, $n_{(Ag)}$ = 13.5−j 75, and the length of the straight waveguide is 1 m. (a). theoretical result. (b). laboratory result.

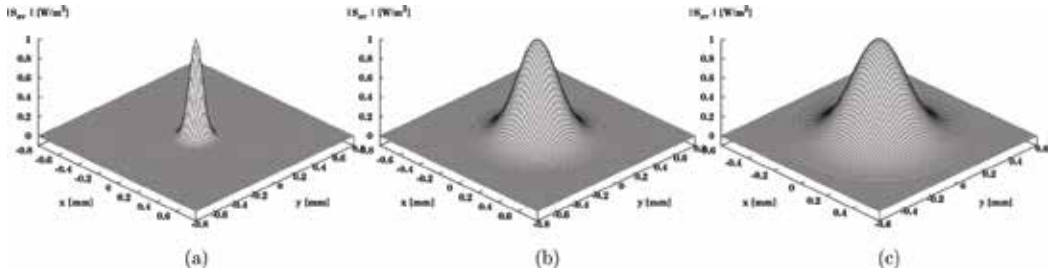


**Figure 8.** The output power density for the straight hollow waveguide with three dielectric layers, where (a). a = 0.8 mm and $w_0$ = 0.1 mm. (b). a = 0.8 mm and $w_0$ = 0.3 mm. (c). a = 0.6 mm and $w_0$ = 0.3 mm. The other parameters are: b = 0.5 mm, $\lambda = 10.6\ \mu m$ , $n_{(0)}$ = 1, $n_1$ = 2.22−j $10^{-6}$, $n_2$ = 4−j $10^{-6}$, $n_3$ = 6−j $10^{-6}$, $n_m = n_{(Ag)}$ = 13.5−j 75.3, and the length of the straight waveguide is 1 m.

By changing only the spot size from $w_0$ = 0.1 to 0.3 mm, with the same other parameters, the output power density is changed, as shown in **Figure 8(a)** and **8(b)**. The results of the output power density ($|S_{av}|$) show the behavior of the solutions for the $TEM_{00}$ mode in excitation. By changing only the spot size from $w_0$ = 0.3 to 0.1 mm, the width of the output Gaussian becomes more narrow. The output field results are strongly affected by the spot size and the structure of the three layers and the metallic layer in the cross section of the straight hollow waveguide.

This mode model can be a useful tool to predict the relevant parameters in the case of the hollow waveguide with three dielectric layers and a metallic layer (Ag) for practical applications (output fields, output power density and output power transmission), before carrying out experiments in the laboratory.

## 5. Conclusions

The main objective of this chapter was to develop the techniques that enable us to solve problems with inhomogeneous dielectric materials in the cross section of the straight rectangular and circular waveguides. The proposed techniques are very effective in relation to the conventional methods because they allow the development of expressions in the cross section only according to the specific discontinuous problem. In this way, the mode model methods become an improved methods to solve discontinuous problems in the cross section (and not only for continuous problems).

Three examples of inhomogeneous dielectric profiles in the cross section of the straight waveguides were shown in **Figure 1(a)–(c)**. **Figure 1(a)** and **1(b)** show the rectangular and circular profiles in the cross section of the straight rectangular waveguide, respectively. **Figure 1(c)** shows three dielectric layers and a metallic layer in the cross section of the straight hollow waveguide. The second objective is to understand the influence of the inhomogeneous dielectric materials on the output fields.

The proposed techniques are important to improve the methods that are based on Laplace and Fourier transforms and their inverse transforms also for the discontinuous rectangular and

circular profiles in the cross section. The technique based on $\omega_\varepsilon$ function was explained in detail in this chapter.

The result of the comparison between the theoretical models with the analytical solution [35] is shown in **Figure 4(b)** and the convergence is shown in **Figure 4(c)**. The comparison has shown good agreement.

The results for the rectangular profile in the cross section of the straight rectangular waveguide (**Figure 1(a)**) were shown in **Figure 5(a)–(f)**. **Figure 5(a)–(d)** shows the results of the output field as a response to a half-sine ($TE_{10}$) input-wave profile. The output fields are strongly affected by the input wave profile ($TE_{10}$ mode), the rectangular profile, and the location of the center of the rectangle (0.5 a, 0.5 b).

By increasing only the value of $\epsilon_r$ of the rectangular dielectric material, the Gaussian shape of the output field increased, the $TE_{10}$ wave profile decreased, the relative amplitude decreased, and the width of the Gaussian shape decreased. The output field approaches to the final output field, by increasing only the parameter of the order N, as shown in **Figure 5(f)**.

The results for the circular profile in the cross section of the straight rectangular waveguide (**Figure 1(b)**) were shown in **Figure 6(a)–(f)**. **Figure 6(a)–(d)** shows the results of the output field as a response to a half-sine ($TE_{10}$) input-wave profile.

By increasing only the value of the parameter $\epsilon_r$ of the circular dielectric material (**Figure 1(b)**) in the rectangular cross section from 3 to 10, the Gaussian shape of the output transverse profile of the field increased, the $TE_{10}$ wave profile decreased, and the relative amplitude of the output field decreased.

The output fields of **Figure 5(a)–(f)** and **Figure 6(a)–(f)** are strongly affected by the input wave profile ($TE_{10}$ mode), the rectangular profile or circular profile, and the location of the center of the rectangle or the circle (0.5 a, 0.5 b).

It is interesting to see a similar behavior of the output results in the cases of rectangular profiles (**Figure 5(a)–(f)**) that relate to **Figure 1(a)** and in the cases of circular profiles (**Figure 6(a)–(f)**) that relate to **Figure 1(b)**, for every value of $\epsilon_r$, respectively. According to these output results, we see the similar behavior for every value of $\epsilon_r$, but the amplitudes of the output fields are different.

The comparison between our theoretical result (**Figure 7(a)**) and the published experimental data [37], as shown also in **Figure 7(b)** shows good agreement of a Gaussian shape as expected, except for the secondary small propagation mode. The experimental result is taken into account the roughness of the internal wall of the waveguide, but our theoretical model is not taken the roughness.

The output power density for the straight hollow waveguide with three dielectric layers (**Figure 1(c)**) is shown in **Figure 8(a)–(c)**. The output field results are strongly affected by the spot size and the structure of the three layers and the metallic layer in the cross section of the straight hollow waveguide.

These models are useful to predict the structure of the output fields for rectangular and circular profiles in straight waveguides in the cases of microwave and millimeter-wave regimes and in

the cases of infrared regime. These models can be a useful tool to predict the relevant parameters for practical applications, before carrying out experiments in the laboratory.

## Author details

Zion Menachem

Address all correspondence to: zionm@post.tau.ac.il

Department of Electrical Engineering, Sami Shamoon College of Engineering, Beer Sheva, Israel

## References

[1] Chiang KS. Review of numerical and approximate methods for the modal analysis of general optical dielectric waveguides. Optical and Quantum Electronics. 1993;**26**:S113-S134

[2] Zhao S. Full-vectorial matched interface and boundary (MIB) method for the modal analysis of dielectric waveguides. Journal of Lightwave Technology. 2008;**26**:2251-2259

[3] Harrington JA, Matsuura Y. Review of hollow waveguide technology. SPIE. 1995;**2396**: 4-14

[4] Harrington JA, Harris DM, Katzir A, editors. Biomedical Optoelectronic Instrumentation. 1995;**2396**:4-14

[5] Harrington JA. A review of IR transmitting, hollow waveguides. Fiber and Integrated Optics. 2000;**19**:211-228

[6] Marhic ME. Mode-coupling analysis of bending losses in IR metallic waveguides. Applied Optics. 1981;**20**:3436-3441

[7] Croitoru N, Goldenberg E, Mendlovic D, Ruschin S, Shamir N. Infrared chalcogenide tube waveguides. SPIE. 1986;**618**:140-145

[8] Jiao CQ. Selective suppression of electromagnetic modes in a rectangular waveguide by using distributed wall losses. Progress in Electromagnetics Research Letters. 2011;**22**:119-128

[9] Mineo M, Di Carlo A, Paoloni C. Analytical design method for corrugated rectangular waveguide SWS THZ vacuum tubes. Journal of Electromagnetic Waves and Applications. 2010;**24**:2479-2494

[10] Smartt CJ, Benson TM, Kendall PC. Exact transcendental equation for scalar modes of rectangular dielectric waveguides. Optical and Quantum Electronics. 1994;**26**:641-644

[11] Chen TT. Wave propagation in an inhomogeneous transversely magnetized rectangular waveguide. Applied Scientific Research. 1960;**8**:141-148

[12] Yeap KH, Tham CY, Yassin G, Yeong KC. Attenuation in rectangular waveguides with finite conductivity walls. Radioengineering. 2011;**20**:472-478

[13] Sharma J. Full-wave analysis of dielectric rectangular waveguides. Progress In Electromagnetics Research. 2010;**13**:121-131

[14] Sumathy M, Vinoy KJ, Datta SK. Analysis of rectangular folded-waveguide millimeter-wave slow-wave structures using conformal transformations. Journal of Infrared, Millimeter, and Terahertz Waves. 2009;**30**:294-301

[15] Rothwell EJ, Temme A, Crowgey B. Pulse reflection from a dielectric discontinuity in a rectangular waveguide. Progress In Electromagnetics Research. 2009;**97**:11-25

[16] Liu S, Li LW, Leong MS, Yeo TS. Rectangular conducting waveguide filled with uniaxial anisotropic media: a modal analysis and dyadic Green's function. Progress In Electromagnetics Research. 2000;**25**:111-129

[17] Han SH, Wang XL, Fan Y. Improved generalized admittance matrix technique and its applications to rigorous analysis of millimeter-wave devices in rectangular waveguide. International Journal of Infrared and Millimeter Waves. 2006;**27**:1391-1402

[18] Lu W, Lu YY. Waveguide mode solver based on Neumann-to-Dirichlet operators and boundary integral equations. Journal of Computational Physics. 2012;**231**:1360-1371

[19] Eyges L, Gianino P. Modes of dielectric waveguides of arbitrary cross sectional shape. Journal of the Optical Society of America. 1979;**69**:1226-1235

[20] Abbas Z, Pollard RD, Kelsall W. A rectangular dielectric waveguide technique for determination of permittivity of materials at W-band. IEEE Transactions on Microwave Theory and Techniques. 1998;**46**:2011-2015

[21] Hewlett SJ, Ladouceur F. Fourier decomposition method applied to mapped infinite domains: scalar analysis of dielectric waveguides down to modal cutoff. Journal of Lightwave Technology. 1995;**13**:375-383

[22] Hernandez-Lopez MA, Quintillan M. Propagation characteristics of modes in some rectangular waveguides using the finite-difference time-domain method. Journal of Electromagnetic Waves and Applications. 2000;**14**:1707-1722

[23] Vaish A, Parthasarathy H. Analysis of rectangular waveguide using finite element method. Progress In Electromagnetics Research C. 2008;**2**:117-125

[24] Baganas K. Inhomogeneous dielectric media: Wave propagation and dielectric permittivity reconstruction in the case of a rectangular waveguide. Journal of Electromagnetic Waves and Applications. 2002;**16**:1371-1392

[25] Novotny L, Hafner C. Light propagation in a cylindrical waveguide with a complex, metallc, dielectric function. Physical Review E. 1994;**50**:4094-4106

[26] Yener N. Advancement of algebraic function approximation in eigenvalue problems of lossless metallic waveguides to infinite dimensions, part I: Properties of the operator in infinite dimensions. Journal of Electromagnetic Waves and Applications. 2006;**20**:1611-1628

[27] Yener N. Algebraic function approximation in eigenvalue problems of lossless metallic waveguides: Examples. Journal of Electromagnetic Waves and Applications. 2006;**20**:731-745

[28] Khalaj-Amirhosseini M. Analysis of longitudinally inhomogeneous waveguides using Taylor's series expansion. Journal of Electromagnetic Waves and Applications. 2006;**20**: 1093-1100

[29] Khalaj-Amirhosseini M. Analysis of longitudinally inhomogeneous waveguides using the Fourier series expansion. Journal of Electromagnetic Waves and Applications. 2006;**20**: 1299-1310

[30] Reutskiy SY. The methods of external excitation for analysis of arbitrarily-shaped hollow conducting waveguides. Progress in Electromagnetics Research. 2008;**82**:203-226

[31] Miyagi M, Kawakami S. Design theory of dielectric-coated circular metallic waveguides for infrared transmission. Journal of Lightwave Technology. 1984;**LT-2**:116-126

[32] Menachem Z, Jerby E. Transfer matrix function (TMF) for propagation in dielectric waveguides with arbitrary transverse profiles. IEEE Transactions on Microwave Theory and Techniques. 1998;**46**:975-982

[33] Menachem Z, Tapuchi S. Influence of the spot-size and cross-section on the output fields and power density along the straight hollow waveguide. Progress in Electromagnetics Research. 2013;**48**:151-173

[34] Vladimirov V. Equations of Mathematical Physics. New York: Marcel Dekker, Inc.; 1971

[35] Collin RE. Foundation for Microwave engineering. New York: McGraw-Hill; 1996

[36] Miyagi M, Harada K, Kawakami S. Wave propagation and attenuation in the general class of circular hollow waveguides with uniform curvature. IEEE Transactions on Microwave Theory and Techniques. 1984;**32**:513-521

[37] Croitoru N, Inberg A, Oksman M, Ben-David M. Hollow silica, metal and plastic waveguides for hard tissue medical applications. SPIE. 1997;**2977**:30-35

Chapter 17

# Periodic Rectangular and Circular Profiles in the Cross Section of the Straight Waveguide Based on Laplace and Fourier Transforms and Their Inverse Transforms and Applications

Zion Menachem

Additional information is available at the end of the chapter

http://dx.doi.org/10.5772/intechopen.76794

**Abstract**

This chapter presents propagation along the straight rectangular waveguide with periodic rectangular and circular profiles in the cross section. The objectives in this study are to explore the effect of the periodic rectangular and circular profiles in the cross section of the straight waveguide on the output field and to develop the technique to calculate two kinds of the periodic profiles. The method is based on Laplace and Fourier transforms and the inverse Laplace and Fourier transforms. The contribution of the proposed technique is important to improve the method that is based on Laplace and Fourier transforms and their inverse transforms also for the discontinuous periodic rectangular and circular profiles in the cross section (and not only for the continuous profiles). The proposed technique is very effective to solve complex problems, in relation to the conventional methods, especially when we have a large numbers of dielectric profiles. The application is useful for straight waveguides in the microwave and the millimeter wave regimes, with periodic rectangular and circular profiles in the cross section of the straight waveguide.

**Keywords:** wave propagation, helical waveguide, dielectric waveguide, power transmission

## 1. Introduction

Review of numerical and approximate methods for the modal analysis of general optical dielectric waveguides with emphasis on recent developments has been published [1]. Examples of interesting methods, such as the finite difference method and the finite element method have been reviewed. The method for the eigenmode analysis of two-dimensional step-index waveguides has been proposed [2]. The method distinguishes itself other existing interface methods by avoiding the use of the Taylor series expansion and by introducing the concept of the iterative use of low-order jump conditions.

The method of selective suppression of electromagnetic modes in a rectangular waveguides by using distributed wall losses has been proposed [3]. Analytical design method for corrugated rectangular waveguide has been proposed [4].

A Fourier operator method has been used to derive for the first time an exact closed-form eigenvalue equation for the scalar mode propagation constants of a buried rectangular dielectric waveguide [5]. Wave propagation in an inhomogeneous transversely magnetized rectangular waveguide has been studied with the aid of a modified Sturm-Liouville differential equation [6]. A fundamental and accurate technique to compute the propagation constant of waves in a lossy rectangular waveguide has been proposed [7]. This method is based on matching the electric and magnetic fields at the boundary and allowing the wave numbers to take complex values.

A great amount of numerical results for cylindrical dielectric waveguide array have been presented [8]. Dielectric cylinders have been arrayed by a rectangular mode. When the area of dielectric cylinder in a unit cell varied from a small number to a big one and even maximum, interactions between space harmonics firstly got stronger but finally got weaker. Full-wave analysis of dielectric rectangular waveguides has been presented [9]. The waveguide properties of permeable one-dimensional periodic acoustic structures have been studied [10]. Analysis of rectangular folded-waveguide millimeter wave slow-wave structure using conformal transformation has been developed [11].

A simple closed-form expression to compute the time-domain reflection coefficient for a transient $TE_{10}$ mode wave incident on a dielectric step discontinuity in a rectangular waveguide has been presented [12]. In this paper, an exponential series approximation was provided for efficient computation of the reflected and transmitted field waveforms.

A waveguide with layered-periodic walls for different relations between the dielectric permittivities of the central layer and the superlattice layers has been proposed [13]. A full-vectorial boundary integral equation method for computing guided modes of optical waveguides has been presented [14]. A method for the propagation constants of arbitrary cross-sectional shapes has been described [15]. Experiment and simulation of $TE_{10}$ cut-off reflection phase in gentle rectangular downtapers has been studied [16].

The rectangular dielectric waveguide technique for the determination of complex permittivity of a wide class of dielectric materials of various thicknesses and cross sections has been described [17]. In this paper, the technique has been presented to determine the dielectric constant of materials. Fourier decomposition method applied to mapped infinite domains has

been described [18], and this method is reliable down to modal cutoff. Analysis for new types of waveguide with Fourier's expansion differential method has been proposed [19].

Propagation characteristics of modes in some rectangular waveguides using the finite-difference time-domain method have been proposed [20]. Analysis of rectangular waveguide using finite element method has been presented for arbitrarily shaped waveguide [21]. Wave propagation and dielectric permittivity reconstruction in the case of a rectangular waveguide have been studied [22].

Important method for the analysis of electromagnetic wave propagation along the straight dielectric waveguide with arbitrary profiles has been proposed [23]. The mode model method for wave propagation in the straight waveguide with a circular cross section has been proposed [24]. This method in Refs. [23, 24] related to the methods based on Laplace and Fourier transforms and the inverse Laplace and Fourier transforms.

The objectives in this chapter are to explore the effect of the periodic rectangular and circular profiles in the cross section of the straight waveguide on the output field and to develop the technique to calculate the dielectric profile, the elements of the matrix, and its derivatives of the dielectric profile. The proposed technique is important to improve the mode model also for the periodic rectangular and circular profiles and not only for the continuous profiles.

## 2. Periodic rectangular and circular profiles in the cross section of the straight waveguide

In this chapter we introduce two different techniques, and the particular applications allow us to improve the mode model so that we can solve inhomogeneous problems also for periodic profiles in the cross section of the straight waveguide. Thus, in this chapter we introduce two techniques to calculate the dielectric profile, the elements of the matrix, and its derivatives of dielectric profile in the cases of periodic rectangular and circular profiles in the cross section of the straight rectangular waveguide.

The proposed techniques are very effective in relation to the conventional methods because they allow the development of expressions in the cross section only according to the specific discontinuous problem. In this way, the mode model method becomes an improved method to solve discontinuous problems in the cross section (and not only for continuous problems).

Three examples of periodic rectangular profiles are shown in **Figure 1(a–c)**, and three examples of periodic circular profiles are shown in **Figure 1(d–f)** in the cross section of the straight rectangular waveguide.

An example of periodic structure with two rectangular profiles along x-axis is shown in **Figure 1(a)**, where the centers of the left rectangle and right rectangle are located at the points (0.25 a, 0.5 b) and (0.75 a, 0.5 b), respectively. An example of periodic structure with two rectangular profiles along y-axis is shown in **Figure 1(b)**, where the centers of the upper rectangle and lower rectangle are located at the points (0.5 a, 0.75 b) and (0.5 a, 0.25 b).

An example of periodic structure with four rectangular profiles along x-axis and y-axis is shown in **Figure 1(c)**. The center of the first rectangle is located at the point (0.25 a, 0.25 b),

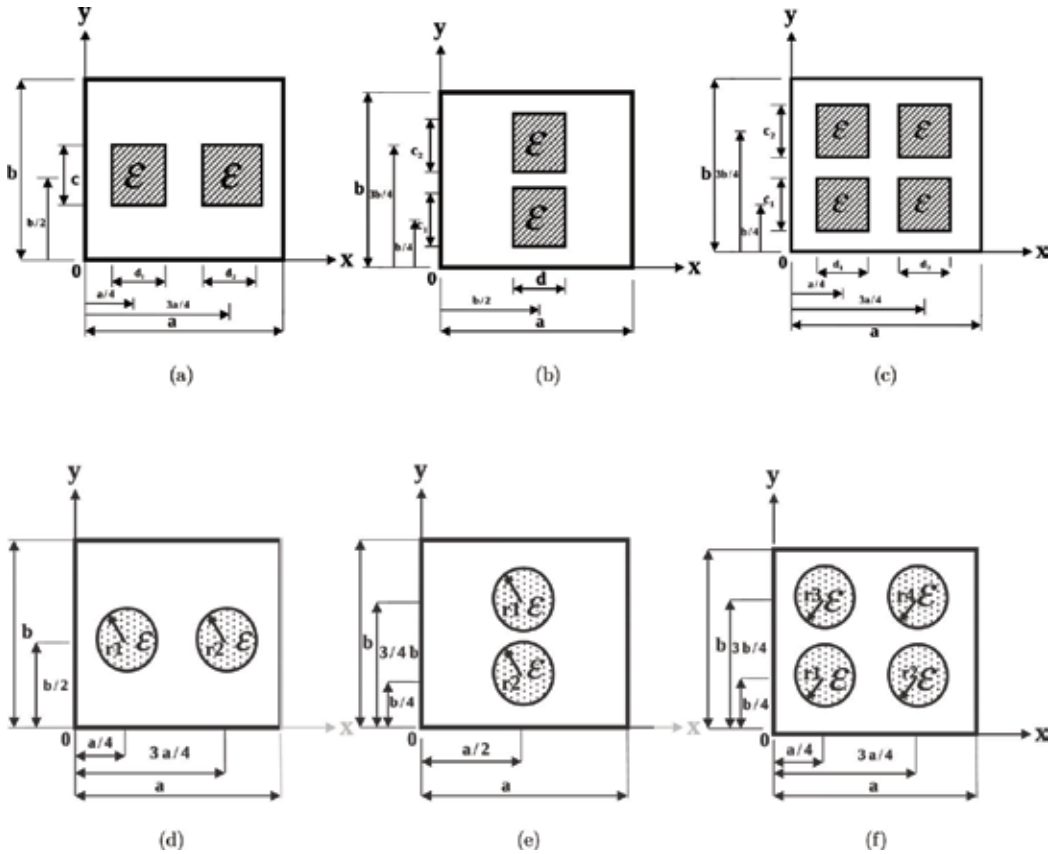


**Figure 1.** Examples of the periodic rectangular profiles (a–c) and periodic circular profiles (d–f) in the cross section of the straight rectangular waveguide.

the center of the second rectangle is located at the point (0.75 a, 0.25 b), the center of the third rectangle is located at the point (0.25 a, 0.75 b), and the center of the fourth rectangle is located at the point (0.75 a, 0.75 b).

An example of periodic structure with two circular profiles along x-axis is shown in **Figure 1(d)**, where the centers of the left circle and right circle are located at the points (0.25 a, 0.5 b) and (0.75 a, 0.5 b). An example of periodic structure with two circular profiles along y-axis is shown in **Figure 1(e)**, where the centers of the upper circle and lower circle are located at the points (0.5 a, 0.75 b) and (0.5 a, 0.25 b).

An example of periodic structure with four circular profiles along x-axis and y-axis is shown in **Figure 1(f)**. The center of the first circle is located at the point (0.25 a, 0.25 b), the center of the second circle is located at the point (0.75 a, 0.25 b), the center of the third circle is located at the point (0.25 a, 0.75 b), and the center of the fourth circle is located at the point (0.75 a, 0.75 b).

The objective of this chapter is to introduce two different techniques that allow us to improve the model so that we can solve nonhomogeneous problems also for periodic profiles in the

http://dx.doi.org/10.5772/intechopen.76794

cross section of the straight rectangular waveguide. Thus, we need to introduce a technique and a particular application for the two geometric shapes composed of rectangles or circles in the cross section. We need to calculate the dielectric profile, the elements of the matrix, and its derivatives of the dielectric profile in the cases of periodic rectangular profiles (**Figure 1(a–c)**) and periodic circular profiles (**Figure 1(d–f)**) in the cross section of the straight rectangular waveguide.

It is very interesting to compare between two different techniques of the two different kinds of the profiles (rectangular and circular) in the cross section of the rectangular straight waveguide.

## 3. The techniques to solve two different profiles in the cross section

The two kinds of the different techniques enable us to solve practical problems for the periodic rectangular profiles (**Figure 1(a–c)**) and periodic circular profiles (**Figure 1(d–f)**) in the cross section of the straight rectangular waveguide.

**Figure 2(a)** shows one rectangular profile where the center of the rectangle is located at the point (0.5 a, 0.5 b). **Figure 2(b)** shows one circular profile where the center is located at the point (0.5 a, 0.5 b). The proposed techniques to solve discontinuous problems with two different profiles (rectangular and circular) in the cross section will introduce according to **Figure 2(a** and **b)**.

**Figure 2(a)** shows one rectangular profile in the cross section, and **Figure 2(b)** shows one circular profile in the cross section. The dielectric profile $g(x,y)$ is given according to $\epsilon(x,y) = \epsilon_0(1+g(x,y))$. According to **Figure 3(a** and **b)** and for $g(x,y) = g_0$, we obtain

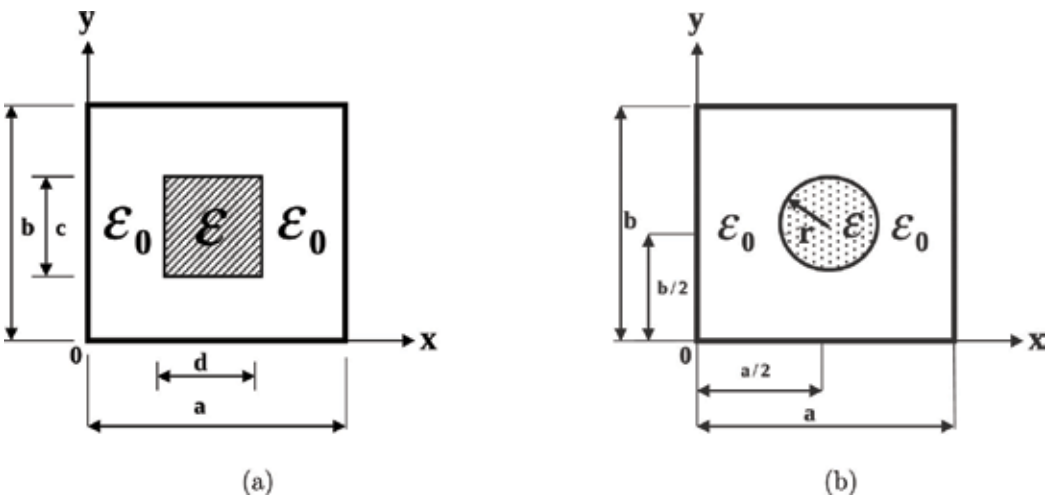


**Figure 2.** Examples of the rectangular and circular profiles in the cross section of the straight rectangular waveguide. (a) One rectangular profile. (b) One circular profile.

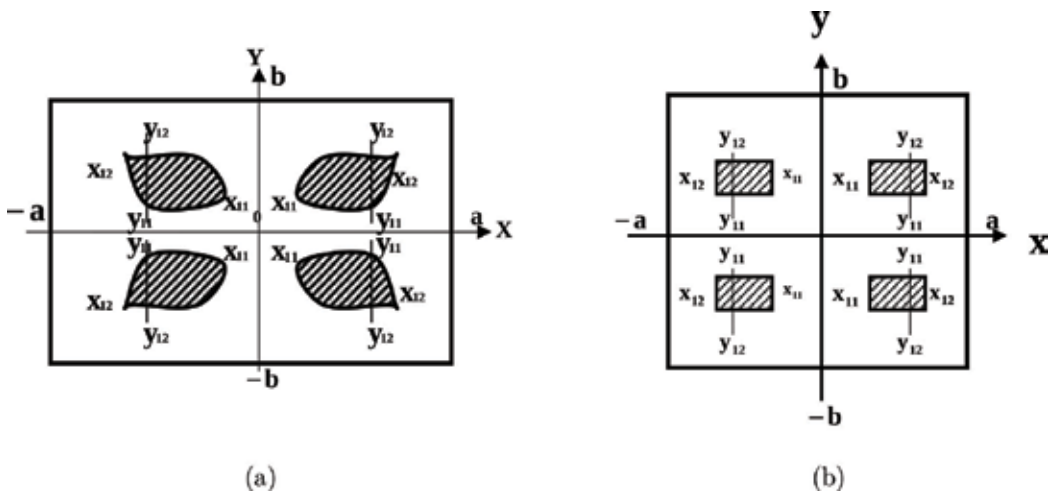


**Figure 3.** (a) The arbitrary profile in the cross section. (b) The rectangular profile in the cross section, as shown in **Figure 2(a)**.

$$g(n,m) = \frac{g_0}{4ab}\left\{\int_{x_{11}}^{x_{12}} dx \int_{y_{11}}^{y_{12}} \exp\left(-j\left(k_x x + k_y y\right)\right)dy + \int_{-x_{12}}^{-x_{11}} dx \int_{y_{11}}^{y_{12}} \exp\left(-j\left(k_x x + k_y y\right)\right)dy \right.$$
$$\left. + \int_{-x_{12}}^{-x_{11}} dx \int_{-y_{12}}^{-y_{11}} \exp\left(-j\left(k_x x + k_y y\right)\right)dy + \int_{x_{11}}^{x_{12}} dx \int_{-y_{12}}^{-y_{11}} \exp\left(-j\left(k_x x + k_y y\right)\right)dy\right\}. \quad (1)$$

If $y_{11}$ and $y_{12}$ are not functions of x, then the dielectric profile is given by

$$g(n,m) = \frac{g_0}{ab}\int_{x_{11}}^{x_{12}} \cos(k_x x)dx \int_{y_{11}}^{y_{12}} \cos\left(k_y y\right)dy. \quad (2)$$

The derivative of the dielectric profile in the case of $y_{11}$ and $y_{12}$ which are functions of x is given by

$$g_x(n,m) = \frac{2}{am\pi}\int_{x_{11}}^{x_{12}} g_x(x,y)\sin\left[\frac{k_y}{2}\left(y_{12} - y_{11}\right)\right]\cos\left[\frac{k_y}{2}\left(y_{12} + y_{11}\right)\right]\cos(k_x x)dx, \quad (3)$$

where $g_x(x,y) = (1/\epsilon(x,y))(d\epsilon(x,y)/dx)$, $\epsilon(x,y) = \epsilon_0(1 + g(x,y))$, $k_x = (n\pi x)/a$, and $k_y = (m\pi y)/b$. Similarly, we can calculate the value of $g_y(n,m)$, where $g_y(x,y) = (1/\epsilon(x,y))\ (d\epsilon(x,y)/dy)$.

For the cross section as shown in **Figure 2(a)** and according to **Figure 3(b)**, the center of the rectangle is located at (0.5 a, 0.5 b), $y_{12}$ = b/2 + c/2, and $y_{11}$ = b/2 − c/2. Thus, for this case, $y_{12} - y_{11}$ = c and $y_{12} + y_{11}$ = b. In the same principle, the location of the rectangle should be taken into account.

http://dx.doi.org/10.5772/intechopen.76794

The particular application is based on the $\omega_\varepsilon$ function [25]. The $\omega_\varepsilon$ function is used in order to solve rectangular profile, periodic rectangular profiles, circular profile, and periodic circular profile in the cross section of the straight waveguide. The $\omega_\varepsilon$ function is defined as $\omega_\varepsilon(r) = C_\varepsilon \exp\left[-\varepsilon^2/\left(\varepsilon^2 - |r|^2\right)\right]$ for $|r| > \varepsilon$, where $C_\varepsilon$ is a constant and $\int \omega_\varepsilon(r)dr = 1$. In the limit $\varepsilon \to 0$, the $\omega_\varepsilon$ function is shown in **Figure 4**.

The technique based on $\omega_\varepsilon$ function is very effective to solve complex problems, in relation to the conventional methods, especially when we have a large number of dielectric profiles, as shown in **Figure 1(c** and **f)**. We will demonstrate how to use with the proposed technique for all the cases that are shown in the examples of **Figure 1(a–f)**.

### 3.1. The technique based on $\omega_\varepsilon$ function for the periodic rectangular profile in the cross section

**Figure 1(a)** shows the periodic rectangular profile where the center of the left rectangle is located at (0.25 a, 0.5 b) and the right rectangle is located at (0.75 a, 0.5 b). This dielectric profile is given by

$$g(x) = \begin{cases} g_0 \exp\left(1 - q_1(x)\right) & ((a/2) - d_1 - \varepsilon)/2 \le x < ((a/2) - d_1 + \varepsilon)/2 \\ g_0 & ((a/2) - d_1 + \varepsilon)/2 < x < ((a/2) + d_1 - \varepsilon)/2 \\ g_0 \exp\left(1 - q_2(x)\right) & ((a/2) + d_1 - \varepsilon)/2 \le x < ((a/2) + d_1 + \varepsilon)/2 \\ g_0 \exp\left(1 - q_3(x)\right) & ((3a/2) - d_2 - \varepsilon)/2 \le x < ((3a/2) - d_2 + \varepsilon)/2 \\ g_0 & ((3a/2) - d_2 + \varepsilon)/2 < x < ((3a/2) + d_2 - \varepsilon)/2 \\ g_0 \exp\left(1 - q_4(x)\right) & ((3a/2) + d_2 - \varepsilon)/2 \le x < ((3a/2) + d_2 + \varepsilon)/2 \\ 0 & else \end{cases}, \tag{4a}$$

and

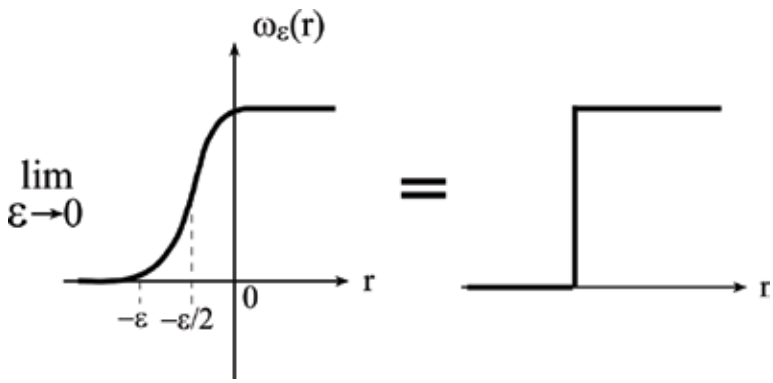


**Figure 4.** The technique based on $\omega_\varepsilon$ function in the limit $\varepsilon \to 0$ to solve discontinuous problems.

$$g(y)=\begin{cases} g_0\exp\left(1-q_5(y)\right) & (b-c-\varepsilon)/2\le y<(b-c+\varepsilon)/2 \\ g_0 & (b-c+\varepsilon)/2<y<(b+c-\varepsilon)/2 \\ g_0\exp\left(1-q_6(y)\right) & (b+c-\varepsilon)/2\le y<(b+c+\varepsilon)/2 \\ 0 & else \end{cases}, \tag{4b}$$

where

$$q_1(x)=\frac{\varepsilon^2}{\varepsilon^2-[x-((a/2)-d_1+\varepsilon)/2]^2} \quad , \quad q_2(x)=\frac{\varepsilon^2}{\varepsilon^2-[x-((a/2)+d_1-\varepsilon)/2]^2},$$
$$q_3(x)=\frac{\varepsilon^2}{\varepsilon^2-[x-((3a/2)-d_2+\varepsilon)/2]^2} \quad , \quad q_4(x)=\frac{\varepsilon^2}{\varepsilon^2-[x-((3a/2)+d_2-\varepsilon)/2]^2}$$
$$q_5(y)=\frac{\varepsilon^2}{\varepsilon^2-[y-(b-c+\varepsilon)/2]^2} \quad , \quad q_6(y)=\frac{\varepsilon^2}{\varepsilon^2-[y-(b+c-\varepsilon)/2]^2} \quad .$$

The elements of the matrix are given in this case by

$$\begin{aligned} g(n,m)=\frac{g_0}{ab}\Bigg\{ & \int_{((a/2)-d_1-\varepsilon)/2}^{((a/2)-d_1+\varepsilon)/2}\exp\left(1-q_1(x)\right)\cos\left(\frac{n\pi x}{a}\right)dx+ \\ & \int_{((a/2)-d_1+\varepsilon)/2}^{((a/2)+d_1-\varepsilon)/2}\cos\left(\frac{n\pi x}{a}\right)dx+\int_{((a/2)+d_1-\varepsilon)/2}^{((a/2)+d_1+\varepsilon)/2}\exp\left(1-q_2(x)\right)\cos\left(\frac{n\pi x}{a}\right)dx+ \\ & \int_{((3a/2)-d_2-\varepsilon)/2}^{((3a/2)-d_2+\varepsilon)/2}\exp\left(1-q_3(x)\right)\cos\left(\frac{n\pi x}{a}\right)dx+ \\ & \int_{((3a/2)-d_2+\varepsilon)/2}^{((3a/2)+d_2-\varepsilon)/2}\cos\left(\frac{n\pi x}{a}\right)dx+\int_{((3a/2)+d_2-\varepsilon)/2}^{((3a/2)+d_2+\varepsilon)/2}\exp\left(1-q_4(x)\right)\cos\left(\frac{n\pi x}{a}\right)dx\Bigg\} \\ & \Bigg\{\int_{(b-c-\varepsilon)/2}^{(b-c+\varepsilon)/2}\exp\left(1-q_5(y)\right)\cos\left(\frac{m\pi y}{b}\right)dy+\int_{(b-c+\varepsilon)/2}^{(b+c-\varepsilon)/2}\cos\left(\frac{m\pi y}{b}\right)dy+ \\ & \int_{(b+c-\varepsilon)/2}^{(b+c+\varepsilon)/2}\exp\left(1-q_6(y)\right)\cos\left(\frac{m\pi y}{b}\right)dy\Bigg\}. \end{aligned} \tag{5}$$

The derivatives of the dielectric profile are given in this case by

$$g_x=\begin{cases} \dfrac{d}{dx}\left(\ln\left(1+g_0\ q_1(x)\right)\right) & ((a/2)-d_1-\varepsilon)/2\le x<((a/2)-d_1+\varepsilon)/2 \\ \dfrac{d}{dx}\left(\ln\left(1+g_0\ q_2(x)\right)\right) & ((a/2)+d_1-\varepsilon)/2\le x<((a/2)+d_1+\varepsilon)/2 \\ \dfrac{d}{dx}\left(\ln\left(1+g_0\ q_3(x)\right)\right) & ((3a/2)-d_2-\varepsilon)/2\le x<((3a/2)-d_2+\varepsilon)/2' \\ \dfrac{d}{dx}\left(\ln\left(1+g_0\ g_4(x)\right)\right) & ((3a/2)+d_2-\varepsilon)/2\le x<((3a/2)+d_2+\varepsilon)/2 \\ 0 & else \end{cases} \tag{6a}$$

and

$$g_y = \begin{cases} \frac{d}{dx}\left(\ln\left(1+g_0\ \ q_5(y)\right)\right) & (b-c-\varepsilon)/2 \le y < (b-c+\varepsilon)/2 \\ \frac{d}{dx}\left(\ln\left(1+g_0\ \ q_6(y)\right)\right) & (b+c-\varepsilon)/2 \le x < (b+c+\varepsilon)/2 \\ 0 & else \end{cases}. \tag{6b}$$

The derivative of the dielectric profile for m = 0 in the case of the periodic profile (**Figure 1(a)**) in the cross section of the waveguide is given in the limit $\varepsilon \to 0$ by

$$\begin{aligned} g_x(n, m=0) = \frac{1}{a}\Bigg\{ & \int_{((a/2)-d_1-\varepsilon)/2}^{((a/2)-d_1+\varepsilon)/2} \cos(k_x x)\frac{d}{dx}\left[\ln\left(1+g_0\ \ q_1(x)\right)\right]dx \\ & + \int_{((a/2)+d_1-\varepsilon)/2}^{((a/2)+d_1+\varepsilon)/2} \cos(k_x x)\frac{d}{dx}\left[\ln\left(1+g_0\ \ q_2(x)\right)\right]dx \\ & + \int_{((3a/2)-d_2-\varepsilon)/2}^{((3a/2)-d_2+\varepsilon)/2} \cos(k_x x)\frac{d}{dx}\left[\ln\left(1+g_0\ \ q_3(x)\right)\right]dx \\ & + \int_{((3a/2)+d_2-\varepsilon)/2}^{((3a/2)+d_2+\varepsilon)/2} \cos(k_x x)\frac{d}{dx}\left[\ln\left(1+g_0\ \ q_4(x)\right)\right]dx \Bigg\}. \end{aligned}$$

Similarly, we can calculate the derivative of the dielectric profile for any value of n and m.

### 3.2. The technique based on $\omega_\varepsilon$ function for one circular profile in the cross section

The dielectric profile for one circle is given where the center is located at (0.5 a, 0.5 b) (**Figure 2(b)**) by

$$g(x,y) = \begin{cases} g_0 & 0 \le r < r_1 - \varepsilon_1/2 \\ g_0 \exp\left[1 - q_\varepsilon(r)\right] & r_1 - \varepsilon_1/2 \le r < r_1 + \varepsilon_1/2' \end{cases} \tag{7}$$

where

$$q_\epsilon(r) = \frac{{\varepsilon_1}^2}{{\varepsilon_1}^2 - \left[r - (r_1 - \varepsilon_1/2)\right]^2},$$

else $g(x,y) = 0$.

The radius of the circle is given by

$$r = \sqrt{(x - a/2)^2 + (y - b/2)^2}.$$

Similarly, we can calculate the periodic circular profiles according to their location.

Thus, the derivatives of the dielectric profile for one circle are given where the center is located at (0.5 a, 0.5 b) (**Figure 2(b)**) in the region $r_1 - \varepsilon_1/2 \le r < r_1 + \varepsilon_1/2$ by

$$g_x = \frac{-2\ g_0\ \cos\theta \exp\left[1 - q_\epsilon(r)\right][r - (r_1 - \varepsilon_1/2)]{\varepsilon_1}^2}{\left\{1 + g_0 \exp\left[1 - q_\epsilon(r)\right]\right\}\left[{\varepsilon_1}^2 - [r - (r_1 - \varepsilon_1/2)]^2\right]^2}, \tag{8a}$$

$$g_y = \frac{-2\ g_0\ \sin\theta \exp\left[1 - q_\epsilon(r)\right][r - (r_1 - \varepsilon_1/2)]{\varepsilon_1}^2}{\left\{1 + g_0 \exp\left[1 - q_\epsilon(r)\right]\right\}\left[{\varepsilon_1}^2 - [r - (r_1 - \varepsilon_1/2)]^2\right]^2}, \tag{8b}$$

else $g_x = 0$, and $g_y = 0$.

The elements of the matrices for one circle are given where the center is located at (0.5 a, 0.5 b) (**Figure 2(b)**) by

$$g(n,m) = \frac{g_0}{ab}\left\{\int_0^{2\pi}\int_0^{r_1-\epsilon_1/2} \cos\left[\frac{n\pi}{a}\left(r\cos\theta + \frac{a}{2}\right)\right]\cos\left[\frac{m\pi}{b}\left(r\sin\theta + \frac{b}{2}\right)\right] + \right.$$
$$\left.\int_0^{2\pi}\int_{r_1-\epsilon_1/2}^{r_1+\epsilon_1/2} \cos\left[\frac{n\pi}{a}\left(r\cos\theta + \frac{a}{2}\right)\right]\cos\left[\frac{m\pi}{b}\left(r\sin\theta + \frac{b}{2}\right)\right]\exp\left[1 - q_\varepsilon(r)\right]\right\} r dr d\theta, \tag{9}$$

$$g_x(n,m) = -\frac{2g_0}{ab}\left\{\int_0^{2\pi}\int_{r_1-\epsilon_1/2}^{r_1+\epsilon_1/2} \frac{{\epsilon_1}^2[r - (r_1 - \epsilon_1/2)]\exp\left[1 - q_\epsilon(r)\right]\cos\theta}{\left[{\epsilon_1}^2 - [r - (r_1 - \epsilon_1/2)]^2\right]^2\left[1 + g_0\exp\left[1 - q_\epsilon(r)\right]\right]}\right.$$
$$\left.\cos\left[\frac{n\pi}{a}\left(r\cos\theta + \frac{a}{2}\right)\right]\cos\left[\frac{m\pi}{b}\left(r\sin\theta + \frac{b}{2}\right)\right]\right\} r dr d\theta, \tag{10a}$$

$$g_y(n,m) = -\frac{2g_0}{ab}\left\{\int_0^{2\pi}\int_{r_1-\epsilon_1/2}^{r_1+\epsilon_1/2} \frac{{\epsilon_1}^2[r - (r_1 - \epsilon_1/2)]\exp\left[1 - q_\epsilon(r)\right]\sin\theta}{\left[{\epsilon_1}^2 - [r - (r_1 - \epsilon_1/2)]^2\right]^2\left[1 + g_0\exp\left[1 - q_\epsilon(r)\right]\right]}\right.$$
$$\left.\cos\left[\frac{n\pi}{a}\left(r\cos\theta + \frac{a}{2}\right)\right]\cos\left[\frac{m\pi}{b}\left(r\sin\theta + \frac{b}{2}\right)\right]\right\} r dr d\theta, \tag{10b}$$

where $r = \sqrt{(x - a/2)^2 + (y - b/2)^2}$.

Similarly, we can calculate the periodic circular profile according to the number of the circles and the locations of their centers.

The matrix **G** is given by the form

$$\mathbf{G} = \begin{bmatrix} g_{00} & g_{-10} & g_{-20} & \cdots & g_{-nm} & \cdots & g_{-NM} \\ g_{10} & g_{00} & g_{-10} & \cdots & g_{-(n-1)m} & \cdots & g_{-(N-1)M} \\ g_{20} & g_{10} & \ddots & \ddots & \ddots & & \\ \vdots & g_{20} & \ddots & \ddots & \ddots & & \\ g_{nm} & \ddots & \ddots & \ddots & g_{00} & \vdots & \\ \vdots & & & & & & \\ g_{NM} & \cdots & \cdots & \cdots & \cdots & \cdots & g_{00} \end{bmatrix}. \tag{11}$$

http://dx.doi.org/10.5772/intechopen.76794

Similarly, the $\mathbf{G_x}$ and $\mathbf{G_y}$ matrices are obtained by the derivatives of the dielectric profile. These matrices relate to the method that is based on the Laplace and Fourier transforms and their inverse transforms [23].

The technique is important to solve discontinuous periodic rectangular and circular profiles in the cross section of the straight waveguide. The graphical results in the next section will be demonstrated as a response to a half-sine ($TE_{10}$) input-wave profile.

## 4. Numerical results of periodic rectangular and circular dielectric materials

All the graphical results are demonstrated as a response to a half-sine ($TE_{10}$) input-wave profile for the periodic rectangular profiles (**Figure 1(a–c)**) and the periodic circular profiles (**Figure 1(d–f)**) in the cross section of the straight rectangular waveguide.

The output fields for the periodic structure with the two rectangular profiles along x-axis (**Figure 1(a)**) are demonstrated in **Figure 5(a** and **b)** for $\epsilon_r = 3$ and for $\epsilon_r = 10$, respectively. In this examples, the left rectangle is located at the point (0.25 a, 0.5 b), and the center of the right rectangle is located at the point (0.75 a, 0.5 b). **Figure 5(c)** shows the output field as the function of x-axis where y = b/2 = 10 mm for four values of $\epsilon_r = 3, 5, 7$, and 10, respectively.

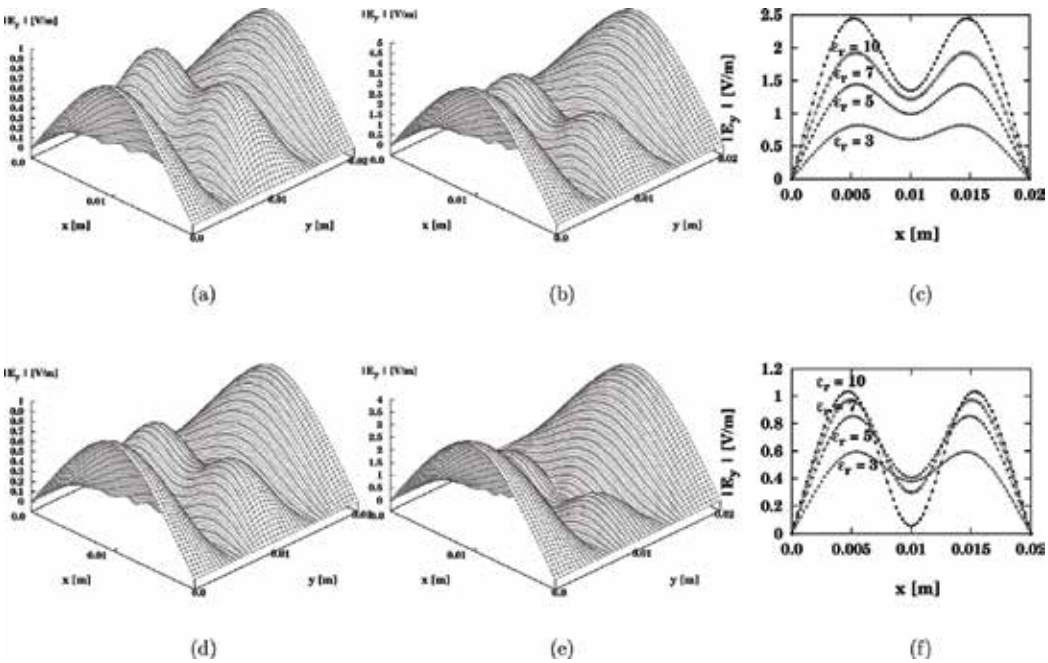


**Figure 5.** The output field as a response to a half-sine ($TE_{10}$) input-wave profile for the periodic rectangular profiles (a–c) that relate to cross section (**Figure 1(a)**) and for the periodic circular profiles (d–f) that relate to cross section (**Figure 1(d)**). The results are shown for (a) $\epsilon_r = 3$; (b) $\epsilon_r = 10$; (c) $\epsilon_r = 3, 5, 7$, and 10; (d) $\epsilon_r = 3$; (e) $\epsilon_r = 10$; and (f) $\epsilon_r = 3, 5, 7$, and 10.

The parameters of these examples are $a = 2\,cm$, $b = 2\,cm$, $\lambda = 3.75\,cm$, $\beta = 58\,1/m$, $k_0 = 167\,1/m$, and $z = 15\,cm$.

The output fields for the periodic structure with the two circular profiles along x-axis (**Figure 1(d)**) are demonstrated in **Figure 5(d** and **e)** for $\epsilon_r = 3$ and for $\epsilon_r = 10$, respectively. In this examples, the left circle is located at the point (0.25 a, 0.5 b), and the center of the right circle is located at the point (0.75 a, 0.5 b). **Figure 5(f)** shows the output field as the function of x-axis where y = b/2 = 10 mm for four values of $\epsilon_r = 3, 5, 7,$ and 10, respectively.

It is interesting to see a similar behavior of the output results in the cases of periodic rectangular profiles (**Figure 5(a–c)**) that relate to **Figure 1(a)** and in the cases of periodic circular profiles (**Figure 5(d–f)**) that relate to **Figure 1(d)**, where $\epsilon_r = 3$ and 10, respectively. The behavior is similar, but not for every $\epsilon_r$, and the amplitudes of the output fields are different.

The output fields (**Figure 5(a–f)**) are strongly affected by the input-wave profile ($TE_{10}$ mode), the periodic structure with the two rectangular profiles or the two circular profiles along x-axis, and the distance between the two centers of the rectangular or the circular profiles.

The output fields for the periodic structure with the two rectangular profiles along y-axis (**Figure 1(b)**) are demonstrated in **Figure 6(a–c)** for $\epsilon_r = 3, 5,$ and 10, respectively. The centers of the upper rectangle and the lower rectangle are located at the points (0.5 a, 0.75 b) and

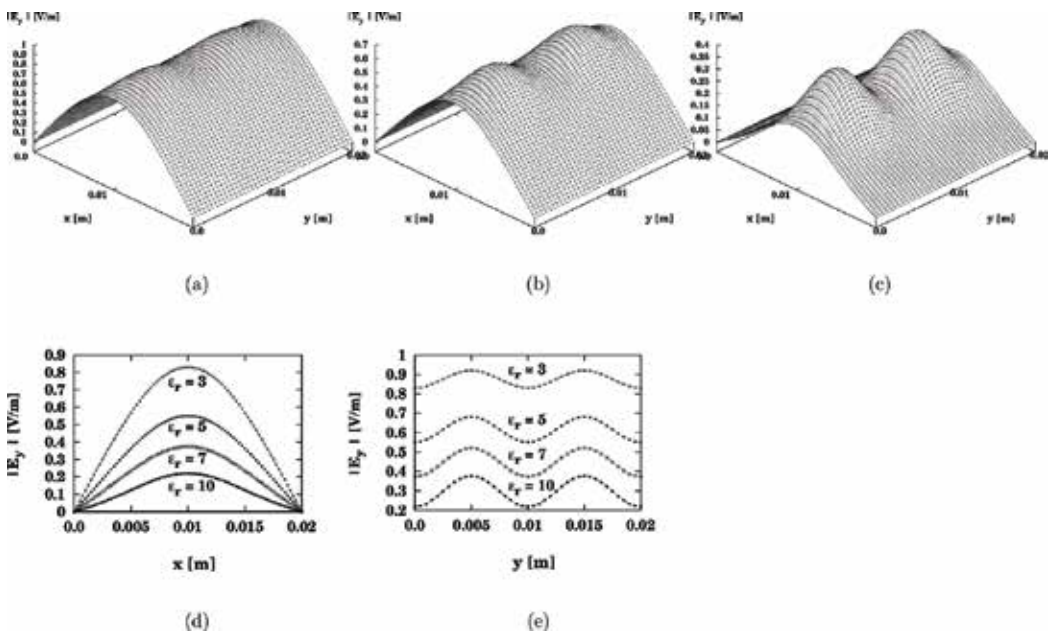


**Figure 6.** The output field as a response to a half-sine ($TE_{10}$) input-wave profile for the periodic rectangular profiles (a–c) that relate to cross section (**Figure 1(b)**). The results are shown for (a) $\epsilon_r = 3$; (b) $\epsilon_r = 5$; (c) $\epsilon_r = 10$; (d) $\epsilon_r = 3, 5, 7,$ and 10; and (e) $\epsilon_r = 3, 5, 7,$ and 10.

http://dx.doi.org/10.5772/intechopen.76794

(0.5 a, 0.25 b), respectively. The output field is shown in **Figure 6(d)** for x-axis where y = b/2 = 10 mm and is shown in **Figure 6(e)** for y-axis where x = a/2 = 10 mm and for $\epsilon_r = 3, 5, 7$, and 10, respectively.

The parameters of these examples are a $= 2\ cm$, b $= 2\ cm$, c $= 2.5\ mm$, d $= 2.5\ mm$, $\lambda = 3.75\ cm$, $\beta = 58\ 1/m$, $k_0 = 167\ 1/m$, and z $= 15\ cm$.

By changing only the parameter $\epsilon_r$ from 3 to 10, the relative profile of the output field is changed from a half-sine ($TE_{10}$) profile to a Gaussian shape profile, as shown in **Figure 6(d)**. The output field in **Figure 6(e)** demonstrates the periodic structure with the two rectangular profiles for $\epsilon_r = 3, 5, 7$, and 10.

The output fields for the periodic structure with the two circular profiles along y-axis (**Figure 1(e)**) are demonstrated in **Figure 7(a–c)** for $\epsilon_r = 3, 5$, and 10, respectively. The centers of the upper circle and the lower circle are located at the points (0.5 a, 0.75 b) and (0.5 a, 0.25 b), respectively. The output field is shown in **Figure 7(d)** for x-axis where y = b/2 = 10 mm and is shown in **Figure 7(e)** for y-axis where x = a/2 = 10 mm for $\epsilon_r = 3, 5, 7$, and 10, respectively.

By changing only the parameter $\epsilon_r$ from 3 to 10, the relative profile of the output field is changed from a half-sine ($TE_{10}$) profile to a Gaussian shape profile. The output field in **Figure 7 (e)** demonstrates the periodic structure with the two circular profiles for $\epsilon_r = 3, 5, 7$, and 10.

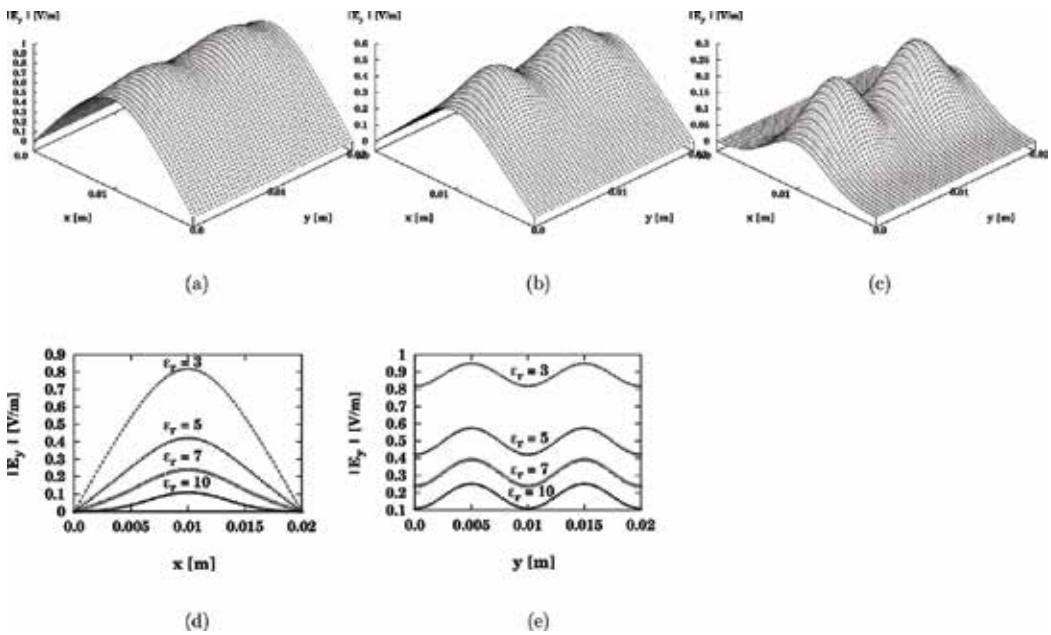


**Figure 7.** The output field as a response to a half-sine ($TE_{10}$) input-wave profile for the periodic circular profiles (a–c) that relate to cross section (**Figure 1(e)**). The results are shown for (a) $\epsilon_r = 3$; (b) $\epsilon_r = 5$; (c) $\epsilon_r = 10$; (d) $\epsilon_r = 3, 5, 7$, and 10; and (e) $\epsilon_r = 3, 5, 7$, and 10.

The parameters of these examples are a $= 2\ cm$, b $= 2\ cm$, c $= 2.5\ mm$, d $= 2.5\ mm$, $\lambda = 3.75\ cm$, $\beta = 58\ 1/m$, $k_0 = 167\ 1/m$, and z $= 15\ cm$. The radius of the circle is equal to $2.5\ mm$.

The output fields (**Figure 6(a–e)**) and **Figure 7(a–e)**) are strongly affected by the input-wave profile ($TE_{10}$ mode), the periodic structure with the two rectangular profiles (**Figure 1(b)**) or circular profiles (**Figure 1(e)**) along y-axis, and the distance between the two centers of the profiles.

It is interesting to see a similar behavior of the output results in the cases of periodic rectangular profiles (**Figure 6(a–e)**) that relate to **Figure 1(b)** and in the cases of periodic circular profiles (**Figure 7(a–e)**) that relate to **Figure 1(e)**, for every value of $\epsilon_r$, respectively. According to these output results, we see the similar behavior for every value of $\epsilon_r$, but the amplitudes of the output fields are different.

The output fields for the periodic structure with four rectangular profiles along x-axis and y-axis (**Figure 1(c)**) are demonstrated in **Figure 8(a** and **b)** for $\epsilon_r = 1.2$ and 1.4, respectively. The center of the first rectangle is located at the point (0.25 a, 0.25 b), the center of the second rectangle is located at the point (0.75 a, 0.25 b), the center of the third rectangle is located at the point (0.25 a, 0.75 b), and the center of the firth rectangle is located at the point (0.75 a, 0.75 b).

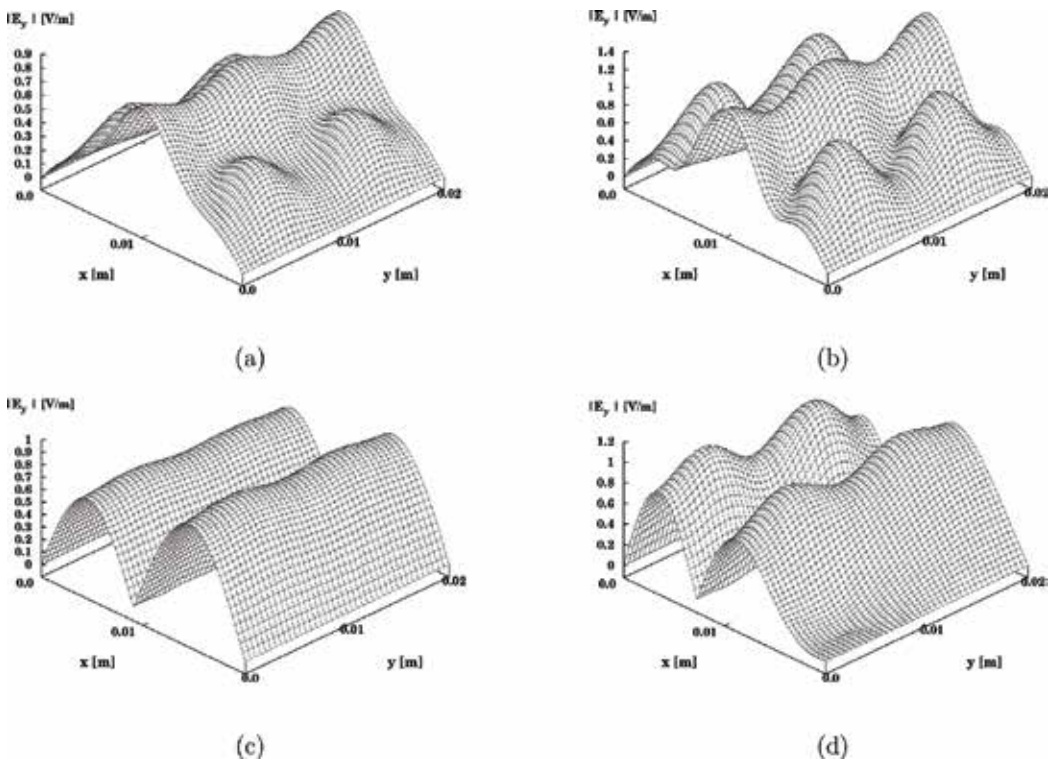


**Figure 8.** The output field as a response to a half-sine ($TE_{10}$) input-wave profile in the case of four rectangular profiles along x-axis and along y-axis (**Figure 1(c)**) for (a) $\epsilon_r = 1.2$ and (b) $\epsilon_r = 1.4$. The output field as a response to a half-sine ($TE_{10}$) input-wave profile in the case of four circular profiles along x-axis and along y-axis (**Figure 1(f)**) for (c) $\epsilon_r = 4$ and (b). $\epsilon_r = 10$.

By increasing the parameter $\epsilon_r$ from 1.2 to 1.4, the output dielectric profile of the structure of the periodic rectangular profile increased, the output profile of the half-sine ($TE_{10}$) profile decreased, and the output amplitude increased. These results are strongly affected by the half-sine ($TE_{10}$) input-wave profile and the locations of the rectangular profiles along x-axis and along y-axis. The parameters are a $= 2\ cm$, b $= 2\ cm$, z $= 15\ cm$, $k_0 = 167\ 1/m$, $\lambda = 3.75\ cm$, and $\beta = 58\ 1/m$.

The output fields for the periodic structure with four circular profiles along x-axis and y-axis (**Figure 1(f)**) are demonstrated in **Figure 8(c** and **d)** for $\epsilon_r$ = 4 and 10, respectively. The center of the first circle is located at the point (0.25 a, 0.25 b), the center of the second circle is located at the point (0.75 a, 0.25 b), the center of the third circle is located at the point (0.25 a, 0.75 b), and the center of the firth circle is located at the point (0.75 a, 0.75 b). The parameters are a $= 2\ cm$, b $= 2\ cm$, z $= 15\ cm$, $k_0 = 167\ 1/m$, $\lambda = 3.75\ cm$, and $\beta = 58\ 1/m$.

These results are strongly affected by the half-sine ($TE_{10}$) input-wave profile, the locations of the rectangular profiles (**Figure 1(c)**) or circular profiles (**Figure 1(f)**) along x-axis and along y-axis, and the distance between the centers of the profiles. By increasing the parameter $\varepsilon_r$, the Gaussian shape of the output field increased.

## 5. Conclusions

The main objective of this research was to understand the influence of the periodic rectangular and circular profiles in the cross section along the straight rectangular waveguide on the output field. The second objective was to develop the technique to calculate two kinds of the proposed periodic profiles in the cross section. The calculations are based on using Laplace and Fourier transforms, and the output fields are computed by the inverse Laplace and Fourier transforms.

The contribution of the technique and the particular application is important to improve the method that is based on Laplace and Fourier transforms and their inverse transforms also for the discontinuous problems of the periodic rectangular and circular profiles in the cross section (and not only for the continuous profiles). The particular application is based on the $\omega_\varepsilon$ function. Thus, the proposed techniques are very effective in relation to the conventional methods because they allow the development of expressions in the cross section only according to the specific discontinuous problem.

All the graphical results were demonstrated as a response to a half-sine ($TE_{10}$) input-wave profile and the periodic profiles in the cross section of the straight rectangular waveguide.

Three examples of periodic rectangular profiles are shown in **Figure 1(a–c)**, and three examples of periodic circular profiles are shown in **Figure 1(d–f)** in the cross section of the straight rectangular waveguide. It is very interesting to compare between two different techniques of the two different kinds of the profiles (rectangular and circular) in the cross section of the rectangular straight waveguide.

**Figure 5(a–c)** relates to **Figure 1(a)** and **Figure 5(d–f)** relates to **Figure 1(d)**. The output fields (**Figure 6(a–f)**) are strongly affected by the input-wave profile ($TE_{10}$ mode), the periodic structure with the two rectangular profiles or the two circular profiles along x-axis, and the distance between the two centers of the rectangular or the circular profiles.

It is interesting to see a similar behavior of the output results in the cases of periodic rectangular profiles (**Figure 5(a–c)**) that relate to **Figure 1(a)** and in the cases of circular profiles (**Figure 5(d–f)**) that relate to **Figure 1(d)**, where $\epsilon_r = 3$ and 10, respectively. The behavior is similar, but not for every $\epsilon_r$, and the amplitudes of the output fields are different.

**Figure 6(a–e)** relates to **Figure 1(b)** and **Figure 7(a–e)** relates to **Figure 1(e)**. The output fields (**Figure 6(a–e)** and **Figure 7(a–e)**) are strongly affected by the input-wave profile ($TE_{10}$ mode), the periodic structure with the two rectangular profiles (**Figure 1(b)**) or circular profiles (**Figure 1(e)**) along y-axis, and the distance between the two centers of the profiles.

By changing only the parameter $\epsilon_r$ from 3 to 10, the relative profile of the output field is changed from a half-sine ($TE_{10}$) profile to a Gaussian shape profile, as shown in **Figure 6(d)** and **Figure 7(d)**. The output fields in **Figure 6(e)** and in **Figure 7(e)** demonstrate the periodic structure with the two rectangular and circular profiles for $\epsilon_r = 3, 5, 7,$ and 10.

It is interesting to see a similar behavior of the output results in the cases of periodic rectangular profiles (**Figure 6(a–e)**) that relate to **Figure 1(b)** and in the cases of periodic circular profiles (**Figure 7(a–e)**) that relate to **Figure 1(e)**, for every value of $\epsilon_r$, respectively. According to these output results, we see the similar behavior for every value of $\epsilon_r$, but the amplitudes of the output fields are different.

The results of the periodic structures of the output field along x-axis and y-axis are demonstrated in **Figure 8(a–d)**. **Figure 8(a** and **b)** relates to **Figure 1(c)** and **Figure 8(c** and **d)** relates to **Figure 1(f)**. By increasing the parameter $\epsilon_r$, the output dielectric profile of the structure of the periodic rectangular profile increased, the output profile of the half-sine ($TE_{10}$) profile decreased, and the output amplitude increased. The results are strongly affected by the half-sine ($TE_{10}$) input-wave profile and the locations of the rectangular or circular profiles. The results show in general similar behavior of the output field, but not the same results, and also the amplitudes of the output fields are different.

The application is useful for straight waveguides in the microwave and the millimeter wave regimes, with periodic rectangular and periodic circular profiles in the cross section of the straight waveguide.

## Author details

Zion Menachem

Address all correspondence to: zionm@post.tau.ac.il

Department of Electrical Engineering, Sami Shamoon College of Engineering, Beer Sheva, Israel

## References

[1] Chiang KS. Review of numerical and approximate methods for the modal analysis of general optical dielectric waveguides. Optical and Quantum Electronics. 1993;**26**:S113-S134

[2] Zhao S. Full-vectorial matched interface and boundary (MIB) method for the modal analysis of dielectric waveguides. Journal of Lightwave Technology. 2008;**26**:2251-2259

[3] Jiao CQ. Selective suppression of electromagnetic modes in a rectangular waveguide by using distributed wall losses. Progress in Electromagnetics Research Letters. 2011;**22**:119-128

[4] Mineo M, Carlo AD, Paoloni C. Analytical design method for corrugated rectangular waveguide SWS THZ vacuum tubes. Journal of Electromagnetic Waves and Applications. 2010;**24**:2479-2494

[5] Smartt CJ, Benson TM, Kendall PC. Exact transcendental equation for scalar modes of rectangular dielectric waveguides. Optical and Quantum Electronics. 1994;**26**:641-644

[6] Chen TT. Wave propagation in an inhomogeneous transversely magnetized rectangular waveguide. Applied Scientific Research. 1960;**8**:141-148

[7] Yeap KH, Tham CY, Yassin G, Yeong KC. Attenuation in rectangular waveguides with finite conductivity walls. Radioengineering. 2011;**20**:472-478

[8] Tian JS, Tian LD. Rigorous analysis of electromagnetic wave propagation in cylindrical dielectric waveguide array. International Journal of Infrared and Millimeter Waves. 2003; **24**:1885-1891

[9] Sharma J. Full-wave analysis of dielectric rectangular waveguides. Progress in Electromagnetics Research. 2010;**13**:121-131

[10] Sukhinin SV. Waveguide effect in a one-dimensional periodically penetrable structure. Journal of Applied Mechanics and Technical Physics. 1990;**31**:580-588

[11] Sumathy M, Vinoy KJ, Datta SK. Analysis of rectangular folded-waveguide millimeter-wave slow-wave structures using conformal transformations. Journal of Infrared, Millimeter, and Terahertz Waves. 2009;**30**:294-301

[12] Rothwell EJ, Temme A, Crowgey B. Pulse reflection from a dielectric discontinuity in a rectangular waveguide. Progress in Electromagnetics Research. 2009;**97**:11-25

[13] Bulgakov AA, Kostylyova OV, Meriuts AV. Electrodynamic properties of a waveguide with layered-periodic walls. Radiophsics and Quantum Electronics. 2005;**48**:48-56

[14] Lu W, Lu YY. Waveguide mode solver based on Neumann-to-Dirichlet operators and boundary integral equations. Journal of Computational Physics. 2012;**231**:1360-1371

[15] Eyges L, Gianino P. Modes of dielectric waveguides of arbitrary cross sectional shape. Journal of the Optical Society of America. 1979;**69**:1226-1235

[16] Soekmadji H, Liao SL, Vernon RJ. Experiment and simulation on $TE_{10}$ cut-off reflection phase in gentle rectangular downtapers. Progress in Electromagnetics Research Letters. 2009;**12**:79-85

[17] Abbas Z, Pollard RD, Kelsall W. A rectangular dielectric waveguide technique for determination of permittivity of materials at W-band. IEEE Transactions on Microwave Theory and Techniques. 1998;**46**:2011-2015

[18] Hewlett SJ, Ladouceur F. Fourier decomposition method applied to mapped infinite domains: scalar analysis of dielectric waveguides down to modal cutoff. Journal of Lightwave Technology. 1995;**13**:375-383

[19] Binzhao C, Fuyong X. Analysis for new types of waveguide with Fourier's expansion-differential method. International Journal of Infrared and Millimeter Waves. 2008;**29**:240-248

[20] Hernandez-Lopez MA, Quintillan M. Propagation characteristics of modes in some rectangular waveguides using the finite-difference time-domain method. Journal of Electromagnetic Waves and Applications. 2000;**14**:1707-1722

[21] Vaish A, Parthasarathy H. Analysis of rectangular waveguide using finite element method. Progress in Electromagnetics Research C. 2008;**2**:117-125

[22] Baganas K. Inhomogeneous dielectric media: wave propagation and dielectric permittivity reconstruction in the case of a rectangular waveguide. Journal of Electromagnetic Waves and Applications. 2002;**16**:1371-1392

[23] Menachem Z, Jerby E. Transfer matrix function (TMF) for propagation in dielectric waveguides with arbitrary transverse profiles. IEEE Transactions on Microwave Theory and Techniques. 1998;**46**:975-982

[24] Menachem Z, Tapuchi S. Influence of the spot-size and cross-section on the output fields and power density along the straight hollow waveguide. Progress in Electromagnetics Research. 2013;**48**:151-173

[25] Vladimirov V. Equations of Mathematical Physics. New York (NY): Marcel Dekker, Inc., 1971

Chapter 18

# A Theoretical Model of the Holographic Formation of Controllable Waveguide Channels System in Photopolymer Liquid Crystalline Composition

Artem Semkin and Sergey Sharangovich

Additional information is available at the end of the chapter

http://dx.doi.org/10.5772/intechopen.74838

**Abstract**

Rapid development of the integrated optics and photonics makes it necessary to create cheap and simple technology of optical waveguide systems formation. Photolithography methods, widely used for these tasks recently, require the production of a number of precision amplitude and phase masks. This fact makes this technology expensive and the formation process long. On another side there is a cheap and one-step holographic recording method in photopolymer compositions. Parameters of the waveguide system formed by this method are determined by recording geometry and material's properties. Besides, compositions may contain liquid crystals that make it possible to create elements, controllable by external electric field. In this chapter, the theoretical model of the holographic formation of controllable waveguide channels system in photopolymer liquid crystalline composition is developed. Special attention is paid to localization of waveguides in the media caused by light field attenuation during the formation process.

**Keywords:** photopolymer, liquid crystal, waveguide, holography

## 1. Introduction

The ability to form waveguide systems for optical and terahertz radiation in photopolymerizable compositions recently is of great interest among researchers: [1–4]. Formed holographically or by photolithography methods, such waveguides are widely used in the integrated optics and photonics devices. Besides, it seems urgent to create the manageable light guides, in which the light propagation conditions can be controlled by external influences, such as an electric field.

One of the possible solutions of this problem is a holographic recording of the waveguide channels in a photopolymer composition containing liquid crystals.

The aim of this chapter is to develop the theoretical model of holographic formation of controllable waveguide channels system in photopolymer liquid crystalline composition with dye sensitizer, also known as polymer-dispersed (PDLC) or polymer-stabilized (PSLC) liquid crystals.

## 2. Theoretical model

We consider the incidence of two plane monochromatic waves $\mathbf{E}_0$ and $\mathbf{E}_1$ with incidence angles $\theta_0$ and $\theta_1$ on the PDLC (PSLC) sample for two formation geometries: transmission (**Figure 1a**) and reflection (**Figure 1b**) ones.

Thus, recording waves in the general case can be described as:

$$\begin{aligned}\mathbf{E}_0(\mathbf{r},t) &= \mathbf{e}_0 \cdot E_0(\mathbf{r}) \cdot e^{i\cdot\left(\omega t-\mathbf{k_0}\cdot\mathbf{r}-\varphi_0(\mathbf{r})\right)-\alpha(\mathbf{r},t)\cdot(\mathbf{N}_0\cdot\mathbf{r})},\\ \mathbf{E}_1(\mathbf{r},t) &= \mathbf{e}_1 \cdot E_1(\mathbf{r}) \cdot e^{i\cdot\left(\omega t-\mathbf{k}_1\cdot\mathbf{r}-\varphi_1(\mathbf{r})\right)-\alpha(\mathbf{r},t)\cdot(\mathbf{N}_1\cdot\mathbf{r}),}\end{aligned} \tag{1}$$

where $\mathbf{e}_0$, $\mathbf{e}_1$ are the unit polarizations vectors of the beams; $E_0(\mathbf{r})$, $E_1(\mathbf{r})$ are the spatial amplitude distributions; $\varphi_0(\mathbf{r})$, $\varphi_1(\mathbf{r})$ are spatial phase distributions; $\mathbf{k_0}$, $\mathbf{k}_1$ are the wave vectors; $\mathbf{N}_0$, $\mathbf{N}_1$ are wave normals; $\alpha(\mathbf{r},t)$ is the absorption coefficient; $\omega = 2\pi/\lambda$, $\lambda$ is the wavelength of the recording radiation.

Investigated material is characterized by optical anisotropy properties; thus, in the material, each of recording wave (Eq. (1)) will be divided into two mutually orthogonal ones called ordinary and extraordinary. So, in the sample, Eq. (1) should be rewritten as:

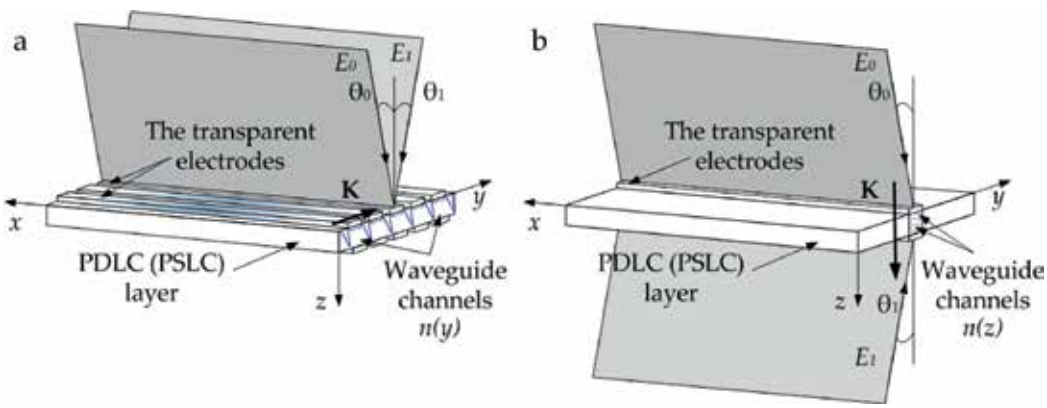


**Figure 1.** Waveguide channels holographic formation: (a) transmission recording geometry and (b) reflection recording geometry.

$$\begin{aligned}\mathbf{E}_0(\mathbf{r},t) &= \sum_{m=o,\,e} \mathbf{e}_0^m \cdot E_0(\mathbf{r}) \cdot e^{i\cdot\left(\omega t-\mathbf{k}_0^m\cdot\mathbf{r}-\varphi_0(\mathbf{r})\right)-\alpha(\mathbf{r},t)\cdot\left(\mathbf{N}_0^m\cdot\mathbf{r}\right)},\\ \mathbf{E}_1(\mathbf{r},t) &= \sum_{m=o,\,e} \mathbf{e}_1^m \cdot E_1(\mathbf{r}) \cdot e^{i\cdot\left(\omega t-\mathbf{k}_1^m\cdot\mathbf{r}-\varphi_1(\mathbf{r})\right)-\alpha(\mathbf{r},t)\cdot\left(\mathbf{N}_1^m\cdot\mathbf{r}\right)},\end{aligned} \tag{2}$$

where $m = o$ corresponds to ordinary waves and $m = e$ corresponds to extraordinary waves, respectively.

For two recording geometries (see **Figure 1**), the spatial distributions of the forming field intensities are determined by the following expression:

$$\begin{aligned}I^T(\mathbf{r},t) &= \sum_{m=o,\,e} I^0(\mathbf{r}) \cdot e^{-\alpha(\mathbf{r},t)\cdot\left[\left(\mathbf{N}_0^m+\mathbf{N}_1^m\right)\cdot\mathbf{r}\right]} \cdot \left[1+m^m(\mathbf{r})\cos\left(\mathbf{K}^m\cdot\mathbf{r}+\varphi_0(\mathbf{r})-\varphi_1(\mathbf{r})\right)\right]\\ I^R(\mathbf{r},t) &= \sum_{m=o,\,e} I^0(\mathbf{r}) \cdot e^{\left[\frac{-\alpha(\mathbf{r},t)\cdot d}{2}\right]} \cdot \mathrm{ch}\left\{\alpha(\mathbf{r},t)\cdot\left[\left(\mathbf{N}_0^m+\mathbf{N}_1^m\right)\cdot\mathbf{r}-\frac{d}{2}\right]\right\}\cdot\left[1+m^m(\mathbf{r})\cos\left(\mathbf{K}^m\cdot\mathbf{r}+\varphi_0(\mathbf{r})-\varphi_1(\mathbf{r})\right)\right],\end{aligned} \tag{3}$$

where $I^T(\mathbf{r},t)$, $I^R(\mathbf{r},t)$ are the spatial distributions of light field intensity for transmission and reflection geometries, respectively; $I^0(\mathbf{r}) = E_0^2(\mathbf{r}) + E_1^2(\mathbf{r})$, $m^m(\mathbf{r}) = \frac{2E_0(\mathbf{r})\cdot E_1(\mathbf{r})}{E_0^2(\mathbf{r})+E_1^2(\mathbf{r})}\cdot\left(\mathbf{e}_0^m\cdot\mathbf{e}_1^m\right)$ are the local contrasts of interference patterns; $\mathbf{K}^m = \mathbf{k}_0^m - \mathbf{k}_1^m$; $d$ is the thickness of the material.

Under the influence of light field in photopolymer liquid crystalline composition with dye sensitizer, the dye molecule absorbs a light radiation quantum with the dye radical and the primary radical initiator formation. The radical of dye is not involved in further chemical reactions and turns to colorless leuco form.

Thus, during the waveguide channel system formation, dye concentration decreases. This fact causes the light-induced decreasing of light absorption. The absorption coefficient dependence of a mount of absorbed radiation can be written as [5]:

$$-\frac{d\alpha(\mathbf{r},t)}{dt} = \beta_q\cdot\alpha_0\cdot I_{abs}(\mathbf{r},t), \tag{4}$$

where $\alpha(\mathbf{r},t) = \alpha_0\cdot K_d(\mathbf{r},t)$ is the absorption coefficient with light-induced change taken into account; $K_d(\mathbf{r},t)$ is dye concentration; $\alpha_0$ is the absorption of one molecule; $\beta_q$ is quantum yield of dye; and $I_{abs}(\mathbf{r},t)$ is the light intensity from Bouguer-Lambert law:

$$\begin{aligned}I_{abs}^T(\mathbf{r},t) &= \sum_{m=o,\,e} E_0^2(\mathbf{r})\cdot\left(1-e^{-\alpha(\mathbf{r},t)\cdot\left[\mathbf{N}_0^m\cdot\mathbf{r}\right]}\right)+E_1^2(\mathbf{r})\cdot\left(1-e^{-\alpha(\mathbf{r},t)\cdot\left[\mathbf{N}_1^m\cdot\mathbf{r}\right]}\right)\\ I_{abs}^R(\mathbf{r},t) &= \sum_{m=o,\,e} E_0^2(\mathbf{r})\cdot\left(1-e^{-\alpha(\mathbf{r},t)\cdot\left[\mathbf{N}_0^m\cdot\mathbf{r}\right]}\right)+E_1^2(\mathbf{r})\cdot\left(1-e^{-\alpha(\mathbf{r},t)\cdot\left[d-\mathbf{N}_1^m\cdot\mathbf{r}\right]}\right)'\end{aligned} \tag{5}$$

where $I_{abs}^T(\mathbf{r},t)$, $I_{abs}^R(\mathbf{r},t)$ are defined for transmission and reflection geometries, respectively.

Then, the solution of Eq. (3) for light-induced absorption change for transmission and reflection geometries is obtained in [5] as follows:

$$\begin{aligned}\alpha_T^m(\mathbf{r},t) &= \alpha_{sub} + \alpha_0 K_{d0} \cdot e^{-\beta_q \cdot \alpha_0 \cdot \left[\left(\mathbf{N}_0^m + \mathbf{N}_1^m\right)\cdot \mathbf{r} \cdot t\right]} \\ \alpha_R^m(\mathbf{r},t) &= \alpha_{sub} + \alpha_0 K_{d0} \cdot e^{-\beta_q \cdot \alpha_0 \cdot \left[\left(\mathbf{N}_0^m \cdot \mathbf{r} + d - \mathbf{N}_1^m \cdot \mathbf{r}\right)\cdot t\right]}\end{aligned}, \tag{6}$$

where $\alpha_{sub}$ is the substrate absorption coefficient and $K_{d0}$ is the initial dye concentration.

The process of waveguide channels' holographic formation is described by the kinetic equations system (KES), written for monomer concentration and refraction index [6–8]:

$$\frac{\partial M^m(\mathbf{r},t)}{\partial t} = \operatorname{div}\left[D_M^m(\mathbf{r},t)\operatorname{grad} M^m(\mathbf{r},t)\right] - K_g \cdot \left[\frac{\alpha_0 \beta K_{d0} \tau_0 I^m(\mathbf{r},t)}{K_b}\right]^{0,5} M^m(\mathbf{r},t), \tag{7}$$

$$\frac{\partial n^m(\mathbf{r},t)}{\partial t} = \delta n_p \cdot K_g \cdot \left[\frac{\alpha_0 \beta K_{d0} \tau_0 I^m(\mathbf{r},t)}{K_b}\right]^{0,5} \frac{M^m(\mathbf{r},t)}{M_n} + \delta n_{lc} \operatorname{div}\left[D_{LC}^m(\mathbf{r},t)\operatorname{grad}\frac{M^m(\mathbf{r},t)}{M_n}\right], \tag{8}$$

where $M_n$ is the initial concentration of the monomer; $K_g$, $K_b$ are parameters of the rate of growth and breakage of the polymer chain, respectively; $\beta$ is the parameter of initiation reaction; $\tau_0$ is lifetime of the excited state of the dye molecule; $D_M^m(\mathbf{r},t)$, $D_{LC}^m(\mathbf{r},t)$ are the diffusion coefficients of the monomer and liquid crystal, respectively; $\delta n_p$, $\delta n_{lc}$ are weight coefficients of the contribution of photopolymerization and diffusion processes; and $I^m(\mathbf{r},t)$ is the intensity distribution (Eq. (3)).

Diffusion coefficients can be defined from the following equations:

$$\begin{aligned}D_M^m(\mathbf{r},t) &= D_{Mn}\exp\left[-s_M\left(1 - \frac{M^m(\mathbf{r},t)}{M_n}\right)\right] \\ D_{LC}^m(\mathbf{r},t) &= D_{LCn}\exp\left[-s_{LC}\left(1 - \frac{L^m(\mathbf{r},t)}{L_n}\right)\right]\end{aligned}, \tag{9}$$

where $D_{Mn}$ and $D_{LCn}$ are the initial diffusion coefficients, respectively; $s_M$, $s_{LC}$ are rates of reduction in time; $L_n$, $L^m(\mathbf{r},t)$ are the initial and current concentrations of liquid crystal.

Weight coefficients $\delta n_p$ and $\delta n_{lc}$ from Eq. (7) are found from the Lorentz-Lorentz formula [8]:

$$\delta n_p = \frac{4\pi}{3} \cdot \frac{\left(n_{st}^2 + 2\right)}{6 n_{st}^2} \cdot \left(\alpha_M + \frac{\alpha_P}{l}\right) \cdot \frac{\rho_M}{W_M}, \tag{10}$$

$$\delta n_{lc} = \frac{4\pi}{3} \cdot \frac{\left(n_{st}^2 + 2\right)}{6 n_{st}^2} \cdot \left(\alpha_M \frac{\rho_M}{W_M} + \alpha_{LC} \frac{\rho_{LC}}{W_{LC}}\right), \tag{11}$$

where $\alpha_M$, $\alpha_P$, $\alpha_{LC}$ are the polarizability of monomer, polymer, and liquid crystal molecules, respectively; $\rho_M$, $\rho_{LC}$ are the density of the monomer and liquid crystal, respectively; $W_M$, $W_{LC}$ are molecular weights; $l$ is the average length of polymeric chains; and $n_{st}$ is the refractive index of the composition prior to the start of the recording process, determined by the Lorentz-Lorentz formula from the refractive indices of the monomer and the liquid crystal [8]:

http://dx.doi.org/10.5772/intechopen.74838

$$n_{st} = M_n \cdot \frac{n_M^2 - 1}{n_M^2 + 2} + L_n \cdot \frac{n_{LC}^2 - 1}{n_{LC}^2 + 2}, \tag{12}$$

where $n_M$, $n_{LC}$ are the monomer and liquid crystal refractive indices.

Because of periodical character of the forming fields' intensities' spatial distributions, solution of KES can be found as a sum of $H$ spatial harmonics [8]:

$$M^m(\mathbf{r},\tau) = \sum_{j=0}^{H} M_j^m(\mathbf{r},\tau)\cos(j\mathbf{K}^m\mathbf{r}), \quad n^m(\mathbf{r},\tau) = n_{st} + \sum_{j=0}^{H} n_j^m(\mathbf{r},\tau)\cos(j\mathbf{K}^m\mathbf{r}), \tag{13}$$

where $M_j^m(\mathbf{r},\tau) = \frac{1}{2\pi}\int_{-\pi}^{\pi} M_j^m(\mathbf{r},\tau)\cos(j\mathbf{K}^m\mathbf{r})\ d(\mathbf{K}^m\mathbf{r})$, $n_j^m(\mathbf{r},\tau) = \frac{1}{2\pi}\int_{-\pi}^{\pi} n_j^m(\mathbf{r},\tau)\cos(j\mathbf{K}^m\mathbf{r})\ d(\mathbf{K}^m\mathbf{r})$ are the monomer concentration and refractive index harmonics amplitudes, respectively; $n_{st}$ is the PDLC (PSLC) refractive index at $\tau = 0$; $\tau = t/T_M^m$ is the relative time; $T_M^m = \frac{1}{D_{Mn}^m \cdot |\mathbf{K}^m|^2}$ is the components' diffusion characteristic time.

By substituting Eq. (13) to the KES (Eqs. (7 and 8)) and using the orthogonality of spatial harmonics, a system of coupled kinetic differential equations for the amplitudes of monomer concentration harmonics can be obtained for $D_M^m(\mathbf{r},t) = D_{LC}^m(\mathbf{r},t) = D_{Mn}^m$ (stable diffusion coefficients) and $K_d(\mathbf{r},t) = K_{d0}$ (stable absorption) [6]:

$$\begin{cases} \dfrac{\partial M_0^m(\mathbf{r},\tau)}{\partial\tau} = \sum\limits_{l=0}^{H} a_{0,l}^m(\mathbf{r}) M_l^m(\mathbf{r},\tau) \\ \dfrac{\partial M_1^m(\mathbf{r},\tau)}{\partial\tau} = -M_1^m(\mathbf{r},\tau) + \sum\limits_{l=0}^{H} a_{1,l}^m(\mathbf{r}) M_l^m(\mathbf{r},\tau) \\ \cdots\cdots\cdots\cdots\cdots\cdots\cdots\cdots\cdots\cdots \\ \dfrac{\partial M_H^m(\mathbf{r},\tau)}{\partial\tau} = -N^2 M_H^m(\mathbf{r},\tau) + \sum\limits_{l=0}^{H} a_{N,l}^m(\mathbf{r}) M_l^m(\mathbf{r},\tau) \end{cases}, \tag{14}$$

and also a system of differential equations for the amplitudes of refraction index harmonics:

$$\begin{cases} \dfrac{\partial n_0^m(\mathbf{r},\tau)}{\partial\tau} M_n = -\delta n_p \sum\limits_{l=0}^{H} a_{0,l}^m(\mathbf{r}) M_l^m(\mathbf{r},\tau) \\ \dfrac{\partial n_1^m(\mathbf{r},\tau)}{\partial\tau} M_n = -\delta n_p \sum\limits_{l=0}^{H} a_{1,l}^m(\mathbf{r}) M_l^m(\mathbf{r},\tau) + \delta n_{lc} M_1^m(\mathbf{r},\tau) \\ \cdots\cdots\cdots\cdots\cdots\cdots\cdots\cdots\cdots\cdots\cdots\cdots\cdots\cdots \\ \dfrac{\partial n_H^m(\mathbf{r},\tau)}{\partial\tau} M_n = -\delta n_p \sum\limits_{l=0}^{H} a_{H,l}^m(\mathbf{r}) M_l^m(\mathbf{r},\tau) + \delta n_{lc} H^2 M_H^m(\mathbf{r},\tau) \end{cases}. \tag{15}$$

In equation systems Eqs. (14) and (15), a coefficient matrix is introduced [6]:

$$a_{j,l}^{m}(\mathbf{r}) = -\begin{Bmatrix} e_1^m & e_2^m & e_3^m & 0 & 0 & 0 & . & 0 & 0 & 0 & 0 \\ 2e_2^m & e_{11}^m & e_2^m & e_3^m & 0 & 0. & . & 0 & 0 & 0 & 0 \\ 2e_3^m & e_2^m & e_1^m & e_2^m & e_3^m & 0 & . & 0 & 0 & 0 & 0 \\ 0 & e_3^m & e_2^m & e_1^m & e_2^m & e_3^m & . & 0 & 0 & 0 & 0 \\ 0 & 0 & e_3^m & e_2^m & e_1^m & e_2^m & . & 0 & 0 & 0 & 0 \\ 0 & 0 & 0 & e_3^m & e_2^m & e_1^m & . & 0 & 0 & 0 & 0 \\ . & . & . & . & . & . & . & . & . & . & . \\ 0 & 0 & 0 & 0 & 0 & 0 & . & e_1^m & e_2^m & e_3^m & 0 \\ 0 & 0 & 0 & 0 & 0 & 0 & . & e_2^m & e_1^m & e_2^m & e_3^m \\ 0 & 0 & 0 & 0 & 0 & 0 & . & e_3^m & e_2^m & e_1^m & e_2^m \\ 0 & 0 & 0 & 0 & 0 & 0 & . & 0 & e_3^m & e_2^m & e_1^m \end{Bmatrix}, \tag{16}$$

where $e_1^m = \frac{\sqrt{2}}{b_s^m}\left(1 + L_s^m\right)$; $e_{11}^m = \frac{\sqrt{2}}{b_s^m}\left(1 + 3L_s^m/2\right)$; $e_2^m = \frac{\sqrt{2}m_s^m}{4b_s^m}$; $e_3^m = \frac{\sqrt{2}}{b_s^m}L_s^m/2$; $m_s^m = m^m(\mathbf{r})$; $L_s^m = L^m(\mathbf{r}) = -[m^m(\mathbf{r})]^2/16$; $b_s^m = b^m(\mathbf{r}) = \frac{T_p^m(\mathbf{r})}{T_M^m(\mathbf{r})}$ are the parameters that characterize the ratio of polymerization and diffusion rates; and $T_p^m(\mathbf{r})$ is the characteristic polymerization time:

$$T_p^m(\mathbf{r}) = \frac{1}{K_g} \cdot \left[\frac{2K_b}{\alpha_0 \beta K_{d0} \tau_0 I^m(\mathbf{r})}\right]^{0,5}, \tag{17}$$

$T_M^m(\mathbf{r})$ is the characteristic diffusion time:

$$T_M^m(\mathbf{r}) = \frac{1}{D_{Mn}^m \cdot \left[\mathbf{K}^m \cdot \mathbf{r} + \varphi_0(\mathbf{r}) - \varphi_1(\mathbf{r})\right]^2}. \tag{18}$$

Coefficients $a_{j,l}^m(\mathbf{r})$ describe the contributions of photopolymerization and diffusion recording mechanisms. However, for analysis of equation systems Eqs. (14) and (15), it is convenient to introduce the coupling coefficients $c_{j,l}^m(\mathbf{r}) = a_{j,l}^m(\mathbf{r}) - j^2\delta_{j,l}$ ($\delta_{j,l}$ is the Kronecker symbol), which characterizes the coupling between j and l harmonics. The difference between coefficients $c_{j,l}^m(\mathbf{r})$ and $a_{j,l}^m(\mathbf{r})$ characterizes the contribution of monomer diffusion to the recording process and it is proportional to the second degree of the harmonic's number. The increase of this contribution according to the harmonic's number is due to grating period decrease and, respectively, the diffusion characteristic time decrease for this harmonic.

For solution of the coupled differential equations system (14), the initial conditions should be introduced:

$$M_0^m(\mathbf{r}, \tau = 0) = M_n, M_1^m(\mathbf{r}, \tau = 0) = 0, \ldots, M_H^m(\mathbf{r}, \tau = 0) = 0. \tag{19}$$

The solution can be found using the operator method [6]. The general solution for the spatial amplitude profiles of monomer concentration harmonics will be:

$$M_j^m(\mathbf{r},\tau) = M_n \sum_{l=0}^{H} A_{j,l}^m(\mathbf{r}) \exp\left[\lambda_l^m(\mathbf{r})\cdot\tau\right], \tag{20}$$

where functional dependencies of coefficients $\lambda_l^m(\mathbf{r})$ are defined as the roots of the characteristic equation $\left|c_{j,l}^m(\mathbf{r}) - \lambda_l^m(\mathbf{r})\right| = 0$. Analysis shows that $\lambda_l^m(\mathbf{r})$ is real, different, and negative. Coefficients $A_{j,l}^m(\mathbf{r})$ are defined as solutions of a system of linear algebraic equations:

$$\begin{Bmatrix} 1 & 1 & 1 & . & 1 \\ \lambda_0^m & \lambda_1^m & \lambda_2^m & . & \lambda_H^m \\ \lambda_0^{m^2} & \lambda_1^{m^2} & \lambda_2^{m^2} & . & \lambda_H^{m^2} \\ \lambda_0^{m^3} & \lambda_1^{m^3} & \lambda_2^{m^3} & . & \lambda_H^{m^3} \\ \lambda_0^{m^4} & \lambda_1^{m^4} & \lambda_2^{m^4} & . & \lambda_H^{m^4} \\ . & . & . & . & . \\ \lambda_0^{m^H} & \lambda_1^{m^H} & \lambda_2^{m^H} & . & \lambda_H^{m^H} \end{Bmatrix} \times \begin{Bmatrix} A_{j,0}^m \\ A_{j,1}^m \\ A_{j,2}^m \\ A_{j,3}^m \\ A_{j,4}^m \\ \cdots \\ A_{j,H}^m \end{Bmatrix} = M_n \begin{Bmatrix} \delta_{j,0} \\ c_{j,0}^m \\ \sum_{i_0=0}^{H} c_{j,i_0}^m c_{i_0,0}^m \\ \sum_{i_1=0}^{H} c_{j,i_1}^m \sum_{i_0=0}^{H} c_{i_1,i_0}^m c_{i_0,0}^m \\ \cdots\cdots\cdots\cdots\cdots\cdots\cdots\cdots\cdots\cdots \\ \sum_{i_{(N-2)}=0}^{H} c_{j,i_{N-1}}^m \cdots \sum_{i_2=0}^{H} c_{i_3,i_2}^m \sum_{i_1=0}^{H} c_{i_2,i_1}^m \sum_{i_0=0}^{H} c_{i_1,i_0}^m c_{i_0,0}^m \end{Bmatrix}, \tag{21}$$

where $\lambda_l^m = \lambda_l^m(\mathbf{r})$, $A_{j,l}^m = A_{j,l}^m(\mathbf{r})$, $c_{j,l}^m = c_{j,l}^m(\mathbf{r})$.

Then, by substituting (20) to (15) and by integrating the resulting differential equations with initial conditions, we get.

$$n_0^m(\mathbf{r},\tau=0) = 0, n_1^m(\mathbf{r},\tau=0) = 0, \ldots n_H^m(\mathbf{r},\tau=0) = 0 \tag{22}$$

The general solution for the amplitude of $j$-harmonic of the refractive index can be found:

$$n_j^m(\mathbf{r},\tau) = n_{pj}^m(\mathbf{r},\tau) + n_{lcj}^m(\mathbf{r},\tau), \tag{23}$$

where $n_{pj}^m(\mathbf{r},\tau) = \delta n_p \sum_{l=0}^{H} a_{j,l}^m(\mathbf{r}) \sum_{q=0}^{H} A_{l,q}^m(\mathbf{r}) \frac{1-\exp\left[\lambda_q^m(\mathbf{r})\cdot\tau\right]}{\lambda_q^m(\mathbf{r})}$, $n_{lcj}^m(\mathbf{r},\tau) = -\delta n_{lc}\cdot j^2 \sum_{q=0}^{H} A_{j,q}^m(\mathbf{r}) \frac{1-\exp\left[\lambda_q^m(\mathbf{r})\cdot\tau\right]}{\lambda_q^m(\mathbf{r})}$, $j = 0,\ldots,H$.

Thus, Eqs. (13), (20), and (23) are the general solutions of nonlinear photopolymerization diffusion holographic recording of waveguide channels system in PDLCs (PSLCs) in the case of stable diffusion coefficients and stable absorption. They define kinetics of spatial profiles of monomer concentration—$M^m(\mathbf{r},\tau)$ and refractive index $n^m(\mathbf{r},\tau)$.

In case of high nonlinearity, it is possible to form the specific spatial profile of refractive index. The nonlinearity of recording is achieved by changing the ratio of the photopolymerization and diffusion mechanism contributions to the process of structure's formation.

## 3. Numerical simulations

To investigate the formation processes, numerical simulations of first four refractive index harmonics kinetics for transmission and reflection geometries were made with the following parameters: $\lambda = 633$ nm and $\theta_0 = -\theta_1 = 30^\circ$ for transmission geometry (**Figure 1a**) and $\theta_0 = -\theta_1 = 60^\circ$ for reflection geometry (**Figure 1b**); $E_0(\mathbf{r}) = E_1(\mathbf{r}) = 1$; $\varphi_0(\mathbf{r}), = \varphi_1(\mathbf{r}) = 0$; $\mathbf{e}_0$, $\mathbf{e}_1$ are oriented with respect to extraordinary waves in material; $d = 10$ μm; $\delta n_p/\delta n_i = 0.5$; and for two values of parameter $b = b^e = 0.2$ and $b = b^e = 5$ in the absence of absorption. Values $b = 0.2$ and 5 are chosen as an example to investigate two common cases: $b << 1$ and $b >> 1$. Simulations were made by Eq. (23); results are shown in **Figure 2**.

As can be seen from **Figure 2**, in the case of predomination of polymerization ($b^e = 0.2$, **Figure 2a**), the structure forms quickly, but amplitudes of higher harmonics are high, so the spatial profile of refractive index changes has an inharmonic character. In another case of diffusion predominance ($b^e = 5$, **Figure 2b**), spatial profile is quasi-sinusoidal, but it is slower. These effects can be explained by the following. When polymerization is rapid, in the area of the maximum of intensity distribution (Eq. (3)), molecules of liquid crystal do not have time to diffuse, so the concentrations' gradient is not high enough; monomer molecules do not diffuse from minimums of intensity distribution. Thus, profile of refractive index distribution becomes inharmonic. So, it can be concluded that ratio of polymerization and diffusion rates $b^m(\mathbf{r}, \tau)$ defines the distribution $n^m(\mathbf{r}, \tau)$.

Corresponding distributions $n^e(\mathbf{r}, \tau = 50)$ for two examined cases in the absence of absorption are shown in **Figure 3**.

In **Figure 3**, a new spatial coordinate is introduced: $\xi = y$ for transmission geometry (see **Figure 1a**) and $\xi = z$ for reflection geometry (see **Figure 1b**).

According to Eqs. (17) and (18), parameter $b^m(\mathbf{r}, \tau)$ depends on formation field's amplitude and phase distributions as well as material properties. So, by controlling these parameters one can create any distribution of refractive index $n^m(\mathbf{r}, \tau)$. As is shown in **Figure 3**, distributions can be quasi-rectangular (**Figure 3a**) and quasi-sinusoidal (**Figure 3b**), so they can be mentioned as waveguides systems.

It should be also noted that the amplitude of refractive index change when $b = 0.2$ (**Figure 3a**), due to high amplitudes of higher harmonics (see **Figure 2a**), is lower than in the case of $b = 5$.

To investigate the impact of absorption on the spatial profile of structure along the thickness of the sample, numerical simulations were made with the following parameters: $\lambda = 633$ nm; $\theta_0 = -\theta_1 = 30^\circ$ for transmission geometry (**Figure 1a**) and $\theta_0 = -\theta_1 = 60^\circ$ for reflection geometry (**Figure 1b**); $E_0(\mathbf{r}) = E_1(\mathbf{r}) = 1$; $\varphi_0(\mathbf{r}), = \varphi_1(\mathbf{r}) = 0$; $\mathbf{e}_0, \mathbf{e}_1$ are oriented with respect to extraordinary waves in material; $d = 10$ μm; $\delta n_p/\delta n_i = 0.5$; $b = b^e = 5$; $\alpha d = 2$ *Np*. Simulations were made by Eq. (23) for the amplitude of the first harmonic of refractive index and for two formation geometries. Results are shown in **Figure 4**.

http://dx.doi.org/10.5772/intechopen.74838

As shown in **Figure 4**, absorption of the formation field causes dependence of the first harmonic on $z$-coordinate (see **Figure 1**) during the recording process. Thus, the spatial profile of refractive index changes its character in time and space.

In **Figure 4**, some characteristic cases of localization of maximum of refractive index change in the thickness can be seen. In particular, in the case of transmission geometry (**Figure 4a**) at $\tau = 2.5$, maximum is localized between 1.5 and 3.5 μm of the material thickness. For reflection geometry (**Figure 4b**), one maximum is localized near 5 μm at $\tau = 1.25$, and there are two

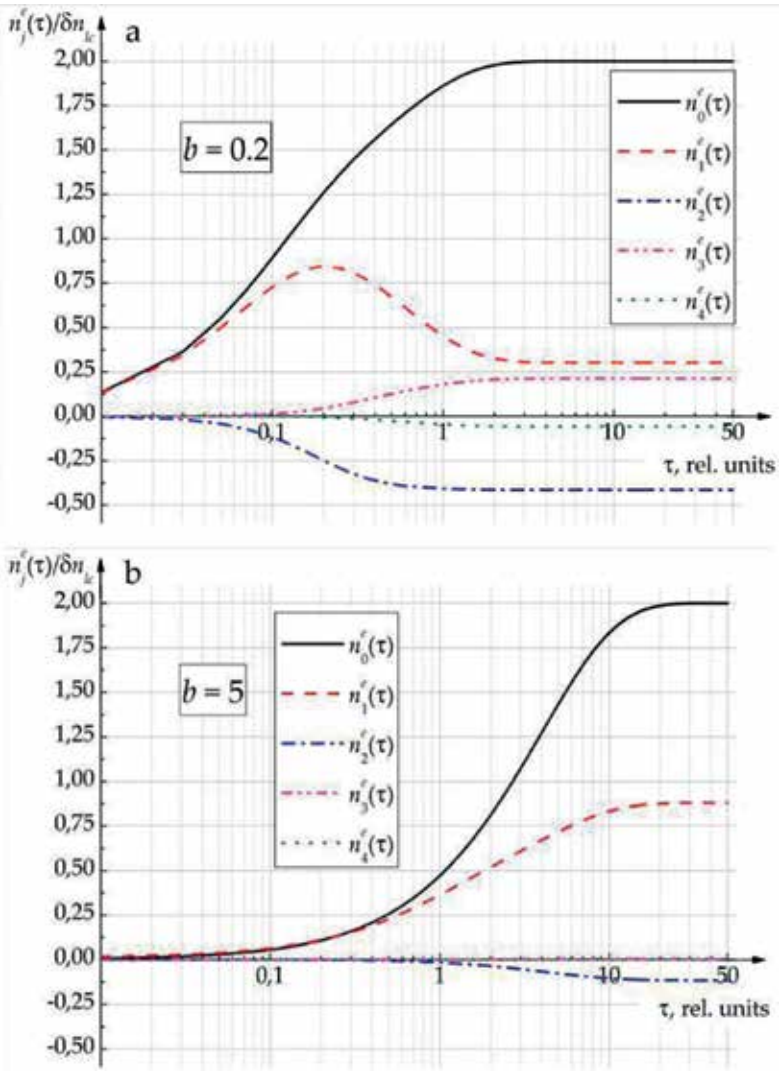


**Figure 2.** Refractive index harmonics kinetics for $b = 0.2$ (a) and $b = 5$ (b).

other maximums at $\tau > 2.5$. These effects take place because of dependence $b^m(\mathbf{r})$. Absorption causes the dependence on $z$-coordinate and spatial distributions of amplitude, and the phase of recording field (Eqs. (1) and (2)) causes the dependence on $x$ and $y$ coordinates. In more general cases, there is also a temporal dependence $b^m(\mathbf{r}, \tau)$ caused by photo-induced effects (Eq. (6)).

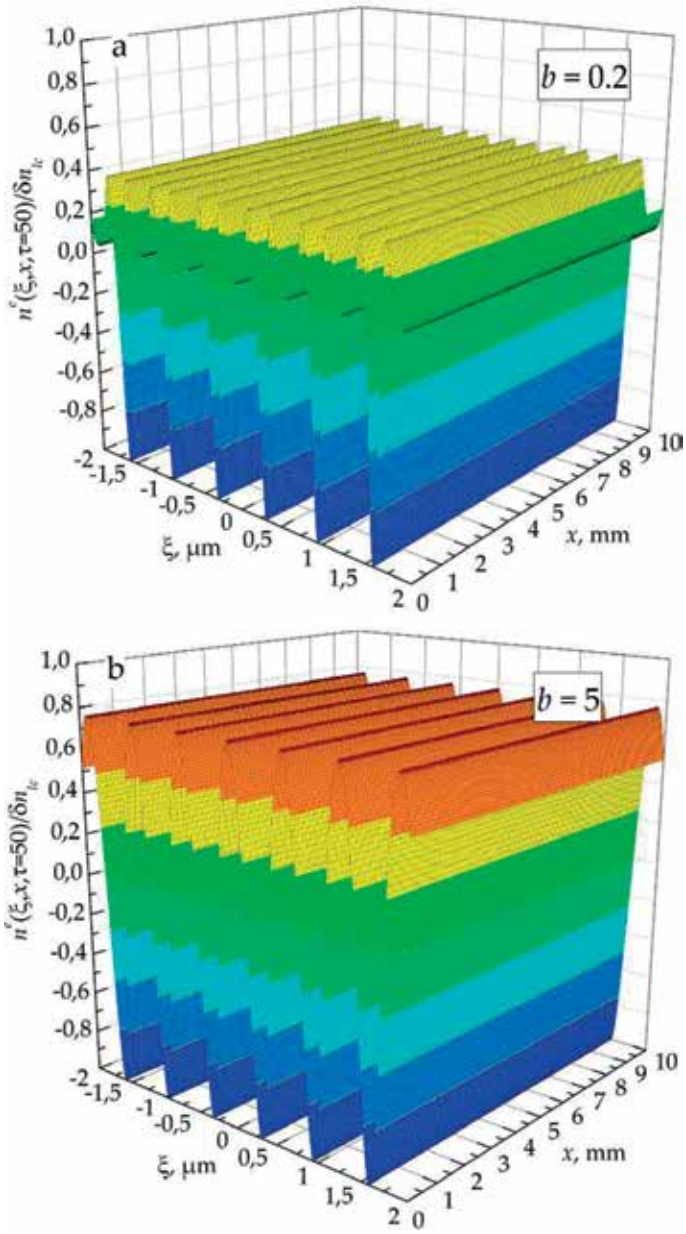


**Figure 3.** Refractive index distributions for $b = 0.2$ (a) and $b = 5$ (b).

http://dx.doi.org/10.5772/intechopen.74838

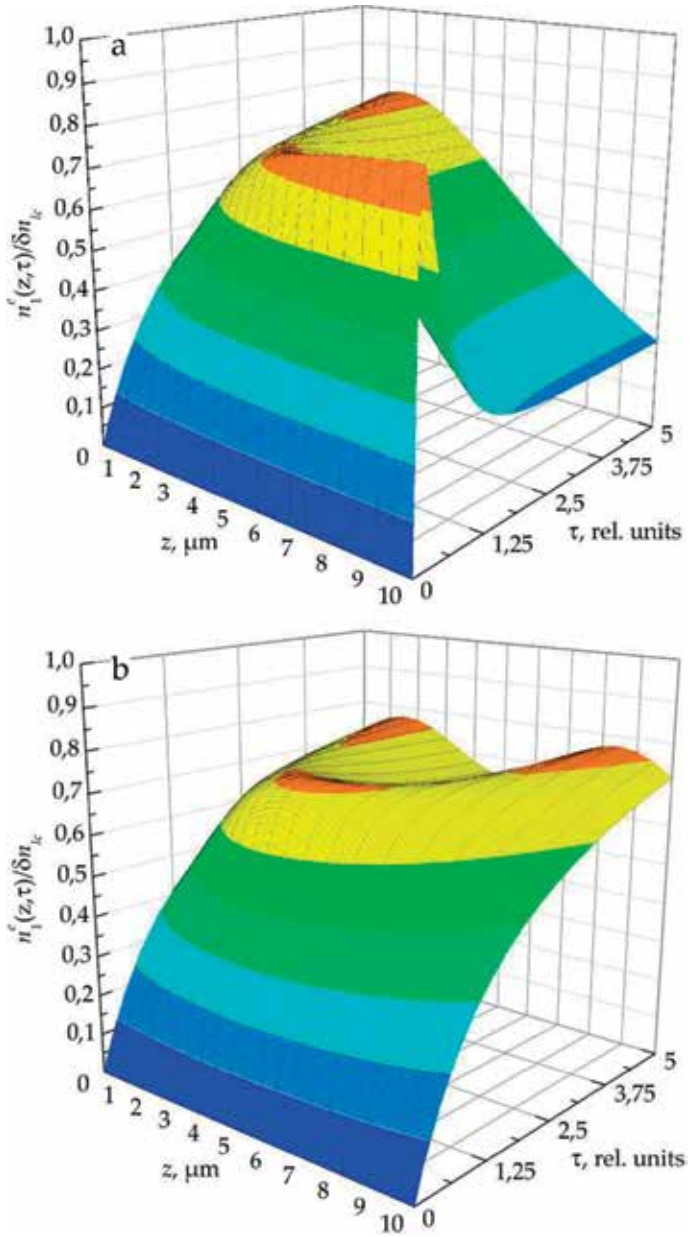


**Figure 4.** Impact of light absorption: transmission geometry (a) and reflection geometry (b).

To illustrate the localization of waveguide channels into the material, in **Figure 5**, there are some more two-dimensional spatial distributions of refractive index, obtained by Eq. (23) for transmission and reflection geometries—$b = b^e = 5$ and for different values of $\tau$.

It follows from the abovementioned that by controlling the spatial distribution of light field and taking the absorption effects into account, the waveguide systems localized into the

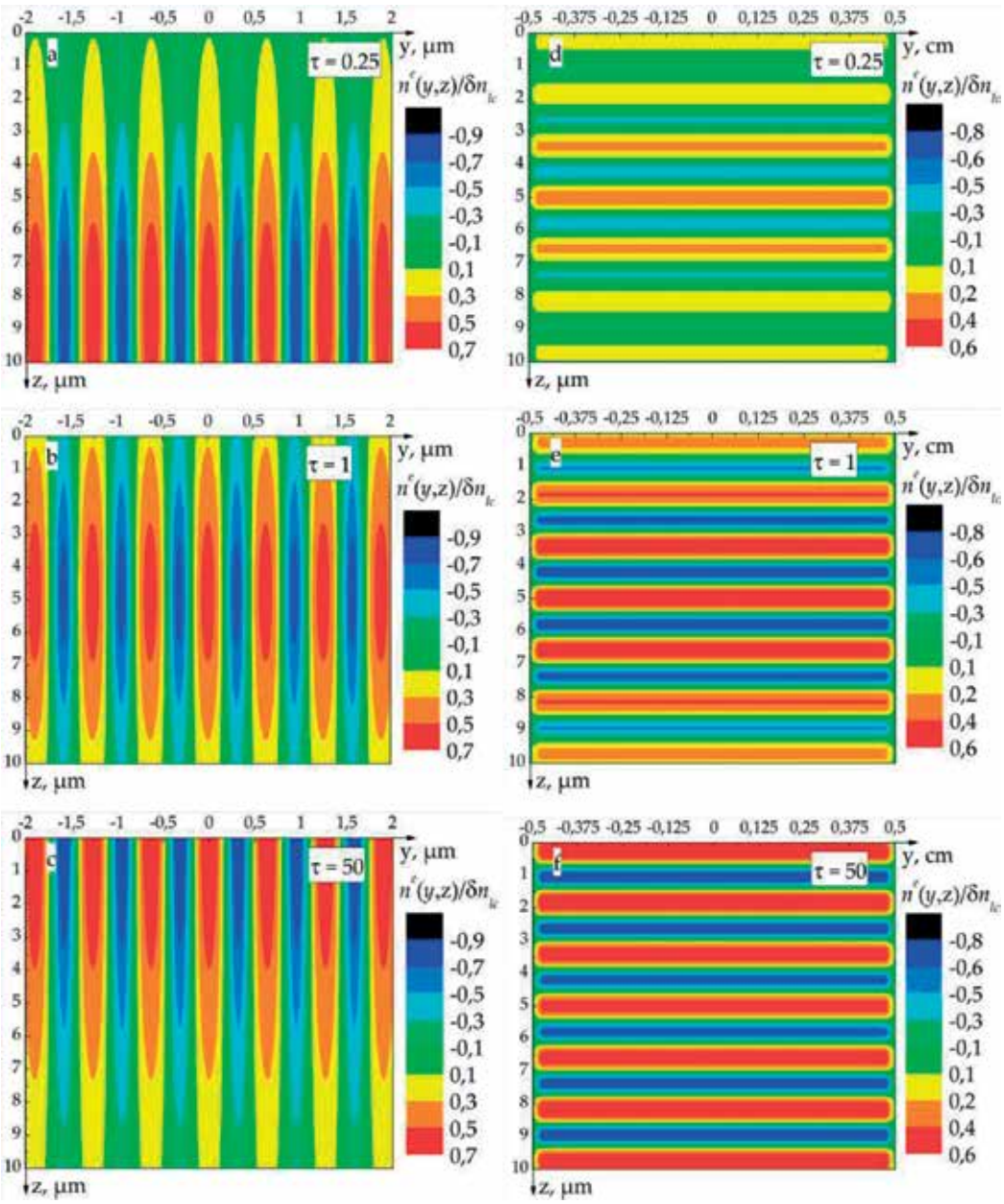


**Figure 5.** Two-dimensional refractive index distributions: transmission geometry (a–c) and reflection geometry (d–f).

material can be holographically formed. Localization is important because of the necessity to create a predetermined refractive index profile independent from properties of possible substrates (electrodes, glass, polymer layers, etc.). In particular, to create the waveguide system localized near the bottom substrate, formation geometry should be transmissive and formation

should be stopped before $\tau = 0.5$, for localization into the center of the sample—$0.5 < \tau < 2.5$—for transmission and reflection geometries, and for $\tau > 2.5$, waveguides will be localized near the top substrate for transmission geometry and not localized for reflection geometry. The given values of $\tau$ are valid for the formation parameters given earlier.

In our recent works [9–18], we have seen that the impact of the external electric field on the holographic structure formed in PDLC (PSLC) leads to the refractive index change due to electro-optical orientation mechanisms, that is typical to liquid crystals, and the recorded structure can be "erased". So, it can be supposed that the impact of external electric field on individual waveguides will lead to its "erasing", and it is possible to "switch off" some waveguides or change the system's period, and so on.

## 4. Conclusion

Thus, in this chapter, the theoretical model of holographic formation of controllable waveguide channels system in photopolymer liquid crystalline composition is developed. The most general cases are described by the developed model, and numerical simulations were made for plane recording waves and stable absorption cases. Special attention is paid to localization of waveguides in the media caused by light field attenuation during the formation process.

It is shown that parameters of the waveguide system formed by holography's methods are determined by recording geometry and material's properties. Also, by control of these parameters, waveguides can be localized into the sample that makes them independent from substrates. Also, introduced compositions contain liquid crystals that make it possible to create elements, controllable by external electric field.

Obtained results can be used for new photonics devices based on photopolymer liquid crystalline composition development.

## Acknowledgements

The work is performed as a project that is part of Government Task of Russian Ministry of Education (project No. 3.1110.2017/4.6).

## Author details

Artem Semkin and Sergey Sharangovich*

*Address all correspondence to: shr@tusur.ru

Tomsk State University of Control Systems and Radioelectronics, Tomsk, Russia

## References

[1] Keil N, Zawadski C, Zhang Z, Wang J, Mettbach N, Grote N, Schell M. Polymer PLC as an Optical Integration Bench. Optical Fiber Communication Conference and Exposition (OFC/NFOEC) and the National Fiber Optic Engineers Conference. 2011;**2011**:1-3

[2] Li H, Qi Y, Mallah R, Sheridan J. Modeling the nonlinear photoabsorptive behavior during self-written waveguide formation in a photopolymer. JOSA B. 2015;**32**:912-922. DOI: 10.1364/JOSAB.32.000912

[3] Zhang Z, Felipe D, Katopodis V, Groumas P, Kouloumentas Ch, et al. Hybrid photonic integration on a polymer platform. Photonics. 2015;**2**:1005-1026. DOI: 10.3390/photonics2031005

[4] Zhang Z, Mettbach N, Zawadski C, Wang J, Schmidt D, Brinker W, Grote N, Schell M, Keil N. Polymer-based photonic toolbox: Passive components, hybrid integration and polarisation control. IET Optoelectronics. 2010;**5**:226-232. DOI: 10.1049/iet-opt.2010.0054

[5] Dovolnov E, Ustyuzhanin S, Sharangovich S. Formation of holographic transmission and reflecting gratings in photopolymers under light-induced absorption. Russian Physics Journal. 2006;**49**:1129-1138. DOI: 10.1007/s11182-006-0233-3

[6] Dovolnov E, Sharangovich S. Nonlinear model of record and readout of holographic transmission diffraction gratings in absorbent photopolymers. Part I. Theoretical analysis. Russian Physics Journal. 2005;**48**:501-510. DOI: 10.1007/s11182-005-0159-1

[7] Dovolnov E, Sharangovich S. Nonlinear model of record and readout of holographic transmission diffraction gratings in absorbent photopolymers. Part II. Numerical modelling and experiment. Russian Physics Journal. 2005;**48**:766-774. DOI: 10.1007/s11182-005-0199-6

[8] Dovolnov E, Sharangovich S. Analysis of dynamics of holographic grating formation withinharmonic spatial distribution in photopolymer + liquid crystalcompounds. Proceedings of SPIE. 2005;**6023**:602301. DOI: 10.1117/12.646947

[9] Ustyuzhanin S, Nozdrevatykh B, Sharangovich S. Anisotropic light beam diffraction on electrical controlled holographic gratings in photopolymer-dispersed liquid crystals. International Conference on Advanced Optoelectronics and Lasers (CAOL), IEEE. 2008: 407-409. DOI: 10.1109/CAOL.2008.4671969

[10] Ustyuzhanin S, Nozdrevatykh B, Sharangovich S. Transfer functions of nonuniform transmission photonic structures in polymer-dispersed liquid-crystal materials. Physics of Wave Phenomena. 2010;**18**:289-293. DOI: 10.3103/S1541308X10040102

[11] Ustyuzhanin S, Sharangovich S. Analytical model of light beam diffraction by one-dimensional electrically controlled non-uniform transmission photon PDLC structures. Russian Physics Journal. 2011;**54**:172-179. DOI: 10.1007/s11182-011-9595-2

[12] Semkin A, Sharangovich S. Diffraction characteristics of the PDLC photonic structures under the influence of alternating electric fields. Bulletin of Russian Academy of Sciences: Physics. 2013;**77**:1416-1419. DOI: 10.3103/S1062873813120125

[13] Semkin A, Sharangovich S. The analytical model of light beams diffraction on the holographic photonic PDLC structure under the influence of an alternating electric field. Pacific Science Review A. 2013;**15**:118-124

[14] Semkin A, Sharangovich S. The PDLC photonic structures diffraction characteristics managing by the spatially non-uniform electric field. International Conference on Advanced Optoelectronics and Lasers (CAOL), IEEE. 2013:48-49. DOI: 10.1109/CAOL.2013.6657522

[15] Semkin A, Sharangovich S. Analytical model of light beam diffraction on holographic polarization spatially inhomogeneous photonic PDLC structures. Physics Procedia. 2015; **73**:41-48. DOI: 10.1016/j.phpro.2015.09.119

[16] Semkin A, Sharangovich S. Light beam diffraction on inhomogeneous holographic photonic PDLC structures under the influence of spatially non-uniform electric field. Journal of Physics: Conference Series. 2016;**735**:012030. DOI: 10.1088/1742-6596/735/1/012030

[17] Semkin A, Sharangovich S. Highly effective light beam diffraction on holographic PDLC photonic structure, controllable by the spatially inhomogeneous electric field. Physics Procedia. 2017;**86**:160-165. DOI: 10.1016/j.phpro.2017.01.011

[18] Semkin A, Sharangovich S. Theoretical model of controllable waveguide channels system holographic formation in photopolymer-liquid crystalline composition. Physics Procedia. 2017;**86**:181-186. DOI: 10.1016/j.phpro.2017.01.020

Chapter 19

# Application of Numeric Routine for Simulating Transients in Power Line Communication (PLC) Systems

Afonso José do Prado, Luis Henrique Jus,
Melissa de Oliveira Santos, Elmer Mateus Gennaro,
André Alves Ferreira, Thainá Guimarães Pereira,
Aghatta Cioqueta Moreira,
Juliana Semiramis Menzinger,
Caio Vinícius Colozzo Grilo,
Marinez Cargnin Stieler and José Pissolato Filho

Additional information is available at the end of the chapter

http://dx.doi.org/10.5772/intechopen.74753

**Abstract**

Applying numerical routines based on trapezoidal rule of integration (Heun's method for numerical integration), simple models of transmission lines are used to analyze and simulate the propagation of communication signals in PLC-type systems (power line communication systems). Such systems are shared by the same systems for the transfer of electrical power and signal transmission. For the mentioned routines, the main objectives are: simulate the propagation of electromagnetic transients in these systems and analyze the interference of such phenomena in the transmitted signal. Such simulations are performed with classical structures that represent infinitesimal units of transmission lines. Modifications in the structure of such units are analyzed to improve the results obtained by the mentioned simulations.

**Keywords:** waveguide, electromagnetic transient, eigenvalues and eigenfunctions, linear systems, numerical analysis, simulation, state space methods, numerical integration method, transmission line modeling

## 1. Introduction

Systems of conductors for signal transmission or power transmission, that are, in general, classified as waveguide systems, systems of protection, coordination and control of the main system, the waveguide system, are as important as the conductors that are used. For projecting these accessory systems, analysis of short-circuit levels, overvoltages, as well as the duration of transient phenomena are very important [1–9]. In several situations, it is not possible to perform tests related to the occurrence of transient electromagnetic phenomena in actual transmission systems [10]. One situation for this is when the systems are in the design phase and have not yet been built or fabricated. Another situation is where the system cannot be shut down for maintenance or testing, for example, in the case of transmission lines responsible for interconnecting great power plants to great consumer centers. Because the theory and equations related to the propagation of electromagnetic fields in systems of conductors can be related to power and signal transmissions, different transmission systems are modeled as transmission lines or waveguides [1–14]. For example, systems with low voltage, low power and very high frequency for signal transmission and systems with very high voltage, very high power and low frequency can be modeled as transmission lines or waveguides. In analyses of these types of electrical systems affected by electromagnetic transient phenomena, time-domain and frequency-dependent models are considered efficient and accurate for applications in this field [1–16]. Ways to improve these models have been researched yet, searching for increasing the accuracy of the results and the efficiency of the applied methods. For the analysis of the propagation of transient electromagnetic phenomena in electrical networks using transmission line theory, the waveguides can be decomposed into infinitesimal parts modeled by $\pi$ circuits or T circuits [3–11, 17]. Simple numerical routines for this type of analysis can be good tools for undergraduate students to investigate and simulate these types of phenomena [11, 18–20] and to test improvements in the numerical model applied to the mentioned analyses. On the other hand, for more complex numerical or simpler numerical models, to a greater or lesser degree, respectively, numerical routines are influenced by numerical errors [1–23].

Considering the simplified representation of a transmission line by $\pi$ circuit cascades, the solution of this system is obtained with the application of trapezoidal integration, and the results are affected by numerical oscillations or Gibbs' oscillations [1–27]. It is possible to minimize the influence of numerical oscillations or Gibbs' oscillations, in the obtained results, by means of structural modifications of these circuits [11, 17]. The proposed modification initially involves adding damping resistors ($R_D$) in all $\pi$ circuits [11, 17]. These resistors are introduced in parallel with the elements in a series of the $\pi$ circuits (elements representing the longitudinal parameters of transmission lines or waveguides) [28]. However, in spite of decreasing the effects of numerical oscillations considerably, the incorporation of damping resistances in each circuit of the cascade increases the computational time to perform the analyses and simulations of electromagnetic phenomena propagation. So, an alternative structure for the $\pi$ circuit cascade is proposed, which involves the absence of damping resistance in half of all $\pi$ circuits, all of which circuits are grouped in the center of the cascade. In other cases, the different structures of $\pi$ circuits, with and without damping resistance, are applied

alternately in the composition of the cascade used to represent transmission lines or waveguides for analysis and simulations of transient electromagnetic phenomena propagation [29–32]. If the damping resistances are not applied in each π circuit of the cascade that represents the waveguides or the transmission lines, the numerical simulation can be numerically unstable [28–32]. The results of several simulations that will be used to compare and determine which structure is adequate to reduce Gibbs' oscillations without compromising the computational time will be presented. In this case, it is considered cascades with classical π circuits and cascades with damping resistances applied in each π circuit. The results presented for these comparisons are based on output voltage versus time graphs and three-dimensional graphs that establish the relationship between the first voltage peaks with the number of π circuits and the damping resistance values during the first voltage reflection to the end of the line.

## 2. Trapezoidal rule

The trapezoidal rule or Heun's method is a numerical integration method based on the transformation of differential equations into their algebraic equivalents. The integral of a function is approximated by the first-degree function related to the original function (the area of a trapezoid) where the endpoints are approximated by points of intersection between the original and the first-degree functions. By improving approximation accuracy, a large range of independent variable values can be subdivided into equally small portions, called integration steps (**Figure 1**).

Applying the trapezoidal rule, the equation below is obtained:

$$\int_{t(k)}^{t(k+1)} f(t)\,dt \approx \frac{\Delta t}{2}\left[f(t_{k+1}) + f(t_k)\right] \tag{1}$$

The time step is

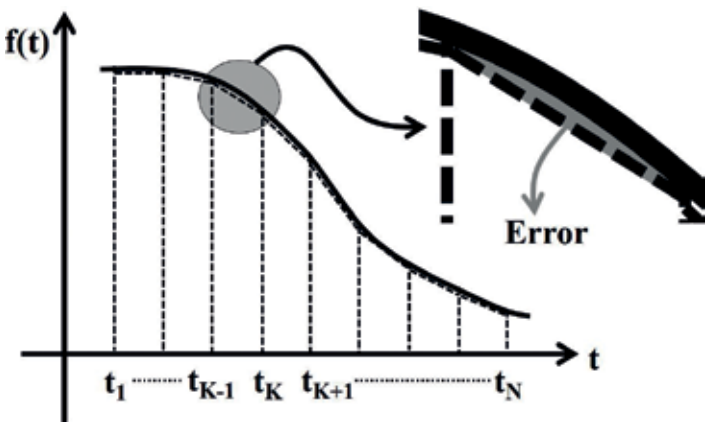


**Figure 1.** Schema of trapezoidal rule for numerical integration.

$$\Delta t = t_{k+1} - t_k \tag{2}$$

Using Eq. (1), Eq. (3) is obtained:

$$\int_{t(k)}^{t(k+1)} f(t)\,dt \approx y_{t+1} - y_t = \Delta y \quad \rightarrow \quad y_{t+1} = y_t + \frac{\Delta t}{2}[f(t_k) + f(t_{k+1})] \tag{3}$$

Considering a model of a physical system (or physical phenomenon), x is a vector composed by state variables of the mentioned system. Also, considering that the physical system is described by the first-order differential linear system, Eq. (4) is obtained:

$$\frac{dx}{dt} = Ax + Bu \quad \rightarrow \quad \dot{x} = Ax + Bu \tag{4}$$

In this case, the $A$ matrix represents the system, the $B$ matrix is related to independent inputs of the system, the $u$ vector is the input vector, and the $x$ vector is the vector of the state variables of the system. For numerical applications, Eq. (5) is considered:

$$\frac{\Delta x}{\Delta t} \approx \frac{dx}{dt}, \quad if \;\; \Delta t \to 0 \tag{5}$$

From Eqs. (3)–(5), for very small time step, Eq. (6) is obtained:

$$x_{t+1} = x_t + \frac{\Delta t}{2}\left[\dot{x}_{t+1} + \dot{x}_t\right] \quad \rightarrow \quad x_{t+1} = x_t + \frac{\Delta t}{2}[Ax_{t+1} + Bu_{t+1} + Ax_t + Bu_t] \tag{6}$$

Simplifying Eq. (6) and considering that $I$ is the identity matrix, Eq. (7) is obtained:

$$\begin{aligned} x_{t+1} &= \left[I - \frac{\Delta t}{2}A\right]^{-1} \cdot \left[I + \frac{\Delta t}{2}A\right]x_t + \left[I - \frac{\Delta t}{2}A\right]^{-1} \cdot \frac{\Delta t}{2}B[u_{t+1} + u_t] \\ x_{t+1} &= A_1A_2x_t + A_1B_1[u_{t+1} + u_t] \end{aligned} \tag{7}$$

In this case, $A_1$, $A_2$, and $B_1$ elements in Eq. (7) are

$$\begin{aligned} y_{t+1} &= \left[I - \frac{\Delta t}{2}A\right]^{-1} \cdot \left[I + \frac{\Delta t}{2}A\right]y_t + \left[I - \frac{\Delta t}{2}A\right]^{-1} \cdot \frac{\Delta t}{2}B[u_{t+1} + u_t] \\ y_{t+1} &= A_1A_2y_t + A_1B_1[u_{t+1} + u_t] \end{aligned} \tag{8}$$

Using Eq. (7), it is possible to determine the next state ($x_{t+1}$) of the analyzed system, if the current state ($x_t$) is known. This characteristic is very important for numerical applications where the functions that describe the physical system are not known or do not exist.

## 3. Transmission line equivalent circuit model

Analyzing the propagation of waves in transmission lines or waveguides, these systems can be decomposed into infinitesimal portions that can be represented by $\pi$ circuits. For representing

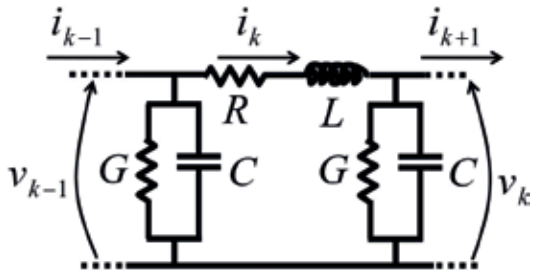


**Figure 2.** The generic unit of π circuits.

the whole system, there is a need to use a cascade with a large number of π circuits. The generic unit of π circuits is shown in **Figure 2**.

Based on the structure of π circuit and Kirchhoff's laws, the relations of voltages and currents for this generic unit are determined by Eq. (9):

$$\frac{di_k}{dt} = \dot{i}_k = \frac{1}{L}(v_{k-1} - R \cdot i_k - v_k) \quad and \quad \frac{dv_k}{dt} = \dot{v}_k = \frac{1}{C}(i_k - G \cdot v_k - i_{k+1}) \tag{9}$$

Each π circuit has two state variables: the transversal voltage ($v_k$) and the longitudinal current ($i_k$). For describing the whole transmission line or the waveguide, it is necessary to use an *n*-order linear numerical system. So, the *x* vector is

$$x = [\, i_1 \quad v_1 \quad i_2 \quad v_2 \quad \cdots \quad i_k \quad v_k \quad \cdots \quad i_n \quad v_n \,]^T \tag{10}$$

In this case, the structure of the *A* matrix is based on Eq. (9):

$$A = \begin{bmatrix} -\frac{R}{L} & -\frac{1}{L} & 0 & \cdots & \cdots & 0 \\ \frac{1}{C} & -\frac{G}{C} & -\frac{1}{C} & \ddots & \ddots & \vdots \\ 0 & \ddots & \ddots & \ddots & \ddots & \vdots \\ \vdots & \ddots & \frac{1}{C} & -\frac{G}{C} & -\frac{1}{C} & 0 \\ \vdots & \ddots & \ddots & \frac{1}{L} & -\frac{R}{L} & -\frac{1}{L} \\ 0 & \cdots & \cdots & 0 & \frac{2}{C} & -\frac{G}{C} \end{bmatrix} \tag{11}$$

Considering only one voltage source in the initial of the transmission line or the waveguide, the *B* vector is in Eq. (12). If other sources are connected to the system in different points, the *B* vector should be adequately changed:

$$B = \begin{bmatrix} \frac{1}{L} & 0 & \cdots & 0 \end{bmatrix}^T \tag{12}$$

If damping resistances are included in π circuits, this is shown in **Figure 3**. The relations of voltages and currents for the generic unit of π circuits are in Eq. (13):

$$\dot{i}_k = \frac{v_{k-1} - R \cdot i_k - v_k}{L} \quad and \quad \dot{v}_k = \frac{i_k - (2G_D + G)\, v_k + G_D(v_{k-1} + v_{k+1}) - i_{k+1}}{C} \tag{13}$$

Based on **Figure 3** and Eq. (12), the structure of the $B$ vector is in Eq. (14). In this case, only one voltage source at the initial of the waveguide is considered:

$$B = \left[ {}^{1}\!/_{L} \quad {}^{G_D}\!/_{C}\, 0 \cdots 0 \right]^T \tag{14}$$

Also, based on **Figure 3** and Eq. (12), the structure of the $A$ matrix is in Eq. (15). In this case, new non-null elements are included because of the application of damping resistances:

$$A = \begin{bmatrix} -\frac{R}{L} & -\frac{1}{L} & 0 & \cdots & \cdots & \cdots & \cdots & 0 \\ \frac{1}{C} & -\frac{(G+2G_D)}{C} & -\frac{1}{C} & \frac{G_D}{C} & \ddots & \ddots & \ddots & \vdots \\ 0 & \ddots & \ddots & \ddots & \ddots & \ddots & \ddots & \vdots \\ \vdots & \ddots & \frac{1}{L} & -\frac{R}{L} & -\frac{1}{L} & \ddots & \ddots & \vdots \\ \vdots & \ddots & \frac{G_D}{C} & \frac{1}{C} & -\frac{(G+2G_D)}{C} & -\frac{1}{C} & \frac{G_D}{C} & \vdots \\ \vdots & \ddots & \ddots & \ddots & \ddots & \ddots & \ddots & 0 \\ \vdots & \ddots & \ddots & \ddots & \ddots & \frac{1}{L} & -\frac{R}{L} & -\frac{1}{L} \\ 0 & \cdots & \cdots & \cdots & 0 & \frac{G_D}{C} & \frac{2}{C} & -\frac{(G+2G_D)}{C} \end{bmatrix} \tag{15}$$

The damping resistance is determined by

$$R_D = k_D \frac{2L}{\Delta t}, \quad G_D = \frac{1}{R_D}, \quad k_D = \frac{R_D \Delta t}{2L} = \frac{\Delta t}{2LG_D} \tag{16}$$

The $R$, $L$, $G$, and $C$ values are calculated by Eq. (17) where d is the line length and $n$ is the number of $\pi$ circuits:

$$R = R' \cdot \frac{d}{n}, \qquad L = L' \cdot \frac{d}{n}, \qquad G = G' \cdot \frac{d}{n}, \qquad C = C' \cdot \frac{d}{n} \tag{17}$$

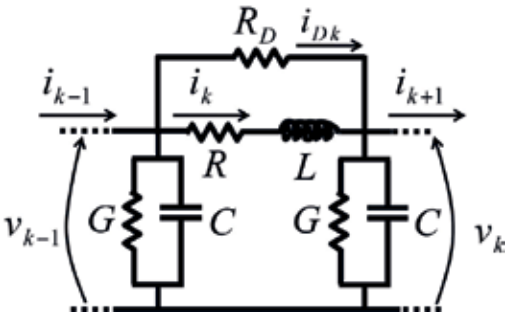


**Figure 3.** Introduction of damping resistances in $\pi$ circuits.

http://dx.doi.org/10.5772/intechopen.74753

## 4. Numerical computation

In **Figure 4**, the flowchart applied to obtain the results of electromagnetic transient phenomena simulations without the introduction of damping resistances is shown.

In case of **Figure 4**, the flowchart is based on Eq. (6) to Eq. (12). The simulations are carried out considering that the analyzed waveguide or the transmission line is connected to an independent step voltage source of 1 pu. The end line is opened, and, because of this, the value of the propagated voltage wave is doubled compared to the voltage value at the initial line. Using the flowchart of **Figure 4**, the parameter values applied to the obtained results are $R'$ = 0.03 Ω/km, $L'$ = 1.2 mH/km, $G'$ = 0.5 μS/km, $C'$ = 10 nF/km, $\Delta t$ = 50 ns, and $d$ = 5 km.

In **Figure 5**, the flowchart related to the inclusion of damping resistances in the π circuits for representing the analyzed waveguide or the transmission line is shown. The values of $R'$, $L'$,

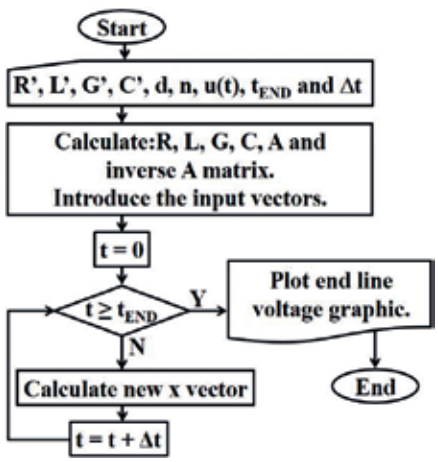


**Figure 4.** Flowchart for numerical simulations without application of damping resistances.

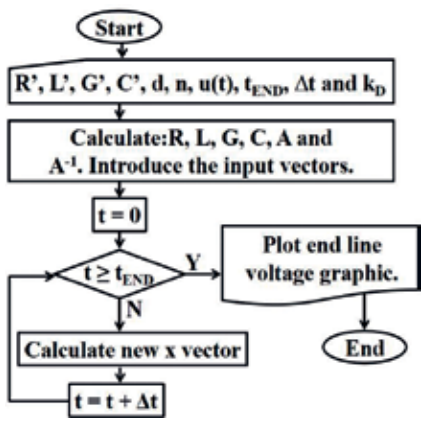


**Figure 5.** Flowchart for numerical simulations with applications of damping resistances.

$G'$, $C'$, $\Delta t$, and $n$ are the same that were used to simulations without damping resistances. The analyzed system is also connected to the 1 pu step voltage, and the end line is also opened.

## 5. Effects of the simulation accuracy without damping resistance

Applying the flowchart of **Figure 4**, the main obtained results are shown in **Figure 6**. For these results, the time step ($\Delta t$) is 50 ns, and the number of π circuits is changed from 50 to 500 with step variation of 1 unit. In general, when the voltage waves are reflected the first time at the end line, the voltage values reach 2.5 pu, initially. This initial value is due to the influence of numerical oscillations or Gibbs' oscillations. These oscillations cause numerical errors of 25% because, in this case, the exact values should be 2 pu. While the reflected voltage wave is propagated to the line initial, after new reflection at the initial line, Gibbs' oscillations are being damped. In case of the second voltage wave reflection at the end line, the voltage values should be null ones. In this instant time, there are numerical problems again that are also represented by Gibbs' oscillations. So, the results obtained from numerical routine based on the flowchart without the application of damping resistances are highly influenced by numerical oscillations during abrupt changes at voltage related to the energization of the transmission line or the waveguide. For the systems modeled by the transmission line theory concepts, the step voltage source represents the main problems that introduce abrupt changes in voltages in the line.

The numerical routine described by the flowchart is simple. Despite this characteristic, the numerical simulations lead to results with errors of 25% independently that the number of π circuits is applied. The increase of the number of π circuits is not related to a correspondent decrease of the numerical errors and numerical oscillations in the obtained results. A proposed alternative is the introduction of damping resistances for decreasing numerical errors and Gibbs' oscillations in the obtained results. Next, both items show the results obtained with this alternative.

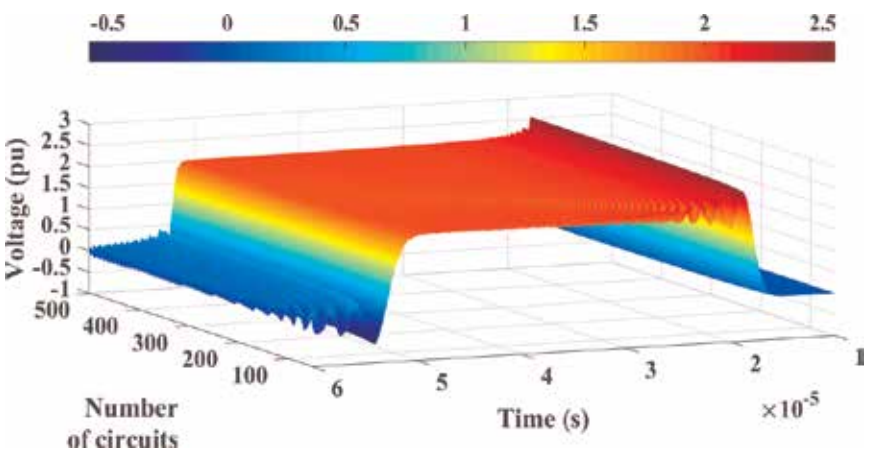


**Figure 6.** The step voltage wave propagation varying the number of circuits for the first reflection at the analyzed end line without the application of damping resistances.

http://dx.doi.org/10.5772/intechopen.74753

## 6. Improvement of the simulation accuracy with damping resistance

Applying damping resistances and using the $k_D$ factor as 2.5, the obtained results are shown in **Figure 7**. Comparing **Figure 7** to **Figure 6**, if the number of π circuits is increased, numerical oscillations or Gibbs' oscillations are decreased. So, considering a constant value for the $k_D$ factor, if an adequate number of π circuits is applied, numerical oscillations can be minimized. Similar results can be obtained changing the value of the $k_D$ factor. In this case, in **Figure 8**, the results are obtained using 200 π circuits for different values of the $k_D$ factor. Based on these results, the numerical oscillations are decreased if the factor is decreased. Because in this chapter the $k_D$ is the integer, the lower value of $k_D$ is 1, and the best reductions of numerical

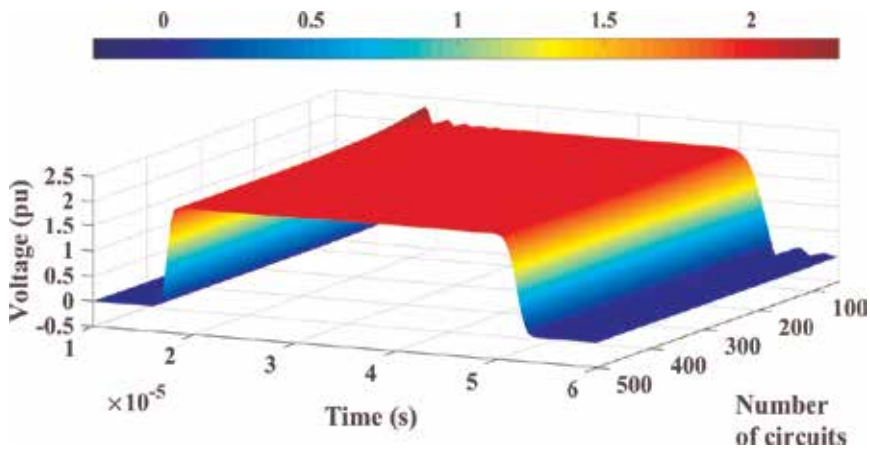


**Figure 7.** The step voltage wave propagation varying the number of circuits for the first reflection at the analyzed end line with the application of damping resistances and $k_D = 2.5$.

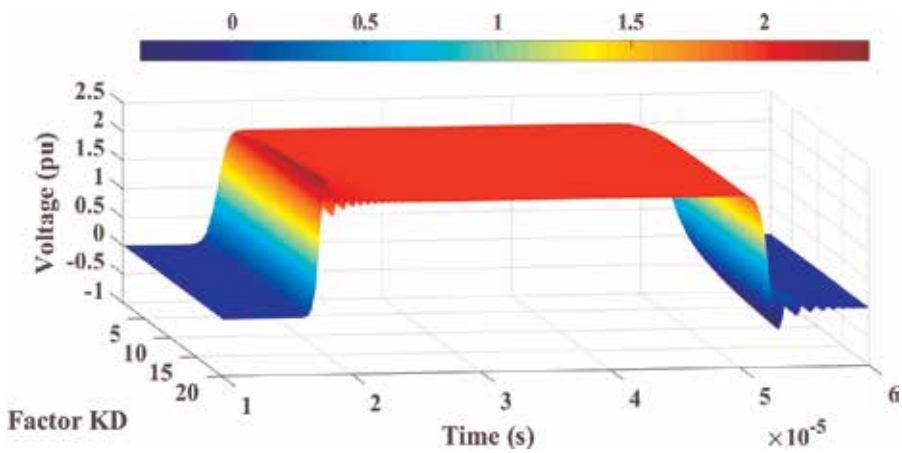


**Figure 8.** The step voltage wave propagation varying the factor $k_D$ for the first reflection at the analyzed end line with the application of damping resistances and $n = 200$.

oscillations are obtained for this value. Based on **Figures 7** and **8**, there are two parameters that can minimize numerical oscillations: the number of π circuits and the value of the $k_D$ factor.

## 7. Effects of $k_D$ factor variation

Applying damping resistances, from **Figures 9–15**, the number of π circuits is changed from 50 to 500 for different values of the $k_D$ factor. In **Figure 9**, the results are related to $k_D = 1$. For this value of the $k_D$ factor, the numerical oscillations are highly minimized. Low numerical oscillations are observed for the number of π circuits about 50. In **Figure 10**, with $k_D = 2.5$, the numerical oscillations reach higher values than the results shown in **Figure 9**, and they are related to a range from 50 to about 100 that is bigger than the range observed in **Figure 9**. In

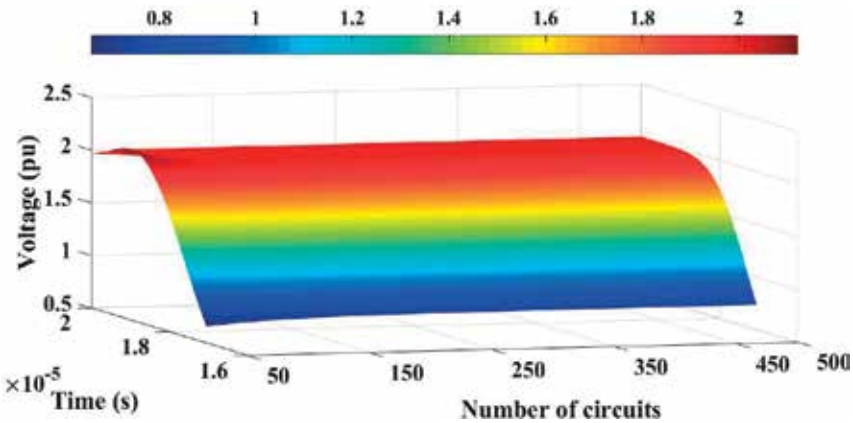


**Figure 9.** Results for different quantities of π circuits and $k_D = 1$.

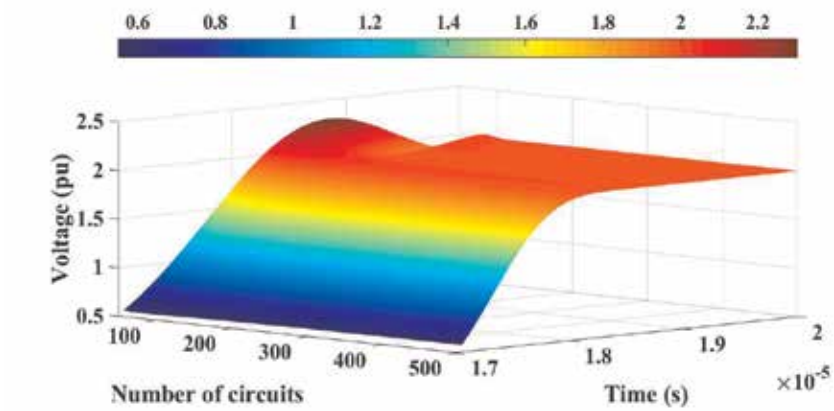


**Figure 10.** Results for different quantities of π circuits and $k_D = 2.5$.

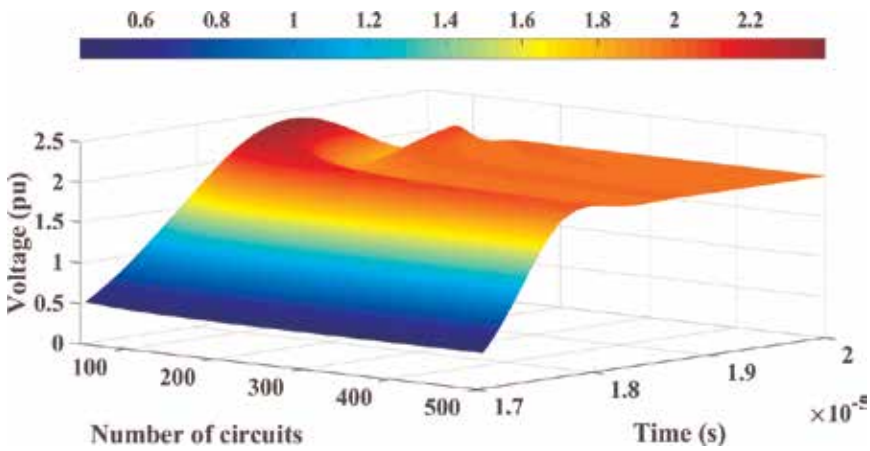


**Figure 11.** Results for different quantities of π circuits and $k_D = 5$.

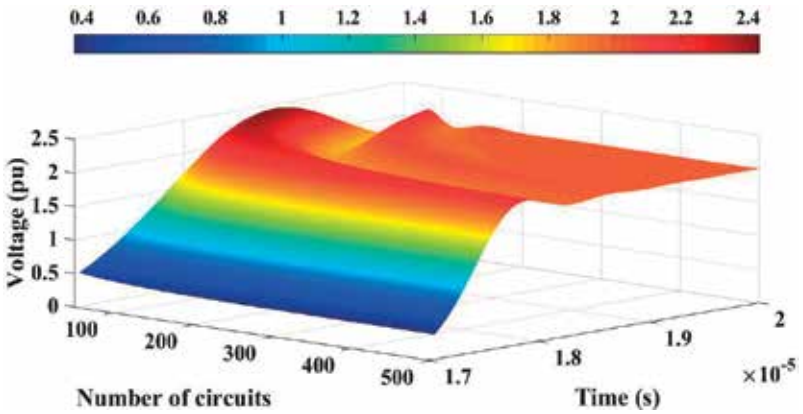


**Figure 12.** Results for different quantities of π circuits and $k_D = 7.5$.

**Figure 10**, the second overvoltage peak that is lower than the first overvoltage peak is also observed. Both overvoltage peaks are caused by numerical oscillations. Compared to **Figure 9**, in **Figure 10**, for the same time interval, the number of overvoltage peaks is increased showing that the damping of numerical oscillations is not effective as well as when the $k_D$ factor is equal to 1. Based on Eq. (16), the $k_D$ factor is related to the time step ($\Delta t$), and the value of this factor is also related to the frequency of the oscillations that are significantly reduced by the application of damping resistances. So, increasing the value of the $k_D$ factor, not all numerical oscillations are damped. Because of this, the overvoltage peaks are increased, and other lower overvoltage peaks arise.

Increasing the value of the $k_D$ factor, the influence of damping resistances is decreased. So, the voltage peaks caused by Gibbs' oscillations are increased, if the $k_D$ factor is increased. This

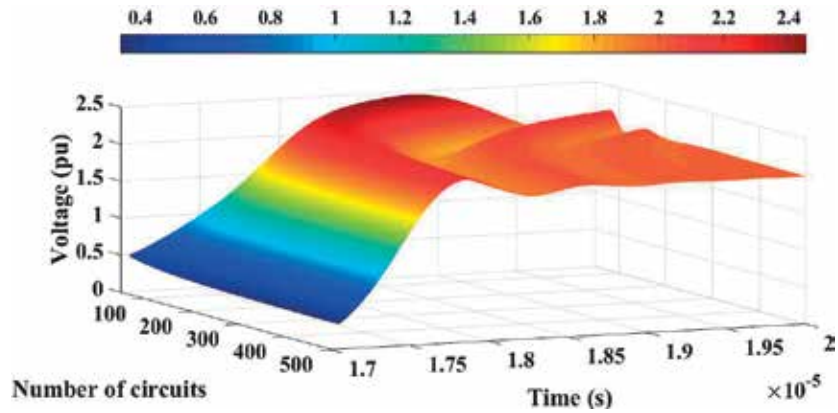


**Figure 13.** Results for different quantities of π circuits and $k_D$ = 10.

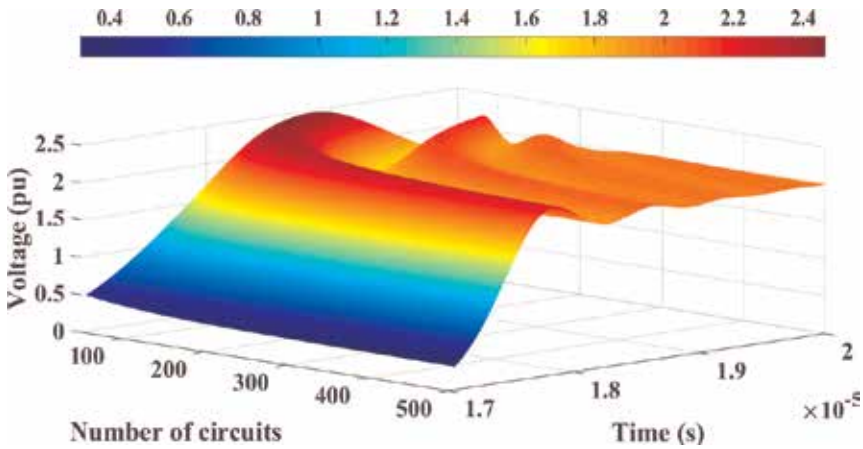


**Figure 14.** Results for different quantities of π circuits and $k_D$ = 12.5.

effect is observed in **Figures 11–15**. The highest voltage peak for each value of the $k_D$ factor is about 2.5 pu. Another consequence is that the second voltage peak is increased, while the $k_D$ factor is decreased. The influence of damping resistances for minimizing the numerical oscillations in proposed transmission line model is more effective for small values for the $k_D$ factor, considering the lower limit as 1.

Analyzing the results from **Figures 9–15**, the highest voltage peak for each value of the $k_D$ factor is related to the lowest number of π circuits. Increasing the number of π circuits for the same $k_D$ factor value, the voltage peak values can be decreased. Changing adequately the $k_D$ factor and the number of π circuits, Gibbs' oscillations can be minimized. The sets of $k_D$ values and the numbers of π circuits that minimize the numerical oscillations can be determined by analyzing the first voltage peaks of a great number of simulations.

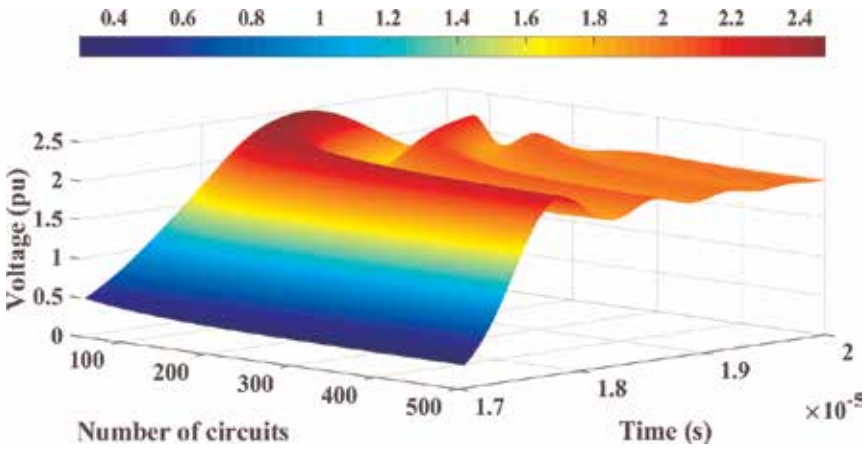


**Figure 15.** Results for different quantities of π circuits and $k_D$ = 15.

## 8. Number of π circuit variation

Setting the number of π circuits, the results are analyzed considering the $k_D$ changing from 1 to 10. Applying 50 units of π circuits, the voltage peaks are not damped significantly if the $k_D$ is changed. It is observed in **Figure 16**. For 100 units of π circuits, the voltage peaks are damped for values of the $k_D$ factor from 1 to about 3 (**Figure 17**).

Considering 150 units of π circuits, the range of the $k_D$ factor that the voltage peaks are damped is bigger than the previous results. It is shown in **Figure 18**. In this case, this $k_D$ factor range is from 1 to about 4. For 200 units of π circuits, the higher limit of the mentioned range is increased to about 5 (**Figure 19**). If 250 units of π circuits are applied, the range is further increased and the higher limit is about 6 (**Figure 20**). Similar relations are observed in

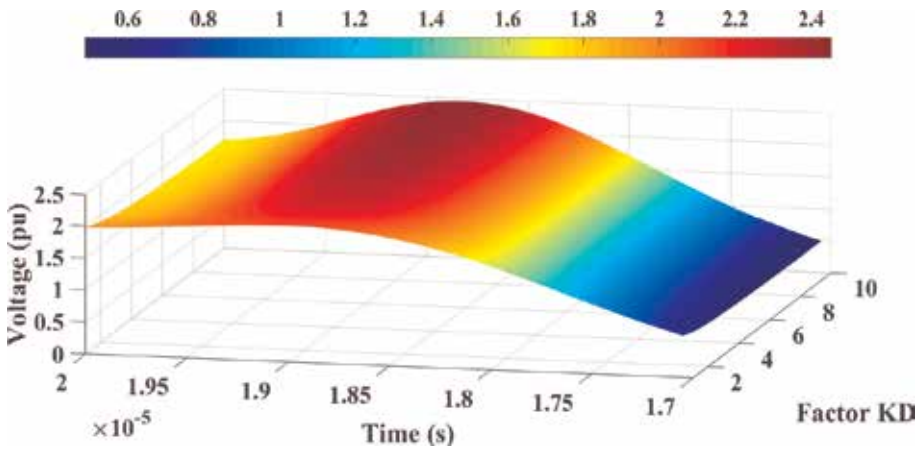


**Figure 16.** Results for different values of the $k_D$ factor and $n$ = 50.

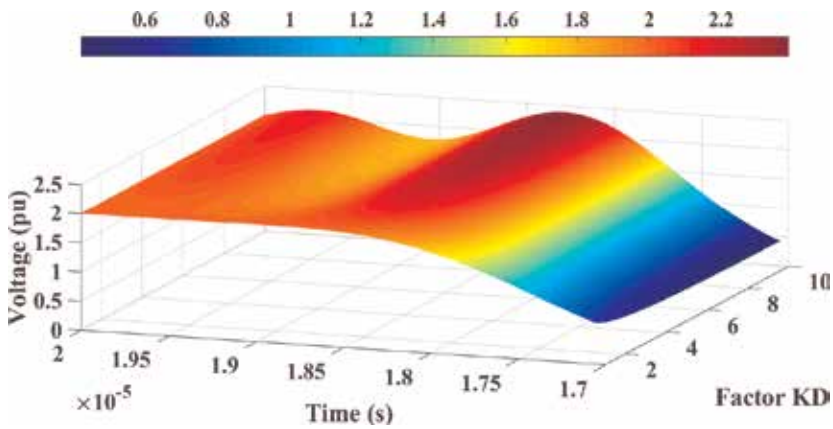


**Figure 17.** Results for different values of the $k_D$ factor and $n$ = 100.

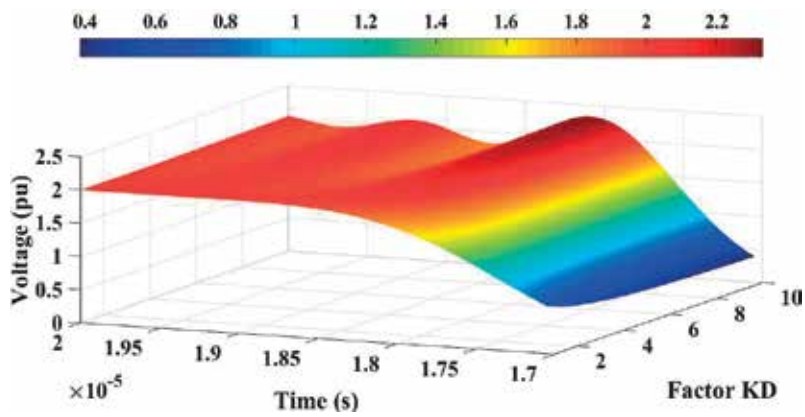


**Figure 18.** Results for different values of the $k_D$ factor and $n$ = 150.

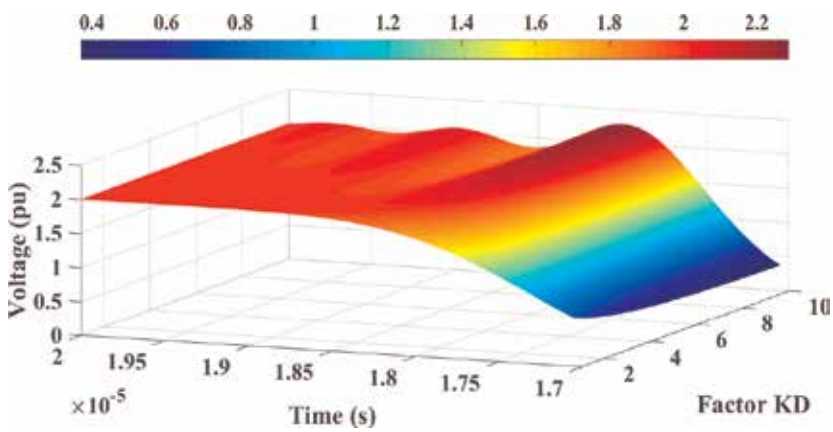


**Figure 19.** Results for different values of the $k_D$ factor and $n$ = 200.

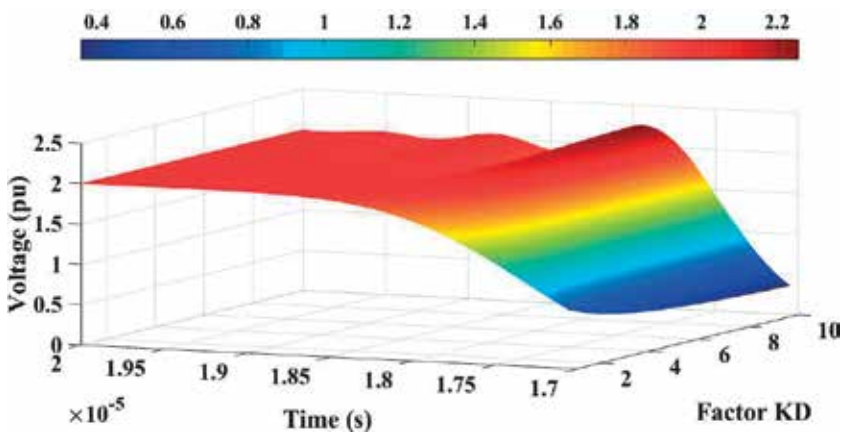


**Figure 20.** Results for different values of the $k_D$ factor and $n$ = 250.

**Figures 21–23**. If the quantity of π circuits is increased, the range of the $k_D$ factor that is related to the minimization of Gibbs' oscillations is increased. In this case, the increase of this quantity is directly related to the increase of the simulation time.

Still analyzing **Figures 21–23**, it is observed that the relation between the number of the π circuits and the influence of the $k_D$ factor in minimizing the voltage peaks is not linear. There is a saturation point where the increase of the number of π circuits can no longer minimize significant Gibbs' oscillations and, consequently, the voltage peaks in obtained simulations. Because of this, another type of analysis is shown in **Figure 24**. In this case, the voltage peaks are related to the correspondent values of the $k_D$ factor and the number of π circuits. In case of **Figure 24**, the results are obtained to a time step ($\Delta t$) of 50 ns. A region where the numerical oscillations are critically damped and there are no voltage peaks can be observed. In this case, the voltage value is 2 pu and corresponds to the exact values that can be obtained using a numerical routine of Laplace's transformation. So, a specific type of analysis is related to the

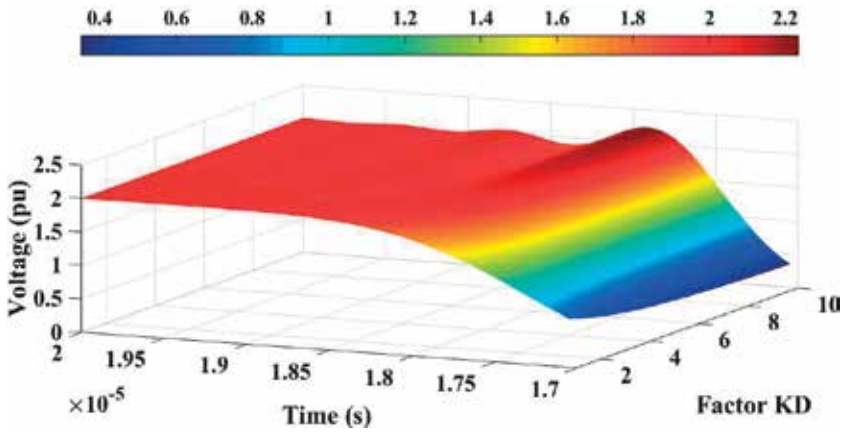


**Figure 21.** Results for different values of the $k_D$ factor and $n$ = 300.

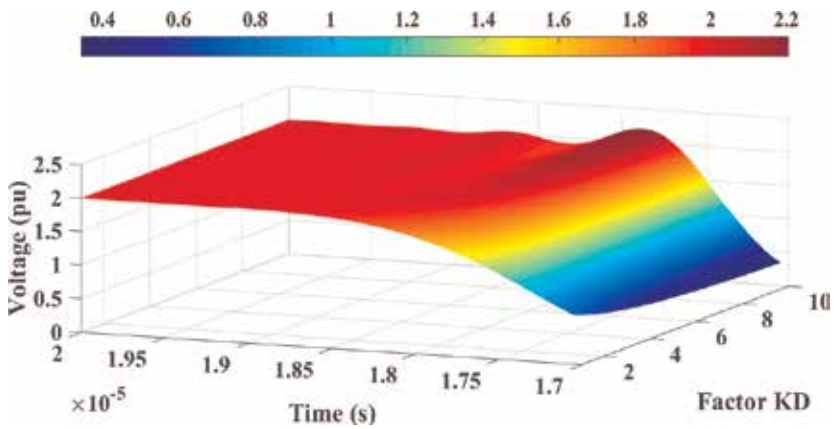


**Figure 22.** Results for different values of the $k_D$ factor and $n$ = 400.

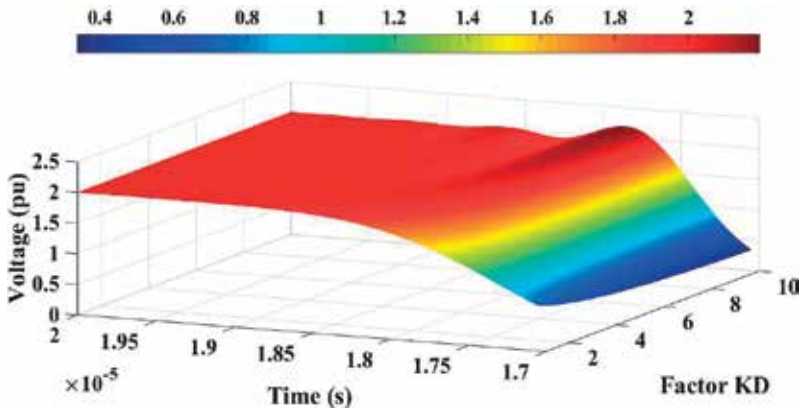


**Figure 23.** Results for different values of the $k_D$ factor and $n$ = 500.

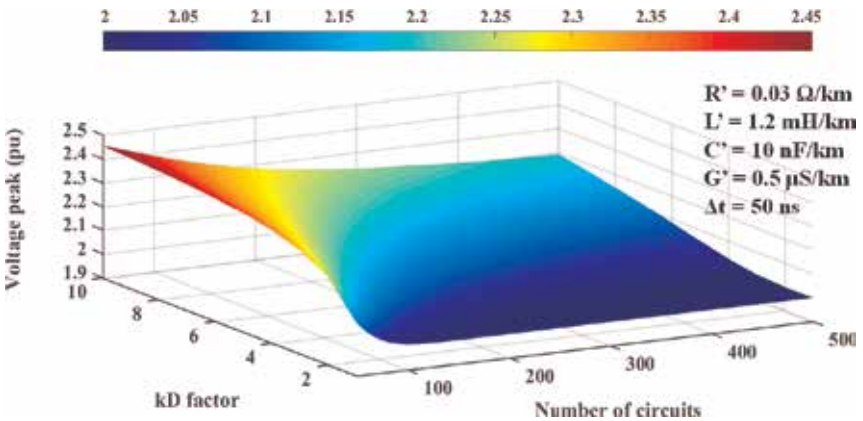


**Figure 24.** Voltage peaks related to the $k_D$ factor and the number of π circuits for $\Delta t$ = 50 ns.

application of three-dimensional graphics showing the influence of the $k_D$ factor values and the number of π circuits on the voltage peaks obtained during the numerical simulations. It is shown in the next section.

## 9. Other analyses

Based on the results shown in the previous sections, it is concluded that the numerical oscillations and, consequently, the voltage peaks obtained by the proposed model are influenced jointly by two factors: the damping resistance value and the number of π circuits applied to the numerical simulations of electromagnetic phenomena in waveguides or transmission lines. Because of this, the analyses of this joint influence must be based on three-dimensional graphics. In **Figure 24**, the highest voltage peaks during the first wave reflection on the transmission end line or the receiving end terminal of the waveguide are shown. These peaks depend on the $k_D$ factor and the number of π circuits considering the time step as 50 ns. In **Figures 25** and **26**, the time steps are 10 ns and 200 ns, respectively. These graphics are used for completing the analyses carried out in the previous sections.

Based on the last three sets of obtained results of this chapter (**Figures 24**–**26**), for a specific time step, there are sets of the number of π circuits and the $k_D$ factor values adequate for minimizing Gibbs' oscillations and, consequently, the voltage peaks in simulations of electromagnetic transient phenomena in transmission lines using the numerical routine proposed in this chapter. The time step choice or determination is related to the fundamental frequency of the simulated phenomena. This choice or determination can be related to the type of the analyzed circuit. For example, transmission lines for power systems or waveguides for data transmission can be mentioned.

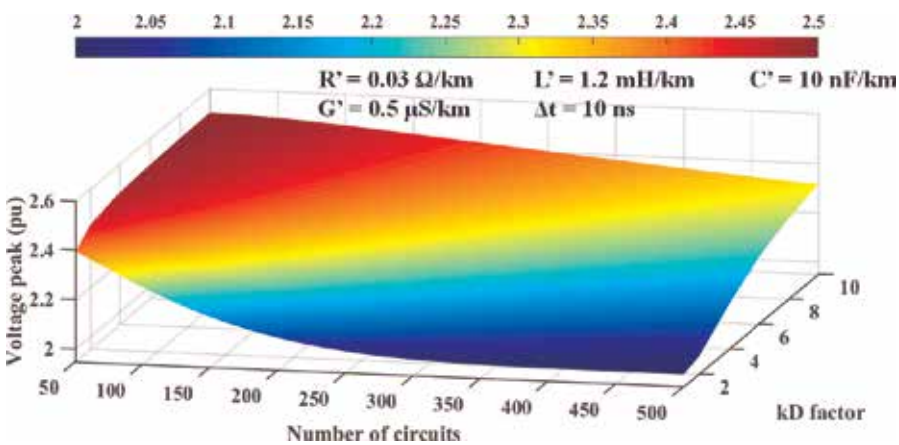


**Figure 25.** Voltage peaks related to the $k_D$ factor and the number of π circuits for $\Delta t$ = 10 ns.

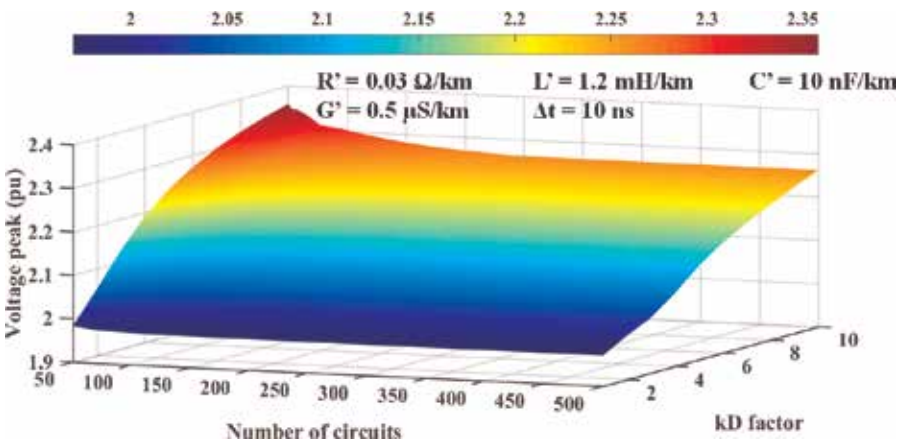


**Figure 26.** Voltage peaks related to the $k_D$ factor and the number of $\pi$ circuits for $\Delta t$ = 200 ns.

## 10. Conclusions

Modifications on the classical structure of $\pi$ circuits for modeling transmission lines are presented. These modified $\pi$ circuits are applied to obtain a cascade that represents the analyzed transmission lines. Based on the electromagnetic basic concepts, very long circuits for power transmission and circuits for data transmission can be analyzed using the theoretical bases of the transmission lines. So, a numerical routine for simulating electromagnetic transient phenomena in waveguides (transmission lines for power systems or data transmission) is obtained.

In the proposed numerical routine, damping resistances for minimizing Gibbs' oscillations or numerical oscillations are included. These oscillations are caused by the numerical integration method applied to the solution of the linear system that describes the waveguide. Applying this proposed numerical routine, several results of simulations varying the number of $\pi$ circuits, the $k_D$ factor, and the time step are obtained. These results are concentrated on three-dimensional graphics where the joint influence is shown.

Based on the obtained results, it is observed that there are ranges of the model parameters adequate for the minimization of numerical oscillations that influence these results. The main model parameters that influence the minimization of numerical oscillations are the number of $\pi$ circuits and the $k_D$ factor. The $k_D$ factor is applied to calculate the value of damping resistances included in each $\pi$ circuit of the mentioned cascade.

## Acknowledgements

The authors would like to thank the financial support by FAPESP (The São Paulo Research Foundation). The following processes are related to the results shown in this chapter: 2015/21390-7, 2015/20590-2, 2015/20684-7, 2016/02559-3, 2017/05988-5, 2017/05995-1, and 2017/23430-1.

## Author details

Afonso José do Prado[1]*, Luis Henrique Jus[1], Melissa de Oliveira Santos[1], Elmer Mateus Gennaro[1], André Alves Ferreira[1], Thainá Guimarães Pereira[1], Aghatta Cioqueta Moreira[1], Juliana Semiramis Menzinger[1], Caio Vinícius Colozzo Grilo[1], Marinez Cargnin Stieler[2] and José Pissolato Filho[3]

*Address all correspondence to: afonsojp@uol.com.br

1 Campus of São João da Boa Vista, São Paulo State University (UNESP), São João da Boa Vista, São Paulo State, Brazil

2 Campus of Tangará da Serra, The University of Mato Grosso State (UNEMAT), Tangará da Serra, Mato Grosso State, Brazil

3 The University of Campinas (UNICAMP), Campinas, São Paulo State, Brazil

## References

[1] Macías JAR, Expósito AG, Soler AB. A comparison of techniques for state-space transient analysis of transmission lines. IEEE Transactions on Power Delivery. April, 2005;**20**(2): 894-903

[2] Macías JAR, Expósito AG, Soler AB. Correction to "a comparison of techniques for state-space transient analysis of transmission lines". IEEE Transactions on Power Delivery. July, 2005;**20**(3):2358

[3] Nelms RM, Newton SR, Sheble GB, Grigsby LL. Simulation of transmission line transients using a personal computer. IEEE Conference Record of the 1988 Eighteenth Power Modulator Symposium. 20–22 June 1998, Hilton Head, South Carolina, USA. pp. 229-232

[4] Nelms RM, Sheble GB, Newton SR, Grigsby LL. Using a personal computer to teach power system transients. IEEE Transactions on Power Systems. August, 1989;**4**(3):1293-1294

[5] Mamis MS, Koksal M. Transient analysis of nonuniform lossy transmission lines with frequency dependent parameters. Electric Power Systems Research. December, 1999;**52**(3): 223-228

[6] Mamis MS. Computation of electromagnetic transients on transmission lines with nonlinear components. IEEE Proceeding of Generation, Transmission and Distribution. March, 2003; **150**(2):200-204

[7] Mamis MS¸ Koksal M, Solution of eigenproblems for state-space transient analysis of transmission lines. Electric Power Systems Research. July, 2000;**55**(1):7-14

[8] Mamis MS¸ Meral ME. State-space modeling and analysis of fault arcs. Electric Power Systems Research. September, 2005;**76**(1–3):46-51

[9] Dommel HW. Electromagnetic Transients Program - Rule Book. Oregon; 1984

[10] Dommel HW. EMTP Theory Book. 2ª edition. Vancouver; April 1996

[11] Prado AJ, Lessa LS, Monzani RF, Bovolato LF, Pissolato Filho J. Modified routine for decreasing numeric oscillations at associations of lumped elements. Electric Power Systems Research. July 2014;**112**(1):56-64

[12] Brandão Faria JA. Overhead three-phase transmission lines – Non diagonalizable situations. IEEE Transactions on Power Delivery. October 1988;**3**(4)

[13] Brandão Faria JA, Briceño Mendez J. Modal analysis of untransposed bilateral three-phase lines - a perturbation approach. IEEE Transactions on Power Delivery. January 1997;**12**(1)

[14] Brandão Faria JA, Briceño Mendez J. On the modal analysis of asymmetrical three-phase transmission lines using standard transformation matrices. IEEE Transactions on Power Delivery. October 1997;**12**(4)

[15] Morched A, Gustavsen B, Tartibi M. A universal model for accurate calculation of electromagnetic transients on overhead lines and underground cables. IEEE Transactions on Power Delivery. July 1999;**14**(3):1032-1038

[16] Gustavsen B, Semlyen A. Combined phase and modal domain calculation of transmission line transients based on vector fitting. IEEE Transactions on Power Delivery. April 1998;**13**(2)

[17] Chrysochos AI, Tsolaridis GP, Papadopoulos TA, Papagiannis GK. Damping of oscillations related to lumped-parameter transmission line modeling. In: Conf. on Power Systems Transients (IPST 2015). 7. pp. 2015

[18] Monzani RC, Prado AJ, Kurokawa S, Bovolato LF, Pissolato Filho J. Using a low complexity numeric routine for solving electromagnetic transient simulations. (DOI 10.5772/48507) in Matlab - a fundamental tool for scientific computing and engineering applications. Rijeka, Croatia: InTech - Open Access Publisher. 2012, pp. 463-484

[19] Lessa LS, Prado AJ, Kurokawa S, Bovolato LF, Pissolato Filho J. The MatLab Software Application for Electrical Engineering Simulations and Power System Analyses (DOI 10.5772/48555) in Matlab - a fundamental tool for scientific computing and engineering applications. Rijeka, Croatia: InTech - Open Access Publisher. 2012. pp. 433-462

[20] Prikler L, Hoidalen HK. ATPDraw Version 3.5 – Users' Manual. Trondheim, Norway; August 2002

[21] Galvão RKH, Hadjiloucas S, Kienitz KH, Paiva HM, Afonso RJM. Fractional order modeling of large three-dimensional RC networks. IEEE Transactions on Circuits and Systems – I: Regular Papers. March, 2013;**60**(3):624-637

[22] Gustavsen B. Avoiding numerical instabilities in the universal line model by a two-segment interpolation scheme. IEEE Transactions on Power Delivery. July, 2013;**28**(3):1643-1651

[23] Moreno P, Ramirez A. Implementation of the numerical Laplace transform: A review. IEEE Transactions on Power Delivery. October, 2008;**23**(4):2599-2609

[24] Nguyen TT, Chan HY. Evaluation of modal transformation matrices for overhead transmission lines and underground cables by optimization method. IEEE Transactions on Power Delivery. January, 2002;**17**(1):200-209

[25] Marti JR. Accurate modelling of frequency-dependent transmission lines in electromagnetic transients simulations. IEEE Transactions on PAS. January 1982;**101**:147-155

[26] Martí JR, Lin J. Suppression of numerical oscillations in the EMTP. IEEE Transactions on Power Systems. May 1989;**4**(2)

[27] Lin J, Martí JR. Implementation of the CDA procedure in the EMTP. IEEE Transactions on Power Systems. May 1990;**5**(2)

[28] Prado AJ, Bespalhuk KJ, Silva BF, Conceição KO, Cargnin-Stieler M, Gennaro EM, Pissolato Filho J. Influences of damping resistances on transient simulations in transmission lines. Progress in Electromagnetics Research B. 2017;**75**:27-39

[29] Santos MO, Jus LH, Prado AJ, Gennaro EM, Pissolato Filho J. Influence of damping resistance in electromagnetic transients using alternate structures of circuits. Progress in Electromagnetics Research Symposium - PIERS 2017. 22–25 May 2017, St. Petersburg Russia

[30] Prado AJ, Lessa LS, Assunção E, Teixeira MCM, Monzani RC, Pissolato Filho J. Laplace's analyses for application of p circuits" associations in digital simulations. Progress in Electromagnetic Research Symposium - PIERS 2016, 8–11 August 2016, Shanghai, China

[31] Prado AJ, Conceição KO, Bespalhulk KJ, Silva BF, Gennaro EM, Cargnin-Stieler M, Pissolato Filho J. Minimization of Gibb's oscillations in transients" simulations using damping resistance. Progress in Electromagnetic Research Symposium - PIERS 2016, 8–11 August 2016, Shanghai, China

[32] Jus LH, Moreira AC, Oliveira MO, Pereira TG, Prado AJ, Gennaro EM, Pissolato Filho J. Transmission lines model with different basic structures applied to transient electromagnetic simulations. The 6th IASTED International Conference on Modelling, Simulation and Identification - MSI 2016, v. 1, pp. 118–122, 16–18 August 2016, Campinas, Brazil

*Edited by Kok Yeow You*

Recently, the rapid development of radiofrequency (RF)/microwave and photonic/optical waveguide technologies has had a significant impact on the current electronic industrial, medical and information and communication technology (ICT) fields. This book is a self-contained collection of valuable scholarly papers related to waveguide design, modeling, and applications. This book contains 20 chapters that cover three main subtopics of waveguide technologies, namely RF and microwave waveguide, photonic and optical waveguide and waveguide analytical solutions. Hence, this book is particularly useful to the academics, scientists, practicing researchers and postgraduate students whose work relates to the latest waveguide technologies.

Published in London, UK


IntechOpen

ISBN 978-1-83881-516-5